

Hubless Wheel Design and Calculations

Said Bera ÇİVİ^{1*}, Veysel TÜRKEL²

¹Osen Mobilya Aksesuarları Ltd. Şti, Esenyurt, İstanbul

²İstanbul Teknik Üniversitesi, ARDES, Maslak, Sarıyer, İstanbul

Sait Bera ÇİVİ ORCID No: 0000-0002-1040-8689

Veysel TÜRKEL ORCID No: 0000-0003-4174-1406

*Corresponding author: turkelv@itu.edu.tr

(Received: 18.07.2023, Accepted: 8.10.2023, Online Publication: 28.12.2023)

Keywords

Helicar gear,
Stabilization,
Mechanical
design

Abstract: In this study, Helical gear design, analysis and calculations, chain gear system design and calculations, lubrication system, brake disc, caliper, original stabilization part and system, transmission shaft design, calculations and analysis, wedge calculations analysis and design, bearing, ring selection and necessary information about dimensioning of the system, mechanical design, system components and methods are presented. The advantages and disadvantages of the system compared to conventional wheels have been reviewed and a cost analysis has been made. Since the system has a disadvantageous efficiency compared to traditional wheels, it has been tried to increase the efficiency and life of the current design and to create a usage area in the market.

Göbeksiz Tekerlek Tasarımı ve Hesaplamaları

1

Anahtar Kelimeler

Helisel dişli,
Stabilizasyon,
Mekanik
dizayn

Öz: Bu çalışmada, Helisel dişli, zincir dişli sistemi, yağlama sistemi, fren diski, kaliper, özgün stabilizasyon parçası ve sistemi, aktarma mili tasarımı, kama hesapları, analizleri ve tasarımları yanı sıra rulman, segman seçimi ve sistemin boyutlandırılması, mekanik dizaynı, sistem bileşenleri ve yöntemleri hakkında gerekli bilgiler verilmiştir. Sistemin geleneksel tekerleklere kıyasla avantaj ve dezavantajları gözden geçirilmiş ve maliyet analizi yapılmıştır. Bu analiz sonucunda sistem geleneksel tekerleklere göre dezavantajlı verime sahip olması sebebiyle güncel tasarımın verimi ve ömrü arttırılmaya çalışılarak piyasa içerisinde bir kullanım alanı oluşturmak amaçlanmıştır.

1. INTRODUCTION

A hubless wheel refers to wheel designs that do not have a rotating hub at the center of the wheel. The advantages of using such a wheel include reducing the rotating inertia of the wheel and creating an empty space by eliminating the spoke wires and weights inside the hub used in motorcycle rims [1]. Additionally, this design is much more appealing compared to traditional wheel designs. This design was initially invented by Franco Sbarro [2,3], the founder of Sbarro automobiles, in 1989, and during that time, it gained recognition for its striking appearance. However, hubless wheels, compared to traditional wheels, come with disadvantages such as the complexity of manufacturing, more components involved, increased calculation requirements, and higher costs. These factors pose obstacles to their alternative and widespread use and development. The existing

drivetrain system found in current cars is problematic because the options for transferring power in traditional systems are limited to belt pulleys or chain gears, which do not allow the use of axles and constant velocity joints [4-6]. In addition, in the 2010 film *Tron: Legacy*, scenes featuring hubless wheeled motorcycles were showcased with the inclusion of light animations, which brought the concept of hubless wheels back into the spotlight within the automotive industry. The company responsible for the motorcycle design in the film, Hammacher Schlemmer, stated that many people were fascinated by the wheels of the motorcycle and that numerous manufacturing companies sought inspiration from them [7,8]. This film inspired many engineers and companies to start developing new designs. To add a new design element to this unique concept and to treat it as a thesis project, a decision was made to design a hubless wheel.

The aim of this study is to achieve a durable, long-lasting, and original design from mechanical and intricate hubless wheels and, most importantly, to create a new market niche. Among these goals are the entertainment industry, racing tracks, and everyday usage. If successful results are obtained from this project, it will not only lead to high-value production but also create employment opportunities in various regions of our country. Additionally, when increased energy production and the electric vehicle sector come together, it will significantly reduce our unemployment rate. This will demonstrate to the world that we exhibit an innovative approach rather than traditionalism, contributing to our country in many aspects. These contributions include inspiring various industries, including the existing automotive sector. Furthermore, this design highlights the necessity of promoting high-value product manufacturing within Turkey.

2. MATERIAL AND METHOD

There are four important factors to consider in the design of the system, these are:

- Transmission System
- Lubrication System
- Stabilization
- Brake System

2.1. Transmission System

One of the key aspects of the system is how the initial power from the engine will be transferred. Hubless wheel designs require the necessity of working with rotating motion and torque transfer, such as belts, pulleys, or chain gears. Instead of focusing on solving this problem, it was deemed more suitable to adapt the design from cars to motorcycles. The second aspect is how the power obtained from the chain gear will be transmitted to the wheel. Many designers have chosen to transfer the power from the engine to the traditional wheel located at the rear, rather than the hubless wheel. As an alternative to this choice, it is considered beneficial to design a large gear that matches the diameter of the rim and mount the gear directly onto the rim when transferring power with a chain gear.

If it is possible to provide the transmission through a large hubless chain gear, this design approach will significantly reduce the number of parts and costs. With this design, components such as the drive shaft, pinion, internal helical gear, auxiliary bearing, segments, and wedges will no longer be needed. However, the transition from a small gear to a large gear will still result in a significant RPM drop. To overcome this issue, a reducer of the same size or motor power should be planned and designed. However, the standard power of motors available in the market is limited to a maximum of 3000 RPM. Therefore, within the existing transmission system, two helical pinion gears placed on the drive shaft and two internal helical gears connected to the rim are used for power transmission.

2.2. Lubrication Issue

Another problem of hubless wheels is the lubrication issue. The biggest criticism of this system is that, unlike traditional wheels, no matter how much manual lubrication is applied, the system still experiences dry friction. Additionally, due to the presence of more interacting components compared to traditional wheels, friction is significantly increased. Moreover, due to the open nature of the hubless system, the transmission components are more exposed to foreign particles from the outside. The solution method identified for this problem is to ensure sealing only at the points where the transmission occurs. This is referred to as transitioning to a lubrication method while the entire system is closed. Lubrication calculations were performed to address this issue, and a closed lubrication system was deemed necessary for long-term durability.

2.3. Stabilization

Once the general design of the hubless wheel is completed, the following questions arise: How will the wheel be connected to the engine? Will it be able to maintain a stable and smooth movement while also accommodating the chain gear design? What should the design be like? Where should the bearing of the drive shaft be located? Will there be any friction during these processes? These questions need to be addressed. Stabilization is the most crucial component of the system, responsible for keeping the system together and creating a socket for attaching the wheel system to the chassis. In the assembled system, there are bearings in the form of balls that serve as the connection between the rim and the stabilization component. These balls, similar to the gears, are subjected to a closed lubrication system and are designed to be suitable for production and assembly. The axle connection and bearing housing points, which will connect the chassis to the wheel, are also present on the stabilization component.

2.4. Brake System

In previous designs, the braking system was not integrated into the system. This was due to the lack of designed brake discs and calipers that would be suitable for the system. Additionally, the brake system was not separated from the lubrication system. Therefore, it was decided that the use of a closed lubrication system would prevent oil from coming into contact with the brake disc. The brake system in the design is located in the center of the hub. This is made possible by the closed design of the lubrication system and the unique components used in the brake system. When looking at other Hubless Wheel designs, it can be observed that the brake caliper and disc are located either on the right or left, similar to traditional wheels. However, in this new design, moving the brake caliper and disc to the center of the system is crucial to balance the stresses that occur during braking.

3. RESULTS

Taking a general overview of the design, it consists of several key elements: the initial power provided by the electric motor connected to the chassis, the transmission of the driving force to the drive shaft through the chain gear, the rotation of the drive shaft with the help of wedge, bearing, and segment auxiliary materials, and the engagement of two helical pinion gears fixed to the drive shaft. The pinion helical gears start rotating the internally fixed helical gears on the rim at a gear ratio of $i=4.17$. Simultaneously, the brake disc connected to the internal helical gear starts rotating with the system. However, the caliper is fixed to the lubrication chamber to ensure its stability.

Based on the calculations, the required motor power is determined to be 8 kW. The motor output torque is 1456 Nm, and its speed is 1200 rpm. Under these conditions, the analysis has been conducted to calculate the environmental forces and the values of the external forces (Figure 1 and Figure 2).

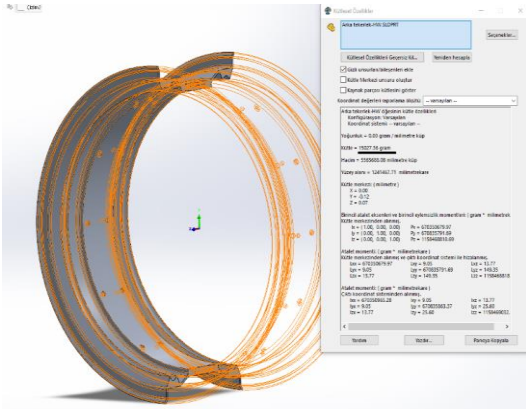


Figure 1. Mass measurement results of hubless rim design

Hubless rim design;

$$\begin{aligned}
 m &= 14,07 \text{ kg} \\
 r_1 &= 260 \text{ mm} \\
 r_2 &= 274,25 \text{ mm} \\
 I_z &= \frac{1}{2} \times m \times (r_1^2 + r_2^2) = \frac{1}{2} \times 14,07 \times \\
 &\quad (260^2 + 274,25^2) \\
 &= 998732 \text{ kgmm}^2 \\
 I_x &= \frac{1}{12} \times m \times (3(r_1^2 \times r_2^2) + h^2) = 1/12 \times 14 \times \\
 &\quad (3 \times (260^2 + 274,5^2) + 257,82^2) \\
 &= 576423,1687 \text{ kgmm}^2 \quad (1)
 \end{aligned}$$

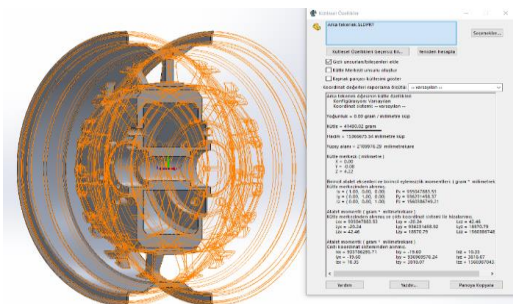


Figure 2. Estimated rim mass measurement with hub motor mounted.

Hub Motor Rim design;

$$\begin{aligned}
 m &= 47,89 \text{ kg} \\
 r &= 280 \text{ mm} \\
 I_z &= m \times \frac{r^2}{2} = 47,89 \times \frac{280^2}{2} \\
 &= 1842400 \text{ kgmm}^2 \\
 I_x &= \frac{m}{12} \times (3 \times r^2 + h^2) = \frac{47,89}{12} \times (3 \times 280^2 + 257^2) \\
 &= 1179891,917 \text{ kgmm}^2
 \end{aligned} \quad (2)$$

According to the results obtained, the hubless wheel, compared to the hubless motorized wheel, has an advantage in terms of the moment of inertia.

3.1. Design Elements

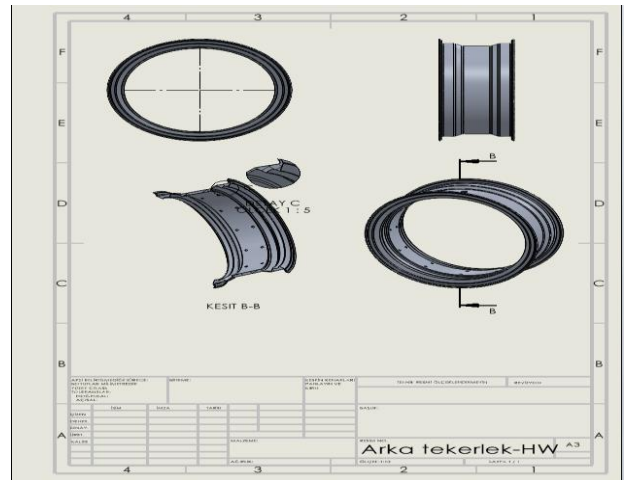


Figure 3. Rim Technical Drawing

Aluminum alloy, specifically Aluminum 1060 Alloy, has been chosen as the material for the wheel rim due to its widespread use in the automotive industry. This alloy consists of approximately 90% aluminum and 10% silicon. It may also contain trace amounts (less than 1%) of titanium, magnesium, and other metals. Aluminum 1060 Alloy is deemed suitable for use as a rim material due to its strength values and lightweight characteristics, as shown in Table 1.

Table 1. Rim Material Values

Material	Aluminum 1060 Alloy
Tensile Strength	68,9356 Mpa
Yield Strength	27,5742 Mpa
Crushing Strength	Pem = 13,7871 Mpa

The rim has metric 6 bolt holes on its inner side. The assembly of internal helical gears is done in these holes. When looking at the auxiliary view of section B-B, a separate circular void is observed, which is placed between the part that provides stabilization of the wheel and the rim. To prevent friction and ensure movement capability, sockets have been created for the bearings.

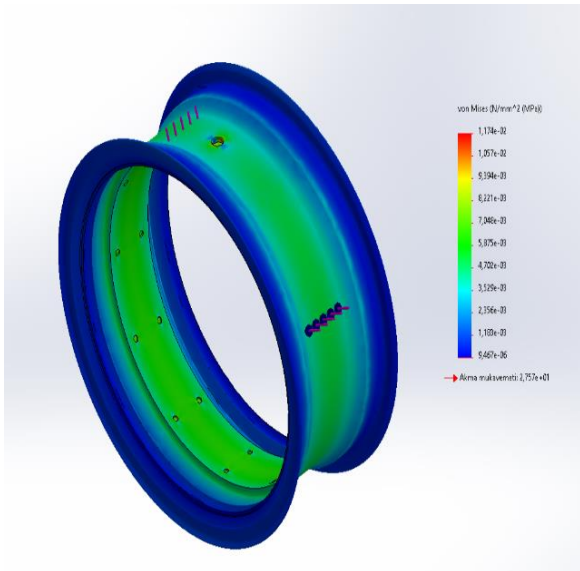


Figure 4. Rim Strength Analysis-1

Table 2. Rim Analysis Results-1

Safe crushing stress	13,5784 Mpa
Yield strength	27,5742 Mpa
Maximum tension	$1,174 \times 10^{-1} Mpa$
Minimum tension	$9,467 \times 10^{-6} Mpa$

Figure 5. Rim Strength Analysis-2

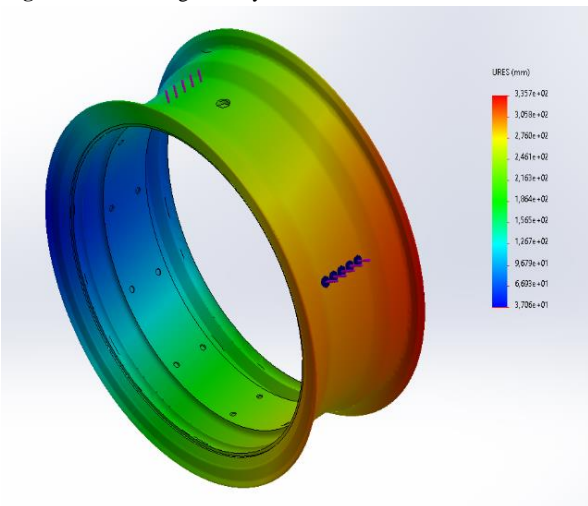


Table 3. Rim Analysis Results-2

Maximum amount of deflection	Minimum amount of deflection
33,57mm	3,706 mm

The results of the strength and deflection analyses conducted in Figures 4 and 5 are provided in Table 2 and Table 3, respectively. The results show that the stresses generated are lower than the safe stress limit, indicating that the material and design have sufficient strength.

3.1.1. Stabilization Component

The role of the stabilization component is to house the connection points of the primary transmission elements. It accommodates the connection points of the chain sprocket, which transfers power from the engine to the wheel, and the shaft, which transfers rotational force from the gear to the reducer.

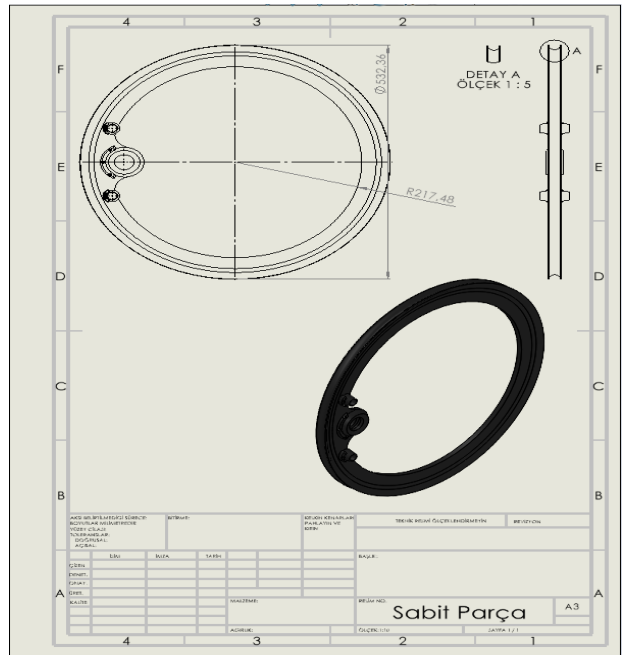


Figure 6. Stabilization Piece Technical Drawing

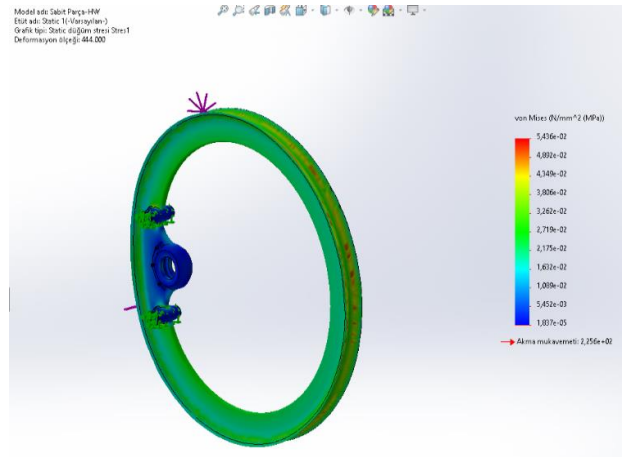


Figure 7. Equivalent stress view

Table 4. Equivalent stress results

Yield strength	Safe crush strength	Maximum stress	Minimum stress
225,6 Mpa	45,12 Mpa	$5,346 \times 10^{-2} Mpa$	$1,837 \times 10^{-5} Mpa$

As seen in Figure 7 and Table 4, the maximum stress obtained from the equivalent stress analysis falls within the safe strength range, ensuring safety.

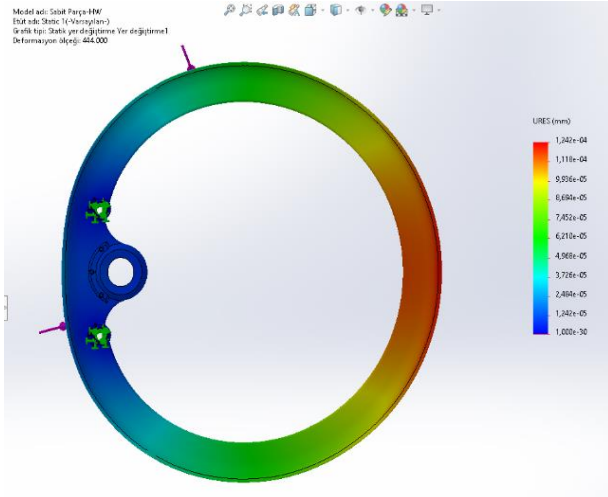


Figure 8. Deflection view

Table 5. Deflection amount

Maximum deflection	Minimum deflection	Deformation scale
$1,242 \times 10^{-4} mm$	$1 \times 10^{-30} mm$	444.000

The deflection amount is a deformation scale that needs to be considered. As can be understood from Figure 8 and Table 5, in order to make the resulting deformation visible to the naked eye, it has been added to the representation with a magnification of 444,000 times.

3.2. Necessary Calculations for Helical Gears

The dimensioning of the helical gear mechanism is based on the gear ratio $i = n_1/n_2 = 1750/408 = 4.2892$ and the torque $M = 42.7358 Nm$.

3.2.1. Pressure angle

The pressure angle of standard-sized helical gears is $\alpha_n = 20^\circ$

3.2.2. Helix angle

If β is small, efficiency increases and the added load decreases. However, as β increases, the engagement path lengthens, leading to multiple teeth engaging simultaneously. When necessary, the gear can be narrowed by increasing β . β is taken as 15° .

3.2.3. Face width coefficient

Table 6. Width Coefficient Based on Surface Finish and Shaft Bearing Condition (Bozacı et al., 1989)

Surface Finish and Bearing Condition	ψ_m	ψ_d
Unprocessed Cast Gears	4÷5	0,23÷0,28
Processed Gears	7÷9	0,4÷0,5
Precision Processed Gears	14÷16	0,7÷0,9
Precision Processed Gears with Bearings on Both Sides	18÷23	1÷1,3
Precision Processed Helical Gears with Bearings on Both Sides	20÷40	1,1÷2

Note: ψ_m is taken as 20 using the last row of Table 6.

3.2.4. Number of teeth on the driving gear

For the purpose of counting in the normal plane, $Z_1 = 28$.

3.2.5. Form factor K_{fn}

Table 7. K_{fn} form factor ruler according to the number of teeth for $\alpha_n = 20^\circ$ for DIN 867 (Bozacı vd., 1989)

Z	13	14	15	16	18	20	22	24
K_{fn}	3,5	3,3	3,23	3,85	3,4	2,95	2,85	2,78
Z	26	28	30	35	40	50	70	100
K_{fn}	2,7	2,64	2,6	2,51	2,4	2,37	2,28	2,2

Theoretical equivalent will be selected according to the number of teeth. For $z_n = \frac{z_1}{\cos^3 \beta} = \frac{28}{\cos^3 15} = 31,06 \cong 31$ pieces, K_{fn} is taken 2,65 from Table 7 by interpolation.

3.2.6. Profile grip ratio

For $\alpha_n = 20^\circ$ ve $\beta = 15^\circ$ ϵ is taken as 1,65

3.2.7. Number of dynamic loads

K_d is taken as 1.16, assuming that the workmanship is sensitive and the peripheral speed is $\frac{1750}{60} = 29,16$ cycle/s and $29,16 \times 2 \times 3,14 \times 0,113926 = 20,86 \frac{m}{s} \cong 21$ m/s. The overload safety factor (S) is taken as 1.25.

3.2.8. Material

One of the most sought-after characteristics in gear wheels is hardness. Both gears were selected to be made of Ck 60 material. Yield $\sigma_{Ak} = 390 \frac{N}{mm^2}$, rupture $\sigma_k = 700 \frac{N}{mm^2}$, hardness $H_B = 2410 \frac{N}{mm^2}$. $\sigma_D \approx 0,5 \times \sigma_K = 350 \frac{N}{mm^2}$. $\sigma_{em} = \frac{\sigma_D}{K_\zeta} = \frac{350}{1,5} = 233 \frac{N}{mm^2}$. The pressure that can be transported safely is taken as $P_{em} = 0,25H_B = 602 \frac{N}{mm^2}$.

3.2.9. Moment to be transmitted

Moment $M = 42,7358 Nm = 42735,8 Nmm$, conversion Rate $i = 4.2892$

3.2.10. Determining the module

According to the gear bottom strength;

$$m_n = \sqrt[3]{\frac{2 \times S \times M_{d1} \times K_D \times K_{fn} \times \cos \beta}{z_1 \times \psi_m \times \sigma_{em} \times \epsilon}}$$

$$= \sqrt[3]{\frac{2 \times 1,25 \times 42735,8 \times 1,6 \times 2,65 \times \cos 15^\circ}{28 \times 20 \times 233 \times 1,65}} = 1.2319 \text{ mm}(3)$$

According to abrasion and crushing, m_n has been obtain as following;

$$m_n = \sqrt[3]{\frac{2 \times S \times M_{d1} \times E \times K_d \times \cos^4 \beta}{z_1^2 \times P_{em} \times \varepsilon \times \psi_m} \times \frac{i+1}{1}} \quad (4)$$

$$m_n = \sqrt[3]{\frac{2 \times 1,25 \times 42735,8 \times 2,1 \times 1,6 \times \cos^4 15^\circ}{28^2 \times 602^2 \times 1,65 \times 20 \times \frac{4,2982 + 1}{1}}} = 1,4937 \text{ m}$$

$$m_n = 2 \text{ mm}$$

3.2.11. Dimensioning

Table 8. Gear Dimensioning Table

Dimensioning parameters	Driving gear	Driven gear
Normal module	2mm	2mm
Forehead Module	2,07	2,07
Tooth width	41,4110	41,4110
Rolling circle diameter	115,92	453,68
Number of teeth	28 pieces	122 pieces
Head circle diameter	119,92	457,63
Base circle diameter	110,92	448,68

3.2.12. Forces acting on shaft bearings

$$\text{Perimeter force } F_p = 2 \times S \times \frac{M_{d1}}{d_1} = 2 \times 1,25 \times \frac{42,7358}{50,68} = 2108 \text{ N} \quad (5)$$

$$\text{Tooth force } F_t = \frac{F_c}{\cos(\alpha_n) \times \cos(\beta)} = \frac{2108}{\cos(20^\circ)} \times \cos(15^\circ) = 2322,42 \text{ N} \quad (6)$$

$$\text{Radial Force } F_r = F_z \sin \alpha_n = 2322,42 \times \sin 20 = 794,17 \text{ N} \quad (7)$$

$$\text{Axial Force } F_a = F_c \times \tan \beta = 2108 \times \tan 15 = 564,83 \text{ N} \quad (8)$$

3.3. Calculations Required for Wedge

Wedge refers to the small components that allow the connection of elements such as gears, pulleys to shafts in a detachable manner, enabling the transmission of motion from the shaft to the hub or from the hub to the shaft. Among the types of wedges, the embedded key is the most commonly used and cost-effective type available in the market. Therefore, an embedded key has been used in the design.

3.3.1. Calculation of wedge length

The only calculation required for fit wedges is the determination of the wedge length.

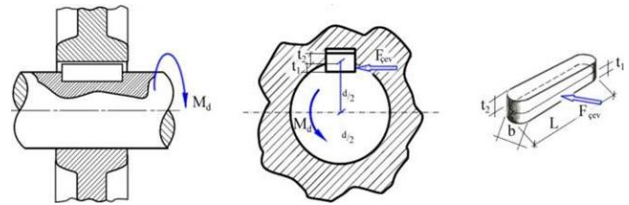


Figure 9. Forces and Dimensioning of Fit Wedges

If the $t_1 \times L$ surface is subjected to crushing, either the shaft or the hub will be crushed. To prevent damage to the shaft, the wedge material should be chosen weaker than the shaft.

$$P = \frac{F_{cev}}{A_1} = \frac{F_{cev}}{L \times t_1} \quad (9)$$

The same calculation should also be performed for the $t_2 \times L$ surface, and in this calculation, the crushing of the wedge or the hub should be checked to prevent damage.

$$P = \frac{F_{cev}}{A_2} = \frac{F_{cev}}{t_2 \times L} \quad (10)$$

Calculations should be performed to assess the lateral crushing of the wedge. The intersection point of the hub and the shaft should also be checked to ensure that the hub shaft is not cut or damaged.

$$T = \frac{F_{cev}}{A_3} = \frac{F_{cev}}{b \times L} \quad (11)$$

The longest among the three wedge lengths should be considered as the reference for the wedge length in these calculations. Additionally, one of the upper limits from the standard wedge lengths should be selected. The standard wedge lengths available in the market are as follows;

L = 6, 8, 10, 12, 14, 18, 20, 22, 25, 28, 32, 36, 40, 45, 50, 63, 70, 80, 90, 100, 110, 125, 140, 160, 180, 200, 220, 250, 280, 315, 355, 400 mm

Figure 10. Standard Dimensions of Fit Wedges

Transfer from sprocket gear to transmission shaft:

RPM = 1750 rpm

Torque = 42.7358 Nm

Safety Factor (S) = Light Impact, Variable Load = 5

Shaft_{material} = Fe 50

$$\sigma_{Ak} = 450 \frac{N}{mm^2}$$

$$T_{bD} = 150 \frac{N}{mm^2}$$

$$T_{em} = \frac{150}{5} = 30 \text{ N/mm}^2,$$

$$P_{em} = \frac{\sigma_{ak}}{S} = \frac{450}{5} = 90 \text{ N/mm}^2$$

Wedge_{material} = Fe 42

$$\sigma_{ak} = 380 \frac{N}{mm^2}$$

$$T_{bD} = 130 \frac{N}{mm^2}$$

$$T_{em} = \frac{130}{5} = 26 \text{ N/mm}^2$$

$$P_{em} = \frac{\sigma_{ak}}{5} = 76 \frac{N}{mm^2}$$

$$\begin{aligned}
 H_{ub_{material}} &= Fe\ 50 \\
 \sigma_{Ak} &= 450 \frac{N}{mm^2} \\
 T_{bD} &= 150 \frac{N}{mm^2} \\
 T_{em} &= \frac{150}{5} = 30\ N/mm^2, \\
 P_{em} &= \frac{\sigma_{ak}}{S} = \frac{450}{5} = 90\ N/mm^2
 \end{aligned}$$

Mil çapları	den büyük	6	8	10	12	17	22	30	38	44	50	58	65	75	85	95	110	130	150	170	200	230	260	290	330	380	440	
Feder kesiti	Genişlik b	2	3	4	5	6	8	10	12	14	16	18	20	22	25	28	32	36	40	45	50	56	63	70	80	90	100	
	Yükseklik h	2	3	4	5	6	7	8	9	10	11	12	14	14	16	18	20	22	25	28	32	32	32	36	40	45	50	
Yuva derinliği (Norma)	Hüde r ₁	1,2	1,8	2,5	3,0	3,5	4,0	5	5	5,5	6	7	7,5	8,5	9,0	10	11	12	13	15	17	19	20	22	25	28	31	
	Göbekte r ₂	1	1,4	1,8	2,3	2,8	3,3	3,3	3,8	4,3	4,4	4,9	5,4	5,9	6,4	7,4	8,4	9,4	10,4	11,4	12,4	13,4	14,4	15,4	17,4	19,5		
	f ₁	+0,05					+0,1														+0,15							
	Yuva derinlik toleransı	-0,00					-0,00															-0,00						
	f ₂	+0,05					+0,1														+0,15							
	-0,00						-0,00														-0,00							
Federin pah veya radyüsü	r _{max}	0,25			0,35		0,55				0,80				1,30		2,00			3,00							2,95	
	r _{min}	0,16			0,25		0,40				0,60				1,00		1,60			2,50							2,50	
Yuva radyüsü	r ₂ max	0,16			0,25		0,40				0,60				1,00		1,60			2,50							2,50	
Feder uzunluğu	L min	6	6	8	10	14	18	22	28	36	45	50	56	63	71	80	90	100	110	125	140	160	180	200	230	250	280	
	L max	20	36	45	50	71	90	110	140	160	180	200	230	250	280	320	360	400	400	400	400	400	400	400	400	400	400	400

Figure 11. Wedge Sizes according to Shaft Diameter

Wedge sizes according to shaft diameter:

$$\begin{aligned}
 d &= \sqrt[3]{\frac{16 \times M_d}{\pi \times T_{em}}} = \sqrt[3]{\frac{16 \times 42,78 \times 1000}{3,14 \times 30}} \\
 &= 19,36\ mm
 \end{aligned} \tag{12}$$

Shaft Diameter (d): 20 mm
 Width (b): 6 mm
 Height (h): 6 mm
 Shaft Depth (t1): 3.5 mm
 Hub Depth (t2): 2.8 mm

$$M_d = F_C \times \frac{d}{2}$$

$$F_C = 2 \times \frac{M_d}{d} = 2 \times 42,7358 \times \frac{1000}{20} = 4278\ N$$

The wedge length based on the crushing;

$$P = \frac{F_C}{t_1 \times L}$$

$$L_{wedge} = \frac{F_C}{t_1 \times P} = \frac{4278}{3,5 \times 76} = 9,09\ mm \tag{13}$$

The wedge length based on the shear stress;

$$\begin{aligned}
 T &= \frac{F_{cev}}{A_3} = \frac{F_{cev}}{b \times L} \\
 L_{wedge} &= \frac{F_{cev}}{T \times b} = \frac{4278}{26 \times 10} = 16,45\ mm
 \end{aligned} \tag{14}$$

Based on the provided standard wedge length;
L = 18 mm

3.4. Calculations Required for Sprocket Gear

The sprocket gear is the component used to transfer the motor output power to the transmission shaft. It plays a crucial role in the power transmission system. (See Figure 12).

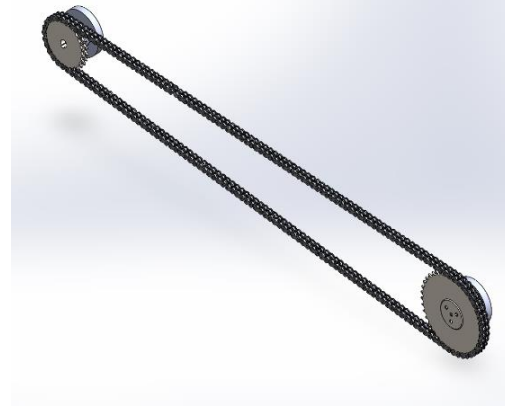


Figure 12. Assembly of Sprocket Gear Transmission

3.4.1. Calculation of chain-sprocket gear (Based on ANSI standards)

$$\begin{aligned}
 1KW &= 1,341\ Hp \\
 8KW &= 10.789\ Hp
 \end{aligned}$$

3.4.2. Operating factor

The machine is considered to have heavy impact loads. Due to being driven by an electric motor $\delta_1 = 1.5$, since it operates in a clean environment $\delta_2 = 1.2$, with an estimated operating time of over 10 hours $\delta_3 = 1.4$.

$$\delta = \delta_1 \times \delta_2 \times \delta_3 \tag{15}$$

So, it is accepted as follows;
 $\delta = 1,5 \times 1,2 \times 1,4 = 2,52$

3.4.3. Design power (Hp)

Design power refers to the power that needs to be transmitted with a safety margin

$$P_{hes} = P_g \times \frac{\delta}{Sira\ Katsayisi} \tag{16}$$

$$P_{hes} = 10,789 \times \frac{2,52}{1} = 27\ Hp$$

Pre-selection

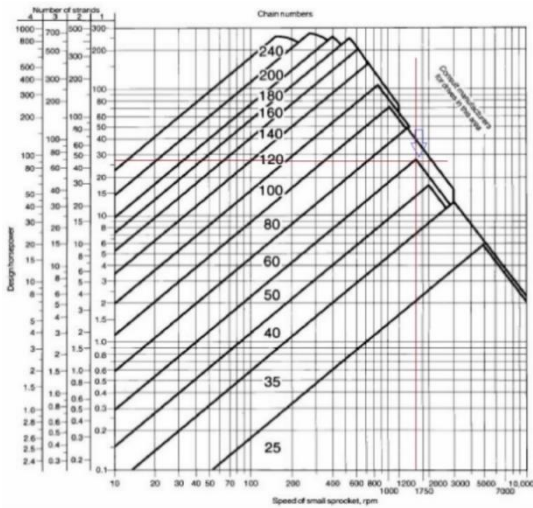


Figure 13. Chain Model Power Diagram

The power diagram, a chain with number 50 was selected for $n_1 = 1600 \text{ rpm}$ $P_{hes} = 27,1882 \text{ BG}$. The chain pitch (P) was read as $(P) = \frac{5}{8}''$.

3.4.4. Final selection

Based on the power evaluation table, for the given chain with $n_1 = 1600 \text{ rpm}$ and $P_{hes} = 27.1882 \text{ hp}$, it is observed that it guarantees the required power when used with a gear with $z_1 = 20,1 \cong 20$ teeth.

3.4.5. Selection of the driven gear

The gear ratio is calculated as $i = 1600/1750 = 0.9142$. The number of teeth on the driven gear is calculated as $z_2 = i \times z_1 = 0.9142 \times 20.1 \approx 18$. Therefore, the driven gear is selected to have approximately 18 teeth.

3.4.6. Chain length

The chain length can be calculated using Equation (17):

$$Z = \frac{2a}{P} + \frac{z_2 + z_1}{2} + \left(\frac{z_2 - z_1}{2\pi}\right)^2 \times \frac{P}{a} \tag{17}$$

$$Z = 2 \times \frac{657,8}{1} + \frac{18+20}{2} + \left(\frac{18-20}{2 \times 3,14}\right)^2 \times \frac{1}{657,8} = 1333,6001 \cong 1334$$

When rounded to the nearest even number, a total of 1334 links will be required for the chain.

3.4.7. Chain maintenance and lubrication

As indicated in the power evaluation table, the chain should be lubricated using the immersion method with a type B oil bath. This method involves immersing the chain in an oil bath for lubrication and maintenance purposes.

3.5. Transmission Shaft Assembly

Table 9. Assigned Material Values for Transmission Shaft

Material	Density	Yield Strength	Thermal Conductivity	Poisson's Ratio
Case-hardened Steel	7800 kg/m ³	8*10 ⁸ N/m ²	14 W/ m*K	0,28

The transmission shaft is supported by bearings at both ends. Due to its location in the hub, analysis is deemed necessary. The resistances considered in the analysis include the resistance caused by initial motion due to friction and acceleration. The stresses and deflections on the shaft caused by the circumferential force of $80 + 80 = 160 \text{ N}$ applied to the wedges have been measured.

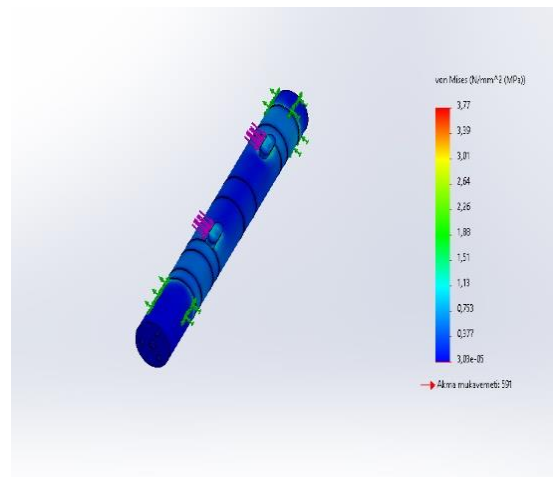


Figure 14. Representation of Equivalent Stress

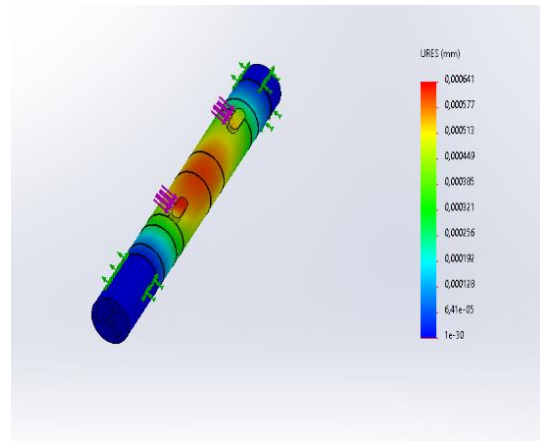


Figure 15. Representation of Displacement of Transmission Shaft

Table 10. Stress Analysis Results

Circumferential Force	Maximum Equivalent Stress	Minimum Equivalent Stress	Maximum Displacement
80 N	3,77 Mpa	0,377 Mpa	0,000641mm

Based on the values provided in Figure 14, Figure 15, and Table 8, the analysis was conducted assuming that the transmission shaft is supported by bearings at both ends and considering two circumferential forces of 80 N applied to the wedges.

3.6. Brake Disc

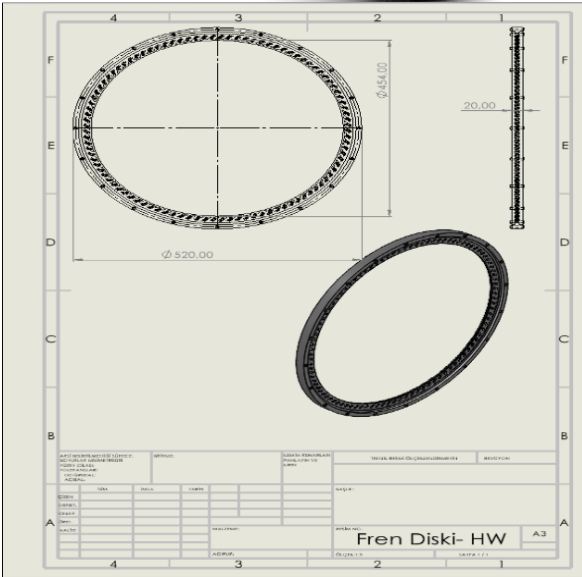


Figure 16. Technical Drawing of Brake Disc

Figure 16 depicts the Brake Disc specifically designed for the system, aiming to be secured by a circumferential loop of 20 M10 bolts.

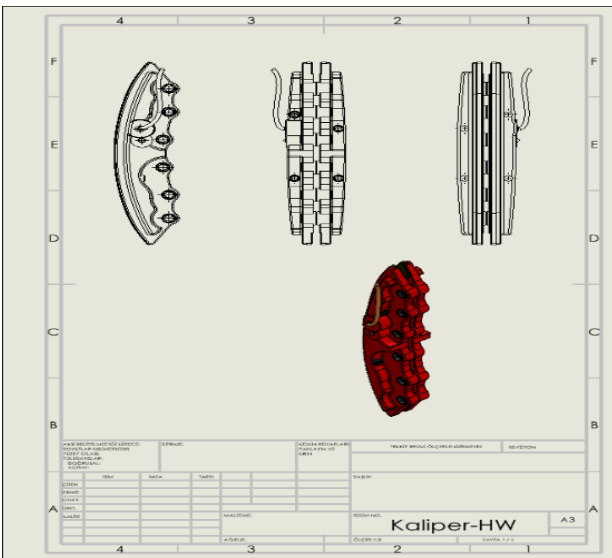


Figure 17. Technical Drawing of Caliper

3.7. Caliper

Figure 17 illustrates a reverse caliper design that differs from standard brake calipers by compressing from inside

the frame, rather than from the outside, in accordance with the design of the brake disc. The renders shown in figure 18 were created using Autodesk VRED Pro software.



Figure 18. Hubless Wheel Render views

4. DISCUSSION AND CONCLUSION

The mechanical friction, which was one of the issues in previous versions of the hubless wheel system, has been minimized with the new design. The number of components has been reduced, making the system more manufacturable. The existing advantages and disadvantages of the system have been reevaluated and presented to you in this section with an objective approach. The design includes 2 sets of stabilizers, internal helical gears, and a helical pinion gear, which differentiate it from traditional wheels. Additionally, there are 1 transmission shaft, 4 bearings, 8 segments, 80 ball bearings, 4 sealing components, 2 wedges, and 1 closed lubrication system, totaling 106 additional parts and 10 different components. The excessive number of components compared to traditional wheels leads to mechanical losses, additional cost expenses, and challenges in assembly and production. The additional cost expenses pose a significant problem for both consumers and manufacturers. Everything, from the machinery used in production to the storage space allocated for extra parts, reflects in the prices. Furthermore, the reduced number of components in traditional wheel designs allows for faster and more efficient production processes compared to hubless wheels. From a consumer perspective, the disadvantages include not only the product price but also the need for spare parts that may arise in case of accidents. However, when comparing the hubless wheel to a wheel with a hub-mounted motor, the hubless wheel has an advantage in terms of moment of inertia. Additionally, the design and layout of hubless wheels make it easier for them to find a place in the market. As mentioned in the introduction, many companies, especially in the

motorcycle industry, have started transitioning to this design. Efforts are also being made to explore alternative solutions to overcome the disadvantages of this design. It is evident that sacrificing the number of components in the hubless wheel design to reduce costs, ease assembly and production, and increase efficiency makes the Hubless DC electric motor design the most suitable option. The use and application areas of hubless motors are increasing in today's market. This growth encompasses various areas such as bicycles, scooters, motorcycles, and current ATV and UTV models. The hubless design that covers all these models is a very sleek and elegant design. Furthermore, the advantage of utilizing the difference in moment of inertia is a significant advantage.

CONFLICT OF INTEREST

The authors have no known conflict of interest or any shared interests with any institution, organization, or individual.

AUTHOR CONTRIBUTIONS

Veysel Türkel contributed to the identification and management of conceptual and design processes, while Said Bera Çivi played an active role in data collection, analysis, and interpretation.

REFERENCES

- [1] Mopare, S., Patel, M., Bhosale, A., Detke, R., Bindu, R. (2018) Design and development of an innovative hubless wheel, IOSR Journal of Mechanical and Civil Engineering, 15(3), 01-14.
- [2] <http://sbarro.phcalvet.fr/>, Erişim Tarihi: Ocak 2018, Konu: Franco Sbarro, Another Vision of Car 2000.
- [3] RMK's hubless rear Wheel drive under construction | Electric Vehicle Sbarro Orbital Wheel, 1929-Franco Sbarro
- [4] Karayolunda Seyreden Araçlara Etkiyen Dirençler | Bölüm 4 (2009) Akdeniz Üniversitesi-Karayolları Müh.
- [5] Mopare, S., Patel, M., Bhosale, A., Detke, R., Bindu, R. (2018) Design and development of an innovative hubless wheel, IOSR Journal of Mechanical and Civil Engineering, 15(3), 01-14.
- [6] Bozacı, A., Koçaş, İ. ve Çolak, Ö. Ü. (1989) Makina Elemanlarının Projelendirilmesi. Seç Yayın Dağıtım, İstanbul.
- [7] Trivini, R. (2010) Hubless castor wheel construction, particularly for furniture articles, U.S. Patent No. 7,657,969. Washington, DC: U.S. Patent and Trademark Office.
- [8] Wang, X.P. ve Feng, L. inventors; Shanghai Magic Wheels Sporting Goods Co Ltd, assignee. Hubless wheel. United States patent US 9,573,417. 2017 Feb 21.

Evaluation of Sugar, HMF, pH, and Acidity Content in Some Popular Soft Drinks Sold in Türkiye

Ramazan GÜN^{1*} , İnan DURSUN² 

¹ Bingöl University, Faculty of Health Sciences, Department of Nutrition and Dietetics, Bingöl, Türkiye

² Bingöl University, Vocational School of Food, Agriculture and Livestock, Department of Beekeeping, Bingöl, Türkiye

Ramazan GÜN ORCID No: 0000-0001-9309-6408

İnan DURSUN ORCID No: 0000-0003-1717-8166

*Corresponding author: rgun@bingol.edu.tr

(Received: 15.06.2023, Accepted: 14.10.2023, Online Publication: 28.12.2023)

Keywords

Erosive effect,
HMF,
Public health,
Soft drinks,
Sugars,
Tax on sugar

Abstract: It is well-known that high consumption of sugary drinks causes negative effects on human health. This study aims to determine the sugar, HMF, pH, and titratable acidity values of soft drinks (n = 25) sold in Türkiye. All the samples were purchased from chain supermarkets in the city of Bingöl, Türkiye. HPLC-RID and HPLC-DAD were used to determine sugar profile (glucose, fructose, sucrose, and maltose) and HMF content of the samples, respectively. Results showed that the total sugar and HMF contents of the samples were found to range from 0.23 to 13.85 % and from 0.65 to 27.76 mg/L respectively. In 9 out of 25 samples HMF were not detected. Furthermore, the pH and acidity values of the samples were found to vary from 1.96 to 6.34 and from 0.73 to 22.07 mEq/L, respectively. The samples were classified based on their total sugar content (from sugar free to very high sugar) and pH erosive capacity (from minimally erosive to extremely erosive). Most of the samples (15 out of 25 samples) were classified in the high sugar content soft drinks (>8g/100ml) and 14 out of 25 samples were found to be considered as extremely erosive (pH<3).

Türkiye'de Satılan Bazı Popüler Meşrubatların Şeker, HMF, pH ve Asitlik İçeriğinin Değerlendirilmesi

Anahtar Kelimeler

Eroziv etki,
HMF,
Halk sağlığı,
Meşrubatlar,
Şekerler,
Şeker vergisi

Öz: Şekerli içeceklerin yüksek tüketiminin insan sağlığı üzerinde olumsuz etkilere neden olduğu bilinmektedir. Bu çalışma, Türkiye'de satılan meşrubatların (n=25) şeker, HMF, pH ve titre edilebilir asitlik değerlerini belirlemeyi amaçlamaktadır. Tüm örnekler, Türkiye'nin Bingöl ilindeki zincir süpermarketlerden satın alınmıştır. Numunelerin şeker profilini (glukoz, fruktoz, sukroz ve maltoz) ve HMF içeriğini belirlemek için sırasıyla HPLC-RID ve HPLC-DAD kullanılmıştır. Elde edilen sonuçlara göre, örneklerin toplam şeker ve HMF içeriklerinin sırasıyla % 0,23 - % 13,85 ve 0,65 - 27,76 mg/L arasında değiştiği belirlenmiştir. 25 örneğin 9'unda HMF tespit edilmiştir. Ayrıca örneklerin pH ve asitlik değerleri sırasıyla 1,96 - 6,34 ve 0,73 - 22,07 mEq/L arasında olduğu tespit edilmiştir. Numuneler, toplam şeker içeriklerine (şekersizden - çok yüksek şeker) ve pH eroziv kapasitelerine (minimum erozivden - aşırı erozive) göre sınıflandırılmıştır. Örneklerin çoğu (25 örnekten 15'i) yüksek şeker içerikli meşrubatlar (>8g/100ml) sınıfına girmiş ve 25 örnekten 14'ünün aşırı eroziv (pH<3) olarak değerlendirilebileceği saptanmıştır.

1. INTRODUCTION

Soft drinks comprise sugar sweetened beverages which are so called 'sugary drinks' and 'no added sugar' drinks that just contain naturally occurring sugars. The WHO (World Health Organization) defines sugary drinks as "all types of beverages containing free sugars and these include carbonated or non-carbonated soft drinks,

fruit/vegetable juices and drinks, liquid and powder concentrates, flavoured water, energy and sports drinks, ready-to-drink tea, ready-to-drink coffee, and flavoured milk drinks." The WHO in its report recommended that countries should implement fiscal policies to reduce the consumption of sugary drinks [1]. Hence, some countries have made legal arrangements taking into account the WHO's suggestion. For example, the government of the UK brought the Soft Drinks Industry Levy into force in

2018. According to this levy, companies will be extra charged 24p/L, and 18p/L respectively if soft drinks include added sugars ≥ 8 g / 100 mL, and between ≤ 8 g / 100 mL - ≥ 5 g / 100 mL. [2]. Similar taxations in different rates on sugar added soft drinks have been implemented in France, the Philippines, Chile, Mexico, Switzerland [3]. Furthermore, regardless of amount of sugar content of sugar added soft drinks are subject to excise duty between 10 % - 35 % rates in Türkiye. According to the law, coke drinks are subjected to 35 % and other soft drinks including fruit juices, vegetable juices, mineral waters, sodas, and non-alcoholic drinks are subjected to 10% special consumption tax. These extra costs are paid directly by the consumers [4].

Soft drinks are very popular especially among children due to the taste, relatively low cost and preferred to be consumed at any time in any place; with meal, between meals. They are also a source of hydration and allow for quenching consumer's thirst [5, 6]. Turkish Statistical Institute [7] announced that children constitute 26.9 % of Türkiye's population (84 million 680 thousand 283). According to data obtained from Statista, 2377 million litres of soft drinks equivalent to 27.95 litres per person were consumed in Türkiye in 2021 [8]. In order to maintain a balanced and healthy diet, the WHO recommended that free sugar intake for adults and children should be less than 10% of daily energy intake [1].

There is a relationship among acidity, pH, sugar content, and HMF concentration. Soft drinks generally have low pH and high acidity values. The sources of acidity and low pH could be from their natural occurrence in

ingredients and from added acidulants. Low pH and high acidity eliminate microbial growth which occurs due to a high percentage of moisture and give beverages extra flavour [9, 10, 11]. Presence of HMF is an important quality indicator in many foods, although it is still not considered as a hazardous substance [12]. HMF has been identified in many food products including honey, syrups, and roasted foods such as coffee, malt, caramels [13]. Generally, its presence in soft drinks is an indicator for heat treatment. Heat treatment is an essential part of soft drink processing [14]. During thermal processing, in an aqueous solution with the presence of sugars, amino acids, and under acidic conditions high heating treatment for a certain time triggers to generate HMF [15].

The primary objectives of this study are: (i) to identify the sugar profile of the soft drinks and classify them depending on their total sugar content (from sugar free to very high sugar content) according to legislations; (ii) to analyse HMF content of the soft drinks; (iii) to determine pH and titratable acidity of the soft drinks and categorise them according to their erosive capacity.

2. MATERIAL AND METHOD

2.1. Material

Twenty-five soft drinks were purchased from a chain supermarket in city of Bingöl, Türkiye in January 2021. The selected chain supermarket has branches in all cities. Thus, beverages are available to be purchased by consumers in all cities of Türkiye. Type of samples and some of the labelling information were demonstrated in Table 1.

Table 1. Type of samples and some of the labelling information

Sample ID	Sample Type	Added sugar /syrup content	Acidulant content	Expiry Date/Batch No
SD1	Orange juice from concentrate	No sugar added	No acidulant added	19.07.2021/005016
SD2	Squeezed Orange juice	No sugar added	No acidulant added	11.08.2021/IZ-1112 0348813
SD3	Apricot juice from concentrate	Sucrose/fructose-glucose	Citric acid	26.11.2021/2611-IZ-M26
SD4	Grape juice from concentrate	Beet sugar	Citric acid	29.10.2021/2910-IZ-M25
SD5	Mango juice from concentrate	Beet sugar	Citric acid	24.04.2021/2404-IZ-M26
SD6	Pineapple juice from concentrate	Sucrose/fructose-glucose	Citric acid, trisodium citrate	04.11.2021/0411-IZ-M26
SD7	Apple juice from concentrate	Sucrose/fructose-glucose	Malic acid	15.03.2022/1512-IZ-M26
SD8	Squeezed apple juice	No sugar added	No acidulant added	17.07.2021/IZ-1711 000344
SD9	Squeezed pomegranate juice	No sugar added	No acidulant added	16.07.2021/IZ – 1611 020250
SD10	Cherry juice from concentrate	Beet sugar	Concentrated lemon juice	14.12.2021/1412 IZ-M22
SD11	Squeezed tomato juice	No sugar added	No acidulant added	07.10.2021/TT2047 071020
SD12	Lemonade soda	Sucrose	Concentrated lemon juice	25.08.2021/61211221
SD13	Lemonade soda	Sucrose/fructose-glucose	Citric acid, sodium citrate	11.05.2021/AA1612 111120-S
SD14	Mixed fruit flavoured soda	Sucrose/fructose-glucose	Citric acid	03.03.2021/0145CR03111203
SD15	Orange flavoured soda	Sucrose/fructose-glucose	Citric acid, malic acid, sodium citrate	29.04.2021/EN011 290720-S
SD16	Lemon flavoured Iced Tea	Sucrose	Citric acid, trisodium citrate	19.03.2022/14
SD17	Lemon flavoured Iced Tea	Sucrose/fructose-glucose	Citric acid, sodium citrate	17.04.2021/EN0204 170720-S
SD18	Lemon flavoured Iced Tea	Sucrose, fructose	Trisodium citrate, concentrated lemon juice	17.09.2021/0844AD 1709201(S)
SD19	Energy drink	Sucrose	Citric acid, sodium citrate	12.12.2022/EN0245 121220
SD20	Energy drink	Sucrose, glucose	Citric acid, sodium bicarbonate	27.11.2022/1879741
SD21	Energy drink	Sucrose/fructose-glucose	Citric acid, phosphoric acid, sodium bicarbonate	27.11.2021/AA0430 271120-S
SD22	Coke	Sucrose/fructose-glucose	Phosphoric acid	20.10.2021/DZ0037 201020-S
SD23	Coke	Sucrose/fructose-glucose	Ammonium sulfate	06.10.2021/1927CR0610201 (S)
SD24	Iced Coffee (Americano)	No sugar added	Sodium bicarbonate, tripotassium citrate	05/2021/02262226
SD25	Pineapple Flavoured Malt drink	Sucrose/fructose-glucose	Citric acid	06.11.2022/21.06 3H S

2.1. Method

2.2.1. Sugar profile analysis by HPLC- RID

2.2.1.1. Standard solution preparation

Sugar profile analyses of the samples were performed using the modified method of TS 13359 [16]. Stoke solution of fructose (D(-)-fructose, Sigma Aldrich), glucose (D-glucose anhydrous, Fluka), sucrose (Fluka), maltose (D-(+)- maltose monohydrate, Fluka) were prepared by dissolving them with ultrapure water (generated from Sartorius H2O-I-1-UV-T Arium Comfort; resistivity 18.2 MΩ.cm) in a beaker. The prepared solution was transferred to a 100 mL flask and then 25 mL methanol (Chromasolv grade, Sigma Aldrich) added to the flask. Later the flask was made up to mark by the addition of ultrapure water. By diluting the prepared stoke solution, seven points standard series was prepared to produce calibration curves. Calibration curves were created by plotting the area of the sugar compound against the concentration of the sugar compound. All the calibration curves showed good linear regressions in the range of 0.9993 – 0.9998 illustrated in Figure 1.

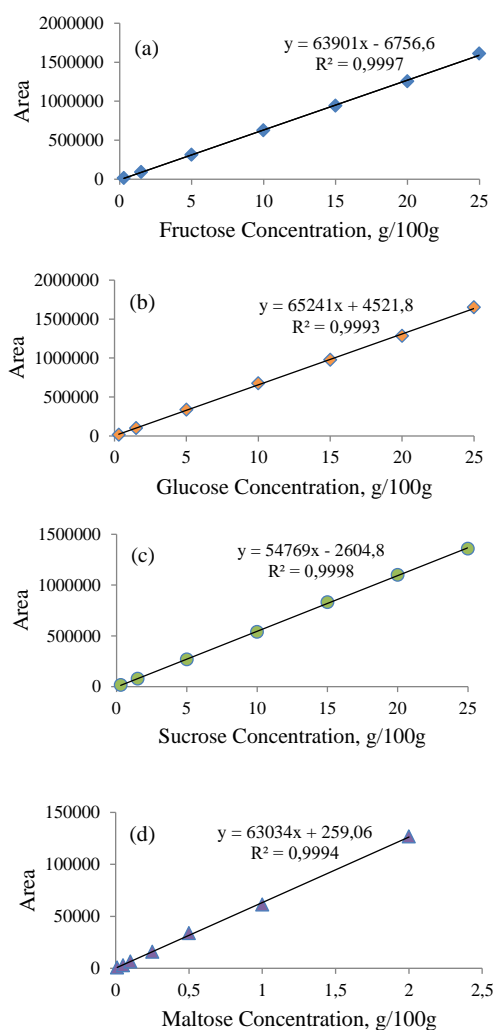


Figure 1. Calibration curves of: (a) fructose, (b) glucose, (c) sucrose and (d) maltose sugars standards

2.2.1.2. Sample preparation and data acquisition

5 g sample was weighed in a beaker and transferred to a volumetric 100 mL flask, and then 25 mL methanol was added to the flask. Later the flask was filled to the mark with ultrapure water and the flask was homogenised by shaking gently. The prepared solution was filtered through a 0.45 μm filter (Sartorius Stedim Biotech GmbH, Goettingen, Germany) into a 2 mL autosampler vial and then introduced to the HPLC instrument (Infinity II, Agilent Technologies) equipped with Refractive Index Detector (RID, 1260 Infinity II), using an EC 250/4.6 NUCLEODUR 100–5 NH2 RP column (250 mm, 4.6 mm, Macherey-Nagel) with EC HPLC guard column NUCLEODUR 100-5 NH2-RP (5 μm, 4x3 mm, Macherey-Nagel). Analysis was performed in isocratic elution mode with a mobile phase composed of acetonitrile (HPLC grade, Sigma Aldrich) - water (80:20 v/v) at a flow rate of 1.3 mL/min, injection volume of 10 μl at 30 °C column and detector temperature. Agilent LC Solutions software was used for data acquisition. All the measurements were done in triplicate.

2.2.2. HMF analysis by HPLC- DAD

2.2.2.1. Standard solution preparation

HMF content of the samples was performed by a modified IHC method [17]. In order to prepare 100 mg/L HMF Stock solution, 10 mg HMF standard (J&K, Haihang Industry Co., Ltd.) was weighed using micro analytical balance (XP6, Metler – Toledo). The weighted standard transferred in a 50 mL beaker and dissolved with 90:10 v/v water-methanol and then put into a 100 mL flask filled up with 90:10 v/v water-methanol. Later, the solution was diluted to obtain concentrations of 0.5 mg/L, 1 mg/L, 2 mg/L, 4 mg/L, 8 mg/L, 10 mg/L. 6 points standard series was prepared showing good linear regression ($R^2 = 0.9998$) given in Figure 2.

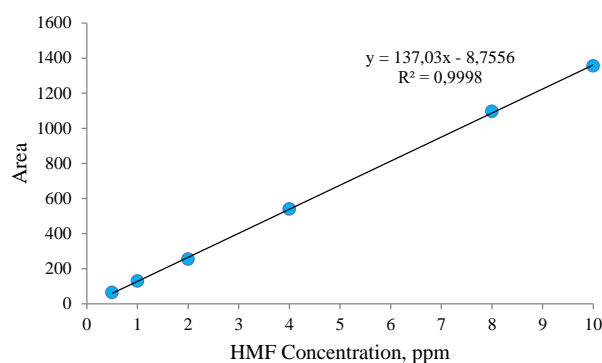


Figure 2. Calibration curve of HMF standard

2.2.2.2. Sample preparation and data acquisition

10 g of sample was weighed in a 50 mL beaker then dissolved with 40 mL ultrapure water. The solution was transferred in a 50 mL flask then 0.5 mL of Carrez I and 0.5 mL Carrez II solutions was added and was filled up 50 mL with ultrapure water. Prepared solution was shaken vigorously then held at ambient temperature for 14 hours. Supernatant was filtered through a paper filter

(MN 615 110 nm Macherey-Nagel). Later, the obtained solution was filtered through 0.45 µm filter (Sartorius Stedim Biotech GmbH, Goettingen, Germany) into a 2 mL autosampler then introduced to the HPLC instrument coupled with Diode Array Detector (DAD 1260 Infinity II WR) using an ACE 5 C18 (250 x 4.6mm id) column. The analysis was carried out in isocratic elution mode with a mobile phase composed of 90:10 v/v water-methanol. The flow rate was 1mL/min, a wavelength of 285nm, and 30 °C column temperature. Agilent LC solutions software was used for data acquisition. All the measurements were done in triplicate.

2.2.3. pH and titratable acidity

The pH was measured soon after opening the package. pH and titratable acidity were performed according to TS 1125 ISO 750. Firstly, pH meter (Orion 3-Star, Thermo Fisher Scientific Inc.) was calibrated using buffer solutions of pH 4, 7, and 10 (Thermo Scientific Inc.). Then, 25 mL of sample was added to a 250 mL beaker and placed on a magnetic stirrer. Later, the electrode was immersed into stirred sample solution and pH of the sample was noted at ambient temperature. The sample was then titrated with 0.1 mol/L NaOH (Sigma - Aldrich) to pH 8.1. Finally, titratable acidity was calculated as follows:

$$\text{Titratable acidity} = \frac{1000 \times V_1 \times C}{V_0} \quad (1)$$

where

V_1 : Volume of NaOH used for titration

C : Concentration of NaOH used for titration

V_0 : Total volume of the sample

All the measurements were done in triplicate.

3. RESULTS AND DISCUSSION

3.1. Sugar Analysis by HPLC- RID

Sugar profiles of the soft drinks including glucose, fructose, sucrose and maltose have been determined using HPLC-RID instrument. A typical sample chromatogram is given in Figure 3. The sugar concentration of the samples were calculated based on the peak areas of calibration curves of the standards by substituting the samples peak area.

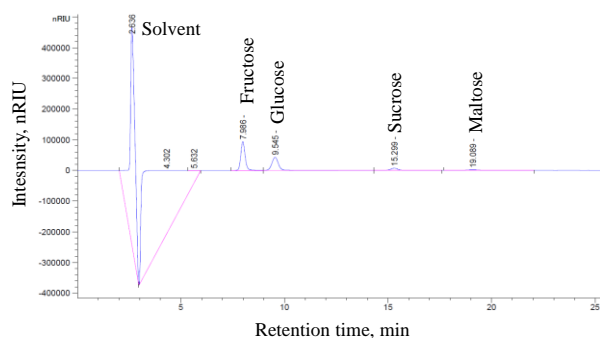


Figure 3. An example of a typical sample chromatogram for sugar components

Total sugar content of the samples were given in Table 2 and illustrated in Figure 4. Concentration of total sugar content of the samples ranged between 0.23 and 13.85 g/100 mL. The mean value of total sugar content of the samples was determined as 8.79 g/100 mL. Sucrose was found to be the most abundant sugar with the mean amount of 3.71 g/100 mL and maltose was found to be the least abundant sugar compound with the mean amount of 0.02 g/100 mL. Most frequently detected sugar components were fructose and glucose to be found in 24 out of 25 samples whilst maltose as least common sugar component were detected in only 3 samples. Unexpectedly, while 9.55% total sugar consisting of 1.02% fructose, 0.98% glucose, and 7.63% sucrose was detected in the sample of SD25 (pineapple flavoured malt drink), no maltose was found in the sample. The highest and the lowest total sugar concentration were found in SD19 (energy drink) sample and SD24 (iced coffee) sample as 13.22 and 0.23 g/100 mL, respectively. According to Nutrition and Health Claims Regulation (EC, 2006), soft drinks were classified in four levels according to their sugar content as sugar-free, moderate sugar content, high sugar content, and very high sugar content.

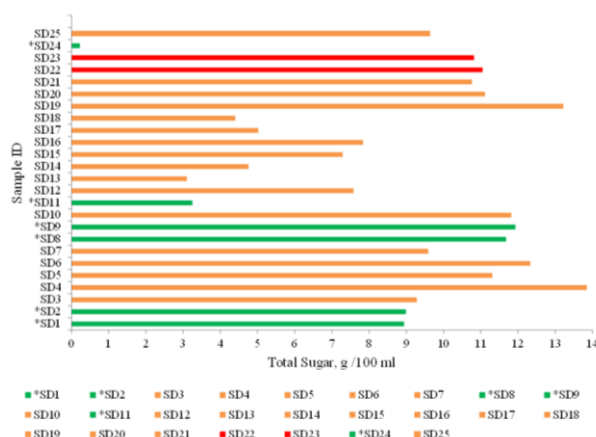


Figure 4. Total sugar content of the samples (green bars represent no taxation, orange bars represent 10% taxation, red bars represent 30% taxation, and '*' indicates the samples does not contain added sugar)

The evaluation of sugar content of the samples according to their sugar levels are illustrated in Figure 5. Most of the products (n=15) were to be determined in 'very high sugar' class. The rest number of 4, 5, and 1 sample were included in 'high', 'moderate' and 'free-sugar' classes, respectively.

Huizinga and Hubert [19] in their study analysed sugar content of the 463 soft drink products and resulted that 171 products were found to be in 'very high sugar' class, 103 products were included in the 'high sugar' class, 134 products were involved in 'moderate sugar' class, and 55 products were get involved in 'sugar-free' class. Silva et al. [20] stated that 48 out of 68 soft drinks including colas, juice drinks, iced teas, and flavoured drinks contained free sugars in their contents. The total sugar

contents including fructose, glucose and sucrose sugars were found ranging between 0.8 and 11 g/100 mL. They detected that colas and juice drinks contained higher total sugars comparing to other type of drinks. It was concluded that, after the sugar tax on soft drinks enforced in Portugal in 2017 [21], sugar concentration of most samples were found to be below to 8 g/100 mL which were less than those from 2008.

According to sugars contents of the samples declared on the Nutrition Facts labels, 20 out of 25 samples contain at least one of the ‘added (free) sugars’ of sucrose, glucose syrup, fructose syrup, and beet sugar. It was specified on the label of these 20 products that sucrose, fructose syrup, and glucose syrup were added to 20, 13, and 13 out of 20 samples, respectively. However, results obtained from HPLC showed that SD5, SD14, and SD24 did not contain sucrose sugar. This may be because consumers consider sucrose as less harmful than fructose and glucose sugar syrups in Türkiye. For this reason, the manufacturers misled consumers by stating that they added sucrose sugar even if they used glucose and fructose. SD1, SD2, SD8, SD9, SD11, and SD24

samples were labelled as no sugar added samples given in Table 1. According to Turkish food codex, there is no tax on beverages that do not contain added sugar. In this case, samples of SD1, SD2, SD8, SD9, SD11, and SD24 that are labelled as ‘no sugar added’ are not taxed. Furthermore, regardless of their sugar content SD22 and SD23 coke samples are taxed at 35% and other all samples are taxed at 10%. In this case, 19 out of 25 samples are taxed in Türkiye [4].

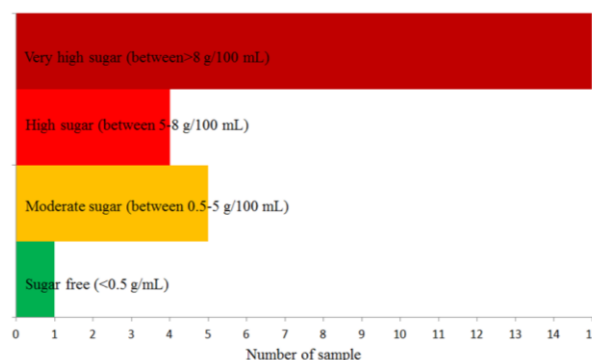


Figure 5. The classification of the samples according to their total sugar levels

Table 2. Sugar, HMF, pH, and titratable acidity values of the samples

Sample ID	Sugar Profile (g/100 mL)					HMF (mg/L)	pH	Titratable acidity (mEq/L)
	Fructose	Glucose	Sucrose	Maltose	Total			
SD1	2.74±0.02	2.72±0.05	3.48±0.04	ND	8.94	ND	3.41±0.01	14.20±0.35
SD2	3.06±0.01	3.16±0.02	2.77±0.02	ND	8.99	3.39±0.06	3.38±0.01	11.67±0.12
SD3	4.27±0.03	4.05±0.07	0.96±0.04	ND	9.28	6.00±0.08	3.83±0.01	5.73±0.12
SD4	2.55±0.02	2.84±0.04	8.46±0.04	ND	13.85	ND	2.78±0.01	6.67±0.12
SD5	5.82±0.04	5.18±0.09	ND	0.31±0.01	11.31	3.07±0.05	2.49±0.01	4.73±0.12
SD6	1.76±0.01	1.78±0.01	8.79±0.03	ND	12.33	0.65±0.01	2.60±0.01	5.80±0.20
SD7	5.23±0.24	3.86±0.14	0.50±0.01	ND	9.59	22.72±0.18	2.86±0.01	5.27±0.12
SD8	6.46±0.02	3.62±0.07	1.60±0.04	ND	11.68	8.13±0.06	3.61±0.01	4.13±0.12
SD9	5.62±0.02	6.31±0.05	ND	ND	11.93	16.82±0.44	2.93±0.01	22.07±0.12
SD10	2.09±0.02	2.91±0.11	6.82±0.2	ND	11.82	1.21±0.01	3.13±0.01	11.20±0.00
SD11	1.27±0.01	1.98±0.10	ND	ND	3.25	ND	4.24±0.01	5.13±0.12
SD12	3.39±0.02	3.59±0.15	0.60±0.02	ND	7.58	1.21±0.01	2.36±0.01	8.27±0.12
SD13	0.27±0.01	0.08±0.00	2.75±0.02	ND	3.10	ND	2.78±0.01	6.00±0.12
SD14	2.74±0.01	2.02±0.02	ND	ND	4.76	2.16±0.09	2.54±0.01	4.67±0.20
SD15	1.87±0.02	1.89±0.03	3.53±0.06	ND	7.29	ND	2.68±0.01	6.13±0.12
SD16	1.70±0.01	1.50±0.01	4.64±0.13	ND	7.84	0.80±0.03	3.19±0.01	3.67±0.12
SD17	1.41±0.04	1.37±0.05	2.24±0.05	ND	5.02	ND	3.15±0.01	3.27±0.12
SD18	1.43±0.02	0.57±0.02	2.40±0.02	ND	4.40	6.49±0.14	3.15±0.01	2.93±0.12
SD19	1.24±0.00	1.19±0.00	10.79±0.02	ND	13.22	ND	1.99±0.01	12.27±0.20
SD20	0.52±0.01	2.18±0.03	8.41±0.07	ND	11.11	2.59±0.01	2.97±0.01	12.33±0.12
SD21	0.71±0.01	0.89±0.04	9.16±0.02	ND	10.76	ND	2.36±0.01	5.80±0.23
SD22	2.43±0.01	2.58±0.02	6.04±0.07	ND	11.05	ND	1.96±0.01	4.93±0.12
SD23	4.55±0.00	5.06±0.04	1.21±0.01	ND	10.82	1.82±0.08	2.03±0.01	3.33±0.31
SD24	ND	ND	ND	0.23±0.01	0.23	27.76±0.08	6.34±0.01	0.73±0.12
SD25	1.02±0.00	0.98±0.08	7.63±0.08	ND	9.63	2.39±0.12	2.21±0.01	8.27±0.20
Average	2.57	2.49	3.71	0.02	8.79	4.29	3.00	7.17

ND: Not detected

3.2. HMF Analysis by HPLC-DAD

Generally, the main sources of HMF are sugars such as glucose and fructose. It occurs in the presence of acids at high temperature thermal processing and bad storage conditions during the Maillard reaction and caramelization. It is commonly found in sugar syrups

and thermally processed foods such as fruit juices, vinegars, baby food, honey and coffee [13]. Therefore, quantification of HMF analysis in soft drinks is very crucial and can be counted as one of the indispensable quality parameters. However there are legal limits set for some foods such as honey [22], and there is no limit established for the concentration of HMF in soft drinks.

The HMF concentrations of the samples were calculated by Agilent LC solutions software using peak areas of calibration curves. An example of HMF sample chromatogram is given in Figure 6.

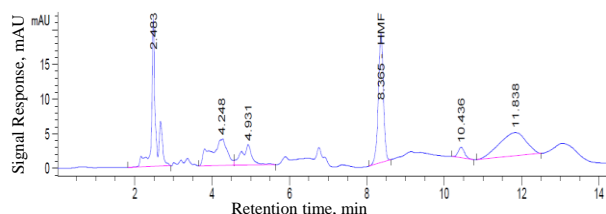


Figure 6. An example of a typical sample chromatogram for HMF component

HMF was not detected in 9 out of 25. The level of HMF content of the samples was found to be ranging from 0.65 to 27.76 mg/L and the mean value of the samples was detected as 4.17 mg/L. Although the lowest total sugar content (0.23 g/100 mL) and the highest pH (6.34) was identified in the iced coffee sample, the highest amount of HMF content was detected as 27.76 mg/L. This could be as a result of coffee roasting and exposing it to high temperature [23]. HMF content in sugar syrups is seen as major public health concern. The generation of HMF in syrups could be as a result of the heating process [24]. Thus, the addition of sugar syrups may cause an increase in the HMF content of the samples. HMF contents of SD7 (sugar-added apple juice) including sucrose / fructose-glucose syrup and SD8 (squeezed apple juice) no sugar-added samples were detected as 22.77 and 8.13 mg/L, respectively. The sugar-added apple juice (SD7) had almost 3 times more HMF than squeezed apple juice (SD8). In a previous study performed by Czerwonka et al. [25], HMF content in different beverages including apple juices, tomato juices, blackcurrant nectars, coke drinks, and citrus flavoured soft drinks was examined. HMF contents were found in a very wide range of values ranging from 0.23 mg/L to 110.75 mg/L. The highest and the lowest mean HMF contents were detected in apple juice samples and orange juice samples as 17.33 and 0.87 mg/L, respectively. Furthermore, HMF levels of roasted and instant coffee samples were also determined. The coffee samples were prepared from 10 g and 6 g of coffee beans and instant coffee assuming them as a cup of ready-to-drink coffee. The results show that HMF contents of the coffee samples were found to be relatively high compared to the drink samples. Mean HMF values of the roasted and instant coffee samples were determined at the amount of 347.6 and 3351 mg/L, respectively. It is stated that, the reason of instant coffee has about ten times higher than roasted coffee was due to instant coffee being subjected to heat treatment during production process.

3.3. pH and Titratable Acidity

The terms of pH and acidity are interrelated to each other representing acidity in aqueous media [26]. In general, soft drinks are naturally acidic [27]. Drinks that are not naturally acidic gain acidity with the addition of acidity regulators which are defined as acidulants. Acidulants as

an essential part of soft drink formulations are also added for the inhibition of microbial growth to extend the shelf-life of the products. Furthermore, they are added to balance the sweetness. Consequently, acidulants are giving them a distinctive taste [28, 29, 30]. According to labelling information, all the 'sugar-added' soft drink samples contain at least one acidulant. Citric acid, trisodium citrate, malic acid, concentrate lemon juice, sodium citrate, sodium bicarbonate, phosphoric acid, and ammonium sulfate (see Table 1) are used as acidulants in the samples. The soft drink samples that are free of added sugar do not contain acidulants except sample of SD24 (iced coffee). Among the acidulants, the most commonly used acidulant was citric acid. It was added in 13 out of 25 samples. Furthermore, concentrated lemon juice was used in 3 samples as a source of citric acid as well. This acidulant is commonly required in sucrose-based carbonated soft drinks due to its relatively low toxicity compared to other acidulants. In addition to that, it is also used for pH adjustment and stronger tartness because it has relatively high equivalent weight (70.05 EW) compared to other acidulants such as malic acid, phosphoric acid, and acetic acid [26, 31].

The pH values of the samples ranged between 1.96 and 6.34 and the mean value of the samples was found to be at the amount of 3.12. The lowest and the highest pH values are detected in SD22 coke sample and SD24 iced coffee sample as 6.34 and 1.96, respectively (see Table 2). Titratable acidities of the samples were detected as ranging between 0.8 and 14.80 mEq/kg and the mean values of the samples were found at the amount of 9.92 mEq/L. The highest and the lowest titratable acidity were found in the SD9 squeezed pomegranate juice sample and SD24 iced coffee sample at the amounts of 22.07 and 0.73 mEq, respectively (see Table 2).

Although acidulants and low pH provide advantages for the end product in the beverage industry mentioned above, they have negative effects on consumer's health. It has been reported in the study that soft drinks that have low pH and high acidity cause tooth erosion including enamel erosion and dental material corrosion [32, 33, 34]. Reddy et al. [28] classified the corrosive degree of soft drinks based on apatite solubility quoted from a study conducted by Larsen and Nyvad [32]. According to this classification soft drinks were classified based on their pH values as extremely erosive (pH<3), erosive (pH between 3 and 4), and minimally erosive pH ≥4 (see Figure 7).

Taking into account of this classification, most of the pH values of the samples were considered as extremely erosive. Among the samples, 14 out of 25 samples were found to be extremely erosive, 9 samples were detected as erosive, and 2 samples were in the class of minimally erosive (see Figure 8). Reddy et al. [28] collected 379 soft drink samples including juices, energy drinks, sodas, flavoured waters, iced teas for pH analysis. It was concluded that 39% of the samples were found extremely erosive, 54% of the samples were considered erosive and only 7% (25 out of 379) of the samples were classified as minimally erosive.

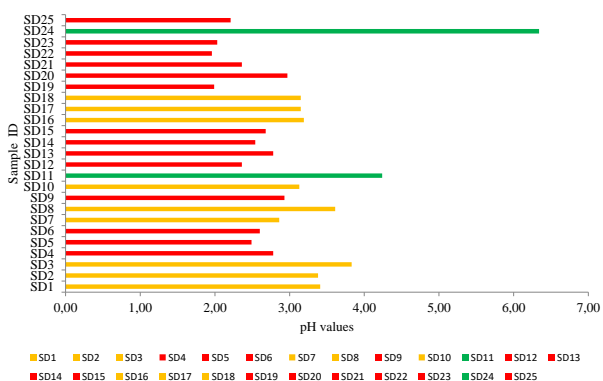


Figure 7. pH values and erosive capacities of the samples (Green, orange, and red bars indicate the erosive capacity of the drinks. Red is for extremely corrosive, orange is for erosive, and green is for minimally erosive)

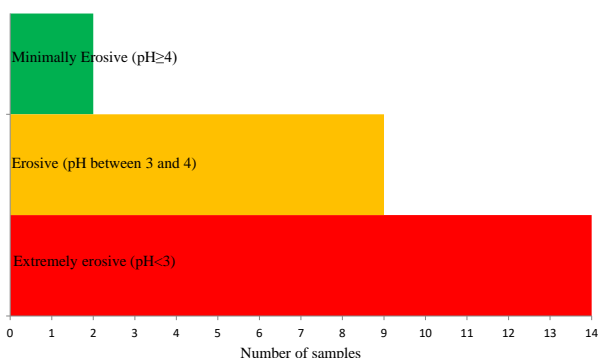


Figure 8. Relative erosivity of the samples (Green, orange, and red bars indicate the erosive capacity of the drinks. Red is for extremely corrosive, orange is for erosive, and green is for minimally erosive)

3.4. Pearson Correlation Matrix Among the Total Sugar, HMF, pH, and Acidity Values

Pearson correlation was conducted in the IBM SPSS Statistics software package program. It was found that Pearson correlation coefficients (PCC) among the total sugar, HMF, pH, and acidity values show that there were negative correlations among the all parameters. The highest and the lowest PCC value were obtained between HMF – pH and acidity – HMF as -0.583 and -0.022, respectively. Furthermore, PCC values for total sugar – pH, total sugar - HMF, pH – acidity, and total sugar – acidity were found as -0.583, -0.245, -0.210 and -0.450, respectively (see Figure 9).

P	Total sugar	HMF	pH	Acidity
Total sugar	1			
HMF	-0.245	1		
pH	-0.583	-0.588	1	
Acidity	-0.45	-0.022	-0.21	1

Figure 9. The Pearson correlation coefficients between the parameters (in figure, P represents parameter)

4. CONCLUSIONS

While, among the sugars; fructose, glucose, sucrose and maltose, the most frequently found sugar was sucrose at the average level of 3.71 g/100 mL in the samples, maltose was found only in two samples and had an average of 0.02 g/100 mL. The most common sugars were fructose and glucose detected in 24 out of 25 samples. Most of the samples (15 out of 25) were to be in a ‘high sugar content’ class ranging between 8.94 and 13.22 g/100 mL. HMF was identified in 16 out of 25 samples ranging from 0.65 to 27.76 mg/L. pH values of the samples were found to be in very wide ranges changing between 1.96 and 6.34. According to erosive capacity, 14 out of 25 samples were considered to be in extremely erosive class (pH<3). The titratable acidity of the samples was found to be between 0.8 and 14.80 mEq/L. As a conclusion, most of the samples were found to be categorised in ‘high sugar content’ and ‘extremely erosive’ classes. From this perspective, it can be said that the soft drink samples could have negative impact on the consumer’s health.

Acknowledgement

This work supported by Bingöl University Central Laboratory Application and Research Center. The authors also would like to thank Bingöl University Scientific Research Projects Coordination Unit (BÜBAP) (Project Number: PİKOM-Ar1.2018.008) for equipment (HPLC) support. I owe special thanks to my dear colleague, Assoc. Prof. Dr. Süleyman İPEK, for his endless support and encouragement.

REFERENCES

- [1] World Health Organization. Guideline: sugars intake for adults and children. World Health Organization; 2015.
- [2] HM Revenue & Customs. The soft drinks industry levy regulations; 2018 [cited 2023 May 14] Available from: http://www.legislation.gov.uk/ukxi/2018/41/pdfs/uk_si_20180041_en.pdf
- [3] Sousa A, Sych J, Rohrmann S, Faeh D. The Importance of Sweet Beverage Definitions When Targeting Health Policies—The Case of Switzerland. *Nutrients*. 2020;12(7):1976.
- [4] Official gazette. 26/05/2022 tarihli ve 5416 sayılı karar; 2022 [cited 2023 May 11] Available from: https://www.resmigazete.gov.tr/eskiler/2022/05/20_220527-9.pdf
- [5] McEwan JA, Colwill JS. The sensory assessment of the thirst-quenching characteristics of drinks. *Food Quality and Preference*. 1996; 7(2):101-11.
- [6] Bandy LK, Scarborough P, Harrington RA, Rayner M, Jebb SA. Reductions in sugar sales from soft drinks in the UK from 2015 to 2018. *BMC medicine*. 2020;18(1):1-0.
- [7] TUIK. [cited 2023 May 7] Available from: <https://data.tuik.gov.tr/Bulten/Index?p=45500>
- [8] Statista. Non-Alcoholic Drinks –Turkey. 2021. [cited 2023 May 11]. Available from:

- <https://www.statista.com/outlook/cmo/non-alcoholic-drinks/turkey#sales-channels>
- [9] von Fraunhofer JA, Rogers MM. Dissolution of dental enamel in soft drinks. *General dentistry*. 2004;52(4):308-12.
- [10] Ivanišová E, Meňhartová K, Terentjeva M, Harangozo L, Kántor A, Kačániová M. The evaluation of chemical, antioxidant, antimicrobial and sensory properties of kombucha tea beverage. *Journal of food science and technology*. 2020;57:1840-6.
- [11] Ribeiro KC, Coutinho NM, Silveira MR, Rocha RS, Arruda HS, Pastore GM, Neto RP, Tavares MI, Pimentel TC, Silva PH, Freitas MQ. Impact of cold plasma on the techno-functional and sensory properties of whey dairy beverage added with xylooligosaccharide. *Food Research International*. 2021;142:110232.
- [12] Rada-Mendoza M, Villamiel M, Ramírez A, Usuriaga Y, Montilla A. Quality indicators in lactose hydrolyzed milks and soy beverages from Colombia. *Journal of Food Science and Technology*. 2021; 12:1-9.
- [13] Bonwick GA, Birch CS. European regulation of process contaminants in food. In: *Mitigating Contamination from Food Processing*. Royal Society of Chemistry, London, UK. 2019. pp. 1–16.
- [14] Adu JK, Orman E, Amengor CD, Peprah P, Danso N, Azumah JA. Assessment of 5-hydroxymethylfurfural levels in carbonated soft drinks and milk products on the markets in the Kumasi Metropolis of Ghana. *Scientific African*. 2022; 1;17:e01346.
- [15] Mtaoua H, Sánchez-Vega R, Ferchichi A, Martín-Belloso O. Impact of high-intensity pulsed electric fields or thermal treatment on the quality attributes of date juice through storage. *Journal of Food Processing and Preservation*. 2017; 41(4):e13052.
- [16] TS 13359. Determination of Fructose, glucose, saccharose, turanose and Maltose of Honey by High Performance Liquid Chromatography. Turkish Standard Institute. 2008. Ankara.
- [17] International Honey Commission (IHC). *Harmonised Methods of the International Honey Commission*. 2009. Available from: <https://www.ihc-platform.net/ihcmethods2009.pdf>.
- [18] TS 1125 ISO 750. The titratable acidity analysis of fruits and vegetables. Turkish Standard Institute. 2002. Ankara.
- [19] Huizinga O, Hubert M. The content of caloric and non-caloric sweeteners in soft drinks in Germany. *Obesity Medicine*. 2017; 1;6:11-4.
- [20] Silva PD, Cruz R, Casal S. Sugars and artificial sweeteners in soft drinks: a decade of evolution in Portugal. *Food Control*. 2021;120:107481.
- [21] OE. Orçamento do Estado para. 2017. In *Da República (Ed.), Diário da República 2016; Vol. 42*, pp. 4875–5107.
- [22] European Union (EU). Council. Council Directive 2001/11 O/EC of 20 December 2001 relating to honey. *Official Journal of the European Communities*. 2002; L10, 47-52.
- [23] Murkovic M, Bornik MA. Formation of 5-hydroxymethyl-2-furfural (HMF) and 5-hydroxymethyl-2-furoic acid during roasting of coffee. *Molecular nutrition & food research*. 2007;51(4):390-4.
- [24] Ros-Polski V, Popović V, Koutchma T. Effect of ultraviolet-C light treatment on Hydroxymethylfurfural (5-HMF) content in high fructose corn syrup (HFCS) and model syrups. *Journal of food engineering*. 2016;179:78-87.
- [25] Czerwonka M, Opilka J, Tokarz A. Evaluation of 5-hydroxymethylfurfural content in non-alcoholic drinks. *European Food Research and Technology*. 2018 Jan;244:11-8.
- [26] Tyl C, Sadler GD. pH and titratable acidity. *Food analysis*. 2017; 389-406.
- [27] Jain P, Nihill P, Sobkowski J, Agustin MZ. Commercial soft drinks: pH and in vitro dissolution of enamel. *General dentistry*. 2007; 1;55(2):150-4.
- [28] Reddy A, Norris DF, Momeni SS, Waldo B, Ruby JD. The pH of beverages in the United States. *The Journal of the American Dental Association*. 2016; 1;147(4):255-63.
- [29] Bamise CT, Ogunbodede EO, Olusile AO, Esan TA. Erosive potential of soft drinks in Nigeria. *World Journal of Medical Sciences*. 2007; 2 (2): 115-119.
- [30] Frederick V, Obed H. Knowledge, practice and perception of taking soft drinks with food and the metabolic effect on high school students in Ghana. *Endocrinol Metab*. 2017;1(1):103-19.
- [31] Soccol CR, Vandenberghe LP, Rodrigues C, Pandey A. New perspectives for citric acid production and application. *Food Technology and Biotechnology*. 2006; 44(2):141-9.
- [32] Larsen MJ, Nyvad B. Enamel erosion by some soft drinks and orange juices relative to their pH, buffering effect and contents of calcium phosphate. *Caries research*. 1999; 33(1):81-7.
- [33] Khoda MO, Heravi F, Shafae H, Mollahassani H. The effect of different soft drinks on the shear bond strength of orthodontic brackets. *Journal of Dentistry (Tehran, Iran)*. 2012; 9(2):145.
- [34] Poggio C, Lombardini M, Colombo M, Bianchi S. Impact of two toothpastes on repairing enamel erosion produced by a soft drink: an AFM in vitro study. *Journal of dentistry*. 2010; 1;38(11):868-74.

Optimizing the Na₂O Dosage to Develop Mechanical Properties of Ferrochrome Slag-Based Alkali-Activated Mortar

Murat DENER^{1*} 

¹Bingöl University, Faculty of Engineering and Architecture, Civil Engineering Department, Bingöl, Türkiye
Murat DENER ORCID No: 0000-0001-6430-8854

*Corresponding author: mdener@bingol.edu.tr

(Received: 14.08.2023, Accepted: 22.10.2023, Online Publication: 28.12.2023)

Keywords

Alkali-activated cement, Na₂O dosage, Ferrochrome slag, Portland cement, Compressive strength

Abstract: The purpose of this study is to investigate the effect of Na₂O dosage on the compressive strength and ultrasonic pulse velocity (UPV) of alkali-activated ferrochrome slag/Portland cement mortar. A total of eight mortar mixtures were produced. While four of the mixtures contain 15% Portland cement, the binder material of the other four mixtures consists entirely of ferrochrome slag. These alkali-activated mortar mixtures were prepared with four Na₂O dosages (4%, 6%, 8%, and 10%). The alkali modulus of all mixtures was kept constant at 1.4. Compressive strength and UPV tests were performed to examine the effect of alkali dosage on both PC-substituted and PC-free mortars. As the Na₂O dosage increased, the compressive strengths of both PC-substituted and unsubstituted mortar specimens increased. It was seen that the critical Na₂O dosage of the alkali-activated mortar was 6%. Compressive strength and UPV values of the mortar specimens increased significantly with PC substitution.

Ferrokrom Cüruf Bazlı Alkali-Aktif Harcın Mekanik Özelliklerini Geliştirmek İçin Na₂O Dozajının Optimize Edilmesi

Anahtar Kelimeler

Alkali-aktif çimento, Alkali dozajı, Ferrokrom cürufu, Portland çimentosu, Basınç dayanımı

Öz: Bu çalışmanın amacı alkali Na₂O dozajının alkali-aktif ferrokrom cürufu/Portland çimentosunun basınç dayanımı ve ultrases geçiş hızı (UGH) üzerindeki etkisini incelemektir. Bu amaç doğrultusunda toplamda sekiz harç karışımı hazırlanmıştır. Karışımların dördü %15 oranında Portland çimentosu içerirken, diğer dördünün bağlayıcı malzemesi tamamen ferrokrom cürufundan oluşmaktadır. Alkali-aktif harçlar dört farklı Na₂O dozajı (4%, 6%, 8% ve 10%) ile hazırlanmıştır. Tüm karışımların alkali modülü 1.4 olarak belirlenmiştir. Na₂O dozajının hem PÇ ikameli hem de PÇ içermeyen harçlar üzerindeki etkisini incelemek için basınç dayanımı ve UGH deneyleri gerçekleştirilmiştir. Na₂O dozajı arttıkça hem PÇ ikameli hem de ikamesiz harç numunelerinin basınç dayanımları artmıştır. Alkali-aktif harç için kritik Na₂O dozajının %6 olduğu görülmüştür. PÇ ikamesi ile harç numunelerinin basınç dayanımı ve UGH değerleri önemli ölçüde artmıştır.

1. INTRODUCTION

Portland cement (PC) is one of the building materials broadly used in the construction industry [1]. It is very advantageous in terms of strength and durability. However, despite all these great features, it has a disadvantage that pushes researchers to look for alternative materials to PC: High CO₂ emissions released into the atmosphere [2,3]. PC is responsible for about 7-8% of the CO₂ emissions released into the atmosphere from human activities. The emissions are mainly due to the decomposition of calcium carbonate (CaCO₃) to generate the calcium silicate and aluminate phases.

Another cause of emissions is the use of fossil fuels [4,5].

Alkali-activated materials (AAMs) serve as an exemplary instance of alternative binders being developed with the primary objective of achieving environmental savings. These materials show promise in reducing the environmental impact associated with traditional cement production. The term of alkali activation refers to the reaction of a solid aluminum silicate material with alkali activator to obtain a hardened binder. Aluminum silicate materials are termed precursor materials [6]. Pozzolan additives, which are

used to replace PC in certain proportions in traditional concrete production [7], can be used in AAM production. Some examples of these materials are blast furnace slag, metakaolin, fly ash and ferrochrome slag (FS) [4,8–10].

Karakoç et al. [11] studied the usability of FS in AAM production. It was stated that it is possible to produce AAM by using a mixture of sodium hydroxide (NaOH) and sodium silicate (Na_2SiO_3) as activator. Yadolahi and Dener stated [12] that the compressive strength of the paste sample consisting entirely of FS was 43.92 MPa. Nath [13] stated that FS addition resulted better compressive strength and well bridged microstructures.

In a study [9] examining the effect of PC substitution on alkali activated FS cement, it was stated that there were increases in compressive strength with PC substitutions. It was also stated that the highest compressive strength was obtained with 15% PC substitution. Mechanical properties and durability of AAM are primarily influenced by the dosage of the activator. Although there are many studies [14–17] examining the effect of Na_2O dosage on the properties of alkali activated blast furnace slag, studies examining the effect on alkali-activated ferrochrome slag (AAFS) are very limited [11]. Karakoç et al. [11] investigated the effect of Na_2O dosage on mixtures prepared using 100% FS. It was stated that the quality of AAFS cement highly depends on Na_2O dosage. It was stated that the highest 28-day compressive strength was obtained when the silica modulus was 0.7 and the Na_2O dosage was 7%.

The literature review shows that there aren't enough studies examining the effect of Na_2O dosage on AAFS based composites. To the best of the author knowledge, there is no study on how the alkali dosage will affect the strength of AAFS composite containing PC. Within the scope of this study, the effect of Na_2O dosage on PC-substituted AAFS mortar was investigated.

2. MATERIAL AND METHOD

2.1. Materials

In this study, the binder materials employed were FS and PC. The type of PC was CEM I 42.5 R [18] which corresponds to ASTM type 1. The properties of the FS and the PC are presented in Table 1.

Table 1. Chemical composition of PC and FS.

Constituent	PC	FS
SiO_2	18.48	33.8
Al_2O_3	4.4	25.48
Fe_2O_3	3.12	0.61
CaO	64.13	1.1
MgO	1.2	35.88
SO_3	0.17	-
Na_2O	0.66	-
K_2O	0.81	-
Cl_2O_3	-	2.12
Specific gravity	3.1	2.85

River aggregate with a maximum diameter of 4 mm was utilized. The size distribution of the aggregate used is shown in Fig 1.

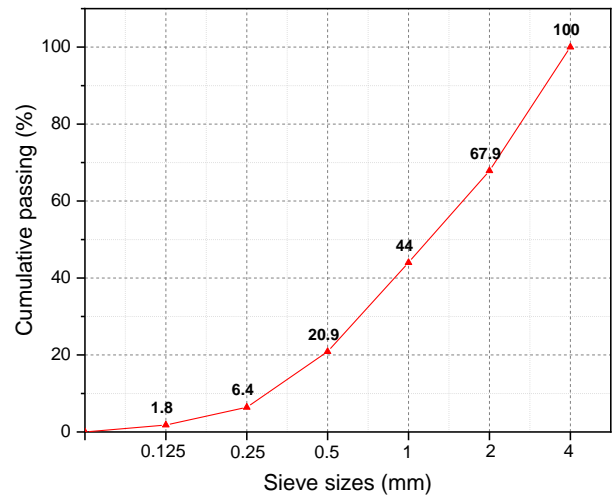


Figure 1. Size distribution of the aggregate.

A mix of Na_2SiO_3 and NaOH was used as alkali activator. NaOH (99% purity) solution was prepared by dissolving NaOH pellets in tap water, then kept at room temperature for 24 h to cool down. Na_2SiO_3 solution composed of 28% SiO_2 , 9% Na_2O , and 63% water content by weight with a silica modulus of 3.11. NaOH and Na_2SiO_3 solutions were mixed to achieve the desired Na_2O dosage.

2.2. Mix Proportions and Test Procedure

A total of eight mortar mixes were prepared to examine the effect of Na_2O dosage. The mixture proportions are given in Table 2.

Table 2. Mix proportions.

Mix codes	FS (wt.%)	Na_2O dosage (%)	A/B	W/B
N4FS100	100	4	2.75	0.45
N6FS100		6	2.75	0.45
N8FS100		8	2.75	0.45
N10FS100		10	2.75	0.45
N4FS85	85	4	2.75	0.45
N6FS85		6	2.75	0.45
N8FS85		8	2.75	0.45
N10FS85		10	2.75	0.45

The term " Na_2O dosage" refers to the weight ratio of the total sodium oxide content in the activator mixture to the binder material. Silica modulus (Ms) indicates the ratio of silicon oxide-to-sodium oxide ($\text{SiO}_2/\text{Na}_2\text{O}$) in the activator mix. A set of AAFS mixtures were prepared with four Na_2O dosages (4%, 6%, 8% and 10%). The Ms of all mixtures were kept constant at 1.4. Aggregate-to-binder (A/B) ratio of all mixtures was determined as 2.75/1. All mixes were produced with a water-to-binder (W/B) ratio of 0.45. Four of the mixtures contain 15% PC, while the other four are produced entirely from FS. All samples were cured at 75 °C for 24 hours and then kept at room temperature until testing day (28 day).

The compressive strength test was conducted following the guidelines outlined in ASTM C109 [19]. The ultrasonic pulse velocity (UPV) test was performed in accordance with ASTM C597 [20]. Fig. 2a and Fig. 2b

show the compressive strength and UPV measurement tests, respectively.

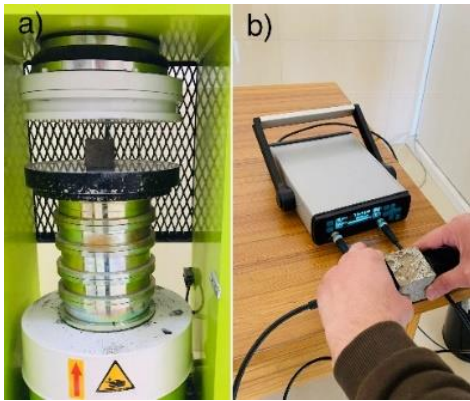


Figure 2. a) compressive strength test b) UPV test.

2.3. Specimen preparation

Firstly, dry materials (FS or FS + PC, and aggregate) were mixed for 30 seconds. Then, NaOH and Na₂SiO₃ solutions were added to the dry mixture. The mixing process continued until a homogeneous mixture (2 min) was obtained. One of the prepared fresh mortars are shown in Fig. 3.



Figure 3. A fresh mortar mixture.

Prepared fresh mortar mixtures were cast into steel molds (50*50*50 mm³). After that, the steel molds were wrapped with a stretch film as shown in Fig. 4.



Figure 4. A wrapped mold.

3. RESULTS AND DISCUSSION

3.1. Compressive strength results

Fig. 5 presents the 28-day compressive strength results for mortar specimens without PC substitution.

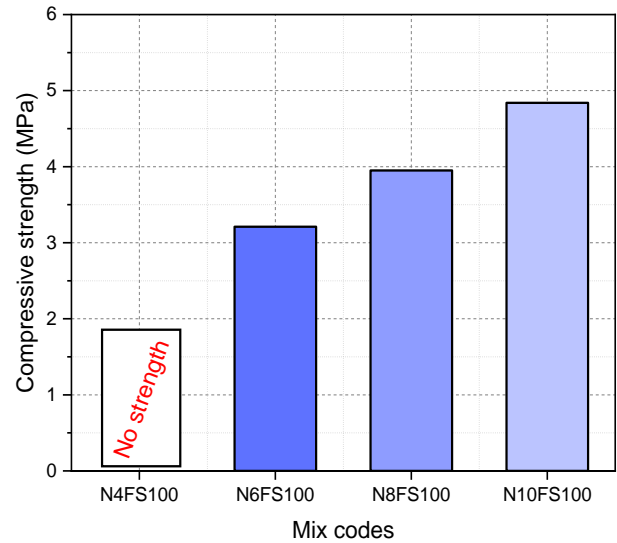


Figure 5. Compressive strength of PC-free specimens.

Mortar specimen with 4% Na₂O dosage, coded as N4FS100, did not have any compressive strength. N4FS100 coded mortar specimen is shown in Fig. 6. The mortar specimen was easily dispersed. The compressive strengths of the N6FS100, N8FS100 and N10FS100 mortar specimens with 6%, 8% and 10% Na₂O dosages were 3.21, 3.95 and 4.84 MPa, respectively. Regardless of the Na₂O% used, the 28-day compressive strength of all PC-free mortar specimens was quite low. However, it was noted that the compressive strength exhibited an increase with an increase in the Na₂O dosage.



Figure 6. N4FS100 coded mortar specimen.

Raising the Na₂O dosage intensifies hydration, leading to a denser microstructure and increased compressive strength [16]. While the strength of samples without PC did increase with an increase in dosage, the highest compressive strength attained remained low at 4.84 MPa. Employing a higher curing temperature to enhance the geopolymerization process can indeed lead to an improvement in compressive strength. However, it's

worth noting that this approach comes with a drawback in terms of increased energy consumption. To enhance compressive strength without the need to raise the curing temperature, a 15% PC substitution was introduced in the mixtures. Fig. 7 presents the 28-day compressive strength results for mortar specimens with 15% PC substitution.

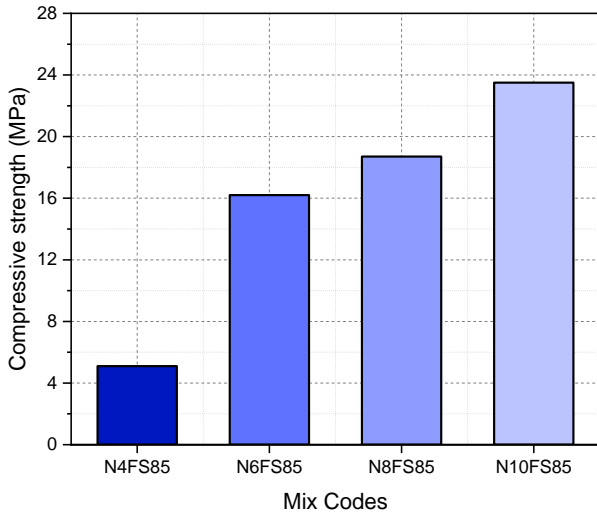


Figure 7. Compressive strength of PC-substituted specimens.

The first thing to note is that the compressive strength increased considerably with the PC substitution. At 4% Na_2O dosage, a compressive strength of the specimen without PC substitution was not obtained, while the compressive strength of the specimen with 15% PC substitute was 5.1 MPa. The compressive strengths of the N6FS85, N8FS85 and N10FS85 mortar specimens with 6%, 8% and 10% Na_2O dosages were 16.2, 18.7 and 23.5 MPa, respectively. It was observed that the critical Na_2O dosage for the alkali activated FS/PC mortar was 6%. Compressive strength of N4FS85 coded specimen was 5.1 MPa. When the Na_2O dosage was increased from 4% to 6%, the compressive strength increased by 217%. The highest compressive strength was obtained from N10FS15 specimen with the highest Na_2O dosage. When 15% PC was added to N6F100, N8F100, N10F100 coded specimens, their compressive strengths increased by 404, 374 and 385%, respectively. The enhancement in compressive strength with PC replacement may be attributed to the formation of calcium silicate hydrate (CSH) and calcium aluminate silicate hydrate (CASH) gels [21].

3.1. Ultrasonic pulse velocity results

Fig. 8 presents the 28-day UPV results for mortar specimens without Portland cement substitution.

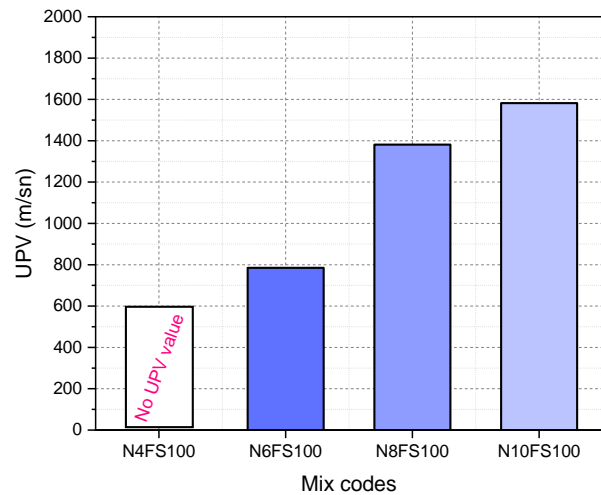


Figure 8. UPV results of PC-free specimens.

Consistent with the compressive strength results, no UPV value was obtained from the N4FS100 coded mortar specimen with 4 Na_2O dosage. The UPV values of the N6FS100, N8FS100 and N10FS100 mortar specimens with 6%, 8% and 10 Na_2O dosages were 785, 1381 and 1582 m/s, respectively. As the Na_2O increased, the UPV values increased. Fig. 9 presents the 28-day UPV measurement results for mortar specimens with 15% PC substitution.

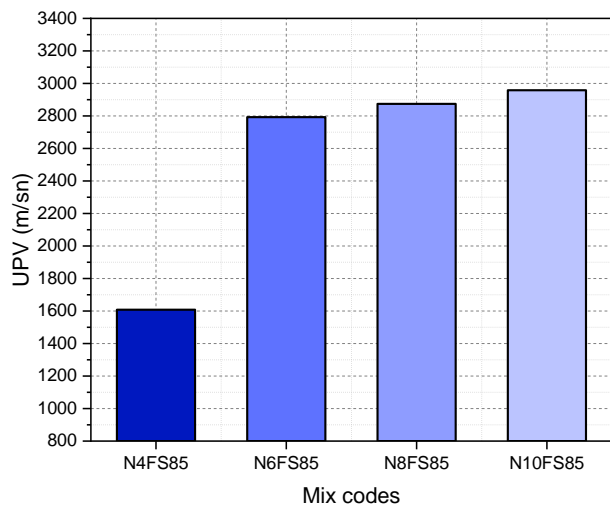


Figure 9. UPV results of PC-substituted specimens.

Like the compressive strength results, significant increases occurred in UPV values with the PC substitution. While No UPV value could be obtained in the mortar specimen coded N4FS100, the UPV value of the N4FS85 coded mortar specimen with 15% PC substitution was 1608 m/s. The UPV values of the N6FS85, N8FS85 and N10FS85 mortar specimens with 6%, 8% and 10% Na_2O dosages were 1608, 2793, 2874 and 2958 m/s, respectively. Compressive strength increased by 74% when Na_2O dosage was increased from 4% to 6% for 15% PC substitution. The UPV values of the N6FS85, N8FS85 and N10FS85 coded mortar specimens were 105, 108 and 87% higher than their PC unsubstituted counterparts. The relationship between the compressive strength and the UPV values of

the specimens with no PC substitution and with 15% PC substitution is given in Fig. 10.

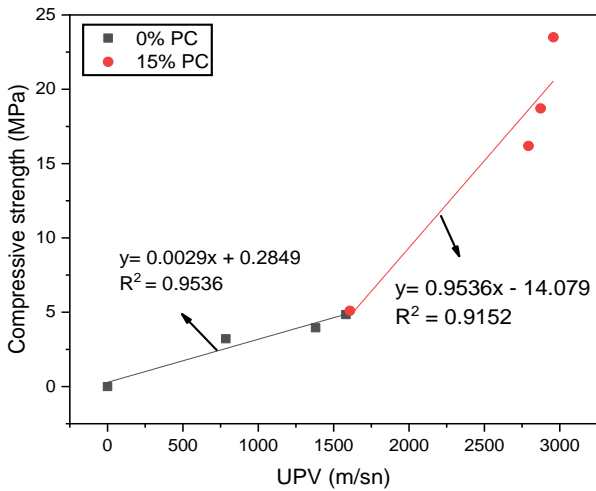


Figure 10. Correlation between compressive strength and UPV values

While the coefficient of determination (R^2) between the compressive strength and the UPV value was 0.95 for the samples without PC substitution, this coefficient was 0.92 for the samples with PC substitution.

4. CONCLUSION



In this study, the effect of Na_2O dosage on the compressive strength and UPV value of alkali-activated FS/PC cement was investigated. In terms of both compressive strength and UPV value, it was observed that the critical Na_2O dosage of the alkali-activated mortar was 6%. As the Na_2O dosage increased, the compressive strength of both PC-substituted and unsubstituted specimens increased. Even at the highest Na_2O dosage, the compressive strength of the mortar specimen without PC substitution were quite low. Both compressive strengths and UPV values increased significantly with PC substitution. The compressive strengths of the N6FS85, N8FS85 and N10FS85 coded mortar specimens were 404, 374 and 385% higher than their PC unsubstituted counterparts. It was observed that the production of AAM using entirely FS was challenging, even with an increasing alkali concentration. It was concluded that to effectively utilize FS in AAM production, it should be blended with materials possessing a high CaO content, such as PC.

REFERENCES

- [1] Sedaghatdoost A, Behfarnia K, Bayati M, Vaezi M sadegh. Influence of recycled concrete aggregates on alkali-activated slag mortar exposed to elevated temperatures. *J Build Eng* 2019;26:100871. <https://doi.org/10.1016/j.jobbe.2019.100871>.
- [2] Provis JL, Palomo A, Shi C. Advances in understanding alkali-activated materials. *Cem Concr Res* 2015;78:110–25. <https://doi.org/10.1016/j.cemconres.2015.04.013>.
- [3] Yön MŞ, Karataş M. Evaluation of the mechanical properties and durability of self-compacting alkali-activated mortar made from boron waste and granulated blast furnace slag. *J Build Eng* 2022;61:105263.
- [4] Provis JL, Bernal SA. Geopolymers and Related Alkali-Activated Materials. *Annu Rev Mater Res* 2014;44:299–327. <https://doi.org/10.1146/annurev-matsci-070813-113515>.
- [5] Ulucan M, Alyamac KE. A comprehensive assessment of mechanical and environmental properties of green concretes produced using recycled concrete aggregates and supplementary cementitious material. *Environ Sci Pollut Res* 2023. <https://doi.org/10.1007/s11356-023-29197-y>.
- [6] Provis JL. Alkali-activated materials. *Cem Concr Res* 2018. <https://doi.org/10.1016/j.cemconres.2017.02.009>.
- [7] Yön MŞ, Arslan F, Karatas M, Benli A. High-temperature and abrasion resistance of self-compacting mortars incorporating binary and ternary blends of silica fume and slag. *Constr Build Mater* 2022;355:129244.
- [8] Dener M, Karatas M, Mohabbi M. Sulfate resistance of alkali-activated slag/Portland cement mortar produced with lightweight pumice aggregate. *Constr Build Mater* 2021;304:124671.
- [9] Dener M, Karatas M, Mohabbi M. High temperature resistance of self compacting alkali activated slag/portland cement composite using lightweight aggregate. *Constr Build Mater* 2021;290. <https://doi.org/10.1016/j.conbuildmat.2021.123250>.
- [10] Özcan A, Karakoç MB. The Resistance of Blast Furnace Slag- and Ferrochrome Slag-Based Geopolymer Concrete Against Acid Attack. *Int J Civ Eng* 2019;17:1571–83. <https://doi.org/10.1007/s40999-019-00425-2>.
- [11] Karakoç MB, Türkmen I, Maraş MM, Kantarci F, Demirboğa R, Uşur Toprak M. Mechanical properties and setting time of ferrochrome slag based geopolymer paste and mortar. *Constr Build Mater* 2014;72:283–92. <https://doi.org/10.1016/j.conbuildmat.2014.09.021>.
- [12] Mohabbi Yadollahi M, Dener M. Investigation of elevated temperature on compressive strength and microstructure of alkali activated slag based cements. *Eur J Environ Civ Eng* 2019. <https://doi.org/10.1080/19648189.2018.1557562>.
- [13] Nath SK. Geopolymerization behavior of ferrochrome slag and fly ash blends. *Constr Build Mater* 2018;181:487–94. <https://doi.org/10.1016/j.conbuildmat.2018.06.070>.
- [14] Karahan O, Yakupoğlu A. Resistance of alkali-activated slag mortar to abrasion and fire. *Adv Cem Res* 2011;23:289–97. <https://doi.org/10.1680/adcr.2011.23.6.289>.
- [15] Abubakr AE, Soliman AM, Diab SH. Effect of activator nature on the impact behaviour of Alkali-Activated slag mortar. *Constr Build Mater* 2020;257:119531. <https://doi.org/10.1016/j.conbuildmat.2020.119531>.
- [16] Fang S, Lam ESS, Li B, Wu B. Effect of alkali contents, moduli and curing time on engineering properties of alkali activated slag. *Constr Build Mater* 2020;249.

- <https://doi.org/10.1016/j.conbuildmat.2020.118799>.
- [17] Shi Z, Shi C, Wan S, Zhang Z. Effects of alkali dosage and silicate modulus on alkali-silica reaction in alkali-activated slag mortars. *Cem Concr Res* 2018;111:104–15. <https://doi.org/10.1016/j.cemconres.2018.06.005>.
- [18] Institution) TSE (Turkish S. TS EN 197-1: Cement Part 1: Composition, specification and conformity criteria for common cements 2012.
- [19] ASTM C109/C109M A. Compressive Strength of Hydraulic Cement Mortars (Using 2-in . or [50-mm] Cube Specimens) 1. Am Soc Test Mater 2007.
- [20] ASTM C597. Standard Test Method for Pulse Velocity Through Concrete. Am Soc Test Mater West Conshohocken, PA, USA 2016.
- [21] Saloni, Parveen, Yan Lim Y, Pham TM. Influence of Portland cement on performance of fine rice husk ash geopolymer concrete: Strength and permeability properties. *Constr Build Mater* 2021. <https://doi.org/10.1016/j.conbuildmat.2021.124321>.

Comparative Analysis of Optimization Algorithms in Overcurrent Relay Optimization

Özge ÖZGÜNER^{1*} , Ebubekir SEYYARER² 

¹ Van Yuzuncu Yıl University, Distance Education Research and Application Center, Van, Türkiye

² Van Yuzuncu Yıl University, Faculty of Engineering, Computer Engineering Department, Van, Türkiye

Özge ÖZGÜNER ORCID No: 0000-0002-4162-9038

Ebubekir SEYYARER ORCID No: 0000-0002-8981-0266

*Corresponding author: ozgeozguner@yyu.edu.tr

(Received: 7.06.2023, Accepted: 25.10.2023, Online Publication: 28.12.2023)

Keywords

Saplings Growing up Algorithm, League Championship Algorithm, Genetic Algorithm, Whale Optimization Algorithm, Overcurrent Relay Coordination

Abstract: Optimization algorithms are commonly used to solve problems aiming to find the minimum or maximum value of a specific objective function. Optimization methods use both mathematical and heuristic approaches to select the best alternative. This study aims to minimize the Overcurrent Relay Coordination (ORC) problem of Overcurrent Relays using four optimization algorithms and compare the results. Overcurrent relays are critical protective devices that detect faults and minimize damage in power systems. Proper selection and adjustment of protective relays are essential to ensure the security of power systems. ORC consider numerous constraints such as relay operation times and settings, load changes, and maintenance requirements in an electric distribution system. The results generated by the Saplings Growing up Algorithm (SGA), League Championship Algorithm (LCA), Genetic Algorithm (GA), and Whale Optimization Algorithm (WOA) for the ORC problem in Hasaңcelebi transformer substation are compared. According to the results obtained, it is observed that the WOA produces faster results than other optimization algorithms.

Aşırı Akım Röle Optimizasyonunda Optimizasyon Algoritmalarının Karşılaştırmalı Analizi

Anahtar Kelimeler

Fidan Gelişim Algoritması, Lig Şampiyonluk Algoritması, Genetik Algoritma, Balina Optimizasyon Algoritması, Aşırı – Akım Röle Koordinasyonu

Öz: Optimizasyon algoritmaları, belirli bir amaç fonksiyonunun minimum veya maksimum değerini bulmayı amaçlayan problemleri çözmeye yaygın olarak kullanılmaktadır. Optimizasyon yöntemleri, en iyi alternatifi seçmek için hem matematiksel hem de sezgisel yaklaşımları kullanmaktadır. Bu çalışmada Aşırı Akım Rölelerinin Koordinasyon (Overcurrent Relay Coordination - ORC) problemini dört optimizasyon algoritması kullanarak en aza indirmeyi ve sonuçlarını karşılaştırmayı amaçlanmaktadır. Aşırı akım röleleri, güç sistemlerinde arızaları tespit eden ve hasarı en aza indiren kritik koruyucu cihazlardır. Güç sistemlerinin güvenliğini sağlamak için koruma rölelerinin doğru seçimi ve ayarlanması önem arz etmektedir. ORC, bir elektrik dağıtım sisteminde röle çalışma süreleri ve ayarları, yük değişiklikleri ve bakım gereksinimleri gibi çok sayıda kısıtlamanın dikkate alınmasını içermektedir. Hasaңcelebi trafo merkezinin ORC sorunu için Fidan Gelişim Algoritması (Saplings Growing up Algorithm -SGA), Lig Şampiyonluk Algoritması (League Championship Algorithm - LCA), Genetik Algoritma (Genetic Algorithm - GA) ve Balina Optimizasyon Algoritması (Whale Optimization Algorithm - WOA) ile üretilen sonuçlar karşılaştırılmaktadır. Elde edilen sonuçlara göre, WOA'nın diğer optimizasyon algoritmalarına göre daha hızlı sonuçlar ürettiği görülmektedir.

1. INTRODUCTION

Many problems are frequently solved using optimization methods. In mathematics, optimization is the process of determining the minimum or maximum quantity of an

equation. The goal of optimization theory and methods is to choose the optimum option given the objective function [1]. In addition to using mathematical approaches, heuristic techniques are also employed to solve optimization systems [2]. The words Meta and Heuristics are combined to generate the phrase Meta-

Heuristics in literature. It is described as a collection of techniques for solving issues using predetermined guidelines and processes [3]. This study intends to reduce the ORC problem utilizing two optimization methods and compare the outcomes with two previously investigated algorithms.

The structure of power systems has become increasingly complex with today's technological developments [4]. During the operation of power systems, protective relays are of great importance [5]. The principal purpose of protective relays is to quickly identify errors that may occur in electrical systems and to reduce or eliminate the damage caused by these faults. In this way, the damages that may occur during the operation of power systems can be prevented and the safety of electrical systems can be ensured. Protective relays include types such as distance protection, overcurrent, and differential relays. Ensuring the continuity and protection of energy in power systems is also an important issue in the field of engineering. Therefore, the correct selection and adjustment of protective relays are crucial for the protection of power systems [6]. The structures of power systems can encounter both permanent and temporary faults. These faults can negatively affect the operation of network equipment and even cause high-amplitude currents to damage network equipment. Therefore, taking safety measures in the structure of power systems is important [7]. One of the most common protective relays is the overcurrent relay [8].

Overcurrent relays are the primary protection devices of electrical distribution systems and prevent malfunction of power systems. These relays work in case of malfunction and take preventive measures to prevent damage to the system. In the past, communication between overcurrent relays was done with traditional methods, but later computerized methods were used [9, 10]. Traditional methods require manual processes such as determining the operating times and order of operation of relays, while computerized methods enable these processes to be carried out in a computer environment. Thanks to these methods, ORC can be performed more effectively and quickly [9, 11].

ORC requires consideration of numerous constraints in an electricity distribution system [12]. These constraints can include factors such as relay operating times, operating sequences, and operating frequencies. Therefore, in order to be properly implemented, ORC has to be formulated as an optimization problem that considers a number of constraints. This optimization problem aims to determine the operating times and sequences of relays and to find the optimal solution. This enables ORC to be conducted more efficiently and ensures system safety. Various optimization techniques are recommended for optimal coordination [13, 14]. Metaheuristic algorithms are algorithms that solve optimization problems by combining different methods. These algorithms are generally used to increase the solution time and/or solution quality of classical optimization algorithms. Additionally, metaheuristic algorithms have been used for ORC issues, with

successful results in terms of both solution speed and quality. For example, metaheuristic algorithms such as Continuous Genetic Algorithm (CGA) [15] and Chaotic Firefly Algorithm (CFA) [16] provide effective results in ORC problems [12].

Razavi et al. [17], used GA for ORC. The presented objective function (OF) can solve coordination problems as well as problems with continuous or discrete time-setting multipliers (TSM) or time-dial settings (TDS). Two distinct power system network configurations were used to test the study. The outcomes attained show that this new approach is a flexible and successful method.

Alam et al. [18] examined the performance of five different meta-heuristic algorithms, including GA, Particle Swarm Optimization (PSO), Differential Evolution (DE), Harmony Search (HS), and Seeker Optimization Algorithm (SOA) for solving the protection coordination problem of oriented overcurrent relays. According to the study, among the five algorithms looked at, the DE algorithm fared the best.

Gaikwad et al. [19] used a tournament championship strategy in their study on the CloudSim simulator to enhance business planning for cloud architecture. Reducing time to market and offering cloud services at reasonable prices are the major objectives. The most effective strategy, according to the data, is ILCA.

Langazane et al. [20] study the effects of particle swarm optimization and genetic algorithms on overcurrent relay sensitivity and speed. The study has shown that evolutionary algorithm control parameters affect relay performance. Experimental results show that PSO converges faster than GA.

According to Rizal et al.'s [21] research utilizing genetic algorithms, the approach of choosing overcurrent relay settings with MATHCAD is still not ideal since it needs certain changes. Compared to conventional optimization strategies, this research appeared to offer an improvement in Overcurrent Relay coordination optimization.

Wadood et al. [22] evaluated the problem of optimally coordinating Directional Overcurrent Relays (DOCR) using the WOA algorithm. It has been put into use in six different systems to assess how well the suggested WOA is working. The six problematic models appear to be successfully minimized in simulation results of the WOA method. The results attested to the effectiveness and dependability of the suggested WOA as a tool for directional overcurrent relay coordination. Additionally, it is determined that the WOA findings outperform numerous well-known and up-to-date methods mentioned in the literature.

For optimal coordination of overcurrent relays in distribution systems, the GA approach was utilized in the work of Bedekar et al. [23]. But, a new target function was used to convert the constrained optimization problem into an unconstrained one using a penalty

method, and during the mapping of binary variables to decimal values, TMS limits were used as variable limits due to relay operating time limits. In both examples, a minimum operating time of 0.2 s was assumed for each relay. The CTI value was taken as 0.57 s for Illustration I and 0.6 s for Illustration II. This shows that constraints can be created based on relay and breaker characteristics and system requirements, and the best coordination can be achieved. The algorithm has been tried on numerous systems and has consistently produced positive outcomes [23].

In their study, Khurshaid et al. [24], proposed hybrid metaheuristic algorithms based on WOA. The outcomes show that the suggested HWOA is a useful and trustworthy technique for directed ORC. The results obtained using HWOA suggest that it is better than WOA and many algorithms mentioned in the literature.

Seyyarer et al. [25], used SGA and LCA for ideal coordination of overcurrent relays in their study. In the study, TEIAS (Turkish Electricity Transmission Corporation) focused on the results of the ORC, which is commonly used in power systems, based on the inverse time setting in phase-to-phase short circuit faults.

In this study, the ORC problem is calculated using GA and WOA. A comparison of the results of these two algorithms with the previous LCA [25, 26] and SGA [25] studies is discussed. The findings show that WOA produces faster results compared to other algorithms.

2. MATERIAL AND METHOD

2.1. Saplings Growing up Algorithm

SGA is a meta-heuristic optimization algorithm designed by inspiring the growth process of saplings. This method places the parameters necessary for solving the problem on the saplings and performs operations on these saplings. The operators in the algorithm are designed to mimic the growth process of seedlings. The sapling planting operator is used to ensure the formation of saplings with a regular distribution in the search space. The branching operator is used in local search operations, while the matching operator is used to provide global search operations. In addition, the Vaccinating operator is used to facilitate information exchange between similar saplings [25-27].

In this way, candidate solutions in SGA are initially distributed regularly in the search space. Later on, both local and global search operations are performed and information exchange is made among similar solutions [27].

Since all of the seedlings in the solution space may be compared to plants, they must all be dispersed equally around the garden (Fig. 1).. Unless it is a problem with several criteria, each seedling represents a potential solution. All seedlings are solutions in a circumstance with several conditions. In order for seedlings to develop

more quickly, a farmer will want to put them evenly spaced apart (Fig. 1) [28].

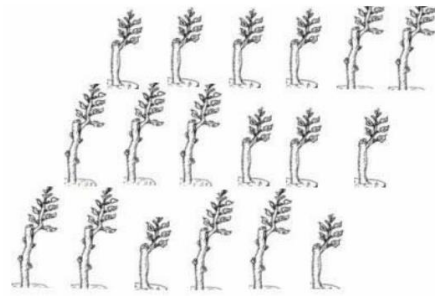


Figure 1. Evenly distributing saplings in the garden [28].

SGA can be implemented in two different ways; the pseudocode of the SGA-1 method is given in Algorithm 1, and the pseudocode of the SGA-2 method is given in Algorithm 2.

Algorithm 1: Pseudocode for SGA-1 [27]

1.	$t \leftarrow 0$ // Starting Time
2.	Saplings Planting ($P(t)$) // Initialization of Starting Population
3.	Fitness Evaluation ($P(t)$)
4.	while Termination Criteria not met do
5.	$P1(t) \leftarrow$ Mating ($P(t)$)
6.	$P2(t) \leftarrow$ Branching ($P(t)$)
7.	$P3(t) \leftarrow$ Vaccinating ($P(t)$)
8.	Fitness Evaluation ($P1(t) \cup P2(t) \cup P3(t)$)
9.	$P(t+1) \leftarrow$ Selection ($P1(t) \cup P2(t) \cup P3(t)$)
10.	$t \leftarrow t + 1$

Algorithm 2: Pseudocode for SGA-2 [27]

1.	$t \leftarrow 0$ // Starting Time
2.	Sapling Planting ($P(t)$) // Setting up the initial population
3.	Calculate Fitness Values ($P(t)$)
4.	while Termination Criteria not met do
5.	$P1(t) \leftarrow$ Mating ($P(t)$)
6.	Calculate Fitness Values ($P1(t)$)
7.	$Pm(t) \leftarrow$ Selection ($P1(t) \cup P(t)$)
8.	$P2(t) \leftarrow$ Branching ($Pm(t)$)
9.	Calculate Fitness Values ($P2(t)$)
10.	$Pb(t) \leftarrow$ Selection ($P2(t) \cup Pm(t)$)
11.	$P3(t) \leftarrow$ Vaccinating ($Pb(t)$)
12.	Calculate Fitness Values ($P3(t)$)
13.	$P(t+1) \leftarrow$ Selection ($P3(t) \cup Pb(t)$)
14.	$t \leftarrow t + 1$

2.2. League Championship Algorithm

Firstly, it is necessary to look at the terms related to team sports for LCA proposed by Kashan. Sports leagues are competitions where a certain number of teams compete and are usually focused on team sports. The championship can be challenged by considering different criteria. Teams try to have the best record by competing with other teams in a certain number of matches. In order to judge if a scenario is a victory, a loss, or a tie, a rigorous win-loss-tie system or a scoring system with a set amount of points is employed. In some cases, bonus points can also be given to teams that meet certain criteria [25, 26, 29].

Similar to other algorithms inspired by nature, LCA evolves a population of solutions in the direction of an ideal solution. Each team (person) in the framework of a sports league symbolizes a viable answer to the issue that has to be resolved and is made up of n players, which corresponds to the number of variables. Team i plays against team j , which is related to its playing strength (fitness) according to an artificial weekly league program. The teams involved play against one another for $S \times (L - 1)$ weeks, where S is the number of seasons and week t is specified. This is used to determine the winning or losing team. Each team reviews the outcomes of the previous week's matches to prepare for the upcoming game and utilizes this data to create its new team. The expected efficient team formation is guided by the formation of a team with better playing strength than the current best team [29, 30].

LCA involves three main concepts:

- How the league schedule will be created.
- How winning or losing teams will be determined.
- How a new team will be created.

A schematic flowchart such as the one in Figure 2 can be used to illustrate the fundamental phases of the League championship algorithm [31].

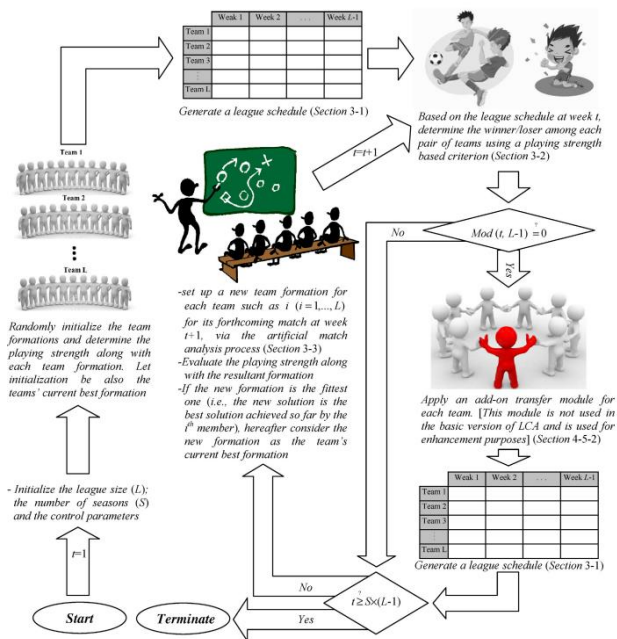


Figure 2. The league championship algorithm (LCA) flowchart [31].

Algorithm 3 provides the pseudocode for the LCA method.

Algorithm 3: Pseudocode for LCA [29]

1.	Set $t = 1$ and initialize the league size (L) and season count (S)
2.	Design a league schedule;
3.	Determine the playing strengths (function or fitness value) of each team by creating a population of L solutions. Permit each team's first formation to be the most effective one at the moment;
4.	While $t \leq S \cdot (L - 1)$
5.	According to the league schedule for week t , determine the winner/loser among each pair of teams using a criteria based on game strength;
6.	$t = t + 1$;
7.	For $i = 1$ to L
8.	Using the team i 's current best configuration and past occurrences, devise a new formation for the upcoming game. The resulting formation's playing strength should be evaluated;
9.	In the event that the new formation is superior (i.e., the outcome is the best outcome thus far for the i -th member of the population), accept the new formation as the team's current best configuration;
10.	End for
11.	If $\text{mod}(t, L - 1) = 0$
12.	Design a new league schedule;
13.	End if
14.	End while

2.3. Genetic Algorithm

GA's are a class of computer models that were influenced by evolution. These algorithms employ recombination operators to basic data structures that resemble chromosomes to encode the probable solution of a particular issue and preserve crucial information. GA usually starts with a population of chromosomes that were produced at random [32]. After that, these structures are assessed, and opportunities for reproduction are given to chromosomes that represent better answers to the goal problem, giving them a greater opportunity to "breed" than those that represent inferior solutions. A solution's "goodness" is often determined in relation to the present population [32].

There are four main concepts in GA. These are:

- Initialization
- Selection
- Reproduction
- Termination

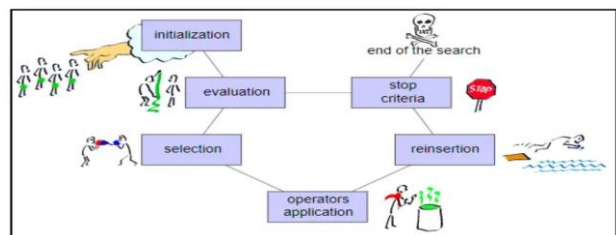


Figure 3. General scheme of GA [33].

Up till the termination condition is satisfied, this generational process is repeated [34]. Algorithm 4 contains the GA method's pseudocode.

Algorithm 4: Pseudocode for GA [34]

1.	Initialize $t = 1$. Produce N solutions randomly to create the initial population $P1$. Analyze the solutions in $P1$'s fitness values.
2.	Crossover: Create a child population Qt by following the steps below:
3.	Based on the fitness values, choose two Pt solutions, x and y .
4.	Create kids using the crossover operator, then include them in Qt .
5.	Mutation: Apply mutation with a predetermined mutation rate to each Qt solution.
6.	Fitness assignment: Based on each solution's goal function value and fitness standing, assign a fitness value to it.
7.	Selection: Based on their fitness values, choose N solutions from Qt , and copy them to $Pt + 1$.
8.	Stop the search and return the current population if the termination requirement is satisfied. Otherwise, increment t by one and go to Step 2.

2.4. Whale Optimization Algorithm

Seyedali Mirjalili and Andrew Lewis first presented WOA in 2016, an algorithm based on humpback whales' fishing strategies [35]. Humpback whales usually feed on flocks of small fish near the water surface, and when they approach they form air bubbles to keep the fish together. This allows them to approach the fish unnoticed [36]. Figure 1 depicts the humpback whales' fishing strategies.

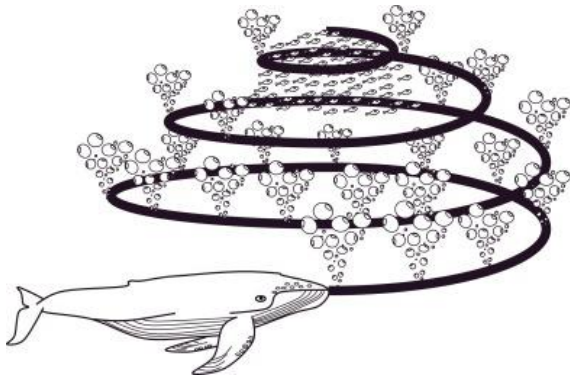


Figure 4. Hunting strategy of humpback whales [35].

In WOA, mathematical equations are created based on this hunting method. \vec{A} and \vec{C} are coefficient vectors, t is the current iteration, and X^* denotes the ideal solution vector. During each iteration, the value of a linearly decreases from 2 to 0, and r contains random vector variables between [0.1] [35].

There are three main concepts in WOA:

- Surrounding prey
- Bubble-net attack method (exploitation phase)
- Search for prey (exploration phase)

Algorithm 5 contains the WOA method's pseudocode.

Algorithm 5: Pseudocode of WOA [35]

1.	Determine the whales' starting population
2.	$Xi (i = 1, 2, \dots, n)$
3.	Determine each search agent's fitness.
4.	$X^* =$ Best-known search agent.
5.	$t = 0$
6.	while ($t <$ maximum number of iterations)
7.	for: All search agents.
8.	Update a, A, C, l , and p
9.	if ($p < 0.5$)
10.	if ($ A < 1$)
11.	else if ($ A \geq 1$)
12.	Choose a search agent at random (Xrand)
13.	Adjust the chosen agent's position.
14.	end if
15.	else if ($p \geq 0.5$)
16.	Update the position of the selected agent.
17.	end if
18.	end for
19.	Check if the selected agent goes outside the boundaries. If it does, give it the boundary values.
20.	Determine each search agent's fitness. Update X^* if a better solution is discovered.
21.	$t = t + 1$
22.	end while
23.	return X^*

2.5. Overcurrent Relay Coordination

Faults can occur in power systems due to various reasons, most of which are caused by the flow of current into the power system that exceeds the nominal level [30, 37]. One significant challenge that many power systems face is coordination problems. Either linear programming or nonlinear programming can be used to solve this issue. The pickup current settings in the linear coordination model are preset at values between the maximum load current and the minimum fault current, and optimization is accomplished by altering only the time dial. This model aims to prevent fault conditions that may occur in the power system, depending on the operating characteristics of the relays and system conditions. Depending on the properties of the relays, the nonlinear coordination model concurrently optimizes the time dial and pickup current settings. This model offers a more flexible approach and can more effectively prevent various fault conditions that may occur in the power system. However, the optimization of the nonlinear model can be more difficult and time-consuming [38].

Overcurrent relays operate in two types of modes, time-delayed and instantaneous. In our country, they are set to inverse time for phase-to-phase faults and to fixed time for phase-to-ground faults. These relays can provide protection in either forward or reverse direction depending on the power flow [6]. In this study, the settings of overcurrent relays used for the ORC in the TEIAS power system were investigated. In this system, coordination was based on inverse time settings to prevent phase-to-phase short-circuit (154 kV/OG 3-Phase Overcurrent) faults (Fig. 5). This coordination helps to prevent overcurrent faults that may occur in the system and reduce damage that may occur during system operation [26].

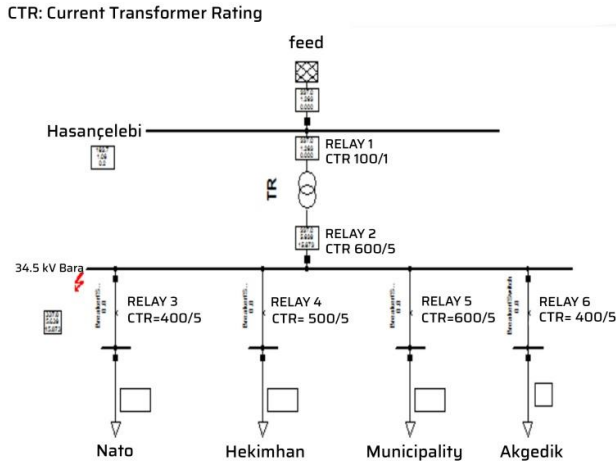


Figure 5. Example Transformer Substation Single Line update [25].

2.5.1. Formulation of overcurrent relay coordination problem

This study’s primary goal is to reduce the operation times of overcurrent relays. To achieve this goal, an optimization is carried out assuming that all relays have the same characteristic features. The findings of this study show that overcurrent relay running periods may be significantly reduced, making a substantial contribution to electrical system safety [26].

The objective function in the ORC is expressed as equation 1.

$$Objective\ Function = \min \sum_{i=1}^n (ti) . m \quad (1)$$

In this study, n represents the number of overcurrent relays in the power system, ti represents the operating time of each overcurrent relay, and m represents the probability of faults occurring in the power system. Considering phase-to-phase faults, the total minimum time of the relays is calculated based on the standard inverse-time characteristic. The characteristic equation used in this study is the standard inverse-time characteristic, expressed in equation 2 [26].

$$ti = \frac{0.14.td}{\left(\frac{Ikd}{Ip}\right)^{0.02}-1} \quad (2)$$

The value of Ikd in Equation 2 is constant and represents the short-circuit current value. The pickup current of the relay is represented by the value of Ip . Relay operation time is represented by ti , while operating characteristic values are represented by td . The constraints used in optimization can be expressed within an estimated range based on the values used in the TEIAS system. These are:

The value of Ikd for relay 1 is 1263A, and for relays 2, 3, 4, 5, and 6, it is 5639A.

Constraint 1: $ti_{min} \leq ti \leq ti_{max} = 1s \leq ti \leq 2.2s$

The first constraint specifies the time order of the six relays as $t6, t5, t4, t3 \leq t2 \leq t1$. It states that the time of Relay 1, $t1$, should be greater than the time of Relay 2, $t2$. Additionally, the time of Relay 2, $t2$, should be greater than the times of the other relays. However, the times of Relays 3, 4, 5, and 6 are not ordered among themselves. Only these relay values should be less than $t2$ and $t1$. $t1$ should be 0.3 seconds greater than $t2$, and $t2$ should be 0.3 seconds greater than the times of the other relays.

Constraint 2: $tdmin \leq td \leq tdmax (0.2 \leq td \leq 1)$

This constraint has been determined in accordance with the approach used by TEIAS in their system.

Constraint 3: This constraint concerns the starting times, therefore it includes Ip .

Relay 1	$117.152 \leq Ip \leq 128.65$
Relay 2	$523 \leq Ip \leq 575$
Relay 3	$400 \leq Ip \leq 420$
Relay 4	$500 \leq Ip \leq 510$
Relay 5	$600 \leq Ip \leq 610$
Relay 6	$400 \leq Ip \leq 420$

ti values will be calculated according to these constraints [26].

3. APPLICATIONS AND NUMERICAL RESULTS

Table 1 presents the results of SGA, LCA, GA, and WOA.

Table 1. Results of SGA, LCA, GA, and WOA

	Relay-1	Relay-2	Relay-3	Relay-4	Relay-5	Relay-6	
$T_i(s)$	SGA	1.617	1.311	1.005	1.005	1.005	1.005
	LCA	1.605	1.305	1.001	1.001	1	1.005
	GA	1.606	1.305	1.002	1	1	1.001
	WOA	1.602	1.301	1	1	1	1

The results of SGA and LCA for the relay coordination problem of the Hasançelebi substation, as well as the results of GA and WOA, are presented in tables in this section. The minimum ti values obtained with SGA, LCA, GA and WOA are depicted in Table 2.

Table 2. Comparison of Results of Methods.

Metho d	Total T_i (s)
SGA	6.948
LCA	6.917
GA	6.914
WOA	6.903

The minimum ti values obtained from these four methods are shown graphically in Table 2. The results obtained are very close to the lower limits in the given constraints. The WOA method has, nevertheless, taken less time to compute than the other algorithms.

4. CONCLUSION

In this study, the performance of four distinct algorithms—SGA, LCA, GA, and WOA—for resolving the ORC issue was examined. Each algorithm was run 1000 times. SGA examines both global and local search steps and works with a small number of input parameters without using additional functions. The high success rate is mainly due to the fact that the initial population is not randomly selected. LCA, on the other hand, produces successful results by performing a high number of iterations in a short time. Traditional optimization methods can be limited in finding the global optimum point and sometimes get stuck at a local optimum point. Compared to conventional single-point search methods, GA claims to use a multi-point search strategy to locate the global optimal point. GA provides successful results in taking large search spaces and finding optimal combinations and solutions.

WOA provides faster results compared to other algorithms. When compared to other algorithms, WOA has a high search capacity and convergence speed, making it unique in its ability to use search agents to locate the best answer. The case studies in this paper are also analyzed using several optimization algorithms as demonstrated in the literature, and the suggested WOA algorithm produces a better optimum solution than the alternatives. Comparing the output values obtained by solving other problems using the four optimization algorithms included in this study is among the planned studies.

REFERENCES

- [1] Chong EK, Żak SH. Gradient methods. An Introduction to Optimization (Fourth ed.). Hoboken: Wiley. 2013:131-60.
- [2] Govan A. Introduction to optimization. In North Carolina State University, SAMSI NDHS, Undergraduate workshop 2006 (Vol. 3, p. 6).
- [3] Aydın A. Metasezgisel yöntemlerle uçak çizelgeleme problemi optimizasyonu [Doctoral dissertation]. Turkey: Marmara University; 2009.
- [4] Nevzat ON. Trends in Power System Protection Researches: A Review of Fundamental Relays. *Balkan Journal of Electrical and Computer Engineering*. 2018 Oct 10;6(4):247-56.
- [5] Zeineldin HH, Sharaf HM, Ibrahim DK, Abou El-Zahab EE. Optimal protection coordination for meshed distribution systems with DG using dual setting directional over-current relays. *IEEE transactions on smart grid*. 2014 Sep 24;6(1):115-23.
- [6] Akdağ O, Yeroğlu C. Güç sistemlerinde aşırı akım koruma koordinasyon modelinin oluşturulması, benzetimi ve optimizasyonu. *Erzincan University Journal of Science and Technology*. 2019 Mar 3;12(1):202-14.
- [7] Ortmeyer TH, Hiyama T, Salehfar H. Power quality effects of distribution system faults. *International Journal of Electrical Power & Energy Systems*. 1996 Jun 1;18(5):323-9.
- [8] Zeineldin H, El-Saadany EF, Salama MA. Optimal coordination of directional overcurrent relay coordination. In *IEEE Power Engineering Society General Meeting, 2005* 2005 Jun 16 (pp. 1101-1106). IEEE.
- [9] So CW, Li KK. Overcurrent relay coordination by evolutionary programming. *Electric power systems research*. 2000 Feb 1;53(2):83-90.
- [10] Meskin M, Domijan A, Grinberg I. Optimal coordination of overcurrent relays in the interconnected power systems using break points. *Electric Power Systems Research*. 2015 Oct 1;127:53-63.
- [11] Acharya D, Das DK. Güç dağıtım sisteminde optimum aşırı akım röle koordinasyonu için etkili bir optimizasyon algoritması. *Uygulamalarla uzmanlık sistemleri*. 1 Ağustos 2022;199:116858.
- [12] Atsever MB, Hocaoğlu MH. Aşırı Akım Röle Koordinasyonu için Bozkurt Algoritmasının Kapsamlı Performans Analizi. *Türk Mühendislik Araştırma ve Eğitimi Dergisi*. 2022 Nov 11;1(2):52-61.
- [13] Noghahi AS, Sadeh J, Mashhadi HR. Considering different network topologies in optimal overcurrent relay coordination using a hybrid GA. *IEEE Transactions on Power Delivery*. 2009 Sep 22;24(4):1857-63.
- [14] Soman SA. Lectures on power system protection. NPTEL, [online] Available: www.cdeep.iitb.ac.in. 2010.
- [15] Uthitsunthorn D, Kulworawanichpong T. Optimal overcurrent relay coordination using genetic algorithms. In *2010 international conference on advances in energy engineering 2010 Jun 19* (pp. 162-165). IEEE.
- [16] Gokhale SS, Kale VS. An application of a tent map initiated Chaotic Firefly algorithm for optimal overcurrent relay coordination. *International Journal of Electrical Power & Energy Systems*. 2016 Jun 1;78:336-42.
- [17] Razavi F, Abyaneh HA, Al-Dabbagh M, Mohammadi R, Torkaman H. A new comprehensive genetic algorithm method for optimal overcurrent relays coordination. *Electric Power Systems Research*. 2008 Apr 1;78(4):713-20.
- [18] Alam MN, Das B, Pant V. A comparative study of metaheuristic optimization approaches for directional overcurrent relays coordination. *Electric Power Systems Research*. 2015 Nov 1;128:39-52.
- [19] Gaikwad AD, Kavita S. Improved League Championship Algorithm (ILCA) for Load Balancing in Cloud Computing. *International Journal of Next-Generation Computing*. 13.5 2022.
- [20] Langazane SN, Akshay KS. Effects of particle swarm optimization and genetic algorithm control parameters on overcurrent relay selectivity and speed. *IEEE Access* 10. 2022: 4550-4567.
- [21] Rizal AS, Umam MN, Syaputra AM, Gemayel A. Study of overcurrent relays coordination optimization based on genetic algorithms. In *2020 international conference on technology and policy*

- in energy and electric power (ICT-PEP) IEEE. 2020 Sep: 100-103.
- [22] Wadood A, Khurshaid T, Farkoush SG, Yu J, Kim CH, Rhee SB. Nature-inspired whale optimization algorithm for optimal coordination of directional overcurrent relays in power systems. *Energies*. 2019.
- [23] Bedekar PP, Bhide SR, Kale VS. Optimum coordination of overcurrent relays in distribution system using genetic algorithm. In 2009 International Conference on Power Systems 2009 Dec 27 (pp. 1-6). IEEE.
- [24] Khurshaid T, Wadood A, Farkoush SG, Yu J, Kim CH, Rhee SB. An improved optimal solution for the directional overcurrent relays coordination using hybridized whale optimization algorithm in complex power systems. *IEEE Access*. 2019 Jul 1;7:90418-35.
- [25] Seyyarer E, Cengiz HA, Ayata F, Uçkan T, Karci A. Fidan Gelişim ve Lig Şampiyonluk Algoritmaları Kullanarak Aşırı-Akım Rölelerin Optimum Koordinasyonu. *Computer Science*. 2018 Sep 9;3(2):1-4.
- [26] Seyyarer A, Akdağ O, Hark C, Karci A, Yeroğlu C. Overcurrent relay coordination of 154/34, 5 kV Hasaңcelebi substation by league championship algorithm. In 2017 International Artificial Intelligence and Data Processing Symposium (IDAP) 2017 Sep 16 (pp. 1-6). IEEE.
- [27] Karci A. Natural inspired computational intelligence method: saplings growing up algorithm. In 2007 IEEE International Conference on Computational Cybernetics 2007 Oct 19 (pp. 221-226). IEEE.
- [28] Karci A, Alatas B. Thinking capability of saplings growing up algorithm. International conference on intelligent data engineering and automated learning. Berlin, Heidelberg: Springer Berlin Heidelberg, 2006.
- [29] Kashan AH. League championship algorithm: a new algorithm for numerical function optimization. In 2009 international conference of soft computing and pattern recognition 2009 Dec 4 (pp. 43-48). IEEE.
- [30] Wangchamhan T, Chiewchanwattana S, Sunat K. Efficient algorithms based on the k-means and Chaotic League Championship Algorithm for numeric, categorical, and mixed-type data clustering. *Expert Systems with Applications*. 2017 Dec 30;90:146-67.
- [31] Kashan AH. League Championship Algorithm (LCA): An algorithm for global optimization inspired by sport championships. *Applied Soft Computing* 16. 2014: 171-200.
- [32] Mathew TV. Genetic algorithm. Report submitted at IIT Bombay. 2012:53.
- [33] Keshav R. Sharma [Internet]. 2022 [Cited 2023 Sep 21]. Available from: <https://vidyasheela.com/post/gentle-introduction-to-genetic-algorithm>
- [34] Kumar M, Husain DM, Upreti N, Gupta D. Genetic algorithm: Review and application. Available at SSRN 3529843. 2010 Dec 1.
- [35] Mirjalili S, Lewis A. The whale optimization algorithm. *Advances in engineering software*. 2016 May 1;95:51-67.
- [36] Goldbogen JA, Friedlaender AS, Calambokidis J, Mckenna MF, Simon M, Nowacek DP. Integrative approaches to the study of baleen whale diving behavior, feeding performance, and foraging ecology. *BioScience*. 2013 Feb 1;63(2):90-100.
- [37] Karababa S. Harmoniklerin dijital aşırı akım röleleri üzerine etkisinin incelenmesi [Master's dissertation]. Turkey: Yıldız Technical University; 2008.
- [38] Amraee T. Coordination of directional overcurrent relays using seeker algorithm. *IEEE Transactions on Power Delivery*. 2012 Apr 10;27(3):1415-22.

Determination of Harm Forms in Grain Fields of the Genus *Platycleis* Fieber, 1853 (Orthoptera: Tettigoniidae) in Güroymak, Bitlis, Türkiye

Mustafa İLÇİN^{1*} 

¹ Bingöl University, Agriculture Faculty, Plant of Protection Department, Bingöl, Türkiye
Mustafa İLÇİN ORCID No: 0000-0002-2542-9503

*Corresponding author: milcin@bingol.edu.tr

(Received: 24.05.2023, Accepted: 25.10.2023, Online Publication: 28.12.2023)

Keywords
Platycleis,
Agriculture,
Harmful,
Biological
control

Abstract: In this study, species belonging to the genus: *Platycleis* Fieber 1853 which have shown large population increases in agricultural lands and especially in cereal products in recent years, have been identified and species identifications have been made. Species identified are *Platycleis affinis* Fieber, 1853, *P. intermedia* Serville, 1838 and *P. escaleari escaleari* Bolivar, 1899. These species reach a density of 30-50 per m² in the lands where they are found, and it has been determined that they damage plant products. Although the numbers reached by the species could not reach a herd-like reproduction, it was determined that they caused damage after a certain density. However, it has been observed that they cause economic loss in products. It has been determined that these species increase the damage size by intensifying in certain periods on the crops they damage, wild wheat, wheat, barley, and corn plants. In-plant protection against these pests, preventive measures within the framework of integrated pest management principles, cultural control practices, and the use of biological control agents at the focal point show significant results that appear to have been taken.

33

Platycleis Fieber, 1853 cinsine ait bazı türlerin tahıl arazilerinde zarar biçimlerinin belirlenmesi, Güroymak, Bitlis, Türkiye

Anahtar Kelimeler
Platycleis,
Tarım,
Zararlı,
Biyolojik
mücadele

Öz: Bu çalışmada, son yıllarda başta tahıl ürünleri olmak üzere tarım arazilerinde büyük popülasyon artışları gösteren ve zarara neden olan *Platycleis* Fieber, 1853 cinsine ait türler tespit edilerek teşhisleri yapılmıştır. Teşhisi yapılan taksonlar; *Platycleis affinis*, Fieber, 1853; *P. intermedia* Serville, 1838 ve *P. escaleari escaleari* Bolivar, 1899' dir. Bu türlerin buldukları arazilerde m²'de 30-50 adet arasında bir yoğunluğa ulaşmakla birlikte bitkisel ürünlere zarar verdikleri tespit edilmiştir. Türlerin ulaştıkları sayılar sürü şeklinde bir çoğalmaya ulaşmasa da bu yoğunluktan sonra zarar oluşturdukları belirlenmiştir. Ayrıca ürünlerde ekonomik kayba neden oldukları görülmüştür. Bu türlerin zarar verdikleri ürünler; buğdaygillerden yabani buğday, buğday, arpa ve mısır'dır. Bu çalışma ile bu türlerin ürünlerin belli dönemlerinde bitkiler üzerinde yoğunlaşarak zarar boyutunu artırdıkları tespit edilmiştir. Bu zararlılara karşı bitki korumada, entegre zararlı yönetimi ilkeleri çerçevesinde koruyucu önlemler, kültürel mücadele uygulamaları ve odak noktada biyolojik mücadele ajanlarının kullanımının sonucunda önemli sonuçlar elde edildiği, daha hızlı sonuç alınmak istenirse son uygulamalar olarak çeşitli bitkisel kaynaklı ekstraktlar ile biyopestisitlerin kullanılmasıyla da zararlılar ile mücadelede etkin sonuçlar alındığı görülmektedir.

1. INTRODUCTION

Insects, which constitute a large part of the biological diversity on earth, are an important group in the ecological and economic lives of humans and other living things. Members of this group are found almost everywhere from the equator to the poles, from deserts to forests, from high

mountain areas to low plains, from swamps to caves, from cold water sources to agricultural areas, and from our homes to hot springs [1].

Insects are a class with very different characteristics from all living. The species has been always dominant in systematics and deserves to be a superior living group

with its population characteristics and various other adaptation differences. Grasshoppers, which stand out with their many features, are in the Orthoptera order and show different characteristics from other orders among insects. Grasshoppers are an essential component of both healthy and degraded grassland ecosystems. Many of these insects are found in natural and anthropogenic habitats (pastures, wetlands, agricultural fields, lawns, etc.). Grasshoppers stimulate plant growth, participate in the nutrient cycle, and play an important role in food chains [2,3,4,5,6]. Some locusts are proposed as ecological indicators of ecosystem qualities and the effectiveness of ecological networks [7]. On the other hand, when their populations reach catastrophic proportions, locusts are among farmers' most devastating enemies. Locust epidemics (infestation); occur with *Schistocerca gregaria* (Forskål, 1775), *Nomadacris septemfasciata* (Serville, 1838), *Locusta migratoria* Linnaeus, 1758, *Calliptamus italicus* (Linnaeus, 1758) and *Docostaurus maroccanus* (Thunberg, 1815). Locusts continue to occur in abundance on all continents except Antarctica, affecting the livelihoods of one in ten people in the world. Today, locust outbreaks are decreasing in frequency and size with better control and implementation of preventive strategies [8,9]. However, the invasions of the herds continued in certain years. During the 2003–2005 outbreak of the Desert locust *S. gregaria* in Africa, more than eight million people experienced crop loss of around 80% to 100% [10]. Broad-spectrum neurotoxins have been used on a total of 13 million hectares in 22 countries on three continents to combat locust swarms. Such transcontinental operation, including food aid for the infested population, has cost the world community more than half a billion dollars [1].

The spawning period of grasshoppers is 10 days, and their number varies between 80-180 individuals. They reach adulthood in about 6-7 weeks. The most effective factor in the formation of grasshoppers is temperature. While the temperature is between 25-35 °C under optimum conditions, it can sometimes rise to 35 °C. Annual total locust loss is between 5% and 65% for various reasons. About 10% of these are habitat-based, 3-4% cannot spawn, 40% become prey, and 10% are mold, bacteria, etc. shows features. The number of grasshoppers increases 400 times during the summer months. It is reported that they destroyed the food of 35 thousand people in 1 day and traveled 150 km. It has been reported that the number of locusts in 1 km² is between 40-80 million [11].

2. MATERIAL AND METHOD

In this study, the visual inspection method, gauze trapping method and pitfall trap method were used to obtain specimens. In the visual control method, by going diagonally in the area where the survey was made, the above-ground organs of the plant in the agricultural lands were visually examined, and samples were collected from the nymphs and adults of the species belonging to the order Orthoptera. In the pitfall trap method, before the harmful species in the nymph stage are transformed into winged form, wide and deep pits are opened in front of

them in the field, and the sample species are ensured to fall into these pits and are caught in this way and taken into insecticide boxes. This method, within the framework of plant protection control methods, is an important application in controlling the population numbers of winged grasshoppers until the 2nd nymph stage and in all life stages of wingless forms, and in neutralizing harmful species. The gauze trapping method is applied as a method that allows catching winged grasshoppers and obtaining samples in this way by using a 30x45 cm circle and a device made of tulle wrapped around this circle with a handle attached to it. Samples of this study were collected between April and September of 2019-2021. The study was carried out over two years and 12 months. Areas where the land is densely built; It was ensured that the sample species were obtained collected and analyzed under laboratory conditions in the wheat fields located in the Güroymak district and rural areas between the of Bitlis and Muş provinces. [Figure 4].

3. RESULTS

Classis: Insecta

Ordo: Orthoptera

Subordo: Ensifera

Family: Tettigoniidae Krauss, 1902

Genus: *Platypleis* Fieber 1853

The structure of the head is generally small and the pronotum is flat. Wings specifically front ones usually mottled, and hind wings are transparent and plain. The ovipositor is in an upward direction. The first part of the titulators is spineless (Figure 1). Carinas are usually prominent in metazoa and the significant difference between species is determined by the wing structure and color. The average length of the ovipositor is between 9-17 mm [Figure 2,3] [12,13].



Figure 1. *Platypleis affinis* Fieber 1853 [14].



Figure 2. Figure 2. *Platypleis affinis* Fieber 1853 [15].



Figure 3. Figure 4. *P. escalerai escalerai* Bolivar, 1899 [16].



Figure 4. Figure 1. Research area in Bitlis-Güroymak.

4. DISCUSSION AND CONCLUSION

Genus *Platypleis* is the structure of the head generally small and the pronotum flat. The wings, specifically the front ones, are usually spotted, while the hind wings are transparent and plain. The ovipositor is pointed upwards. The first part of the titillators is spineless. Carinae are generally evident in metazoans, and the significant differences between species are determined by the wing structure and color. The average length of the ovipositor is between 9-17 mm. Grasshoppers appear as a systematic category that causes the most damage in agricultural production within the class of insects. With its biological characteristics and adaptation abilities to climatic changes, it can spread to very wide areas. It can reach very large populations, especially due to its herd-forming abilities, and can destroy many other plant products, especially cultivated plants, by living and acting together. It has been understood that the increase in the reproductive capacity of grasshoppers depending on the developmental stages is mainly because of atmospheric events, especially the increase in temperature and precipitation are the determining factors in this situation. It is seen that drought conditions experienced in certain periods can also lead to an increase or decrease in grasshopper populations. It should not be forgotten that swarm movements of locusts threaten the lives of many people and have increasing importance in terms of food security. It has been determined that when they form a herd, they consume enough food for thousands of people in one day, and they move very fast and travel very long distances. Taking precautions against locusts within the framework of scientific methods, applying warning and monitoring systems effectively, and timely implementing control strategies-methods in plant protection are seen as inevitable. Some of the natural enemies of locusts have undertaken certain tasks in biological control. Certain bird species in nature are among the most important of these creatures. It is known that there are partridge, crow, stork,

starling, and goldfinch species that gather in flocks to reduce the species population of grasshoppers, especially during the nymph period. It has been determined that the birds known as starlings among the people seriously affect the grasshopper population in a flock and their harmful potential is extremely reduced. Several Orthoptera species were identified as primary pests, and their populations were found to be under pressure from their natural enemies. By recognizing and managing these natural enemies very well, it will be ensured that residue problems do not occur without the need for chemical control. As a result, ensuring the continuity of ecological balance, protecting natural resources, and preventing them from being damaged can be achieved with these measures.

Acknowledgement

I would like to thank my student Şakir YILDIZ for his support in collecting the samples in this study.

REFERENCES

- [1] FAO, 2020. Food and Agriculture Organization of the United Nations, Desert Locust Crisis, Appeal Rapid Response and Anticipatory Action in the Greater Horn of Africa.
- [2] Stebaev, I. V., 1972. Periodic changes in the ecological distribution of grasshoppers in the temperate and the extreme continental steppe regions, and their importance for the local ecosystems,” in Proceedings of the International Study Conference on the Current and Future Problems of Acridology, pp. 207–213, Centre for Overseas Pest Research, London, UK.
- [3] Hewitt, G. B. and Onsager, J. A., 1982. A method for forecasting potential losses from grasshopper feeding on northern mixed prairie forages,” *Journal of Range Management*, vol. 35, pp. 53–57.
- [4] Olfert, O. O. and M. K. Mukerji, 1983. Effects of acute simulated and acute grasshopper (Orthoptera: Acrididae) damage on growth rates and yield in spring wheat (*Triticum aestivum*),” *The Canadian Entomologist*, vol. 115, no. 6, pp. 629–639.
- [5] Sergeev, M. G., 2000. Zonal-landscape distribution of Orthoptera zoomass in Middle Region of the USSR,” *Geographia in Prirodnyje Resursy*, no. 2, pp. 89–92, Russian.
- [6] Lockwood, J. A., Latchininsky, A. V. and Sergeev, M. G., 2000. Kluwer Academic Publishers, Eds., pp. 7–30, Dordrecht, Netherlands.
- [7] Bazelet, C. S., 2011. Grasshopper bioindicators of effective large-scale ecological networks, Ph.D. Dissertation, Department of Conservation Ecology and Entomology, Stellenbosch University, South Africa.
- [8] Magor, J. I., Lecoq, M. and Hunter, D. M., 2008. Preventive control and Desert Locust plagues,” *Crop Protection*, vol. 27, no. 12, pp. 1527–1533.
- [9] Sword, G. A., Lecoq, M. and Simpson, S. J., 2010. Phase polyphenism and preventative locust management, *Journal of Insect Physiology*, vol. 56, no. 8, pp. 949–957.

- [10] Brader, L., Djibo, H. and Faye, F. G., 2005. Towards a More Effective Response to Desert Locusts and Their Impacts on Food Insecurity, Livelihoods and Poverty. Independent Multilateral Evaluation of the 2003–2005 Desert Locust Campaign, FAO, Rome, Italy.
- [11] Gullan, P. J. Cranston P.S. 2012. The Insect an Outline of Entomology, A. John Wiley and Sons, Ltd. Publication.
- [12] İlçin, M., 2015 “Batman İli Ekili Alanlarda Bulunan Orthoptera:Insecta Faunasının Araştırılması ve Tarım Alanlarında Zarar Oluşturabilecek Türlerin Belirlenmesi”(Doktora Tezi) Dicle Üniversite-si, Fen Bilimleri Enstitüsü, Diyarbakır, pp. 186.
- [13] Çiplak, B., Heller, K-G. Demirsoy, A., 2002. Review and key to species of Platycleis from Turkey (Orthoptera:Tettigoniidae) with descriptions of Yalvaciana subgen. and two new species, Journal of Natural History, 2002, 36, 197–236.
- [14] https://commons.wikimedia.org/wiki/File:Platycleis_affinis_%28SainteRadegonde%29_23082014_01.jpg
- [15] <https://biodiv.cevennes-parcnational.fr/espece/65705>
- [16] <http://orthoptera.speciesfile.org/Common/basic/ShowImage.aspx?TaxonNameID=1142535&ImageID=142642>

Numerical Analysis of Different Slit-Check Dams

Erdinç İKİNCİOĞULLARI^{1*}, Muhammet Emin EMİROĞLU²

¹ Bingöl University, Engineering and Architecture Faculty, Civil Engineering Department, Bingöl, Türkiye

² Fırat University, Engineering Faculty, Civil Engineering Department, Elazığ, Türkiye

Erdinç İKİNCİOĞULLARI ORCID No: 0000-0003-2518-980X

Muhammet Emin EMİROĞLU ORCID No: 0000-0002-3603-0274

*Corresponding author: eikinciogullari@bingol.edu.tr

(Received: 3.10.2023, Accepted: 5.11.2023, Online Publication: 28.12.2023)

Keywords

Slit check dam,
OpenFOAM,
Horizontal
openings,
Vertical openings,
Angled openings,
CFD

Abstract: Check dam designs have attracted attention recently due to the clogging of classical check dam structures with sediment and wooden material carried during the flood quickly. These structures regulate flow characteristics and debris flow. However, until now, the impacts of these structures on flow characteristics have received little attention in the literature. Therefore, it is necessary to develop new models to increase these structures' trapping capacity or extend the clogging time. In this study, the flow characteristics of check dams with horizontal, vertical, and angled openings were numerically analyzed for two-phase (water and air) flow. The numerical model was validated using experimental results in the literature. For the study in which twelve analyses were performed, four different check dam models (i.e., check dam with the classical, the narrow horizontal opening, the vertical openings, and angled openings) and three different unit flows (0.04, 0.03, and 0.02 m³ s⁻¹ m⁻¹) were used in the analysis. The open-source software OpenFOAM and the k- ω SST turbulence model were used for the numerical analysis using the Computational Fluid Dynamics (CFD) method. At maximum unit flow, the highest energy dissipation rate among slit check dam models was seen in Model-3, which has vertical openings. At minimum unit flow, the highest energy dissipation rate was attained in Model 2, which has horizontal openings. There is no difference in the energy dissipation rate at low unit flows whether the openings are positioned vertically or angled; nevertheless, the vertical model (Model-3) is observed to be more efficient at maximum unit flow.

Farklı Geçirgen Kontrol Barajlarının Sayısal Analizi

Anahtar

Kelimeler

Geçirgen kontrol
barajı,
OpenFOAM,
Yatay açıklıklı
kontrol barajı,
Düşey açıklıklı
kontrol barajı,
Açılı açıklıklı
kontrol barajı,
HAD

Öz: Klasik kontrol barajları, taşkın sırasında taşınan tortu ve ahşap malzeme sebebiyle kısa sürede tıkanmaktadır. Bu nedenle klasik kontrol barajların tutma kapasitesini artırmak veya tıkanma süresini uzatmak için yeni modellerin geliştirilmesi gerekmektedir. Araştırmacılar, son yıllarda alternatif modeller üzerinde çalışmışlardır. Ancak bugüne kadar bu yapıların akış üzerindeki etkileri literatürde çok az ilgi görmüştür. Bu çalışmada; yatay, dikey ve açılı açıklıklı kontrol barajların akış özellikleri iki fazlı (su ve hava) akış için sayısal olarak incelenmiştir. Sayısal modelde kullanılan sınır şartları ve çözüm ağı, literatürdeki deneysel sonuçlar kullanılarak doğrulanmıştır. Toplamda 12 analizin gerçekleştirildiği bu çalışma için dört farklı baraj modeli (klasik, yatay açıklıklı, dikey açıklıklı ve açılı açıklıklı) ve üç farklı birim debi (0,04; 0,03 ve 0,02 m³ s⁻¹ m⁻¹) kullanılmıştır. Sayısal analizler için açık kaynak kodlu OpenFOAM yazılımı ve k- ω SST türbülans modeli kullanılmıştır. Elde edilen sonuçlara göre, geçirgen kontrol baraj modelleri arasında en yüksek enerji sönmüleme oranı maksimum birim debide, düşey açıklıklı model olan Model-3'te gözlenirken; minimum birim debide, yatay açıklıklı model olan Model-2'de gözlenmiştir. Açıklıkların dikey veya açılı konumlandırılmasının düşük birim debide enerji sönmüleme oranına bir etkisi olmazken, maksimum birim debide dikey modelin (Model-3) daha verimli olduğu gözlenmiştir.

1. INTRODUCTION

Global warming is an issue that has attracted the world's attention in recent years. While drought is observed in some regions due to climate change, loss of life and property occurs due to excessive rainfall in some regions. In recent years, researchers have made suggestions to reduce the impact of these losses by making regional risk assessments [1–3]. The clogging of the bridge and culvert, frequently seen especially in flood regions, increases the losses. For this reason, check dams are used to keep these transported materials.

Check dams are important water structures commonly used to prevent soil and water loss in stream beds or sloping lands to control water flow (Fig. 1a). These structures are designed to prevent erosion and ensure the sustainability of agricultural lands and can be constructed from various materials such as stone, logs, bricks, and cement. The history of the check dams is based on the information that the first example was made of wood for flood protection in Italy in 1537, and their number increased in the following years [4]. These structures are also known as control dams and offer various ecological benefits, such as improving water quality, recharge of groundwater, and development of coastal ecosystems [4].

Check dams cause a decrease in the channel slope and flow rate of the sediment accumulated during the flood, thus increasing the flow depth [5]. This situation can cause significant problems when the natural material in the stream bed and the woody material around the canal during floods cause blockages [6]. Conventional control structures, especially those built of stone walls, may be poor at providing adequate resistance to the dynamic effects of debris flows and can cause damage in the downstream region [7]. Therefore, permeable slopes have been investigated to control the transport of sediment and woody material more effectively [8,9].

Conventional control dams, especially those built of stone walls, may be poor at providing adequate resistance to the dynamic effects of debris flows, and the downstream region may suffer due to the "hungry water effect" [7]. According to the studies, approximately 65% of such structures are destroyed due to the increase in the bed depth of the sediment [10,11]. For this reason, experimental studies have been carried out using slit check dam to control the transport of sediment and woody material [8,9]. The use of slit check dams has the potential to prevent the accumulation of sediment and woody material and offers a more effective solution in stream management. These experimental studies provide important guidance in the design and implementation processes to improve weirs' performance and effectively control sediment and woody material transport.

Slit check dams (see Fig. 1b) protect the ecosystem balance and prevent downstream scours by keeping the sediment and wood materials transported during the flood under control [12]. These structures keep the sedimentary material behind the dam, thanks to the

openings that allow the passage of sediment of a certain diameter (Fig. 1b). This situation helps to reduce the possible damages of flood by preventing the clogging of downstream structures such as bridges and culverts [8]. In addition, thanks to the self-cleaning feature of the slit dams [13], it contributes to the cleaning of the accumulated sediment over time. However, due to the sediment accumulating in their gratings during a severe flood, these structures may also become clogged and inoperable, like classical dams [12]. For this reason, these structures should be used and developed more effectively to minimize the possible damages, especially in flood areas. Researches and experimental studies provide important clues for increasing the performance of slit check dams and minimizing the flood effect. In this way, it aims to use water structures as more durable, efficient structures and maintain the ecosystem balance.

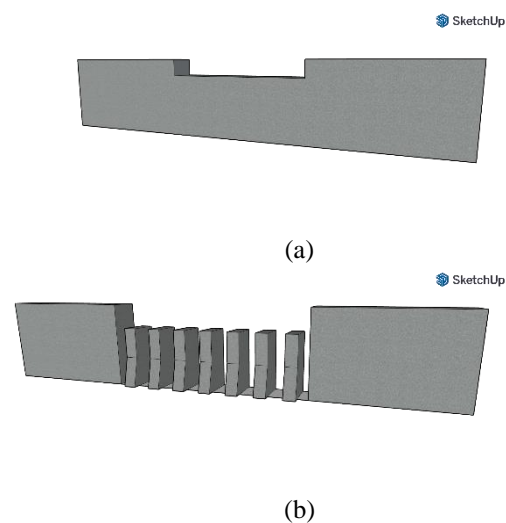


Figure 1. a) Classical check dam, b) Slit check dam

Literature studies reveal that many models related to slit check dams have been proposed, but no effective results have been reached yet [14]. The study by Piton and Recking [14] provides a comprehensive review of the design of slit check dams and discusses the applications of these structures in flood hazard mitigation. They introduced the general context and functions of these structures, and the shape of the openings and hydraulic design criteria for different types are summarized in detail. In addition, the dynamics of sediment deposition were also studied in depth. As a result of their study, the researchers emphasized that the behavior of slit check dams can be significantly affected by the presence of woody material. That is, the presence of woody material can significantly affect the performance and effectiveness of structures. Therefore, the containment and management of woody material is essential to operate slit check dams successfully. In another study prepared by the same researchers [15], models used to control residual materials were examined. They explained how slit check dams are designed and used to hold the sedimentary material effectively. Different design models and structures of slit check dams offer alternative solutions for residual material control, and the need for further research and development in this regard

has been emphasized. Aydin et al. [16] worked on the hydraulics of the slit-check dam for subcritical flow regimes. The hydraulic characteristics of slit-check dams were studied using the numerical and experimental determination of the flow's energy dissipation performances and water surface profiles. According to the findings, a slit-check dam with blocks causes hydraulic jumps and important energy losses in a subcritical flow. These findings demonstrated the effectiveness of slit-check dams with blocks for debris breaking, energy dissipation, and flow management in flood and normal flow situations.

As seen in the literature review, many researchers have conducted different studies on slit check dams in recent years and emphasized that more studies are needed to eliminate the uncertainties on this subject. In this study, the flow characteristics of the check dams for four different geometries were numerically investigated for water flow condition. It is aimed to provide preliminary information for future studies by comparing the results obtained.

2. METHODOLOGY

In this study, the flow characteristics of classical and slit check dams with different openings were compared numerically. The analyses were carried out for a channel with a length of 4.80 m, a width of 0.52 m, and a height of 0.75 m. The check dam was located 1.50 m away from the upstream part of the channel, and a 0.10 m high threshold was added to the end of the channel (Fig. 2). The height of the dams is 0.50 m and their thickness is 0.05 m.

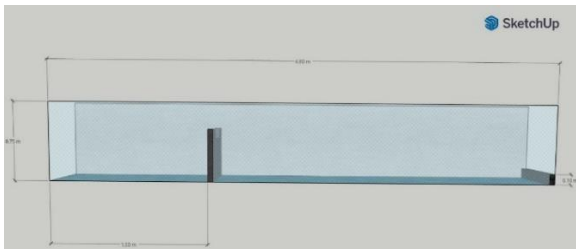


Figure 2. Longitudinal section of the channel

Within the scope of the study, a total of twelve analyses were conducted for three different unit flow rates ($0.04-0.03-0.02 \text{ m}^3 \text{ s}^{-1} \text{ m}^{-1}$) and four check dam models. One of these models is the classic check dam, while the other models are designed using openings placed in different directions (horizontal, vertical, and angled) on the body of the classic check dam (Fig. 3). The dimensions of these openings are the same, and the ratio of the area of the filled part to the area of the empty part is equal for all slit check dams.

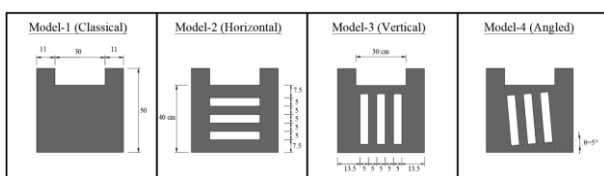


Figure 3. Check dam models considered in the study

Numerical analyses were carried out using the interFoam solver, which can solve two-phase (water and air) flow in the OpenFOAM software (v7). Previous studies [17,18] were validated mesh domain and boundary conditions for stepped spillway using the snappyHexMesh mesh generation method and the $k-\omega$ SST turbulence method (Table 1). In this study, the maximum cell dimensions are 0.05 m, and the minimum cell dimensions are gradually reduced to 0.001 m, as in the mentioned studies [17,18] (Fig. 4). Analyses to determine the solution time were continued for 80 seconds. Although the flow reached a steady state after the 30th second, all analyses were continued for an additional 50 seconds (Fig. 5).

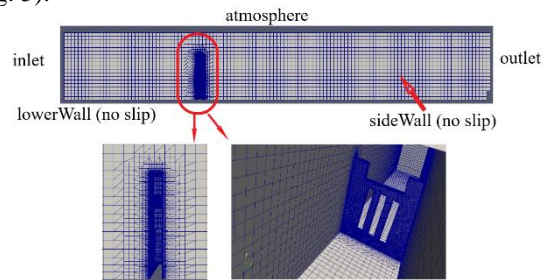


Figure 4. Mesh domain and boundary conditions

Table 1. Parameters in the boundary conditions [17,18]

	<i>inlet</i>	<i>outlet</i>	<i>lowerWall-sideWall</i>	<i>atmosphere</i>
<i>U</i>	variableHeightFlowRateInletVelocity	zeroGradient	noSlip	pressureInletOutletVelocity
<i>omega</i>	fixedValue	inletOutlet	omegaWallFunction	inletOutlet
<i>k</i>	fixedValue	inletOutlet	kqRWallFunction	inletOutlet
<i>nut</i>	calculated	calculated	nutkWallFunction	calculated
<i>p_rgh</i>	zeroGradient	zeroGradient	fixedFluxPressure	totalPressure
<i>Alpha.water</i>	variableHeightFlowRate	zeroGradient	zeroGradient	inletOutlet

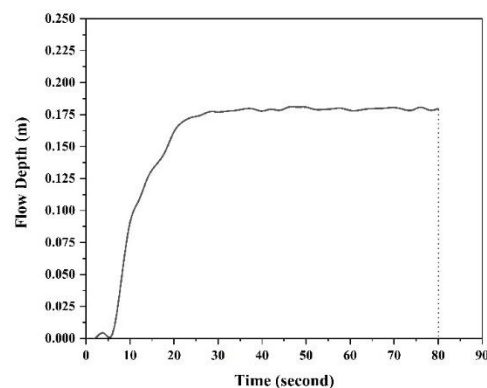


Figure 5. Variation of flow depth throughout the analysis time

3. RESULTS AND DISCUSSION

According to the results, an increase in water heights is observed as the unit flow increases. Due to the increased momentum, the hydraulic jump's length also increases in all models. Although the water height upstream of the classic check dam is considerably higher than in other models, no significant difference was observed between the downstream water heights (Fig. 6). However, since the height of the water surface in the region where the water falls in the classic check dam decrease due to the impact, it is thought that the amount of scour in this region will be higher compared to other models [19].

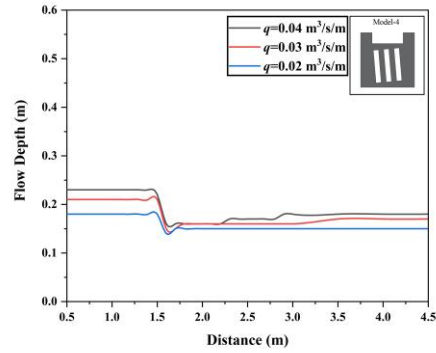


Figure 6. Water surface profiles

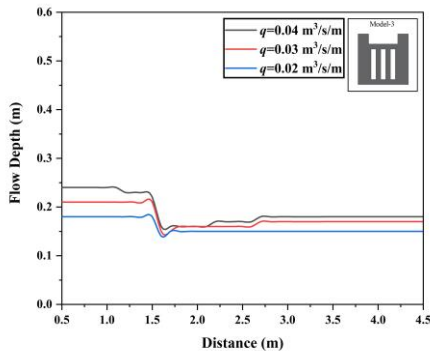
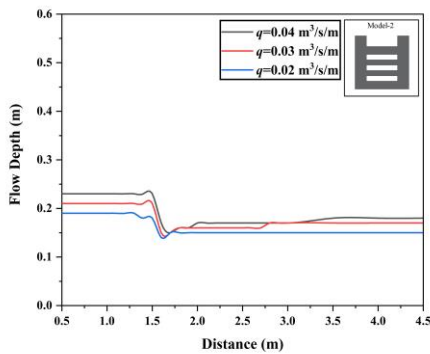
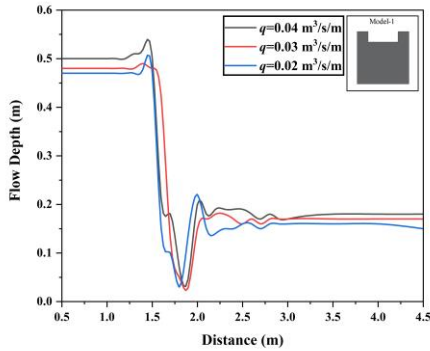
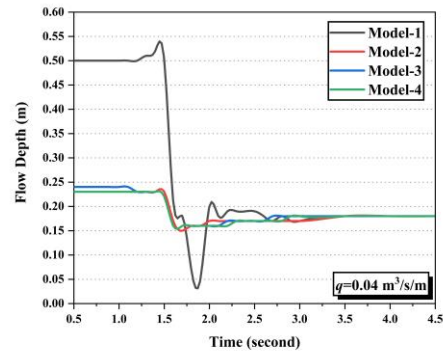
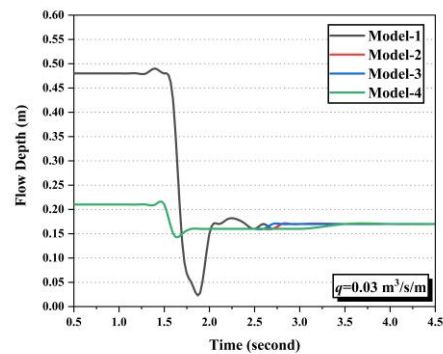


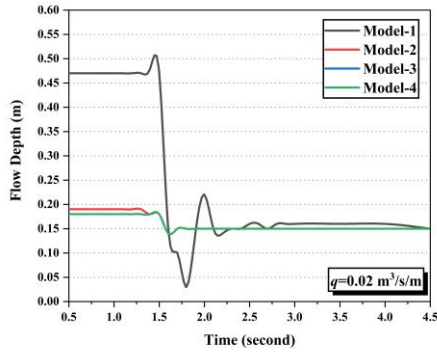
Figure 7 compares the water surface profiles of check dam types for three different flow discharges. Generally, water surface levels rise upstream of check dams and begin to fall downstream due to increased flow velocity. Larger discharges have visible effects on the surface profiles (Fig. 7a), whereas small discharges have a negligible effect on the water surface profiles (Fig. 7c). The model with the longest hydraulic jump length at maximum unit flow is Model-2, while at medium unit flow it is Model-4. The model with the shortest hydraulic jump length is Model-3.



(a)



(b)



(c)

Figure 7. Comparison of the water surface profile for: a) $q=0.04 \text{ m}^3 \text{ s}^{-1} \text{ m}^{-1}$, b) $q=0.03 \text{ m}^3 \text{ s}^{-1} \text{ m}^{-1}$, and c) $q=0.02 \text{ m}^3 \text{ s}^{-1} \text{ m}^{-1}$

The subcritical upstream flow condition ($Fr < 1$) was used for all numerical simulations. The flow's depth decreases, and velocity increases throughout the slit models. Thus, the supercritical flow regime is observed downstream of the slit models. Then, the flow energy is dissipated due to the hydraulic jump, and the flow regime returns to the subcritical flow regime. This situation is important for stream regulation and flood control, particularly during high discharge during floods. The energy dissipation ratio was calculated using the following equations.

$$E = \frac{V^2}{2g} + h \quad (1)$$

$$\Delta E(\%) = \frac{E_1 - E_2}{E_1} \quad (2)$$

where, E_1 and E_2 are the specific energy at the upstream and downstream of the check dam, respectively. V is the mean velocity, and h is the flow depth.

The energy dissipation rates of the models are given in Table 2. The upstream Froude number (Fr_1) defines the subcritical flow regime, which ranges from 0.02 to 0.12. According to the results, while the energy dissipation rate increases as the unit flow rate increases in slit check dam models, the situation is the opposite for classical check dams. The energy dissipation rate varies between 63.5-65.8% for Model-1, 18.7-21.2% for Model-2, 16.5-24.4% for Model-3, and 16.5-21.2% for Model-4. According to these results, the highest energy dissipation rate among slit check dam models was observed in Model-3 at maximum flow rate, while it was obtained for Model-2 at minimum flow rate. As for the vertical or angled placement of the openings, no difference in energy dissipation rate is observed at low flow rates, while the vertical model (Model-3) is seen to be more effective at maximum flow rate.

Table 2. Energy dissipation rates

	q	h_1	h_2	V_1	Fr_1	V_2	E_1	E_2	$\% \Delta E$
Model-1	0.04	0.50	0.18	0.08	0.04	0.22	0.50	0.18	63.5
	0.03	0.48	0.17	0.06	0.03	0.18	0.48	0.17	64.3
	0.02	0.47	0.16	0.04	0.02	0.13	0.47	0.16	65.8
Model-2	0.04	0.23	0.18	0.17	0.12	0.22	0.23	0.18	21.2
	0.03	0.21	0.17	0.14	0.10	0.18	0.21	0.17	18.7
	0.02	0.19	0.15	0.11	0.08	0.13	0.19	0.15	20.8
Model-3	0.04	0.24	0.18	0.17	0.11	0.22	0.24	0.18	24.4
	0.03	0.21	0.17	0.14	0.10	0.18	0.21	0.17	18.7
	0.02	0.18	0.15	0.11	0.08	0.13	0.18	0.15	16.5
Model-4	0.04	0.23	0.18	0.17	0.12	0.22	0.23	0.18	21.2
	0.03	0.21	0.17	0.14	0.10	0.18	0.21	0.17	18.7
	0.02	0.18	0.15	0.11	0.08	0.13	0.18	0.15	16.5

4. CONCLUSION

In this study, the flow characteristics of the classical check dam and three different slit check dam models were compared, and 12 analyses were conducted for the subcritical flow regime ($Fr < 1$) using OpenFOAM software and $k-\omega$ SST turbulence method. The results obtained are listed below.

- While the highest energy dissipation rate was observed in the classical check dam, the risk of scouring the downstream of these structures may be higher than in the slit check dams.
- Among the slit check dam models, the highest energy dissipation rate was obtained in Model-3 at maximum unit flow and Model-2 at minimum unit flow.
- While the energy dissipation ratios of model 2 and model 4 for maximum unit flow are equal to each other, for medium unit flow rate, the energy dissipation rates of all slit check dam models were equal.
- The model with the longest hydraulic jump length is Model-2.
- It has been observed that placing the openings vertically or at an angle does not change the energy dissipation rate at low unit flow, and the vertical model is more effective at high unit flow.

Declaration of conflicting interests

The authors declared no potential conflicts of interest with respect to the research, authorship, and/or publication of this article.

Acknowledgement

The numerical analyses of this paper were performed entirely at TUBITAK ULAKBIM, High Performance and Grid Computing Center (TRUBA resources).

REFERENCES

- [1] Erol U, Kızmaz Y, Özden A, Ceyhunlu Aİ. Evaluation of the Transportation Infrastructure Vulnerability in Kaynarca, Sakarya Basin from a Flood Spread Risk Perspective n.d. <https://doi.org/10.52114/apjhad.1128037>.
- [2] Abdelkareem M, Mansour AM. Risk assessment and management of vulnerable areas to flash flood hazards in arid regions using remote sensing and GIS-based knowledge-driven techniques. *Nat Hazards* 2023;117:2269–95. <https://doi.org/10.1007/S11069-023-05942-x/figures/15>.
- [3] Ceribasi G, Ceyhunlu AI. Generation of 1D and 2D flood maps of Sakarya river passing through Geyve district of Sakarya city in Turkey. *Nat Hazards* 2021;105:631–42. <https://doi.org/10.1007/S11069-020-04327-8/figures/12>.
- [4] Abbasi NA, Xu X, Lucas-Borja ME, Dang W, Liu B. The use of check dams in watershed management projects: Examples from around the world. *Sci Total Environ* 2019;676:683–91. <https://doi.org/10.1016/j.scitotenv.2019.04.249>.
- [5] Castillo VM, Mosch WM, García CC, Barberá GG, Cano JAN, López-Bermúdez F. Effectiveness and geomorphological impacts of check dams for soil erosion control in a semiarid Mediterranean catchment: El Cárcavo (Murcia, Spain). *CATENA* 2007;70:416–27. <https://doi.org/10.1016/j.catena.2006.11.009>.
- [6] D'Agostino V, Degetto M, Righetti M. Experimental investigation on open check dam for coarse woody debris control 2000;20:201–12.
- [7] Lucas-Borja ME, Piton G, Yu Y, Castillo C, Antonio Zema D. Check dams worldwide: Objectives, functions, effectiveness and undesired effects. *Catena* 2021;204:105390. <https://doi.org/10.1016/j.catena.2021.105390>.
- [8] Armanini A, Larcher M. Rational Criterion for Designing Opening of Slit-Check Dam. *J Hydraul Eng* 2001;127:94–104. [https://doi.org/10.1061/\(ASCE\)0733-9429\(2001\)127:2\(94\)](https://doi.org/10.1061/(ASCE)0733-9429(2001)127:2(94)).
- [9] Schwindt S, Franca MJ, De Cesare G, Schleiss AJ. Analysis of mechanical-hydraulic bedload deposition control measures. *Geomorphology* 2017;295:467–79. <https://doi.org/10.1016/j.geomorph.2017.07.020>.
- [10] Lyu X bo, You Y, Wang Z, Liu J feng, Sun H, Zhao W yu. Characteristics of gully bed scour and siltation between check dams. *J Mt Sci* 2023;20:49–64. <https://doi.org/10.1007/S11629-022-7474-7/metrics>.
- [11] Pan HL, Huang JC, Wei LQ, Ou GQ. A Study on Scouring Laws Downstream of Debris Flow Sabo Dams. *Appl Mech Mater* 2012;170–173:2071–6. <https://doi.org/10.4028/www.scientific.net/amm.170-173.2071>.
- [12] Akçalı E. Taşkın ve Rüşubat Kontrolünde Yeni Öneri: Gemiburnu Tip Geçirgen Bent. *Tek Dergi* 2022;33:12847–61. <https://doi.org/10.18400/tekderg.880224>.
- [13] Catella M, Paris E, Solari L. Case Study: Efficiency of Slit-Check Dams in the Mountain Region of Versilia Basin. *J Hydraul Eng* 2005;131:145–52. [https://doi.org/10.1061/\(ASCE\)0733-9429\(2005\)131:3\(145\)](https://doi.org/10.1061/(ASCE)0733-9429(2005)131:3(145)).
- [14] Piton G, Recking A. Design of Sediment Traps with Open Check Dams. I: Hydraulic and Deposition Processes. *J Hydraul Eng* 2015;142:04015045. [https://doi.org/10.1061/\(ASCE\)HY.1943-7900.0001048](https://doi.org/10.1061/(ASCE)HY.1943-7900.0001048).
- [15] Piton G, Recking A. Design of Sediment Traps with Open Check Dams. II: Woody Debris. *J Hydraul Eng* 2015;142:04015046. [https://doi.org/10.1061/\(ASCE\)HY.1943-7900.0001049](https://doi.org/10.1061/(ASCE)HY.1943-7900.0001049).
- [16] Aydin MC, Aytemur HS, Ulu AE. Experimental and Numerical Investigation on Hydraulic Performance of Slit-check Dams in Subcritical Flow Condition. *Water Resour Manag* 2022;36:1693–710. <https://doi.org/10.1007/S11269-022-03103-6/figures/11>.
- [17] İkinciogullari E. Efficiency of Mesh Generation Utilities on Energy Dissipation for a Stepped Spillway Model. *ICHEAS 3rd Int. Conf. Appl. Sci., Cape Town, South Africa: 2023*.
- [18] İkinciogullari E. A novel design for stepped spillway using staggered labyrinth trapezoidal steps. *Flow Meas Instrum* 2023;93:102439. <https://doi.org/10.1016/j.flowmeasinst.2023.102439>.
- [19] İkinciogullari E, Emiroglu ME, Aydin MC. Comparison of Scour Properties of Classical and Trapezoidal Labyrinth Weirs. *Arab J Sci Eng* 2022;47:4023–40. <https://doi.org/10.1007/S13369-021-05832-z/figures/15>.

Isothermic and Thermodynamic Approaches in Cadmium (II) Adsorption with Sivas Province Nanoclay

Nilgün ONURSAL 

¹ Siirt University, Education Faculty, Science Department, Siirt, Türkiye
Nilgün ONURSAL ORCID No: 0000-0002-2460-6475

*Corresponding author: nilgun.onursal@gmail.com

(Received: 7.08.2023, Accepted: 5.11.2023, Online Publication: 28.12.2023)

Keywords
Nanoclay,
Adsorption,
Cadmium,
Temkin,
Adsorption
Thermodynamics.

Abstract: In this study, the nano clay obtained by grinding clay from Sivas Yıldızeli region, Sivas Nano Clay (SNC), was used as adsorbent for the removal of cadmium from the solution. For the characterization of nano clay; XRD, SEM-EDX, BET and TGA analyses were performed. The surface area of the adsorbent was measured as 153.364 m²/g and the pore size as 3.835 nm. Parameters affecting adsorption such as temperature, adsorbent amount and speed were investigated. The contact time was determined as 180 min. The studies on adsorption equilibrium were applied to Langmuir, Freundlich, Temkin and Dubinin-Radushkevich isotherm models. As a result of the regression on the isotherm models, it was found that the adsorption fit the Temkin model. The adsorption capacity of nano clay was determined as 53.48, 49.50 and 48.54 gm⁻¹ for 298, 308 and 318 K temperatures. Adsorption thermodynamic study, ΔG° values were found to be -26.553, -27.673, -28.796 kJmol⁻¹ ΔH° value 6,823 kJmol⁻¹ and ΔS° value 0.112 kJmol⁻¹K⁻¹ for 298, 308, 318 K, respectively. The positive value of ΔH° indicates that the event is endothermic. The positive value also indicates that the event is chemical. The negative sign of ΔG° indicates that the event is spontaneous

43

Sivas İli Nanokil İle Kadmiyum (II) Adsorpsiyonunda İzotermik ve Termodinamik Yaklaşımlar

Anahtar Kelimeler
Nanokil,
Adsorpsiyon,
Kadmiyum,
Temkin,
Adsorpsiyon
Termodinamiği.

Öz: Bu çalışmada atık sulardaki ağır metallerin uzaklaştırılması için en uygun yöntemlerden biri olan adsorpsiyon yöntemi tercih edilmiş ve kadmiyumun çözüldüğü ortamdan giderimi için adsorban olarak Sivas Yıldızeli bölgesinden alınan kilin öğütülmesi ile elde edilen nanokil Sivas Nano Clay (SNC) kullanılmıştır. Nanokilin karakterizasyonu için; XRD, SEM-EDX, BET ve TGA analizleri yapılmıştır. Adsorplayıcının yüzey alanı 153.364 m²g⁻¹ olarak, gözenek boyutu 3.835 nm olarak ölçülmüştür. Adsorpsiyonu etkileyen parametrelerden sıcaklık, adsorban miktarı ve hız gibi parametreler incelenmiştir. Temas süresi 180 dk olarak belirlenmiştir. Adsorpsiyon dengesi üzerine yapılan çalışmalar ise, Langmuir, Freundlich, Temkin ve Dubinin-Radushkevich izoterm modellerine uygulanmıştır. İzoterm modelleri ile ilgili yapılan regresyon sonucunda adsorpsiyonun Temkin modeline uyduğu tespit edilmiştir. Nanokilin adsorplama kapasitesi 298, 308 ve 318 K sıcaklıkları için 53.48, 49.50 ve 48.54 gm⁻¹ olarak belirlenmiştir. Adsorpsiyon termodinamiği çalışması ΔG° değerleri 298, 308, 318 K için sırasıyla -26.553, -27.673, -28.796 kJmol⁻¹ ΔH° değeri 6,823 kJmol⁻¹ ve ΔS° değeri 0.112 kJmol⁻¹K⁻¹ olarak bulunmuştur. ΔH° 'ın pozitif değeri oluşu olayın endotermik olduğunu göstermektedir. Pozitif değer ayrıca olayın kimyasal olduğunu göstermektedir. ve ΔG° 'ın negatif işarete sahip olması olayın kendiliğinden yürüdüğünü göstermektedir.

1. INTRODUCTION

One of the most important environmental pollution types is water pollution. Water pollution, which is a problem all over the world, will start to decrease the amount of water due to the unconscious and irresponsible use of water and may bring water wars as an inevitable end. In this context, it has become a necessity to reduce water pollution and to raise awareness of people on this issue [1]. Among the studies on this subject, adsorption is one of the effective and cheap methods. Adsorption is the accumulation of ions or molecules in solution on the appropriate contact surface or interface between two phases. These phases can be liquid-liquid, solid-liquid or gas-liquid, or gas-solid combination [2].

The substance deposited on the contacted surface is called adsorbed (adsorbate) and the adsorber is called adsorbent. It is possible to talk about three types of adsorptions: physical, ion exchange and chemical adsorption. In physical adsorption, there is an adsorption based on Van der Waals attraction force, which is a weak interaction force between molecules [2]. The main reason why an ion is selectively retained on the surface of a solid is due to electrostatic attraction. The reversible exchange of ions between some solids and the electrolyte solution is referred to as ion exchange. However, although the ion exchange process is much more complex than adsorption, the data obtained with general techniques are quite similar [3]. In chemical adsorption, both covalent and ionic bond interactions take place between the molecules of the adsorbate and the molecules on the surface of the adsorber. In this process, a single layer is formed on the surface of the adsorbate. The factor that causes this is the chemical interaction between the adsorber and the adsorbate. In chemical adsorption, the process is irreversible [4]. While applying this method, the most efficient isotherm analysis should be performed. For this reason, among the models in which chemical adsorption is applied, the most commonly used ones are Langmuir, Freundlich, Temkin, Dubinin-Radushkevich and Harkins-Jura [5]. The recognition of adsorption phenomenon dates back to ancient times. However, its scientific use and the development of its application areas has been mostly in the twentieth century. It has almost reached its peak, especially in wastewater treatment. This is due to its easy availability and low cost [1,6].

1.1. Clay

Clays are key elements not only in geological and environmental processes but also in many human activities. In the description of the clay research organization known as the Association Internationale Pour L'etude des Argiles (AIPEA), the most important element that distinguishes clay from other soils is its plasticity. This is also emphasized as a distinctive feature. However, there is no reliable criteria for plasticity. This makes particle size criteria common. Clay research disciplines have different understandings about the definition of clay. Geologists consider it to be $2\mu\text{m}$ and colloidal, sedimentologists consider it to be $< 4\mu\text{m}$ in

particle size (equivalent spherical diameter), and chemists consider it to be only $1\mu\text{m}$. [7].

Zeolite, clay diatomite, wheat straw, activated carbon, montmorillonite, waste biomass and many natural adsorbents have been used. [8]. Canpolat and his friends was used Midyat stone as an adsorbent. [9].

1.1.1. Nanoclay

The literal meaning of nano is expressed as one billionth of a physical size. Nanometer means a length equal to one billionth of a meter. To understand how small the nanometer is, it would be enough to think that the diameter of a human hair is around $100\,000\text{ nm}$. If 100 to 1000 atoms of the atoms that make up an object come together, the nano size is formed. Nano technology or nanoscience is certain to be the most used and brightest field of the 21st century and beyond. Because many countries in the world are making investments and research on this subject [10].

Towards the end of the 20th century, scientists discovered the scanning tunneling microscope which can directly image atoms and its derivative, the atomic force microscope. With these discoveries, they brought different perspectives to physics and chemistry at the nanometer scale. In this way, by observing chemical reactions, a wide range of processes and their interactions, it has become possible to obtain artificial materials by moving atoms one by one to the desired locations in a controlled manner [11]. By reducing the material at the nano-size level, its properties change too. For example, when the size of the ceramic particle, which is fragile, is reduced to the nanometer level, it can be deformed and shaped. In other words, it is defined as the processing, creation and manipulation of tools, materials and structures at the molecular level. Due to the decline in profits in manufacturing sectors similar to the automotive sector, economists in the US recognized these opportunities and accepted nanotechnology as a priority area by elucidating the situation to then President Clinton. After that, it spread rapidly all over the world [12].

1.2. Heavy Metals

Heavy metals are naturally occurring elements with high atomic weights and a density almost five times that of water. Today, there are many different definitions. They are defined according to their atomic weight, density, chemical properties or toxicity. In reality, they are defined as metals with a density greater than 5g/cm^3 . In medicine, however, the situation is different. Regardless of the atomic weights of the elements, they are described as metals with all toxic properties [13].

Heavy metals, which are used in a wide range of applications, are preferred especially in industry, technology, domestic, agricultural, and medical fields. Their excessive use adversely affects human health and the environment and raises concerns. Because depending on the toxicity dose of heavy metals, many factors such as age, gender, genetics, exposure pattern and even

nutritional status of the individuals exposed to them are important. Elements such as lead, arsenic, mercury, cadmium and chromium, which have extreme toxicity, are among the most important metals in terms of public health. Since exposure to even low doses of these elements can cause multiple organ failure, they are classified as human carcinogens (known or probable) by both the International Agency for Research on Cancer and the US Environmental Protection Agency [14]. Many studies on the adsorption of heavy metals have taken their place in the literature [15,17].

1.2.1. Cadmium (Cd)

Cadmium, which is in group II B of the periodic table, is a silver-white metal element. In nature, it is usually found in the form of CdS (cadmium sulfide) and among zinc ores. Cadmium, which is a by-product of zinc production, is between zinc and mercury in terms of chemical properties. Most of its compounds are used as red and yellow pigments in paints. It is mostly coated on iron, zinc, steel, and copper, making them resistant to

corrosion. Accumulators with cadmium electrodes last much longer than lead batteries [17]. Cadmium, which is used extensively in industry and is among the important environmental pollutants, can cause life-threatening hazards due to exposure in daily life. Cd, which has a long half-life, is known to cause direct or indirect toxicity in cardiovascular, respiratory, nervous system, urinary, gastrointestinal and bones. In addition, if it accumulates in the body in excess, it can cause many diseases such as anemia, osteoporosis, anosmia, eosinophilia, and chronic rhinitis [18].

1.2.2. Adsorption Isotherm Models

Adsorption isotherms are concerned with the behavior of adsorbents in equilibrium at constant temperature. Depending on the interaction between the adsorbent and the absorber, adsorption processes can be either physisorption or chemisorption [5,19]. The following table provides the most commonly used adsorption isotherm models.

Table 1. Table of adsorption isotherm models

Isotherm Model	Formulas	Remarks
Freundlich Isotherm Model	$q_e = K_F C_e^{\frac{1}{n}} \quad \text{Eq. (1)}$ (Non-Linear) $\log q_e = \log K_F + \frac{1}{n} \log C_e \quad \text{Eq. (2)}$ (Linear Form)	<ul style="list-style-type: none"> The linear state of the equation of the Freundlich model, which is an experimental (empirical) model, is obtained by taking the logarithm of the two sides of the equation in the first part. Here; C_e; represents concentration in equilibrium state (mgL^{-1}), q_e; the amount of adsorbed substance in equilibrium (mgg^{-1}), K_F; The Freundlich constant (mgg^{-1}), n; the adsorption intensity values. k – constant indicating the relative adsorption capacity of the adsorbent ($\text{mgg}^{-1})(\text{Lm}^{-1})^{1/n}$; $1/n$ – constant for the intensity of the adsorption, $0 < 1/n < 1$; C_e – equilibrium concentration of the solute in the solution (mgL^{-1}), equation (1 and 2). [5,21].
Langmuir Isotherm Model	$q_e = \frac{Q_0 K_L C_e^{\theta}}{1 + K_L C_e} \quad \text{Eq. (3)}$ (Non-Linear) $\frac{C_e}{q_e} = \frac{1}{K_L Q_0} + \frac{C_e}{K_L} \quad \text{Eq. (4)}$ (Linear Form)	<ul style="list-style-type: none"> In the Langmuir isotherm model, it is stated that the distribution of reactive groups on the surface of particles is homogeneous. This model was developed based on gas theory and is widely used to describe gas adsorption on solids. q_{max} - maximum adsorption capacity (mgg^{-1}); b – constant related to the free energy of adsorption (Lmg^{-1}), equation (3 and 4). [21,22].
Temkin Isotherm Model	$q_e = B \ln A_T + B \ln C_e \quad \text{Eq. (5)}$ (Linear Form)	<ul style="list-style-type: none"> According to this model, the heat of adsorption in a linear order is due to the interaction between the adsorbent and the adsorbate. The decrease in adsorption energy is linear, not exponential [5]. Here the b value is the constant related to the adsorption heat (J.mol^{-1}) and is expressed as $B = RT/bT$. bT is the Temkin isotherm constant. A_T is the equilibrium binding constant (L g^{-1}). T is the absolute temperature (K). R is the ideal gas constant ($\text{J mol}^{-1} \text{K}^{-1}$). The values B and A_T are calculated from the slope and cut-off point of the linear plot plotted by $\ln C_e$ versus q_e respectively, equation (5).
Dubinin-Radushkevich (D-R) Isotherm	$\ln q_e = \ln q_m - K_{DR} \varepsilon^2 \quad \text{Eq. (6)}$ $\varepsilon = RT \ln \left(1 + \frac{1}{C_e} \right)$	<ul style="list-style-type: none"> The D-R isotherm model refers to the potential change that occurs on a heterogeneous surface. Here, E represents the average adsorption energy and allows us to find out the mechanism of adsorption. As for K_{DR}, it is the isotherm constant in the adsorption energy [22]. ε: shows Polanyi's potential and q_m: shows adsorption capacity (molg^{-1}), equation (6 and 7) [24]. (Saloğlu, 2019)

Halsey Isotherm Model	$E = \frac{1}{\sqrt{2K_{DR}}}$ Eq. (7) $\ln q_e = \left[\left(\frac{1}{n} \right) \ln K \right] - \left(\frac{1}{n} \right) \ln C_e$ Eq. (8)	<ul style="list-style-type: none"> The Halsey isotherm model can be used in case of the presence of multi-layered and irregular porous structures, equation (8) [24].
Jovanovich Isotherm Model	$q_e = q_{max}(1 - e^{-k_j C_e})$ Eq. (9) (Non-Linear) $\ln q_e = \ln q_m - K_j C_e$ Eq. (10) (Linear Form)	<ul style="list-style-type: none"> It is a mathematical concept derived from the mechanism of adsorption on homogeneous solid surfaces according to the Jovanovich isotherm model. This model assumes that the adsorption event is non-specific, without side interactions and that the solid surface where the adsorption function takes place is covered by a monolayer mechanism. The second equation on the left-hand side gives its linear form. K_j – Jovanovic constant (Lmg^{-1}). equation (9 and 10). [20,23.]

1.4. Thermodynamic Definitions

Enthalpy; It refers to the total energy change of a substance at constant pressure. Its unit is $Jmol^{-1}$, its symbol is ΔH . ΔH provides information about whether a reaction is exothermic or endothermic. If the sign of ΔH is positive, the reaction is endothermic and if it is negative, the reaction is exothermic. While physical adsorption is only exothermic, chemical adsorption can be endothermic or exothermic. ΔG , called Gibbs free energy, determines whether a reaction is spontaneous or not. Its unit is $Jmol^{-1}$. A negative sign of ΔG indicates that the event occurred spontaneously, while a positive sign indicates that it is not possible for the event to occur, but that an event in the opposite direction can only occur by 'expending energy'. ΔG is a valuable concept of very critical value for the science of chemistry, which tries to understand the behavior of matter by linking it to its structure. ΔS is called entropy. It is a measure of the irregularity of matter. Its unit is entropy of the system decreases. The Gibbs equation connects these concepts [25].

$$\Delta G = \Delta H - T\Delta S \quad (11)$$

2. MATERIAL AND METHOD

In this study, nanoclay obtained from Yıldızeli district of Sivas province was used to remove cadmium element from aqueous media. The clay was centrifuged at a speed of 14000 rpm in a Thermo- SL-16R model device. The colloidal part was taken into a container and kept for 15 days, and the upper non-collapsing clayey part was centrifuged again in the same device. Then the colloidal liquid part was filtered through 2 layers of filter paper. The filtrate was dried in an oven at 110 °C and beaten in a porcelain pestle. Then it was ground in a Retsch Brand ball grinder and tried to be brought to nano size. The sample obtained was tested in the SEM device and it was determined to be approximately 336.8 nm in size. This value is due to the fact that the dry clay could not be refined too much in the ball grinder.

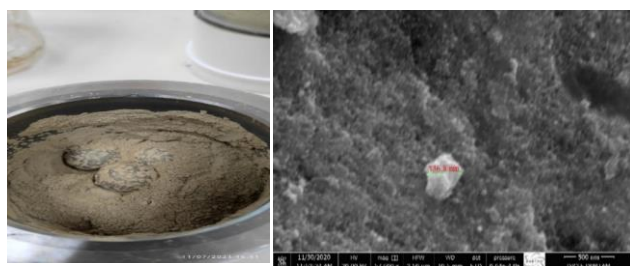


Figure 1. The obtained nanoclay milled in a ball grinder and SEM analysis image

2.1. Characterization

The characterization of the prepared sample was performed on SEM -EDX (Quanta FEG 250)), BET (Quantachrome Nova Win) branded device. Multipoint surface area and pore size determination analysis was performed by applying vacuum process at 105°C for 20 hours. XRF analysis was performed using UQ program of Thermo ARL XRF device. for XRD, Bruker -D8-advance, FT-IR analysis was performed on Perkin Elmer device and Shimadzu-DTG-60H was used for TGA. For the analysis results, Agilent 200 Series AA device was used.

3. RESULTS

3.1. SEM Analysis

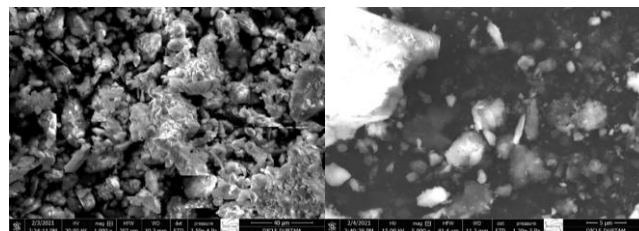
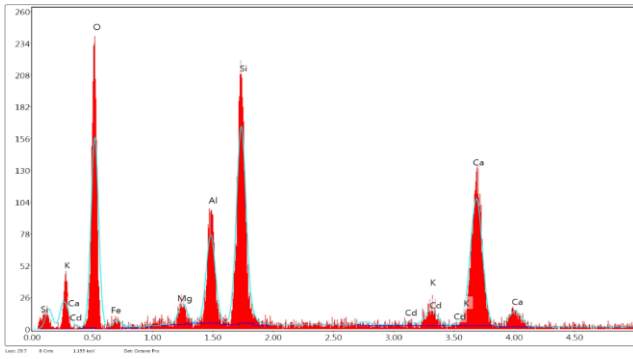


Figure 2. Natural and Cd-treated SEM images of the nanoclay.

Figure 2 clearly shows the peaks of Cd ion in the FE-SEM image of the nanocomposite used in the study. In the EDX diagram, the ratio of Cd retained is given.



Element	Wt %	Atomic %	Error %	Net Int.	Net Error %	K Ratio	Z	R	A	F
O K	53.56	70.74	11.22	82.08	2.65	0.1302	1.0590	0.9650	0.2296	1.0000
Mg K	1.90	1.65	22.35	9.92	15.99	0.0066	0.9802	0.9995	0.4569	1.0077
Al K	6.88	5.39	9.92	45.28	4.89	0.0389	0.9442	1.0068	0.5930	1.0103
Si K	14.41	10.84	7.10	105.68	2.78	0.0930	0.9652	1.0137	0.6638	1.0074
Cd L	0.59	0.11	59.18	1.91	57.01	0.0048	0.7074	1.2351	1.0855	1.0606
K K	1.39	0.75	23.28	8.72	21.28	0.0124	0.8958	1.0429	0.9334	1.0621
Ca K	16.61	8.76	5.29	86.16	3.67	0.1472	0.9123	1.0477	0.9530	1.0193
Fe K	4.66	1.76	21.55	11.86	19.83	0.0399	0.8140	1.0690	0.9895	1.0640

Figure 3. EDX diagram obtained as a result of interaction of nano clay with metal.

When the data in this diagram are examined, it is understood that cadmium element is adsorbed by nanoclay.

Table 2. Classification values of the sample according to SiO₂ ratios

SiO ₂ Ratio (%)	Type
>63	Acidic
63-52	Medium
52-45	Basic
<45	Ultrabasic

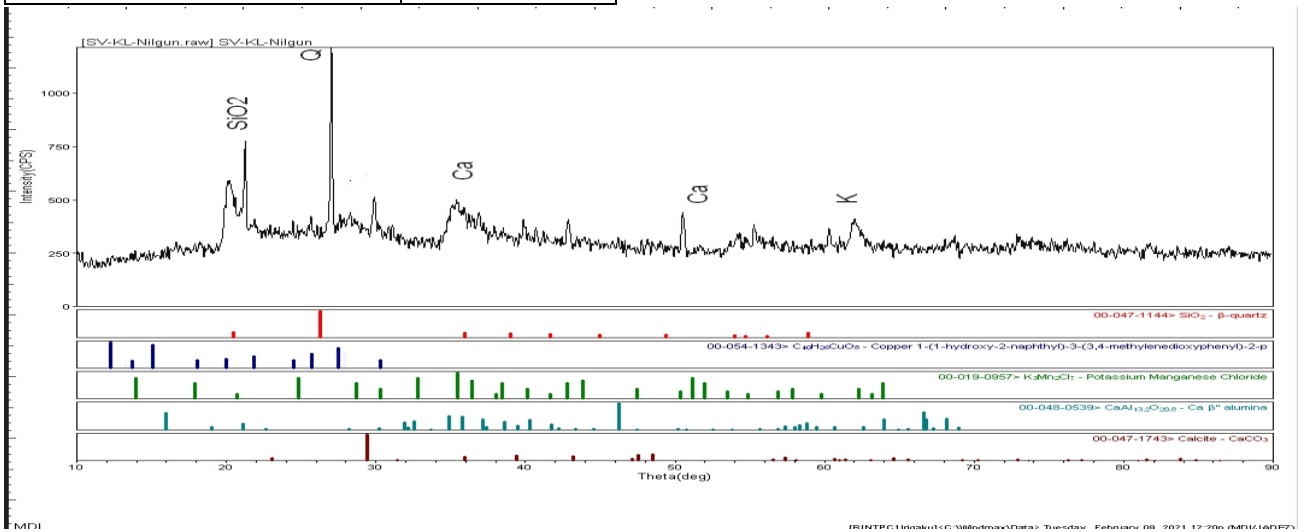


Figure 4. XRD diffractogram of nanoclay.

On the diffractogram, quartz peak is striking.

3.4. TGA Analysis

The amount of volatile matter in the sample was determined by thermal gravimetric analysis. Looking at the TGA peak (25-800°C), there is a decrease around 100°C due to humidity, while the situation is relatively

When the data in this table are evaluated, it is understood that the clay has a moderate SiO₂ ratio [5].

3.2. XRF Analysis

XRF analysis of clay was performed and the results obtained are given in the table below.

Table 3. Clay XRF Results

Sample Sign %	Sivas Nanoclay
LOI	10.50
Al ₂ O ₃	14.7
CaO	3.7
Fe ₂ O ₃	7.5
K ₂ O	1.0
MgO	4.3
MnO	0.1
Na ₂ O	0.1
P ₂ O ₅	<0.1
SiO ₂	57.1
TiO ₂	0.6

When the data in Figure 3 and Table 3 are analyzed, it is understood that there is a consistency between the SEM-EDX and XRF results and the microscopic and macroscopic data and that they support each other

3.3. XRD Analysis

The structure of the obtained nanoclay was determined by X-ray powder diffraction (XRD) method. These measurements were performed with a Bruker D8 Discover X-ray diffractometer. The diffractogram of the composite is given in Figure 4

stable between 100-600°C. The % decrease between 600-800 °C is due to the thermal decomposition of CaCO₃, the main ingredient of calcite, turns into limestone (CaO) by releasing CO₂ or dehydration of the Al-OH bond. As a result of the analysis, it was determined that the mass had approximately 25% volatile matter.

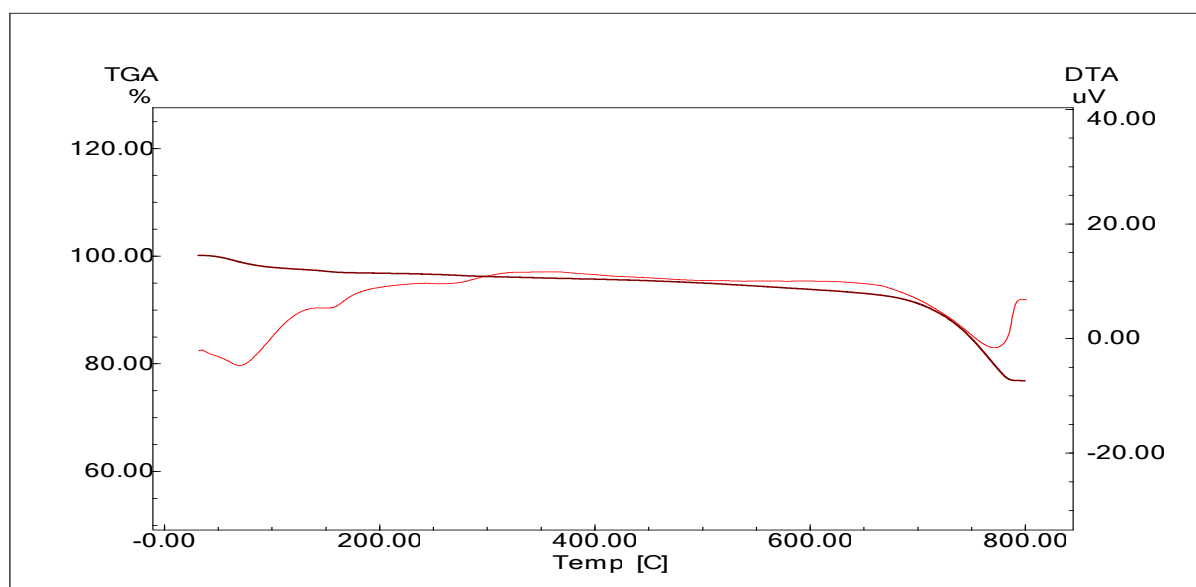


Figure 5. TGA diagram of the nanoclay

3.5. BET Analysis.

At 77.3 K temperature and low pressure, BET (Braun Emmet Teller) method was applied with nitrogen gas

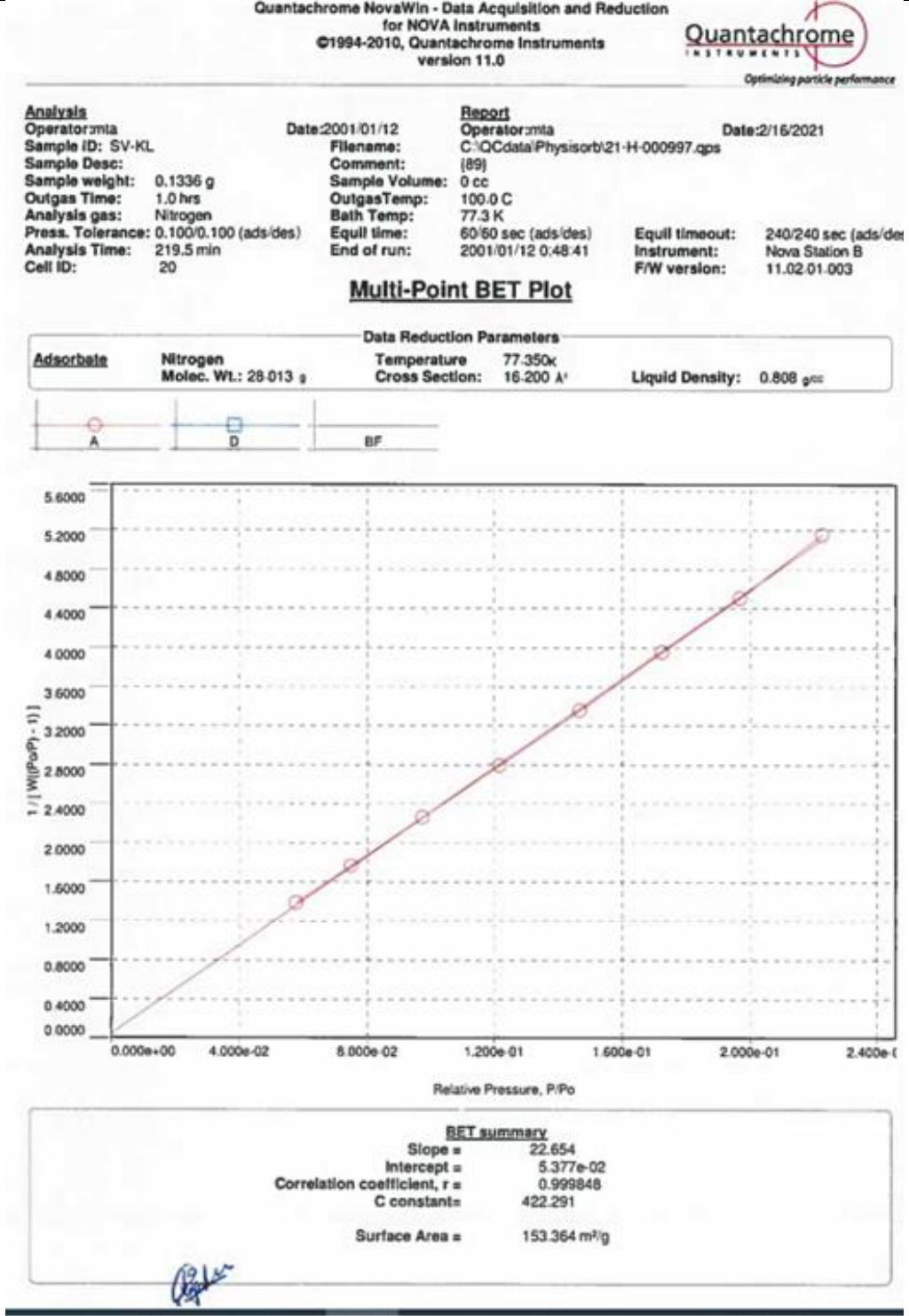
adsorption and the surface area was measured as 153.364 m²/g. BET detail table is given below.

Table 4. BET detail data table

Surface Area Data	
Multi Point BET.....	1.534e+02 m ² /g
BJH method cumulative adsorption surface area.....	3.897e+01 m ² /g
BJH method cumulative desorption surface area	7.257e+01 m ² /g
DH method cumulative adsorption surface area.....	3.957e+01 m ² /g
DH method cumulative desorption surface area.....	7.400e+01 m ² /g
method external surface area.....	9.391e+01 m ² /g
t- method micropore surface area.....	5.945e+01 m ² /g
NLDFT cumulative surface area.....	1.148e+02 m ² /g
.....	3.794e+00 nm
Pore Volume Data	
Total pore volume for pores with Diameter	
Less than 131.14 nm at P/Po=0.985135.....	1.470e-01 cc/g
BJH method cumulative adsorption pore volume.....	8.512e-02 cc/g
BJH method cumulative desorption pore volume.. ..	9.910e-02 cc/g
DH method cumulative adsorption pore volume	8.406e-02 cc/g
DH method cumulative desorption pore volume	9.713e-02 cc/g
t- method micropore volume	2.714e+01 cc/g
HK method cumulative pore volume	8.543e+01cc/g
SF method cumulative pore volume	8.565e+01cc/g
NLDFT method cumulative pore volume	1.322e+01cc/g

Pore Size Data

Average pore Diameter.....3.835e+00 nm
 BJH method adsorption pore Diameter (Mode Dv (d)).....3.146e+00 nm
 BJH method desorption pore Diameter (Mode Dv (d)).....3.709e+00 nm
 DH method adsorption pore Diameter (Mode Dv (d))3.146e+00 nm
 DH method desorption pore Diameter (Mode Dv (d))3.709e+00 nm
 HK method pore Diameter (Mode).....4.315e+01 nm
 SF method pore Diameter (Mode).....3.508e+01 nm
 NLDFT pore Diameter (Mode)



AREA-Volume Summary
 Data Reduction Parameters Data

Adsorbate: Nitrogen	Temperature: 77.350 K
Molec. Wt. 28.013 g	Cross Section 16.200 Å ² Liquid Density: 0.808 g/cc

3.6. Adsorption Models

3.6.1. Isotherm Studies

The experimental and instrumental studies of the adsorption isotherm followed a similar path to the kinetic studies. The adsorption of cadmium ion was carried out at 3 temperatures of 298, 308 and 318 K. Adsorption was

carried out at different concentrations until equilibrium was reached. The solutions obtained as a result of the process were analyzed in AAS device and data were obtained. These data were applied to Langmuir, Freundlich, Temkin, Dubinin-Radushkevich, Halsey and Jovanovich isotherm models.

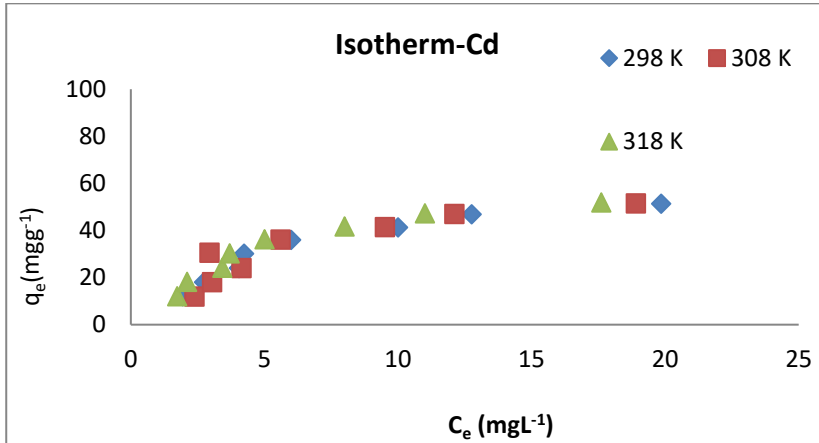


Figure 6. Isotherm plots of Cd (II) at 298,308 and 318

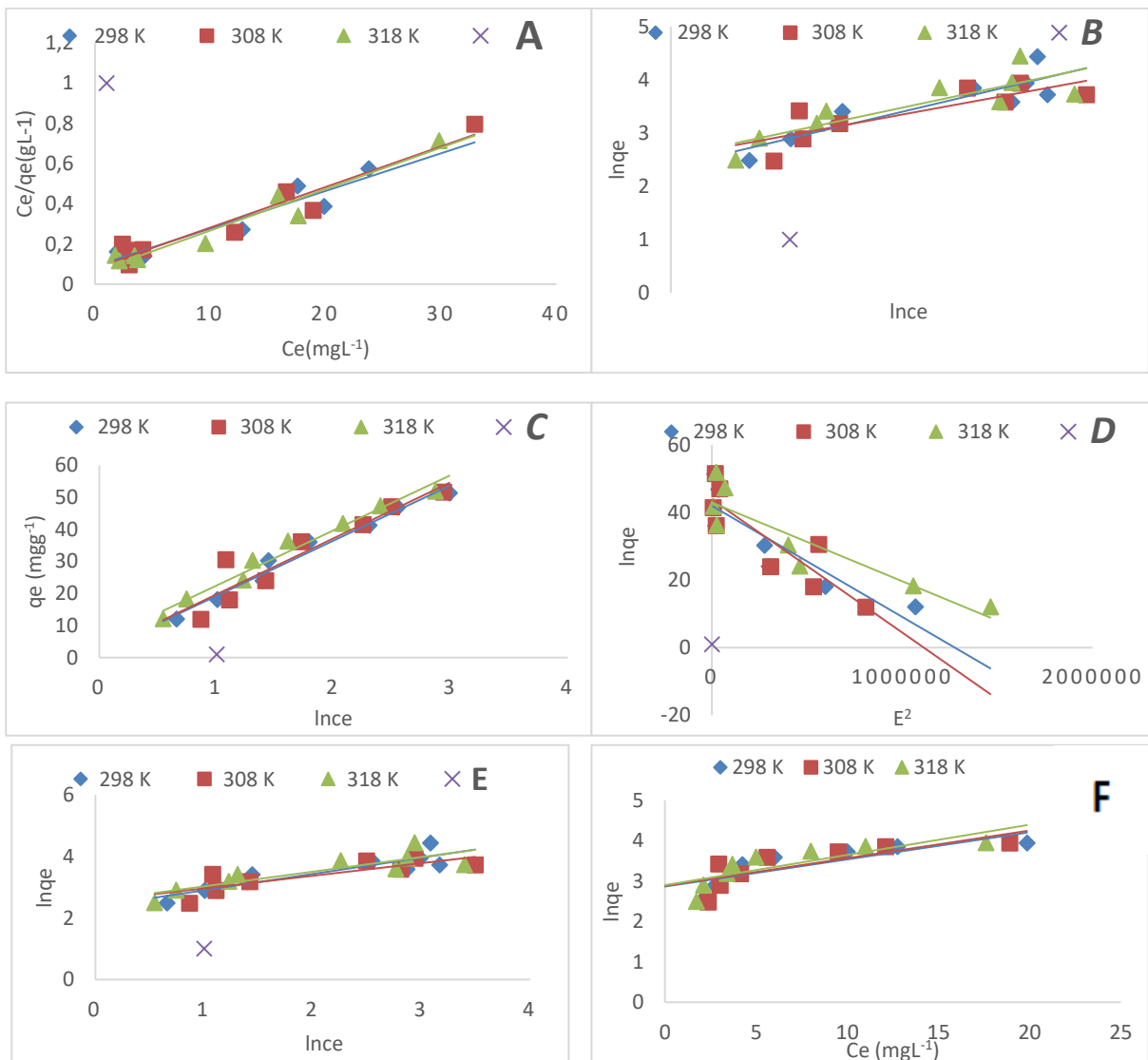


Figure 7. (a) Langmuir, (b) Freundlich, (c) Temkin, (d) Dubinin-Radushkevich, (e) Halsey, (f) Jovanovich plots of Cd (II) at 298,308 and 318 K

Thus, Langmuir, Freundlich, Temkin, Dubinin-Radushkevich, Halsey and Jovanovich isotherm linear plots were obtained. The necessary parameters of these

models were obtained from these plots. These parameters are given in table.7.

Table 5. Constants achieved from Adsorption Isotherm Experiment

Langmuir Isotherm				Freundlich Isotherm			Temkin Isotherm			Dubinin-Radushkevich Isotherm		
T (K)	K_L (L/mg)	q_{max} (mg/g)	R^2	K_F	n	R^2	B	K_{TM}	R^2	K_{DR} (L/mg)	E (kJ/mol)	R^2
298	0.208	53.476	0.915	234.423	1.885	0.8041	17.242	1.123	0.9745	$3E.10^{-5}$	129	0.7932
308	0.253	49.50	0.928	356.396	2.438	0.6811	17.490	1.134	0.8829	$4E.10^{-5}$	111.8	0.7778
318	0.338	48.54	0.946	357.026	2.101	0.7366	17.227	1.354	0.9728	$2E.10^{-5}$	158.1	0.8216
Halsey Isotherm				Jovanovich Isotherm								
T	K_H	n	R^2	K_J	q_{max}	R^2						
298	-4.468	-1.885	0.804	-0.0672	17.544	0.677						
308	-6.223	-2.438	0.681	-0.0684	17.849	0.616						
318	-5.364	-2.101	0.737	-0.0748	18.143	0.654						

3.6.2. Thermodynamic studies

ΔH and ΔS values can be found from the formula $\ln Kd^0 = -\Delta H/R + \Delta S/R$. For this, it is essential to find the $\ln Kd^0$

value. Therefore, the plot given in figure 10 was created and $\ln Kd^0$ values were found for each temperature from the shift of the plot.

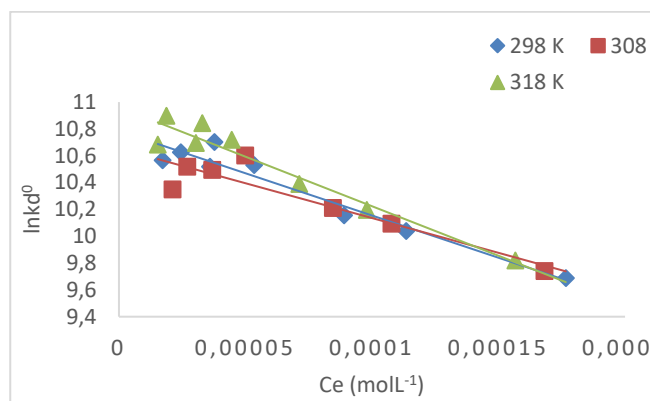


Figure 8. $\ln Kd^0$ plot of different concentration values of Cd (II)

The $\ln Kd^0$ values found were plotted with corresponding $1/T$ values and the Van't Hoff plot given in figure 11 was obtained.

Figure. 10 shows the Gibbs equation in its Onursal notation. The shift of the equation of the plot directly gives ΔH and the negative value of the slope directly gives the entropy.

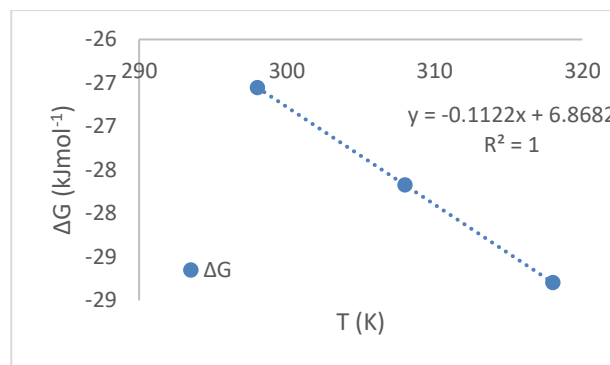


Figure 10. Onursal representation of the Gibbs formula.

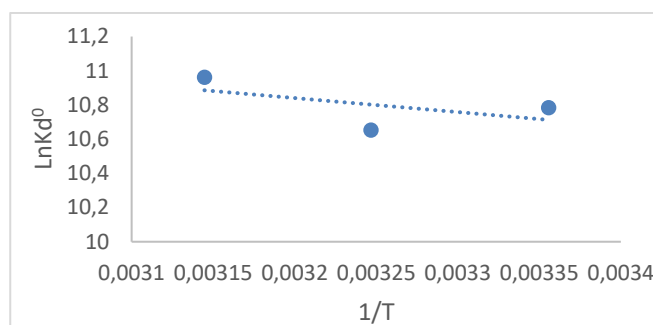


Figure 9. Van't Hoff plot of Cd (II)

The equation obtained from the plot is applied to Gibbs' equation: The obtained ΔG , ΔH and ΔS values are given in table.7.

3.6.3. Adsorbent Quantity

In figure 11, the variation of the amount of adsorbed material with the amount of adsorbent is plotted. As can be seen, although the amount of adsorbent is inversely proportional to q_e , it converges to a base value. This has two meanings. The first is that as adsorbent concentration rises, efficiency falls. The second meaning is that q_e does not increase after a certain point, regardless of how much the amount of adsorbent increases.

Table 6. Thermodynamic parameters related to the adsorption of Cd (II) on nanoclay.

T (K)	$\ln K^0$	ΔG (kJmol ⁻¹)	ΔH (kJmol ⁻¹)	ΔS (kJmol ⁻¹ K ⁻¹)
298	10.784	-26.553	6.823	0.112
308	10.654	-27.673		
318	10.962	-28.796		

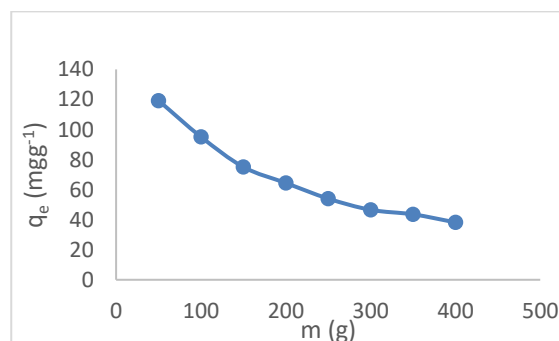


Figure 11. Quantity plot of Cd (II)

4. DISCUSSION AND CONCLUSION

The purpose of this study was to investigate the adsorption method for removing cadmium and to look at the variables that affect adsorption.

According to the results of the analysis, it was understood that it contains the materials that make up the clay. Both vesicular appearance, SEM images and XRF analysis results showed that the material is natural clay. Especially the SiO₂ value is proof of this. SEM_EDX results show that the clay adsorbs Cd (II). Instrumental analysis methods such as XRD, XRF, BET and SEM-EDX were also used to characterize the adsorber. The adsorber pore size was measured as 3.835 nm and the surface area was measured as 153.364 m²g⁻¹. In kinetic studies, 180 min was determined as the working time and the equilibration time was measured as 45 min on average.

In the studies on adsorption equilibrium, Langmuir, Freundlich, Temkin and Dubinin-Radushkevich, Halsey and Jovanovich isotherm models were applied. As a result of the regression on the isotherm models, it was found that the adsorption complied with the Temkin model. The adsorption capacity of SNC was determined as 53.48, 49.50 and 48.54 mgg⁻¹ for 298, 308 and 318 K temperatures.

As a result of the adsorption thermodynamic study, ΔG° values were found to be -26.553, -27.673, -28.796 kJmol⁻¹, ΔH° value 6.823 kJmol⁻¹ and ΔS° value 0.112 kJmol⁻¹K⁻¹ for 298, 308, 318 K, respectively. The positive value of ΔH° indicates that the event is endothermic. The positive value also indicates that the event is chemical. The negative sign of ΔG° indicates that the event is spontaneous.

As a result, it was determined that SNC can be used as an effective adsorbent due to its high capacity and rapid equilibration.

REFERENCES

- [1] Onursal, N., Dal, M. C., Kul, A. R., & Yavuz, Ö. (2020). Cu(II) İyonlarının Doğal Karışık Tipteki Kil İle Sulu Ortamdan Uzaklaştırılması, İzoterm, Kinetik ve Termodinamik Parametrelerin İncelenmesi. *Euroasia Journal of Mathematics, Engineering, Natural & Medical Sciences*, 85-103.
- [2] Okumuş, E. (2007). Küçükçekmece Gölü Sedimentinde Ağır Metal (Zn²⁺, Fe²⁺, Cu²⁺) Adsorpsiyonu. Yıldız teknik Üniversitesi Fen Bilimleri Enstitüsü/Yüksek Lisans Tezi. İstanbul: Yıldız teknik Üniversitesi.
- [3] Karşlı, U. (2019). Yüze Modifiyeli Şeker Pancarı Küspesi Adsorbentle Cr(VI) İyon Adsorpsiyonunun Kesikli Ve Sürekli Sistemlerde İncelenmesi. Hacettepe Üniversitesi Fen Bilimleri Enstitüsü-Yüksek Lisans tezi. Ankara: Hacettepe Üniversitesi.
- [4] Buldağ, E. (2018). Nikel(II) ve Mangan (II)'nin Sulu Çözeltilerden Klorit İhtiva Eden Killerle Uzaklaştırılması. Yüksek Lisans/Dicle Üniversitesi Fen Bilimleri Enstitüsü . Diyarbakır: Dicle Üniversitesi.
- [5] Dal, M. C. (2022). Adsorpsiyon Dengesi Ve İzoterm Modelleri. *Fen Bilimleri ve matematik Alanında Yeni Trendler*. içinde İzmir: Duvar yayınları.
- [6] Alacabey, İ. (2014). Doğal ve aktive edilmiş Van Gölü sediment (dip çamuru) örneklerinin bazı ağır metallerle adsorpsiyonunun izoterm ve termodinamik analizi. *Yüzüncü Yıl Üniversitesi Fen Bilimleri Enstitüsü/Yüksek Lisans Tezi*. Van: Yüzüncü Yıl Üniversitesi .
- [7] Maroto, M. M., & Azcárate, J. A. (2018). What is clay? A new definition of "clay" based on
- [8] plasticity and its impact on the most widespread soil classification systems. *Applied Clay Science*, 57-63.
- [9] Onursal N, Altunkaynak Y, Baran A, Dal MC. Adsorption of nickel(II) ions from aqueous solutions using Malatya clay: Equilibrium, kinetic, and thermodynamic studies. *Environ Prog Sustainable Energy*. 2023;e14150. doi:10.1002/ep.14150.
- [10] Canpolat M. , Altunkaynak Y. , Yavuz Ö. Kimyasal olarak işlenmemiş Midyat taşı kullanılarak sulu çözeltilerden Pb(II) iyonlarının etkin bir şekilde uzaklaştırılması: İzoterm, kinetik ve termodinamik çalışmalar. *NÖHÜ Müh. Bilim. Derg.*. 2022; 11(4): 1085-1096.
- [11] Kaştan, A.,Y. Yalçın, H. Ünal ve Ş. Talaş, (2015).PA 6/ YYPE / Nanokil Kompozitlerin Mekanik Özelliklerinin İncelenmesi,» Afyon Kocatepe Üniversitesi Fen ve Mühendislik Bilimleri Dergisi, pp. 9-20.
- [12] Celep, Ş., & Koç, E. (2008). Nanoteknoloji ve Tekstil Uygulama Alanları. *Ç.Ü Fen Bilimleri Enstitüsü*, 43-52.
- [13] Güneşoğlu, C., & Kut, D. (2005). Nanoteknoloji ve Tekstil Sektöründeki Uygulamaları (Nano Tekstiller). *Mühendis ve Makina*, Cilt 50, sayı 591, 25-34.
- [14] Özbolat, G., & Tuli, A. (2016). Ağır Metal Toksisitesinin İnsan Sağlığına Etkileri. *Ç.ü. Tıp fakültesi, Arşiv Kaynak Tarama Dergisi*, 502-521.
- [15] Tchounwou, P. B., Yedjou, C. G., Patlolla, A. K., & Sutton, D. J. (2014). "Heavy Metals Toxicity and the Environment, . *Molecular Clinical and Environmental Toxicology*, 101., 133-164.
- [16] Altunkaynak Y. , Canpolat M. Sulu Çözeltilerden Nikel(II) İyonlarının Uzaklaştırılmasında Portakal Kabuğu Atığının Kullanılması: Denge, Kinetik Ve Termodinamik Çalışmalar. *JARNAS*. 2022; 8(2): 322-339.
- [17] Altunkaynak, Y. Effectively removing Cu(II) and Ni(II) ions from aqueous solutions using chemically non-processed Midyat stone: equivalent, kinetic and thermodynamic studies. *J IRAN CHEM SOC* **19**, 3357–3370 (2022). <https://doi.org/10.1007/s13738-022-02529-4>.
- [18] Onursal, N., Dal, M.C. (2023). Investigation of isotherm and thermodynamic parameters of adsorption of copper (II) ions in aqueous solution with natural mixed type Siirt clay (NMTSC-2) and new (second) linear equation derived from Harkins–Jura isotherm. *Chem. Pap.* <https://doi.org/10.1007/s11696-023-03116-4>
- [19] Dal, M.C., Onursal, N. (2023). Two new linearized equations derived from a pseudo-second-order

- kinetic model. Desalination and Water Treatment. doi: 10.5004/dwt.2023.29992
- [20] Babamuradov, A. (2022). Cevher hazırlama Tesis Proje. Eskişehir Osmangazi Üniversitesi Maden Mühendisliği Bölümü, (ESOGÜ-CHTP-2022). Eskişehir: Eskişehir Osmangazi Üniversitesi Maden Mühendisliği Bölümü.
- [21] Coşan, D. T., Dal, A., Soyocak, A., Çolak, E., Çiçek, A., & Kurt, H. (2017). Kadmiyum Toksikitesi Oluşturulan Sıçanlarda Tannik Asitin, Ağır Metal Giderimi Ve Bazı Biyokimyasal Değerler Üzerine Etkisinin Araştırılması. Kocatepe Tıp Dergisi, 18, 146-153.
- [22] Rosca, M., Diaconu, M., Hlihor, R., & Petronela, C. (2020). Prediction of Equilibrium Sorption Isotherm for Cadmium Biosorption by Microorganisms: Comparison of Linear and Nonlinear Methods. 2020 International Conference on e-Health and Bioengineering (EHB) (s. 1-4). Romania, : DOI:10.1109/EHB50910.2020.9280180.
- [23] Ehiomogbe, P., Ahuchaogu, I. I., & Ahaneku, I. E. (2022). Review Of Adsorption Isotherms Models. Acta Technica Corwiniensis-Bulletin of Engineering-Fascicule .4, 87-96.
- [24] Okumuş, Ç. Z., & Doğan, T. H. (2019). Biyodizeldeki Suyun Reçine ile Uzaklaştırılması: Adsorpsiyon. Avrupa Bilim ve Teknoloji Dergisi, Sayı 15, 561-570.
- [25] Saloğlu, D. (2019). Mikro Kirletici Naproksenin Atık Sulardan Spirulina platensis ile Modifiye Edilmiş Kitosan-Polivinilalkol Biyokompozitleri ile Adsorpsiyonu. BEÜ Fen Bilimleri Dergisi, 8(2), 506-520.
- [26] Altunkaynak, Y., Canpolat, M. & Yavuz, Ö. Adsorption of cobalt (II) ions from aqueous solution using orange peel waste: equilibrium, kinetic and thermodynamic studies. J IRAN CEMH SOC 19, 2437–2448 (2022). <https://doi.org/10.1007/s13738-021-02458-8>.

Investigation of Anticancer and Antimicrobial Properties of Fluorinated Salicylaldehydes

Fatma OZER^{1*}, Bestoon SHEKHANY^{1,2}, Mustafa Unal BOYRAZ³, Hasan Ali Zafer SAK⁴,
Saduman ERSOZ¹, Ali Osman GÜROL^{5,6}, Faruk SUZERGOZ¹

¹ Department of Biology Science Art Faculty, Harran University, Sanliurfa, Türkiye

² Department of Medical Laboratory Technology, Shaqlawa Technical College, Erbil Polytechnic University, Erbil, Iraq

³ Department of Histology and Embriology, Veterinary Faculty, Harran University, Sanliurfa, Türkiye

⁴ Department of Chest Disease, Medical Faculty, Harran University, Sanliurfa, Türkiye

⁵ Department of Immunology, Aziz Sancar Institute of Experimental Medicine, Istanbul University, Istanbul-Türkiye.

⁶ Department of Medical Pharmacology Istanbul Medical Faculty, Istanbul University, Istanbul-Türkiye.

Fatma OZER ORCID1 0000-0002-6424-7235

Bestoon SHEKHANY ORCID 0000-0001-8849-4153

Mustafa Unal BOYRAZ ORCID 0000-0002-5455-0353

Hasan Ali Zafer SAK ORCID 0000-0002-2388-2259

Saduman ERSOZ ORCID 0000-0001-5137-2814

Ali Osman GÜROL ORCID 0000-0001-6682-4289

Faruk SUZERGOZ ORCID 0000-0001-5000-0998

* Corresponding author Fatma OZER: fozer@harran.edu.tr

(Received: 24.05.2023, Accepted: 14.11.2023, Online Publication: 28.12.2023)

Keywords

Anticancer,
Antimicrobial,
Fluor,
Schiff base,
Apoptosis

Abstract: Multidrug resistance (MDR) to anticancer and antimicrobial drugs has become a global health problem. Schiff bases are referred to as special ligands due to the functional azomethine (C=N) group in their structure and are used in the pharmaceutical industry. Approximately one-fourth of the drugs used in human and animal health contain fluorine atoms. In this study, the cytotoxic and antiproliferative effects of the synthesized fluorinated Schiff bases on the A549 cell line were investigated by MTT assay and 5 (6)-carboxyfluorescein succinimidyl ester (CFSE) staining technique, respectively. The ability of the compounds to induce apoptosis was investigated by Rhodamine 123 staining technique, the inhibitory effects on mitochondrial membrane potential, active caspase-3 analysis by immunofluorescence test, and morphological effects by hematoxylin-eosin (H&E), Giemsa and Papanicolaou (PAP) protocols. Antimicrobial effects of the compounds were investigated by MTT test on *P. aeruginosa*, *E. coli*, and *S. aureus*. The compounds used in the study were generally potent (IC₅₀:1,4-31,5 µM) and Compound 7 (IC₅₀:1,4 µM) exhibited a stronger cytotoxic effect than Doxorubicin (IC₅₀: 1.9 µM). The strongest antiproliferative effect was obtained with Compound 10 (PI:2,1). The strongest antiproliferative effect was obtained with Compound 10 (PI:2,1). The strongest ability to inhibit mitochondrial membrane potential was obtained with Compound 4 (1330). Immunofluorescence studies showed active caspase-3 and morphological studies showed findings indicating apoptosis such as chromatin condensation and DNA fragmentation. The antimicrobial effects of the compounds on *P. aeruginosa*, *E. coli*, and *S. aureus* (MIC₅₀:18,6-49,3 µM) were observed to be lower than Gentamicin (MIC₅₀:1,5-2,2 µM) used as the positive control. It can be said that the fluorinated Schiff Bases synthesized in the study especially Compound 7 are promising for the treatment of multidrug resistance to anticancer drugs and for in vivo studies.

Florlu Salisilaldiminlerin Antikanser ve Antimikrobiyal Özelliklerinin Araştırılması**Anahtar****Kelimeler**

Antikanser,
Antimikrobiyal,
Flor,
Schiff bazı,
Apoptozis

Öz: Antikanser ve antimikrobiyal ilaçlara karşı gelişen çoklu ilaç direnci (MDR) global bir sağlık sorunu haline gelmiştir. Schiff Bazları yapılarındaki fonksiyonel azometin (C=N) grubundan dolayı özel ligandlar olarak anılmakta ve ilaç endüstrisine kullanılmaktadır. İnsan ve hayvan sağlığı alanında kullanılan ilaçların yaklaşık dörtte biri flor atomu içermektedir. Bu çalışmada sentezlenen florlu schiff bazlarının A549 hücre hattında sitotoksik etkileri MTT testi ile, antiproliferatif etkileri; 5 (6)-karboksifluoresan süksinimidil ester (CFSE) boyama tekniği ile araştırıldı. Bileşiklerini apoptozu indükleme yetenekleri ise mitokondriyal membran potansiyeli üzerine olan inhibe edici etkileri Rhodamin 123 boyama tekniği ile, aktif kaspaz-3 analizi immünfloresan testi ile, morfolojik etkileri ise Hematoksilen-eozin (H&E), Giemsa ve Papanicolaou (PAP) protokolleri ile araştırıldı. Bileşiklerin antimikrobiyal etkileri; *P. aeruginosa*, *E. coli* ve *S. aureus* üzerinde MTT testi ile araştırıldı. Çalışmada kullanılan bileşiklerin genel olarak güçlü düzeyde (IC₅₀:1,4-31,5 µM) ve Bileşik 7'nin (IC₅₀:1,4 µM) Doxorubicin' den (IC₅₀:1,9 µM) daha güçlü sitotoksik etki sergilediği saptandı. En güçlü antiproliferatif etki Bileşik 10 (PI:2,1) ile elde edilmiştir. En güçlü mitokondriyal membran potansiyelini inhibe etme yeteneği Bileşik 4 (1330) ile elde edilmiştir. İmmünfloresan çalışmalarda aktif kaspaz-3, morfolojik çalışmalarda ise kromatin kondenzasyonu, DNA fragmentasyonu gibi apoptozu işaret eden bulgular gözlemlendi. Bileşiklerin *P. aeruginosa*, *E. coli* ve *S. aureus* üzerindeki antimikrobiyal etkileri (MİK₅₀:18,6-49,3 µM) pozitif kontrol olarak kullanılan Gentamisin (MİK₅₀:1,5-2,2 µM)'e göre düşük seviyede olduğu gözlemlendi. Çalışmada sentezlenen florlu Schiff Bazlarının ve özellikle Bileşik 7'nin antikanser ilaçlara karşı gelişen çoklu ilaç direnci tedavisinde ve in vivo çalışmalar için umut vaad ettiği söylenebilir.

1. INTRODUCTION

Patients with aggressive cancer exhibit high mortality rates, increasing the demand for new chemotherapeutic drugs with improved therapeutic effects and lower toxicity [1,2]. In cancer biology, controlling cancer remains a big challenge. Cancerous cells in patients are intrinsically resistant to standard chemotherapy, where resistant cells lead to treatment failure [3,4]. Thereby, treatment by traditional chemotherapeutic approaches is primarily limited due to acquired multidrug resistance (MDR) [5,6].

The development of resistance to at least one of three or more drugs with different mechanisms of action is defined as MDR [7,8]. MDR cancer cells and pathogenic microorganisms against drugs adversely affect the success of treatment and often cause deaths [9,10]. Due to the change in the drug target sites of cancer cells or bacteria and the increase in efflux pumps, drug entry into the cell is reduced, and at the same time, the drugs are pumped out of the cell. As a result of the weakening of the immune system caused by anticancer drugs, serious infections develop in about half of the patients. The infection of resistant bacteria with cancer worsens the prognosis in patients [11,12].

Cellular or bacterial MDR is tried to be treated with increasing drug doses or drug combinations, and therefore, undesirable conditions such as anemia, infections, nausea, and hair loss may occur due to the cytotoxic effects of drugs on cancer cells as well as on constant proliferating healthy cells [13]. The failure of treatments due to the development of MDR causes researchers to focus on new alternative compounds obtained from plants, microorganisms, and marine invertebrates, and newly synthesized synthetic chemicals are being tested to develop new alternatives to MDR [14,15,16].

Schiff Bases (SB) are known as special ligands due to the flexible, variable, and electronic properties of the functional azomethine bond (C=N) in their structures. They are used in many different fields from analytical chemistry to the pharmaceutical industry [17]. One of the most important areas of SB study is the biological activity of the compounds. The main goal is to find safe and effective therapeutic agents to treat bacterial infections and cancer [18].

Approximately 25% of the drugs used in the field of human and animal health contain one or more fluorine atoms. The fluorine atom increases the lipophilicity and thermal stability of drugs with its electronegative property and contributes to the formation of stronger bonds of drugs with enzymes and their receptors [19,20]. Apoptosis is a form of programmed death that requires energy and occurs in cells that become unable to sustain life as a result of internal and external effects. Caspase enzymes play an important role in the process of apoptosis. Apoptosis process; It occurs with the activation of initiating caspase (2,8,9,10), terminator caspase (3,6,7), and inflammatory (1,4,5,11,12,13,14) caspase enzymes that enable apoptosis. Situations such as irreparable DNA damage in the cell, exposure to cytotoxic drugs, and an increase in reactive oxygen species cause the internal apoptosis mechanism to be activated [21,22,23]. Cytochrome C is a structure located between the membranes of healthy cell mitochondria and plays an important role in obtaining energy. In the cell undergoing apoptosis, cytochrome c passes into the cytoplasm due to the decrease in the mitochondrial membrane potential [21]. The combination of the apoptosis-activating factor, cytochrome c, and caspase-9 forms apoptosome. The apoptosome binds to inactive caspase 3, enabling its activation. With the activation of Caspase-3 in the process of apoptosis, the cell enters the path of irreversible death. Active caspase- 3; Chromatin condensation, DNA fragmentation in cells causes the

formation of apoptotic bodies and the apoptosis process is completed [22,24,25].

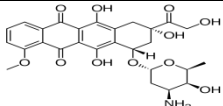
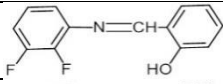
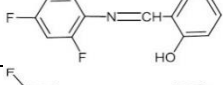
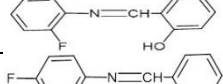
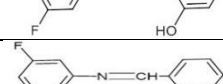
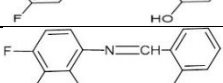
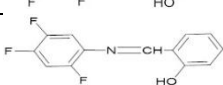
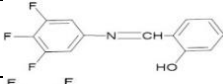
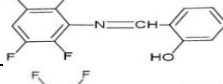
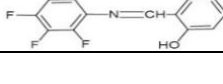

In this study, the cytotoxic, antiproliferative and apoptotic properties of fluorinated salicylamidine derivative (SB) ligands were investigated on A549 cells representing non-small cell lung cancer and some bacteria species *Escherichia coli* (*E. coli*), *Staphylococcus aureus* (*S. aureus*) and *Pseudomonas aureginosa* (*P. aureginosa*) that are at risk for the development of drug resistance.

2. MATERIAL AND METHOD

2.1. Chemicals

The compounds used in the study were synthesized from salicylaldehydes with anilines containing fluorine in different numbers and positions (Table 1). Their cytotoxic, antiproliferative, antiapoptotic, and antimicrobial properties were tested Doxorubicin (DOX) was used as a positive control for anticancer studies, and gentamicin (GEN) was used for antimicrobial studies. Compounds were dissolved in ethyl alcohol at a dose of 10 mM and sterilized by passing through syringe type 20 µm pore size filters and stored at 4°C.

Table 1. Chemical properties of DOX and fluorinated SB ligands

Compound	Chemical name	Chemical Formula	Structure	MW(g/mol)
DOX	Doxorubicin	C ₂₇ H ₂₉ N ₁ O ₁₁		543
C1	F _{2,3} -SAL	C ₁₃ H ₉ NO F ₂		233
C2	F _{2,4} -SAL	C ₁₃ H ₉ NO F ₂		233
C3	F _{2,5} -SAL	C ₁₃ H ₉ NO F ₂		233
C4	F _{3,4} -SAL	C ₁₃ H ₉ NO F ₂		233
C5	F _{3,5} -SAL	C ₁₃ H ₉ NO F ₂		233
C6	F _{2,3,4} -SAL	C ₁₃ H ₈ NO F ₃		251
C7	F _{2,4,5} -SAL	C ₁₃ H ₈ NO F ₃		251
C8	F _{3,4,5} -SAL	C ₁₃ H ₈ NO F ₃		251
C9	F ₄ -SAL	C ₁₃ H ₇ NO F ₄		269
C10	F ₅ -SAL	C ₁₃ H ₆ NO F ₅		287

2.2. Cell Line and Bacterial Strains

A549 cells (ATCC) a lung adenocarcinoma cell line derived from human non-small cell lung cancer cells were cultured in DMEM+F12 medium containing 10% fetal calf serum. Bacterial stock strains for *E. coli* (ATCC, 25922), *S. aureus* (ATCC, 29213), and *P. aureginosa* (ATCC, 27853) were cultured in Mueller-Hinton (MH) broth.

2.3. MTT Analysis for Cell Cytotoxicity

DOX and SB ligands (C1-10) were added to 96-well culture plates at 1, 10, 100, and 1000 µM concentration in triple order. A549 cells were suspended at 10⁵ cells ml⁻¹ and then added to each culture well in a volume of 100 µl. The culture plates were incubated at 37°C in a humidified environment containing 5% CO₂ for 72 h. At the end of culture period, 10 µl MTT solution (3-(4,5-dimethylthiazol-2-yl)-2,5-diphenyltetrazolium bromide, Sigma) at 250 µM concentration was added to each well and then incubated for more 4 h. MTT-formazan crystals were dissolved by adding 100 µl of dimethyl sulfoxide (DMSO, Sigma) to each well. Culture plates were read at an ELIZA microplate reader (MD Spectramax, M5) at a wavelength of 570 nm and optical density (OD) values were recorded for each well. IC₅₀ values were calculated by nonlinear regression analysis using OD values.

2.4. CFSE Analysis for Cell Proliferation

A549 cells were incubated with CFSE (5(6)-Carboxyfluorescein diacetate N-succinimidyl ester, Sigma) at 1,5 µM concentration for 20 min in the dark at 37°C under a humidified 5% CO₂ atmosphere. After incubation, CFSE was removed by washing twice with PBS and then analyzed at flow cytometry in FL-1 (green fluorescent channel in the range 10⁰ - 10⁴) to determine the maximum fluorescence intensity of the cells (Navios, Beckman Coulter). Unstained cells were used to determine autofluorescence. CFSE-stained cells were incubated at 10⁵ ml⁻¹ concentration with IC₅₀ doses of DOX and SB ligands at 37°C in a humidified atmosphere containing 5% CO₂ for 72 h. After incubation, the fluorescent intensity of cells was determined by using an FL1 histogram (Figure 1). Proliferative indexes (PI) were calculated using LISTMOD data by FacsExpress flow cytometry software.

2.5. Rho123 Analysis for Determining Mitochondrial Potential

A549 cells were added to each well at 10⁵ ml⁻¹ doses and incubated with DOX and FSB ligands in IC₅₀ doses at 37°C in a humidified atmosphere containing 5% CO₂ for 72 h. After incubation, cells were treated with 10 µl of Rho123 (1 mg ml⁻¹, Sigma) at 37°C for 60 min at 37°C in a humidified atmosphere containing 5% CO₂ in the dark. Rho123 accumulation levels of the cells were determined by flow cytometry using FL-1 histogram (Figure 2). Unstained cells were used for autofluorescence determination.

2.6. Cleaved Caspase-3 Expression Analysis for Detection of Apoptosis

A549 cells at 10^5 ml⁻¹ doses were incubated with an IC₅₀ dose of DOX and FSB ligands at 37°C in a humidified atmosphere containing 5% CO₂ for 72 h. After incubation, cells have been rinsed within PBS and then fixed with 4% paraformaldehyde at 37 °C for 20 min. Cells were incubated for 15 min with 1% Triton® X-100 for permeabilization. Cells then were treated for 30 min with 3% of BSA/PBS for blocking. Eventually, cells were incubated with anti-cleaved caspase-3 monoclonal antibody (Alexa Fluor® 488 conjugate, Cell Signaling Technology) at room temperature for 2 h in the dark. Cells were examined by using a fluorescent microscope to determine cleaved caspase-3 expressions.

2.7. Histopathological Morphology Analyses

A549 cells were added to each well at 10^5 ml⁻¹ doses and incubated with DOX and FSB ligands in IC₅₀ doses at 37°C in a humidified atmosphere containing 5% CO₂ for 72 h. After incubation, morphological cell analysis was performed using standard hematoxylin-eosin (H&E), Giemsa, and Papanicolaou (PAP) staining protocols. Cells were examined under a light microscope to determine the morphological changes indicating apoptosis formation in the cells.

2.8. MTT Analysis for Determining Antibacterial Effects

1 ml of each pre-culture suspension of bacterial strains was transferred into 50 ml Mueller Hinton (MH) broth for sub-culturing. Gentamycin (GEN) and SB ligands were added to 96-well culture plates in triple order as 1, 10, 100, and 1000 µM. The bacteria suspension in MH medium was adjusted to 0.5 McFarland standards and 100 µl of suspension was added to each well and then incubated at 37°C for 18 h. After incubation, 10 µl of 250 µM MTT solution was added to each well and incubated for another 4 h 100 µl of DMSO was added to the culture wells to dissolve the MTT-formazan crystals. Culture plates were read at 570 nm in the ELIZA microplate reader and OD values were recorded for each culture plate well. MIC₅₀ values were calculated by linear regression analysis using OD values.

2.9. Statistical Analysis

Analysis of data, determination of IC₅₀ values, and MIC₅₀ values of each compound were performed using GraphPad Prism version 9.1.1 (GraphPad Software, La Jolla California USA). The ANOVA test was used to compare the dose-dependent cytotoxic effects of each compound on A549 cells. SPSS (IBM AMOS VERSION) was used for the ANOVA test. The reliability of the antibacterial data was obtained by performing the homogeneity test from the OD values. Differences between data sets were considered statistically significant when the p-value was less than 0.05.

3. RESULTS

3.1. Cytotoxicity

IC₅₀ (half-maximal inhibitory concentration) is an informative measure of the efficacy of a drug [26]. The IC₅₀ values are used to determine the potency of DOX and SB ligands to inhibit the biological functions of A549 cells. The strongest cytotoxic effect on A549 cells was obtained with C7 (F2,4,5-SAL, IC₅₀: 1.4 µM), which has 3 fluorine atoms in its structure, showed stronger cytotoxic activity than DOX (IC₅₀: 1.9 µM) which is a standard chemotherapy drug (Table 2).

3.2. Antiproliferative Effects

PI gives information about the proliferation ability of cells [27] The lowness of this index determines the power of DOX or SB ligands to inhibit the proliferation of A549 cells. It was observed that C8 (F3,4,5-SAL) and C10 (F5-SAL) showed the strongest antiproliferative activity (respectively PI: 2.1 and 2.2) according to the PI values giving information about the antiproliferative capacity of SB ligands on A549 cells. DOX (PI: 1.5) was found to have stronger antiproliferative capacity than SB ligands in terms of antiproliferative capacity (Table 2).

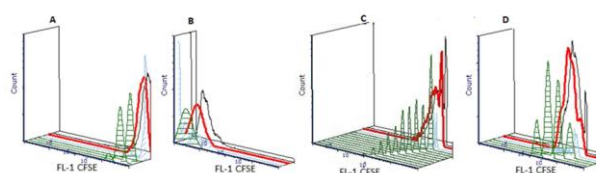


Figure 1. CFSE analysis by flow cytometry (A) Fluorescent intensity of the cells zero h CFSE staining (B) Fluorescent intensity of the cells 72 h after CFSE staining (C) Fluorescent intensity of the cells after 72 h with DOX (D) Fluorescent intensity of the cells after 72 h with Salicylaldehyde compound

Table 2. Cytotoxic, antiproliferative, apoptotic effects of DOX and fluorinated SB ligands on A549 cells

	Bacteria	<i>E. coli</i>	<i>S. aureus</i>	<i>P. aeruginosa</i>
MIC ₅₀ (µM)	GEN	1.5	1.7	2.2
	C1	35.0	49.3	42.8
	C2	32.6	50.1	40.4
	C3	33.7	27.3	41.2
	C4	33.0	24.3	36.2
	C5	33.1	24.1	37.3
	C6	36.5	38.5	43.5
	C7	35.8	26.9	46.2
	C8	32.2	54.5	36.5
	C9	32.8	18.6	42.2
C10	32.8	23.04	43.0	

3.3. Mitochondrial Membrane Potential

Changes in mitochondrial membrane potential can be determined by flow cytometry analysis of Rho123 accumulation in cells. This loss of potency is associated with the development of apoptosis in cells. In flow cytometric analysis which has been performed after the application of DOX and SB ligands, it was observed that there were decreases in Rho123 accumulation at varying levels in the cells. Among the SB compounds, the lowest

accumulation of Rho123 was found in cells treated with C5 (F3.5-SAL, mean fluorescent channel: 1330), and this level was higher than in cells treated with DOX (mean fluorescence channel: 1574), (Table 2).

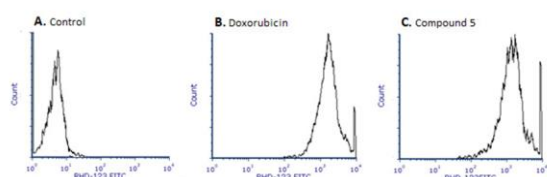


Figure 2. Rho123 analysis by flow cytometry. A) Unstained cells used for determining auto-fluorescent B) DOX-treated cells stained with Rho123 C) Salicylaldehyde compound (C5) treated cells stained with Rho123.

3.4. Cleaved Caspase-3 Expression

Caspase-3 is a critical implementer of apoptosis, as it is partially or completely responsible for the proteolytic cleavage of many important key proteins. Active caspase-3 is expressed in the cells when a cell is driven to apoptosis [22]. Determination of cleaved caspase-3 expression in A549 cells treated with DOX and SB ligands indicates that the cytotoxic effect in cells occurs via apoptosis (Figure 3).

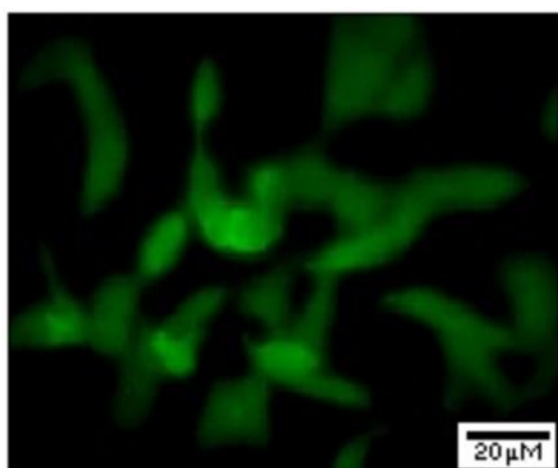


Figure 3. Cleaved caspase-3 expression of A549 cells treated with fluorosalicylaldehydes. Cells were stained with anti-cleaved caspase-3 after 72 h incubation with synthesized fluorinated fluorosalicylaldehydes and then examined under a fluorescent microscope (Mag).

3.5. Cell Morphology

The occurrence of apoptosis in cells can be characterized by a series of typical morphological features that can be followed by staining the cells with dyes used in histopathology and then microscopic examinations [25]. Chromatin condensation and marginalization, bubbling and shrinkage on the cell surface, and the presence of apoptotic bodies and ghost cells in microscopic evaluation after Giemsa, H&E, and PAP staining are important evidence that DOX and SB ligands triggered apoptosis in cells (Figure 4A, B and C)

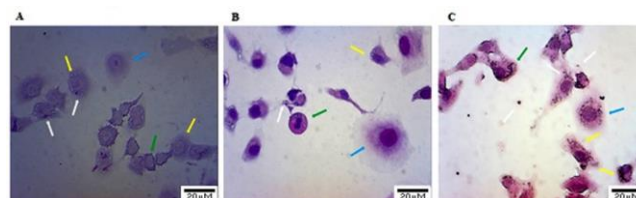


Figure 4. A) Giemsa, B) H&E, and C) PAP staining of the cells after cultured 72 h with chemicals. Green arrows: chromatin condensation and marginalization, white arrows: apoptotic bodies, blue arrow: ghost cell, yellow arrows: cell membrane blebbing and blistering

3.6. Antibacterial Activity

The MIC value is the minimum dose of antimicrobial agent concentration that is needed to inhibit the growth of a target microorganism. MIC₅₀ more specifically indicates the intrinsic potency of an antimicrobial and is used in studies to describe how effective a particular antimicrobial is on a species [28]. GEN used as a positive control showed strong antimicrobial capacity on *E. coli*, *S. aureus*, and *P. aeruginosa* (MIC₅₀: 1.5, 1.7, and 2.2 μM, respectively), but the antimicrobial effects of SB ligands on these bacterial species (MIC₅₀: ranged 32.2-36.5, 18.6-54.5, 36.2-46.2 μM, respectively) were not found remarkable.

Table 3. Antibacterial effects of GEN and fluorinated SB ligands on the bacteria species

	Parameters	IC ₅₀ (μM)	Proliferative Index (PI)	Rho123 (FL-1*)
Compounds	DOX	1.9	1.5	1574
	C1	11.6	2.4	1571
	C2	12.3	2.4	2700
	C3	6.1	2.3	2305
	C4	2.1	2.4	1444
	C5	5.2	3.9	1330
	C6	2.5	4.6	2986
	C7	1.4	2.6	2609
	C8	4.1	2.2	2521
	C9	31.5	2.4	3615
C10	13.9	2.1	2031	

4. DISCUSSION AND CONCLUSION

The development of new effective anti-tumor agents based on new chemical compositions with novel structures is important to cope with this drug resistance [29]. In this respect, SB compounds are of great interest in the field of new alternative drug research [30]. The discovery of compounds with both anticancer and antimicrobial effects is of great importance as cancer cells and bacteria have similar resistance mechanisms, such as increasing the extracellular excretion of drugs and changing drug target sites [31,32].

Replacing the Hydrogen (H) atom with Fluorine (F) is a frequently used strategy in new drug studies to increase the efficacy of existing drugs. F atom in drugs prevents enzymes involved in metabolic events such as Krebs cycle and glycolysis in cells, prevents protein synthesis, damages lysosomes, and reduces cell membrane potential by inhibiting sodium ATPase [33,34,35]. It is sometimes stated that Fluorinated SB derivatives exhibit stronger effects than anticancer and antimicrobial drugs used as positive controls [36,37,38]. In addition, it can be said that fluorine-containing SB derivatives exhibit

strong cytotoxic effects on cancer cells, while they show low cytotoxicity on normal cells with high proliferation rates [39,40].

It has been reported in some studies that Schiff bases containing fluorine or trifluoromethyl in the phenyl ring exhibit potent cytotoxic effects on A549 cancer cells [40,41]. The biological activities of fluorine-substituted SB compounds are affected by the number and position of fluorine atoms, and it has been reported that the compound containing 5 fluorine atoms has the strongest cytotoxic effect on A549 cells [42]. In a study that investigated the anticancer effects of SB compounds carrying fluorine atoms on A549, Hep G-2, and HeLa cells, it is emphasized that the compound carrying two fluorine atoms has stronger anticancer effects than cisplatin and the position of the fluorine atom is important in the activities of the compounds [38]. In this study, we can state that the fluorine atom numbers and positions of the SB ligands are effective in cytotoxicity and that the compounds containing 3 fluorines show stronger cytotoxic effects 2, 4, and 5, and the difference in the cytotoxic effects of the 3-fluorinated ligands varies depending on the positions of the fluorine atoms.

Determining the antiproliferative capacities of a compound on cancer cells is of great importance in the discovery of new chemotherapeutic agents. In a recent study, aminophenylhydrazine SB compounds were tested for their antiproliferative capacity on A549 cells and showed that those containing two fluorine atoms had the strongest antiproliferative effect compared to five fluorine atoms [42]. Another study with SB compounds carrying fluorine atoms in the ortho and para positions showed that the antiproliferative effects of the compounds on K562 cells were lower than that of DOX [43]. In our study, although the lowest PI value among SB ligands was obtained with 5 fluorinated compounds, this antiproliferative capacity lagged behind DOX, which is the standard chemotherapeutic drug.

Determination of mitochondrial membrane potential is considered an important criterion in determining the apoptotic effect of compounds on cells. In a study that tested the apoptotic effects of N-phenyl carbazole triphenyl amine modified semi-sandwich (III) SB compounds and their complexes with iridium on A549, HeLa, BEAS cells, it was emphasized that the decrease in mitochondrial membrane potential indicates that apoptosis is effective in the death of cells [35]. In our study, it was observed that SB ligands with difluorine atoms had a stronger effect on mitochondrial membrane potential in A549 cells than DOX, whereas ligands containing three, four, and five fluorine atoms had a lower capacity than DOX. We understand that there is a negative correlation between the number of fluorine atoms of ligands and their ability to reduce mitochondrial membrane potential, thereby driving cells into apoptosis.

Cleaved caspase-3 expression is one of the most important molecular biomarkers that indicate the occurrence of apoptosis in cells. Cell death is a process

with many types; It occurs in different ways such as apoptosis, pyroptosis, and autophagy. The role of apoptosis in cancer treatment and prognosis is very important. Recently, it has been suggested that caspase-3 may associate apoptosis with pyroptosis which causes inflammatory cell death. It is stated that the induction of both apoptosis and pyroptosis with the effectiveness of chemotherapeutics is an important modality for cancer treatment and caspase-3 is an important stimulator for both [44]. The observation of cleaved caspase-3 expression in A549 cells in our study indicates that the cytotoxic effects of DOX and SB ligands occur through the induction of apoptosis in the cells.

Cell morphology analyses provide useful data for obtaining information about cell cytotoxicity. Morphological changes indicative of apoptosis such as cytoplasmic shrinkage, membrane overflow, and DNA fragmentation were observed in cells treated with SB copper coordinated compound [45]. Observation of cellular morphological changes such as chromatin condensation and marginalization, presence of apoptotic bodies, ghost cells, and cell membrane swelling and shrinkage, which indicate apoptosis in A549 cells in our study, is another important finding that apoptosis is effective in cell cytotoxicity of FSB ligands.

Many studies show that SB compounds have antimicrobial properties. Fluorinated SB containing F or CF₃ at the meta position on the N-aryl ring has been found to exhibit potent antimicrobial activity on *S. aureus*, *B. subtilis*, *E. coli*, and *K. pneumoniae* [46]. It has been determined that the fluorine-bearing compound in the para position of the phenol ring shows strong antimicrobial activity and has a stronger antifungal effect than fluconazole, which is currently used in the treatment of fungal infections [47]. In a study that investigated the antimicrobial properties of six SB compounds derived from 3-fluoro salicylaldehyde on *K. pneumoniae*, *S. typhi*, *S. aureus*, *B. subtilis*, *P. aeruginosa*, *E. coli* bacteria and *P. chrysogenum*, *C. albicans*, *A. niger* and *A. flavus*. It has been determined that most of the compounds have antibacterial and antifungal activity on these bacteria [48]. In this study, contrary to the other presented studies, it was observed that the antimicrobial effects of fluorinated salicylaldehyde SB compounds on *E. coli*, *S. aureus*, and *P. aeruginosa* were lower than gentamicin, a standard antibacterial drug, and none of the compounds had significant effects on the tested bacteria. Salicylaldehyde derivative Schiff Base compounds containing fluorine atoms in different numbers and positions show promising anti-cancer properties such as cytotoxicity, inhibiting proliferation, and directing A549 lung cancer cells to apoptosis but, they remained unremarkable in terms of their antibacterial effect on *E. coli*, *S. aureus* and *P. aeruginosa*.

In this study, the anticancer and antimicrobial properties of Schiff base derivative (C1-C10) containing fluorine atoms in different numbers and positions were investigated. Cytotoxic, antiproliferative, and apoptotic properties of the synthesized compounds were examined

on A549 cells. Its antimicrobial properties were investigated on *E. coli*, *P. aureginosa*, and *S. aureus* bacterial strains. It was observed that these synthesized compounds exhibited strong cytotoxic effects on A 549 cells. It was determined that Compound 7 (IC₅₀: 1.4 µM), which has fluorine atoms attached at the –middle, -meta, and –para positions, exhibited a stronger cytotoxic effect than DOX (IC₅₀: 1.9 µM), which was used as a positive control. Compound 4 (2.1 µM) and Compound 6 (2.5 µM) showed cytotoxic effects close to DOX. The synthesized compounds showed high (Compound 3, 4, 5, 6, 7, and 8) and moderate (1, 2, 9, and 10) cytotoxic effects. Compounds 1, 2, 3, 4, 5, 7, 8, 9, and 10 (PI values 2.4, 2.4, 2.3, 2.4, 2.6, 2.2, 2.4, and 2.1, respectively) were used as positive control near DOX (PI: 1.5). It has been determined that it exhibits antiproliferative effects. Compounds 1, 4, and 5 (Rho 123 values 1571, 1444, and 1330, respectively) were found to be more potent in reducing mitochondrial membrane potential than Dox (Rho 123:1574). It was determined that the compounds caused decreases in mitochondrial membrane potential, thus the release of active caspase-3. After the release of active caspase-3 in cells, DNA fragmentation, apoptotic bodies, ghost cells, etc. occur. By observing the structures microscopically after Hematoxylin-Eosin, Giemsa, and PAP staining, it can be said that the synthesized compounds are successful in directing A549 cells to apoptosis. When evaluated as antimicrobials, the MIC₅₀ values of the synthesized compounds on *E. coli*, *P. aureginosa*, and *S. aureus* strains were found to vary between 18.50 and 49.3. It can be said that the compounds showed moderate antimicrobial effects compared to Gentamicin (MIC₅₀ values of 1.5, 1.7, and 2.2, respectively), which was used as a positive control. It can be said that the results of the study are promising for the use of the synthesized compounds in vivo studies.

Acknowledgement

This study is supported by the Harran University Scientific Research Project Coordination Unit (Project No: 20160). Supplying chemical compounds, Prof. Dr. Thank you Veli KASUMOV.

There is no need for an ethics Committee Document for our study.

REFERENCES

- [1] Chabner BA, Roberts TG Jr. Chemotherapy and the war on cancer. *Nat Rev Cancer*.2005;5: 65–72.
- [2] Kamb A, Wee S, Lengauer C. Why is cancer drug discovery so difficult? *Nat Rev Drug Disc*. 2007; 6: 115–120.
- [3] Shilpa BS, Padmamma S, Kumara AT. Mapping of scientific articles on Leukemia: A scientometric study. *Libr Philos Pract*. 2019; 1: 1-24.
- [4] Aktimur SH, Gunes AK, Akidan O. Efficacy of the Combination of Venetoclax and Azacitidine in Elderly of Frail Relapsed/Refractory Patients with Acute Myeloid Leukemia, First Multi-Institutional Real World Experience from Türkiye. *J Hematol Oncol*. 2020; 31(4): 213.
- [5] Kankala RK, Liu CG, Yang DY. Ultrasmall platinum nanoparticles enable deep tumor penetration and synergistic therapeutic abilities through free radical species-assisted catalysis to combat cancer multidrug resistance. *Chem Eng J*. 2020;383: 123.
- [6] Sonbol, H., Ameen, F., AlYahya, S., Almansob, A., & Alwakeel, S. Padina Boryana mediated green synthesis of crystalline palladium nanoparticles as potential nanodrug against multidrug-resistant bacteria and cancer cells. *Scientific reports*. 2021; 11(1), 1-19.
- [7] Magiorakos, A. P., Srinivasan, A., Carey, R. B., Carmeli, Y., Falagas, M. E., Giske, C. G., Monnet, D. L. Multidrug-resistant, extensively drug-resistant and pan drug-resistant bacteria: an international expert proposal for interim standard definitions for acquired resistance. *Clinical microbiology and infection*. 2012;18(3), 268-281.
- [8] Moitra K. Overcoming Multidrug Resistance in Cancer Stem Cells. *Biomed Res Int*. 2015:635745.
- [9] Wang, X., Zhang, H., & Chen, X. Drug resistance and combating drug resistance in cancer. *Cancer Drug Resistance*. 2019; 2(2), 141.
- [10] Orsi, G. B., Falcone, M., & Venditti, M. (2011). Surveillance and management of multidrug-resistant microorganisms. *Expert Review of Anti-Infective Therapy*. 2019; 9(8), 653-679.
- [11] Peraman, R., Sure, S. K., Dusthacker, V. N., Chilamakuru, N. B., Yiragamreddy, P. R., Pokuri, C., et.al. Insights on recent approaches in drug discovery strategies and untapped drug targets against drug resistance. *Future Journal of Pharmaceutical Sciences*. 2021; 7(1), 1-25.
- [12] WC Soo, V., Kwan, B. W., Quezada, H., Castillo-Juárez, I., Pérez-Eretza, B., Julieta García-Contreras, S., García-Contreras, R. Repurposing of anticancer drugs for the treatment of bacterial infections. *Current topics in medicinal chemistry*. 2017; 17(10), 1157-1176.
- [13] Can, G. Side effects of antineoplastic drugs and nursing approaches. *Journal of Education and Research in Nursing*. 2005; 2(2), 8-15.
- [14] Majolo, F., Delwing, L. K. D. O. B., Marmitt, D. J., Bustamante-Filho, I. C., & Goettert, M. I. Medicinal plants and bioactive natural compounds for cancer treatment: Important advances for drug discovery. *Phytochemistry Letters*. 2019; 31, 196-207.
- [15] Temel, M. K. The development of cytotoxic chemotherapeutics in the twentieth century. *Turkish Journal of Oncology*. 2015; 30(2).
- [16] Bukowski, K., Kciuk, M., & Kontek, R. Mechanisms of multidrug resistance in cancer chemotherapy. *International journal of molecular sciences*. 2020; 21(9), 3233.
- [17] Uddin, M. N., Ahmed, S. S., & Alam, S. R. Biomedical applications of Schiff base metal complexes. *Journal of Coordination Chemistry*. 2020; 73(23), 3109-3149.

- [18] Matela, G. Schiff bases and complexes: a review on anti-cancer activity. *Anti-Cancer Agents in Medicinal Chemistry*. 2020; 20(16), 1908-1917.
- [19] Al-Harthy, T., Zoghaib, W., & Abdel-Jalil, R. Importance of fluorine in benzazole compounds. *Molecules*. 2020; 25(20), 4677.
- [20] Inoue, M., Sumii, Y., & Shibata, N. Contribution of organofluorine compounds to pharmaceuticals. *ACS omega*. 2020; 5(19), 10633-10640.
- [21] Bildik A, Bayar İ. Kanserde apoptotik Yolakların İnhibisyonu. *Türkiye Klinikleri J Vet Sci*. 2018; 9(2):42-51.
- [22] Kaya C, Çalışkan Y, Yönden Z. Apoptozis. *The Medical Journal of Mustafa Kemal University*. 2012; 3(11); 26-37.
- [23] Atagün G, Zafer, E, Gürkanlı İ. Apoptoziste mitokondrinin rolü. *Türk Bilimsel Derlemeler Dergisi*. 2011; 4(2): 9-53.
- [24] Dağdeviren T. Programlı hücre ölümü; Apoptoz. *Gaziosmanpaşa Üniversitesi Tıp Fakültesi Dergisi*. 2021; 3(3), 120-135.
- [25] Coşkun G, Özgür H. Apoptoz ve nekrozun moleküler mekanizması. *Arşiv Kaynak Tarama Dergisi*. 2012; 20(3): 145-158.
- [26] Berrouet C, Dorilas N, Rejniak K A, Tuncer N. Comparison of drug inhibitory effects (IC 50) in monolayer and spheroid cultures. *Bulletin of Mathematical Biology*, 2020; 82(6) 68.
- [27] Elias J M. Cell proliferation indexes: a biomarker in solid tumors. *Biotechnic & histochemistry*, 1997; 72(2): 78-85.
- [28] Schwarz S, Silley P, Simjee S, Woodford N, van Duijkeren E, Johnson A P., et al. (Assessing the antimicrobial susceptibility of bacteria obtained from animals. *Journal of antimicrobial chemotherapy*. 2010; 65(4): 601-604.
- [29] Rice, L. B. Unmet medical needs in antibacterial therapy. *Biochemical pharmacology*. 2006; 71(7), 991-995.
- [30] Fekri R, Salehi M, Asadi A. Synthesis, characterization, anticancer and antibacterial evaluation of Schiff base ligands derived from hydrazone and their transition metal complexes. *Inorganica Chim Acta*. 2019; 484: 245-254.
- [31] Kumar, A., Chakma, U., Chandra, A., Howlader, D., Akash, S., Kobir, M., et.al. Modified D-glucofuranose computationally screening for inhibitor of breast cancer and triple breast cancer: Chemical descriptor, molecular docking, molecular dynamics, and QSAR. *Journal of the Chilean Chemical Society*. 2022; 67(3), 5623-5635.
- [32] Housman, G., Byler, S., Heerboth, S., Lapinska, K., Longacre, M., Snyder, N., & et.al. Drug resistance in cancer: an overview. *Cancers*. 2014; 6(3), 1769-1792.
- [33] Strunecká, A., Patočka, J., & Connett, P. Fluorine in medicine. *J Appl Biomed*. 2004; 2, 141-150.
- [34] Kurtdede, E. Türkiye'de florozis sorunu ve florun biyokimyasal etkileşimi. *Atatürk Üniversitesi Veteriner Bilimleri Dergisi*. 2017; 2(3), 320-326.
- [35] Chen, S., Liu, X., Ge, X., Wang, Q., Xie, Y., Hao, Y., et.al. Lysosome-targeted iridium (III) compounds with pyridine-triphenylamine Schiff base ligands: Syntheses, antitumor applications and mechanisms. *Inorganic Chemistry Frontiers*. 2020; 7(1), 91-100.
- [36] Gupta, D., & Jain, D. K. Synthesis, antifungal and antibacterial activity of novel 1, 2, 4-triazole derivatives. *Journal of advanced pharmaceutical technology & research*. 2015; 6(3), 141.
- [37] Avila-Sorrosa, A., Bando-Vázquez, A. Y., Alvarez-Alvarez, V., Suarez-Contreras, E., Nieto-Meneses, R., Noguera-Torres, B., et. al. Synthesis, characterization and preliminary in vitro trypanocidal activity of N-arylfluorinated hydroxylated-Schiff bases. *Journal of Molecular Structure*. 2020; 1218, 128520.
- [38] Wu, R., Bi, C., Zhang, X., Zong, Z., Fan, C., Zhang, X., et.al. Syntheses, crystal structure and biological evaluation of three novel Cu (II) complexes with Schiff base derived from fluorinated amino acid and Salicylaldehyde. *Applied Organometallic Chemistry*. 2020; 34(1), e5264.
- [38] Würtenberger, I., Follia, V., Lerch, F., Cwikla, C., Fahrner, N., Kalchschmidt, C., et. Al. Fluorinated Fe (III) salophene complexes: optimization of tumor cell-specific activity and utilization of fluorine labeling for in vitro analysis. *Journal of Medicinal Chemistry*. 2015; 58(2), 588-597.
- [40] Zeng, L., Deng, Y., Weng, L., Yang, Z., Chen, H., Liu, Q. Synthesis and Anti-Tumor Activities of Fluoride-Containing Gossypol Derivatives Compounds. *Natural Science*. 2017; 9(9), 312-318.
- [41] Mahal, A., Wu, P., Jiang, Z. H., & Wei, X. Schiff bases of tetrahydro curcumin as potential anticancer agents. *Chemistry Select*. 2019; 4(1), 366-369.
- [42] Sak, Z. H. A., Süzergöz, F., Kasumov, V. T., Gürol, A. O. Anticancer Properties of Fluorinated Aminophenylhydrazines on A549 Lung Carcinoma Cell Line. *Iranian Journal of Public Health*. 2021; 50(3), 550-556.
- [43] Gurol, A. O., Kasim, V., Suzergoz, F. Antiproliferative effects of fluorine substitute 3, 5-di-tert-butylphenol bearing Schiff bases using CFSE-based cell proliferation assay. *Current Science*. 2017; 619-624.
- [44] Li, L., Wang, S., & Zhou, W. Balance. Cell Apoptosis and Pyroptosis of Caspase-3-Activating Chemotherapy for Better Antitumor Therapy. *Cancers*. 2022; 15(1), 26.
- [45] Xia, Y., Liu, X., Zhang, L., Zhang, J., Li, C., Zhang, N., Li, Y. A new Schiff base coordinated copper (II) compound induces apoptosis and inhibits tumor growth in gastric cancer. *Cancer Cell International*. 2019; 19, 1-11.
- [46] Avila-Sorrosa, A., Hernández-González, J. I., Reyes-Arellano, A., Toscano, R. A., Reyes-Martínez, R., Pioquinto-Mendoza, J. R., et.al. Synthesis, structural characterization and biological activity of fluorinated Schiff-bases of the type [C6H4-1-(OH)-3-(CHNArF)]. *Journal of Molecular Structure*. 2015; 1085, 249-257.
- [47] Carreño A, Rodríguez L, Páez-Hernández D, Martín-Trasanco R, Zúñiga C, Oyarzún DP, et.al. Two New Fluorinated Phenol Derivatives Pyridine

Schiff Bases: Synthesis, Spectral, Theoretical Characterization, Inclusion in Epichlorohydrin- β -Cyclodextrin Polymer, and Antifungal Effect. *Front Chem.* 2018;30; 6:312.

- [48] Shanmugam M, Narayanan K, Mahalakshmi M, Kabilan S, Chidambaranathan V. Synthesis, characterization and biological studies of some novel 3-fluorosalicylaldehyde based amine derivatives. *Spectrochim Acta A Mol Biomol Spectrosc.* 2013; 116:394-400.

Classification of Circular Knitting Fabric Defects Using MobileNetV2 Model

Kazım HANBAY^{1*} 

¹ İnönü University, Engineering Faculty, Software Engineering Department, Malatya, Türkiye
Kazım HANBAY ORCID No: 0000-0003-1374-1417

*Corresponding author: kazimhanbay@gmail.com

(Received: 15.07.2023, Accepted: 16.11.2023, Online Publication: 28.12.2023)

Keywords

Fabric defect
detection,
Deep learning,
Image processing,
Circular knitting

Abstract: Fabric defects cause both labor and raw material losses and energy costs. These undesirable situations negatively affect the competitiveness of companies in the textile sector. Traditionally, human-oriented quality control also has important limitations such as lack of attention and fatigue. Robust and efficient defect detection systems can be developed with image processing and artificial intelligence methods. This study proposes a deep learning-based method to detect and classify common fabric defects in circular knitting fabrics. The proposed method adds a fine-tuned mechanism to the MobileNetV2 deep learning model. The added fine-tuned mechanism is optimized to classify fabric defects. The proposed model has been tested on a fabric dataset containing circular knitting fabric defects. Obtained results proven that the proposed method produced desired results in fabric defect detection.

MobileNetV2 Modeli Kullanılarak Yuvarlak Örgü Kumaş Hatalarının Sınıflandırması

Anahtar Kelimeler

Kumaş hatası
tespiti,
Derin öğrenme,
Görüntü işleme,
Yuvarlak örgü

Öz: Kumaş hataları hem işçilik ve hammadde kayıplarına hem de enerji maliyetlerine neden olur. Bu istenmeyen durumlar tekstil sektöründeki firmaların rekabet gücünü olumsuz etkilemektedir. Geleneksel olarak, insan odaklı kalite kontrolü dikkat eksikliği ve yorgunluk gibi önemli sınırlamalara sahiptir. Görüntü işleme ve yapay zeka yöntemleri ile sağlam ve verimli hata tespit sistemleri geliştirilebilir. Bu çalışma, yuvarlak örgü kumaşlarda yaygın kumaş hatalarını tespit etmek ve sınıflandırmak için derin öğrenme tabanlı bir yöntem önermektedir. Önerilen yöntem, MobileNetV2 derin öğrenme modeline ince ayarlı bir mekanizma eklemektedir. Eklenen ince ayarlı mekanizma, kumaş hatalarını sınıflandırmak için optimize edilmiştir. Önerilen model, yuvarlak örgü kumaş hataları içeren bir kumaş veri seti üzerinde test edilmiştir. Elde edilen sonuçlar, önerilen yöntemin kumaş hatası tespitinde istenilen sonuçları verdiğini kanıtlamıştır.

1. INTRODUCTION

Fabric defect detection is the process of identifying and localizing defects or flaws in textile fabrics using automated or computerized methods. This can be done using image processing and machine learning techniques that analyze images of the fabric and identify any areas that differ from the normal fabric pattern, such as holes, stains, or discolorations. Fabric defect detection is important in ensuring the quality of textile products and reducing waste in manufacturing processes. The goal of fabric defect detection is to improve quality control in textile industry and ensure that only high-quality products are released to the market.

Traditional human-oriented fabric defect detection methods include various difficulties such as labor cost and eye strain. Therefore, artificial intelligence-based defect detection methods have been developed. Fabric defect detection studies made with machine learning and image processing methods can be examined in two groups in general: Motif-based methods and non-motif-based methods. The motif-based methods use a defect-free ground truth fabric image for comparison of the all fabric motifs. But in practice it is difficult to work with these methods as there are so many fabric and defect types. Therefore, there has been more interest in non-motif-based studies. The five primary categories of non-motif-based investigations are structural [1], statistical [2], model-based [3], learning-based [4] and spectral [5].

This study focuses on the ability of deep learning methods to detect circular knitting fabric defects. To classify different fabric patterns, robust and efficient methods have been developed by using deep learning architectures separately or together. Fabric images have regular shape and patterns. When defects occur, these regular shape and patterns are broken. At this point, these deteriorations are detected with strong pattern analysis and deep learning methods. In this paper, powerful deep learning model (i.e., MobileNet) is used to obtain better performance for specific fabric defects. To keep the model's initial learned parameters, alternative architecture is designed in a parallel configuration. Thus the proposed model achieves high defect detection results for circular knitting fabric defects.

From this point of view, this paper uses the MobileNetV2 deep learning model to detect common defects in circular knitting fabrics. The most important innovation point is that the proposed transfer learning-based model has been designed for circular knitting fabric defects. In addition, there are several advantages of the employed deep learning method:

Improved accuracy: The proposed approach, which makes use of the MobileNetV2 model, outperforms more established techniques like the shearlet transform and GLCM models in terms of accuracy.

Increased robustness: The proposed deep learning model can be more robust to noise and low contrast in the fabric images. By incorporating different convolution layers, the overall model can be more resistant to overfitting and generalization errors.

Faster training: Our deep learning model can often be trained more quickly than other deep models.

The rest of the paper is organized as follows. Section 2 introduces the prior works about the fabric defect detection. Section 3 presents the proposed hybrid deep learning model. Section 4 provides the experimental results and Section 5 concludes the paper.

2. LITERATURE REVIEW

Fabric defect detection is traditionally performed in a human inspection way. However, artificial intelligence and image processing methods are used in modern defect detection systems. There are many related literature papers about fabric defect detection. Also, there are different comprehensive reviews of fabric defect detection techniques using computer vision, including both traditional and deep learning-based approaches [6,7]. Mak et al. [8] presents a method for fabric defect detection that uses Gabor filters and morphological operations to enhance the texture and identify the defect regions. Huang and Xiang [4] developed a defect detection model based on CNN model and repeated pattern analysis. Their model uses both DeeplabV3+ and GhostNet to perform lightweight fabric defect detection. Zhou and Wang [9] proposed a unsupervised defect detection model by using local patch approximation. They used 2D maximum

entropy model to distinguish defective pixel regions from the abnormal map. High detection rates were taken on 54 defective fabrics.

Another paper proposes a texture analysis-based approach for fabric defect detection using support vector machines (SVMs) [10]. The method extracts texture features from the fabric image and uses SVMs to detect the defective regions. Zhao et al. [11] performed a defect detection system based on deep learning using a Faster R-CNN network. They used a normalization step to reduce some undesired situations such as brightness changes and noise. They performed detailed experimental works to compare the proposed model. The proposed model achieved more high detection results than Yolo, YoloV3 and SSD models. In a recent study, deep learning and contrast enhancement method were used together [12]. Inception v3 model was used to extract fabric feature extraction. The three types of defective fabric that this model can identify are holes, vertical defects, and horizontal defects. In a study using the MobileNetV2 model, fabric defect detection was made quickly on the NVIDIA Jetson Nano card [13]. Deep neural network model consists of a channel attention mechanism. This mechanism emphasizes defect features and suppress background noise components. Comprehensive analyzes were performed in a study comparing the discrete curvelet transform, wavelet transform and GLCM methods [14]. The best results have been achieved by using the discrete curvelet transform and GLCM features together. CNN-based architecture with adaptive threshold-based have been developed to determine fabric defect classes [15]. Adaptive threshold mechanism is used for class determination. Two different real fabric datasets are used. The proposed model achieved an average of 90% success in defect detection. Pourkaramdel et al. [16] proposed a local quartet patterns based method to obtain discriminative texture features of fabric images. This model is robust to noise and it can be use in industrial defect detection problems.

Recently, deep learning-based defect detection models have been developed. Vgg16 deep learning model was used to detect circular knitting fabric defects [17]. The proposed method produced better results than shearlet transform and GLCM methods. In a recent study, a specific deep learning architecture has been developed to detect circular knitting fabric defects [18]. This architecture has obtained more high defect detection rates than InceptionV3, MobileNetV2, Xception and ResNet50 models. A model was developed based on the YOLOX-Nano model to develop an optimized deep model for defect classification [19]. To classify the woven fabrics which distributed along the warp and weft directions, proper convolution kernels have been developed. The proposed deep model has a balance in terms of fabric size, accuracy and speed for defect detection. In a recent study, circular knitting fabric defects were detected using 3 different deep learning architectures [20]. Detection of fabric defects with the machine vision mechanism installed on the circular knitting machine is an important and valuable task. Fabric defects were detected with 98% success with ResNet architecture. An intelligent

automation system was developed for fabric inception machines [21]. The developed intelligent and PLC-controlled system examines and reports the fabric rolls in terms of quality control.

The results of the literature review revealed that the studies on fabric defect detection may be divided into two primary categories. The first group is studies using traditional image analysis and machine learning approaches such as GLCM, wavelet transform and support vector machines. The second group uses deep learning methods. It is pointed that defect detection methods made with deep learning methods stand out as very powerful and highly distinctive studies. However, deep learning based works have some disadvantages such as computational cost and numerous parameters. Especially the number of methods developed to detect circular knitting fabric defects is very limited. However, knitted fabrics are widely used in daily life including t-shirts, sweaters, socks, leggings and tights, hats and scarves. Overall, knitting fabrics are versatile and widely used in the production of various types of clothing due to their stretch ability, comfort, and ability to provide texture and warmth.

3. MOBILENETV2-BASED FABRIC DEFECT DETECTION

There exist different deep learning models like VGG19, MobileNet, ResNet and InceptionV3. These models have been shown to work well in a variety of computer vision applications, including pattern recognition and texture classification. In this paper, MobileNetV2 model is used to detect circular knitting fabric defects. However, it is aimed that the model produces the best results by performing different ablation studies.

MobileNetV2 a deep learning architecture that was specifically developed for efficient computation on mobile and embedded devices [22]. This architecture was developed by researchers at Google and is based on a combination of depth wise separable convolutions and pointwise convolutions. Depth wise separable convolutions are a form of convolution that factorizes a standard convolution into a depth wise convolution and a pointwise convolution. This approach reduces the computational cost of the deep model.

The pre-trained MobileNet presents a module that contains inverting residual structure. The initial of MobileNetV2 begins with fully convolutional layers. This first layers include 32 filters and 19 residual bottlenecks. The obvious structure of this block can be examine in Table 1 [22].

Table 1. Bottleneck residual block (Here k , s and t show the channel, stride and expansion factor, respectively).

Input	Operator	Output
$h \times w \times k$	1×1 conv2d, ReLU	$h \times w \times (tk)$
$h \times w \times k$	3×3 dwise $s=S$ ReLU	$\frac{h}{s} \times \frac{w}{s} \times (tk)$
$\frac{h}{s} \times \frac{w}{s} \times tk$	Linear 1×1 conv2d	$\frac{h}{s} \times \frac{w}{s} \times k'$

As shown in Table 1, MobileNetV2 layer blocks include commonly composed of 1×1 convolution and 3×3 depth wise separable convolutions (DW Conv). Therefore MobileNetV2 deep network model consists of a series of a convolution and DW Conv blocks [13]. In this model, linear bottlenecks and depth wise separable convolutions has been integrated into inverting residual structure with linear bottlenecks. Two types of convolution layers in MobileNetV2 architecture can be seen Figure 1.

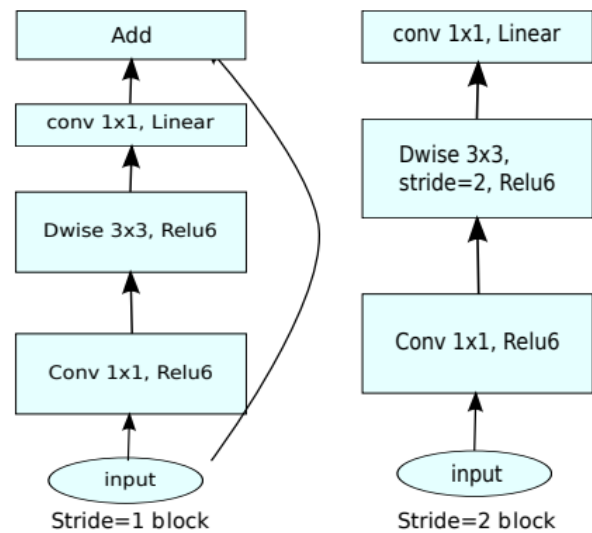


Figure 1. The block structure of MobileNetV2 [22]

In this paper, ReLU6 activation function is used to ensure non-linearity and enhance sparsity. Thus MobileNetV2 model is robust to conditions such as low-precision computation. During training, kernel size is used as 3×3 . Also dropout and batch normalization operations are used. Constant expansion strategy is used except for the first layer. As a result of the experimental studies, expansion factor is determined as 5. This means that if a bottleneck layer takes 64-channel input tensor, it generates a tensor with 128 channels. Therefore intermediate expansion layer has $64 \times 5 = 320$ channels [22].

Original MobileNetV2 architecture cannot give the desired results in circular fabric defect detection. In this paper, the images in the circular knitting fabric database contain some undesirable situations such as noise, light change and rotation. At this point, it is necessary to perform parameter optimization and fine-tuning of the MobileNetV2 model.

Fine-tuning is a well-known optimization strategy for enhancing model performance. To increase the accuracy of the MobileNetV2, fine-tuned block can be added following the 16 blocks of the MobileNetV2 architecture. Based on similar studies in the literature [23], this paper uses a fine-tuned block to enhance the classification performance of MobileNetV2. Thus, an efficient MobileNetV2 architecture is developed for detecting the defects in circular knitting fabrics. Fine-tuned block includes 3 main sub-layer: feature extraction, pooled feature map and last block. Especially feature extraction layers in fine-tuned block have critical role since MobileNetV2 model performs over-abstract representations fabric images. Over-abstraction leads to lose of distinctive defect features. The structure of the fine-tuned block used in the proposed model and the layers it contains are shown in the Figure 2. As shown in Fig. 2, fine-tuned block has the two convolution layer, batch normalization, a dropout layer, flatten layer and dense layer. Pool size of AveragePooling2D is 2x2. Dropout layer and ReLU activation function have 32 channels. Finally, fine-tuned block consists of the flatten and dense layers. Learning rate is 0.001.

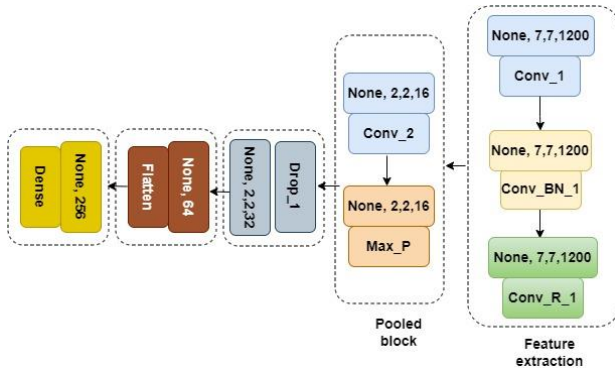


Figure 2. The block structure map of fine-tuning approach

4. EXPERIMENTAL RESULTS

In this section, the results of the fine-tuned MobileNetV2 architecture on a fabric database containing circular knitting fabric defects are presented. Firstly, some general explanations about the fabric database have been given. Then, the experimental results obtained are discussed.

4.1. Fabric Dataset

The dataset used in the study was created on a knitting machine in a textile factory [24]. Fabric production was monitored by installing a line scanning camera and a line light system on the circular knitting machine. Table 3 present information about the fabric dataset.

Table 2. Fabric defect classes and number of image in fabric dataset

Defect types				Defect-free
Needle breakages	Holes/tear	Press-off	Gout	
2493	219	243	45	10820

There are the most common circular knitting fabric defects, including needle breakages, hole, press-off and gout. There are 13820 images in the database. The size of images is 256x250. Figure 3 shows some representative defect samples.

Images in this dataset contain a lack of contrast and noise. Therefore, a pre-processing step was applied. In this paper, gaussian smoothing is used to pre-processing step for denoising fabric images. Gaussian filtering is applied to improve visual quality at various scales. As a result of the preprocessing, the defective pixel regions were better highlighted. Also, the performance of deep learning algorithms is improved by minimizing the noise components.

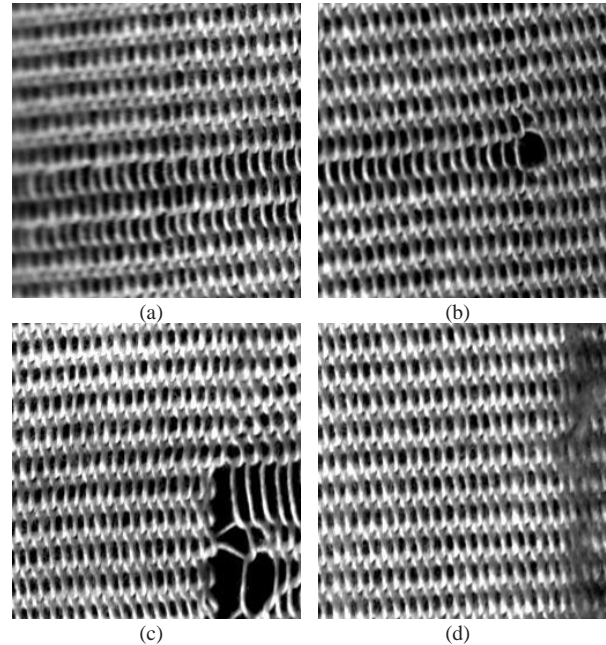


Figure 3. The representative defected samples of the fabric dataset: (a) needle breakages, (b) holes/tear, (c) press-off, (d) gout

4.2. Defect Detection Results

The proposed MobileNetV2 model is compared with InceptionV3 [25] and Xception [26] architectures. Accuracy, precision, recall and F1-score are used as comparison metrics. Thus, comparisons could be performed within the framework of different parameters. The methods used in the comparison have been tested and trained with optimal values. Xception is version of a well-known Inception module. There are some differences between Inception and Xception models. Readers can be read these differences from their original papers.

Deep models were trained using circular knitting fabrics. In experimental works, the circular knitting dataset was split into 90% and 10% for training and testing, respectively. With the use of this method, training data that won't be used in testing can be provided. Validation set was 10% of the training image set. Hyperparameters of deep models were determined on the basis of the validation set. Experimental results were obtained 5 times and the average classification results were reported.

The first experiment has been performed in the form of binary classification of fabric images defected and defect-free. Therefore, it does not include classification results among four different defect types. The classification results of the deep architectures are given in Table 3. As can be seen from these results, the proposed fine-tuned MobileNetV3 model produced the highest results. The

original MobileNetV2 model produced poor results in fabric defect detection [18]. However, the feature extraction capacity of this deep model has been improved with the fine-tuned MobileNetV2 version. In addition, the images in the fabric database were pre-processed before the classification process. Thus, noise and brightness changes in the images are reduced. This has positively affected the performance of the fine-tuned MobileNetV2 model. The obtained results encouraged the use of deep learning-based methods to detect circular knit fabric defects.

The feature extraction and pooling layer structure in fine-tuned blocks are arranged for fabric defect detection. This had a positive effect on the performance of the MobileNetV2. The performances of the Inception and Xception models can be improved with some adjustments to these models. Especially in the inception connection model, the number of convolution operations and kernel sizes can be rearranged. The Xception model, which was developed on the basis of the Inception model, can be re-designed in a similar way. In addition, all models can be trained with a larger number of fabric images to improve their performance.

Table 3. Overall classification results InceptionV3, Xception and fine-tuned MobileNetV2 models on fabric dataset

	Accuracy	precision	recall	F1-score
InceptionV3	78.30	78.32	78.29	78.14
Xception	80.45	80.38	80.47	80.24
Fine-tuned MobileNetV2	92.13	92.15	92.19	91.96

The second experiment has been carried out to distinguish between 4 different fabric defect in the dataset. Classification result are given in Table 4. The proposed fine-tuned MobileNetV2 architecture achieves effective results. In particular, needle breakages and hole fabric defects, which have similar visual characteristics, are effectively distinguished. It has been understood that existing architectures should be configured according to error types. With fine-tuned block, it is clear that MobileNetV2 has a strong ability to find the four most prevalent fabric defects. Of the four defect kinds, the needle breakages defect has the lowest detection accuracy. The most important reason for this is that the defected region resembles a defect-free image pattern. InceptionV3 and Xception models obtain lower classification results. When the results between Table 3 and Table 4 are compared, it is seen that the success of the methods in distinguishing 4 different classes is partially lower. The main reason for this is both the high number of classes and the low number of faulty examples in the database.

Table 4. Classification accuracies of InceptionV3, Xception and fine-tuned MobileNetV2 models on 4 fabric defects

	Needle breakages	Holes/tear	Press-off	Gout
InceptionV3	74.23	76.27	76.72	75.53
Xception	73.49	77.13	76.41	76.81
Fine-tuned MobileNetV2	89.28	91.24	90.43	90.17

5. CONCLUSION

In this paper, fine-tuned MobileNetV2 architecture is proposed to detect the most common fabric defects in circular knitting fabrics. Considering the fabric database used, MobileNetV2 architecture is used for the first time to detect circular knitting fabric defects. Pre-processing steps have been performed to the images in the fabric database. Thus, improvements have been made against undesired situations such as lack of contrast, noise and blurring. Fine-tuned blocks have been added to the MobileNetV3 architecture to detect types of circular knitting fabric defects. Thus, the feature extraction capacity of the model is improved. Convolution and pooling kernels in blocks are determined by experimental testing.

The proposed model produced better results than Inception and Xception models. The proposed model contains fewer hyperparameters than the other two models. Therefore, the model requires less time to train and test. Future research will lead to the development of hybrid deep learning models. Thus, more powerful methods will be developed in detecting circular knitting fabric defects.

REFERENCES

- [1] Abouelela A, Abbas HM, Eldeeb H, Wahdan AA, Nassar SM. Automated vision system for localizing structural defects in textile fabrics. *Pattern Recognit Lett* 2005;26:1435–43.
- [2] Tajeripour F, Kabir E, Sheikhi A. Fabric Defect Detection Using Modified Local Binary Patterns. *EURASIP J Adv Signal Process* 2008 20081 2007;2008:1–12.
- [3] Li P, Zhang H, Jing J, Li R, Zhao J. Fabric defect detection based on multi-scale wavelet transform and Gaussian mixture model method. 2014;106:587–92.
- [4] Huang Y, Xiang Z. RPDNet: Automatic Fabric Defect Detection Based on a Convolutional Neural Network and Repeated Pattern Analysis. *Sensors* 2022, Vol 22, Page 6226 2022;22:6226.
- [5] Raheja JL, Kumar S, Chaudhary A. Fabric defect detection based on GLCM and Gabor filter: A comparison. *Optik (Stuttg)* 2013;124:6469–74.
- [6] Hanbay K, Talu MF, Özgüven ÖF. Fabric defect detection systems and methods—A systematic literature review. *Optik (Stuttg)* 2016;127:11960–73.
- [7] Rasheed A, Zafar B, Rasheed A, Ali N, Sajid M, Dar SH, et al. Fabric Defect Detection Using Computer Vision Techniques: A Comprehensive Review. *Math Probl Eng* 2020;2020.
- [8] Mak KL, Peng P, Yiu KFC. Fabric defect detection using morphological filters. *Image Vis Comput* 2009;27:1585–92.
- [9] Zhou J, Wang J. Unsupervised fabric defect segmentation using local patch approximation. 2016;107:800–9.

- [10] Bumrungkun P. Defect detection in textile fabrics with snake active contour and support vector machines. *J Phys Conf Ser* 2019;1195:012006.
- [11] Zhao S, Yin L, Zhang J, Wang J, Zhong R. Real-time fabric defect detection based on multi-scale convolutional neural network. *IET Collab Intell Manuf* 2020;2:189–96.
- [12] Alruwais N, Alabdulkreem E, Mahmood K, Marzouk R, Assiri M, Abdelmageed AA, et al. Hybrid mutation moth flame optimization with deep learning-based smart fabric defect detection. *Comput Electr Eng* 2023;108:108706.
- [13] Zhang J, Jing J, Lu P, Song S. Improved MobileNetV2-SSDLite for automatic fabric defect detection system based on cloud-edge computing. *Measurement* 2022;201:111665.
- [14] Anandan P, Sabeenian RS. Fabric defect detection using Discrete Curvelet Transform. *Procedia Comput Sci* 2018;133:1056–65.
- [15] Suryarasmı A, Chang CC, Akhmalia R, Marshallia M, Wang WJ, Liang D. FN-Net: A lightweight CNN-based architecture for fabric defect detection with adaptive threshold-based class determination. *Displays* 2022;73:102241.
- [16] Pourkaramdel Z, Fekri-Ershad S, Nanni L. Fabric defect detection based on completed local quartet patterns and majority decision algorithm. *Expert Syst Appl* 2022;198:116827.
- [17] Hanbay K. Detecting of Circular Knitting Fabric Defects Using VGG16 Architecture. *Turkish J Nat Sci* 2022;11:125–9.
- [18] Hatami Varjovi M, Fatih TALU M, Hanbay K. Fabric Defect Detection Using Customized Deep Convolutional Neural Network for Circular Knitting Fabrics. *Turkish J Nat Sci* 2022;11:160–5.
- [19] Yin YY, Li LQ. A lightweight algorithm for woven fabric defect detection. *China Autom. Congr., Institute of Electrical and Electronics Engineers (IEEE); 2022, p. 1025–9.*
- [20] ÇELİK Hİ, DÜLGER LC, ÖZTAŞ B, KERTMEN M, GÜLTEKİN E. A Novel Industrial Application of CNN Approach: Real Time Fabric Inspection and Defect Classification on Circular Knitting Machine. *Tekst ve Konfeksiyon* 2022;32:344–52.
- [21] Arıkan CO. Developing an intelligent automation and reporting system for fabric inspection machines. *Tekst ve Konfeksiyon* 2019;29:93–100.
- [22] Sandler M, Howard A, Zhu M, Zhmoginov A, Chen L-C. *MobileNetV2: Inverted Residuals and Linear Bottlenecks* n.d.
- [23] Shamrat FJM, Azam S, Karim A, Ahmed K, Bui FM, De Boer F. High-precision multiclass classification of lung disease through customized MobileNetV2 from chest X-ray images. *Comput Biol Med* 2023;155:106646.
- [24] Hanbay K, Talu MF, Özgüve ÖF, Öztürk D. Real-time detection of knitting fabric defects using shearlet transform. *Tekst ve Konfeksiyon* 2019;29:1–10.
- [25] Szegedy C, Vanhoucke V, Ioffe S, Shlens J, Wojna Z. Rethinking the Inception Architecture for Computer Vision. *Proc IEEE Comput Soc Conf Comput Vis Pattern Recognit* 2015;2016-December:2818–26.
- [26] Chollet F. Xception: Deep Learning with Depthwise Separable Convolutions. *Proc. IEEE Conf. Comput. Vis. Pattern Recognit.*, 2017, p. 1251–8.



On Generic Submersion in the Contact Context

Cem SAYAR^{1*}

¹ Florida International University, Department of Mathematics and Statistics, Miami, FL, US
 Cem Sayar ORCID No: 0000-0002-8339-4396

*Corresponding author: csayer@fiu.edu.tr

(Received: 15.05.2023, Accepted: 21.11.2023, Online Publication: 28.12.2023)

Keywords

Riemannian
 Submersion,
 Almost contact metric
 manifolds,
 Distribution,
 Reeb vector field

Abstract: In the present paper, we introduce a new type of Riemannian submersion in the contact framework such that the fibers of such submersion are generic submanifolds, as given in [10]. This type of submersion is a generalization of many kinds of submersion introduced before in the literature. Once the Reeb vector field ξ is tangent to the fibers, its position is given such that it should lie in the anti-invariant distribution D^0 , which is given in the definition of the generic submersion. Moreover, we give an example and some results for such submersions.

Kontakt Geometride Kapsamlı Submersiyonlar Üzerine

Anahtar Kelimeler

Riemann submersiyon,
 Hemen hemen kontakt
 metrik manifold,
 Distribüsyon,
 Reeb vektör alanı

Öz: Makalede, bu tür submersiyonların liflerinin kapsamlı alt manifoldlar ([10]'da verildiği gibi) olacağı şekilde, kontakt çerçevede, yeni bir Riemann submersiyon tanımlıyoruz. Bu tür submersiyonlar daha önce literatürde tanımlanan bir çok submersiyon çeşidinin genelleştirilmesidir. Reeb vektör alanı liflere teğet olduğu durumda kapsamlı submersiyon tanımında verilen D^0 distribüsyonunda yer alması gerektiği sonucu verildi. Dahası, kapsamlı submersiyon örneği ve bazı sonuçlar verildi.

1. INTRODUCTION

The theory of submanifolds has always been a trending topic in differential geometry. This fact inspired most geometers to define and study new submanifolds. After O'Neill [1] and Gray [2] introduced the concept of Riemannian submersion between two Riemann manifolds, the verity; fibers of a Riemannian submersion are a submanifold of the total manifold, put the geometers in a direction to focus on the theory of submersion. Besides this, Watson considered the Riemannian submersions in a complex context and defined and studied so-called almost Hermitian submersions [3]. Later, the theory of submersion became a popular field, and it has also been worked in the contact context [4,5]. Most recent submersion studies can be found in the books [6,7].

Ronsse defined generic submanifolds in the complex context [8]. Based on the given idea in this work, generic submersions were defined in the complex context [9]. Later on, the concept given by Ronsse was introduced in contact geometry [10]. In this paper, we construct

generic submersions using the idea presented in [10] for generic submanifolds.

The current paper is organized as follows:

Section 2 includes the fundamental literature, which is used throughout the paper. Generic submersion in the contact context is defined and studied in Section 3. In this section, the position of the Reeb vector field, when it is tangent to the fibers, is given. Moreover, an original example is introduced and some results are given.

2. PRELIMINARIES

2.1. Riemannian Submersions

This section is devoted to Riemannian submersion and some related preliminaries.

Let (M, g) and (N, h) be Riemannian maifolds, here $\dim(M) > \dim(N)$. A surjective mapping

$$\pi: (M, g) \rightarrow (N, h)$$

is called a *Riemannian submersion* [1] if

- π has maximal rank, and

- the restriction of π_* on $\ker\pi_*^\perp$ is a linear isometry.

In this case, for each point q in N , $\pi^{-1}(q)$ is a k – dimensional submanifold of M is called a *fiber*, where $k = \dim(M) - \dim(N)$. A vector field on M is called a *vertical* (resp. *horizontal*) if it is always tangent (resp. orthogonal) to the fibers. A vector field X on M is called *basic* if X is horizontal and π –related to a vector field X_* on N , i.e. $\pi_*X_p = X_{*\pi(p)}$ for all $p \in M$. We will denote by \mathcal{V} and \mathcal{H} the projections on the vertical distribution $\ker\pi_*$, and the horizontal distribution $\ker\pi_*^\perp$, respectively. Here, the manifold (M, g) is called total manifold and (N, h) is called base manifold of the submersion $\pi: (M, g) \rightarrow (N, h)$.

The geometry of the Riemannian submersions is characterized by O’Neill tensors \mathcal{T} and \mathcal{A} , defined as follows:

$$\mathcal{T}_U V = \mathcal{V}\nabla_{\mathcal{V}U}\mathcal{H}V + \mathcal{H}\nabla_{\mathcal{V}U}\mathcal{V}V \quad (1)$$

$$\mathcal{A}_U V = \mathcal{V}\nabla_{\mathcal{H}U}\mathcal{H}V + \mathcal{H}\nabla_{\mathcal{H}U}\mathcal{V}V \quad (2)$$

for any vector fields U and V on M , here ∇ is the Levi-Civita connection of g . One can see that \mathcal{T}_U and \mathcal{A}_U are skew-symmetric operators on the tangent bundle of the total manifold M reversing the vertical and horizontal distributions.

Here we give some of the properties of the O’Neill tensors \mathcal{T} and \mathcal{A} , which will be helpful for the following sections.

Let V, W be vertical and X, Y be horizontal vector fields on M , then we have

$$\mathcal{T}_V W = \mathcal{T}_W V, \quad (3)$$

$$\mathcal{A}_X Y = -\mathcal{A}_Y X = \frac{1}{2}\mathcal{V}[X, Y]. \quad (4)$$

On the other hand, (1) and (2) yield us

$$\nabla_V W = \mathcal{T}_V W + \widehat{\nabla}_V W, \quad (5)$$

$$\nabla_V X = \mathcal{T}_V X + \mathcal{H}\nabla_V X, \quad (6)$$

$$\nabla_X V = \mathcal{A}_X V + \mathcal{V}\nabla_X V, \quad (7)$$

$$\nabla_X Y = \mathcal{H}\nabla_X Y + \mathcal{A}_X Y, \quad (8)$$

where $\widehat{\nabla}_V W = \mathcal{V}\nabla_V W$. Moreover, if X is basic

$$\mathcal{H}\nabla_V X = \mathcal{A}_X V.$$

Remark 1.

- In this paper, we will assume all the horizontal vector fields as basic.
- One can observe that \mathcal{T} acts on the fibers as the second fundamental form while \mathcal{A} acts on the horizontal distribution and measures of the obstruction to the integrability of it.

To see more details, we refer to the paper [1] and the book [7].

Lemma 1. [1] Let $\pi: M \rightarrow N$ be a Riemannian submersion between Riemannian manifolds and X, Y be basic vector fields of M . Then

- $g(X, Y) = h(X_*, Y_*) \circ \pi$,
- the horizontal part $[X, Y]^{\mathcal{H}}$ of $[X, Y]$ is a basic vector field and corresponds to $[X_*, Y_*]$, i.e. $\pi_*([X, Y]^{\mathcal{H}}) = [X_*, Y_*]$,
- $[V, X]$ is vertical for any vector field V of $\ker\pi_*$,
- $(\nabla_X Y)^{\mathcal{H}}$ is the basic vector field corresponding to $\nabla_{X_*} Y_*$.

2.2. Almost Contact Metric Manifolds

Let M be a C^∞ – differentiable manifold. An *almost contact structure* on M , denoted by (ϕ, ξ, η) , consists of a $(1,1)$ tensor field ϕ (called the structure tensor field), a vector field ξ (called Reeb vector field) and a 1-form η (the dual of ξ) such that

$$\phi^2 = -I + \eta \otimes \xi \quad (9)$$

and

$$\eta(\xi) = 1, \quad (10)$$

where I denotes the identity endomorphism of the fiber bundle TM . In this case, (M, ϕ, ξ, η, g) is called an *almost contact manifold*. One can see that the manifold has odd dimension and it follows that

$$F\xi = 0, \quad \eta \circ F = 0. \quad (11)$$

If a Riemannian metric g on M satisfies

$g(\phi X, \phi Y) = g(X, Y) - \eta(X)\eta(Y)$, $\forall X, Y \in \Gamma(TM)$, 12 then g is said to be adapted to the almost contact structure (ϕ, ξ, η) . In this case, (ϕ, ξ, η, g) (resp. (M, ϕ, ξ, η, g)) is called *almost contact metric structure* (resp. *almost contact metric manifold*). By using (9) and (12), the following relation can be obtained:

$$\eta(X) = g(X, \xi), \quad \forall X \in \Gamma(TM). \quad (13)$$

Let $\mathcal{D} = \text{Im}F = \text{Ker} \eta$ denote the contact distribution of the manifold M . Hence the tangent bundle decomposes into the orthogonal sum:

$$TM = \mathcal{D} \oplus \text{span} \xi. \quad (14)$$

From (9) and (12), it follows that ϕ is skew-symmetric with respect to g , which allows one to define the 2-form α , called the fundamental 2-form of the almost contact metric structure on M , by [11]

$$\alpha(X, Y) = g(X, \phi Y), \quad \forall X, Y \in \Gamma(TM). \quad (15)$$

Therefore, (M, α) is an almost symplectic manifold.

3. GENERIC SUBMERSIONS

In this section we define and study the concept of generic submersion from an almost contact metric manifold onto a Riemannian manifold.

We would like to mention that there are other notions of generic submanifolds, [12,13,14].

First, we give some facts on generic submanifolds in the almost contact context, [10].

3.1. Generic Submanifolds of Almost Contact Metric Manifolds

In [Bejan and me], the concept generic submanifold of an almost contact metric manifold is defined and studied.

Now, we recall some fundamental knowledge.

Let (B, ϕ, ξ, η, g) be an almost contact metric manifold and let M be a Riemannian submanifold of B . For any $X \in \Gamma(TM)$, we may write

$$\phi X = PX + NX, \tag{18}$$

where $PX \in \Gamma(TM)$ and $NX \in \Gamma(TM^\perp)$.

Proposition 1. [Bejan and me] Let M be a submanifold of an almost contact metric manifold (B, ϕ, ξ, η, g) and let P the operator defined by (18). Then

- P is skew-symmetric with respect to g on M ;
- P^2 is symmetric with respect to g ;
- all eigenvalues of P^2 are contained in $[-1,0]$.

Remark 2. [Bejan and me] From Proposition 1, P^2 has at each point the associated matrix diagonalizable.

Let $-\beta^2$ be an eigenvalue of P^2 whose corresponding eigen distribution will be denoted by D^β . Since P^2 is diagonalizable we may take $-\beta_i^2(p)$, $i = 1, \dots, n$, to be all distinct eigenvalues of P^2 at any point $p \in M$, which yields the decomposition of T_pM into the direct orthogonal sum, i.e.

$$T_pM = D_p^{\beta_1} \oplus D_p^{\beta_2} \oplus \dots \oplus D_p^{\beta_n}. \tag{19}$$

Corresponding to Ronsse's definition [8] of generic and skew CR-submanifolds in almost Hermitian context, it is introduced in almost contact framework the following:

Definition 1. [10] A submanifold M of an almost contact metric manifold (B, ϕ, ξ, η, g) is called generic if there exist some functions

$$\beta_1, \dots, \beta_n: M \rightarrow (0,1),$$

for a positive integer k , such that at each point $p \in M$:

- $-\beta_i^2(p)$, $i = 1, \dots, n$ are distinct eigenvalues of P^2 ;
- the dimension of each $D_p^{\beta_1}, D_p^{\beta_2}, \dots, D_p^{\beta_n}$ is independent of $p \in M$, where D_p^β denotes the

eigenspace corresponding to the eigenvalue $-\beta_i^2(p)$ of P^2 , for $\beta \in \{0,1, \beta_1, \beta_2, \dots, \beta_n\}$;

- the tangent space decomposes into the direct orthogonal sum

$$T_pM = D_p^0 \oplus D_p^1 \oplus D_p^{\beta_1} \oplus \dots \oplus D_p^{\beta_n}.$$

When β_1, \dots, β_n are constants, M is called a skew CR-submanifold.

3.2. Generic submersions in contact geometry

This section will define the generic submersions in the contact context. Since the fibers of a submersion is a submanifold of the total manifold, we will follow the idea of generic submanifold given in the Section 3.1. to construct the generic submersions.

Let (M, ϕ, ξ, η, g) be an almost contact metric manifold, (N, h) be a Riemannian manifold and

$$\pi: (M, \phi, \xi, \eta, g) \rightarrow (N, h)$$

be a Riemannian submersion. For any $X \in \Gamma(\ker \pi_*)$ and $U \in \Gamma(\ker \pi_*^\perp)$, we can set

$$\phi X = PX + QX, \tag{20}$$

$$\phi U = tU + nU, \tag{21}$$

where $PX, tU \in \Gamma(\ker \pi_*)$ and $QU, nU \in \Gamma(\ker \pi_*^\perp)$.

Now, we define a generic submersion in the contact context.

Definition 2. Let (M, ϕ, ξ, η, g) be an almost contact metric manifold, (N, h) be a Riemannian manifold and

$$\pi: (M, \phi, \xi, \eta, g) \rightarrow (N, h)$$

be a Riemannian submersion. Then, π is called a *generic submersion* (resp. *skew CR-submersion*) if the fibers of the submersion π are generic submanifold (resp. Skew CR-submanifold) of M .

Remark 3. One can see that the definition has no limitation for the Reeb vector field ξ such as tangent or normal. This fact makes this work different than the others given in the literature.

Let (M, ϕ, ξ, η, g) be an almost contact metric manifold, (N, h) be a Riemannian manifold and

$$\pi: (M, \phi, \xi, \eta, g) \rightarrow (N, h)$$

be a generic submersion (or skew CR-submersion). In this case, there are k functions (or constant functions) β_1, \dots, β_k defined on the fibers with the values in the open interval $(0,1)$ such that $\ker \pi_*$ is decomposed as

$$\ker \pi_* = D^0 \oplus D^1 \oplus D^{\beta_1} \oplus \dots \oplus D^{\beta_k}, \tag{22}$$

where D^1 is invariant, D^0 is anti-invariant, D^{β_i} is pointwise slant distribution (or slant distribution) with

slant function θ_i and $-\beta_i^2$ is a distinct eigenvalue of P^2 for each $i = 1, \dots, k$.

Proposition 2. Let (M, ϕ, ξ, η, g) be an almost contact metric manifold, (N, h) be a Riemannian manifold and

$$\pi: (M, \phi, \xi, \eta, g) \rightarrow (N, h)$$

be a generic submersion. Then,

- P is skew-symmetric with respect to the metric g on the fibers;
- any distribution D_p^β is P -invariant, for $\beta \in \{0, 1, \beta_1, \dots, \beta_k\}$;
- for any non-zero eigenvalue, the corresponding eigen distribution is even dimensional.

Proof. For any $X, Y \in \Gamma(\ker \pi_*)$, by using the skew-symmetry of ϕ

$$g(PX, Y) = g(\phi X, Y) = -g(X, \phi Y) = -g(X, PY),$$

which shows the first claim.

Let consider an arbitrary $\beta \in \{0, 1, \beta_1, \dots, \beta_k\}$ and let $-\beta_i^2$ be an eigenvalue of P^2 whose associated eigen distribution is D_p^β . For any $\delta \in \{0, 1, \beta_1, \dots, \beta_k\}$, $\delta \neq \beta$, the skew-symmetry of P yields:

$$\begin{aligned} \beta^2 g(PX, Y) &= -\beta^2 g(X, PY) = g(P^2 X, PY) \\ &= -g(PX, P^2 Y) = \delta^2 g(PX, Y), \forall X \\ &\in \Gamma(D_p^\beta), \forall Y \in \Gamma(D_p^\delta). \end{aligned}$$

Since $\beta \neq \delta$, it follows

$$g(PX, Y) = 0, \forall X \in \Gamma(D_p^\beta), Y \in \Gamma(D_p^\delta),$$

which shows the second claim.

Last claim follows from the other claims.

The following identity gives a relation between certain canonical structures. The idea of the proof is same with Lemma 3.7. in [10].

Lemma 1. Let (M, ϕ, ξ, η, g) be an almost contact metric manifold, (N, h) be a Riemannian manifold and

$$\pi: (M, \phi, \xi, \eta, g) \rightarrow (N, h)$$

be a generic submersion. Then,

$$||QX||^2 = ||X||^2 - (\eta(X))^2 + g(X, P^2 X), \forall X \in \Gamma(\ker \pi_*). \quad (23)$$

Proposition 3. Let (M, ϕ, ξ, η, g) be an almost contact metric manifold, (N, h) be a Riemannian manifold and

$$\pi: (M, \phi, \xi, \eta, g) \rightarrow (N, h)$$

be a generic submersion. Then,

- $D^0 = \ker P$;
- $D^1 = \ker Q \cap \mathcal{D}$.

Proof. If $X \in \Gamma(D^0)$, i.e. $P^2 X = 0$, then from the skew-symmetry of P , we obtain

$$||PX||^2 = -g(P^2 X, X) = 0,$$

which shows the first equality.

Assume that $X \in \Gamma(D^1)$, i.e. $P^2 X = -X$, which makes (23)

$$||QX||^2 = -(\eta(X))^2.$$

Then, the last equality above says that both QX and $\eta(X)$ are supposed to be identically zero, i.e.

$$D^1 \subseteq \ker Q \cap \mathcal{D}.$$

On the other hand, for any $X \in \Gamma(\ker Q \cap \mathcal{D})$, (23) becomes

$$0 = g(X, X) + g(X, P^2 X),$$

Which shows that the only eigenvalue of P^2 is -1 and complete the proof. ■

In the view of Proposition 3., we have the following Lemma:

Lemma 2. Let (M, ϕ, ξ, η, g) be an almost contact metric manifold, (N, h) be a Riemannian manifold and

$$\pi: (M, \phi, \xi, \eta, g) \rightarrow (N, h)$$

be a generic submersion. If the Reeb vector field ξ is tangent to $\ker \pi_*$, then

$$D^0 \cap \ker Q = \text{span}\{\xi\}.$$

Remark 4. In this case of ξ is tangent to the fibers, Lemma 2. gives a decomposition for the anti-invariant distribution D^0 such that

$$D^0 = \widehat{D}^0 \oplus \text{span}\{\xi\}, \quad (24)$$

where \widehat{D}^0 is the orthogonal complementary of $\text{span}\{\xi\}$ in D^0 . In other words, if the Reeb vector field ξ is tangent to the fibers, then it is always perpendicular to all other distributions $(\xi \perp D^\beta, \beta \in \{1, \beta_1, \dots, \beta_k\})$, which gives a new decomposition for the fibers.

Remark 5. As a natural consequence of Remark 4., one can see that

$$\eta(X) = 0, \quad (25)$$

where $X \in \Gamma(\widehat{D}^0 \oplus D^1 \oplus D^{\beta_1} \oplus \dots \oplus D^{\beta_k})$, i.e. \widehat{D}^0 is comprised by the contact distribution \mathcal{D} .

Example 1. Consider a pair of almost complex structures $\{J_1, J_2\}$ on R^{12} as in the following:

$$\begin{aligned} J_1(\partial_1, \dots, \partial_{12}) &= (-\partial_3, -\partial_4, \partial_1, \partial_2, -\partial_7, -\partial_8, \partial_5, \partial_6, -\partial_{11}, -\partial_{12}, \partial_9, \partial_{10}), \\ J_2(\partial_1, \dots, \partial_{12}) &= (-\partial_2, \partial_1, \partial_4, -\partial_3, -\partial_6, \partial_5, \partial_8, -\partial_7, -\partial_{10}, \partial_9, \partial_{12}, -\partial_{11}) \end{aligned}$$

with $\partial_i = \frac{\partial}{\partial x_i}$ for any $i \in \{1, \dots, 12\}$. Thus, (ϕ, ξ, η, g) is an almost contact metric structure on the Euclidean space $R^{13} = R^{11} \times R$ with the coordinates (x_1, \dots, x_{13}) such that

$$\begin{aligned} \phi\left(V + \tau \frac{\partial}{\partial x_{13}}\right) &= (\cos f)J_1V + (\sin f)J_2V, \forall V \\ &\in \Gamma(R^{12}), \\ \xi &= \frac{\partial}{\partial x_{13}}, \eta = dx_{13}, \end{aligned}$$

where g is the Euclidean metric on R^{13} , $\tau: R^{13} \rightarrow R$ and $f: R^{13} \rightarrow R - \{0, \frac{\pi}{2}\}$ are smooth functions on the fibers. Define a map $\pi: R^{13} \rightarrow R^6$ such that

$$\pi(x_1, \dots, x_{13}) = (x_2, x_3, x_6, x_8, x_9, x_{12}).$$

$$\ker \pi_* = \widehat{D}^0 \oplus \text{span}\{\xi\} \oplus D^1 \oplus D^\beta,$$

where

$$\begin{aligned} \widehat{D}^0 &= \text{span}\{\partial x_1, \partial x_4\}, \\ D^1 &= \text{span}\{\partial x_9 - \partial x_{12}, ((\cos f) + (\sin f)) \partial x_{10} \\ &\quad + ((\cos f) - (\sin f)) \partial x_{11}\} \end{aligned}$$

and

$$D^\beta = \text{span}\{\partial x_5, \partial x_7\}$$

such that D^β is of the pointwise slant function f . Moreover,

$$\begin{aligned} (\ker \pi_*)^\perp &= \text{span}\{(\sin f) \partial x_2 \\ &\quad + (\cos f) \partial x_3, (-\cos f) \partial x_2 \\ &\quad + (\sin f) \partial x_3, \partial x_6, \partial x_8, \partial x_9 \\ &\quad + \partial x_{12}, ((\cos f) + (-\sin f)) \partial x_{10} \\ &\quad + ((-\cos f) + (-\sin f)) \partial x_{11}\}. \end{aligned}$$

Therefore, the map π is a generic submersion.

Proposition 4. Let π be a generic submersion from an almost contact metric manifold (M, ϕ, ξ, η, g) onto a Riemannian manifold (N, h) with ξ tangent to the fibers and D^0 is parallel with respect to ξ . Then, any integral curve of ξ is a geodesic on the fibers if and only if \widehat{D}^0 is parallel with respect to ξ .

Proof. Assume that ξ is tangent to the fibers and D^0 is parallel with respect to the Reeb vector field, i.e.

$$\nabla_\xi X \in D^0, \forall X \in \Gamma(D^0),$$

Which gives the following equivalence with Remark 4, for any $Z \in \Gamma(\widehat{D}^0)$,

$$\begin{aligned} \widehat{D}^0 \text{ is parallel with respect to } \xi &\Leftrightarrow \nabla_\xi Z \in \widehat{D}^0 \\ &\Leftrightarrow g(\nabla_\xi Z, \xi) = 0 \Leftrightarrow g(Z, \nabla_\xi \xi) = 0 \\ &\Leftrightarrow \nabla_\xi \xi \in \text{span}\{\xi\}. \end{aligned}$$

On the other hand, since ξ is unitary,

$$\begin{aligned} g(\xi, \xi) = 1 &\Leftrightarrow g(\nabla_\xi \xi, \xi) + g(\xi, \nabla_\xi \xi) = 0 \\ &\Rightarrow g(\xi, \nabla_\xi \xi) = 0 \\ &\Rightarrow \nabla_\xi \xi = 0, \end{aligned}$$

which completes the proof.

Theorem 1. Let π be a generic submersion from an almost contact metric manifold (M, ϕ, ξ, η, g) onto a Riemannian manifold (N, h) . If M is of a closed fundamental 2-form α , then

- the anti-invariant distribution D^0 is integrable,
- if the Reeb vector field ξ is tangent to the fibers, then the distribution \widehat{D}^0 is integrable if and only if the restriction of η on \widehat{D}^0 is closed.

Proof. Let $X, Y \in \Gamma(D^0)$ and $V \in \Gamma(\ker \pi_* - D^0)$. Thus, by Proposition 2, there exists $Z \in \Gamma(\ker \pi_* - D^0)$ such that $PZ = V$. Since $PZ = PV = 0$, we have

$$\begin{aligned} g([X, Y], V) &= g([X, Y], PZ) \\ &= Zg(Y, PX) - Yg(Z, PX) \\ &\quad - Xg(Z, PY) - g([Z, Y], PX) \\ &\quad - g([X, Z], PY) + g([X, Y], PZ) \\ &= Z\alpha(Y, X) - Y\alpha(Z, X) - X\alpha(Z, Y) - \alpha([Z, Y], X) \\ &\quad - \alpha([X, Z], Y) + \alpha([X, Y], Z) \\ &= d\alpha(Z, X, Y) \\ &= 0, \end{aligned}$$

which means $[X, Y] \in \Gamma(D^0)$, i.e. D^0 is integrable.

Now, let $X, Y \in \Gamma(\widehat{D}^0)$. D^0 is integrable implies $[X, Y] \in \Gamma(D^0)$. From Remark 5, it follows that

$$g([X, Y], \xi) = \eta([X, Y]) = d\eta(X, Y).$$

Thus, $[X, Y] \in \Gamma(\widehat{D}^0)$ if and only if $d\eta(X, Y) = 0$. ■

Acknowledgement

Author is grateful for the comments from the Reviewers.

REFERENCES

- [1] O'Neill B. The fundamental equations of a submersion. Michigan Mathematical Journal. 1966 Dec;13(4):459-69.
- [2] Gray A. Pseudo-Riemannian almost product manifolds and submersions. Journal of Mathematics and Mechanics. 1967 Jan 1;16(7):715-37.
- [3] Watson B. Almost hermitian submersions. Journal of Differential Geometry. 1976 Jan;11(1):147-65.
- [4] Prasad R, Akyol MA, Kumar S, Singh PK. Quasi bi-slant submersions in contact geometry. Cubo (Temuco). 2022 Apr;24(1):1-20.

- [5] Sari R, Akyol MA. Hemi-slant ξ -Riemannian submersions in contact geometry. *Filomat*. 2020;34(11):3747-58.
- [6] Sahin B. Riemannian submersions, Riemannian maps in Hermitian geometry, and their applications. Academic Press; 2017 Jan 23.
- [7] Pastore AM, Falcitelli M, Ianus S. Riemannian submersions and related topics. World Scientific; 2004 Jun 21.
- [8] Ronsse, G.B.: Generic and skew CR-submanifolds of a Kaehler manifold. *Bull. Inst. Math. Acad. Sin.* 18, 127–141 (1990)
- [9] Sayar C, Taştan HM, Özdemir F, Tripathi MM. Generic submersions from Kaehler manifolds. *Bulletin of the Malaysian Mathematical Sciences Society*. 2020 Jan;43:809-31.
- [10] Bejan CL, Sayar C. Generic Submanifolds of Almost Contact Metric Manifolds. *Bulletin of the Malaysian Mathematical Sciences Society*. 2022 Sep;45(5):2571-95.
- [11] Blair DE. A survey of Riemannian contact geometry. *Complex Manifolds*. 2019 Jan 1;6(1):31-64.
- [12] Akyol MA. Conformal generic submersions. *Turkish Journal of Mathematics* 45.1 (2021): 201-219.
- [13] Tanveer F, Akyol MA, Alzulaibani AA. "On a submersion of generic submanifold of a nearly Kaehler manifold." *International Journal of Geometric Methods in Modern Physics* 19.04 (2022): 2250048.
- [14] Akyol MA. Generic Riemannian Submersions from Almost Product Riemannian. *Gazi University Journal of Science* 30, no. 3 (2017): 89-100.

Electron Spin Resonance Spectrum Simulations and DFT Calculations for Possible Radicals of the Ketoprofen Molecule

Halil Uğur TAŞDEMİR^{1*} , Ercan TÜRKKAN¹ 

¹ Necmettin Erbakan University, Ahmet Kelesoglu Education Faculty, Physics Education Department, Konya, Türkiye

Halil Uğur TAŞDEMİR ORCID No: 0000-0002-6205-0092

Ercan TÜRKKAN ORCID No: 0000-0003-4365-5544

*Corresponding author: halilugurtasdemir@gmail.com.tr

(Received: 15.02.2023, Accepted: 27.11.2023, Online Publication: 28.12.2023)

Keywords

Electron Spin
Resonance,
Density
Functional
Theory,
Ketoprofen,
Radical
simulations

Abstract: In this study, the molecular structure of the Ketoprofen molecule, which is the drug's active ingredient, was revealed by using theoretical methods. First of all, conformational space scanning in the Ketoprofen molecule was performed by the Molecular Mechanical Force Field method. Then, the most stable structure, geometry parameters, Nuclear Magnetic Resonance parameters of the ketoprofen molecule was found with the help of the Density Functional Theory method. Further, Possible radicals were modeled using the most stable structure of the ketoprofen molecule. Electron Spin Resonance parameters of these possible radicals were also calculated with the Density Functions Theory method. Finally, using these parameters theoretical Electron Spin Resonance spectra of possible radicals were obtained by simulation program.

Ketoprofen Molekülünün Olası Radikalleri İçin Elektron Spin Rezonans Spektrum Simülasyonları ve DFT Hesaplamaları

Anahtar Kelimeler

Elektron Spin
Rezoanans,
Yoğunluk
Fonksiyonelleri
Teorisi,
Ketoprofen,
Radikal
simülasyonları

Öz: Bu çalışmada ilaç etken maddesi olan Ketoprofen molekülünün moleküler yapısı teorik yöntemler kullanılarak açığa çıkarılmıştır. Öncelikle Ketoprofen molekülünün konformasyonel uzay taraması Moleküler Mekanik Kuvvet Alanları metodu kullanılarak gerçekleştirilmiştir. Daha sonra ketoprofen molekülünün en kararlı yapısı, geometri parametreleri, Nükleer Manyetik Rezonans parametreleri Yoğunluk Fonksiyonel Teorisi yöntemi yardımıyla bulunmuştur. Ayrıca ketoprofen molekülünün en kararlı yapısı kullanılarak olası radikaller modellendi. Son olarak, bu parametreler kullanılarak olası radikallerin teorik Elektron Spin Rezonans spektrumları simülasyon program ile elde edilmiştir.

1. INTRODUCTION

Ketoprofen is a kind of non-steroid anti-inflammatory drugs (NSAID) which are widely used around the world due to their pain and inflammation-reducing properties. Ketoprofen is a benzophenone derivative, especially used in the treatment of moderate pain [1-6]. Since it is a drug active ingredient, it is important to reveal the structure of the Ketoprofen molecule correctly. The electronic properties (energy, dipole moment etc.) of a molecule are closely related to its molecular structure. If the molecular structure is correctly detected, other electronic properties of the molecule can also be accurately detected. The molecular structure of a

molecule may be revealed by X-ray study or by spectroscopic methods such as Nuclear Magnetic Resonance (NMR) spectroscopy. NMR spectroscopy provides information about molecular structure and is a frequently used method to explain molecular structure [7-9]. The Density Functional Theory (DFT) method is a very successful theoretical method in revealing the molecular structures of molecules and calculating NMR parameters [10-14]. Drugs may be exposed to radiation for sterilization purposes or accidentally. As a result of drug interaction with radiation, radicals may form in the drug [15, 16]. Electron Spin Resonance (ESR) technique is one of the commonly used methods to detect the radical formed in the drug [17,18]. ESR technique can detect even a very small amount of paramagnetic center,

namely radical, in the sample [19-21]. The g and hyperfine coupling constant (hfcc) parameters obtained from the ESR spectrum give us important information about the paramagnetic center. However, it is often not easy to analyze an ESR spectrum and accurately determine the ESR parameters from that spectrum. The DFT method can help analysis of ESR spectra [22-25].

2. MATERIAL AND METHOD

The theoretical calculation of the Ketoprofen molecule started with conformation analysis. The conformation analysis of the Ketoprofen molecule was carried out using the Molecular Mechanical Force Fields (MMFF) method by the Spartan08 program [26]. As a result of the conformation analysis, 19 conformations of the Ketoprofen molecule were obtained. The most stable conformation of the Ketoprofen molecule was determined by optimization and frequency calculation for each conformer using the B3LYP/6-311++G(d,p) method basis set combination [27,28]. As a result of optimization and frequency calculations, the most stable structure and its geometry parameters were determined. Nuclear Magnetic Resonance parameters (^1H and ^{13}C chemical shift values) of the Ketoprofen molecule were calculated using the B3LYP/6-311++G(d,p) method-basis set combination. Seven possible radicals of the Ketoprofen molecule were modeled using the B3LYP/6-311++G(d,p) method basis set combination. ESR parameters (g value and hfcc values) of seven possible radicals were also calculated using the same method and basis set. All calculations except the conformation analysis were performed using the Gaussian03 program [29]. ESR spectrum patterns of possible radicals were obtained by using the calculated ESR parameters of possible radicals in the JEOL IsoSimu/ Fa Version 2.2.0 simulation program.

3. RESULTS AND DISCUSSION

The structure of the most stable conformer of the Ketoprofen molecule is shown Figure 1.

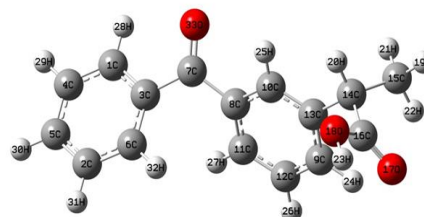


Figure 1. The most stable structure of Ketoprofen molecule

The geometry parameters of the optimized structure are given in Table 1. It is seen that the geometry parameters given in Table 1 of the most stable structure of the Ketoprofen molecule are compatible with the experimental and theoretical studies previously studied in the literature [3,6]. One of the methods used to determine the molecular structure is the NMR spectroscopy method. Experimental NMR parameters of Ketoprofen molecule (^1H and ^{13}C chemical shift values) are available in the literature [30].

NMR parameters (^1H and ^{13}C chemical shift values) calculated using the B3LYP/6-311++G(d,p) method basis set combination of the Ketoprofen molecule are given in Table 2. Defining the molecular structure correctly will increase the accuracy of the calculation to be made using that molecular structure. As can be seen from Table 2, the experimental and calculated chemical shift values are compatible for the Ketoprofen molecule. The fact that the theoretical and experimental NMR parameters are compatible with each other is a situation that shows the accuracy of the theoretically found molecular structure.

Table 1. The calculated and experimental geometry parameter of the Ketoprofen molecule

	Bond Lengths (Å ^o)			Bond Angles (degree)	
	Experimental [6]	Calculated		Experimental [6]	Calculated
C1-C3	1.388	1.402	C2-C6-C3	120.3	120.3
C3-C6	1.393	1.400	C6-C3-C7	122.5	122.6
C6-C2	1.382	1.393	C1-C3-C7	118.9	118.1
C2-C5	1.374	1.399	C3-C7-O33	119.0	119.9
C5-C4	1.367	1.396	C3-C7-C8	121.4	120.1
C4-C1	1.378	1.389	C7-C8-C11	121.5	122.7
C3-C7	1.487	1.500	C7-C8-C10	118.6	117.9
C7-O33	1.218	1.221	C8-C10-C13	121.4	121.3
C7-C8	1.488	1.501	C10-C13-C9	118.6	118.8
C8-C11	1.395	1.399	C13-C9-C12	121.1	120.5
C11-C12	1.381	1.394	C9-C12-C11	120.1	120.4
C12-C9	1.392	1.392	C12-C11-C8	119.1	119.9
C9-C13	1.385	1.402	C11-C8-C10	119.8	119.2
C13-C10	1.367	1.392	C13-C14-C15	112.4	112.3
C13-C14	1.532	1.528	C13-C14-C16	110.3	109.4
C14-C15	1.518	1.537	C15-C14-C16	110.0	110.7
C14-C16	1.515	1.523	C18-C16-O17	123.3	122.5
C16-O17	1.248	1.206		Dihedral Angles (degree)	
C16-O18	1.254	1.355	C6-C3-C7-C8	-36.0	32.9
	Bond Angles (degree)		C8-C7-C3-C1	147.5	-150.8
C4-C1-C3	120.4	120.4	C3-C7-C8-C11	-25.3	31.4
C1-C4-C5	120.6	120.0	C10-C8-C7-C3	159.3	-152.6
C4-C5-C2	119.9	119.9	C13-C14-C16-O17	-107.3	90.0
C5-C2-C6	120.2	120.1	C13-C14-C16-O17	72.2	88.8
C6-C3-C1	118.5	119.2	C9-C13-C14-C16	-67.6	-58.5
			C10-C13-C14-C16	116.0	123.3

Table 2. Experimental and Theoretical ^1H Chemical Shift values of Ketoprofen molecule in ppm

	CH ₃ peak value	CH peak value	Phenyl peak values
Experimental [23]	1.377	3.771	7.436-7.639
This study	1.422	4.112	7.842-8.274

Defining the molecular structure correctly will increase the accuracy of the calculation to be made using that molecular structure. As can be seen from Table 2, the experimental and calculated chemical shift values are compatible for the Ketoprofen molecule. The fact that the theoretical and experimental NMR parameters are compatible with each other is a situation that shows the accuracy of the theoretically found molecular structure. Katusin-Razem et al., mentioned that a radical was formed in the sample in their study in 2005 years for the sterilization of the Ketoprofen molecule. In this study, Katusin-Razem et al. discussed possible radicals for the ketoprofen molecule [31]. Spin trapping EPR studies of the Ketoprofen molecule are also available in the literature [32]. However, there is no definition in the literature of the radical(s) that will occur due to the irradiation of Ketoprofen. Six possible radicals were modeled using the B3LYP/6-311++G(d, p) method basis set combination considering the studies in the literature for the Ketoprofen molecule. The radicals were named as Rad1, Rad2, Rad3, ..., Rad6. H23 atom for Rad1 radical ($\text{RCCH}_3\text{CO}\dot{\text{O}}$), H23 and O18 atoms

for Rad2 radical ($\text{RCH}_3\dot{\text{C}}\text{O}$), H20 atom for Rad3 radical ($\text{RC}\dot{\text{C}}\text{H}_3\text{COOH}$), H19 atom for Rad4 radical ($\text{RC}\dot{\text{C}}\text{H}_2\text{COOH}$), C15-H19-H21-H22 atoms for Rad5 radical ($\text{RC}\dot{\text{C}}\text{OOH}$) were modeled by removing them from the Ketoprofen molecule. The Ketoprofen molecule is modeled anionic for Rad 6 radical ($\text{RCCH}_3\text{COOH}^-$). Possible radicals modeled are shown in Figure 2.

ESR parameters (g and hfcc values) of the modeled radicals were calculated using the same method and basis set. The calculated isotropic ESR parameters of the modeled radicals are given in Table 3.

ESR spectra may not be easily resolved due to overlaps. In such cases, spectra can be analyzed with simulations. Values such as g and hfcc values of the radical(s) that are assumed to occur are needed for simulation. The g and hfcc values required for simulation can be obtained from theoretical calculations. More than one radical can form in the molecule, in which case the analysis of the spectrum will become more complicated. Theoretical calculations can be used to analyze such complex spectra, and the success of the DFT method in calculating ESR parameters is known from previous studies [33,34].

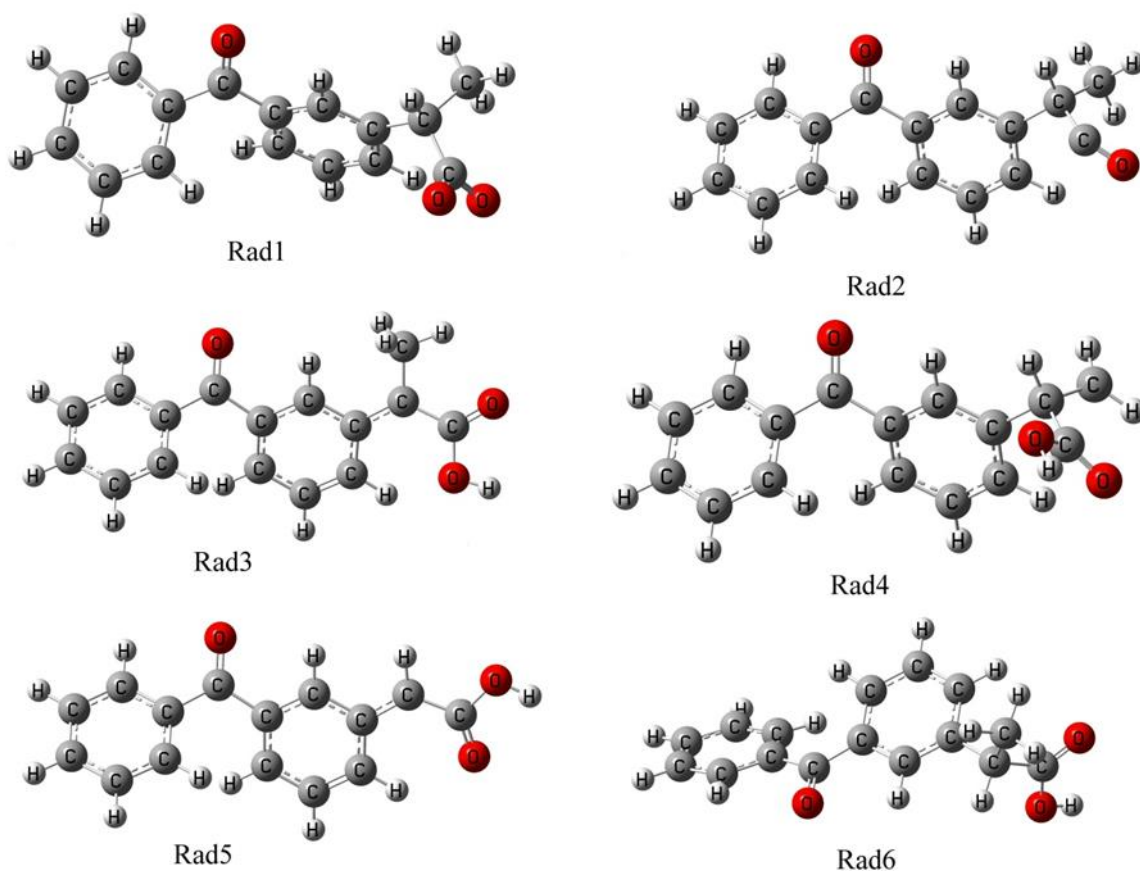
**Figure 2.** The possible radicals of Ketoprofen molecule

Table 3. The calculated hfcc(in Gauss) and g values of six possible radicals

Atom	Rad1	Rad2	Rad3	Rad4	Rad5	Rad6
H19			2.4			
H20	3.9	1.9		23.0	14.1	
H21	1.5	4.9	28.4	21.5		
H22			16.3	22.4		
H23					1.1	
H24			3.8		4.5	4.1
H25			4.3		4.9	2.6
H26			1.6		1.8	
H27			4.1		5.1	2.0
H28						2.3
H30						3.3
H32						1.7
g_{iso}	2.0096	2.0007	2.0033	2.0026	2.0033	2.0040

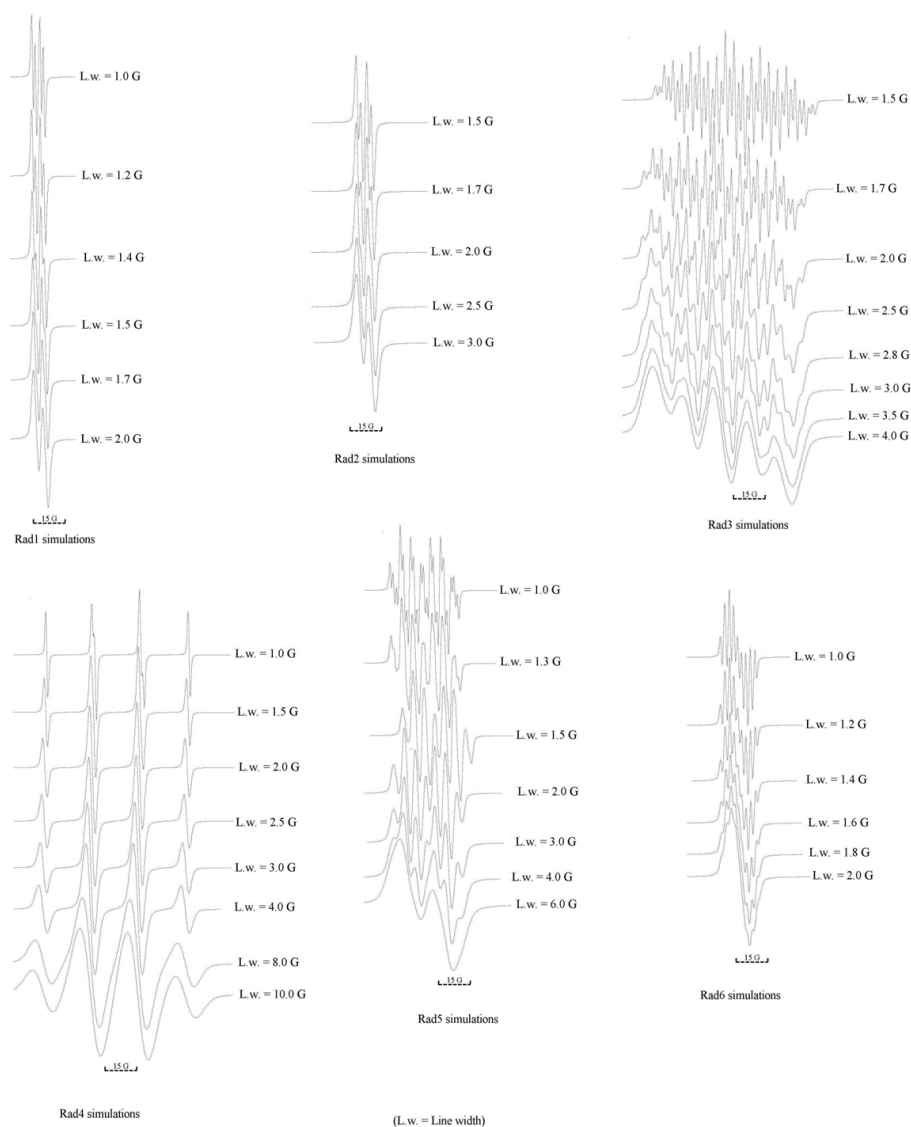
For the radical modeled as $RCCH_3CO\dot{O}$, the calculation could not be completed with B3LYP/6-311++G(d,p) base set combination. In order to calculate the g and hfcc values of the $RCCH_3CO\dot{O}$ radical, the basis set was changed. The isotropic g and hfcc values of $RCCH_3CO\dot{O}$ radical were calculated using four different basis set combinations. Thus, the effect of different basis sets on the calculation was also investigated. The isotropic g and hfcc values calculated with different

basis sets are given in Table 4 for the $RCCH_3CO\dot{O}$ radical.

Table 4. The g and hfcc (in Gauss) values of the Rad1 radical calculated with different basis sets

Atoms	Basis Sets			
	6-31+ (d)	6-311+(d)	6-31+(d,p)	6-311 (d,p)
H20	3.8	4.1	3.8	4.0
H21	1.5	1.4	1.6	1.3
g_{iso}	2.0094	2.0098	2.0094	2.0099

When Table 4 is examined, the g value and hfcc values for Rad1 model radical do not change much with the change of the basis set. In other words, the change of the basis set does not affect the calculation results much. Possible ESR spectra were obtained by using the ESR parameters given in Table 2 in the JEOL IsoSimu/Fa Version 2.2.0 simulation program. Spectra with different line widths were simulated for each radical. The simulations were created by taking the average of the isotropic g and hfcc values given in Table 3 for the $RCCH_3CO\dot{O}$ radical. The line width of the simulations is indicated on the spectra. The simulated ESR spectra are given in Figure 3.

**Figure 3.** Electron Spin Resonance spectrum simulations of the modeled radicals

It is possible to reproduce the simulations given in Figure 3. When the spectra in Figure 3 are examined, the shape of the spectra changes depending on the line width. Although the line width is kept small when recording the ESR spectrum, the line width will increase due to overlaps. Therefore, the appearance of the spectrum will change. More than one simulation spectra of a radical are given. Since it is not possible to predict what kind of overlap will occur in the experiment. The first thing the experimenter encounters in ESR spectroscopy analysis is the spectrum pattern. It can measure the g and $hfcc$ values from the spectrum after being able to analyze the spectrum pattern. In this sense, spectra created based on theoretical values can guide experimenters. Of course, simulations with the same spectrum patterns can also be seen here. In simulations with similar spectrum patterns, the differences between the theoretical and experimental values of g and $hfcc$ are calculated to decide which radical is formed. For g values, the difference between the experiment and the theoretical calculation should be at most 1000 ppm [35]. For $hfcc$ values, the difference between the experiment and the theoretical calculation should not exceed % 20 [36].

4. CONCLUSIONS

In this study, the molecular structure of the Ketoprofen molecule and the radicals that may occur in the Ketoprofen molecule when exposed to radiation were investigated. Using the ESR parameters of the modeled radicals, theoretical ESR spectra were generated for each radical. The parameters required to construct the ESR spectra of the radical can be derived by theoretical calculation methods. How to use the ESR parameters obtained by theoretical calculations in spectrum simulations is presented to the literature. The values of the ESR parameters of the radical(s) formed by the irradiation of the ketoprofen molecule are not available in the literature. These parameters have been presented in the literature with this study.

Acknowledgement

This study was presented as a abstract at the 33rd Physics Congress of the Turkish Physical Society.

REFERENCES

- [1] El-Kamel AH, Sokar MS, Al Gamal SS, Naggar VF. Preparation and evaluation of ketoprofen floating oral delivery system. *International Journal of Pharmaceutics*. 2001; 220 (1-2): 13-21.
- [2] Kokki H, Karvinen M, Jekunen A. Pharmacokinetics of a 24-hour intravenous ketoprofen infusion in children. *Acta Anaesthesiologica Scandinavica*. 2002; 46(2): 194-98.
- [3] Vueba ML, Batista de Carvalho LAE, Veiga F, Sousa JJ, Pina ME. Influence of cellulose ether polymers on ketoprofen release from hydrophilic matrix tablets. *European Journal of Pharmaceutics and Biopharmaceutics*. 2004; 58(1): 51-59.
- [4] Earley B, Crowe MA. Effects of ketoprofen alone or in combination with local anesthesia during the castration of bull calves on plasma cortisol, immunological, and inflammatory responses. *Journal of Animal Science*. 2002; 80(4): 1044-52.
- [5] Chuang YP, Xue J, Du Y, Li M, An HY, Phillips DL. Time-Resolved Resonance Raman and Density Functional Theory Investigation of the Photochemistry of (S)-Ketoprofen. *Journal of Physical Chemistry B*. 2009; 113(30): 10530-39.
- [6] Lekun L, Gao H. First principles study on the molecular structure and vibrational spectra of ketoprofen. *Spectrochimica Acta PartA*. 2012; 97: 329-39.
- [7] Abdel-Shafi AA. Effect of β -cyclodextrin on the excited state proton transfer in 1-naphthol-2-sulfonate. *Spectrochimica Acta PartA*. 2001; 57(9): 1819-28.
- [8] Dodziuk H, Demchuk OM, Schilf W, Dolgonos G. Synthesis and NMR study of a first generation dendrimer having four branches involving four glycine and one carbomoyl-(3,7-dimethoxy-2-naphthalene) groups and attempts to complex it with α -, β -or γ -cyclodextrins. *Journal of Molecular Structure*. 2004; 693(1-3): 145-51.
- [9] Beraldo H, Nacif WF, West DX. Spectral studies of semicarbazones derived from 3- and 4-formylpyridine and 3- and 4-acetylpyridine: crystal and molecular structure of 3-formylpyridine semicarbazone. *Spectrochimica Acta PartA*. 2001; 57(9): 1847-54.
- [10] Osmialowski O, Kolehmainen E, Gawinecki R. GIAO/DFT calculated chemical shifts of tautomeric species. 2-Phenacylpyridines and (Z)-2-(2-hydroxy-2-phenylvinyl)pyridines. *Magnetic Resonance in Chemistry*. 2001; 39(6): 334-40.
- [11] Meng Z, Carper WR. GIAO NMR calculations for atrazine and atrazine dimers: comparison of theoretical and experimental ^1H and ^{13}C chemical shifts. *Journal of Molecular Structure Theochem*. 2002; 588(1-3): 45-53.
- [12] Laihia K, Kolehmainen E, Kauppinen R, Lorenc J, Puzsko A. Multinuclear ^1H , ^{13}C and ^{15}N NMR study of some substituted 2-amino-4-nitropyridines and their N-oxides. *Spectrochimica Acta PartA*. 2002; 58(7): 1425-35.
- [13] Depature L, Surpateanu G. Carbanion substituent effects on 1-disubstituted 4-(4'-pyridyl)pyridinium methylide structures using ^{13}C NMR spectroscopy and DFT method. *Spectrochimica Acta PartA*. 2003; 59(13): 3029-39.
- [14] Dega-Szafran Z, Katrusiak A, Szafran M. X-ray, NMR and DFT studies of the complex of 1,4-dimethylpiperazine mono-betaine with p-hydroxybenzoic acid. *Journal of Molecular Structure*. 2006; 785(1-3):160-66.
- [15] Basly JP, Longy I, Bernard, M. ESR identification of radiosterilized pharmaceuticals: latamoxef and ceftriaxone. *International Journal of Pharmaceutics*. 1997; 58(8):241-45.

- [16] Basly JP, Basly I, Bernard M. Electron spin resonance detection of radiosterilization of pharmaceuticals: application to four nitrofurans. *Analyst*.1998; 123(8):1753-56.
- [17] Ece E, Tasdemir HU, Biyik R, Ozmen A, Sayin U. Paramagnetic characterization and dosimetric properties of Airfix drug and its ingredients (Montelukast sodium, Sorbitol): An EPR and DFT study. *Radiation Physics and Chemistry*. 2022; 1995: 110082.
- [18] Ece E, Ozmen A, Biyik R, Sayin U. Gamma irradiation effect on some asthma drugs: EPR detection of radiosterilization. *Radiation Protection Dosimetry*. 2023; 199(14): 1600-1604.
- [19] Koksall F, Koseoglu R. EPR of gamma irradiation induced radicals in NaHCO₃, CsHCO₃ and Na₂CO₃. *Radiation Physics and Chemistry*. 2000; 57(1): 59-61.
- [20] Damian G. EPR investigation of γ -irradiated anti-emetic drugs. *Talanta*. 2003; 60(5): 923-27.
- [21] Yordanov ND, Mladenova, R. EPR study of free radicals in bread. *Spectro- Chim Acta Part A*. 2004; 60(6): 1395-1400.
- [22] Ciofini I, Adamo C, Barone VJ. Complete structural and magnetic characterization of biological radicals in solution by an integrated quantum mechanical approach: Glycyl radical as a case study. *Journal of Chemical Physics*. 2004; 121(14): 6710-18.
- [23] Harriman J E. *Theoretical Foundation of Electron Spin Resonance*. New York: Academic Press; 1978.
- [24] Tasdemir HU, Türkkan E, Sayin U, Ozmen A. EPR study of gamma-irradiated 2-Bromo-4'-methoxyacetophenone single crystals. *Radiation Effect and Defect in Solids*. 2016; 171(3-4): 214-22.
- [25] Tasdemir HU, Sayin U, Turkkan E, Ozmen A. EPR investigation of gamma irradiated single crystal guaifenesin: A combined experimental and computational study. *Radiation Physics and Chemistry*. 2016; 121: 61-68.
- [26] Shao Y, Molnar L, Jung Y, Kussmann J, Ochsenfeld C, Brown S, et al. Spartan'08, Wavefunction, Inc. Irvine, CA. *Physical Chemistry Chemical Physics*.2006;8:3172-91.
- [27] Becke AD. Density Functional thermochemistry. III. The role of exact exchange. *Journal of Chemical Physics*. 1993; 98(7): 5648-52.
- [28] Lee C, Yang W, Parr RG. Development of the Colle- Salvetti correlation- energy formula into a functional of the electron density. *Physical Review B*.1988; 37: 785-89.
- [29] Frisch MJ, Trucks GW, Schlegel HB, Scuseria GE, Robb MA, Cheeseman JR, et al. Gaussian 03, Revision E.01, Gaussian, Inc., Pittsburgh, PA. 2003.
- [30] Guo H, Cai C, Gong H, Chen X. Multi-spectroscopic method study the interaction of anti-inflammatory drug ketoprofen and calf thymus DNA and its analytical application. *Spectrochimica Acta Part A*. 2011; 79(1): 92-96.
- [31] Katusin-Razem B, Hamitouchei K, Maltar-Strmecki N, Kos K, Pucic I, Britvic-Budicin S, et al. Radiation sterilization of ketoprofen. *Radiation Physics and Chemistry* 2005; 73(2): 111-16.
- [32] Nakajima A, Tahara M, Yoshimura Y, Nakazawa H. Determination of free radicals generated from light exposed ketoprofen. *Journal of Photochemistry and Photobiology A:Chemistry*. 2005;174(2): 87-89.
- [33] Mattar SM, Stephens AD. Magnetic Inequivalency, Electron Paramagnetic Resonance, Electronic Structure, Optimal Geometry, and Electronic Spectra of the 4,5-Bis(trifluoromethyl)-1,3,2-dithiazol-2-yl, Radical. *Journal of Physical Chemistry A*. 2000; 104(16): 3718-32.
- [34] Ban F, Gauld JW, Wetmore SD, Boyd RJ. In *EPR of Free Rad. in Sol. Trends in Methods and App*. The Netherlands: Kluwer Academic Pub. Chapter 6; 2003.
- [35] Neese F. Prediction of electron paramagnetic resonance g-values by coupled perturbed Hartree–Fock and Kohn–Sham theory. *Journal Chemical Physics*. 2001;115(24):11080-96.
- [36] Chipman DM. *Quantum Mechanical Electronic Structure Calculations with Chemical Accuracy*. Netherlands: Kluwer Academic Press; 1995. p. 109-138.

Investigation of the Thermal, Kinetic, and Dielectric Properties of a Novel Methacrylate Polymer Derived from Naphthol-Containing Cinnamic Acid Derivative

Eray ÇALIŞKAN^{1*}, Kenan KORAN², Fatih BİRYAN²

¹ Bingöl University, Faculty of Science and Arts, Chemistry Department, Bingöl, Türkiye

² Fırat University, Faculty of Science, Chemistry Department, Elazığ, Türkiye

Eray ÇALIŞKAN ORCID No: 0000-0003-2399-4100

Kenan KORAN ORCID No: 0000-0002-2218-7211

Fatih BİRYAN ORCID No: 0000-0001-9198-3329

*Corresponding author: ecaliskan@bingol.edu.tr

(Received: 16.10.2023, Accepted: 30.11.2023, Online Publication: 28.12.2023)

Keywords

Polymer,
Dielectric,
Thermal
stability,
Cinnamic
acid

Abstract: The study investigates the thermal, kinetic, and dielectric properties of a novel methacrylate polymer synthesized from a naphthol-containing cinnamic acid derivative. Notably, the glass transition temperature (T_g) of the polymer, a crucial parameter for amorphous polymers, was found to be significantly higher than traditional methacrylate polymers, owing to the presence of the naphthol group within the polymer structure. The research also delves into the thermal stability and activation energy of the polymer using thermal analysis techniques. Additionally, the dielectric properties of the homopolymer were explored with a focus on the temperature-dependent changes in the dielectric constant and its behavior with varying frequencies.

Naftol İçeren Sınammik Asit Türevinden Türetilen Yeni Bir Metakrilat Polimerinin Termal, Kinetik ve Dielektrik Özelliklerinin İncelenmesi

Anahtar

Kelimeler
Polimer,
Dielektrik,
Termal
kararlılık
Sınammik
asit

Öz: Bu çalışmada, naftol içeren bir sınammik asit türevinden sentezlenen yeni bir metakrilat polimerinin termal, kinetik ve dielektrik özellikleri incelenmiştir. Özellikle, amorf polimerler için çok önemli bir parametre olan polimerin camsı geçiş sıcaklığının (T_g), polimer yapısındaki naftol grubunun varlığı nedeniyle geleneksel metakrilat polimerlerinden önemli ölçüde daha yüksek olduğu bulunmuştur. Araştırmada ayrıca termal analiz teknikleri kullanılarak polimerin termal kararlılığı ve aktivasyon enerjisi de incelenmiştir. Ek olarak, homopolimerin dielektrik özellikleri, dielektrik sabitindeki sıcaklığa bağlı değişikliklere ve değişen frekanslardaki davranışına odaklanılarak araştırılmıştır. Bu çalışma, naftol içeren bir sınammik asit türevinden sentezlenen yeni bir metakrilat polimerinin termal, kinetik ve dielektrik özelliklerini araştırmaktadır. Özellikle, amorf polimerler için çok önemli bir parametre olan polimerin camsı geçiş sıcaklığının (T_g), polimer yapısındaki naftol grubunun varlığı nedeniyle geleneksel metakrilat polimerlerinden önemli ölçüde daha yüksek olduğu bulunmuştur. Araştırmada ayrıca termal analiz teknikleri kullanılarak polimerin termal kararlılığı ve aktivasyon enerjisi de incelenmiştir. Ek olarak, homopolimerin dielektrik özellikleri, dielektrik sabitindeki sıcaklığa bağlı değişikliklere ve değişen frekanslardaki davranışına odaklanılarak araştırılmıştır.

1. INTRODUCTION

Methacrylate polymer derivatives are a group of polymers that are derived from methacrylate monomers but have been modified or functionalized to exhibit specific properties or applications[1-3]. These derivatives can have a wide range of physical properties and applications, depending on the nature of the modifications. Methacrylate polymers can be functionalized with various

groups or additives to impart specific properties, such as conductivity, flame resistance, or antimicrobial properties. These functional polymers have applications in electronics, textiles, and healthcare [4, 5].

The electrical and thermal behavior of polymers with methacrylate main chains has been the subject of extensive study, owing to their diverse application [6-8]. With a well-established understanding of the degradation

mechanisms inherent to methacrylate polymers, various investigations have delved into elucidating rate constants and activation energy values associated with their thermal degradation. The thermal stability of polymers is of paramount significance due to its critical role in numerous applications. In recent years, the research landscape has expanded to encompass studies concerning the thermal degradation of methacrylate and acrylate main chain polymers bearing distinctly different side groups, further enhancing our understanding of these materials [9-13].

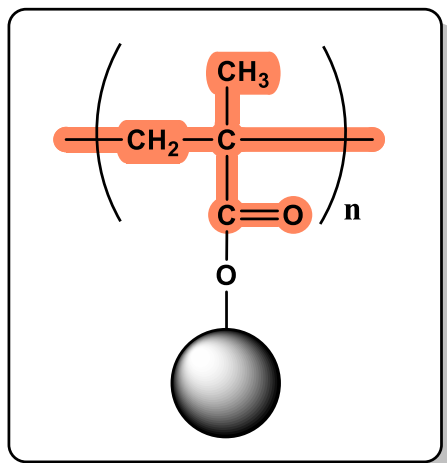


Figure 1. The general structure representation of modified methacrylate polymer

In this study, we synthesized a homopolymer utilizing a monomer derived from a naphthol-containing cinnamic acid derivative and methacryloyl chloride through free radical polymerization techniques. The resulting polymer was characterized extensively to explore its thermal, kinetic, and dielectric properties. Comparative analyses were conducted with existing literature data to gain insights into the unique behavior and performance of this novel polymer. Our findings provide valuable contributions to the evolving knowledge of methacrylate-based polymers and offer potential avenues for their enhanced utilization in various technological applications.

2. MATERIAL AND METHOD

This section begins with an overview of the four synthesis steps employed to create the polymer: the synthesis of naphthyl acrylic acid, attachment of a linker (4-amino phenol), and formation of the monomer using methacryloyl chloride. The use of free radical polymerization with AIBN as the initiator is explained. It also details the physical measurements performed, such as thermal analysis, determination of the activation energy, and dielectric properties analysis.

2.1. Synthesis

2.1.1. General synthesis for compounds

The synthesis started with the reaction of malonic acid and naphthaldehyde under basic conditions to obtain a cinnamic acid derivative. Then, 4-amino phenol was used as a linker before the monomer step. After having (*E*)-*N*-(4-hydroxyphenyl)-3-(naphthalene-1-yl)acrylamide, the

free radical polymerization method was preferred due to the suitability of the monomer.

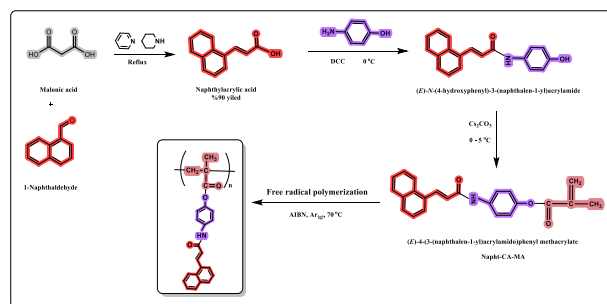


Figure 2. General synthesis steps for homopolymer

Free radical polymerization method was used for the polymerization of the monomer in the presence of a radical initiator (AIBN). Then, it was passed through argon gas and kept in an Oil Bath at 70 °C for 24 hours. Then obtained crude product was precipitated in ethanol and filtered. Obtained solid was dried under vacuum and characterized via spectroscopic methods.

2.2. Characterization of Compounds

2.2.1. Characterization of naphthol-cinnamic acid

^1H NMR (400 MHz, $\text{DMSO-}d_6$) δ 12.49 (s, 1H), 8.40 (d, $J = 15.7$ Hz, 1H), 8.21 (d, $J = 8.2$ Hz, 1H), 8.08 – 7.87 (m, 3H), 7.70 – 7.49 (m, 3H), 6.61 (d, $J = 15.8$ Hz, 1H). ^{13}C NMR (101 MHz, DMSO) δ 122.40, 123.45, 125.70, 126.20, 126.77, 127.62, 129.20, 130.85, 131.22, 131.46, 133.77, 140.64, 167.90.

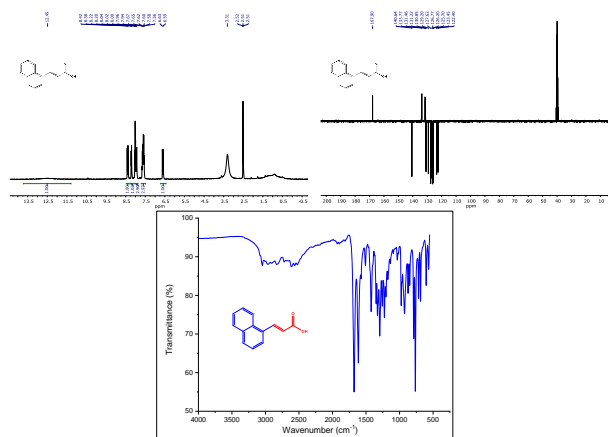


Figure 3. ^1H , ^{13}C and FT-IR spectra of cinnamic acid compound

2.2.2. Characterization of intermediate compound

^1H NMR (400 MHz, $\text{DMSO-}d_6$) δ 10.06 (s, 1H), 9.26 (s, 1H), 8.33 (d, $J = 15.5$ Hz, 1H), 8.25 (d, $J = 8.4$ Hz, 1H), 8.01 (d, $J = 8.1$ Hz, 2H), 7.84 (d, $J = 7.3$ Hz, 1H), 7.62 (dt, $J = 15.2, 7.8$ Hz, 3H), 7.55 (d, $J = 8.4$ Hz, 2H), 6.89 (d, $J = 15.4$ Hz, 1H), 6.81 – 6.73 (m, 2H). ^{13}C NMR (101 MHz, DMSO) δ 39.72, 115.46, 115.70, 120.71, 121.51, 123.04, 123.71, 125.08, 126.08, 126.24, 126.74, 127.43, 129.16, 130.16, 136.37, 154.05, 163.33.

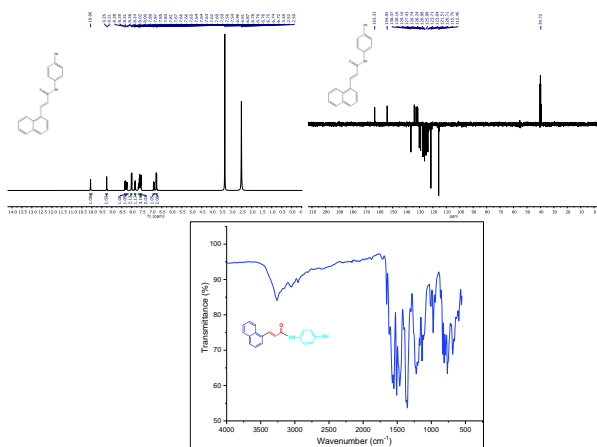


Figure 4. ^1H , ^{13}C and FT-IR spectra of intermediate compound

2.2.3. Characterization of monomer

^1H NMR (400 MHz, $\text{DMSO-}d_6$) δ 10.40 (d, $J = 9.1$ Hz, 1H), 8.61 – 8.18 (m, 4H), 8.02 (dd, $J = 8.1, 3.7$ Hz, 4H), 7.93 – 7.71 (m, 5H), 7.61 (tt, $J = 21.6, 19.3, 6.9$ Hz, 6H), 7.36 – 7.09 (m, 3H), 7.05 – 6.72 (m, 2H), 6.30 (d, $J = 4.6$ Hz, 1H), 5.90 (s, 1H), 2.03 (d, $J = 4.6$ Hz, 3H). ^{13}C NMR (101 MHz, DMSO) δ 39.72, 115.46, 115.70, 120.71, 121.51, 123.04, 123.71, 125.08, 126.08, 126.24, 126.74, 127.43, 129.16, 130.16, 136.37, 154.05, 163.33.

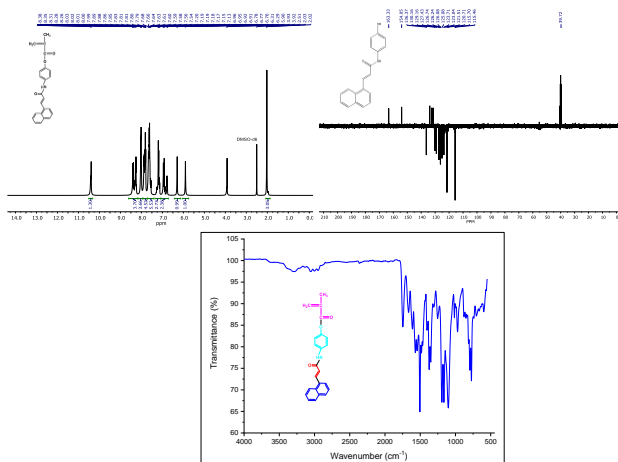


Figure 5. ^1H , ^{13}C and FT-IR spectra of monomer

2.2.4. Characterization of polymer compound

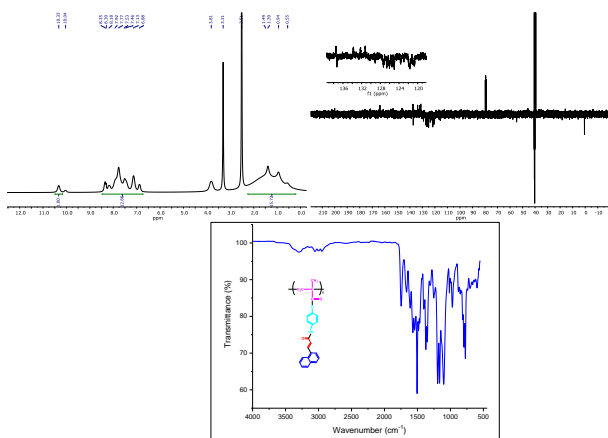


Figure 6. ^1H , ^{13}C and FT-IR spectra of polymer compound

2.3. Physical Measurements

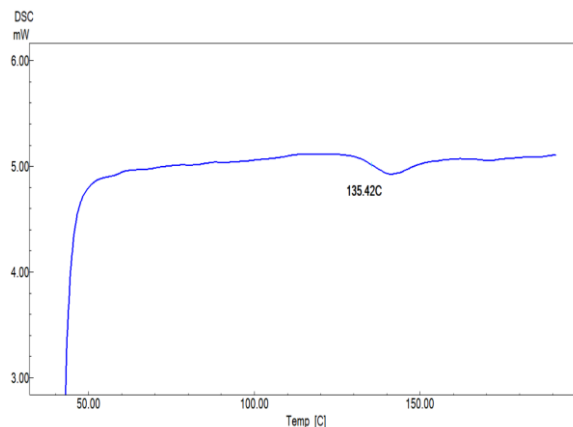


Figure 7. The glass transition temperature of polymer

DSC analysis was performed under a nitrogen atmosphere from ambient temperature to 200 °C at a heating rate of 20 °C min⁻¹. The glass transition temperature was determined as 135.42 °C. This temperature is considerably higher than some methacrylate polymers in the literature. This is thought to be due to the presence of the naphthol group, which is a hard and bulky structure, in the side chain of the homopolymer. The glass transition temperature of amorphous polymers is related to the chain flexibility. Naphthol group in the structure of polymer decreases chain flexibility and increase Tg.

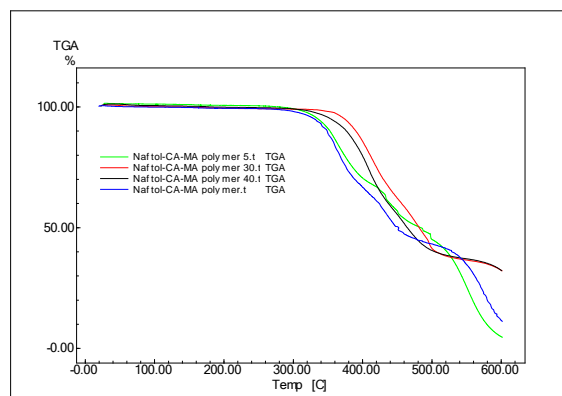


Figure 8. TGA analysis of polymer

In order to determine the thermal stability of the naphthol polymer, TGA analyses were performed in an argon atmosphere. The decomposition temperature was determined as 332 °C in the analysis performed at a heating rate of °C min⁻¹.

Thermal degradation activation energy values were calculated from TGA analysis of the polymer at different heating rates. The activation energies calculated according to the conversion percentages in the range of 2% to 35% were determined in the range of 115.37-187.18 kJ mol⁻¹. The average activation energy was calculated as 139.22 kJ mol⁻¹.

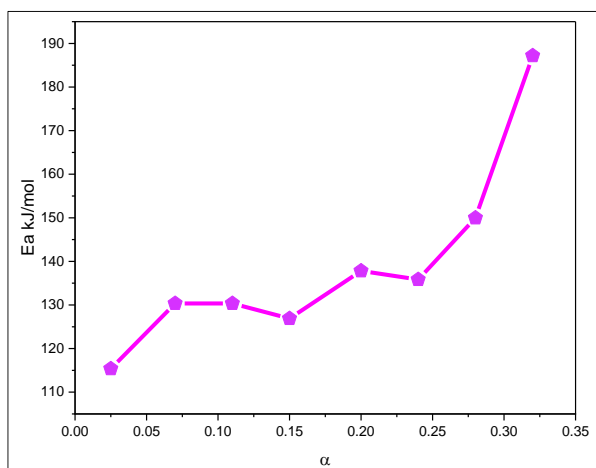


Figure 9. Activation energy graph of polymer

Table 1. Thermal properties of polymer different heating rates

Sample	T _{initial} (°C)	Residue at 400 °C	Residue at 600 °C
5 °C/min	332	66	4
10 °C/min	338	70	11
30 °C/min	356	81	31
40 °C/min	367	87	31

Table 2. Dielectric parameters of samples at 1 kHz at various temperature

Sample	Dielectric constant	AC conductivity (S/cm)	Log σ_{ac}
273K	8.47	2.55×10^{-10}	-9.593
300K	10.80	1.03×10^{-08}	-7.731
320K	10.83	1.86×10^{-08}	-7.524
355K	13.44	9.57×10^{-07}	-6.018

Dielectric behaviors of homopolymer were performed as a function of frequency in the 100 Hz to 70 kHz range. The dielectric constant decreases with increasing frequency. Dipole movements are constrained and the polarization effect is diminished in a stronger electric field. The ac conductivity values for alternating current are also in a similar state. A significant change was observed in the dielectric constant of the polymer with the increase in temperature. The dielectric constant increased from 8.47 to 13.44 at 1 kHz from room temperature to 355K.

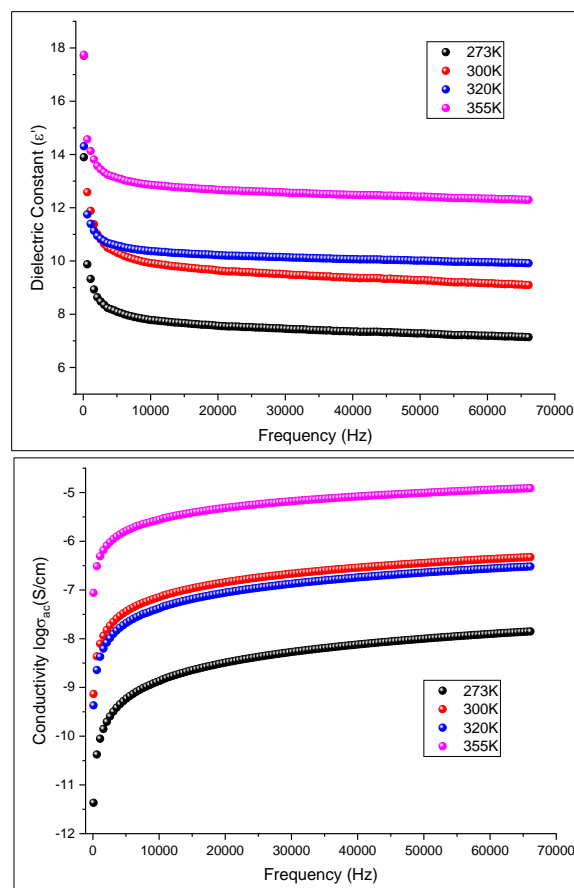


Figure 10. Dielectric properties of polymer

3. RESULTS

The results indicates that the polymer's glass transition temperature (T_g), measured at 135.42 °C. The significantly higher T_g , compared to other methacrylate polymers, is attributed to the presence of the naphthol group in the polymer's side chain, which reduces chain flexibility and increases T_g . Additionally, the thermal stability of the polymer, as determined by TGA analysis, revealed a decomposition temperature of 332 °C. The activation energy values calculated from TGA analysis at different heating rates were in the range of 115.37-187.18 kJ mol⁻¹, with an average activation energy of 139.22 kJ mol⁻¹. Furthermore, the dielectric behavior of the homopolymer was discussed, focusing on how the dielectric constant changes with increasing frequency and temperature.

4. DISCUSSION AND CONCLUSION

In this section, the results are interpreted and their implications are explained. The significance of the higher T_g , linked to the presence of the naphthol group, is discussed in terms of chain flexibility. The impact of the novel polymer's properties on potential applications is explored, and the practical relevance of these findings is emphasized.

Methacrylate polymers containing cinnamic acid derivative are a type of polymers that incorporate cinnamic acid or its derivatives into the polymer backbone or side chains. These polymers can exhibit improved

thermal stability, optical properties, shape-memory behavior, and biocompatibility [14, 15]. Several examples are given below;

Poly(phenyl cinnamate-co-methyl methacrylate) (PPCM), a copolymer of phenyl cinnamate and methyl methacrylate, which can form liquid crystalline phases and exhibit photoresponsive behavior. Poly(4-hydroxycinnamoyl methacrylate) (PHCMA), a homopolymer of 4-hydroxycinnamoyl methacrylate, which can undergo reversible crosslinking and de-crosslinking upon exposure to UV light and heat, respectively.

Poly(3,4-dihydroxycinnamoyl methacrylate) (PDHCMA), a homopolymer of 3,4-dihydroxycinnamoyl methacrylate, which can form hydrogen-bonded supramolecular networks and exhibit shape-memory and self-healing properties. Poly(3,4-dihydroxycinnamoyl methacrylate-co-methyl methacrylate) (PDHCMA-MMA), a copolymer of 3,4-dihydroxycinnamoyl methacrylate and methyl methacrylate, which can show enhanced mechanical strength and thermal stability compared to PDHCMA. Poly(3,4-dihydroxycinnamoyl methacrylate-co-ethylene glycol dimethacrylate) (PDHCMA-EGDMA), a crosslinked copolymer of 3,4-dihydroxycinnamoyl methacrylate and ethylene glycol dimethacrylate, which can display shape-memory and self-healing properties as well as biodegradability.

In summary, methacrylate polymer derivatives are versatile materials with a broad range of physical properties and applications. Their tunable characteristics make them valuable in various industries, from optics and automotive to healthcare and electronics. We have developed a novel homopolymer by using a cinnamic acid derivative and conducted several physical experiments in order to understand the thermal and dielectric characteristics of the polymer. The results demonstrated potential physical properties, especially, the dielectric constant is considerably high value compared to similar structures in literature. Academic research in this field continually explores new derivatives and applications to meet evolving industrial needs.

Acknowledgement

This work was supported by Firat University Scientific Research Projects Unit under grant number FF.22.14.

REFERENCES

- [1] Soleymani Eil Bakhtiari S, Bakhsheshi-Rad HR, Karbasi S, Tavakoli M, Razzaghi M, Ismail AF, et al. Polymethyl Methacrylate-Based Bone Cements Containing Carbon Nanotubes and Graphene Oxide: An Overview of Physical, Mechanical, and Biological Properties. *Polymers*. 2020;12(7):1469.
- [2] Castillo-Aguirre A, Maldonado M. Preparation of Methacrylate-Based Polymers Modified with Chiral Resorcinarenes and Their Evaluation as Sorbents in Norepinephrine Microextraction. *Polymers*. 2019;11(9):1428.
- [3] Dabrowski ML, Stubenrauch C. Methacrylate-Based Polymer Foams with Controllable Pore Sizes and Controllable Polydispersities via Foamed Emulsion Templating. *Advanced Engineering Materials*. 2021;23(3):2001013.
- [4] Sengwa RJ, Choudhary S. Dielectric properties and fluctuating relaxation processes of poly(methyl methacrylate) based polymeric nanocomposite electrolytes. *Journal of Physics and Chemistry of Solids*. 2014;75(6):765-74.
- [5] Deka N, Bera A, Roy D, De P. Methyl Methacrylate-Based Copolymers: Recent Developments in the Areas of Transparent and Stretchable Active Matrices. *ACS Omega*. 2022;7(42):36929-44.
- [6] Roig A, Ramis X, De la Flor S, Serra À. Dual-cured thermosets from glycidyl methacrylate obtained by epoxy-amine reaction and methacrylate homopolymerization. *Reactive and Functional Polymers*. 2021;159:104822.
- [7] Biryani F, Çalışkan E, Koran K. Kinetic analysis and dielectric properties of tyrosine-based tripeptide side groups carrying novel methacrylate polymers. *Journal of Polymer Research*. 2022;29(10):415.
- [8] Singh N, Agarwal P, Porwal J, Porwal SK. Evaluation of block copolymer and homopolymer of stearyl methacrylate as multifunctional additives for lubricating oil. *Polymer Bulletin*. 2023.
- [9] Arslan Z, Kiliçlar HC, Yağcı Y. Visible Light Induced Degradation of Poly(methyl methacrylate-co-methyl α -chloro acrylate) Copolymer at Ambient Temperature. *Macromolecular Rapid Communications*. 2023;44(9):2300066.
- [10] Baruah U, Dutta PP, Mohan B, Baruah SD, Saikia PJ. Thermal degradation study of poly(ethylene-co-methyl methacrylate) nanospheres synthesized via miniemulsion polymerization. *Journal of Thermal Analysis and Calorimetry*. 2023;148(13):6085-95.
- [11] Atiyah H, Hussein RD, Rashid MM, Powell J, Voisey KT. Thermal degradation and ablation energy of poly (methyl methacrylate). *AIP Conference Proceedings*. 2023;2806(1).
- [12] Hu Z, Cai T, Chi C. Thermoresponsive oligo(ethylene glycol)-methacrylate-based polymers and microgels. *Soft Matter*. 2010;6(10):2115-23.
- [13] Biryani F, Çelik H, Çalışkan E, Koran K. Molecular design of ferrocene-based novel polymer using click chemistry via chemoselective polymerization and investigation of electrical properties as organic Schottky diode. *European Polymer Journal*. 2023;197:112321.
- [14] Fonseca AC, Lima MS, Sousa AF, Silvestre AJ, Coelho JFJ, Serra AC. Cinnamic acid derivatives as promising building blocks for advanced polymers: synthesis, properties and applications. *Polymer Chemistry*. 2019;10(14):1696-723.
- [15] Ruwizhi N, Aderibigbe BA. Cinnamic Acid Derivatives and Their Biological Efficacy. *International Journal of Molecular Sciences*. 2020;21(16):5712.

High Response Hydrogen Gas Sensor Based on Palladium Coated Multi-Walled Carbon Nanotube

Betül CEVİZ ŞAKAR*¹ 

¹ Ataturk University, East Anatolia High Technology Application and Research Center (DAYTAM), Erzurum, 25240, Turkey

Orcid No: 0000-0003-3298-2793

*Corresponding author: betul.sakar@ataunil.edu.tr

(Received: 13.07.2023, Accepted: 01.12.2023, Online Publication: 28.12.2023)

Keywords

H₂ gas sensing, MWCNT, Spin coating, XPS, Pd,

Abstract: H₂, which has a zero-carbon footprint, is expected to be one of the main energy sources in the future. The sensitive detection of H₂ in the transportation, storage and energy production processes will allow the active use of this resource. Recently, there are many studies in which nanotube-shaped structures are used as high-response gas sensors. In this study, H₂ gas response parameters at different temperatures (150, 200 and 250 °C) of multi-walled carbon nanotube (MWCNT), which were grown on quartz substrate by spin coating method and then Pd coated with DC sputtering, were investigated. The measurements were made at a gas concentration of 1000 ppm with the help of a current-sensitive gas sensor system. The crystallographic structure, elemental content, oxidation levels and surface morphological properties of the produced film were determined by XRS, XPS and SEM analysis. XRD and XPS analyzes support that the MWCNT used in the study is well graphitized and the formation of PdO compound in the structure with Pd coating. The temperature-dependent H₂ gas sensing measurements showed that the produced Pd-MWCNT structure had a very high gas response and the highest response was at 200 °C. Comparing the response values obtained with the results of other Pd-CNT structures in the literature, it was determined that the film produced by the economical spin coating method had a very high gas response.

Paladyum Kaplı Çok Duvarlı Karbon Nanotüp Tabanlı Yüksek Yanıtlı Hidrojen Gazı Sensörü

Anahtar Kelimeler

H₂ gaz sensör, MWCNT, Spin kaplama, XPS, Pd,

Öz: Sıfır karbon ayak izine sahip olan H₂'nin gelecekte ana enerji kaynaklarından biri olması bekleniyor. Taşıma, depolama ve enerji üretim süreçlerinde H₂'nin hassas tespiti bu kaynağın aktif olarak kullanılmasını sağlayacaktır. Son zamanlarda nanotüp şeklindeki yapıların yüksek tepkili gaz sensörleri olarak kullanıldığı birçok çalışma bulunmaktadır. Bu çalışmada, cam altlık üzerinde spin kaplama yöntemi ile büyütülen ve daha sonra DC püskürtme ile Pd kaplanan çok duvarlı karbon nanotüpün (MWCNT) farklı sıcaklıklardaki (150, 200 ve 250 °C) H₂ gazı tepki parametreleri incelenmiştir. Ölçümler akıma duyarlı gaz sensör sistemi yardımıyla 1000 ppm gaz konsantrasyonunda yapılmıştır. Üretilen filmin kristalografik yapısı, element içeriği, oksidasyon seviyeleri ve yüzey morfolojik özellikleri XRS, XPS ve SEM analizleri ile belirlenmiştir. XRD ve XPS analizleri, çalışmada kullanılan MWCNT'nin iyi grafitleştiğini ve Pd kaplama ile yapıda PdO bileşiği oluşumunu desteklemektedir. Sıcaklığa bağlı H₂ gazı algılama ölçümleri, üretilen Pd-MWCNT yapısının çok yüksek bir gaz tepkisine sahip olduğunu ve en yüksek tepkinin 200 °C'de olduğunu göstermiştir. Elde edilen tepki değerleri literatürdeki diğer Pd-CNT yapılarının sonuçları ile karşılaştırıldığında, ekonomik spin kaplama yöntemi ile üretilen filmin çok yüksek gaz tepkisine sahip olduğu belirlenmiştir.

1. INTRODUCTION

Today, it is extremely important to meet the increasing energy need from energy sources with zero carbon footprint. As an environmentally friendly energy source, H₂ is one of the most important clean energy sources of the future [1,2]. H₂ is a highly flammable and explosive gas with high heat of combustion (120-142 MJ/g). It has a wide flammable range, especially when its amount in the environment exceeds 4% [3]. In addition to these properties of H₂, its colourless, odourless and tasteless nature makes it impossible for human senses to detect it. Parallel to the increasing use of H₂ energy, this gas needs to be carefully monitored during storage, transportation and usage.

In detecting any gas with the aid of a sensor, it is essential that the sensor has fast response (τ_{res}) and recovery times (τ_{rec}), high response magnitude (R) and chemical stability. In this context, it is requested that the gas sensors that are tried to be developed should have the specified features together [1]. Different semiconductor metal oxides (SMO) such as TiO₂ [4–7], MoO₃ [8], WO₃ [9,10], SnO₂ [11,12], ZnO [13,14] and graphene [15] are used in H₂ gas sensor applications. These SMOs can have different structures such as nanotubes or nanowalls. Many studies emphasize the importance of nanotube structures for obtaining high gas response magnitude and low response times [1]. Nanotubes generally exhibit good gas sensing performance, as their large surface area allows H₂ molecules to interact more. The most well-known of these nanotube structures are single (SWCNT) and multi-walled carbon nanotubes (MWCNT). Both SWCNT and MWCNT are basically different shape formations of graphene. While SWCNTs are the rolled-up form of a single graphene layer, MWCNTs are composed of graphene layers that are concentrically nested within each other. The diameters of CNTs are usually in the order of nanometers [16]. CNTs may exhibit metallic or semiconductor characteristics, depending on the direction of graphene. CNTs have high thermal conductivity at room temperature, superconducting characteristics at low temperatures, and a tensile strength approximately 56 times higher than steel [17]. Both SWCNTs and MWCNTs have a wide range of electro-analytical and radiation applications [18,19]. In addition, there are many studies indicating that CNTs can be used as H₂ gas sensors. Kong et al., published a study suggesting that CNTs could be used as H₂ gas sensors [20]. In that study, SWCNT has been deposited on the silicon substrate by chemical vapor deposition (CVD) method. The authors also coated the film surface they produced with Pd. Response and recovery times for H₂ gas at 400 ppm gas concentration were calculated as 2 and 1.5 s, respectively. Zilli et al., formed Pd-MWCNT nanocomposite structure with CVD growth system and determined the H₂ gas response with a system sensitive to current change [21]. The authors reported that the composite they produced had a response time of 150 s and that the H₂ gas sensing parameters changed significantly with increasing H₂ concentration. Data in the literature indicate that Pd modification is required to increase H₂ gas adsorption

[1]. There are many studies examining the response characteristics of the Pd-CNT structure at different gas concentrations. In different studies, the researchers have been stated that the H₂ gas responses of the structures as 407 at 200 ppm [22], 1000 at 311 ppm [23], 1260 at 3000 ppm [24], 2 at 400 ppm [20] and 400 at 10000 ppm [25].

In this study, the structural, morphological properties and temperature dependent H₂ gas sensor detection capabilities of Pd-MWCNT nanocomposite, were investigated. Gas sensor measurements of the produced nanocomposite were taken at 150, 200 and 250 °C under a constant 1000 ppm H₂ gas concentration. The obtained results are given in comparison with the results of Pd nanocomposites previously published in the literature.

2. MATERIAL AND METHOD

In this study, MWCNTs of 99% purity, 10-20 nm in diameter and 10-30 μ m in length, purchased from Graphene Chemical Industries, were used. For film growth by spin coating, MWCNT was mixed with ethanol at 0.25 mg/ml. The resulting solution was ultrasonicated for 1 hour. The obtained solution was dropped by a micropipette onto the quartz substrate, which was previously subjected to the conventional cleaning procedure. The dripped solution was spinned for 30 s at 3000 rpm at room temperature. These dripping and rotating processes were repeated 3 times. DC sputtering system was used to make Pd modification to the obtained film. During the sputtering process, the sputtering parameters were set as chamber pressure 3 mtorr, deposition time 120 s, substrate temperature 200 °C, deposition power 20 W. In order to take the H₂ gas sensor measurements of the produced Pd-MWCNT structure, IDE (interdigitated digital electrode) Pt contacts were made in the thermal evaporation system.

PANalytical/Empryeon and Specs-Flex devices were used for XRD and XPS analysis, respectively. The average angular resolution of this XRD device, which has a power of 4kW, is 0.026°. In XRD measurements, a Ni-filtered Cu source with a wavelength of 1.54 nm ($K\alpha$) was used to generate X-rays. Obtained XRD and XPS data were analyzed with Origin 8.5 (Demo) and CASAXPS (Demo) and versions. Zeiss Sigma 300 model scanning electron microscope (SEM) device was used to obtain surface morphological images. The gas sensor properties of the synthesized Pd-MWCNT film was determined for H₂ gas for 150, 200 and 250 °C temperature and 1000 ppm gas flow with the Keithley 487 picoammeter in the current-sensitive gas sensor measurement system. In these measurements, a voltage of 1V was applied to the metal contacts on the samples.

3. RESULTS AND DISCUSSION

XRD analysis was carried out to determine whether the Pd coated multi-walled carbon nanotube, which was used as an H₂ gas sensor, was in a crystallographic structure. The XRD profile obtained between $2\theta=10^\circ-90^\circ$ of the examined sample is given in Figure 1. This figure

shows a dominant peak corresponding to $2\theta=26^\circ$ and low intensity peaks corresponding to 36° , 43° and 53° . Except for the peak corresponding to 36° , the others represent the classical crystallographic planes of CNTs (002), (100) and (004). The peak observed at 36° reveals the formation of PdO in the structure during the Pd decoration process. The fact that the 002 plane, one of the crystallographic planes of MWCNT, is very dominant like a single crystal, reveals that the MWCNT examined in the study is well graphitized [26]. The crystallite size for 002 plane of MWCNT calculated as 68.5 nm.

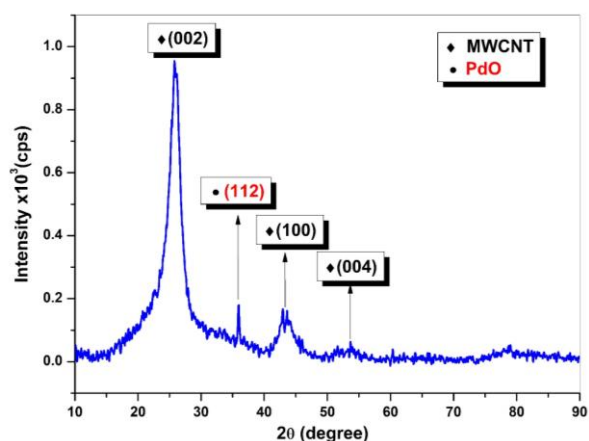


Figure 1. XRD profile of the Pd-MWCNT nanocomposite

Since the gas sensor properties of any material are directly related to the chemical properties and morphology of its surface, both survey and high resolution XPS spectra of the produced film are given in Figure 2 (a-d). From the survey profile given in Figure 2 (a), it is important that only C, Pd and O are present in the structure. This can be considered as an indication that the production stage is designed not to cause any pollution. The high intensities of the peaks of Pd can be seen from Figure 2 (a), as XPS analyses can provide information from the surface of the examined sample to a depth of 10-20 nm. The high resolution XPS spectrum of the Pd 3d orbital is given in Figure 2 (b). From this figure, it is seen that there are two dominant peaks corresponding to Pd 3d_{3/2} and Pd 3d_{5/2} peaks resulting from spin-orbit interaction, and 2 low-intensity peaks supporting PdO formation. The good agreement ($R^2=0.9975$) between the measured raw data and the cumulative peak data obtained after deconvolution can be considered as an indication that the peak separation is done correctly, that is, all formations in the structure of Pd are presented fully. The C1s peak is currently used in almost all XPS studies, both in calibration procedures and in determining the bond structures of C. The specific scanning spectrum of the C1s peak is given in Figure 2 (c). The structure being MWCNT, requires a high proportion of pure C bonds, as expected, with 46.17% of C-C bonds supporting this situation. It was determined that C-C, C-H, C=O and O-C=O formations occurred in the structure, respectively, with the deconvolution of the C1s peak, and their relative distributions were 46.17%, 28.23%, 10.80% and 14.81%. In order to determine the oxidation species and levels of the Pd-decorated MWCNT film, the specific scanning spectrum of the

O1s peak of the film is shown in Figure 2 (d). This spectrum reveals that there is only chemical bonding between C, O and Pd in the structure. That is to say, there are only peaks corresponding to C-O, Pd-O, and O-Pd-O in the deconvoluted spectrum. Among these peaks, it can be clearly seen from the figure that C-O and Pd-O peaks are dominant. According to the elemental analysis processes performed according to XPS analysis, the atomic percentages of O, C and Pd elements in the structure were calculated as 69.113%, 15.745% and 15.141%, respectively. As mentioned before, the fact that XPS is only sensitive to the sample surface caused the Pd and O ratios to be higher than expected. In addition, XPS analyses clearly support the existence of PdO formation, which is thought to exist in the structure according to the XRD results.

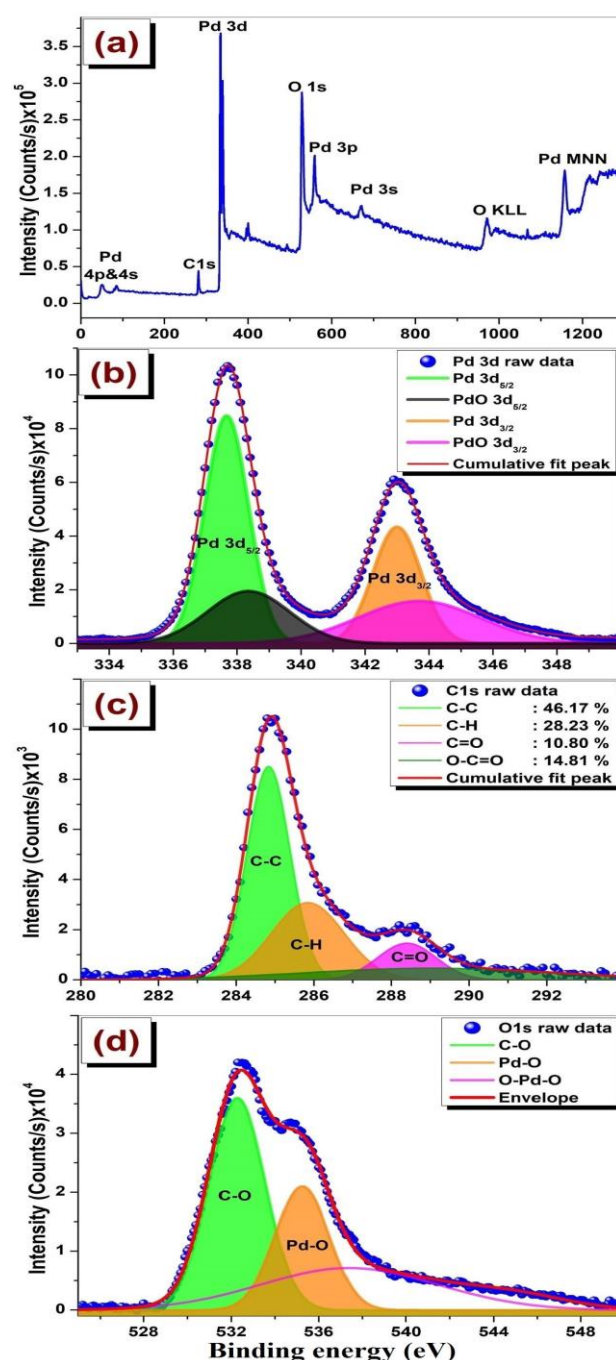


Figure 2. (a) XPS survey spectrum of Pd coated MWCNT (b-d) High resolution spectra of Pd, C and O, respectively

The morphological structure and elemental content of the Pd decorated MWCNT film were investigated using SEM-EDAX. From the 10 KX SEM image given in Figure 3(a), it can be seen that the quartz substrate is almost homogeneously coated with MWCNT. Although it is thought that there may be agglomerations in places, it is clear that MWCNTs completely cover the surface, forming a very tightly packed fibrous structure. From the images in Figures 3 (b) and (c) given for 100 KX and 150 KX magnifications of this film, it is seen that the nanotubes are oriented parallel to the surface and the tube diameters vary between 23.97 nm and 31.99 nm. In addition, it can be seen from Figure 3 (c) that the nanotube surfaces have a porous structure. The energy dependent EDAX spectrum of Pd coated MWCNT is given in Figure 3 (d). The peaks seen in this spectrum belong to C, O and Pd. This supports the qualitative analysis results obtained from XRD and XPS analyses. Elemental percentages by mass obtained by analyzing these peaks were calculated as 83.46%, 6.02% and 10.52% for C, O and Pd, respectively. The fact that the electrons used in EDAX can penetrate more into the structure allows data to be obtained from lower layers compared to XPS. So, this is the main reason why the elemental percentages given look different from XPS.

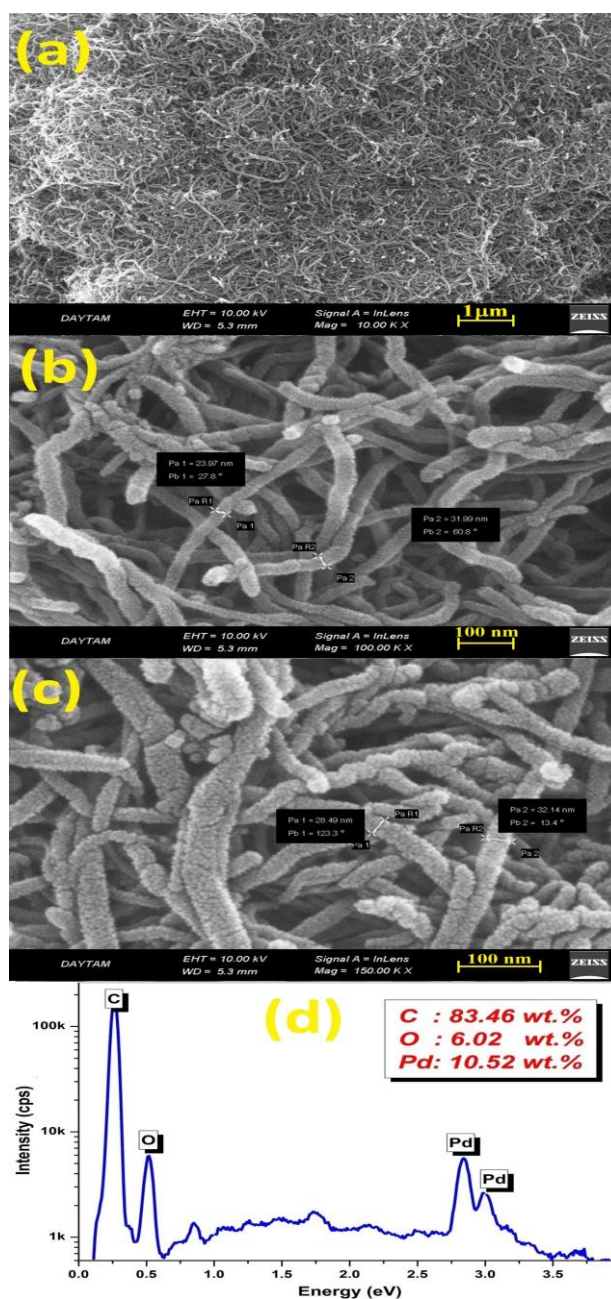


Figure 3. (a-c) SEM images of the Pd coated MWCNT (d) EDAX profile of the MWCNT

The H_2 gas sensor characteristics of Pd coated MWCNT films as a function of temperature are shown in Figures 4 (a) and (b). PdO on the surface of the film exposed to the hydrogen environment undergoes surface reduction. In such a case, palladium hydride is formed by bonding palladium and hydrogen [27]. When the PdO compound homogeneously coated on MWCNTs interacts with H_2 , the number of free electrons in the structure increases. This corresponds to an increase in the carrier charge concentration in the structure, that is, to a decrease in the electrical resistance of the structure. In addition, the coating of high conductivity MWCNTs with PdO causes the gaps between nanotubes to be filled. Due to the conversion of PdO to Pd metal in the hydrogen environment, the conductivity of the structure is further strengthened and its electrical resistance is significantly reduced. In a film produced with such a system, in the H_2 gas environment, it is expected that the electrical resistance will decrease, that is, the current will increase.

This described situation is clearly seen in the PdO coated MWCNT film. When Figure 4 (a) is examined, it is seen that the I/I_0 values show a significant increase in the case of the application of H_2 gas, and that the resistance of the structure increases in the case of gas cut-off. This is a proof that the produced thin film giving response for H_2 gas.

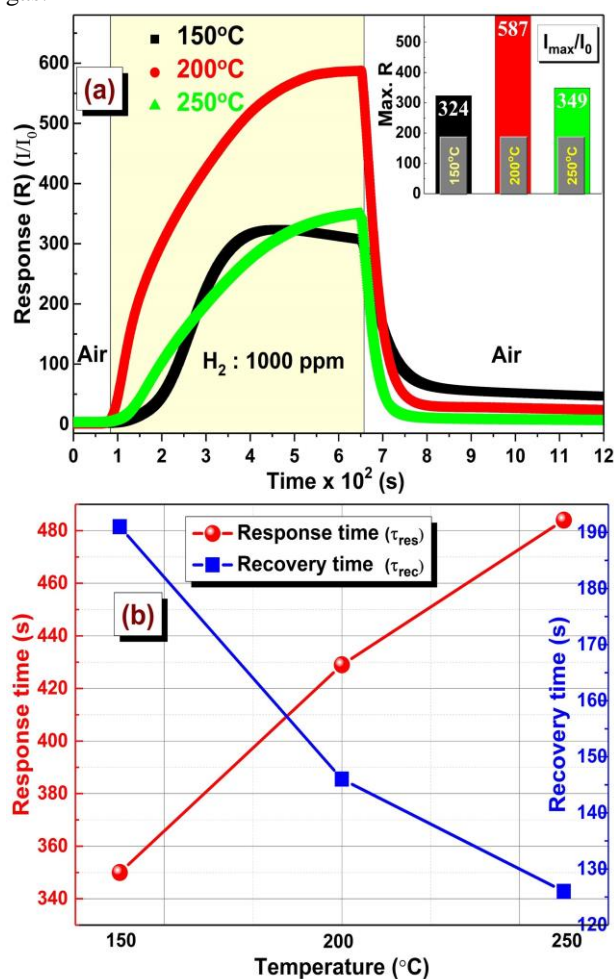


Figure 4. (a) Current-time variations of Pd coated MWCNT for 1000 ppm H_2 gas (b) Variations of temperature dependent response and recovery times

The gas response of any gas sensor device can be determined from changes in current or resistance. An ideal sensor is expected to have a high response value and low response and recovery times. In the calculation of gas responses, some researchers calculate the response values with $100 \times (I_m - I_0)/I_0$, while others use I/I_0 values directly. Essentially, both of these procedures are accurate in determining the gas response, but a normalization is required to compare the gas responses of the produced materials. In this study, the gas response of the produced film was calculated using I/I_0 . In this equation, I represents the current value at any instant, while I_0 corresponds to the minimum current. When the I/I_0 changes of the measurements taken at 150, 200 and 250°C are examined to determine whether the H_2 gas response of the PdO-coated MWCNT film changes with temperature, it is seen that the highest gas response is 587 at 200 °C. The inset plot of Figure 4 (a) reveals that the maximum H_2 gas response values of this film first increase and then decrease with increasing temperature.

From these data, it can be concluded that in order to obtain the maximum H_2 gas response from PdO coated MWCNT films, it is necessary to operate them at an operating temperature of 200 °C. However, it cannot be said that a manufactured material is an ideal candidate for a gas sensor based solely on the magnitude of the response value. Another parameter that can be used for this purpose is the response times. In the calculation of the response times, starting from the minimum current, the time it takes to reach 90% of the time corresponding to the maximum response is used, while in the recovery time, the 90% decrease time from the maximum is used. In the light of this information, the temperature dependent changes of the calculated τ_{res} and τ_{rec} times are shown in Figure 4 (b). Accordingly, the minimum response and recovery times were obtained at 150 and 250 °C, respectively. While the response times have an increase with increasing temperature, the recovery times have an almost regular decrease. From the evaluation of response and recovery times together, it is concluded that the optimum condition is at 200 °C. At this temperature, response and recovery times were calculated as 429 and 146 s, respectively. Therefore, due to both the high gas response and the response times that can be considered optimum compared to other temperatures, it was concluded that it would be appropriate to operate PdO-coated MWCNT films at 200 °C for H_2 gas sensing.

In order to make a meaningful evaluation of the data obtained in this study, the sensing parameters were compared with some studies in the literature. Table 1 shows the response values and response calculation formulas for H_2 gas of some Pd decorated structures (SWNT, MoS_2 , WO_3 , and graphene). When this table is examined, it can be seen that the Pd-MWCNT structure produced in this study has high response values compared to other materials. In some studies, given in the table, it is seen that the equation $(R_a - R_g)/R_a \times 100$ is used to calculate the R parameter. Calculating the R value of any material with this method causes the results to be higher than calculations with R_g/R_a or I/I_0 . Although the I/I_0 method is preferred for the calculation of R values in this study, it is clear that the H_2 gas R values obtained are higher than almost all other materials. If the data obtained in the study are calculated with a result similar to the other equation, the H_2 gas response of Pd-MWCNT measured at 200°C will be 58600. In addition, considering that the measurements in this study were taken at 1000 ppm gas concentration, it can be easily expected that much higher responses will be obtained at 3000 or 10000 ppm values.

4. CONCLUSION

In this study, Pd coated MWCNTs with very high H_2 gas response values were successfully fabricated. It has been determined that the produced nanotube film has response values of 324, 587 and 349 for H_2 gas at 150, 200 and 250 °C, respectively, and the response times are competitive with other studies presented in the literature. From the evaluation of response times and response magnitude values together, it was determined that the

use of Pd coated MWCNT film at 200 °C would give better results. XRD and XPS results indicate that PdO compounds are formed on the surface of the structure with Pd coating. This PdO compound interacts with H₂ and the number of free electrons in the structure increases. This corresponds to a decrease in the electrical resistance of the structure. Moreover, the coating of

MWCNTs with PdO leads to the filling of the gaps between the nanotubes. Due to the conversion of PdO to Pd metal in hydrogen environment, the conductivity of the structure is further enhanced and the electrical resistance is significantly reduced.

Table 1. Comparison of H₂ gas sensing parameters of produced Pd-MWCNT with some studies in literature

Sample	τ_{res} [s]	τ_{rec} [s]	R	G.C. (ppm)	T (°C)	Definition of R	Ref.
Pd-SWNT	420		1260	3000	RT	$(R_a - R_g)/R_a \times 100$	[24]
Pd-SWNT	15	300	400	10000	RT	$(R_a - R_g)/R_a \times 100$	[22]
Pd-WO ₃	42	48	169	1000	80	R_g/R_a	[28]
Pd/MoS ₂	786	902	35	10000	RT	$(R_a - R_g)/R_a \times 100$	[29]
Pd/Graphene	60	--	33	10000	RT	$(R_a - R_g)/R_a \times 100$	[30]
Pd-MWCNT	350	191	324	1000	150	I/I_0	This work
Pd-MWCNT	429	146	587	1000	200	I/I_0	This work
Pd-MWCNT	484	126	349	1000	250	I/I_0	This work

R: Response, T: Temperature, RT: Room Temperature, G.C.: Gas Concentration

REFERENCES

- [1] Yoo IH, Kalanur SS, Seo H. Deposition of Pd nanoparticles on MWCNTs: Green approach and application to hydrogen sensing. *J Alloys Compd.* 2019;788:936–43.
- [2] Elam C. Realizing the hydrogen future: The International Energy Agency's efforts to advance hydrogen energy technologies. *Int J Hydrog Energy.* 2003;28(6):601–7.
- [3] Gu H, Wang Z, Hu Y. Hydrogen Gas Sensors Based on Semiconductor Oxide Nanostructures. *Sensors.* 2012;12(5):5517–50.
- [4] Krško O, Plecenik T, Roch T, Grančič B, Satrapinsky L, Truchlý M, et al. Flexible highly sensitive hydrogen gas sensor based on a TiO₂ thin film on polyimide foil. *Sens Actuators B Chem.* 2017;240:1058–65.
- [5] Li Z, Yao Z, Haidry AA, Plecenik T, Xie L, Sun L, et al. Resistive-type hydrogen gas sensor based on TiO₂: A review. *Int J Hydrog Energy.* 2018;43(45):21114–32.
- [6] Haidry A, Schlosser P, Durina P, Mikula M, Tomasek M, Plecenik T, et al. Hydrogen gas sensors based on nanocrystalline TiO₂ thin films. *Open Phys.* 2014;14; 9(5).
- [7] Ceviz Şakar B. Influence of the Cu doping on the physical and H₂ gas sensing properties of TiO₂. *Int J Hydrog Energy.* 2024;50(Part A):1197-208
- [8] Xu K, Liao N, Xue W, Zhou H. First principles investigation on MoO₃ as room temperature and high temperature hydrogen gas sensor. *Int J Hydrog Energy.* 2020; 45(15):9252–9.
- [9] Mirzaei A, Kim JH, Kim HW, Kim SS. Gasochromic WO₃ Nanostructures for the Detection of Hydrogen Gas: An Overview. *Appl Sci.* 2019;29(9):1775.
- [10] Wu CH, Zhu Z, Huang SY, Wu RJ. Preparation of palladium-doped mesoporous WO₃ for hydrogen gas sensors. *J Alloys Compd.* 2019;776:965–73.
- [11] Katsuki A, Fukui K. H₂ selective gas sensor based on SnO₂. *Sens Actuators B Chem.* 1998;52(1–2):30–7.
- [12] Lu S, Zhang Y, Liu J, Li HY, Hu Z, Luo X, et al. Sensitive H₂ gas sensors based on SnO₂ nanowires. *Sens Actuators B Chem.* 2021;345:130334.
- [13] Al-Hardan NH, Abdullah MJ, Aziz AA. Sensing mechanism of hydrogen gas sensor based on RF-sputtered ZnO thin films. *Int J Hydrog Energy.* 2010;35(9):4428–34.
- [14] Lupan O, Chai G, Chow L. Hydrogen gas sensor based on single ZnO nanorod. *Microelectron Eng.* 2008;85(11):2220–5.
- [15] Hong J, Lee S, Seo J, Pyo S, Kim J, Lee T. A Highly Sensitive Hydrogen Sensor with Gas Selectivity Using a PMMA Membrane-Coated Pd Nanoparticle/Single-Layer Graphene Hybrid. *ACS Appl Mater Interfaces.* 2015;18; 7(6):3554–61.
- [16] Han T, Nag A, Chandra Mukhopadhyay S, Xu Y. Carbon nanotubes and its gas-sensing applications: A review. *Sens Actuators Phys.* 2019; 291:107–43.
- [17] Wong EW, Sheehan PE, Lieber CM. Nanobeam Mechanics: Elasticity, Strength, and Toughness of Nanorods and Nanotubes. *science.* 1997;277(5334):1971-1975.
- [18] Akbaba U, Kasapoğlu AE, Gür E. Gamma and neutron irradiation effects on multi-walled carbon nanotubes. *Diam Relat Mater.* 2018;87:242–7.
- [19] Şakar E, Akbaba U, Zukowski E, Gürol A. Gamma and neutron radiation effect on Compton profile of the multi-walled carbon nanotubes. *Nucl Instrum Methods Phys Res Sect B Beam Interact Mater At.* 2018;437:20–6.
- [20] Kong J, Chapline MG, Dai H. Functionalized carbon nanotubes for molecular hydrogen sensors. *Adv Mater.* 2001;13(18):1384–6.
- [21] Zilli D, Bonelli PR, Cukierman AL. Room temperature hydrogen gas sensor nanocomposite based on Pd-decorated multi-walled carbon nanotubes thin films. *Sens Actuators B Chem.* 2011;157(1):169–76.
- [22] Sun Y, Wang HH. High-Performance, Flexible Hydrogen Sensors That Use Carbon Nanotubes Decorated with Palladium Nanoparticles. *Adv Mater.* 2007 5;19(19):2818–23.
- [23] Xiao M, Liang S, Han J, Zhong D, Liu J, Zhang Z, et al. Batch Fabrication of Ultrasensitive Carbon

- Nanotube Hydrogen Sensors with Sub-ppm Detection Limit. *ACS Sens.* 2018;27;3(4):749–56.
- [24] Mubeen S, Zhang T, Yoo B, Deshusses MA, Myung NV. Palladium Nanoparticles Decorated Single-Walled Carbon Nanotube Hydrogen Sensor. *J Phys Chem C.* 2007;111(17):6321–7.
- [25] Sun Y, Wang HH, Xia M. Single-Walled Carbon Nanotubes Modified with Pd Nanoparticles: Unique Building Blocks for High-Performance, Flexible Hydrogen Sensors. *J Phys Chem C.* 2008;112(4):1250–9.
- [26] Atchudan R, Pandurangan A, Joo J. Effects of Nanofillers on the Thermo-Mechanical Properties and Chemical Resistivity of Epoxy Nanocomposites. *J Nanosci Nanotechnol.* 2015;1;15(6):4255–67.
- [27] Girma HG, Park KH, Ji D, Kim Y, Lee HM, Jeon S, et al. Room-Temperature Hydrogen Sensor with High Sensitivity and Selectivity using Chemically Immobilized Monolayer Single-Walled Carbon Nanotubes. *Adv Funct Mater.* 2023;33(18):2213381.
- [28] Wang Y, Liu B, Xiao S, Li Wang L, Cai D, Wang D, et al. High performance and negative temperature coefficient of low temperature hydrogen gas sensors using palladium decorated tungsten oxide. *J. Mater. Chem. A.* 2015; 3(3):1317-24,
- [29] Baek DH, Kim J. MoS₂ gas sensor functionalized by Pd for the detection of hydrogen. *Sens Actuators B Chem.* 2017;250:686–91.
- [30] Chung MG, Kim DH, Seo DK, Kim T, Im HU, Lee HM, et al. Flexible hydrogen sensors using graphene with palladium nanoparticle decoration. *Sens Actuators B Chem.* 2012;169:387–92.

Root Cause Model Proposal For Human-Related Risks In Occupational Health And Safety Practices Of Special Provincial Administrations

Mustafa ERDEM^{1*} , Alpaslan H. KUZUCUOĞLU² 

¹ Istanbul Gedik University, Graduate Education Institute, Occupational Health and Safety Doctoral Program, Istanbul, Türkiye

² Istanbul Medeniyet University, Literature Faculty, Information And Document Management Department, Istanbul, Türkiye

Mustafa ERDEM ORCID No: 0000-0002-2746-0571

Alpaslan H. KUZUCUOĞLU ORCID No: 0000-0003-3186-2204

*Corresponding author: mustafaerdem073@hotmail.com

(Received: 09.11.2023, Accepted: 01.12.2023, Online Publication: 28.12.2023)

Keywords

Occupational
Health and
Safety,
Special
Provincial
Administrations,
Occupational
Accident

Abstract: Special provincial administrations are autonomous institutions based on the efficiency and effectiveness of local public services, where the people of the region contribute more to the management and democratic elements find a more comprehensive development environment. Local services provided by private administrations directly affect human life. The aim of the study is to propose a root cause model for risks based on human factors in the occupational health and safety (OHS) practices of special provincial administrations. In the research, OHS practices in special provincial administrations were examined. In the section, the importance of OHS in special provincial administrations, the causes of occupational accidents and occupational diseases, and the measures that can be taken to prevent occupational accidents and occupational diseases are included. The research was conducted on employees of special provincial administrations. While the population of the research consists of 11,463 people working in special provincial administrations, the sample was determined as 372 people with a confidence level of 0.95 and a margin of error of 0.05, and the study was conducted with 372 people. SPSS 22.00 was used to analyze the research data. Independent sample t-test was used to compare independent pairs of groups, and one-way variance test was used to compare three or more independent groups. In the study conducted on human-induced risks, OHS practices scores were compared according to the demographic information of the participants, and the relationship between the sub-dimensions and the root cause were examined. The direct and indirect effects of the root problem and cause factor on work accidents were examined. In addition, a root cause analysis was made in the research and a model proposal was made for human-induced.

İl Özel İdarelerinin İş Sağlığı ve Güvenliği Uygulamalarında İnsan Kaynaklı Risklere Yönelik Kök Sebep Modeli Önerisi

Anahtar Kelimeler

İl Özel İdareleri,
İş Kazası,
İş Sağlığı ve
Güvenliği

Öz: İl özel idareleri, bölge insanların daha çok yönetime katkı sağladığı, demokratik unsurların daha kapsamlı bir kalkınma ortamı bulduğu yerel kamu hizmetlerinin verimliliğine ve etkinliğine dayanan otonom kurumlardır. Özel idarelerde sunulan mahalli hizmetler, insan yaşamını doğrudan etkilemektedir. Çalışmada il özel idarelerinin iş sağlığı ve güvenliği (İSG) uygulamalarında insan faktörüne dayalı risklere yönelik, kök sebep modeli önerisinde bulunulması amaçlanmıştır. Araştırmada, il özel idarelerinde İSG uygulamaları konusu incelenmiştir. Bölüm içerisinde il özel idarelerinde İSG'nin önemi, iş kazaları - meslek hastalarının nedenleri, iş kazaları ile meslek hastalıklarının önlenmesinde alınabilecek tedbirlere yer verilmiştir. Araştırma il özel idareleri çalışanları üzerinde yapılmıştır. Araştırmanın evrenini il özel idarelerinde çalışan 11.463 kişi oluştururken örneklemi ise 0.95 güven, 0.05 hata payı ile 372 kişi olarak belirlenmiş ve 372 kişi ile çalışma yapılmıştır. Araştırma verilerinin analizinde SPSS 22.00 kullanılmıştır. Bağımsız ikili grupların

karşılaştırılmasında bağımsız örneklem t-test, üç ve daha fazla bağımsız grupların karşılaştırılmasında ise tek yönlü varyans testi kullanılmıştır. İnsan kaynaklı risklere yönelik yapılan çalışmada, katılımcıların demografik bilgilerine göre İSG uygulamaları puanları karşılaştırılmış, alt boyutlarıyla arasındaki ilişki ve kök neden durumu incelenmiştir. İş kazalarına kök sorun ve neden faktörünün doğrudan ve dolaylı etkileri incelenmiştir. Bununla birlikte araştırmada kök sebep analizi yapılarak insan kaynaklı risklere yönelik bir model önerisi yapılmıştır.

1. INTRODUCTION

Public administration units are of great importance in solving social problems that are intertwined with society in many areas. In parallel with the population growth, there is an increase in the problems that the state needs to solve, and this leads to an increase in the services provided by the state.

The duties, responsibilities and authorities of special provincial administrations are shared between metropolitan municipalities and the state according to their importance in big cities. The study examines the impact of the reform on occupational health and safety of employees in special provincial administrations in Turkey on provincial governments. Community coexistence may mean that people have a desire for a well-managed local governance model. The state determines the need for these demands. The continuous development of social needs and expectations forces institutions to find new resources. For this reason, issues such as the production, transmission and management of public services bring to the fore the need for public administration.

Due to changing conditions and management needs in the constantly developing world, an ongoing construction process has entered the management strategy. In this reform process in Turkey, the understanding of local administrations is being restructured and it is possible to say that many things have changed. The most important one is the creation of municipalities and special provincial administrations. In order to meet the general needs of the provincial population, special administratively and economically autonomous provincial administrations are established, whose decision-making bodies are elected by local voters.

In this study, which was carried out to examine human-related risks in the OHS practices of special provincial administrations, which are a part of local governments, the purpose of OHS in special provincial administrations, the causes of work accidents, approaches to the causes of work accidents in special provincial administrations, the causes of work accidents, work accidents in special provincial administrations and issues regarding the measures that can be taken to prevent accidents are mentioned. It is aimed to propose a root cause model for human-related risks in the OHS practices of special provincial administrations.

In the literature research, the effects of whether the personnel working in special provincial administrations have sufficient knowledge among the main causes of work accidents and occupational diseases were examined. In addition, the importance of factors such as the level of employees in the sector regarding the risks and dangers in their working environments, what differences there are based on factors such as employee awareness, employee education level, age, working hours and previous injuries are mentioned in this research. In this study, it is emphasized that original training plans should be created with different techniques to protect employees from risks in the workplace and to increase their awareness of risks.

Purpose of the research

This study aims to examine the factors related to human-related risks in the occupational health and safety practices of special provincial administrations. Accordingly, the current dangers in terms of health and occupational safety of all employees in special provincial administrations and the risks that they may be involved in have been investigated.

Importance of the research

When the general structure of special provincial administrations is examined, it is observed that they employ personnel in a large number of different working areas. From past to present, technological and scientific advances as well as the development of transportation and communication have affected the distance between rural and urban living standards and caused them to become increasingly closer. Due to this situation, it has become a necessity to provide the same service standards offered by municipalities in rural areas. While services such as irrigation, sewerage, zoning and road works, drinking water, park and garden arrangements, cemetery works and cleaning works in settlements are provided by municipalities in cities; the same services are provided by special provincial administrations in rural areas such as villages and hamlets. [1].

Due to this situation, the occurrence of work accidents and occupational diseases becomes an inevitable situation. After the Occupational Health and Safety Law No. 6331 came into force, more attention is paid to occupational safety than in the past in order to avoid legal sanctions. Personnel working in special provincial administrations must

benefit from health and safety activities in addition to training and performance evaluation duties. It is seen that in workplaces where research on OHS is carried out, it has become mandatory to include OHS in the daily routine in personnel services. In accordance with the purposes of OHS practices, it is important for personnel services to closely follow the development of legislation in the field of labour law and social security.

Various variables such as the size of the business area of special provincial administrations, many different hazard categories and the number of employees emphasize the importance of the research.

Assumptions of the research

Ethics Committee Decision dated 21.02.2023 and numbered 444 was taken for the research.

During the execution of the study; * those who participate in the survey will give sincere and accurate answers to the survey questions. * The employees of the special provincial administrations that constitute the sample group must be representative of the population of the research.

Limitations of the research

Participants will be limited to employees of special provincial administrations, provided that they do not have any mental or communication disabilities.

Causes of work accidents in special provincial administrations

Studies have concluded that the materials used during work play a major role in accidents.

Causes of accidents due to human behaviour (human reasons); they are grouped as personal elements, physiological elements and psychological elements. Accident causes related to physical and mechanical environmental conditions (technical reasons); It is also divided into sub-sets as accident causes related to machinery, accident causes related to production regulations, and accident causes related to environmental conditions.

Causes of accidents related to human behaviour

It is stated that when explaining the causes of occupational accidents or occupational diseases that may occur during work, especially the causes related to human behaviour, it is important to express the concepts of "frequency rate of work accidents", "risk of work accidents" and "proneness of work accidents" in order to better understand the subject [2].

According to the Domino Theory of Work Accidents, when all the mechanisms in the enterprises are taken into consideration, it is obvious that the major factor in the processes until the accident occurs is caused by human-caused dangerous actions and situations. Managerial incompetence, personal inadequacy (lack of

experience, carelessness, forgetfulness, etc.), dangerous situations and actions are the sources of accidents [3].

Personal elements

When talking about individual characteristics that cause work accidents to occur, the first thing that comes to mind is the individuals' age, gender, marital status, position, work experience, education level and habits. There is a connection between the individual characteristics of employees and the high number of accidents in businesses [2].

Physiological elements

Physiological factors, which are one of the factors that cause accidents; although it has not been clearly demonstrated that fatigue, monotony, physical inadequacy and insomnia are indicators of accidents, it has been Psychological Elements

Psychological elements

Psychological factors, which are one of the factors that may affect the occurrence of accidents while performing work; it is examined under the headings of intelligence, emotional state, accident proneness, tension (stress), job satisfaction-motivation.

Causes of accidents due to unsafe conditions and environments

In this regard, the working system, ergonomic structure and physical characteristics of the workplace, which are among the causes of work accidents, are generally mentioned.

Causes of accidents due to physical and mechanical environmental conditions in special provincial administrations

It is known that there are two important concepts in the emergence of the concept of health and safety in the workplace. These concepts are called risk and danger. As a general rule, risk is expressed as the risk area and problem for expansion. The main purpose of health and safety activities is to minimize the problems that may arise from these risks. If evaluated only from this perspective, the importance of the subject has emerged again [5].

Causes of accidents due to physical and mechanical environmental conditions in Special Provincial Administrations; * Causes of Accidents Due to Machinery * Causes of Accidents Due to Production Organizations * Causes of Accidents Due to Environmental Factors * Causes of Accidents Due to Unexpected Events.

Psychological elements

Psychological factors, which are one of the factors that may affect the occurrence of accidents while performing work; it is examined under the headings of intelligence, emotional state, accident proneness, tension (stress), job satisfaction-motivation.

Causes of accidents due to unsafe conditions and environments

In this regard, the working system, ergonomic structure and physical characteristics of the workplace, which are among the causes of work accidents, are generally mentioned.

Causes of accidents due to physical and mechanical environmental conditions in special provincial administrations

It is known that there are two important concepts in the emergence of the concept of health and safety in the workplace. These concepts are called risk and danger. As a general rule, risk is expressed as the risk area and problem for expansion. The main purpose of health and safety activities is to minimize the problems that may arise from these risks. If evaluated only from this perspective, the importance of the subject has emerged again [5].

Causes of accidents due to physical and mechanical environmental conditions in Special Provincial Administrations; * Causes of Accidents Due to Machinery * Causes of Accidents Due to Production Organizations * Causes of Accidents Due to Environmental Factors * Causes of Accidents Due to Unexpected Events

Measures that can be taken to prevent work accidents in special provincial administrations

Statistics show that work accidents and occupational injuries occur every 4 minutes in Turkey. Every minute, 640 people are exposed to work accidents. The cost of accidents that occur when adequate measures for OHS are not taken is 4% of the Gross Domestic Product [6].

Looking at the research, it has been understood that a significant part of work accidents can actually be prevented with simple measures. Failure to take these simple precautions creates negative consequences in workplaces. Measures that can be taken in workplaces to prevent work accidents and occupational diseases can be listed as follows:

Benefiting from the science of ergonomics

Ergonomics science ensures that employees increase productivity and performance by designing the workplace in line with the psychological and physical conditions of the individual, so that they can be active in the workplace in an efficient, safe and healthy way, and by complying with OHS rules. Attention should be paid to the way of working in front of the screen, which is frequently used in office environments, the screens being at eye level and at a certain distance, the low height level, sitting and standing height [7].

Going automated and using personal protective

In industry, management and technical and scientific works, it is important to perform tasks with automatically functioning tools without any

effort [8]. Thanks to the devices, tasks are carried out and employees are removed from dangerous situations. Organizational and technical initiatives are used to ensure occupational safety. Since these techniques eliminate occupational safety risks, they are relatively preferable to the use of personal protective equipment [9].

Organization of occupational safety studies

In the statement in Article 80 of the Labour Law No. 4857, the prevailing opinion is that the measures to be taken in the field of OHS should be taken in the business environment. It is seen that the workplaces that make up the organization are successful in combating work accidents. The issue of occupational safety becomes institutional in businesses within the scope of occupational safety organization. Thus, in addition to the advantages of job security, it is also possible for employees to participate in management, resulting in safer working environments in business life [10].

Training of employees on occupational health and safety

Education is very important when solving OHS-related problems. Article 4 of the OSH Law regulates the responsibility for training that must be provided by the employer, and the employer is obliged to provide organization and take precautions.

2. MATERIAL AND METHOD

In the research, the OHS management practices scale was used primarily to determine the OHS practices of special provincial administrations. The scale was created by adapting Christopher et al.'s article [11] and Glendon and Litherland's safety climate survey. The scale consists of 5 sub-dimensions and is scored with a 5-point Likert system (1: Strongly disagree, 5: Strongly agree).

While the population of the research consists of 11,463 people working in special provincial administrations, the sample was determined as 372 people with a confidence level of 0.95 and a margin of error of 0.05, and the study was conducted with 372 people.

SPSS 22.00 was used to analyse the research data. Independent sample t-test was used to compare independent pairs of groups, and one-way variance test was used to compare three or more independent groups. It was determined that the scale scores showed normal distribution. Histograms, graphs and coefficients of variation related to the relevant scales and dimensions were also examined and it was determined that they were suitable for normal distribution. Additionally, analyzes were carried out using parametric methods. In addition, a root cause analysis was made in the research and a model proposal was made for human-induced risks. Root

Cause Analysis is the work done to identify the real causes. It is a process application that focuses on producing permanent solutions rather than eliminating the apparent causes of problems. In this research, human-related risks were identified in special provincial administrations.

This study was conducted to conduct a root cause study to examine human-related risks in the OHS practices of special provincial administrations and to determine whether the scores they received from the OHS management practices scale changed according to the demographic information of the participants.

For this study, an Ethics Committee Certificate was received from Istanbul Gedik University Ethics Committee Commission with letter dated 21.202.2023 and numbered 444.

3. RESULTS

In this section of the study, the findings of the data obtained from the research and the evaluation of the findings are included.

Table1. Validity and Reliability Analysis of the Research

	Item Numbers	Cronbach Alpha Reliability Coefficients
Security Procedures and Risk Management	6	0.75
Safety and Health Rules	7	0.74
First Aid Support and Training	5	0.71
Preventing Work Accidents	7	0.74
Organizational Security Support	5	0.88
Occupational Health and Safety Practices	30	0.92

Cronbach's alpha coefficient was calculated to determine the validity and reliability of the scale used in the study. As a result of the analyses, the Cronbach alpha coefficient of the scale was found to be 0.92. In order for the scale to be considered

reliable, Cronbach's alpha value must be 0.70 and above [12]. The coefficient value being greater than 0.70 indicates that the scale used in this research has high reliability.

Table 2. Normality Analysis of the Research

	Average	Standard deviation	Skewness	Kurtosis
Security Procedures and Risk Management	3,8642	,71877	-,967	,120
Safety and Health Rules	3,8821	,66708	-1,140	,388
First Aid Support and Training	3,9032	,66136	-,997	,075
Preventing Work Accidents	3,9578	,63722	-,928	,029
Organizational Security Support	3,9011	,55965	-,800	,032
Occupational Health and Safety Practices	3,9017	,55967	-,961	,011

It is considered sufficient for normal distribution if the kurtosis and skewness values obtained from the scale scores are between +3 and -3. Accordingly, it

was determined that the scale scores showed a normal distribution. In this context, analyses were carried out with parametric methods.

Table 3. Distribution of Participants' Demographic Information

		Frequency (n)	Percentage (%)
Gender	Female	166	44,6
	Male	206	55,4
	Total	372	100,0
Age	18-25	70	18,8
	26-34	105	28,2
	35-44	68	18,3
	45-55	62	16,7
	56 and over	67	18,0
	Total	372	100,0
Educational Status	Primary School	19	5,1
	Secondary School	38	10,2
	High School	45	12,1
	Associate's Degree	97	26,1
	Bachelor's Degree	144	38,7
	Postgraduate	29	7,8
Total	372	100,0	
Year of Working in This Job	Less than 10 years	107	28,8
	10-20 years	93	25,0
	20-30 years	87	23,4
	30 and over	85	22,8
	Total	372	100,0
Knowledge of OSH Law and Practices	Yes	196	52,7
	Some	102	27,4
	No	74	19,9
	Total	372	100,0

Having had a work accident at this workplace before	Yes	108	29,0
	No	264	71,0
	Total	372	100,0
Having had a Near Miss Incident at this workplace before	Yes	146	39,2
	No	226	60,8
	Total	372	100,0

Of the participants in the study, 166 were women and 206 were men. 70 of the participants are between the ages of 18-25, 105 are between the ages of 26-34, 68 are between the ages of 35-44, 62 are between the ages of 45-55 and 67 are aged 56 and over. 19 of them are primary school graduates, 38 are secondary school graduates, 45 are high school graduates, 97 are associate degree graduates, 144 are undergraduate and 29 are graduate graduates. 107 of them have been working in this job for less than 10 years, 93 for 10-20 years, 87 for

20-30 years, and 85 for more than 30 years. 196 of the participants have knowledge about OSH law and its practices, 102 have some knowledge, and 74 have no knowledge. While 108 of them had experienced a work accident in this workplace before, 264 of them had not experienced a work accident in this workplace before. While 146 of them had experienced a near miss in this workplace before, 226 of them had not experienced a near miss in this workplace before.

Table 4. Findings Regarding the Difference in OHS Practices Scores According to the Gender of the Participants

	Gender	N	Average	Standard deviation	t	p
Security Procedures and Risk Management	Female	166	3,8785	,75710	,340	,734
	Male	206	3,8528	,68799		
Safety and Health Rules	Female	166	3,9079	,69168	,669	,504
	Male	206	3,8613	,64753		
First Aid Support and Training	Female	166	3,9253	,65816	,577	,564
	Male	206	3,8854	,66500		
Preventing Work Accidents	Female	166	3,9828	,56178	,695	,488
	Male	206	3,9376	,69275		
Organizational Security Support	Female	166	3,9482	,46965	1,503	,134
	Male	206	3,8631	,62133		
Occupational Health and Safety Practices	Female	166	3,9285	,55553	,831	,407
	Male	206	3,8800	,56340		

According to the independent sample t test conducted to determine the differences in OHS practices scores of the participants in the study according to their gender, no statistically significant

differences could be detected between them ($p > 0.05$). Accordingly, OHS practices scores do not vary by gender.

Table 5. Findings Regarding the Difference in Occupational Health and Safety Practices Scores According to the Age of the Participants

		N	Average	Standard deviation	F	P
Preventing Work Accidents	18-25	70	4,2347	,70071	13,083	,000
	26-34	105	3,8966	,67720		
	35-44	68	3,8277	,58645		
	45-55	62	4,2396	,31124		
	56 and over	67	3,6354	,56833		
	Total	372	3,9578	,63722		
Organizational Security Support	18-25	70	3,6914	,54127	9,491	,000
	26-34	105	4,1162	,47619		
	35-44	68	4,0059	,66823		
	45-55	62	3,7226	,68841		
	56 and over	67	3,8418	,20162		
	Total	372	3,9011	,55965		
Occupational Health and Safety Practices	18-25	70	4,0667	,74871	9,929	,000
	26-34	105	3,8980	,57329		
	35-44	68	3,9388	,40003		
	45-55	62	4,0527	,26026		
	56 and over	67	3,5576	,50970		
	Total	372	3,9017	,55967		

According to the one-way variance test performed to determine the differentiation of OHS practices scores of the participants according to their ages, statistically significant differences were detected between them ($p < 0.05$). Accordingly, the total averages of safety procedures and risk management, safety and health rules, first aid support and training, occupational health and safety practices of those aged 18-25 are; Total occupational accident prevention averages for those aged 45-55; the total average of organizational security support for those aged 26-34 is higher.

Table 6. Findings regarding the difference in OHS practices scores according to the educational status of the participant

	Educational Status	N	Average	Standard deviation	F	P
Preventing Work Accidents	Primary School	19	4,1429	,00000	20,680	,000
	Secondary School	38	3,8872	,79516		
	High School	45	3,6889	,46818		
	Associate's Degree	97	4,3829	,23829		
	Bachelor's Degree	144	3,6984	,74242		
	Postgraduate	29	4,2118	,07265		
	Total	372	3,9578	,63722		
Organizational Security Support	Primary School	19	3,8000	,00000	4,279	,001
	Secondary School	38	3,7053	,10120		
	High School	45	4,0933	,34536		
	Associate's Degree	97	3,9072	,70537		
	Bachelor's Degree	144	3,8417	,62796		
	Postgraduate	29	4,2000	,00000		
	Total	372	3,9011	,55965		
Occupational Health and Safety Practices	Primary School	19	3,9552	,00000	19,895	,000
	Secondary School	38	3,7458	,63083		
	High School	45	3,7160	,51992		
	Associate's Degree	97	4,2689	,27610		
	Bachelor's Degree	144	3,6866	,63377		
	Postgraduate	29	4,1990	,00000		
	Total	372	3,9017	,55967		

Statistically significant differences were detected between the OHS practices scores according to the educational level of the participants ($p < 0.05$). Total averages of associate degree graduates' safety procedures and risk management, safety and health

rules, first aid support and training, occupational accident prevention, occupational health and safety practices; Postgraduate graduates' total organizational security support averages are higher.

Table 7. Findings regarding the difference in participants' OHS practice scores according to working year

		N	Average	Standard deviation	F	P
Security Procedures and Risk Management	Less than 10 years	107	3,8660	1,02317	1,926	,125
	10-20 years	93	3,9677	,34948		
	20-30 years	87	3,8966	,72526		
	More than 30 years	85	3,7157	,50318		
	Total	372	3,8642	,71877		
Safety and Health Rules	Less than 10 years	107	3,7490	,95929	5,084	,002
	10-20 years	93	4,0522	,45410		
	20-30 years	87	3,9787	,55136		
	More than 30 years	85	3,7647	,43460		
	Total	372	3,8821	,66708		
First Aid Support and Training	Less than 10 years	107	3,8411	,93475	2,182	,090
	10-20 years	93	4,0151	,45990		
	20-30 years	87	3,9632	,59340		
	More than 30 years	85	3,7976	,45092		
	Total	372	3,9032	,66136		
Preventing Work Accidents	Less than 10 years	107	3,9119	,85143	,850	,467
	10-20 years	93	4,0184	,58342		
	20-30 years	87	4,0049	,54744		
	More than 30 years	85	3,9008	,43197		
	Total	372	3,9578	,63722		
Organizational Security Support	Less than 10 years	107	3,6542	,50250	40,627	,000
	10-20 years	93	4,3720	,28831		
	20-30 years	87	3,8046	,52825		
	More than 30 years	85	3,7953	,58633		
	Total	372	3,9011	,55965		
Occupational Health and Safety Practices	Less than 10 years	107	3,8045	,77587	5,721	,001
	10-20 years	93	4,0851	,41543		
	20-30 years	87	3,9296	,46807		
	More than 30 years	85	3,7948	,38576		
	Total	372	3,9017	,55967		

According to the one-way variance test performed to determine the differentiation of OHS practices scores of the participants according to the working year, statistically significant differences were detected between the working year and occupational health and safety practices and its sub-

dimensions, safety and health rules and organizational safety support ($p < 0.05$). Accordingly, the total averages of OHS practices and sub-dimensions of safety and health rules and organizational security support of employees with 10-20 years of experience are higher.

Table 8. Findings Regarding the Difference in OHS Practices Scores According to the Participants' Knowledge of the OSH Law and Practices

		N	Average	Standard deviation	F	P
Security Procedures and Risk Management	Yes	196	3,7381	,79564	6,995	,001
	Some	102	4,0458	,47150		
	No	74	3,9482	,72880		
	Total	372	3,8642	,71877		
Safety and Health Rules	Yes	196	3,7923	,74439	6,092	,002
	Some	102	4,0714	,47177		
	No	74	3,8591	,63338		
	Total	372	3,8821	,66708		
First Aid Support and Training	Yes	196	3,8102	,72232	4,471	,012
	Some	102	4,0392	,49154		
	No	74	3,9622	,66512		
	Total	372	3,9032	,66136		
Preventing Work Accidents	Yes	196	3,8899	,65686	2,674	,070
	Some	102	4,0014	,57019		
	No	74	4,0772	,65708		
	Total	372	3,9578	,63722		
Organizational Security Support	Yes	196	3,9296	,60743	1,373	,255
	Some	102	3,9157	,49826		
	No	74	3,8054	,50093		
	Total	372	3,9011	,55965		
Occupational Health and Safety Practices	Yes	196	3,8320	,61526	3,750	,024
	Some	102	4,0147	,40971		
	No	74	3,9304	,56279		
	Total	372	3,9017	,55967		

According to the one-way variance test conducted to determine the differentiation of OHS practices scores according to the participants' knowledge about the OSH law and practices, knowledge about the OSH law and practices and OSH practices and its sub-dimensions include safety procedures and risk management, safety and health rules, first aid

support and statistically significant differences were detected between education levels ($p < 0.05$). Accordingly, the total averages of those who have some knowledge are higher on OHS practices and its sub-dimensions: safety procedures and risk management, safety and health rules, first aid support and training.

Table 9. Findings Regarding the Difference in OHS Practices Scores According to the Participants' Previous Occupational Accident in This Workplace

	Having previously had an occupational accident at work	N	Average	Standard deviation	t	p
Security Procedures and Risk Management	Yes	108	3,8302	,56553	-,663	,508
	No	264	3,8782	,77331		
Safety and Health Rules	Yes	108	3,9947	,53378	2,353	,019
	No	264	3,8360	,71027		
First Aid Support and Training	Yes	108	3,9481	,52123	,951	,342
	No	264	3,8848	,71086		
Preventing Work Accidents	Yes	108	4,0026	,48592	1,002	,317
	No	264	3,9394	,68961		
Organizational Security Support	Yes	108	4,2574	,26518	11,406	,000
	No	264	3,7553	,58288		
Occupational Health and Safety Practices	Yes	108	4,0066	,46815	2,558	,011
	No	264	3,8587	,58849		

According to the independent sample t test conducted to determine the difference in OHS practices scores according to the participants' previous occupational accidents at the workplace, statistically significant differences were detected between having a previous occupational accident at this workplace and OHS practices and its sub-

dimensions, safety and health rules and organizational safety support. ($p < 0.05$). Accordingly, the total averages of OHS practices and sub-dimensions of safety and health rules and organizational safety support are higher for those who experienced a work accident.

Table 10. Findings Regarding the Difference in OHS Practices Scores According to the Participants' Previous Near Miss Incident at This Workplace

	Having Had a Near Miss Incident at This Workplace Before	N	Average	Standard deviation	t	p
Security Procedures and Risk Management	Yes	146	4,1712	,63877	7,041	,000
	No	226	3,6659	,69876		
Safety and Health Rules	Yes	146	4,0773	,56227	4,882	,000
	No	226	3,7560	,69951		
First Aid Support and Training	Yes	146	4,1562	,56641	6,446	,000
	No	226	3,7398	,66794		
Preventing Work Accidents	Yes	146	4,2221	,52362	7,126	,000
	No	226	3,7870	,64667		
Organizational Security Support	Yes	146	3,7589	,60750	-	,000
	No	226	3,9929	,50697	4,018	
Occupational Health and Safety Practices	Yes	146	4,0771	,47406	5,240	,000
	No	226	3,7883	,58204		

Statistically significant differences were detected between the participants in the study according to the independent sample t test performed to determine the difference in their OHS practices scores according to whether they had previously experienced a near-miss incident in this workplace ($p < 0.05$). Accordingly, the OHS practices and sub-

dimensions of those who experienced a near-miss incident include safety procedures and risk management, safety and health rules, first aid support and training, prevention of work accidents; the total average of organizational security support for those who did not experience a near-miss incident was higher.

Table 11. Findings Regarding the Examination of the Relationship Between OHS Practices and Sub-Dimensions

		Security Procedures and Risk Management	Safety and Health Rules	First Aid Support and Training	Preventing Work Accidents	Organizational Security Support	Occupational Health and Safety Practices
Security Procedures and Risk Management	Pearson Correlation	1					
	Sig						
	N	372					
Safety and Health Rules	Pearson Correlation	,961**	1				
	Sig	,000					
	N	372	372				
First Aid Support and Training	Pearson Correlation	,984**	,987**	1			
	Sig	,000	,000				
	N	372	372	372			
Preventing Work Accidents	Pearson Correlation	,945**	,950**	,981**	1		
	Sig	,000	,000	,000			
	N	372	372	372	372		
Organizational Security Support	Pearson Correlation	,108*	,230**	,165**	,145**	1	
	Sig	,037	,000	,001	,005		
	N	372	372	372	372	372	
Occupational Health and Safety Practices	Pearson Correlation	,955**	,981**	,981**	,958**	,355**	1
	Sig	,000	,000	,000	,000	,000	
	N	372	372	372	372	372	372

** . The correlation is significant at the 0.01 level (2-tailed).

* . The correlation is significant at the 0.05 level (2-tailed).

As a result of the study, no statistically significant differences could be detected between the participants according to the independent sample t test performed to determine the differences in OHS practices scores according to their gender ($p > 0.05$). Accordingly, OHS practices scores do not vary by gender.

As a result of the Pearson Correlation test conducted to examine the relationship between OHS practices and its sub-dimensions, the relationship between OHS practices and its sub-dimensions, such as safety procedures and risk management, safety and health rules, first aid support and training, and occupational accident

prevention, is found to be at a high level; A moderate, statistically significant relationship was detected between organizational security support and organizational security support ($p < 0.01$). Accordingly, its sub-dimensions positively affect occupational health and safety practices.

In his study, Arat [13] found that the awareness levels and knowledge levels of the participants regarding OHS practices did not vary by gender, there was no statistically significant difference between the groups, the awareness levels of the participants regarding OHS practices differed by gender, and there was a statistically significant difference between the groups.

In this study, no statistically significant differences could be detected between the participants according to the independent sample t test conducted to determine the differences in OHS practices scores according to their gender ($p > 0.05$). Accordingly, OHS practices scores do not vary by gender.

In his study, Arat [13] found that the knowledge, consciousness and awareness levels of the participants regarding OHS differed according to age, and that there was a statistically significant difference between the groups.

In this study, significant differences were detected in the OHS practices scores of the participants according to their ages ($p < 0.05$). Accordingly, the total averages of safety procedures and risk management, safety and health rules, first aid support and training, occupational health and safety practices of those aged 18-25 are; Total occupational accident prevention averages for those aged 45-55; the total average of organizational security support for those aged 26-34 is higher.

As a result of his study, Çelik [14] found that the security communication, security participation and security perception scores of the participants did not show statistically significant differences according to the educational level variable. He stated that there was no difference according to the educational level of the participants, security perception, security communication and security participation.

In his study, Arat [13] found that the awareness levels of the participants regarding OHS did not differ according to their educational level, there was no statistically significant difference between the groups, and the awareness levels and knowledge levels of the participants regarding OHS differed according to the educational level, and it was determined that there was a statistically significant difference between the groups.

In this study, statistically significant differences were detected in OHS practices scores according to the educational level of the participants ($p < 0.05$). Total averages of associate degree graduates' safety procedures and risk management, safety and health rules, first aid support and training, occupational accident prevention, OHS practices; Postgraduate graduates' total organizational security support averages are higher.

In his study, Çelik [14] found that the security participation scores of those with less than 1 year of professional experience (3.467 ± 0.747) were higher than the security participation scores of those with 1-5 years of professional experience (2.961 ± 0.801), and that the security participation scores of those with 11 years or more of

professional experience were higher (3.471 ± 0.738), the security participation scores of those with 1-5 years of professional experience are higher than (2.961 ± 0.801), the security participation scores of those with less than 1 year of professional experience are (3.467 ± 0.747), the security participation scores of those with 6-10 years of professional experience are higher, the security participation scores of those with 11 years of professional experience and above (3.471 ± 0.738) were higher than the security participation scores of those with 6-10 years of professional experience (2.834 ± 0.699).

In his study, Arat [13] found that the awareness levels of the participants regarding OHS did not differ according to professional experience, there was no significant difference between the groups, the awareness levels and knowledge levels of the participants regarding OHS differed according to professional experience, and there was a significant difference between the groups.

In this study, according to the one-way variance test conducted to determine the differentiation of occupational health and safety practices scores of the participants according to their knowledge about the OHS law and its practices, knowledge about the OSH law and its practices and occupational health and safety practices and its sub-dimensions, statistically significant differences were detected between safety procedures, risk management, safety and health rules, first aid support and training ($p < 0.05$). Accordingly, those who have some knowledge have higher total averages of occupational health and safety practices and sub-dimensions of safety procedures and risk management, safety and health rules, first aid support and training.

In this study, statistically significant differences were detected among the participants according to the independent sample t test, which was conducted to determine the difference in occupational health and safety practices scores according to whether they had previously experienced a near-miss incident in this workplace ($p < 0.05$). Accordingly, the occupational health and safety practices of those who experienced a near-miss incident and its sub-dimensions include safety procedures and risk management, safety and health rules, first aid support and training, prevention of work accidents; the total average of organizational security support for those who did not experience a near-miss incident was higher.

As a result of the Pearson Correlation test conducted to examine the relationship between occupational health and safety practices and their sub-dimensions as a result of the data obtained from the study, occupational health and safety practices and their sub-dimensions include safety procedures

and risk management, safety and health rules, first aid support and training, occupational accidents high level of prevention; a moderate, statistically significant relationship was detected between organizational security support and organizational

security support ($p < 0.01$). Accordingly, its sub-dimensions positively affect occupational health and safety practices.

Table 12. Root Cause Analysis [15]

	Root	Cause
Stress, Inattention, Interest		+
Safe Behavior Awareness	+	+
Workplace Environment	+	+
Oral-Written Instructions		+
Legal regulations		+
Equipment	+	+
Problem Concept	+	+
Problem Determination	+	+
Problem Solving	+	+
Security Trainings		+
Hardware		+
Personal Protective Equipment		+
Markings		+
Positive Security Criteria	+	+
Security Policies	+	+
Accident Reports		+
Update	+	+
Improvement	+	+
Employees	+	+
Management-Administration	+	+
Experts	+	+
Auditors		+
Risk Factors	+	+

The root factor, which is classified in two separate categories as root and cause and shown in red in Table 12, has both an indirect and direct effect on the occurrence of accident cases. The reason factor shown in yellow has an indirect effect on the occurrence of accident events. As a result of the research conducted to examine human-related risks, the expressions employees, management - administration and experts are the root problem and indirectly affect the results. Although inspectors, legal regulations, equipment, personal protective equipment, markings and accident reports are not the root problem, they are among the direct causes of the result. Expressions such as verbal and written instructions, safety training, stress, carelessness, interest and intensity are not the root problem, but they are indirect causes. Risk factors, equipment, problem concept, problem identification, problem solving, positive security criteria, security policies, updating, safe behaviour awareness, workplace environment and improvement statements are the root problems and are the reasons that directly affect the results [15].

The root problem in job security is that the security culture is immature in underdeveloped or developing societies. Based on the ability of safety culture to learn and teach, people's awareness of safe behaviour should begin to be transferred from their birth.

Developing technologies should be used in OHS training, which is the most important element in the formation of a safety culture. As a result of the research; the use of artificial intelligence technology and virtual reality-based applications in

training studies ensures that occupational health and safety trainings are highly efficient and effective, increases permanent results in the mind, provides advantages in acquiring knowledge, reduces training costs, contributes to the prevention of work accidents and occupational diseases, and increases the motivation of employees. It is stated that it has positive effects on the formation of a safety culture by instilling the habit of safe behaviour [16].

Cell (security awareness) - Most cellular characteristics are genetically transmitted from parents to new generations. Although the concepts of problem, problem determination and problem solving are acquired through learning, they are generally related to the level of intelligence and are acquired through hereditary means.

Texture (safety culture in the family) - Human beings begin to receive their first education from the family starting from infancy. Thus, all employees derive the foundation of safety culture from their families.

Organ (safety culture in the enterprise) - Management, supervisors and experts serve as the basic organs such as the eyes and ears of the enterprise.

System (industrial safety culture) - In order for the system to run smoothly in the machine order in industrial enterprises; Legal regulations, verbal and written instructions, past accident reports and OHS training are very important.

Organism (national security culture) - Positive security criteria, security policies, awareness of safe behaviour, continuous improvement and updating

steps throughout the country are the most important steps in the formation of national security culture.



Figure 1. Root Cause Organism Model [15]

If the root cause factors from the cell to the organism are examined and the necessary preventive measures are taken in the light of scientific studies, it is envisaged to eliminate 98% of human-caused dangerous situations and dangerous movements and to prevent 100% of occupational accidents and occupational diseases.

4. DISCUSSION AND CONCLUSION

Turkey ranks third in the world and first in Europe in terms of occupational accidents. These losses or injuries cause significant losses, both material and moral, as well as for personnel. This scenario also shows the importance of occupational health and safety. Employers are expected to take all necessary precautions for the health and safety of their employees, correct unsafe working conditions and fulfill all other legal obligations.

For employees who spend one-third of their lives at work, a safe and even encouraging working environment and conditions such as cleanliness may seem expensive for employers at first, but they have become a necessity in terms of productivity.

Occupational health and safety is a branch of science that must be implemented proactively. Organizations must prevent accidents before they happen, rather than after, to protect the health and safety of employees and to review and control the inevitable at the source.

Within the scope of this study conducted on human-related risks in the occupational health and safety practices of special provincial administrations, the scores of occupational health and safety practices were compared according to the demographic information of the participants, and the relationship between them and their sub-dimensions and the root cause were examined.

As a result of the research conducted to examine human-related risks, employees, management - administration expressions are the root problem and indirectly affect the results. Although inspectors, legal regulations, equipment, personal protective equipment, markings and accident reports are not the root problem, they are among the direct causes of the result. Expressions such as verbal and written instructions, safety training, stress, carelessness, interest and intensity are not the root problem, but they are indirect causes. Risk factors, equipment, problem concept, problem identification, problem solving, positive security criteria, security policies, update and improvement statements are the root problems and are the reasons that directly affect the results.

Occupational health and safety legislation for special provincial administrations will increase employer employment and productivity. In the working environment, it is important for the consultant and personnel employed in the consultancy unit to be directly connected to the person responsible for occupational health and safety as employees in a reporting unit, to ensure their professional

independence in accordance with ethical principles and uninterrupted business continuity. In order to identify the hazards and risks present in the special provincial administration units and the deficiencies in the risk assessments to be made and to prevent functional and competence conflicts with other institutional units in the implementation of health and safety-related measures in the workplace, the workplace should be organized hierarchically together with the health and safety unit. It is very important to guarantee that workplace physicians, occupational safety specialists and other health personnel, especially those in decision-making positions in special provincial administrations, can work without being influenced by the administration. One of the most important factors in ensuring that health and safety in the workplace is addressed in detail and adopted by all employees is for employers to express the importance and support they give to this issue. To solve this problem, a health and safety policy that explains the importance of health and safety in the workplace must be established and management must be committed to implementing this policy. This policy and the employer's obligation towards it must be prepared and delivered to all employees, both for the work to be done within the private administrations and for the general secretary and unit directorates. In this regard, the study includes issues aimed at preventing risks in public institutions, aiming to ensure that personnel working in special provincial administrations work in healthy working conditions.

5. SUGGESTIONS

- Since the root cause of occupational accidents and occupational diseases is the human factor, the human factor at the focal point must be taken into consideration as a priority at all stages, starting from the cell (safety awareness) specified in the Organism Model to the formation of the organism (national safety culture).
 - Based on the principle of "If there are no people, there will be no work accidents or occupational diseases", emphasis should be given to studies on the cultural development and change of humans in all OHS studies.
 - In order to create a safety culture in special provincial administrations, OHS awareness should be created among employees and activities should be organized to transform the created awareness into a permanent form of behavior.
 - Occupational health and safety legislation implementations for special provincial administrations will increase employer employment and productivity. Legislation needs to be constantly renewed and keep pace with developments.
 - It is very important to guarantee this independence, especially for employees in management or decision-making positions in special provincial administrations.
- One of the most important factors for employers to ensure that health and safety in the workplace is handled well and adopted by all employees is that they express the importance and support they give to this issue.
- A health and safety policy should be established that explains the importance of health and safety in the workplace, and management should be committed to implementing this policy. This policy and the employer's obligation towards it must be prepared and communicated to all employees, both for the work to be done within the private administrations and for the general secretary and unit directorates.
 - First of all, providing OHS training and employment training by using new technologies such as virtual reality-based and artificial intelligence technologies instead of theoretical / traditional methods will contribute to the training being more effective, more efficient and more successful.
 - By organizing events where employees can express themselves, the problems they encounter in the work environment should be asked, their opinions should be taken and employees should be made to feel that they are valuable to the organization.
 - Employees who are successful in occupational health and safety practices should be rewarded.
 - The success of the study is directly proportional to the number of participants. For this reason, more participants should be able to participate in new OHS studies.
 - Situations that pose security problems should be examined in detail in new studies.
 - More emphasis can be given to occupational health training in the public sphere, and staff awareness can be increased through in-service training.
 - Necessary improvement works should be carried out to create a healthy and safe environment by performing risk analysis and risk assessment at regular periods.
 - OHS performances should be monitored at workplaces at regular intervals and development processes should be followed.
 - Workplace employees should be aware of safe behaviour in the workplace environment.
 - All individuals, including management, should take responsibility to create an OHS culture in all workplaces.
 - More accurate and clear results can be obtained by researchers with more sample groups.

Acknowledgement

This article was derived by the first author from his doctoral thesis titled "Root Cause Model Proposal for Human-Caused Risks in the Occupational Health and Safety Practices of Special Provincial Administrations" at Istanbul Gedik University, Graduate Education Institute, Occupational Health and Safety Doctoral Program. I would like to thank my advisor Alpaslan H. Kuzucuoğlu for her unwavering support during the preparation of this research, and my teachers Mustafa Yağimli and Hilal Arslan for their guidance.

REFERENCES

- [1] Erdem M. Comparative analysis of special provincial administrations in terms of OHS: Bingöl and Elazığ example: Master's thesis. Istanbul: Istanbul Esenyurt University Institute of Science and Technology; 2019.
- [2] Camkurt M. Z. The Effect of Personal Characteristics of Employees on the Occurrence of Work Accidents: TÜHİS Journal of Labor Law and Economics. 2013; 24(6).
- [3] Kuzucuoğlu H. Human-induced risk factors in preventive protection. In: Gedük S, Kuzucuoğlu A. editors. Preventive protection in cultural heritage practices. Hypercast; 2021; p.47-59
- [4] Biçer E. Study on the causes, costs and prevention of work accidents: Master's thesis. Ankara: Gazi University; 2007.
- [5] Algün A. General Principles of Worker Health and Safety, TMMOB Emo Ankara Branch Newsletter; 2014.
- [6] Bilir N. Occupational Health and Safety Profile. Ministry of Labor and Social Security General Publication No: 62. Türkiye: 2017.
- [7] Akpınar T, Çakmakkaya, B. Y., & Batur, N. Ergonomic Science as a Solution Proposal for Protecting the Health of Office Workers: Journal of Balkan and Near East Social Sciences. 2018; 4(2): 76-98.
- [8] Karaçor M, Keleş K. Components of automation systems. VI. Automation Symposium, Samsun: 2007.
- [9] Wentz C. A. Safety, Health And Environmental Protection. McGraw-Hill Book Company; Boston 1998.
- [10] Süzek S. Participation in labor law, gift to Coşkun Kırcı. Galatasaray University, 1996. Ankara: 161-168. (Participation)
- [11] Christopher P, Xin H, Marimuthu A, Linic S. Singular characteristics and unique chemical bond activation mechanisms of photocatalytic reactions on plasmonic nanostructures. Nature materials. 2012; 11(12): 1044-1050.
- [12] Tavşancıl E, Keser H. Development of a likert type attitude scale towards internet usage: Journal of Educational Sciences & Practices. 2002; 1(1).
- [13] Arat O. Analysis of the knowledge, consciousness and awareness of employees in the human resources department regarding occupational health and safety: A field research: Master's thesis. Istanbul: Istanbul University Institute of Social Sciences; 2022.
- [14] Çelik E. A field research to examine the awareness of healthcare professionals regarding occupational health and safety: Master's thesis. Istanbul: Istanbul Gelişim University Institute of Social Sciences; 2016.
- [15] Tunca F, Utlu Z. Root, cause and effect relationship in occupational safety: Journal of Istanbul Aydın University; 2016; 8 (31): 1-14
- [16] Gök Y. Examining the effect of virtual reality applications in occupational health and safety education: Master's thesis. Konya: Selçuk University; 2022.

Investigation of the Protective Effects of Chrysin Against Paclitaxel-Induced Oxidative Stress and Apoptosis in Human Neuronal SH-SY5Y Cells

Adnan AYNA*¹ , Sema Nur VARAN*² 

¹ Bingöl University, Faculty of Arts and Sciences, Chemistry Department, Bingöl, Türkiye

² Bingöl University, Faculty of Arts and Sciences, Chemistry Department, Bingöl, Türkiye

Adnan AYNA ORCID No: 0000-0001-6801-6242

Sema Nur VARAN ORCID No: 0000-0003-2719-6245

*Corresponding author: aayna@bingol.edu.tr

(Received: 12.10.2023, Accepted: 01.12.2023, Online Publication: 28.12.2023)

Keywords

Paclitaxel,
Chrysin,
Apoptosis,
Bcl-2,
Malondialdehyde
levels

Abstract: In this study, the potential protective effects of chrysin, an important flavonoid, against paclitaxel-induced cell toxicity in the SH-SY5Y nerve cell line as an *in vitro* model, were investigated by cell viability analysis, lipid peroxidation analysis and quantitative simultaneous PCR methods. In the study, firstly, paclitaxel and chrysin were applied to the SH-SY5Y cell line at different concentrations in the range of 0-30 μ M, and the results showed that 15 and 30 μ M paclitaxel reduced cell viability, and 500 and 1000 μ M chrysin application reduced these effects. In addition, chrysin application has been shown to significantly reduce malondialdehyde levels in paclitaxel-induced cells. The study also examined the effects of paclitaxel and chrysin application on apoptotic and antiapoptotic genes, mostly located in the intrinsic pathway, and showed that chrysin significantly reduced the levels of *caspase 10*, *caspase 8*, *caspase 6*, *p53* and *NFKB*, and increased the *Bcl-2* level compared to the paclitaxel-treated group. The results of this study suggest that chrysin's suppression of oxidative stress and apoptotic cell death may be an effective strategy for the treatment of paclitaxel-induced SH-SY5Y cytotoxicity.

Krisinin İnsan Nöronal SH-SY5Y Hücrelerinde Paklitaksel Kaynaklı Oksidatif Stres ve Apoptoza Karşı Koruyucu Etkilerinin Araştırılması

Anahtar Kelimeler

Paklitaksel,
Krisin,
Apoptoz,
Bcl-2,
Malondialdehit
düzeyleri

Öz: Bu çalışmada, *in vitro* model olarak SH-SY5Y sinir hücre hattında paklitaksel kaynaklı hücre toksisitesine karşı önemli bir flavonoid olan krisinin potansiyel koruyucu etkileri hücre canlılık analizi, lipid peroksidasyon analizi ve kantitatif eş zamanlı PCR yöntemleri ile araştırılmıştır. Çalışmada ilk olarak SH-SY5Y hücre hattına 0-30 μ M aralığında farklı konsantrasyonlarda paklitaksel ve krisin uygulanmış ve sonuçlar 15 ve 30 μ M paklitakselin hücre canlılığını azalttığını ve 500 ve 1000 μ M krisin uygulamasının da bu etkileri azalttığını göstermiştir. Buna ilaveten, krisin uygulamasının paklitaksel ile indüklenmiş hücrelerde malondialdehit düzeylerini anlamlı ölçüde azalttığı da gösterilmiştir. Araştırmada paklitaksel ve krisin uygulamasının çoğunlukla intrinsic yolakta yer alan apoptotik ve antiapoptotik genler üzerindeki etkileri de incelenmiş ve krisinin *kaspaz 10*, *kaspaz 8*, *kaspaz 6*, *p53* ve *NFKB* seviyelerini anlamlı şekilde azalttığını, *Bcl-2* seviyesini ise paklitaksel uygulanmış gruba göre arttırdığını göstermiştir. Bu çalışmanın sonuçları, krisinin oksidatif stres ve apoptotik hücre ölümünün baskılanmasının, paklitaksel ile indüklenen SH-SY5Y sitotoksitesininin tedavisi için etkili bir strateji olabileceğini göstermektedir.

1. INTRODUCTION

A chemotherapy drug called paclitaxel is used to treat a number of cancers, including breast cancer, ovarian cancer, lung cancer, and others. Paclitaxel can have negative effects, just like many chemotherapy medications. Individuals may experience fewer adverse effects than others, and the intensity of these side effects can vary from person to person. Nausea and vomiting, hair loss, neutropenia, peripheral neuropathy, muscle and joint pain, exhaustion, changes in liver enzymes, and diarrhoea are some of the more frequent side effects of paclitaxel [1-3].

Nowadays, various treatment strategies have been practically applied to reduce side effects [4-8]. One of these strategies and the newest is antioxidants, which have a natural usage area. Natural antioxidants have a slowing and even stopping effect on the course of cancer and can be applied as a combined treatment with chemotherapy.

Flavonoids are an important class of compounds found naturally in plants. They serve as colour pigments in plants and are widely found in various plant materials. Flavonoids play a protective role for plants against environmental stresses and have potential biological effects that may provide beneficial effects to humans. Flavonoids have various effects on health. These effects can be summarized as antioxidant properties, anti-inflammatory effects, cardiovascular effects, anticancer effects, anti-diabetic and antimicrobial effects [9-11]. Chrysin is a bioactive compound naturally found in some plants. It is a type of plant pigments called flavonoids. Chrysin is found primarily in flowering plants and can also be isolated from propolis, honey and some fruits. One of the scientific highlights of chrysin is that it has antioxidant properties. There has also been some research on the anti-inflammatory, antimicrobial and anti-cancer potential of chrysin [12-15].

The aim of this study was to evaluate the possible protective effects of chrysin against paclitaxel-induced toxicity in SH-SY5Y neuron cells as an *in vitro* model through oxidative damage and apoptosis. Thus, possible damage and cell losses that may occur in neuronal cells induced by paclitaxel can be ameliorated. In this study, human neuroblastoma SH-SY5Y cells was used as a model to study neuronal damage caused by paclitaxel-induced oxidative damage and apoptosis in neurodegenerative diseases.

2. MATERIAL AND METHODS

2.1. Materials

SH-SY5Y (ATCC® CRL-2266™) cells were graciously donated by Ataturk University, Turkey. Chrysin was attained from Sigma-Aldrich (St Louis, MO, USA) company with 97% purity. Malondialdehyde bis (PubChem CID:67147) was procured from Merck (Germany). Dulbecco's Modified Eagle Medium

(DMEM) and Fetal Bovine Serum (FBS) were acquired from GIBCO (Gibco, USA).

2.2. Cell Culture

SH-SY5Y cells were grown at 37 °C in a humidified 5% CO₂ environment with 10% FBS and 1% penicillin-streptomycin in DMEM. For 24 hours, the cells were sown in 75 cm² cell culture flasks.

2.3. Cell Proliferation Assay

After the SH-SY5Y cells cultivated in a flask reached sufficient growth, they were removed with Trypsin-EDTA, stained with trypan-blue on the thoma slide, and then counted under an inverted microscope. The calculated cells were seeded in 96-well plates with 7x10³ cells in each well. Then, different concentrations of paclitaxel (3.75 μM, 7.5 μM, 15 μM, 30 μM) were applied to the cells to determine the most effective cytotoxic paclitaxel concentration on the cells. After determining the most effective paclitaxel concentration, chrysin was applied to the cells at different concentrations (125 μM-1000 μM) together with paclitaxel in order to investigate the potential of chrysin to prevent paclitaxel-induced cytotoxicity. After 24 hours of incubation, 3 μl of the WST-1 cell viability kit was added to each well, incubated for 4 hours, and cell viability analyzes were performed by measuring at 595 nm on the ELISA micro plate reader device.

2.4. Measurement of Malondialdehyde Levels

By lipid peroxidation analysis, the extent to which 30 μM Paclitaxel and 500-1000 μM chrysin applied to the SH-SY5Y cell line had a scavenging effect on lipid peroxidation was determined by MDA measurement. The night before, MDA solution (500 μl from the MDA stock was taken and transferred to the tube containing 450 μl of pure water, and 50 μl of the mixture was taken from each tube (except MDA stock) and transferred to the next tube, diluted and kept at +4 °C. In the next stage, SH-SY5Y cells were removed with Trypsin-EDTA solution and then counted on the thoma slide and planted in 6-well plates with 10⁶ cells in each well. After the cells were incubated in a CO₂ incubator for 24 hours, determined amounts of paclitaxel and chrysin were applied to the cells. The next day, the cells were centrifuged and the above cells were incubated. The medium was removed and 1 ml of 0.8% TBA (thiobarbutic acid) solution and 250 μl of TCA (trichloroacetic acid) solution were added and mixed to ensure sufficient homogenization. Afterwards, the cells were boiled in boiling water at 95 °C for 30 minutes. The water bath process was shocked. For this purpose, the cells were placed in ice and treated for 5 minutes. After the quenching process, the cells were centrifuged at 1000 rpm and the supernatant on the cells was removed and transferred to suitable plates for measurement. The absorbance of the cells placed in the ELISA reader device was calculated at 532 nm.

2.5. Real Time PCR

The mRNA transcript level of the genes in the scope of current research were examined via qRT gene expression assay kit procured from Jena Bioscience Company using Rotor-Gene Q (Qiagen) device. For this study, mRNA was isolated utilizing the kit bought from Jena Bioscience. cDNA synthesis was accomplished in line with the supplied kit procedure (Jena Bioscience). The expression levels of apoptotic *caspase 10*, *caspase 8*, *caspase 6*, *p53* and *NFKB*, anti-apoptotic *Bcl-2* and *GAPDH* as a housekeeping gene were analyzed as explained in (Ref). Primer sequences (Molgen Biotechnology, Turkey) were shown in Table 1.

Table 1. Gene-specific primer sequences used in the qRT-PCR study (F: Forward, R: Reverse)

Genes	Primer sequences (5'-3')
<i>Bcl-2</i> (F)	TTAATGTGATTTAGTTATGGCCT
<i>Bcl-2</i> (R)	AATAACAATTCTGTTGACG
<i>Caspase 8</i> (F)	CCTGTCCATCAGTGCCATAG
<i>Caspase 8</i> (R)	CCTGTCCATCAGTGCCATAG
<i>Caspase 6</i> (F)	GACCGACTAAATGCC
<i>Caspase 6</i> (R)	AATACTGTGCAAATGCC
<i>Caspase 10</i> (F)	CCAGGCTATGTATCCTTTCCGGC
<i>Caspase 10</i> (R)	TCGTTGACAGCAGTGAGGATGG
<i>NF-KB</i> (F)	TGCAGCAGAACCAAGGACATG
<i>NF-KB</i> (R)	TGCATTGGGGGCTTTACTGCT
<i>P53</i> (F)	CGACGGTGACACGCTTCC
<i>P53</i> (R)	TTTCTGACTCAGAGGGGGC
<i>GAPDH</i> (F)	GTATCGGACGCCTGGTTACC
<i>GAPDH</i> (R)	TTGAAGTGGCGTGGGTAGAG

2.6. Statistical Analysis

The data obtained from our experimental studies, which were performed in at least 3 repetitions, were statistically evaluated by comparing them with one-way ANOVA Tukey's Multiple Comparison test via GraphPad Prism 5.01 software, and $p < 0.001$ was considered as significant.

3. RESULTS

3.1. Effects of Paclitaxel and Chrysin Application on Cell Viability

To examine the protective effects against paclitaxel-induced oxidative stress and apoptosis in the human

neuronal SH-SY5Y cell line, cells were treated with chrysin and the extent to which the damage was minimized was evaluated by the following cell viability tests. To determine the damage status of SH-SY5Y cells, 4 different doses were applied: 3.75, 7.5, 15, 30 μM . It was observed that 15 to 300 μM paclitaxel caused a significant ($p < 0.001$) decrease in cell proliferation, while 3.75 and 7.5 μM paclitaxel did not cause a significant change in cell proliferation (Figure 1).

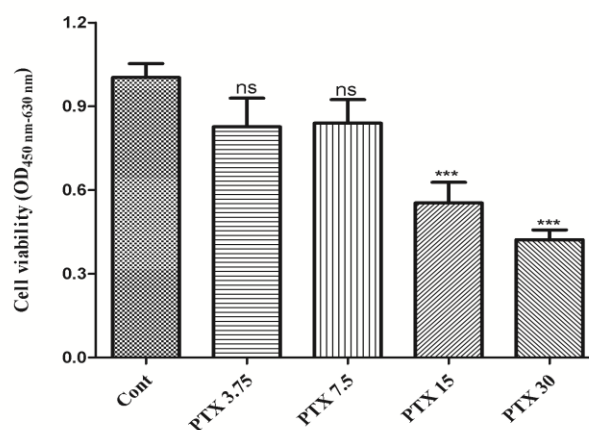


Figure 1. Effect of different doses of paclitaxel on cell proliferation of dopaminergic nerve line (SH-SY5Y) cells. *** $p < 0.001$: statistically significant differences between cont and other groups, ns: nonsignificant

After it was determined that 15 and 30 μM paclitaxel caused a significant ($p < 0.001$) decrease in cell proliferation, 4 different concentrations of chrysin (1000, 500, 250, 125 μM) were injected into the cells together with paclitaxel in order to determine the protective effects of chrysin against paclitaxel-induced toxicity at the relevant dosages. When 1000 μM and 500 μM chrysin were applied to the cells together with 15 μM paclitaxel, it was determined that cell proliferation increased significantly compared to the cells applied paclitaxel, whereas the application of 250 μM and 125 μM chrysin did not show a protective effect (Figure 2). In the light of the findings, subsequent studies were carried out with 500 and 1000 μM chrysin compared to 30 μM paclitaxel.

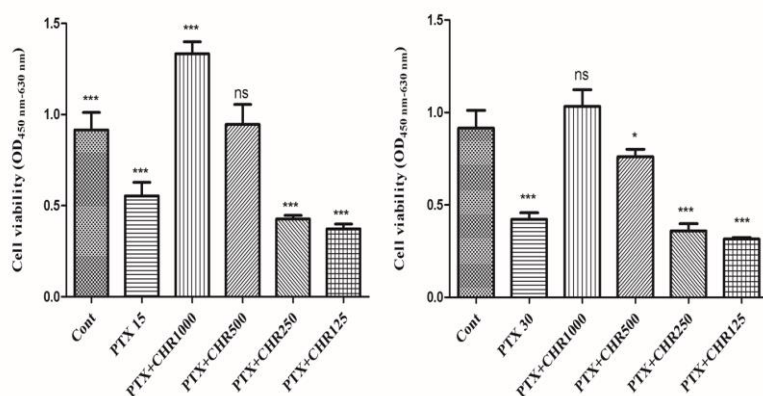


Figure 2. The effects of 500 and 1000 μM chrysin on cell proliferation on SH-SY5Y cells induced by paclitaxel, which was selected as the effective dose (15 and 30 μM). Cont: Control, PTX: Paclitaxel, CHR: Chrysin. *** $p < 0.001$ and * $p < 0.1$: statistically significant differences between cont and other groups, ns: nonsignificant

3.2. Lipid Peroxidation Assay

A lipid peroxidation experiment was conducted to observe to what extent the cells were damaged after the application of 30 μM paclitaxel, one of the paclitaxel-derived chemotherapeutics, to healthy human neuroblastoma cells and to what extent antioxidant treatment minimized this damage, and to determine the malondialdehyde level. To investigate whether chrysin contributes to suppressing nerve cell death from paclitaxel-induced toxicity and to determine the malondialdehyde level, LPO analysis was performed using paclitaxel+500 and 1000 μM chrysin vs 30 μM paclitaxel. While the MDA level in 30 μM paclitaxel-induced SH-SY5Y cells significantly increased ($p < 0.01$), chrysin pretreatment significantly reduced MDA levels compared to paclitaxel-induced SH-SY5Y cells ($p < 0.01$).

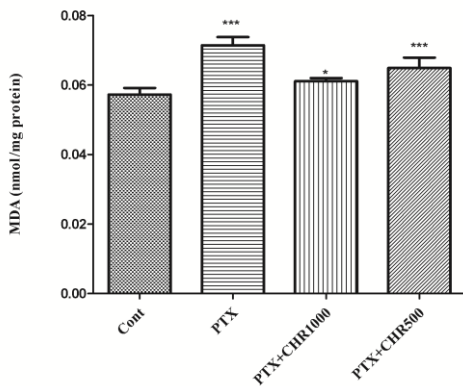


Figure 3. Measurement of MDA (malondialdehyde) released as a result of lipid peroxidation on the SH-SY5Y cell line induced by the simultaneous application of 30 μM paclitaxel, 30 μM paclitaxel + 500 and 1000 μM chrysin using the LPO Assay kit. *** $p < 0.001$ and * $p < 0.1$: statistically significant differences between cont and other groups, ns: nonsignificant

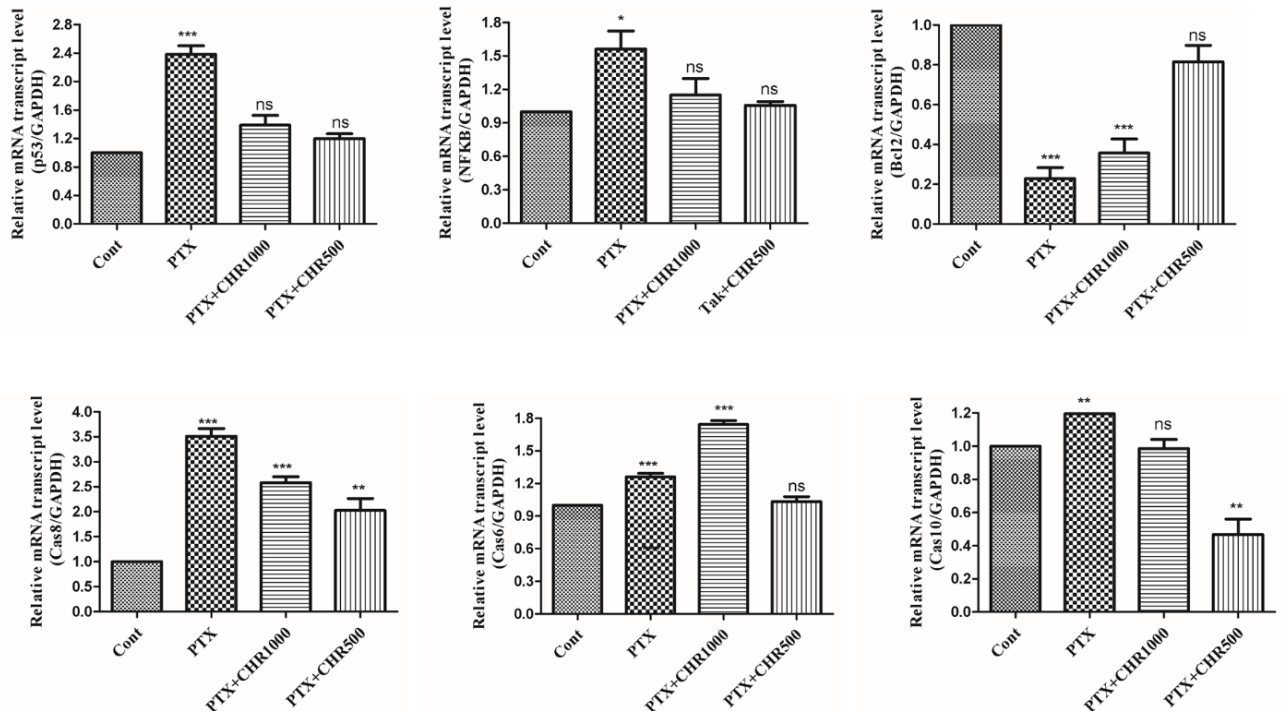


Figure 4. mRNA expression level of apoptotic and anti-apoptotic genes in SH-SY5Y cell line induced by 30 μM paclitaxel, 500 and 1000 μM chrysin. *** $p < 0.001$, ** $p < 0.01$ and * $p < 0.1$: statistically significant differences between cont and other groups, ns: nonsignificant

3.3. qRT-PCR Experiments

To test whether the mRNA transcript levels of anti-apoptotic and apoptotic genes were affected by paclitaxel and chrysin, the expression levels of Bcl-2, P53, Cas-6, Cas-8, Cas-10, and NFKB were measured by qRT-PCR. It was observed that the mRNA transcript levels of *p53*, *Cas-6*, *Cas-8*, *Cas-10* and *NFKB* were significantly increased after treatment with paclitaxel compared to the control, and the mRNA levels of *Bcl-2* were also significantly reduced (Figure 9). When chrysin and paclitaxel were administered together, it was observed that the mRNA transcript levels of *p53*, *Cas-6*, *Cas-8*, *Cas-10* and *NFKB* decreased compared to the paclitaxel-treated group, and the mRNA levels of *Bcl-2* increased significantly.

4. DISCUSSION

Paclitaxel is a chemotherapy drug widely used in the treatment of cancer. Chemotherapy drugs work by killing or preventing cancer cells from growing and multiplying [15]. However, cytotoxic drugs can act on healthy cells as well as cancer cells and cause some side effects. Many chemotherapeutic drugs can create oxidative stress in cells and lead to lipid peroxidation [16]. Paclitaxel may also be one of these mechanisms. When attacking cancer cells, chemotherapy drugs can cause peroxidation of lipids in cell membranes by increasing the formation of free radicals.

Lipid peroxidation is the process by which lipids (fats) in cells undergo oxidative damage. These reactions involve chain reactions initiated by highly reactive molecules called free radicals [17]. Free radicals affect cell membranes and intracellular components, causing a condition called oxidative stress. Lipid peroxidation is a process in which the lipids that make up the cell membrane, such as fatty acids, phospholipids and cholesterol, are targeted. Lipid hydroperoxides are formed by adding hydroxyl groups to these lipids under the influence of free radicals. Lipid hydroperoxides can disrupt the structural integrity of the cell membrane, deplete enzymatic and non-enzymatic antioxidant systems, and interact with other cellular components, leading to cell damage and cell death [18]. Lipid peroxidation is considered a marker of oxidative stress and plays an important role in many diseases. It may be especially effective in the development of cardiovascular diseases, diabetes, cancer, neurodegenerative diseases and other chronic diseases [19]. In response, the body has naturally developed antioxidant defense mechanisms against lipid peroxidation. Adopting a healthy lifestyle, a balanced diet and a diet enriched with antioxidants can play an important role in preventing lipid peroxidation. However, in some cases, especially in chronic diseases or cases of increased oxidative stress, supplements can be used to support a balanced antioxidant system. In a study conducted on experimental animals, it was reported that paclitaxel caused peripheral neuropathy by increasing lipid peroxidation [20]. Another study revealed that royal jelly, rich in antioxidant content, had a reducing effect on paclitaxel-induced lipid peroxidation in heart tissue [21]. In an experimental study conducted by Gür and his colleagues, it was reported that paclitaxel causes lipid peroxidation in liver cells and hesperidin minimizes this effect [22].

Paclitaxel has an effect that inhibits cell division and stops the growth of cancer cells. This effect prevents cancer cells from dividing and proliferating by interfering with the cell cycle [23]. However, paclitaxel also induces apoptosis [24]. Paclitaxel neutralizes structures called microtubules within the cell. Microtubules serve as the skeleton of the cell during cell division. By increasing the stability of these structures, paclitaxel prevents cell division from completing properly and leads to the death of cells [25]. It is known that cancer cells, in particular, divide and multiply faster than normal cells. Therefore, while paclitaxel works as

an effective treatment against the rapid division of cancer cells, it interferes less with the division of normal cells and reduces damage to healthy cells [26]. Paclitaxel's triggering of apoptosis enables cancer cells to enter the process of programmed cell death. Apoptosis is important to keep abnormal growth of cells and potentially cancerous tumours under control. Therefore, drugs that induce apoptosis, such as paclitaxel, may be an effective tool in cancer treatment. However, these drugs can also affect healthy cells and cause some side effects during treatment. Healthy cells may respond in different ways than cancer cells, which can lead to side effects. Paclitaxel can damage healthy cells and cause cells to die by apoptosis. In parallel with the data obtained in the thesis, it has been reported in previous studies that paclitaxel causes apoptosis in the sciatic nerve by increasing *caspase-3* and *Bax* levels and suppressing *Bcl-2* levels [27]. In another study, an increase in the mRNA transcript levels of *caspase-3*, *p53* and *Apaf-1* was observed in both the sciatic nerve and spinal cord after treatment with paclitaxel, while a decrease was observed in the mRNA transcript levels of *Bcl-2* and *Bcl-xL* [28]. Another study shows that chrysin application protects SH-SY5Y cells by reducing the expression of *Cas-3*, *Cyt c* and *Bax* in cyclophosphamide-induced SH-SY5Y cells and reducing the expression of the anti-apoptotic gene *Bcl-2* [6]. According to the results obtained in the study titled neuroprotective effects of chrysin on diclofenac-induced apoptosis in SH-SY5Y cells, chrysin reduces the expression of *Bax*, *cytochrome c*, *cas-3*, *cas-8* and *p53* and reduces the expression of the anti-apoptotic gene *Bcl-2*. It shows that it protects SH-SY5Y cells [29] further indicating that natural antioxidants have a slowing and even stopping effect on the course of cancer and can be applied as a combined treatment with chemotherapy [30,32]. The use of antioxidants as nutritional supplements, and chrysin in particular, reduces the apoptotic effects of paclitaxel in SH-SY5Y cells, which may add depth to therapeutic approaches to paclitaxel-induced cell injuries.

5. CONCLUSIONS

The purpose of this study was to examine the impact of different paclitaxel and chrysin concentrations on SH-SY5Y cell viability, MDA levels and mRNA transcript levels of some apoptotic and anti-apoptotic genes. In this study, the results showed that 15 and 30 μM paclitaxel reduced cell viability, and 500 and 1000 μM chrysin application reduced these effects. Chrysin treatment has been shown to considerably reduce MDA levels in paclitaxel-induced cells. The study also examined the effects of paclitaxel and chrysin application on apoptotic and antiapoptotic genes, and showed that chrysin significantly reduced the levels of *caspase 10*, *caspase 8*, *caspase 6*, *p53* and *NFKB*, and increased the *Bcl-2* level compared to the paclitaxel-treated group

REFERENCES

- [1] Zhao, S., Tang, Y., Wang, R., & Najafi, M. (2022). Mechanisms of cancer cell death induction by paclitaxel: an updated review. *Apoptosis*, 27(9-10), 647-667.
- [2] Sousa-Pimenta, M., Estevinho, L. M., Szopa, A., Basit, M., Khan, K., Armaghan, M., ... & Sharifi-Rad, J. (2023). Chemotherapeutic properties and side-effects associated with the clinical practice of terpene alkaloids: paclitaxel, docetaxel, and cabazitaxel. *Frontiers in Pharmacology*, 14, 1157306.
- [3] Panebianco, C., Pisati, F., Villani, A., Andolfo, A., Ulaszewska, M., Bellini, E., ... & Paziienza, V. (2023). Counteracting gemcitabine+ nab-paclitaxel induced dysbiosis in KRAS wild type and KRASG12D mutated pancreatic cancer *in vivo* model. *Cell Death Discovery*, 9(1), 116.
- [4] Cavalier, A.N., Clayton, Z., Wahl, D., Seals, D., & LaRocca, T. (2020). The Effects of Chemotherapeutic Agents and a Mitochondrial Antioxidant on the Brain Transcriptome and Cognitive Function. *The FASEB Journal*, 34(S1), 1-1.
- [5] Kikuchi, H., Yuan, B., Hu, X., ve Okazaki, M. (2019). Chemopreventive and anticancer activity of flavonoids and its possibility for clinical use by combining with conventional chemotherapeutic agents. *American Journal of Cancer Research*, 9(8), 1517.
- [6] Ayna, A., Özbolat, S.N., & Darendelioglu, E. (2020). Quercetin, chrysin, caffeic acid and ferulic acid ameliorate cyclophosphamide-induced toxicities in SH-SY5Y cells. *Molecular Biology Reports*, 47(11), 8535-8543.
- [7] Celik, Z.B., Cankara, F.N., & Gunaydin, C. (2020). Alterations in the matrix metalloproteinase-3 promoter methylation after common chemotherapeutics: *In vitro* study of paclitaxel, cisplatin and methotrexate in the MCF-7 and SH-SY5Y cell lines. *Molecular Biology Reports*, 47(11), 8987-8995.
- [8] Ayna, A. (2021). Caffeic acid prevents hydrogen peroxide-induced oxidative damage in SH-SY5Y cell line through mitigation of oxidative stress and apoptosis. *Bratislava Medical Journal/Bratislavske Lekarske Listy*, 122(2).
- [9] Shen, N., Wang, T., Gan, Q., Liu, S., Wang, L., & Jin, B. (2022). Plant flavonoids: Classification, distribution, biosynthesis, and antioxidant activity. *Food chemistry*, 383, 132531.
- [10] Panche, A. N., Diwan, A. D., & Chandra, S. R. (2016). Flavonoids: an overview. *Journal of nutritional science*, 5, e47.
- [11] Mani, R., & Natesan, V. (2018). Chrysin: Sources, beneficial pharmacological activities, and molecular mechanism of action. *Phytochemistry*, 145, 187-196.
- [12] Kucukler, S., Benzer, F., Yildirim, S., Gur, C., Kandemir, F. M., Bengu, A. S., ... & Dortbudak, M. B. (2021). Protective effects of chrysin against oxidative stress and inflammation induced by lead acetate in rat kidneys: a biochemical and histopathological approach. *Biological Trace Element Research*, 199(4), 1501-1514.
- [13] Özbolat, S. N., & Ayna, A. (2021). Chrysin suppresses HT-29 cell death induced by diclofenac through apoptosis and oxidative damage. *Nutrition and Cancer*, 73(8), 1419-1428.
- [14] Varışlı, B., Caglayan, C., Kandemir, F. M., Gür, C., Ayna, A., Genç, A., & Taysı, S. (2023). Chrysin mitigates diclofenac-induced hepatotoxicity by modulating oxidative stress, apoptosis, autophagy and endoplasmic reticulum stress in rats. *Molecular Biology Reports*, 50(1), 433-442.
- [15] Zhu, L., & Chen, L. (2019). Progress in research on paclitaxel and tumor immunotherapy. *Cellular & molecular biology letters*, 24, 1-11.
- [16] Saleh, E. A. M., Al-Dolaimy, F., Baymakov, S., Ullah, M. I., Khlewee, I. H., Bisht, Y. S., & Alsaalamy, A. H. (2023). Oxidative stress affects the beginning of the growth of cancer cells through a variety of routes. *Pathology-Research and Practice*, 154664.
- [17] Ursini, F., & Maiorino, M. (2020). Lipid peroxidation and ferroptosis: The role of GSH and GPx4. *Free Radical Biology and Medicine*, 152, 175-185.
- [18] Angelova, P. R., Esteras, N., & Abramov, A. Y. (2021). Mitochondria and lipid peroxidation in the mechanism of neurodegeneration: Finding ways for prevention. *Medicinal Research Reviews*, 41(2), 770-784.
- [19] Negre-Salvayre, A., Auge, N., Ayala, V., Basaga, H., Boada, J., Brenke, R., ... & Zarkovic, N. (2010). Pathological aspects of lipid peroxidation. *Free radical research*, 44(10), 1125-1171.
- [20] Zbârcea, C.E., Ciotu, I.C., Bild, V., Chiriță, C., Tănase, A. M., Șeremet, O.C., ...ve Negreș, S. (2017). Therapeutic potential of certain drug combinations on paclitaxel-induced peripheral neuropathy in rats. *Rom. J. Morphol. Embryol*, 58, 507-516.
- [21] Malekinejad, H., Ahsan, S., Delkosh-Kasmaie, F., Cheraghi, H., Rezaei-Golmisheh, A., ve Janbaz-Acyabar, H. (2016). Cardioprotective effect of royal jelly on paclitaxel-induced cardio-toxicity in rats. *Iranian journal of basic medical sciences*, 19(2), 221.
- [22] Gur, C., Kandemir, F.M., Caglayan, C., ve Satıcı, E. (2022). Chemopreventive effects of hesperidin against paclitaxel-induced hepatotoxicity and nephrotoxicity via amendment of Nrf2/HO-1 and caspase-3/Bax/Bcl-2 signaling pathways. *Chemico-Biological Interactions*, 365, 110073.
- [23] Pasquier, E., Honore, S., Pourroy, B., Jordan, M. A., Lehmann, M., Briand, C., & Braguer, D. (2005). Antiangiogenic concentrations of paclitaxel induce an increase in microtubule dynamics in endothelial cells but not in cancer cells. *Cancer Research*, 65(6), 2433-2440.
- [24] Wang, T. H., Wang, H. S., & Soong, Y. K. (2000). Paclitaxel-induced cell death: where the cell cycle and apoptosis come together. *Cancer:*

Interdisciplinary International Journal of the American Cancer Society, 88(11), 2619-2628

- [25] Horwitz, S. B., Cohen, D., Rao, S., Ringel, I., Shen, H. J., & Yang, C. P. (1993). Taxol: mechanisms of action and resistance. *Journal of the National Cancer Institute. Monographs*, 15, 55-61.
- [26] Sosa, V., Moliné, T., Somoza, R., Paciucci, R., Kondoh, H., & LLeonart, M. E. (2013). Oxidative stress and cancer: an overview. *Ageing research reviews*, 12(1), 376-390.
- [27] Semis, H.S., Kandemir, F. M., Kaynar, O., Dogan, T., Arıkan, S.M. (2021). The protective effects of hesperidin against paclitaxel-induced peripheral neuropathy in rats. *Life Sciences*, 287, 120104.
- [28] Yardım, A., Kandemir, F. M., Çomaklı, S., Özdemir, S., Caglayan, C., Kucukler, S., ve Çelik, H. (2021). Protective effects of curcumin against paclitaxel-induced spinal cord and sciatic nerve injuries in rats. *Neurochemical Research*, 46(2), 379-395.
- [29] Darendelioglu, E. (2020). Neuroprotective effects of chrysin on diclofenac-induced apoptosis in SH-SY5Y cells. *Neurochemical research*, 45(5), 1064-1071.
- [30] Temel, Y., Kucukler, S., Yıldırım, S., Caglayan, C., & Kandemir, F. M. (2020). Protective effect of chrysin on cyclophosphamide-induced hepatotoxicity and nephrotoxicity via the inhibition of oxidative stress, inflammation, and apoptosis. *Naunyn-Schmiedeberg's archives of pharmacology*, 393, 325-337.
- [31] Temel, Y., Çağlayan, C., Ahmed, B. M., Kandemir, F. M., & Çiftci, M. (2021). The effects of chrysin and naringin on cyclophosphamide-induced erythrocyte damage in rats: biochemical evaluation of some enzyme activities in vivo and in vitro. *Naunyn-Schmiedeberg's Archives of Pharmacology*, 394, 645-654.
- [32] Samarghandian, S., Farkhondeh, T., & Azimi-Nezhad, M. (2017). Protective effects of chrysin against drugs and toxic agents. *Dose-Response*, 15(2), 1559325817711782.

Energy-Efficient Lighting Design: An Investigation of Optimal Daylight Use in Different Window Models and Furniture Colors

Aylin DURAK^{1*} , Ahmet ÇİFCİ¹ 

¹ Burdur Mehmet Akif Ersoy University, Faculty of Engineering and Architecture, Department of Electrical-Electronics Engineering, Burdur, Türkiye

Aylin DURAK ORCID No: 0009-0002-6227-5870

Ahmet ÇİFCİ ORCID No: 0000-0001-7679-9945

*Corresponding author: adurak@mehmetakif.edu.tr

(Received: 17.05.2023, Accepted: 05.12.2023, Online Publication: 28.12.2023)

Keywords

Daylight factor,
Window size,
Velux daylight
visualizer,
Energy savings

Abstract: This study presents an investigation aimed at achieving energy savings in lighting by using the ideal window concept and other parameters to optimally benefit from daylight. The study has been applied under overcast sky and deep room conditions, which represent the worst-case scenarios. As an alternative to time-consuming mathematical calculations, the Velux Daylight Visualizer lighting simulation program was used to create three-dimensional designs for horizontal, vertical, square, and roof windows separately, and the effects of these windows on the daylight factor were analyzed. The impact of different furniture colors in the interior space was also examined. Following the investigations, it was observed that roof windows produced more daylight compared to others, with the average daylight factor value at 1.9%. However, since roof windows cannot be used in multi-story buildings, a comparison was made between horizontal, vertical, and square windows, and it was concluded that horizontal windows placed close to the upper wall were more efficient than the others, with the DF value recorded averagely at 1.7%. In addition, it was observed that lighter-colored furniture, among the light and dark furniture, produced more daylight compared to the other.

Enerji Verimli Aydınlatma Tasarımı: Farklı Pencere Modellerinde ve Mobilya Renklerinde Optimum Gün Işığı Kullanımı Üzerine Bir Araştırma

Anahtar Kelimeler

Gün ışığı
faktörü,
Pencere boyutu,
Velux daylight
visualizer,
Enerji tasarrufu

Öz: Bu çalışma, gün ışığından optimum seviyede faydalanmak için, ideal pencere kavramını ve diğer parametreleri kullanarak aydınlatmada enerji tasarrufu sağlamaya yönelik bir araştırma sunmaktadır. Çalışma en kötü durum senaryolarını temsil eden bulutlu gökyüzü ve derin oda koşulları altında uygulanmıştır. Zaman alıcı matematiksel hesaplamalara alternatif olan aydınlatma simülasyon programı Velux Daylight Visualizer ile yatay, dikey, kare ve çatı pencereleri için ayrı ayrı üç boyutlu tasarım yapıp, bu pencerelerin gün ışığı faktörüne etkileri analiz edilmiştir. Ayrıca iç ortamda bulunan farklı mobilya renklerinin etkisi de incelenmiştir. Yapılan incelemelerden sonra, çatı pencerelerinin diğerlerine kıyasla daha fazla gün ışığı ürettiği görülmüştür ve ortalama gün ışığı faktörü değerinin %1,9 olduğu görülmüştür. Fakat çatı pencereleri katlı binalarda kullanılamayacağından yatay, dikey ve kare pencereler arasında karşılaştırma yapılmış ve üst duvara yakın yerleştirilen yatay pencerelerin %1,7'lik ortalama gün ışığı faktörü ile diğerlerine göre daha verimli olduğu sonucuna ulaşılmıştır. Buna ek olarak, açık ve koyu olarak sınıyan mobilyalardan açık renkli olanların diğerine kıyasla daha çok gün ışığı ürettiği görülmüştür.

1. INTRODUCTION

In Türkiye, the use of renewable energy sources is increasing day by day to reduce dependence on foreign energy and meet energy needs in a clean and uninterrupted manner. Among renewable energy sources, the sun, which is the source of many types of energy found in nature, is considered a significant input. Today, all new technologies are based on solar energy, an unlimited, cost-free, and clean energy type. In this context, one of the areas benefiting from solar energy is natural lighting, also known as daylight. Daylight is the most effective primary light source for creating a visual environment and useful energy savings in buildings [1-4]. From the past to the present, it has been scientifically proven that daylight helps people become happier, calmer, healthier, and more productive. Additionally, using daylight in lighting reduces heat exchange between indoor and outdoor spaces to a minimum, which is important for energy savings in buildings [5]. The benefits of effective use of daylight can be categorized into two main groups: visual comfort and energy savings.

According to the European standard EN 12665, visual comfort is described as “a subjective condition of visual well-being induced by the visual environment” [6]. Visual comfort constitutes a crucial element in the design of daylighting systems. Daylight can provide natural lighting that is beneficial for health and well-being, but it can also cause discomfort glare if not properly managed [7, 8]. Several studies have investigated strategies to reduce discomfort glare from daylight [9]. Such strategies encompass the employment of shading mechanisms, innovative side and top daylighting systems, and electric lighting control systems. Modern transparent and/or translucent glazing can also be utilized to avoid glare and diffuse light to wider areas of floor space. Effective daylighting design should include top-lighting, side-lighting, electric lighting controls, and a building explicitly designed to maximize the advantages of daylight. Light shelves, surface colors and textures, ceiling height, and room dividers are some of the building features that can affect visual comfort in daylighting design.

Energy savings is the efficient use of energy without any reduction in production, comfort, or workforce. The rapid and unconscious consumption of our energy sources has led humanity to seek new energy-saving methods. Efficient lighting design and its effective use in buildings are important parameters for achieving energy savings. One of the most significant ways in which daylight can contribute to energy savings is through the use of natural lighting in buildings [10]. By designing buildings with large windows and skylights, it is possible to reduce the need for artificial lighting during the day. This can result in significant energy savings, as lighting accounts for a significant portion of a building’s energy consumption. Lighting constitutes one of the most significant electricity consumers in both the residential and commercial sectors. Globally, lighting accounts for approximately 20% to 30% of total

electricity consumption [11]. However, by transitioning to more energy-efficient lighting technologies, substantial energy savings can be achieved [12]. Trifunovic et al. [13] demonstrated that energy savings of up to 27% in residential and 30% in commercial sectors are possible through the adoption of energy-efficient lighting technologies. On the other hand, the use of large windows may lead to higher energy requirements for space heating due to the insulation properties of glass not being as effective as insulation materials in walls.

The design and placement of windows can significantly impact the amount of natural light that enters a building, which can have a profound effect on the well-being and health of its occupants [14]. Additionally, windows can also contribute to the energy efficiency of a building by reducing the need for artificial lighting and heating or cooling systems [15, 16]. To optimize the quality of daylight in a building, windows should be strategically placed to allow for maximum natural light penetration. The size and orientation of windows should be carefully considered to ensure that they provide adequate illumination while minimizing glare and heat gain. A well-designed window system can provide ample natural light while minimizing heat gain and loss, resulting in a more comfortable and energy-efficient indoor environment.

Several studies have been conducted about daylight, energy savings and window size, orientation and position. Hopkinson et al. [17] have developed a simple formula to calculate the indirect component of the daylight factor (DF). Additionally, they assumed that the total DF obtained by adding the direct and indirect components of daylight is an important factor in determining natural lighting in a room design.

To calculate the DF in an indoor space, Ibarra and Reinhart [18] preferred a classroom model in an L-shape with 69 students. The calculations were simulated using ECOTECH and RADIANCE programs and compared. According to the comparison, the data obtained from the ECOTECH program was found to be lower than that obtained from the RADIANCE program. It was considered more appropriate to use the RADIANCE program for daylight simulations in buildings.

Li [19] made predictions of daylight and energy savings under various sky conditions through mathematical calculations. As a result of the calculations, it was concluded that daylight-dependent lighting contributes significantly to energy efficiency. Vanhoutteghem et al. [20] investigated the impact of façade window design on energy consumption, daylighting, and thermal comfort in nearly zero-energy houses. The study evaluated the relationship between window size, orientation, and glazing properties for different room geometries using EnergyPlus and DAYSIM. The results showed that low U-values are needed in both north- and south-oriented rooms before large window areas lead to reductions in space heating demand.

Mushataha and Shadid [21] measured the indoor light levels with a lux meter to evaluate the daylight performance at the archaeological museum located in Kuwait, and simulated it using computer programs such as ECOTECH and REVIT. Based on the data obtained, they concluded that 45% energy savings could be achieved.

Mangkuto et al. [14] examined how different characteristics of window systems, including wall reflectance, window-to-wall ratio (WWR), and window orientation, influenced daylight metrics and electricity consumption for lighting purposes. Their research focused on an office room in a tropical climate and was among the first to show that the visual aspects of window systems can be included in an optimization process.

Dino and Üçoluk [22] created a tool for optimizing design in high-performance buildings, which they utilized to enhance energy efficiency and daylighting performance across various architectural layouts and building apertures. Fang and Cho [23] improved basic building shapes, as well as the dimensions and positioning of windows and skylights, to enhance energy efficiency and daylighting performance. By employing a genetic algorithm, they achieved an increase of over 28% in daylight performance and a reduction of more than 17% in energy usage across various climatic conditions.

De Gastines and Pattini [24] conducted simulations using the EnergyPlus program under Argentine climate conditions to determine the factors that are effective in energy savings in buildings. They considered window type and location, building geometry, and WWR as simulation parameters. Based on the data obtained, they have proven that the most energy-efficient windows are not the highly insulated ones but the ones with low total solar energy transmittance. They have also shown that adequate architectural design can provide significant energy savings by offering alternative strategies to high-performance window technologies.

This study aimed to achieve energy savings in lighting by utilizing the ideal window concept. The methodology was implemented under simulated conditions representing challenging scenarios with overcast skies and deep rooms. Ankara has been chosen as the location, and the building orientation is set to the north. The main contributions of this paper are as follows:

- To analyze the influence of different window types, including horizontal, vertical, square, and roof windows, the Velux Daylight Visualizer program was used to create three-dimensional designs for each window type separately.
- In addition, the existing literature focuses on increasing energy efficiency by considering factors such as window type, location, and building geometry. However, in this study, the impact of different window sizes on interior daylight is examined and specifically evaluated.

- The resulting DFs were analyzed to evaluate the impact of these window types.
- The study aims not only to contribute to energy savings by maximizing natural light indoors but also to enhance the quality of life by improving the natural lighting of the interior space.
- Furthermore, the study examined how various furniture colors affect the interior space.

The paper is structured as follows: In Section 2, a brief overview is given regarding the Velux Daylight Visualizer simulation software and daylight. In Section 3, results are provided and analyzed. Finally, we end the paper with the discussion and conclusions.

2. MATERIAL AND METHOD

In order to apply the optimal window design, a room with a length of 8 meters, a width of 4 meters, and a height of 3 meters was selected for the study. To observe the impact of window size on daylight distribution in the interior space, window models of five different sizes with an area of 2.5 m² were considered. The Velux Daylight Visualizer program was used to determine the daylight factor in the room and analyze it for different positions and sizes of windows. The Velux Daylight Visualizer program is designed for natural lighting design and allows for the modeling of three-dimensional spaces and the design of openings such as windows. It also provides a visual output of brightness and glare values, as well as DF values, for all relevant designers [25]. Numerous investigations have verified the proper functioning of this computational tool [26, 27], confirming its precision by implementing the CIE (Commission International de l'Eclairage) test cases [28]. At present, several studies focused on daylighting employ this simulation program [29-32].

2.1. Velux Daylight Visualizer

Velux Daylight Visualizer is a useful program for determining the orientation and lighting levels of buildings [33]. As the name suggests, the program carries out daylight studies that have been developed and verified according to CIE test cases [26]. The simulation software offers the ability to select sky conditions (overcast and clear skies), location, interior furnishings, and various window models. As shown in Figure 1 and Figure 2, windows of different sizes and features are available within the program.

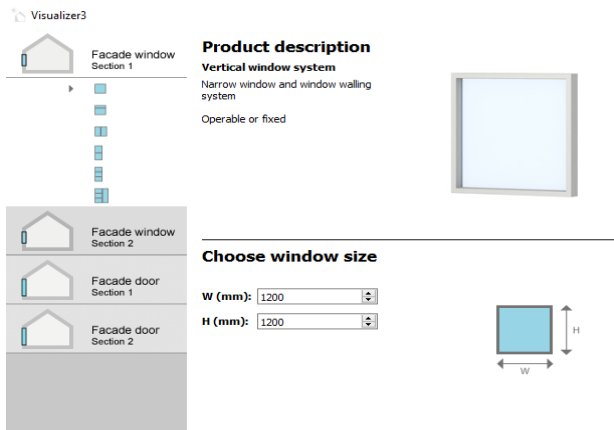


Figure 1. Facade windows in Velux Daylight Visualizer

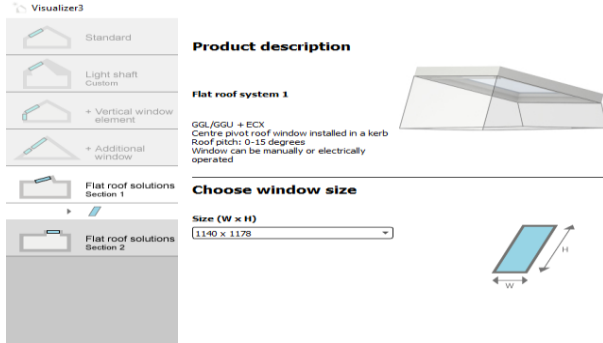


Figure 2. Flat roof windows in Velux Daylight Visualizer

Additionally, the selection of location and various sky conditions (overcast, intermediate, and sunny) is possible (Figure 3).



Figure 3. Selection of location and sky conditions in Velux Daylight Visualizer

The DF is directly proportional to the illumination rate of the space. Spaces with the highest degree of illumination are represented in red, while the amount of illumination decreases towards blue [34]. Figure 4 shows the DF color indicators.

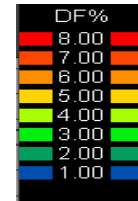


Figure 4. DF color indicators

2.2. Natural Lighting (Daylight)

Natural light has always been the ideal choice for humans, as our eyes naturally adapt to this source of illumination. Taking daylight into consideration in a building provides significant psychological benefits to its occupants. Additionally, it can increase efficiency in the space by reducing the burden of artificial lighting requirements.

The DF is commonly used to measure the amount of natural light in a space, as it illustrates the potential of natural light under unfavorable conditions, such as an overcast sky. The DF is expressed as a percentage and is defined as the ratio of horizontal indoor to outdoor illumination by daylight, assuming constant overcast sky conditions. If the DF is 3%, it means that the illumination present at that point within the building is 3% of the overall external horizontal illumination that has been scattered [35]. The equation (1) below demonstrates how to determine DF from illuminance levels [36].

$$DF = \left(\frac{E_i}{E_o} \right) \times 100 \quad (1)$$

where

E_i = illuminance level inside the space

E_o = illuminance level outside the space

The illuminance at a point inside a building can be divided into three components [37, 38]:

1. Sky Component (SC): This is the direct light coming from a visible portion of the sky at the specific point being considered.
2. Externally Reflected Component (ERC): This refers to the light that is reflected off external surfaces before reaching the point in question.
3. Internally Reflected Component (IRC): This component accounts for the light that reflects off interior surfaces before arriving at the considered point.

Each of these three components is computed separately, and the DF is derived from the sum of these values. Figure 5 shows three components of daylight that contribute to the illuminance on a work plane in a room.

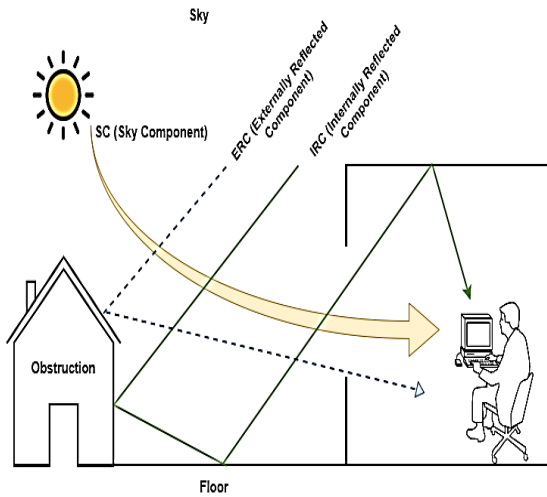


Figure 5. Components of daylight that add to the illuminance at a point within a room As indicated in Table 1, there is inadequate illumination in the environment when the DF value goes below 2%. If it exceeds 5%, there is too much illumination, which causes glare. Glare is recognized as a significant issue in ensuring visual comfort [39]. Ideally, DF should be between 2% and 5%.

Table 1. DF values and their meanings

DF	
Inadequate	● DF < 2%
Optimal	● 2% < DF < 5%
Glare	● DF > 5%



Figure 6. Components of view-roof window and view-facade window situations [40]

2.2.2. Window size and features

One of the primary purposes of using windows is to allow daylight to enter the building; therefore, the design of their dimensions and location directly affects natural lighting design [41]. Appropriately selected windows in terms of size, features, and location increase the amount of energy savings within the building and minimize glare problems that may occur in the interior environment. Window systems play a significant role in heat exchange processes and managing solar energy gains. For this reason, the energy efficiency factor should be considered during the design phase.

To achieve energy savings and visual comfort conditions in lighting, a comprehensive and efficient approach to daylight design is required without compromising illumination quality. Therefore, it is recommended to start by addressing certain design criteria for daylighting. These design criteria are as follows:

- Building design
- Window size and features
- Sky conditions

2.2.1. Building design

In building designs, aesthetic value is often taken into consideration. Alongside the exterior appearance of the building, the distribution of daylight in the interior environment is an important input during the design phase. This is because correctly designed daylight in buildings provides dynamic areas that promote an individual’s visual comfort and actions while also reducing the building’s energy consumption.

External obstructions and reflections (buildings, trees, ground surfaces, etc.) in the surrounding environment greatly affect the amount of natural light reaching the interior. In an effective architectural design, buildings should be positioned so as not to obstruct the intake of daylight into the interior. In accordance with this goal, skylights, as illustrated in Figure 6, are less impacted by surrounding obstructions and provide a larger view of the sky than facade windows [40].

2.2.3. Sky conditions

CIE has mathematically defined 15 general sky conditions [41]. Among these sky conditions, CIE clear sky and CIE overcast sky are two widely used sky models in lighting design and are shown in Figure 7. These sky models are used to determine the amount of natural light that enters a building and to evaluate the lighting system’s energy performance.

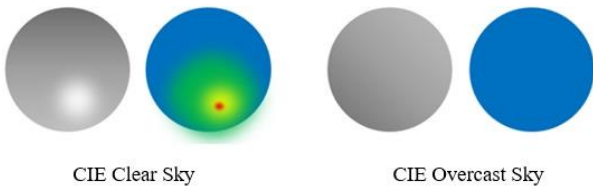


Figure 7. CIE standard clear sky and overcast sky [42]

CIE clear sky represents a cloudless sky with no atmospheric disturbances [43]. This model assumes that the sun is at an altitude greater than 5° and that the brightness of the sky is uniform in all directions. The CIE clear sky model is commonly used to evaluate the amount of direct and diffuse solar radiation that enters a building, as well as the distribution of sunlight throughout the day.

On the other hand, CIE overcast sky represents a cloudy sky with uniform cloud cover. This model assumes that the sun is completely covered by clouds and that the brightness of the sky is uniform in all directions. The CIE overcast sky model is used to evaluate the amount of diffuse radiation that enters a building on cloudy days [44].

3. RESULTS

In the first model, a vertical window model with a width of 1.25 meters, a height of 2 meters, and positioned 50 cm above the floor was chosen. Figure 8 illustrates the results for the vertical window model. Due to the smaller glass surface of vertical windows compared to other window models, the DFs produced at the side points were correspondingly lower. The DF value near the window was measured to be an average of 0.8%. Additionally, it was observed that the daylight distribution was not uniform.

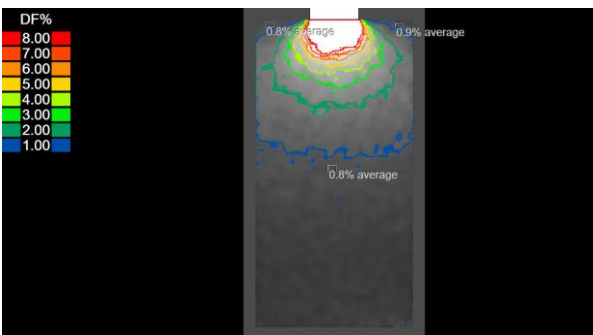


Figure 8. DF for the vertical window model

In the second model, the square window model with a width and length of 1.58 meters was tested. Figure 9 shows the results for the square window model. In this model, the average DF value was measured as 1.1% at the side sections, indicating insufficient transmission of light to the deeper parts of the room.

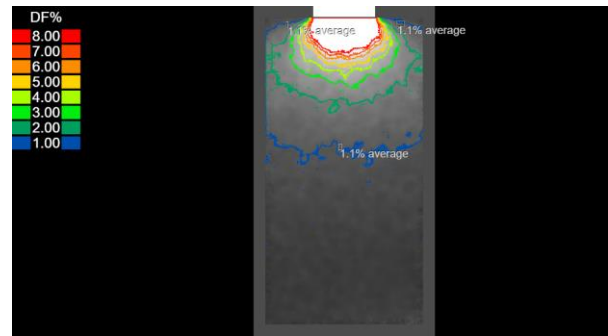


Figure 9. DF for the square window model

In the third model, the horizontal window model with a width of 1.25 meters and a length of 2 meters was selected. Figure 10 depicts the results for the horizontal window model. When compared to the square window model, which is the most similar in terms of shape, the horizontal window model is weaker at transmitting sufficient daylight to the extremities of the room. The average DF value near the window was calculated as 1.7%. Therefore, horizontal windows provide more daylight to a wider area near the window compared to square windows, but as you move away from the window, the amount of sunlight in the middle areas of the room decreases.

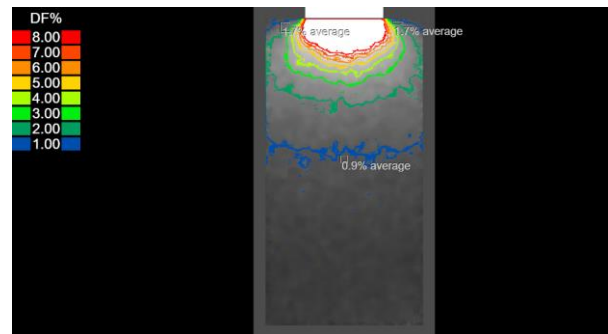


Figure 10. DF for the horizontal window model

The fourth model is the horizontal roof window model, with a width of 1.34 meters and a length of 1.6 meters. Figure 11 illustrates the results for the roof window model. The average DF value was calculated at 1.9%. When compared to the other three windows, it is evident that daylight is distributed more uniformly in the roof window model.

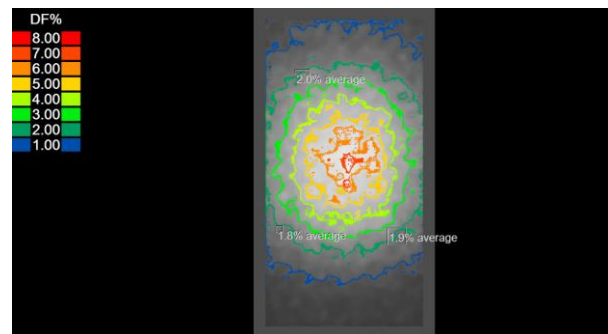


Figure 11. DF for the roof window model

As the fifth and final model, the horizontal window model with a width of 1 meter and a length of 2.5 meters is positioned close to the ceiling at a height of 1.8 meters

from the floor. Figure 12 shows the results for the horizontal window model positioned close to the ceiling. There were no daylight factor values of 5% or higher, indicating glare issues. It also proved to be much more effective in transmitting light to the centre points of the room compared to other window models.

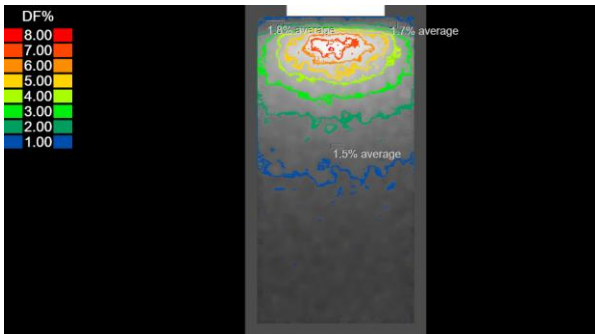


Figure 12. DF for the horizontal window model positioned close to the ceiling

The objects in the indoor environment also have specific reflection values. These values significantly affect daylight performance. In Figure 13, the impact of light and dark-colored furniture on the daylight factor in the interior environment is observed in the system created with the Velux Daylight Visualizer Program under the same room condition and window type, with the dimensions of length and height of 1.2 meters and 2 meters, respectively. Light-colored furniture reflected more light into the indoor environment compared to dark-colored furniture, with an average DF value of 2%.

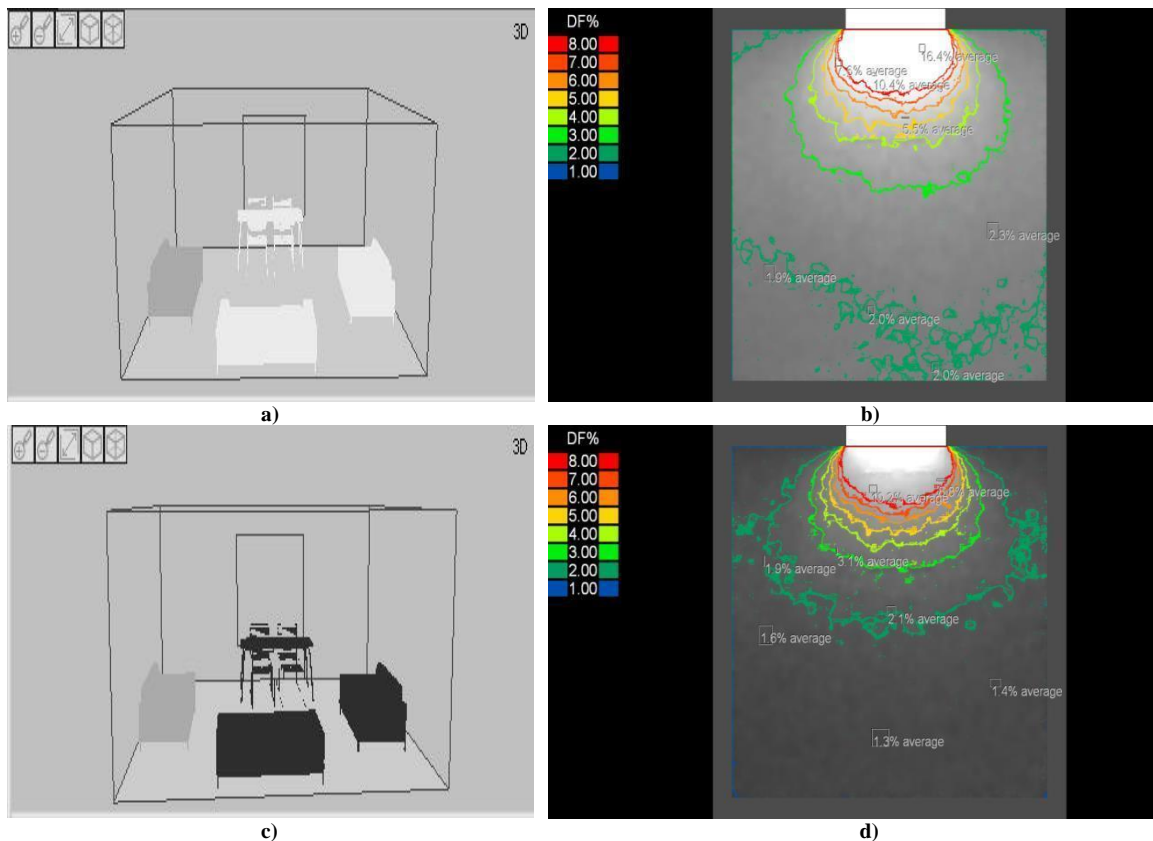


Figure 13. a) Three-dimensional design of white-gray furniture b) DF in the interior space with white-gray furniture with the window type of vertical c) Three-dimensional design of black-gray furniture d) DF in the interior space with black-gray furniture with the window type of vertical

4. DISCUSSION AND CONCLUSION

This study investigated the concept of an ideal window for maximizing daylight utilization in indoor environments and the parameters affecting the distribution of daylight indoors. To reduce costs associated with artificial lighting, the impact of different window sizes was analyzed using the computer simulation software Velux Daylight Visualizer.

The literature usually says that the optimal DF values are between 2% and 5%. However, the values found in this study are not exactly in that range because they were

calculated in difficult conditions like deep rooms and overcast skies. Vertical windows have shown very poor performance in distributing daylight homogeneously. The small glass surfaces (1.25 meters) of these windows have been particularly insufficient in delivering light to the lateral axes. Horizontal windows exhibit a similar trend to the square window model in transmitting daylight to nearby points. The daylight factor is high near the window, but light transmission decreases as the distance increases. However, horizontal windows contribute significantly to energy savings by allowing more light into the interior due to their width, with the DF level at 1.7%. Square windows have shown a more

homogeneous distribution compared to vertical and horizontal windows. Although they produce similar results to horizontal windows at close points, it has been observed that they are better at transmitting light to the middle points of the room compared to horizontal windows, by the DF level of 1.1% at the middle point. Roof windows have produced the most ideal light distribution compared to all other window models. However, since they can only be used in attics, more emphasis has been placed on the other three window models. Horizontal windows placed in the upper position have been more effective in delivering light to the far ends of the room. Being in the upper position has prevented potential glare problems near the window. In addition, since it allows more light into the interior with the DF level at 1.5%, its contribution to energy savings has come to the forefront. In conclusion, the horizontal window model placed in the upper position of the wall will greatly contribute to energy savings by reducing the need for artificial lighting. Under challenging conditions, there may be a decrease in overall light levels, which can impact the performance of window models. In these conditions, it has been observed that horizontal windows contribute more to achieving a homogeneous distribution by allowing more light to enter due to their widths. However, optimal DF values have not been reached.

The light-colored furniture used in the study has contributed to a broader distribution of daylight in the indoor environment by enhancing the reflection of natural light. Light colors can increase the overall light level in the interior by reflecting light rather than absorbing it. On the other hand, dark-colored furniture tends to absorb light and reflect less. This can result in the creation of more shaded areas in areas where furniture is present, making the room darker. In fact, in environments where white furniture is used, an average DF value of 2% is obtained, whereas with dark furniture, this value is determined to be 1.5%.

REFERENCES

- [1] Li DHW, Tsang EKW. An analysis of daylighting performance for office buildings in Hong Kong. *Build Environ.* 2008 Sep 1;43(9):1446–58.
- [2] Kwong QJ. Light level, visual comfort and lighting energy savings potential in a green-certified high-rise building. *Journal of Building Engineering.* 2020 May 1;29:101198.
- [3] Wagiman KR, Abdullah MN, Hassan MY, Mohammad Radzi NH. A new metric for optimal visual comfort and energy efficiency of building lighting system considering daylight using multi-objective particle swarm optimization. *Journal of Building Engineering.* 2021 Nov 1;43:102525.
- [4] Scorpio M, Ciampi G, Gentile N, Sibilio S. Effectiveness of low-cost non-invasive solutions for daylight and electric lighting integration to improve energy efficiency in historical buildings. *Energy and Buildings.* 2022 Sep 1;270:112281.
- [5] Tekbıyık G. Sürdürülebilir mimarlıkta yenilenebilir enerji kaynaklarının kullanımı, kamu binalarında uygulama yöntemleri ve örneklerinin incelenmesi [dissertation]. İstanbul: Fatih Sultan Mehmet Vakıf Üniversitesi; 2018.
- [6] ECS. European committee for standardization; Brussels: 2002. Light and lighting - Basic terms and criteria for specifying lighting requirements (Vol. EN 12665).
- [7] Wilder R, Mukhopadhyay J, Femrite T, Amende K. Evaluating Glare in Leed Certified Buildings To Inform Criteria For Daylighting Credits. *Journal of Green Building.* 2019 Sep 1;14(4):57–76.
- [8] Fakhari M, Fayaz R, Lollini R. The Impact of Evaluated Daylight to the Total Light Ratio on the Comfort Level in Office Buildings. *Buildings.* 2022 Dec;12(12):2161.
- [9] Amirkhani M, Garcia-Hansen V, Isoardi G, Allan A. An Energy Efficient Lighting Design Strategy to Enhance Visual Comfort in Offices with Windows. *Energies.* 2017 Aug;10(8):1126.
- [10] Pilechiha P, Mahdavinejad M, Pour Rahimian F, Carnemolla P, Seyedzadeh S. Multi-objective optimisation framework for designing office windows: quality of view, daylight and energy efficiency. *Applied Energy.* 2020 Mar 1;261:114356.
- [11] Soori PK, Vishwas M. Lighting control strategy for energy efficient office lighting system design. *Energy and Buildings.* 2013 Nov 1;66:329–37.
- [12] Ganandran GSB, Mahlia TMI, Ong HC, Rismanchi B, Chong WT. Cost-Benefit Analysis and Emission Reduction of Energy Efficient Lighting at the Universiti Tenaga Nasional. *ScientificWorldJournal.* 2014;2014:745894.
- [13] Trifunovic J, Mikulovic J, Djuricic Z, Djuric M, Kostic M. Reductions in electricity consumption and power demand in case of the mass use of compact fluorescent lamps. *Energy.* 2009 Sep 1;34(9):1355–63.
- [14] Mangkuto RA, Rohmah M, Asri AD. Design optimisation for window size, orientation, and wall reflectance with regard to various daylight metrics and lighting energy demand: A case study of buildings in the tropics. *Applied Energy.* 2016 Feb 15;164:211–9.
- [15] Hammad F, Abu-Hijleh B. The energy savings potential of using dynamic external louvers in an office building. *Energy and Buildings.* 2010 Oct 1;42(10):1888–95.
- [16] Chow SKH, Li DHW, Lee EWM, Lam JC. Analysis and prediction of daylighting and energy performance in atrium spaces using daylight-linked lighting controls. *Applied Energy.* 2013 Dec 1;112:1016–24.
- [17] Hopkinson RG, Longmore J, Petherbridge P. An Empirical Formula for the Computation of the Indirect Component of Daylight Factor. *Trans Illum Eng Soc.* 1954 Jul 1;19(7_IESTrans):201–19.
- [18] Ibarra D, Reinhart CF. Daylight factor simulations—how close do simulation beginners ‘really’ get. *Building Simulation.* 2009;196:196–203.

- [19] Li DHW. A review of daylight illuminance determinations and energy implications. *Appl Energy*. 2010 Jul 1;87(7):2109–18.
- [20] Vanhoutteghem L, Skarning GCJ, Hviid CA, Svendsen S. Impact of façade window design on energy, daylighting and thermal comfort in nearly zero-energy houses. *Energy and Buildings*. 2015 Sep 1;102:149–56.
- [21] Mushtaha ES, Shadid R. Evaluating daylight performance of Sharjah archaeology museum in UAE with a reference of Kuwait national museum. *J. Civil Eng. Urban*. 2015;5: 265-271.
- [22] Dino IG, Üçoluk G. Multiobjective Design Optimization of Building Space Layout, Energy, and Daylighting Performance. *J Comput Civ Eng*. 2017 Sep 1;31(5):04017025.
- [23] Fang Y, Cho S. Design optimization of building geometry and fenestration for daylighting and energy performance. *Solar Energy*. 2019 Oct 1;191:7–18.
- [24] De Gastines M, Pattini AE. Window energy efficiency in Argentina - Determining factors and energy savings strategies. *J Clean Prod*. 2020 Feb 20;247:119104.
- [25] Kazanasmaz ZT. Binaların doğal aydınlatma performanslarının değerlendirilmesi. V. Ulusal Aydınlatma Sempozyumu ve Sergisi, İzmir; 2009.
- [26] Labayrade R, Jensen HW, Jensen C. Validation of Velux Daylight Visualizer 2 against CIE 171: 2006 test cases. 11th International IBPSA Conference, International Building Performance Simulation Association. Glasgow; 2009. p. 1506-13.
- [27] Labayrade R, Fontoynt M, Mouret C, Avouac P, Jean MC. Assessment of Velux Daylight Visualizer 2 against CIE 171: 2006 test cases. *Ecole Nationale Des Travaux Publics de l'Etat*; 2009.
- [28] CIE. Test cases to assess the accuracy of lighting computer programs, Commission Internationale de l'Éclairage, 2006.
- [29] Kousalyadevi G, Lavanya G. Optimal investigation of daylighting and energy efficiency in industrial building using energy-efficient velux daylighting simulation. *Journal of Asian Architecture and Building Engineering*. 2019 Jul 4;18(4):271–84.
- [30] Lapisa R, Karudin A, Martias M, Krismadinata K, Ambiyar A, Romani Z, et al. Effect of skylight–roof ratio on warehouse building energy balance and thermal–visual comfort in hot-humid climate area. *Asian J Civ Eng*. 2020 Jul 1;21(5):915–23.
- [31] Dolnikova E, Katunsky D, Vertal M, Zozulak M. Influence of Roof Windows Area Changes on the Classroom Indoor Climate in the Attic Space: A Case Study. *Sustainability*. 2020 Jan;12(12):5046.
- [32] Dev G, Saifudeen A. Dynamic facade control systems for optimal daylighting, a case of Kerala. *Sustainability Analytics and Modeling*. 2023 Jan 1;3:100018.
- [33] Vishwas M, Soori PK. Simple Tool for Energy Analysis of Day Lighting and Artificial Lighting for a Typical Office Building Lighting System Design. *Int J Energy Eng*. 2012;2(6):332–8.
- [34] Akatli G, Sağıroğlu Ö. Kutsal Mekanlarda Doğal Işık Tasarımının Etimesgut Cami ve Işık Kilisesi Örnekleri Üzerinden İncelenmesi. *Mimar Ve Yaşam*. 2022 Apr 30;7(1):359–82.
- [35] Simm S, Coley D. The relationship between wall reflectance and daylight factor in real rooms. *Architectural Science Review*. 2011 Nov 1;54:329–34.
- [36] Baker N, Steemers K. *Daylight design of buildings*. London: James & James; 2002. 250 p.
- [37] Ghisi E, Tinker JA. An Ideal Window Area concept for energy efficient integration of daylight and artificial light in buildings. *Building and Environment*. 2005 Jan 1;40(1):51–61.
- [38] Rizal Y, Robandi I, Yuniarno EM. Daylight Factor Estimation Based on Data Sampling Using Distance Weighting. *Energy Procedia*. 2016 Nov 1;100:54–64.
- [39] Iesna LH. *Lighting handbook, reference and application volume*. New York: Illuminating Engineering Society of North America. 45-64; 2000.
- [40] VELUX. Velux Daylight Visualizer;2023 [Internet]. [cited 2023 Feb 30]. Available from: <https://www.velux.com/what-we-do/research-and-knowledge/deic-basic-book/daylight/parameters-influencing-daylighting-performance>
- [41] Phillips D. *Daylighting: natural light in architecture*. Oxford: Architectural Press; 2004. 212 p.
- [42] Uetani Y, Aydinli S, Joukoff A, Kendrick JD, Kittler R, Koga, Y. *Spatial Distribution of Daylight–CIE Standard General Sky*. Vienna, Austria; 2003.
- [43] Kensek K, Suk JY. Daylight factor (overcast sky) versus daylight availability (clear sky) in computer-based daylighting simulations. *Journal of Creative Sustainable Architecture & Built Environment*. 2011;1:3-14.
- [44] Henriques GC, Duarte JP, Leal V. Strategies to control daylight in a responsive skylight system. *Automation in Construction*. 2012 Dec 1;28:91–105.
- [45] Li DHW, Lau CCS, Lam JC. Evaluation of overcast-sky luminance models against measured Hong Kong data. *Applied Energy*. 2001 Dec 1;70(4):321–31.

A Study On The Relationship Between Severity Of Clinical Findings And Serum IL-6 Level In Neonatal Calves With Diarrhoea

Gürsel AYDIN¹ , Mustafa Sinan AKTAŞ^{2*} 

¹ Atatürk University, Graduate School of Health Sciences, Veterinary Internal Medicine Department, Erzurum, Türkiye

² Atatürk University, Veterinary Faculty, Internal Medicine Department, Erzurum, Türkiye

Gürsel AYDIN ORCID No: 0000-0002-0912-3352

Mustafa Sinan AKTAŞ ORCID No: 0000-0002-7206-5757

*Corresponding author: sinanaktas@atauni.edu.tr

(Received: 15.08.2023, Accepted: 06.12.2023, Online Publication: 28.12.2023)

Keywords
Diarrhea,
IL-6,
Neonatal
calves

Abstract: The aim of the study is to investigate the relationship between clinical course and serum IL-6 level in neonatal calves with diarrhea. The study material consisted of 40 calves in the neonatal period. The calves were divided into 4 groups: group I (healthy, control, n=10), group II (with mild diarrhea, n=10), group III (with moderate diarrhea, n=10) and group IV (with severe diarrhea, n=10). The breed, age, sex and clinical findings of the calves were recorded. Etiological analysis was performed on stool samples taken from calves. Haematological analyzes were performed on the blood samples taken and serum IL-6 levels were determined using the ELISA test kit. WBC and NEU numbers of calves with diarrhea in group II, group III and group IV were found to be numerically higher than healthy calves in group I ($P>0.05$). Calves in group II (239.76 ± 11.05), group III (293 ± 48.7) and group IV (300 ± 25.06) had higher serum IL-6 levels than calves in group I (211.58 ± 10.07) ($P<0.01$). While IL-6 levels of group IV were higher than group III ($P>0.05$), IL-6 levels of group III and IV were higher than group II ($P<0.01$). According to the data obtained from this study, it was concluded that serum IL-6 is a significant biomarker indicating the degree of clinical severity.

Neonatal Dönem İshalli Buzağlarda Klinik Bulguların Şiddeti İle Serum IL-6 Düzeyi Arasındaki İlişki Üzerine Bir Araştırma

Anahtar Kelimeler
IL-6,
İshal,
Neonatal
buzağı

Öz: Bu çalışmanın amacı, neonatal dönem ishalleri buzağlarda klinik seyir ile serum IL-6 düzeyi arasındaki ilişkiyi araştırmaktır. Çalışma materyalini neonatal dönemdeki 40 buzağı oluşturdu. Buzağlar grup I (sağlıklı, kontrol, n=10), grup II (hafif ishalleri, n=10), grup III (orta şiddette ishalleri, n=10) ve grup IV (şiddetli ishalleri, n=10) olmak üzere 4 gruba ayrıldı. Buzağların ırk, yaş ve cinsiyet bilgileri ile klinik bulguları kaydedildi. Buzağlardan alınan dışkı örneklerinde etiyolojik analiz yapıldı. Alınan kan örneklerinde hematolojik analizler yapıldı ve serumda IL-6 düzeyleri, ELISA test kiti kullanılarak belirlendi. Grup II, grup III ve grup IV'deki ishalleri buzağlarda WBC ve NEU sayıları grup I'deki sağlıklı buzağlara göre rakamsal olarak yüksek olduğu belirlendi ($P>0.05$). Grup II (239.76 ± 11.05 ng/L), grup III (293 ± 48.7 ng/L) ve grup IV'de (300 ± 25.06 ng/L) bulunan buzağların serum IL-6 düzeyleri grup I'deki (211.58 ± 10.07 ng/L) buzağlara göre daha yüksek olduğu belirlendi ($P<0.01$). Grup IV'ün IL-6 düzeyi grup III'e göre rakamsal olarak yüksekken ($P>0.05$), grup III ve IV'ün IL-6 düzeyleri, grup II'ye göre yüksek olduğu belirlendi ($P<0.01$). Bu çalışmadan elde edilen verilere göre, neonatal dönem ishalleri buzağlarda serum IL-6'nın hastalığın klinik şiddetinin derecesini gösteren önemli bir belirteç olduğu sonucuna varılmıştır.

1. INTRODUCTION

Diarrhea, pneumonia (especially aspiration pneumonia), joint diseases, umbilical cord diseases, vitamin, mineral substance and trace element deficiencies, trauma, congenital anomalies, and nutritional disorders are common neonatal period diseases in calves, and among these diseases, neonatal calf diarrhea is the most common disease throughout the world [1,2,3].

Coronavirus, *Rotavirus*, *Cryptosporidium*, *Clostridium perfringens* (*Cl. perfringens*) and *Escherichia coli* (*E. coli*) are the most common causes of diarrhea in neonatal calves, and they can cause inflammatory and functional damage in the intestine [4,5,6]. The clinical signs observed in diarrhea formed in calves during the neonatal period are very variable and may show a course ranging from mild watery diarrhea to coma from a lying position according as the severity of diarrhea and inflammation [6]. In addition, neonatal calf diarrhea can cause significant changes in haematological parameters such as total leukocytes (WBC), lymphocytes (LYM), neutrophils counts (NEU) and hematocrit concentration (HCT) [7,8].

Interleukins, especially Interleukin-6 (IL-6), are used as an important marker in determining early inflammation and prognosis in various diseases [9]. IL-6 is a cytokine produced in response to tissue damage and infections [10]. Multiple cell types are associated with the production of this cytokine, including fibroblasts, keratinocytes, mesangial cells, vascular endothelial cells, mast cells, macrophages, dendritic cells, T and B cells [11]. The biological consequences of IL-6 production have been associated with both pro- and anti-inflammatory effects [12].

There are few studies evaluating the diagnostic and prognostic potential of IL-6 in cattle [13,14,15]. In neonatal diarrheal calves, on the other hand, IL-6 levels were investigated in methodically different studies such as the comparison of those with diarrhea and healthy ones, and those who recovered and those who did not recover in calves with diarrhea and septicemia [16,17]. Based on the hypothesis of the relationship between the severity of the disease and inflammation, in the presented study, it was aimed to investigate the relationship between clinical course and serum IL-6 level in neonatal calves with diarrhea.

2. MATERIAL AND METHOD

2.1. Animals and Groups

In the study different ages, breeds and sexes 10 healthy and 30 untreated diarrheic neonatal calves were used (Ethics Committee Decision No: 2020-13/191). Clinical findings [body temperature (T, C°), respiration rates (R, num/min), and pulse rates (P, beats/min)], dehydration status, sucking reflexes, and whether they could stand or not of the calves were recorded. Neonatal calves had a

problem other than diarrhea (pneumonia, arthritis, omphalitis, etc.) were not included in the study.

The study population was comprised of 40 neonatal calves, 10 of which had healthy (Group-I) and 30 of which were diarrheic calves, additionally diarrheic calves were divided into three groups as mild (Group-II), moderate (Group-III) and severe (Group-IV) according to the criteria for clinical dehydration and depression [18].

Group-I (Control, n=10): This group consisted of different breeds and sexes, 8.3±4.3 days old, who were healthy calves according to clinical and haematological findings.

Group-II (n=10): This group consisted of different breeds and sexes, 7.9±5.6 days old, and mild diarrheic calves with a clinical score of 1 according to the criteria were given in Table-1.

Group-III (n=10): This group consisted of different breeds and sexes, 7±5 days old, and moderate diarrheic calves with a clinical score of 4 according to the criteria were given in Table-1.

Group-IV (n=10): This group consisted of different breeds and sexes, 7.3±4 days old, and severe diarrheic calves with a clinical score of 7 according to the criteria were given in Table-1.

Table-1: Clinical scoring in neonatal calves with diarrhea [18].

Eyeball retraction	0: Not crashed
	1: Mild crashed
	2: Severe crashed
Skin elasticity	0: Back to normal immediately
	1: Back to normal after 1-3 seconds
	2: Back to normal after ≥4 seconds
Sucking reflex	0: Strong regular suction
	1: Poor ineffective suction
	2: No sucking reflex
Stool consistency score	1: Watery
	2: Pasteus
	3: Solid

2.2. Collections of Samples

Blood samples from all calves were taken from V. Jugularis and transferred into 4 mL tubes with EDTA (Becton Dickinson Co, USA) and 10 mL tubes with gel (BD Vacutainer System, Plymouth, UK). Thereafter serum was obtained by centrifugation at 3000 rpm for 10 minutes. The serum samples were stored at -80 °C until analysis (maximum 3 months) Haematological analysis were performed immediately. Additionally fecal samples were taken into sterile fecal containers by rectal stimulation.

2.3. Diagnosis of Etiologic Agents

Diagnosis of etiologic agents (*Rotavirus*, *Coronavirus*, *Cryptosporidium*, *Cl. perfringens* and *E. coli*/F5-K99) in fecal samples were made using rapid diagnosis test kit (Rainbow Calf Scours-BIO K 306 Ag Test Kit, Biox Diagnostics, Belgium). The use of this kit was carried out in accordance with the manufacturer's instructions.

2.4. Haematologic Analysis

The count of white blood cell (WBC), lymphocyte (LYM), neutrophil (NEU), erythrocyte (RBC), hemoglobin (HGB) and hematocrit (HCT) of the calves were determined by hematology analyzer (Abacus Junior Vet 5® Hungary).

2.5. Determination of IL-6

Determination of IL-6 in serum samples was by a sandwich enzyme-linked immunosorbent assay (ELISA) using bovine IL-6-specific antibody (Sun Red Biotechnology Company, Cat No: 201-04-0008). The analysis was carried out in accordance with the recommendations of the manufacturer.

2.6. Statistical Analyses

The analyzes of the clinical, haematological and IL-6 values of the calves in the groups were performed using the General Linear Model procedure and the SPSS 20.0 package program. Significance controls of means found significant between groups were determined by Duncan Multiple Comparison Test.

3. RESULTS

3.1 Clinical Findings

The findings of the clinical examination [T (C°), P (Beats/min), R (Num/min)] of calves in the groups are presented in Table 2. Body temperatures of the calves in groups III and IV were found to be lower than those of the calves in groups I and II (P<0.01).

Table-2: Clinical findings [T (C°), P (Beats/min), R (Num/min)] of the calves in the groups (Mean ±SE).

Parameter s/Groups	Group I (Mean ±SE)	Grup II (Mean± SE)	Grup III (Mean ±SE)	Grup IV (Mean ±SE)	P
T (C°)	38.5±0.3 ^a	38.6±0.5 ^a	36.9±1.5 ^b	36.07±1.5 ^b	**
P (Beats/min)	113.1±14.3	119.2±33.3	111±25.2	105.8±29.5	NS.
R (Num/min)	30.9±5.4	34.6±10.5	40.7±12.8	35.8±8.0	NS.

a, b: The difference between the means with different letters on the same line is statistically significant. **: P<0.01, NS: Not Significant.

3.2. Etiologic Agent Findings

Enteropathogens diagnosed in the feces of diarrhoeic neonatal calves are given in Table 3. Such as *E. coli*, *Rotavirus*, *Coronavirus*, *Cryptosporidium* and *Cl. perfringens* enteropathogens or their combinations were determined.

Table-3. Etiological findings of calves in all groups

Etiology/Groups	Group I (n=10)	Group II (n=10)	Grup III (n=10)	Group IV (n=10)
<i>E. coli</i>	-	2	5	4
<i>Rotavirus</i>	-	2	2	1
<i>Coronavirus</i>	-	1	-	-
<i>Cryptosporidium</i>	-	2	-	-
<i>Cl. perfringens</i>	-	-	-	-
<i>E.coli + Rotavirus</i>	-	1	1	2
<i>E.coli + Coronavirus</i>	-	-	1	-
<i>Rotavirus + Coronavirus</i>	-	-	-	1
<i>Rotavirus + Cl. perfringens</i>	-	1	1	1
<i>E.coli + Rotavirus + Coronavirus</i>	-	-	-	1
<i>E.coli + Rotavirus + Cryptosporidium</i>	-	1	-	-

3.3. Haematological Findings

The haematological parameters findings of calves in all groups are given in Table-4. It was determined that the WBC and NEU numbers in the group II, III and IV were numerically higher than the group I (P>0.05), and there was no difference in the LYM numbers between the groups (P>0.05). RBC numbers in the group II, and IV were higher than the group I (P<0.01). Additionally, it was detected that the HGB numbers and HCT percentages in the group II, III and IV were higher than the group I (P<0.01).

Table-4: Haematological parameters findings of calves in all groups (Mean ±SE).

Parameters Groups	Group I (n=10)	Group II (n=10)	Group III (n=10)	Group IV (n=10)	P
WBC (10 ³ /μl)	8.8±1.4	13.3±8.4	12.6±5.3	11.7±5.1	NS.
LYM (10 ³ /μl)	4.9±1.1	4.8±2.4	5.7±3.2	3.4±1.4	NS.
NEU (10 ³ /μl)	3.6±1.0	8.2±7.5	6.7±5.9	7.8±3.9	NS.
HCT (%)	22.4±3.7 ^c	36.1±10.8 ^b	35±9.6 ^b	47.2±11.6 ^a	**

a, b, c: The difference between the means with different letters on the same line is statistically significant. **: P<0.01, NS: Not Significant.

3.4. IL-6 Findings

Serum IL-6 levels of calves in all groups are given in Table-5. It was determined that the serum IL-6 levels in the group II, III and IV were higher than the group I (P<0.01).

Table-5: Serum IL-6 levels of calves in all groups (Mean ±SE).

Parameter /Groups	Group I (n=10)	Group II (n=10)	Group III (n=10)	Group IV (n=10)	P
IL-6 (ng/L)	211.58±10.07 ^c	239.76±11.05 ^b	293±48.7 ^a	300±25.06 ^a	**

a, b, c: The difference between the means with different letters on the same line is statistically significant. **: P<0.01.

4. DISCUSSION AND CONCLUSION

Despite the advances in herd management, animal care, stables, animal feeding, cattle industry and timely use of biopharmaceuticals, neonatal calf diarrhea remains a major cause of economic loss in the cattle industry worldwide [19]. IL-6 is defined as an early and reliable prognostic marker in various diseases [20]. In the present study, it was aimed to determine serum IL-6 levels according to the clinical course of the disease in calves with neonatal diarrhea and determine whether a relationship between the clinical course or not IL-6.

Among the many infectious agents that cause diarrhea in neonatal calves, *E. coli*, *Salmonella* and *Clostridium* species are the most common bacterial agents [21], *Rotavirus* and *Coronavirus* are the most common viral agents, and *Cryptosporidium parvum* spp is the most common protozoal agent [22]. In the study presented in accordance with these reports, *Rotavirus*, *Coronavirus*, *E. coli*, *Cryptosporidium*, *Cl. perfringens* or a combination of these agents have been identified. In the neonatal period, *Coronavirus*, *Rotavirus*, *Cryptosporidium* and enterotoxigenic *E. coli* are the most common agents that can cause inflammatory and functional damage, especially in the intestine [4,5].

In calves with diarrhea, body temperature is mostly within the normal range, and in a few cases it may be elevated or decreased due to dehydration [23]. Similar to body temperature, respiration and pulse rates may be normal in diarrhoeic calves [24], and hypothermia and tachypnea may occur [25]. In the present study, although there were no difference between respiratory and pulse rates of calves in the groups II, III and IV, it was determined that body temperatures of calves in the groups III and IV were lower than those in the groups I and II.

White Blood Cell, LYM and NEU numbers may increase in diarrhoeic neonatal calves, and leukocytosis may occur. It is stated that the primary reason for this situation may be related to the reactions of the body's immune system against infectious factors, inflammatory reactions, severity of diarrhea, stress and hemoconcentration [26,27,28,29,30]. Atcali and Yildiz [31], determined that there was no significant difference in LYM levels in neonatal diarrheal calves compared to healthy ones in their study, and they interpreted this situation as etiological differences, duration of diarrhea, severity of inflammation, low number of animals, and the fact that some of the animals were at the initial stage of diarrhea. When the same researchers took into account the haematological values that could not be determined statistically significant in their studies, they observed that the lowest and highest levels of these values were in a very wide range and therefore there was no difference. In the presented study, although the WBC and NEU numbers in the groups II, III and IV were numerically higher than the group I, the possible reason why they were not statistically significant was the high standard deviations of the groups, similar to the reasons stated in the above notifications. Barua et al [32] state that the increase in HCT percentages in calves with diarrhea is due to hemoconcentration associated with dehydration and hypovolemia. In the presented study, HCT percentages in the groups II, III and IV were higher than the in group I. The possible reason for this situation may be hemoconcentration, as stated by Barua et al [32].

Cytokines function in many basic processes for life and disease. Among these different functions, their role in inflammation has attracted attention in relation to disease development and treatment [33]. Interleukins, and especially IL-6, are used as a marker of early inflammation and prognosis in various diseases [9]. An extremely important advantage of IL-6 is that it can stay

in the circulation longer than other proinflammatory cytokines [34].

There are many studies in the literature that have been conducted in different animal species and in which IL-6 has been evaluated. It has been used as a reliable parameter to monitor dogs in intensive care units, the average concentration of IL-6 of these dogs was determined to be significantly higher in the non-survivor group compared to the survivors [35]. In addition, it was determined that serum IL-6 levels were increased in dogs with septic peritonitis [36], babesiosis [37], and different liver diseases [38]; in cats with sepsis and septic shock [39], idiopathic cystitis [40], and feline infectious peritonitis [41]; in horses with metabolic syndrome pain [42]; endurance training [43], and acute abdominal disease [44]; in pigs with vesicular stomatitis [45]; in lambs with experimental endotoxemia [46]; in cattle with subclinical mastitis [15]; subclinical endometritis [47], and subclinical parasitemia [48], compared to healthy ones.

Methodologically, different studies have been conducted to evaluate IL-6 in diarrhoeic neonatal calves. Fischer et al [17], in their study to investigate the value of IL-6 as a prognostic marker in neonatal diarrheal calves, divided the calves into two groups as those who recovered and those who did not, according to their clinical findings on the 7th and 10th days. They determined that IL-6 levels were very high at the onset of diarrhea in non-healing calves. In the results of the study; They concluded that IL-6 is a useful complementary parameter for disease prognosis in neonatal calf diarrhea, and high IL-6 values may prompt the Veterinarian to monitor calves more closely and adapt the therapeutic strategy accordingly, thus avoiding animal suffering and economic losses. Albayrak and Kabu [16] determined that IL-6 levels were significantly higher in calves with diarrhea compared to healthy ones. As a result of their studies, they evaluated that routine measurement of serum IL-6 levels is a valuable parameter in evaluating the course and prognosis of diseases. Carroll et al. [49], determined that serum IL-6 levels were very high compared to the control group in calves to which they administered endotoxin intravenously. Kırbaş et al. [50] determined that calves with septicemia had significantly higher IL-6 levels on day 0 compared to the control group, and determined that the levels were significantly lower than the control group after treatment. Similar to the results obtained in the above reports, in the presented study, it was determined that serum IL-6 levels were parallel to the clinical course in neonatal diarrheal calves. Cytokines often exert stimulant (pro-inflammatory) or depressive (anti-inflammatory) effects in inflammatory conditions [51]. As can be understood from the literature reports given above, IL-6, which is one of the proinflammatory cytokines, increases in all conditions that cause inflammation, including diarrhea. The data obtained from this study also support this information.

It was concluded that serum IL-6 level increased in neonatal diarrheic calves as the disease became clinically

more severe, is an significant biomarker indicating the degree of clinical severity in neonatal diarrheic calves.

Acknowledgement

This study is summarized from the master's thesis of Gürsel Aydın

REFERENCES

- [1] Aslan V. Calf diarrhea and its treatments, neonatal calf losses symposium. Selçuk University, Faculty of Veterinary Medicine, Konya, Turkey, 59-69, 1986.
- [2] Collery P, Bradley J, Fagan J, Jones P, Redehan E, Weavers E. Causes of perinatal calf mortality in the Republic of Ireland. *Irish Veterinary Journal*. 1996; 49: 491-496.
- [3] Poulsen KP, McGuirk SM. Respiratory disease of the bovine neonate. *Veterinary Clinics of North America: Food Animal Practice*. 2009; 25: 121-137.
- [4] Al Mawly J, Grinberg A, Prattley D, Moffat J, French N. Prevalence of endemic enteropathogens of calves in New Zealand dairy farms. *New Zealand Veterinary Journal*. 2015; 63: 147-152.
- [5] Kaske M. Physiological function of the gastrointestinal tract and pathophysiological changes in neonatal diarrhea of calves. *Deutsche tierärztliche Wochenschrift*. 1993; 100: 434-439.
- [6] Merckmanual [Internet]. Diarrhea in neonatal ruminants; 2022 [Cited: January, 2022]. Available from: <https://www.merckvetmanual.com/digestive-system/intestinal-diseases-in-ruminants/diarrhea-in-neonatal-ruminants>
- [7] Taylor JA. Leukocyte responses in ruminants. In: Bernart FF, Joseph GZ, Nemi CJ. Editors. *Schalm's Veterinary Hematology*. Lippincott Williams and Wilkins, Philadelphia; 2000. P. 391-400.
- [8] Uzlu E, Karapehlivan M, Çitil M, Gökçe E, Erdoğan HM. Investigation of serum sialic acid and some biochemical parameters in calf with diarrhea symptoms. *YYÜ Veteriner Fakültesi Dergisi*. 2010; 21: 83-86.
- [9] Rincon M. Interleukin-6: From an inflammatory marker to a target for inflammatory diseases. *Trends Immunology*. 2012; 33: 571-577.
- [10] Tanaka T, Narazaki M, Kishimoto T. IL-6 in inflammation, immunity, and disease. *Cold Spring Harbor Perspectives in Biology*. 2014; 2: 1-17.
- [11] Mauer J, Denson JL, Bruning JC. Versatile functions for IL-6 in metabolism and cancer. *Trends Immunology*. 2015; 36: 92-101.
- [12] Scheller J, Chalaris A, Schmidt-Arras D, Rose-John S. (2011) The pro- and anti-inflammatory properties of the cytokine interleukin-6. *Biochimica et Biophysica Acta*. 2011; 1813: 878-888.
- [13] Ishikawa Y, Nakada K, Hagiwara K, Kirisawa R, Iwai H, Moriyoshi M, Sawamukai Y. Changes in interleukin-6 concentration in peripheral blood of pre- and post-partum dairy cattle and its relationship to postpartum reproductive diseases. *The Journal of Veterinary Medical Science*. 2004; 66: 1403-1408.
- [14] Nakajima Y, Mikami O, Yoshioka M, Motoi Y, Ito T, Ishikawa Y, Fuse M, Nakano K, Yasukawa K. Elevated levels of tumor necrosis factor-alpha (TNF-alpha) and interleukin-6 (IL-6) activities in the sera and milk of cows with naturally occurring coliform mastitis. *Research in Veterinary Science*. 1997; 62: 297-298.
- [15] Sakemi Y, Tamura Y, Hagiwara K. Interleukin-6 in quarter milk as a further prediction marker for bovine subclinical mastitis. *Journal of Dairy Research*. 2011; 78: 118-121.
- [16] Albayrak H, Kabu M. Determining serum haptoglobin and cytokine concentrations in diarrheic calves. *FÜ Sağlık Bilimleri Veteriner Dergisi*. 2016; 30: 113-117.
- [17] Fischer S, Bauerfeind R, Czerny CP, Neumann S. Serum interleukin-6 as a prognostic marker in neonatal calf diarrhea. *Journal of Dairy Science*. 2016; 99: 6563-6571.
- [18] Walker PG, Constable PD, Morin DE, Drackley JK, Foreman JH, Thurmon JC. A reliable, practical, and economical protocol for inducing diarrhea and severe dehydration in the neonatal calf. *Canadian Veterinary Research*. 1998; 62: 205-213.
- [19] Picco NY, Alustiza FE, Bellingeri RV, Grosso MC, Motta CE, Larriestra AJ, Vissio C, Tiranti KI, Terzolo HR, Moreira AR, Vivas AB. Molecular screening of pathogenic *Escherichia coli* strains isolated from dairy neonatal calves in Cordoba province, Argentina. *Revista Argentina de Microbiología*. 2015; 47: 95-102.
- [20] Fisher DT, Michelle M, Appenheimer S, Evans S. The two faces of IL-6 in the tumor microenvironment. *Seminars in Immunology*. 2014; 26: 38-47.
- [21] Kasa A, Tulu D, Negera C. Review of common bacterial cause and management of neonatal calf diarrhea in cattle. *International Journal of Microbiology Research*. 2020; 11: 98-104.
- [22] Kongsted H, Jonach B, Haugegaard S, Angen O, Jorsal SE, Kokotovic B, Larsen L, Jensen TK, Nielsen JP. Microbiological, pathological and histological findings in four Danish pig herds affected by a new neonatal diarrhoea syndrome. *BMC Veterinary Research*. 2013; 9: 206.
- [23] Sahal M, Terzi OS, Ceylan E, Kara E. Calf Diarrhea and Prevention Methods. *Lalahan Hayvancılık Araştırma Enstitüsü Dergisi*. 2018; 58: 41-49.
- [24] Fecteau G, Pare J, Van Metre DC, Smith BP, Holmberg CA, Guterbock W, Jang S. Use of a clinical sepsis score for predicting bacteremia in neonatal dairy calves on a calf rearing farm. *Canadian Veterinary Journal*. 1997; 38: 101-104.
- [25] Lofstedt J, Dohoo IR, Duizer G. Model to predict septicemia in diarrheic calves. *Journal of Veterinary Internal Medicine*. 1999; 13: 81-88.
- [26] Brar A, Ahuja CS, Sood NK, Sandhu BS, Gupta K. Haematological changes in neonatal diarrheic calves of different age groups. *Indian Journal of Veterinary Pathology*. 2015; 39: 73-77.
- [27] Brar TK, Singh KD, Kumar A. Effect of different phases of menstrual cycle on heart rate variability (HRV). *Journal of Clinical Diagnostic Research*. 2015; 9: 1-4.

- [28] Günes V, Unver A, Cital M, Erdoğan HM. The prevalence of *Escherichia coli* O157 serotype and *Clostridium perfringens* type A α -toxin in neonatal diarrhoeic calves in Kars district. *Kafkas Üniversitesi Veteriner Fakültesi Dergisi*. 2004; 10: 41-45.
- [29] Seifi HA, Mohri M, Shoorei E, Farzaneh N. Using haematological and serum biochemical findings as prognostic indicators in calf diarrhoea. *Comparative Clinical Pathology*. 2006; 15: 143-147.
- [30] Sentürk S. Fluid therapy in diarrheic calves. *Journal of Faculty Veterinary Medicine*. 2001; 20: 161-167.
- [31] Atcalı T, Yıldız R. The effects of different factors on hemogram parameters on neonatal calves with diarrhea. *Mehmet Akif Ersoy University Journal of Health Sciences Institute*. 2020; 8: 119-127.
- [32] Barua SR, Rakib TM, Das S, Masuduszaman M, Hossain MA. Haematological and serological changes in neonatal diarrheic calves infected with bovine rotavirus. *Multidisciplinary Advances in Veterinary Science*. 2018; 2: 356-366.
- [33] Hirano T. IL-6 in inflammation, autoimmunity and cancer. *International Immunology*. 2021; 33: 127-148.
- [34] Song M, Kellum JA. Interleukin-6. *Critical Care Medicine*. 2005; 33: 463-465.
- [35] Schüttler J, Neumann S. Interleukin-6 as a prognostic marker in dogs in an intensive care unit. *Veterinary Clinical Pathology*. 2015; 44: 223-228.
- [36] Martiny P, Goggs R. Biomarker guided diagnosis of septic peritonitis in dogs. *Frontiers in Veterinary Science*. 2019; 6: 208.
- [37] Goddard A, Leisewitz AL, Kjelgaard-Hansen M, Kristensen AT, Schoeman JP. Excessive pro-inflammatory serum cytokine concentrations in virulent canine babesiosis. *PLoS ONE*. 2016; 11(3): e0150113.
- [38] Neumann S, Kaup FJ, Scheulen S. Interleukin-6 (IL-6) serum concentrations in dogs with hepatitis and hepatic tumours compared with those with extra-hepatic inflammation and tumours. *Comparative Clinical Pathology*. 2012; 21: 539-544.
- [39] Troia R, Mascalonzi G, Agnoli C, Lalonde-Paul D, Giunti M, Goggs R. Cytokine and chemokine profiling in cats with sepsis and septic shock. *Frontiers in Veterinary Science*. 2020; 7: 305.
- [40] Parys M, Yuzbasiyan-Gurkan V, Kruger JM. Serum cytokine profiling in cats with acute idiopathic cystitis. *Veterinary Internal Medicine*. 2018; 32: 274-279.
- [41] Goitsuka R, Ohashi T, Ono K, Yasukawa K, Koishibara Y, Fukui H, Ohsugi Y, Hasegawa A. IL-6 activity in feline infectious peritonitis. *Journal of Immunology*. 1990; 144: 2599-25603.
- [42] Krzysztof M, Katarzyna B, Nezir Yaşar T, Agnieszka S, Jakub N. The activity of IL-6 and TNF- α in adipose tissue and peripheral blood in horses suffering from equine metabolic syndrome (EMS). *Kafkas Üniversitesi Veteriner Fakültesi Dergisi*. 2014; 20: 493-499.
- [43] Witkowska-Pilaszewicz O, Baska P, Czopowicz M, Zmigrodzka M, Szarska E, Szczepaniak J, Nowak Z, Winnicka A, Cywinska A. Anti-inflammatory state in Arabian Horses introduced to the endurance training. *Animals*. 2019; 9: 616.
- [44] Barton MH, Chrysann C. Tumor necrosis factor and Interleukin-6 activity and endotoxin concentration in peritoneal fluid and blood of horses with acute abdominal disease. *Journal of Veterinary Internal Medicine*. 1999; 13: 457-464.
- [45] Velazquez-Salinas L, Pauszek SJ, Stenfeldt C, O'Hearn ES, Pacheco JM, Borca MV, Verdugo Rodriguez A, Arzt J, Rodriguez JJ. Increased virulence of an epidemic strain of vesicular stomatitis virus is associated with interference of the innate response in pigs. *Frontiers Microbiology*. 2018; 9: 1891.
- [46] Kirbas A, Karakus E, Ozkanlar S, Gedikli S, Hanedan B, Topcu A, Bayraktutan Z. Comparative efficacy of the steroids administered by inhalation and parenteral route in lambs with experimentally induced endotoxemia. *International Journal of Veterinary Science*. 2015; 4: 199-205.
- [47] Brodzki P, Kostro K, Krakowski L, Marczuk J. Inflammatory cytokine and acute phase protein concentrations in the peripheral blood and uterine washings of cows with subclinical endometritis in the late postpartum period. *Veterinary Research Communications*. 2015; 39: 143-149.
- [48] Sevimli K, Kuş FS. Acute-phase proteins and Interleukin-6 (IL-6) in cattle infected with subclinical parasitic infections. *Acta Scientiae Veterinariae*. 2015; 43: 1271.
- [49] Carroll JA, Arthington JD, Chase CC. Early weaning alters the acute-phase reaction to an endotoxin challenge in beef calves. *Journal of Animal Science*. 2009; 87: 4167-4172.
- [50] Kirbas A, Kandemir FM, Celebi D, Hanedan B, Timurkan MO. The use of inflammatory markers as a diagnostic and prognostic approach in neonatal calves with septicaemia. *Acta Veterinaria Hungarica*. 2019; 67: 360-376.
- [51] Moreland LW, Scott SW, Schiff MH, Tindall EA, Fleischmann RM, Weaver AL, Ettlenger RE, Cohen S, Kopman WJ, Mohler K, Widmer MB, Blosch CM. Treatment of rheumatoid arthritis with a recombinant human TNF receptor (p75)-Fc fusion protein. *The New England Journal of Medicine*. 1997; 337: 141-147.

A Study on Body Weight and Carcass Characteristics and Sex in Broilers.

İsmail GÖK^{1*} , Tolga TOLUN² 

¹²Kahramanmaraş Sütçü İmam University, Faculty of Agriculture,
Department of Bioengineering, 46100, Kahramanmaraş, Türkiye.
İsmail GÖK ORCID No: 0000-0002-0759-1187
Tolga TOLUN ORCID No: 0000-0003-4081-1222

*Corresponding author: gkisoo1995@gmail.com

(Received: 09.06.2023, Accepted: 06.12.2023, Online Publication: 28.12.2023)

Keywords

Chicken,
Chicken
parts,
Logistic
regression,
Gender.

Abstract: In this study, it was aimed to determine the level of relationship between the carcass and piece weights of chickens and their gender. The body weight, carcass, thigh, wing, breast, heart, liver and gizzard values obtained for this purpose belong to Ross 308 hybrid broiler chickens from the commercially operating slaughterhouses in Kahramanmaraş. 60 hybrid broiler chickens (30 females-30 males) were obtained from the slaughterhouse and the measurements of the body weight before slaughter and the values of the relevant carcass, chicken parts (leg, breast, wing) and internal organs (heart, liver, gizzard) after slaughter were taken. In the study, the dependent variable was sex, the independent variables were body weight, carcass, thigh, wing, breast, heart, liver and gizzard, and logistic regression binary analysis was used. According to the estimation results, the reference category was male (1), and the probability value in the test of the model coefficients was found to be 0.036 ($p < 0.05$). The most significant independent variable explaining the relationship between carcass and piece weights and gender of chickens compared to other independent variables was found to be breast (0.084), and the most insignificant was gizzard (0.939).

Etlik Piliçlerde Canlı Ağırlık ve Karkas Özellikleri ile Cinsiyet İlişkisi Üzerine Bir Araştırma

Anahtar Kelimeler

Tavuk,
Tavuk
parçaları,
Lojistik
regresyon,
Cinsiyet

Öz: Bu çalışmada, tavukların karkas ve parça ağırlıkları ile cinsiyetleri arasındaki ilişki düzeyinin belirlenmesi amaçlanmıştır. Bu amaçla elde edilen canlı ağırlık, karkas, but, kanat, göğüs, kalp, karaciğer ve taşlık değerleri, Kahramanmaraş ilinde ticari olarak faaliyet göstermekte olan kesimhaneden Ross 308 hibrit etlik piliçlerine aittir. Kesimhaneden 60 adet etlik piliç temin edilmiş (30 dişi-30 erkek birey) ve kesim öncesi canlı ağırlık ve kesim sonrası ilgili karkas, tavuk parçaları (but, göğüs, kanat) ve iç organlara (kalp, karaciğer, taşlık) ait değerlerin ölçümleri alınmıştır. Araştırmada bağımlı değişken cinsiyet, bağımsız değişkenler de canlı ağırlık, karkas, but, kanat, göğüs, kalp, karaciğer ve taşlık olarak alınmış ve lojistik regresyon ikili (binary) analizinden yararlanılmıştır. Tahmin sonuçlarına göre referans kategorisi erkek (1), model katsayılarının testinde olasılık değeri 0.036 ($p < 0.05$) bulunmuştur. Tavukların karkas ve parça ağırlıkları ile cinsiyetleri arasındaki ilişki düzeyinin diğer bağımsız değişkenlere göre en anlamlı şekilde açıklayan bağımsız değişken göğüs (0.084), en anlamsız da taşlık (0.939) olduğu yapılmış analiz ile belirlenmiştir.

1. INTRODUCTION

The importance of taking protein, carbohydrates, fats and vitamins for a healthy and balanced nutrition program is known. In this respect, it is often emphasized that the consumption of red and white meat is sufficient, especially in protein intake [1].

Broilers raised for white meat production and consumption are among the most important protein sources. Broiler production is mostly carried out in modernized, automated and profitable poultry houses. During the production phase, not only chickens but also roosters are raised sexually; Although the female/male ratio varies according to the breeding stock programs of the producer companies, it is usually 10 females/1 male. The chickens produced are slaughtered in fully

automatic and modern slaughterhouses by means of integrated systems; Some of the chickens are cut as carcasses and some of them are cut in the cutting units of commercial companies and delivered to the consumer through the cold chain. In the said slaughterhouses, the carcass, which is defined as the head, neck, feet, feathers and internal organs removed, is divided into main parts such as thigh, wing and breast in the relevant cutting units. In addition, internal organs such as gizzard, heart and liver extracted from the carcass are consumed as chicken offal [1].

Quality; It is the whole of the parameters involved in the determination of the demand that the consumer sees or will see in the effect of the change in the unit product [1]. Detection and analysis of the chemical components of meat (protein, fat, ash and water) are reference information about the relevant meat quality. It is predicted that different lighting programs and gender affect the determination of chicken meat quality in Ross 308 hybrid broilers [2]. In the production-consumption hierarchy, all processes from the first step of production to the consumer can affect meat quality positively or negatively [3]. Factors causing stress before slaughter may adversely affect the quality of chicken meat. In addition, it is explained that breast meat can be affected more than thigh meat [4]. It is reported that carcass, thigh and breast meat weights of different hybrids are also different in broilers [5]. Breast meat of slow-growing broilers (compared to fast-growing ones) has higher protein and lower fat content [6]. The significance of the effect of gender on internal organs (gizzard, liver) and carcass characteristics (breast, neck, wing) in broilers, including feathers and feet removed from the cassette during slaughter, was statistically analyzed [7]. In research it was aimed to determine the level of relationship between the carcass and piece weights of chickens and their gender.

2. MATERIAL AND METHOD

Material

Live weight, carcass, leg, wing, breast, heart, liver and gizzard values obtained in this study were obtained from Ross 308 hybrid broiler chickens sold in commercial slaughterhouses in Kahramanmaraş. For this purpose, during the slaughtering process of 60 broiler chickens (30 females - 30 males), a deep horizontal cut was made in the neck muscle, just below the jawbone, along the front and both sides of the throat, to avoid damaging the skin after the neck cut (skin has a protein structure). For this reason, the feathers were dry plucked. After dry plucking, the feet were separated from the carcass with a sharp knife. After the feet were removed, the internal organs were removed without causing damage using an incision in the lower abdominal area close to the cloaca, and the carcass was prepared by washing with warm water. In addition, based on the application procedures of integrated shredding facilities, the carcass (thigh, wing, breast, heart, liver and gizzard) was shredded and chicken parts (leg, breast, wing) and internal organs (heart, liver, gizzard) were removed. In the selection of broiler chickens included in the study, chickens with

limb deficiencies, diseases or mild disabilities (such as limping) were not selected. The selected chickens were slaughtered at the 6th week (42nd day) of commercial slaughter age. In addition, the selected chickens had access to unlimited feed and water until slaughter, as in standard chicken farming.

Metod

Lojistic regresion

In any multivariate model where the differences between independent and dependent variables are sought, if the scale of a variable is nominal in the dependent variable, the least squares method, which is the normality assumption of the dependent variable, will be incomplete, so discriminant and logistic regression analysis can be preferred in this process [8]. Logistic regression analysis is a regression method that is useful in clustering and transport operations. Continuity and normality assumptions are not required. Three methods are used in logistic regression analysis. These; binary, ordinal and nominal methods [9].

Although the logistics model;

$$\lambda(x_i) = E(y_i | x_i) = \log\left[\frac{P(x_i)}{1-P(x_i)}\right] = \sum_{k=0}^p \beta_k x_{ik} \quad (1)$$

form of equality. ($i=1, 2, \dots, n$; $k=1, 2, \dots, p$; $x_i=1$). where $P(x_i)$ is the density;

$$p(x_i) = \frac{e^{\sum \beta_k x_{ik}}}{1 + e^{\sum \beta_k x_{ik}}} = \frac{e^{\lambda(x_i)}}{1 + e^{\lambda(x_i)}} \quad (2)$$

It is expressed as [10;11].

Binary metod

It is a logistic regression analysis that includes binary responses with the dependent variable or variables. It is used to determine the relationship between one or more explanatory variables and the binary response variable [9]. In the binary logistic regression model, there are two responses, 0 and 1, whether a situation or event occurs or not. Odds ratio is the ratio obtained by dividing the probability of occurrence of a situation or event by the probability of not happening. Odds ratio can take a value between 0 and $+\infty$ [12].

$$\text{Odds Ratio} = \frac{\pi(x)}{1-\pi(x)} = e^{\beta_0 + \beta_1 x} \quad (3)$$

When estimating the regression coefficients in logistic regression analysis, the maximum likelihood estimation method can be preferred instead of the least squares method estimation. In the maximum likelihood estimation method, the probability of an event or situation to occur is desired to be the highest [13].

The maximum likelihood function;

$$L(y_i | x_i, \beta) = \prod_{i=1}^n P(x_i)^{y_i} [1 - P(x_i)]^{1-y_i} \quad (4)$$

can be expressed as [14].

In this study, logistic regression binary method was used to find out whether there is a relationship between the overall and piece weights of chickens slaughtered by sex and their gender.

3. RESULTS

In this study, it was aimed to determine the level of relationship between the carcass and piece weights of chickens and their gender. The body weight, carcass, thigh, wing, breast, heart, liver and gizzard values obtained for this purpose belong to Ross 308 hybrid broiler chickens from the commercially operating slaughterhouses in Kahramanmaraş. 60 broiler chickens (30 females-30 males) were obtained from the slaughterhouse and the measurements of the body weight before slaughter and the values of the relevant carcass, chicken parts (leg, breast, wing) and internal organs (heart, liver, gizzard) after slaughter were taken. In the study, the dependent variable was sex, the independent variables were body weight, carcass, thigh, wing, breast, heart, liver and gizzard, and logistic regression binary analysis was used.

According to the results of the research, the reference category was male (1), and the probability value was 0.036 ($p < 0.02$) in the test of the model coefficients, so H_0 (there is no relationship between the carcass and piece weights of chickens and their gender) was rejected, and thus the established model was determined to be statistically significant. It was determined that the hens explained the carcass and piece weights by 32% in a change in gender, and the classification table was an accurate and compatible model with a model estimate of 73.3% in general. According to the other independent variables, the most significant independent variable explaining the relationship between the carcass and piece weights of chickens and their gender was determined by the analysis as breast ($X_5 = 0.084$), and the most meaningless one was gizzard ($X_8 = 0.939$).

In the data set created according to the estimation results, the probability value was found to be 0.036. It has been determined by scientific analysis that there is a relationship between the carcass and piece weights of chickens and their gender.

In order to obtain better results in the data set obtained with randomly selected chickens from Ross 308 hybrid broiler chickens sold in commercial slaughterhouses in Kahramanmaraş, keeping the number of observations in the data set larger, preferring breeds with better living conditions in the region, preferring more care should be taken and the nutritional habits of the chickens should be considered before slaughtering in the region. In order to avoid these and similar problems in future articles or thesis research, the deficiencies mentioned should not be ignored.

4. DISCUSSION AND CONCLUSION

A data set was created with measurements taken from slaughtered chickens.

A model was established with the help of the obtained data set.

H_0 = There is no relationship between the carcass and piece weights of chickens and their gender.

H_1 = There is a relationship between the carcass and piece weights of chickens and their gender.

The hypotheses are stated and the model is established.

This model:

$$Y_{it} = \beta_0 + \beta_1 X_{1it} + \beta_2 X_{2it} + \beta_3 X_{3it} + \beta_4 X_{4it} + \beta_5 X_{5it} + \beta_6 X_{6it} + \beta_7 X_{7it} + \beta_8 X_{8it} + u_{it} \quad (5)$$

Y_{it} : Sex of Chickens (Male, Female).

X_{1it} : Live weight of chickens.

X_{2it} : The carcass of chickens.

X_{3it} : Leg parts of chickens.

X_{4it} : Wing parts of chickens.

X_{5it} : Chicken breast.

X_{6it} : Heart part of chickens.

X_{7it} : The liver part of chickens.

X_{8it} : The stony part of chickens.

is in the form.

As a result of the analysis;

Table 1. Model Summary.

Model Summary		
-2 Log Likelihood	Cox & Snell R Square	Nagelkerke R Square
66.669 ^a	.241	.321

a. Estimation terminated at iteration number 5 because parameter estimates changed by less than ,001

In the model established in Table 1, it was determined that a change in gender explained the carcass and piece weights of chickens by 32%.

Table 2. Reference Category.

Dependent Variable Encoding	
Original Value	Internal Value
Female	0
Male	1

In Table 2. the reference category is from female to male and it is determined that it is the male reference category.

Table 3. Test of Model Coefficients

Omnibus Tests of Model Coefficients			
	Chi-square	df	Sig.
Step	16.509	8	.036
Block	16.509	8	.036
Model	16.509	8	.036

In Table 3, H_0 (There is no relationship between carcass and piece weights and gender of chickens) was rejected because the probability value was below 0.05 in the test of model coefficients. In other words, the established model was determined to be statistically significant.

Table 4. Classification Table

Classification Table			
Observed	Predicted		Percentage Correct
	Gender		
	Female	Male	

Gender	Female	21	9	70.0
	Male	7	23	76.7
Overall Percentage				73.3

Since 30 females were used in the study in Table 4, 21 of them were found and the correct prediction percentage was calculated as 70.0%, while 23 of the 30 males used in the study were found and the prediction percentage was determined to be 73.3%. In addition, it was determined that the model estimation was correct and compatible with 73.3% of the overall total

Table 5. Established Model Variables.

	Variables in the Model					
	B	S.E.	Wald	df	Sig.	Exp(B)
X1	.002	.001	2.219	1	.136	1.002
X2	-.005	.004	1.621	1	.203	.995
X3	.009	.007	1.579	1	.209	1.009
X4	.004	.018	.052	1	.819	1.004
X5	.012	.007	2.984	1	.084	1.012
X6	.085	.080	1.133	1	.287	1.089
X7	-.036	.031	1.318	1	.251	.965
X8	-.001	.016	.006	1	.939	.999
Costant	-9.366	3.732	6.299	1	.012	.000

In Table 5, the ratio of live weight (X1), which has a relationship between the overall and piece weights and gender of the chickens slaughtered according to their sex, is 0.1336, carcass (X2) 0.203, thigh (X3) 0.209, wing (X4) 0.819, It was determined that chest (X5) explained 0.084 ratio, heart (X6) 0.287 ratio, liver (X7) 0.965 ratio and gizzard (X8) 0.999 ratio. As a result of the analysis, it was determined that the independent variable that explained the determination of the relationship between the sex of the chickens in the most significant way compared to the other independent variables was the breast (X5=0.084). In addition, it was determined that an increase of 1.0112 in the breast, which was determined to be significant compared to the others in chicken slaughter according to gender, could be increased by 1.0112 in the female, which is the opposite of the sex determined in the reference.

In a study conducted, pH, hardness (penetrometer value), L*, a* and b* color criteria with and without skin were obtained in male and female broiler (Ross 308) breast and leg meat samples, which were applied 4 different lighting programs (AP) during the 6-week rearing period. data have been identified. As a result of the research, the AP* gender effect on leg meat pH was found to be significant ($p<0.01$). AP* gender effect on breast and leg meat hardness values was found to be significant ($p<0.01$). While the effect of AP on skinned and skinless breast meat on L, a and b color criteria was found to be significant, skinned and skinless thigh meat had AP on L color criterion ($p<0.01$) and on a color criterion ($p<0.01$) and b color criterion ($p<0.05$).) AP* gender effect was significant [15]. In another study, the effects of 4 different lighting programs (AP) commonly applied in broiler farming on yield performances, slaughter and some carcass characteristics were examined. As a result of the research, the effect of AP on live weight at slaughter age was found to be insignificant. 1-10 in terms of live weight gain. and 11-29. On days 4, the differences between AP and the others

were found to be significant ($P<0.05$) [16]. In a study, data were determined to determine the effects of gender on edible carcass components and offal products in broilers. As a result of the research, differences between males and females were found to be significant in terms of the share of feathers, feet, liver, gizzard, chest, neck and wings in live weight. Compared to males, females were found to have higher percentages of feathers, whole and edible carcasses, heart, liver, gizzard, abdominal fat, breast and feet, rumps and neck [7]. In another study, the effects of gender and early limited feeding program on some productivity and immunological characteristics in broiler flocks were determined. As a result of the research, it was observed that rearing male and female broilers separately had a positive effect on some productivity characteristics and provided some advantages in breeding. It has been observed that applying a restricted feeding program at an early age has a positive effect on some productivity characteristics such as feed conversion, viability and belly fat amount and may be recommended to producers [17]. As a result of a study, ± 0.15 for female quails and $DW= 2.21 \pm 0.01$ $MSE= 35.391 \pm 9.07$, $adj.R^2=0.997 \pm 0.033$, $AIC= |-35,04| \pm 0.29$ and $DW= 2.09 \pm 0.91$ for male quails [18]. In another study, it was found that the individual growth curves of Ramanov lambs with logistic regression method were 0.534 ± 2.215 in females and 2.659 ± 0.476 in males [19]. In another study, the factors affecting the success of university students with the logistic regression method; gender, the university they attended, the way they chose the department, and father's education were found to be effective [20]. In another study, with logistic regression method, weekly egg yields of Nick Brown and Leghorn breed chickens from the 18th week to the 59th week; in both races, Nick Brown; $HKO=0.000007$, $R^2=0.9999$, $\bar{R}^2=0.9998$, $AIC=-392.966$, $DW=1.345$: Leghorn; $PCO=0.0001$, $R^2=0.9998$, $\bar{R}^2 =0.9997$, $AIC=-373.225$, $DW=1.845$ [21].

REFERENCES

- [1] Groom GM. Factors affecting poultry meat quality. CHIEM – Options mediterranees. NAMESAKE. Ministry of Agriculture, Fisheries and Food. 1990; Cambridge, UK.
- [2] Yetişir R, Karakaya M, İlhan F, Yılmaz MT, Özalp B. The effects of different lighting programs and gender on some chicken meat quality traits affecting consumer choice. *Animal Production*, 2008; 49(1):20-28.
- [3] Kahraman T, Nazli B, Ergun O. Effects of electrical stimulation on meat quality. *Journal of Istanbul University Faculty of Veterinary Medicine*, 2006;32(2):23-30.
- [4] Debut M, Berri C, Bae'za E, Sellier N, Arnould C, Guemene D, Jehl N, Boutten B., Jégo Y, Beaumont C, Le Bihan-Duval E. Breeding and genetics. Variation of chicken technological meat quality, 2003;82:1829–1838.
- [5] Ozbek M. Different housing systems and effects of genotype on slaughter and carcass characteristics and meat quality in broilers. Uludağ University,

- Institute of Health Sciences, Department of Veterinary-Zootechnics, 2021, PhD Thesis, Bursa, p. 69.
- [6] Cetin I, Cetin E, Cavusoglu E, Yesilbag D, Abdourhamane, IM, Özbek M, Petek M. Comparison of some meat quality traits in slow and fast growing broilers raised in traditional deep litter and grilled ground. *Journal of Lalahan Livestock Research Institute*, 2018;58(1): 7-13.
- [7] Petek M. "The effect of gender on carcass characteristics and offal products in broilers", *Journal of Uludağ University Faculty of Veterinary Medicine*, 1999; 18(1-2): 195-204.
- [8] Kalayci S. SPSS applied multivariate statistical techniques, Asil Publishing House, 2016; 273-274.
- [9] Ozdamar K. Statistical data analysis with package programs, 2nd Edition, Kaan Bookstore, Kastamonu, 1999; pp.475-479.
- [10] Elhan A. Analysis of Logistic Regression Analysis and Its Application in Medicine, Ankara University, Master Thesis, Ankara, 1997.
- [11] Heise MA, Myers RH. Optimal designs for bivariate logistic regression, *Biometrics*, 1996;14:613-623.
- [12] Agresti A. An Introduction To Categorical Data Analysis, 1996; Vol: 1350, New York: Wiley.
- [13] Alpar R. Multivariate Statistical Methods (4th Edition), Detay Publishing, Ankara, 2013.
- [14] Chatfield C, Collins A. Introduction to Multivariate Analysis, Chapman & Hall, London, 1992.
- [15] Yetişir R, Karakaya M, İlhan F, Yılmaz MT, Özalp B. 2008. Different Lighting Programs and Gender Effects on Some Chicken Meat Quality Characteristics Affecting Consumer Preference. *Journal of Animal Production*, 49(1):20-28.
- [16] İlhan U, Yetişir R. 2009. Comparison of Lighting Programs Commonly Used in Broiler Breeding in Terms of Yield Performance and Some Carcass Characteristics. *Selçuk Journal of Agriculture and Food Science*, 23(47):63-72.
- [17] Atasoy F. 2022. Efficiency of the Same Growth and Short-Term Feed Restriction in the Early Period According to Gender in Broiler Flocks. *Ankara University Faculty of Veterinary Medicine Journal*, 2-3(44):215-223.
- [18] Yavuz E, Önem AB, Kaya F, Çanga D, Şahin M. Modeling of Individual Growth Curves in Japanese Quails. *Black Sea Journal of Engineering and Science*, 2019;2(1):11-15.
- [19] Tahtalı Y, Şahin M, Bayburt L. Comparison of different growth curve models in romanov lambs, *Kafkas University Veterinary Faculty Journal*, 2020;26(5):609-615.
- [20] Eratlı Şirin Y, Şahin M. Investigation of factors affecting the achievement of university students with logistic regression analysis: School of physical education and sport example, *Sage Open*, 2020; 10(1).
- [21] Yalçınöz E, Şahin M. Modeling of egg production curves in poultry. *Kahramanmaraş Sütçü İmam University Journal of Agriculture and Nature*, 2020; 23(5):1373 –1778.

Efficacy of Intravenous Iron Therapy in Female Patients with Iron Deficiency Anemia

Sevgi GÜNEŞ^{1*}, Naci Ömer ALAYUNT², Osman ÖZÜDOĞRU³

¹ Siirt University, Medical Faculty, Department of Biophysics, Siirt, Türkiye

² Siirt University, Medical Faculty, Department of Medical Biochemistry, Siirt, Türkiye

³ Erzincan Binali Yıldırım University, Medical Faculty, Department of Internal Medicine, Erzincan, Türkiye

Sevgi GÜNEŞ ORCID No: 0000-0002-9293-215X

Naci Ömer ALAYUNT ORCID No: 0000-0003-2215-0934

Osman ÖZÜDOĞRU ORCID No: 0000-0003-1212-2251

*Corresponding author: sevgi.gunes@siirt.edu.tr

(Received: 15.08.2023, Accepted: 9.12.2023, Online Publication: 28.12.2023)

Keywords

Iron deficiency anemia,
Iron replacement,
Intravenous carboxymaltose,
Serum TIBC,
Serum folate

Abstract: In this study, it was aimed to show the efficacy of intravenous (IV) ferric carboxymaltose treatment for iron deficiency anemia (IDA), which is a public health problem due to its high prevalence in the world and in Türkiye. Since it is the first study in the region, its importance is increasing even more. Eighty female diagnosed with IDA and treated with IV iron carboxymaltose, who applied to Siirt Training and Research Hospital Internal Diseases Polyclinics between June 2018 and September 2019, were included in the study. Biochemical data before and after treatment from the data recorded in the system of the patients who signed the consent form of Siirt University Research Hospital were included in the study retrospectively. After treatment, hemoglobin (HGB), hematocrit (HTC), mean cell volume (MCV), ferritin, iron and B12 values increased statistically ($p < 0.05$). In addition, platelet (PLT), total iron binding capacity (TIBC) and folate values were statistically significantly lower ($p < 0.05$). Additionally, platelet (PLT), total iron binding capacity (TIBC) and folate values were statistically significantly lower ($p < 0.05$). The study is important in terms of revealing the female IDA profile in the region and showing the positive results of IV iron therapy data. It is thought that the study can be a guide in finding solutions to irrational drug use, prolongation of the treatment period and high expenditures while creating IDA treatment protocols.

Demir Eksikliği Anemili Kadın Hastalarda İntravenöz Demir Tedavisinin Etkinliği

Anahtar Kelimeler

Demir eksikliği anemisi,
Demir replasmanı,
İntravenöz karboksimaltoz,
Serum TIBC,
Serum folat

Öz: Bu çalışmada, dünyada ve Türkiye'de prevalansının yüksek olması nedeniyle bir halk sağlığı sorunu olan demir eksikliği anemisinde (DEA) intravenöz (İV) ferrik karboksimaltoz tedavisinin etkinliğinin gösterilmesi amaçlandı. Bölgedeki ilk çalışma olması nedeniyle önemi daha da artmaktadır. Haziran 2018-Eylül 2019 tarihleri arasında Siirt Eğitim ve Araştırma Hastanesi İç Hastalıkları Polikliniği'ne başvuran, DEA tanılı ve İV demir karboksimaltoz tedavisi uygulanan 80 kadın çalışmaya dahil edildi. Siirt Üniversitesi Araştırma Hastanesi onam formunu imzalayan hastaların sisteme kaydedilmiş verilerinden tedavi öncesi ve sonrası biyokimyasal verileri retrospektif olarak çalışmaya dahil edildi. Tedavi sonrası hemoglobin (HGB), hematokrit (HTC), ortalama hücre hacmi (MCV), ferritin, demir ve B12 değerlerinde istatistiksel olarak artış görüldü ($p < 0.05$). Ayrıca trombosit (PLT), toplam demir bağlama kapasitesi (TIBC) ve folat değerleri istatistiksel olarak anlamlı derecede düşüktü ($p < 0.05$). Çalışma bölgedeki kadın DEA profilini ortaya koyması ve İV demir tedavisi verilerinin olumlu sonuçlarını göstermesi açısından önemlidir. Çalışmanın DEA tedavi protokolleri oluşturulurken akılcı olmayan ilaç kullanımına, tedavi süresinin uzamasına ve yüksek tedavi harcamalarına çözüm bulunmasına yol gösterici olabileceği düşünülmektedir.

1. INTRODUCTION

Iron deficiency anemia (IDA) is the most common type of anemia among the types of anemia, which is common in the world and especially in underdeveloped countries. Although IDA is seen in almost all age groups, it is more common especially in women of childbearing age [1-3]. In studies conducted in different age groups, IDA was found to be at the level of 30-78% in Türkiye [4]. It is defined as a public health problem because it is frequently seen in the world and in Türkiye. Iron replacement therapy is administered to patients with IDA in two ways, orally and parenterally. Today, the major treatment method is oral iron administration [5]. However, due to factors such as the observation of gastrointestinal side effects and long-term use in oral iron treatment, the treatment is limited due to patient incompatibility. For these reasons, there is increasing interest in parenteral iron therapy (as it provides a larger and faster source of iron) [6,7]. According to the definition of the World Health Organization, anemia is expressed as a hemoglobin (Hb) value below 13 g dL⁻¹ in men over the age of 15, 12 g dL⁻¹ in women over the age of 15 and non-pregnant women, and below 11 g dL⁻¹ in pregnant women [8]. The first diagnosis to be considered in the differential diagnosis of the patient with anemia is IDA. In addition to low ferritin and iron levels in the serum, increased total iron binding capacity, erythrocyte protoporphyrin, and transferrin-binding receptors are indicators of IDA. Serum ferritin is the strongest test for IDA marker. It is suggested that the diagnostic cut-off value of IDA is in the range of 12-15 mg L⁻¹ [9,10]. The main causes of IDA are inadequate dietary intake (severe malnutrition), blood losses (traumatic hemorrhages, hemoptysis, hematemesis, hematuria, melena, menorrhagia, pregnancy-birth, unrecognized hemorrhages, etc.), decreased iron absorption (H. pylori infection, atrophic gastritis, bariatric surgery, etc.) and hereditary mutations (SLC11A2 mutation, TMPRSS mutation, etc.). The treatment of patients with IDA should be arranged by considering the etiological reasons listed above [11,12,13]. Ferric carboxymaltose (Ferinject™) is a new IV iron complex with a very low risk of anaphylaxis, hypersensitivity, non-dextran and does not require a test dose [14,15]. A single dose infusion of up to 1000 mg of this IV iron complex can be performed in as little as 15-30 minutes [14,15,16]. Ferric carboxymaltose treatment is preferred because it eliminates the gastrointestinal side effects of oral therapy, shortens hospital stay and reduces cost. Ferric carboxymaltose is superior to other parenteral treatments due to its physical osmolarity and neutral pH level, and single dose administration in a short period of time [17,18].

The fact that there are no IDA studies in the literature in Siirt, which is one of the provinces with high fertility, and the idea of showing the effectiveness (effects and side effects) of IV ferric carboxymaltose constitutes the original value of our study. In this study, we aimed to show the effects of ferric carboxymaltose, which is one of the IV iron treatments, since the IDA profile is not found in the literature in Siirt.

2. MATERIAL AND METHOD

2.1. Participants

While creating the experimental group of this study; Non-Interventional Clinical Research Ethics Committee approval was received for the use of the data in the hospital registry system of the participants who signed the Siirt University Hospital consent form (dated 2020/01.03. and numbered). The study was conducted in accordance with the Declaration of Helsinki. Female patients (80 patients aged 18 to 60 years) who applied to the Siirt Training and Research Hospital Internal Medicine Polyclinics between June 2018 and September 2019 and were found to have IDA were included and the effects of IV iron carboxymaltose treatment were examined. Demographic data of the patients obtained retrospectively, pre- and post-treatment hemogram, iron and ferritin results were included in the study. Patients who underwent erythrocyte replacement were excluded from the study.

2.2. Analyses of Samples

In our study, female patients with anemia who applied to Siirt Training and Research Hospital Internal Medicine Polyclinics were retrospectively identified. Among these patients, those with active vaginal bleeding, gastrointestinal (GI) bleeding, hemoptysis, and hematuria were excluded from the study. By examining the hospital records, eligible patients who received iron carboxy maltose replacement (1000 mg 150 cc in 0.9% physiological saline intravenously over 30 minutes) were identified and included in the study. The records in the biochemistry laboratory of our hospital were evaluated for the patients who had 5-8 cc of venous blood collected in 1 EDTA hemogram tube and 2 gel biochemistry tubes in the polyclinic blood collection department before and after the replacement. Hemogram, iron, ferritin and B12 values taken after 4-6 weeks in the patient records were used for analysis. Hemoglobin, hematocrit, ferritin, iron and B12 values measured before and after iron carboxymaltose replacement are recorded in the hospital system. In the biochemistry laboratory of our hospital, hemogram was studied with the "Roche Diagnostic XN-1000" brand device. In our biochemistry laboratory, iron, ferritin and B12 were studied with the "Beckman Coulter DXC-800" brand device.

2.3. Statistical Analysis

After taking the average of the measurements, the normality of the distributions in terms of continuous variables was determined by the Shapiro-Wilk test. Statistical analysis was performed using the Statistical Package for the Social Sciences (SPSS) for Windows version 24.0, and p value of <0.05 was considered statistically significant. Paired T test was used to compare the data between pre-treatment and post-treatment.

3. RESULTS

The symptoms observed in 80 female patients who participated in our study are given in Table 1.

Table 1. Symptoms observed in patients.

Symptoms (N=80)	Yes N (%)	No N (%)
Headache/dizziness	5.0	95.0
Hypersensitivity	1.3	98.7
Dyspnea	2.5	97.5
GIS Symptoms	6.3	93.7
Myalgia	2.5	97.5
Hypotension/hypertension	0.0	100.0
Skin rash	2.5	97.5
Palpitation	1.3	98.7

The mean, minimum and maximum values of HGB and HTC changes (increase rates) in patients are summarized in Table 2.

Table 2. The mean, min. and max. values of HGB and HTC in patients who participating in the study.

Descriptive statistics (N=80)	Mean	Min.	Max.
Age (years)	32	18	60
Control period (days)	30	18	50
HGB increase amount (g dL ⁻¹)	2.85	0.7	6.1
HTC increase amount (%)	7.6	1.1	16.8

HGB: hemoglobin; HTC: hematocrit, Mean: average, Min: minimum, Max: maximum

3.1. Comparison of Values Before and After Treatment

While there was no significant difference between WBC values as observed in Table 3 in terms of values before and after treatment, a statistically significant increase was found in HGB, HTC, MCV, ferritin, iron and B12 values after treatment ($p < 0.05$). In addition, it was determined that there was a statistically significant decrease in platelet, total iron binding capacity and folate values ($p < 0.05$).

Table 3. Distribution of hematological parameters (iron status markers) in patients before and after treatment.

N=80	Before treatment (Mean±SD)	After treatment (Mean±SD)	P
WBC ($\times 10^9$ L ⁻¹)	6.91 ± 1.71	6.89 ± 1.56	0.907
HGB (g dL ⁻¹)	9.4 ± 1.28	12.41 ± 1.13	<0.001*
HTC (%)	31.42 ± 3.39	39.3 ± 3.1	<0.001*
PLT ($\times 10^9$ L ⁻¹)	311.93 ± 90.26	259.96 ± 74.5	<0.001*
MCV (fL)	71.81 ± 8.9	82.01 ± 6.4	<0.001*
Ferritin (ng mL ⁻¹)	3.85 ± 1.94	156.74 ± 104.75	<0.001*
Serum iron (μ g dL ⁻¹)	16.56 ± 7.84	75.91 ± 25.24	<0.001*
TIBC (μ g dL ⁻¹)	455.91 ± 55.8	232.61 ± 57.23	<0.001*
B12 (pg mL ⁻¹)	314.65 ± 78.58	368.7 ± 193.72	0.008*
Folate (ng mL ⁻¹)	9.1 ± 3.42	8.27 ± 3.61	0.010*

*Significance level was accepted as < 0.05 for Paired T test. WBC: white blood cells, HGB: hemoglobin, HTC: hematocrit, PLT: platelet, MCV: mean corpuscular volume, TIBC: total iron binding capacity, Mean: mean, SD: standard deviation.

4. DISCUSSION AND CONCLUSION

Among the types of anemia, IDA is the most common and most treatable. Although the primary treatment method is oral iron administration [5], treatment is limited due to gastrointestinal side effects, long-term use and patient incompatibility. For such reasons, the trend towards

parenteral iron therapy, which can provide faster iron supply, is increasing day by day [6,7]. However, we can encounter the diversity of IDA tables in Türkiye due to regional dietary patterns and economic factors. Siirt DEA table, which emerged with our study and has not been encountered in the literature before, may draw attention to this difference. In this study, it was found that HGB, HTC, MCV, ferritin, iron and B12 values after IV iron carboxymaltose administration were statistically significantly higher than the pre-treatment data ($p < 0.001$) (Table 3).

Iron sucrose, iron dextran, sodium ferrous gluconate can be used as IV preparations in patients with IDA. The use of these preparations is restricted due to long infusion times (sodium ferrous gluconate), increased hypersensitivity reactions (iron dextran), and multiple use of low doses to replenish iron stores [19]. Iron dextran can cause life-threatening anaphylactic reaction, hypersensitivity, myalgia, arthralgia, fever etc. undesirable effects are encountered.

In the meta-analysis about the safety of intravenous iron therapy; It was determined that no increase in risk in terms of mortality and infection and no serious side effects were observed in the treatment, and it is suggested that fever, arthralgia and myalgia improved [20]. Ferric carboxymaltose, which has physical osmolarity and neutral pH, is claimed to be superior to other parenteral treatments [17,18]. According to our study results, the absence of any significant finding in terms of side effects (symptoms such as headache, hypersensitivity, dyspnea, gastrointestinal system symptoms, myalgia, hypertension/hypotension, skin rash and palpitations) supports the superior aspects of the application.

The World Health Organization (WHO) claims that anemia plays a direct or indirect role in 40% of maternal deaths [21]. In addition, moderate bleeding can be fatal in anemic pregnant women [22]. It has been reported that the clinically administered ferric carboxymaltose treatment in pregnant women is effective [23,24]. In this study, it was revealed that the data obtained from women with IDA in Siirt (Table 3) support the literature. In addition, the fact that the fertility rate in Siirt is higher than that of Türkiye further increases the importance of these data.

In a study, it was reported that IDA reduces maternal tolerance to peripartum blood loss, the risk of hemorrhagic shock and cardiovascular insufficiency increases, and wound healing is impaired [25]. It is suggested that an increase of 1 g dL⁻¹ in the hemogram can significantly reduce maternal mortality [26]. In our study, an increase of 2.85 g dL⁻¹ and 7.6% was observed for the hemogram parameters HGB and HTC, respectively (Table 2). Although there were no pregnant women in our study group, this increase in our findings gains importance because women are prone to anemia and have the potential for pregnancy. When we look at the findings of IDA in the Turkish population in a study conducted in Türkiye, it was revealed that the mean value of TIBC in women was 352 ± 64 μ g dL⁻¹ [27], and in the findings of our study, this value was 455.91 ± 55.8 μ g dL⁻¹

¹ before treatment (Table 3). Thus, it can be said that new and more comprehensive studies are needed to investigate the reasons for the higher IDA profile in Siirt compared to Türkiye. The reasons for this situation may be factors such as nutritional habits, socioeconomic status and environmental conditions. A study conducted in Jordan found that iron deficiency anemia is caused by many factors, and that these factors, such as heavy menstrual periods in women and low consumption of red meat, are associated with the severity of anemia. When the study data were examined, it was seen that the values of HGB 8.47 g dL^{-1} , MCV 66.4 fL , Platelet $333.5 \times 10^9 \text{ L}^{-1}$ and serum ferritin 6.67 ng mL^{-1} in patients with IDA coincided with the pre-replacement values of the patients with IDA in our study. In this case, it can be said that iron deficiency anemia and socioeconomic levels may be related [28]. In addition, IV iron carboxymaltose treatment reduced the TIBC from $455.91 \pm 55.8 \mu\text{g dL}^{-1}$ to $232.61 \pm 57.23 \mu\text{g dL}^{-1}$, which is considered normal in a shorter time ($p < 0.001$) (Table 3). When platelet levels are examined, it is seen that Siirt findings ($311.93 \pm 90.26 \times 10^9 \text{ L}^{-1}$) are above the Türkiye average ($237 \pm 76 \times 10^9 \text{ L}^{-1}$). It was determined that this value decreased to levels such as $259.96 \pm 74 \times 10^9 \text{ L}^{-1}$ with the treatment performed in Siirt ($p < 0.001$) (Table 3). In this study, a statistically significant increase was found after the administration in terms of vitamin B12 as a result of IV iron carboxymaltose treatment. Although the statistically significant increase in vitamin B12 value draws attention to the positive results of the applied treatment, the high level of folate and vitamin B12 deficiency in general suggests that it may be caused by unbalanced nutritional habits. In 2021, Kefeli et al. vitamin B12 deficiency was detected in their study. The study suggests that there is a statistically significant relationship ($p = 0.06$) between red meat consumption and vitamin B12, and that as red meat consumption increases, vitamin B12 deficiency decreases [29]. Similar to the above study, it is thought that the B12 deficiency in the data in our study may be due to the low socioeconomic status of Siirt province.

As a result, it was determined that ferric carboxymaltose administration, which is one of the IV iron treatments, is more reliable in terms of side effects and its effectiveness is higher. In addition, the patient's faster recovery compared to oral administration was one of the important results of this study. We think that the research with the data obtained as a result of ferric carboxymaltose treatment, which is one of the intravenous iron treatments, can contribute to the literature and guide clinicians who regulate the treatment of IDA. This study can create new approaches to increase the awareness of physicians and to create solutions for irrational drug use, prolongation of treatment, harm to patients, and high treatment expenditures while creating treatment protocols for IDA.

Conflict Statement

The authors declare that there is no conflict of interest for the study.

Ethical Approval/Patient Consent

Before starting the study, approval was obtained from Siirt University Non-Interventional Clinical Research

Ethics Committee (dated 2020/01.03. and numbered). The data of the patients who signed the Siirt University Research Hospital consent form were used for the research.

REFERENCES

- [1] Bainton DF, Finch CA. The diagnosis of iron deficiency anemia. *Am J Med*, 1967;37:62-69.
- [2] DeMaeyer E, Adiels-Tegman M. The prevalence of anemia in the world. *World Health Stat Q* 1985;38:302-306.
- [3] Frewin R, Henson A, Provan D. Iron deficiency anemia. *BMJ* 1997;314:360-363.
- [4] T.C. Sağlık Bakanlığı, Anne Çocuk Sağlığı Genel Müdürlüğü. 12- 23 aylık çocuklarda demir kullanımı araştırması raporu, Ankara; 2008.
- [5] Danielson BG, Geisser P, Schneider W. [eds]. Iron therapy with special emphasis on intravenous administration. 1st ed. St. Gallen, Switzerland: Vifor (International) Inc; 1996.
- [6] Huch R, Breyman C. Anaemia in pregnancy and postpartum. 2nd ed. Bremen, Germany: Uni-Med Science Verlag; 2006.
- [7] Chamate E. Treatment of iron deficiency anemia in pregnancy and the immediate puerperium and other ferropenic conditions with saccharated iron administered intravenously in fractionated doses. Abstract at XIVth International Congress of Haematology; Sao Paulo, Brasil; 1972.
- [8] Groenveld HF, Januzzi JL, Damman K, van Wijngaarden J, Hillege HL, van Veldhuisen DJ, et al. Anemia and mortality in heart failure patients: a systematic review and meta-analysis. *Journal of the American College of Cardiology*, 2008;52(10),818–827.
- [9] Goddard AF, McIntyre AS, & Scott BB. Guidelines for the management of iron deficiency anaemia. *British Society of Gastroenterology. Gut*, 46 Suppl 3-4 (Suppl 4), IV1–IV5; 2000.
- [10] Punnonen K, Irjala K, Rajama A. Serum Transferrin Receptor and Its Ratio to Serum Ferritin in the Diagnosis of Iron Deficiency. *Blood* 1997;89:1052-1057.
- [11] Iron Deficiency - Investigation and Management Effective Date: June 15, British Columbia Guidelines & protocols advisory committee, 2010.
- [12] Cook JD. Diagnosis and management of iron-deficiency anaemia. *Best Pract Res Clin Haematol* 2005;18:319.
- [13] Alleyne M, Horne MK, Miller JL. Individualized treatment for iron-deficiency anemia in adults. *Am J Med* 2008;121:943.
- [14] Seid MH, Mangione A, Valaoras TG, Anthony LB, Barish CF. Safety profile of iron carboxymaltose, a new high dose intravenous iron in patients with iron deficiency anemia. *Blood*. 2006;108(11):3739.
- [15] Breyman C, Honegger C, Holzgreve W, Surbek D. Diagnosis and treatment of iron deficiency anaemia during pregnancy and postpartum. *Arch Gynecol Obstet*. 2010;282:577-80.
- [16] Van Wyck DB, Martens MG, Seid MH, Baker JB, Mangione A. Intravenous ferric carboxymaltose

- compared with oral iron in the treatment of postpartum anemia: A randomized controlled trial. *Obstet Gynecol.* 2007;110:267-78.
- [17] Breyman C, Gliga F, Bejenariu C, Strizhova N. Comparative efficacy and safety of intravenous ferric carboxymaltose in the treatment of postpartum iron deficiency anemia. *International Journal of Gynecology and Obstetrics.* 2008;101:67-73.
- [18] Kadiroğulları P, Seçkin KD, Bafalı Oİ, Polat İ. Postpartum Dönemde Demir Eksikliği Anemisi Olan Hastalarda İntravenöz ve Oral Demir Tedavisinin Karşılaştırması. *Turk J Clin Lab.* 2018;4:336-341.
- [19] Auerbach M, Coyne D, Ballard H. Intravenous iron: from anathema to standard of care. *Am J Hematol.* 2008;83:580–88.
- [20] Avni T, Bieber A, Grossman A, Green H, Leibovici L, Gafter-Gvili A. The safety of intravenous iron preparations: systematic review and meta analysis. *Mayo Clin Proc.* 2015;90(1):12-23.
- [21] Khan KS, Wojdyla D, Say L, Gülmezoglu AM, Van Look PF. WHO analysis of causes of maternal death: a systematic review. *Lancet.* 2006;367(9516):1066-1074.
- [22] Vural T, Özcan A, Sancı M. Güncel bilgiler ışığında gebelikte demir eksikliği anemisi: Demir desteği kime? Ne zaman? Ne kadar? *Van Tıp Dergisi.* 2016;23(4):369-376.
- [23] Christoph P, Schuller C, Studer H, Irion O, De Tejada BM, Surbek D. Intravenous iron treatment in pregnancy: comparison of high-dose ferric carboxymaltose vs. iron sucrose. *J Perinat Med.* 2012;40(5):469–74.
- [24] Barut A, Harma M. Intravenous iron treatment for iron deficiency anaemia in pregnancy. *J Turk Ger Gynecol Assoc.* 2009;10:109–115.
- [25] Milman N. Anemia-still a major health problem in many parts of the world! *Ann Haematol.* 2011;90(4):369-377.
- [26] Murray-Kolb L. Maternal mortality, child mortality, perinatal mortality, child cognition, and estimates of prevalence of anemia due to iron deficiency. Baltimore: CHERG; 2012.
- [27] Memişoğulları R, Ak Yıldırım H, Uçgun T, Erkan ME, Güneş C, Erbaş M, et al. Prevalence and etiology of anemias in the adult Turkish population. *Turkish Journal of Medical Sciences.* 2012;42:957-63.
- [28] Awidi M., Bawaneh H., Zureigat H., AlHusban M., & Awidi A. Contributing factors to iron deficiency anemia in women in Jordan: A single-center cross-sectional study. *PLoS One*, 2018;13(11),e0205868.
- [29] Kefeli M., Örnek Z., Kardeş H., & Ekemen C. Okul çağındaki çocuklarda vitamin B12, folat ve demir eksikliği prevalansının değerlendirilmesi. *Ege Tıp Dergisi*, 2021;60(3),244-251.

Investigation of Some Heavy Metal Contents of Soils at Different Distances and Depths in Agricultural Areas Near the Silopi Thermal Power Plant

Bedriye BİLİR^{1*}, Hava Şeyma İNCİ², Seyyid IRMAK³, Mikail DOĞAN⁴

¹ Sırnak University, Faculty of Agriculture, Department of Soil Science and Plant Nutrition, Şırnak, Türkiye

² Bingöl University, Department of Crop and Animal Production, Vocational School of Food, Agriculture and Livestock, Bingöl, Türkiye

³ Sırnak University, Faculty of Agriculture, Department of Horticulture, Şırnak, Türkiye

⁴ Şırnak Provincial Directorate Of Agriculture And Forestry, Şırnak Türkiye

Bedriye BİLİR ORCID No: 0000-0002-0038-9509

Hava Şeyma İNCİ ORCID No: 0000-0002-2670-401x

Seyyid IRMAK ORCID No: 0000-0002-7839-7912

Mikail DOĞAN ORCID No: 0000-0003-4940-0147

*Corresponding author: bbilir@sirnak.edu.tr

(Received: 25.09.2023, Accepted: 12.12.2023, Online Publication: 28.12.2023)

Keywords

Silopi,
Thermal Power
Plant,
Heavy metal,
Soil pollution

Abstract: Silopi Thermal Power Plant is located in Şırnak province and uses asphaltite as its fuel source. Emissions from the power plant chimneys are likely to be dispersed in the region and accumulate on soils due to various factors. This could lead to an increase in the concentrations of some heavy metals (such as Cr, Ni and Cd) in soils. In this study, it was aimed to determine the plant-available (extractable) and total heavy metal contents of soils taken from areas close to the power plant where agriculture is intensively practiced. A total of 42 soil samples were collected from 7 different distance classes (D1, D2, D3, D4, D5, D6 and D7) and 21 soil samples from 3 different points in each class and two different depths (0-30 cm and 30-60 cm) close to Thermal Power Plant. The concentrations of plant-available chromium (Cr), nickel (Ni), cadmium (Cd), cobalt (Co) and lead (Pb) were determined in soil samples. As a result of the research, the extractable concentrations were found to be in the ranges of Cr 0.11-0.29 mg kg⁻¹, Ni 0.4-1.71 mg kg⁻¹, Cd 0.02-0.1 mg kg⁻¹, Co 0.17-0.39 mg kg⁻¹ and Pb 0.82-2.37 mg kg⁻¹; total Cr 22-55 mg kg⁻¹, Ni 56-102 mg kg⁻¹, Cd 0.6-0.7 mg kg⁻¹, Co 41-51 mg kg⁻¹ and Pb 69-93 mg kg⁻¹. Statistically (p<0.01); Ni and Pb were found to be significant for depth and distance averages, while Cd, Cr and Co were not considered significant. The concentrations of Cr and Ni concentrations decreased with distance from the power plant. Pb and Ni concentrations were higher in the 0-30 cm depth than in the 30-60 cm depth, suggesting the possibility of an external contamination of the topsoil. However, as a result, both the total and extractable concentrations of all the heavy metals examined did not exceed the permissible limit values according to the Turkish Soil Pollution Control Regulation.

Silopi Termik Santrali Yakınlarındaki Tarım Alanlarında, Farklı Uzaklık ve Derinlikteki Toprakların Bazı Ağır Metal İçeriklerinin Araştırılması

Anahtar Kelimeler

Silopi, Termik
santrali, Ağır
metal, Toprak
kirliliği

Öz: Silopi Termik Santrali Şırnak ilinde bulunmaktadır ve yakıt olarak asfaltit kullanmaktadır. Santral bacalarından çıkan emisyonlar çeşitli faktörlere bağlı olarak bölgeye dağılım ve toprakta birikme ihtimali taşımaktadır. Bu durum topraktaki bazı ağır metallerin (Cr, Ni ve Cd gibi) konsantrasyonunu arttırabilmektedir. Bu çalışmada, tarımın yoğun olarak yapıldığı santrale yakın alanlardan alınan toprakların bitki tarafından alınabilir (ekstrakte edilebilir) ve toplam ağır metal içeriklerinin belirlenmesi amaçlanmıştır. Silopi Termik Santraline yakın 7 farklı uzaklık sınıfı (U1, U2, U3, U4, U5, U6 ve U7) ve her sınıfta 3 farklı noktadan 21 adet ve 0-30 cm ve 30-60 cm olmak üzere iki farklı derinlikten toplam 42 adet toprak örneği alınmıştır. Toprak örneklerinde bitki tarafından alınabilir, krom (Cr), nikel (Ni), kadmiyum (Cd), kobalt (Co) ve kurşun (Pb) belirlenmiştir. Araştırma sonucunda ekstrakte edilebilir Cr 0.11-0.29 mg kg⁻¹, Ni 0.4-1.71 mg kg⁻¹,

¹, Cd 0.02-0.1 mg kg⁻¹, Co 0.17-0.39 mg kg⁻¹ ve Pb 0.82-2.37 mg kg⁻¹; toplam Cr 22-55 mg kg⁻¹, Ni 56-102 mg kg⁻¹, Cd 0.6-0.7 mg kg⁻¹, Co 41-51 mg kg⁻¹ ve Pb 69-93 mg kg⁻¹ aralığında değişmektedir. Topraklarda istatistiksel anlamda (p<0.01); derinlik ve uzaklık ortalamaları için Ni ve Pb çok önemli bulunurken, Cd, Cr ve Co önemsiz bulunmuştur. Uzaklık bakımından ise santralden uzaklaşıldıkça Cr ve Ni konsantrasyonu azalma göstermiştir. Pb ve Ni konsantrasyonu 0-30 cm derinliğinde 30-60 cm derinliğine göre daha yoğun ölçülmüş ve bu da üst topraklara dışarıdan bir katılım riski ihtimalini düşündürmüştür. Fakat sonuç olarak incelenen tüm ağır metallerin hem toplam hem de ekstrakte edilebilir konsantrasyonlarının Türkiye Toprak Kirliliği Kontrol Yönetmeliği'nde izin verilen sınır değerleri altında olduğu görülmüştür.

1. INTRODUCTION

Since natural gas and fuel oil reserves are limited in Turkey, coal is utilized in electricity generation. Coal is a fossil fuel material that is very difficult at every stage from mining to storage [1]. In Turkey, 37% of electricity generation is generated from coal, 30% from natural gas and 20% from hydraulic energy [2, 3].

Thermal power plants consume substantial quantities of coal in the process of generating electricity. The combustion of coal leads to the release of a considerable amount and variety of trace elements, some of which are potentially toxic, are transferred to the environment through different pathways [4, 5]. The main environmental impacts of thermal power plants include soil, air and water pollution, and negative effects on human health, land use and natural areas [6, 7].

Millions of slag, ash, and various particles resulting from coal combustion in thermal power plants are transported to high altitudes, affecting thousands of hectares of land and subjecting agricultural areas, forests and settlements to significant pollution [8]. Heavy metals such as Cd, Cu and As concentrate in the ashes emitted by flue gases and are carried through the air [9]. In addition, the harmful components that accumulate on the soil surface with fly ashes extend their harmful effects over a broader area by leaching with rainwater, consequently polluting groundwater [10].

The concentrations of heavy metal in the soil near thermal power plants increase depending on the wind direction (with the spread of fly ash from the chimneys of the power plants), and heavy metal concentrations further away from the power plant decrease depending on the distance [11]. Rosenstein [12] reported that the levels of Pb, Cd and As heavy metals emitted from the power plant decreased to normal concentrations at a distance of 30 km from the power plant. Determining the presence of heavy metal pollution in agricultural areas is also important in determining the type of crop production to be carried out there [13]. Potential toxic elements such as Cu, Zn, Ni, Cd, Cr, Pb and Co are among the factors that cause pollution in agricultural areas and pose an increasingly dangerous threat [14, 15].

According to the Turkish Soil Pollution Control Regulation, the limit values of some heavy metals in soil are given in Table 1.1.

Table 1.1. Limit values of some heavy metals in soil according to the Turkish Soil Pollution Control Regulation [22].

Heavy Metals (Total)	Oven Dry Soil (mg kg ⁻¹)	Oven Dry Soil (mg kg ⁻¹)
	pH 5- 6	pH > 6
Cadmium (Cd)	1**	3**
Lead (Pb)	50**	300**
Cobalt (Co)	40**	-
Chromium (Cr)	100**	100**
Nickel (Ni)*	30**	75**

* If the pH value is greater than 7, the Ministry may increase the limit values by up to 50% in cases where it is not harmful to the environment and human health, especially groundwater.

** In areas where fodder crops are grown, these limit values may be allowed to be posted if it is proven by scientific studies that they are not harmful to the environment and human health.

Silopi thermal power plant is located in Şırnak province and has been operating since 2009 using asphaltite as fuel [16]. Asphaltite is a substance that separates from the oil deposit as a result of tectonic movements and settles in cracks and crevices around it and differentiates under the influence of pressure and temperature [17] Asphaltites have high ash contents containing metals such as Ni [18, 19]. Emissions from the power plant chimneys are likely to be dispersed throughout the region by various factors and then deposited on soils. This transport may increase the concentrations of some heavy metals (Cr, Ni, Cd, Co and Pb) that cause pollution in soils.

In this study, it was aimed to determine the plant-available concentrations of some heavy metals in soil samples collected at various distances and depths in areas where agriculture is intensively practiced around the Silopi thermal power plant in Şırnak province.

2. MATERIAL AND METHOD

2.1. Study Area

A large part of the southern and southwestern part of Silopi District, located between 37°31' north latitude and 42°28' east longitude in Şırnak province, is located in the Southeastern Anatolia Region, while the northern and northeastern lands are in the Eastern Anatolia Region [20]. The study was conducted in the Silopi Plain, which is located in the Southeastern Anatolia Region, where there are flat or nearly flat areas with high agricultural potential that may be affected by Silopi Thermal Power Plant emissions. The study was conducted in Çardaklı, Başverimli, Ortaköy, Atak, Bostancı, Çiftlik, Yeniköy, Yolağzı, Üçağaç villages, Şehit Harun Boy neighborhood and Keruh, Bozalan and Doruklu villages located between Cizre-Silopi borders. A total of 42 soil samples were taken from the study area in 7 different distance classes (D1: 9-11 km; D2: 11-14 km; D3: 14-17 km; D4: 17-20 km; D5:

20-23 km, D6: 23-26 km, D7: 26-29 km) and at 3 different points (21 soil samples) and 2 different depths (0-30 cm and 30-60 cm) in each distance class (Figure 2.1).

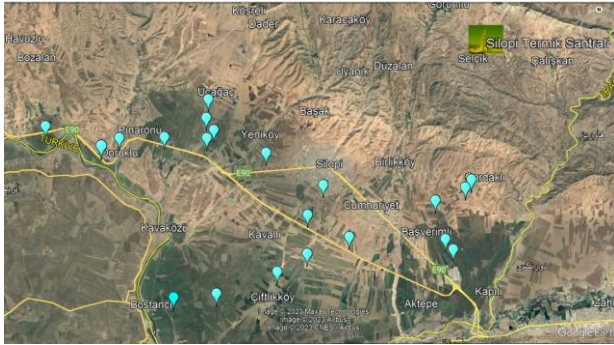


Figure 2.1. Location of the study area and the soil samples taken on the map

The prevalent wind directions of Silopi district of Şırnak province are shown in Figure 2.2.

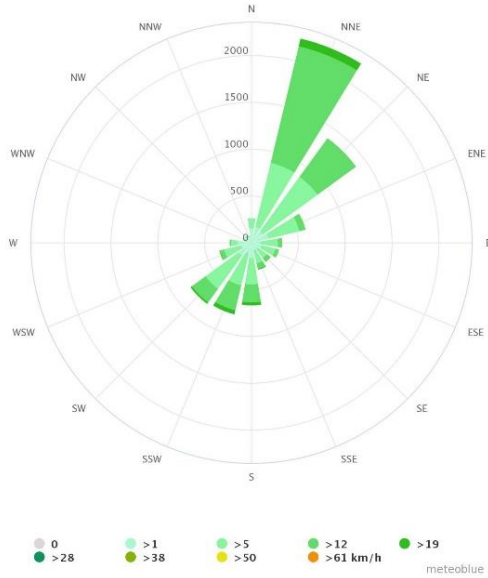


Figure 2.2. The wind vane of Silopi district of Şırnak province [21]

2.1.1. Some properties of the study area soils

The dominant texture class of the topsoil (0-30 cm) and subsoil (30-60 cm) of the study area is sandy clay loam. The pH is slightly and moderately alkaline and most of them do not have salinity problems. Organic matter content was classified as low and very low, while lime content was determined as high. While K, Ca, and Mg contents of the soils are high, Cu, Mn and Fe are sufficient. While phosphorus and Zn contents were sufficient in most of the soils, they were classified as low in some points where soil samples were taken.

2.2. Determination of Cr, Ni, Cd, Co and Pb Concentrations in Soils

Soil samples collected in plastic bags from the Silopi district of Şırnak province were brought to the laboratory and dried in the shade at air dry level. The dried soil samples were then crushed with a mallet sieved through a 2 mm steel sieve and prepared for analysis. The soil samples were prepared according to the DTPA method

developed by Lindsay & Norvell [23] to determine the concentrations of extractable Cr, Ni, Cd, Co and Pb in calcareous soils with near-neutral pH [24] and total Cr, Ni, Cd, Co and Pb concentrations were prepared by digestion with acid mixtures (8 ml HNO₃, 5 ml HCl, 1 ml HF and 5 ml H₃BO₃ mixture) in a microwave sample preparation set. Cr, Ni, Cd, Co and Pb in the filtrates prepared for elemental measurements were determined by atomic absorption spectrophotometer (AAS).

2.3. Statistical Analyses

In the study conducted to determine the effect of Silopi thermal power plant emissions on the soils of the agricultural area, analysis of variance was performed by using the 'JMP 13.2.0' program. Soil samples were divided into groups according to distance and depth from the power plant and the differences between the groups were compared using Tukey test for distance and LSD test for depth [25].

3. RESULTS AND DISCUSSION

Total heavy metal concentrations determined in the study soils (0-30 cm) are shown in Table 3.1.

Table 3.1. Total heavy metal (Cr, Ni, Cd, Co and Pb) concentrations of soils at different distances

Total Concentration (mg kg ⁻¹)	D1	D2	D3	D4	D5	D6	D7
Cr	48.3	49	40.6	45.6	30.6	30.6	39
Ni	98.3	96	90.3	90.3	68.3	68.3	83
Cd	0.6	0.7	0.6	0.6	0.7	0.7	0.6
Co	47.6	47.3	48	47.6	42.6	42.6	46
Pb	77.6	74	79.3	74	90.6	74	76.5

Extractable concentrations of Cr, Ni, Cd, Co and Pb were determined according to the distance and depth of the soil samples. The extractable concentrations of heavy metals (mg kg⁻¹) and the coordinates of the sampling points were used to create an elemental map as shown in Figure 3.1.

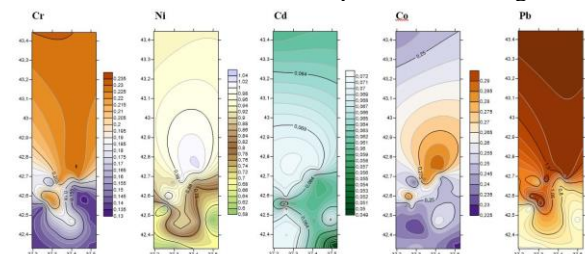


Figure 3.1. Elemental map of Cr, Ni, Cd, Co and Pb concentrations. The color changes in Figure 3.1 express the change in the concentrations of metals. Generally, dark areas represent the region where that metal is in higher concentration.

3.1. Chromium (Cr) Concentration

The mean values of the effect of different depths and distances on Cr concentration in soil samples taken from the vicinity of Silopi Thermal Power Plant are given in Table 3.2. The Cr concentrations between the distance points (D1-D7), 0-30 cm and 30-60 cm were statistically significant at $p < 0.01$ level. Average Cr concentrations of soil samples taken at different depths (0-30 and 30-60 cm) were found statistically non-significant.

Table 3.2. Effect of different depth and distance on Cr concentration of soils

Cr concentrations (mg kg ⁻¹)			
Distances	Depths		Mean
	0-30 cm	30-60 cm	
D1 (9-11 km)	0.23AB**	0.23A**	0.23a**
D2 (11-14 km)	0.25A	0.20AB	0.23a
D3 (14-17 km)	0.19AB	0.20AB	0.19b
D4 (17-20 km)	0.16AB	0.16B	0.16c
D5 (20-23 km)	0.14B	0.14B	0.14c
D6 (23-26 km)	0.13B	0.14B	0.14c
D7 (26-29 km)	0.15AB	0.14B	0.14c
Mean	0.18^{ns}	0.17	
LSD _(0.05)	Depth:-	Distance:0.03	CV(%):8.21

**: $p < 0.01$, ns: non significant

The Cr concentrations of soils at different distances from the power plant were ranked as $D1 = D2 > D3 > D4 = D5 = D6 = D7$. The highest Cr concentration (0.23 mg kg⁻¹) was measured at D1 and D2, the closest group to the power plant, while the lowest Cr concentration was measured at D5, D6 and D7, where the distance to the power plant increased. In general, Cr concentration decreased with increasing distance from the power plant. Cr concentration was higher in soil samples taken from the points closest to the power plant. Mehra et al. [26] reported that Cr concentration in soils around thermal power plants in India decreased with distance from the power plant. Turkmenoglu et al. [11] examined the distribution of Cr and some other heavy metals in the vicinity of thermal power plants about wind direction and distance and reported that Cr concentration decreased with distance in all directions and increased with distance from the power plant.

Cr concentration between soil samples taken from different depths was found to be statistically insignificant. It is thought that Cr pollution from the power plant is not effective on depth. None of the soil samples from the study area had total Cr (Table 3.1) concentrations (22-53 mg kg⁻¹) exceeding the permissible limit value (100 mg kg⁻¹) according to the Turkish Soil Pollution Control Regulation (Table 1.1).

3.2. Nickel (Ni) Concentration

The mean values of the effect of different depths and distances on Ni concentration in soil samples taken from the vicinity of Silopi Thermal Power Plant are given in Table 3.3. Pb concentrations of distance points (U1-U7), average depth, and 0-30 cm were statistically significant at $p < 0.01$. Ni concentrations of soil samples taken at 30-60 cm were statistically insignificant ($p < 0.01$).

Table 3.3. Effect of different depths and distances on Ni concentration of soils

Distances	Depths		Mean
	0-30 cm	30-60 cm	
D1 (9-11 km)	1.27A**	0.77 ^{ns}	1.02a**
D2 (11-14 km)	1.09AB	0.76	0.92ab
D3 (14-17 km)	1.05AB	0.69	0.87abc
D4 (17-20 km)	1.06AB	0.70	0.88abc
D5 (20-23 km)	0.83ABC	0.71	0.77abc
D6 (23-26 km)	0.68BC	0.71	0.70bc
D7 (26-29 km)	0.53C	0.63	0.58c
Mean	0.93a**	0.71b	
LSD _(0.05)	Depth:0.11	Distance:0.32	CV(%):20.83

**: $p < 0.01$, ns: non significant

The Ni concentrations of soils at different distances from the power plant were ranked as $D1 > D2 > D3 = D4 = D5 > D6 > D7$. The highest Ni concentration was determined in D1 (1.02 mg kg⁻¹), the closest group to the power plant, while the lowest Ni concentration was determined in D7 (0.58 mg kg⁻¹), the farthest point. Polat et al. [27] and Koseoglu et al. [28] reported that fly ash released as a result of coal combustion contains significant amounts of heavy metals with different mobility. In this study, it was observed that Ni concentration decreased as the distance from the thermal power plant decreased. With these results, it can be said that the Ni element originated from the power plant and was transported with fly ash. At the same time, Yilmaz et al. [1] reported in a study conducted in the Elbistan thermal power plant that the Ni content of the plants in the region, which they thought to be more polluted, was high and the Ni concentration decreased as they moved away from the power plant and that the fly ash had an effect on this pollution. Simsek et al. [29] determined the concentration of available Ni between 0.02-29.8 mg kg⁻¹ in a study conducted in Osmaniye agricultural areas. Haktanir et al. [30] reported that the extractable Ni content of agricultural and forest soils under the influence of Mugla-Yatagan thermal power plant emissions was between 0.24 mg kg⁻¹-1.65 mg kg⁻¹. The average DTPA-Ni content of surface soils under the influence of the Elbistan Thermal Power Plant was determined as 1.21 mg kg⁻¹ [31].

In the study, the Ni concentration of the topsoil (0-30 cm) was 0.93 mg kg⁻¹ higher than the Ni concentration of the subsoil (30-60 cm) (0.71 mg kg⁻¹). With these results, it can be said that the Ni concentration does not originate

from the parent material and that there is an external contribution. Akbay et al. [31] reported that the elements that are not mobile in the soil should decrease from the surface to the depth if there is pollution caused by the power plant and reported the DTPA-Ni concentration as 1.51 mg kg⁻¹; 1.18 mg kg⁻¹; 1.09 mg kg⁻¹ from top to bottom at three different depths in their study. Kabata-Pendias and Pendias [32] reported that in general, metals such as Ni, Cd, Cu, Hg, Pb, Zn and Cr are taken up by plants by adhering to the soil surface. Plants need trace amounts of nickel, but nickel has high mobility and can be easily taken up by plants in soils with high concentrations and may cause toxic effects [33, [34]. The total Ni concentration (56-102 mg kg⁻¹) of the soil samples taken from the study area (Table 3.1) did not exceed the permissible limit value (75 mg kg⁻¹), taking into account the Turkish Soil Pollution Control Regulation, which states that the ministry may increase the limit values up to 50% if the pH value is greater than 7 and it is not harmful to the environment and human health, especially groundwater (Table 1.1).

3.3. Cadmium (Cd) Concentration

The mean values of the effect of different depth and distance on Cd concentration in soil samples taken from the vicinity of Silopi Thermal Power Plant are given in Table 3.4. Cd concentrations between the distance points (D1-D7), 0-30 cm and 30-60 cm were not statistically significant. Average Cd concentrations of soil samples taken at different depths (0-30 and 30-60 cm) were found statistically non-significant.

Table 3.4. Effect of different depth and distance on Cd concentration of soils

Distances	Cd concentrations (mg kg ⁻¹)		
	Depths		
	0-30 cm	30-60 cm	Mean
D1 (9-11 km)	0.07 ^{ns}	0.07 ^{ns}	0.07^{ns}
D2 (11-14 km)	0.07	0.06	0.06
D3 (14-17 km)	0.07	0.05	0.06
D4 (17-20 km)	0.07	0.07	0.07
D5 (20-23 km)	0.07	0.06	0.06
D6 (23-26 km)	0.05	0.05	0.05
D7 (26-29 km)	0.07	0.07	0.07
Mean	0.07^{ns}	0.06	
LSD _(0.05)	Depth:-	Distance:-	CV(%):18.17

ns:non significant

It is thought that the Silopi thermal power plant does not affect the Cd concentration of soil samples both in terms of distance and depth. As seen in Table 3.4, the concentration of Cd available for uptake by plants varied between 0.05-0.07 mg kg⁻¹ in terms of both distance and depth, while the total Cd concentrations of the soil samples taken in Table 3.1 varied between 0.6-0.7 mg kg⁻¹. Although the power plant did not statistically affect the Cd content, both total Cd and the concentrations of Cd are

below the permissible limit value (3 mg kg⁻¹) according to the Turkish Soil Pollution Control Regulation (Table 1.1). Although the Cd concentration in world soils varies between 0.01-1.0 mg kg⁻¹, the average has been reported as 0.36 mg kg⁻¹ [35]. Mejstřík and Švácha [36] took soil and plant samples from 1, 5, 10, and 15 km distances from 3 different thermal power plants in Czechoslovakia for 7 years and investigated the distribution of Cd and some other heavy metals in the samples. Researchers reported that certain amounts of heavy metal accumulation were detected in the soil and plants around the 3 thermal power plants examined, but the source of this metal accumulation could not be determined with a 7-year monitoring period, and longer periods of investigation were required to determine whether this was due to emissions. Çancı [37] analyzed Pb, Cd and some other heavy metals in fly ash and bottom ash samples from the Seyitömer thermal power plant and soil samples in the vicinity of the power plant and compared the concentrations of soil samples with the upper limits determined for agricultural purposes in different countries and found that Cd and some other heavy metals were below the given values.

3.4. Cobalt (Co) Concentration

The mean values of the effect of different depths and distances on Co concentration in soil samples taken from the vicinity of Silopi Thermal Power Plant are given in Table 3.5. Co concentrations between the distance points (D1-D7), 0-30 cm and 30-60 cm were not statistically significant. Average Co concentrations of soil samples taken at different depths (0-30 and 30-60 cm) were found statistically non-significant.

Table 3.5. Effect of different depths and distances on Co concentration of soils

Distances	Co concentrations (mg kg ⁻¹)		
	Depths		
	0-30 cm	30-60 cm	Mean
D1 (9-11 km)	0.33 ^{ns}	0.25 ^{ns}	0.29^{ns}
D2 (11-14 km)	0.26	0.21	0.24
D3 (14-17 km)	0.27	0.25	0.26
D4 (17-20 km)	0.24	0.22	0.23
D5 (20-23 km)	0.26	0.25	0.25
D6 (23-26 km)	0.21	0.25	0.23
D7 (26-29 km)	0.26	0.23	0.25
Mean	0.26^{ns}	0.24	
LSD _(0.05)	Depth:-	Distance:-	CV(%):15.38

ns:non significant

Sushil and Batra [38] reported that total Cr and Zn content in fly ash and total Mn content in bottom ash were the highest while total Co concentration was the lowest in both. In this study, it is clearly seen that the change in distance does not affect the transport of Co at a statistically significant level. This is related to the fact that heavy metals of lower mass can be transported and precipitated by fly ash, whereas elements of higher mass, such as Co, can precipitate immediately after combustion,

thus enriching the bottom ash in Co [38]. The total Co concentration (41-51 mg kg⁻¹) of soil samples from the study area (Table 3.1) did not exceed the permissible limit value considering the Soil Pollution Control Regulation of Turkey (Table 1.1).

3.5. Lead (Pb) Concentration

The mean values of the effect of different depths and distances on Pb concentration in soil samples taken from the environment of Silopi Thermal Power Plant are given in Table 3.6. Pb concentrations between the distance points (D1-D7) were statistically significant at p<0.01 level. Average Pb concentrations of soil samples taken at different depths (0-30 and 30-60 cm) were found statistically significant (p<0.01) while the 0-30 cm and 30-60 cm were found non-significant.

Table 3.6. Effect of different depths and distances on Pb concentration of soils

Distances	Pb concentrations (mg kg ⁻¹)		Mean
	Depths		
	0-30 cm	30-60 cm	
D1 (9-11 km)	1.53 ^{ns}	1.25 ^{ns}	1.39d**
D2 (11-14 km)	1.43	1.44	1.43cd
D3 (14-17 km)	1.47	1.48	1.47bcd
D4 (17-20 km)	1.72	1.61	1.67b
D5 (20-23 km)	1.32	1.27	1.30d
D6 (23-26 km)	1.63	1.55	1.59bc
D7 (26-29 km)	2.03	1.79	1.91a
Mean	1.59a**	1.48b	
LSD _(0.05)	Depth:0.07	Distance:0.20	CV(%):6.34

**p<0.01, ns:non significant

The Pb concentrations of the soils at different distances from the power plant were ranked as D7>D4>D6>D3>D2>D1=D5. The highest Pb concentration (1.91 mg kg⁻¹) was measured at D7, the furthest group from the power plant, while the lowest Pb concentration was measured at D1 and D5. There was no linear increase or decrease in Pb concentration with increasing distance from the power plant, which can be attributed to the location of the sampling points. Habur Border Gate is located in the Silopi district, so there is heavy vehicle traffic on the highway. Especially since the points in the D7 group are very close to the main road, the Pb elevation may have been caused by this. Seven et al. [39] reported that the extractable Pb concentration in the soil was at the level of 0.05-5 mg kg⁻¹ and that most of the lead causing environmental pollution was caused by tetra ethyl lead resulting from the combustion of gasoline used in motor vehicles. Haktanır et al. [30] determined that the extractable Pb values in the soils of power plant emissions in their study were the lowest 0.09 mg kg⁻¹ and the highest 1.04 mg kg⁻¹ and stated that these values were too low to talk about Pb pollution.

Pb concentration in soil samples taken from different depths decreases with increasing depth. The Pb concentration in the topsoil (0-30 cm) was 1.59 mg kg⁻¹

while it was 1.48 mg kg⁻¹ in the subsoil. Turer et al. [40] in their study on heavy metal contents in the soils around the highway, concluded that heavy metals such as Pb were higher, especially in the topsoil at 0-15 cm depth and that the heavy metal concentration decreased with increasing depth. Akbay et al. [31] found that DTPA-Pb concentration decreased from top to bottom as 1.04 mg kg⁻¹; 0.99 mg kg⁻¹; 0.88 mg kg⁻¹ at three different depths. The total Pb concentration (69-93 mg kg⁻¹) (Table 3.1) of the soil samples taken from the study area did not exceed the permissible limit value (300 mg kg⁻¹) according to the Turkish Soil Pollution Control Regulation (Table 1.1).

4. CONCLUSION

In this study, the variation of plant-available heavy metals such as Pb, Ni, Co, Cr and Cd in the soils of the Thermal Power Plant, which was established very close to the Silopi district where agriculture is intensively practiced, with the distance from the power plant and the depth of the soils was investigated. In this study, the wind direction (Figure 2.2) was not taken into consideration due to safety precautions in soil sampling and the areas where agriculture is intensively practiced were preferred. Among the elements examined, Ni and Cr concentrations decreased significantly at p<0.01 level as the distance from the thermal power plant, confirming the hypothesis of fly ash origin. However, Pb and Ni concentrations were higher in the topsoil (0-30 cm). It is possible to say that these elements are not sourced from the bedrock but are provided by an external contribution. The total concentrations of heavy metals were found to be below the total limit values accepted in soils with pH>6 according to the Regulation on Soil Pollution Control in Turkey. Although the total values of heavy metals measured in the soil were found to be below the limit values, it should be determined by new studies whether there is a transition from the concentration in the soil to the plant and if so, at what level. Although thermal power plants are one of the most talked about issues with their effect on soil pollution today, studies on this issue are very limited in the Silopi district, especially in agricultural areas. For this reason, it is recommended to conduct more comprehensive and long-term studies to determine the heavy metal content of soils and whether heavy metals are added to the food chain by the emissions of Silopi Thermal Power Plant, which has an important place in energy production in the region. The values obtained from the sampling points in this study will constitute a database for monitoring the changes that will occur in the soils of the region.

Acknowledgment

This study was prepared by making additional analyzes for the project titled "Nutrient Element Status of Agricultural Lands in Şırnak-Silopi District and Its Relationship with Some Soil Properties". The study was supported by Şırnak University BAP unit (Project No: 2022.FNAP.05.01.01). We would like to thank Şırnak University BAP unit for their support.

REFERENCES

- [1] Yilmaz K, Inac S, Dikici H, Reyhanli AC. The Effects of A Coal Power Plant on The Environment and Wildlife in Southeastern Turkey. *Journal of Environmental Biology*. 2004;25(4):423-429.
- [2] ETBK. Electricity Republic of Turkey Ministry of Energy and Natural Resourcesenerji ;2020 (15.09.2023). Available from:gov.tr/tr-TR/Sayfalar/Elektrik”.
- [3] Uzun A, Arslan F. Social Acceptance of Thermal Power Plant Projects: Pasakoy (Balıkesir) Thermal Power Plant. *Balıkesir University The Journal of Social Sciences Institute*. 2018;21(40): 27-52.
- [4] Llorens JF, Fernandez-Turiel JL, Querol X. The fate of trace elements in a large coal-fired power plant. *Environmental Geology*. 2001;40(4-5):409-416.
- [5] Goodarzi F, Huggins FE, Sanei H. Assessment of elements, speciation of As, Cr, Ni and emitted Hg for a Canadian power plant burning bituminous coal. *International Journal of Coal Geology*. 2008;74(1):1-12.
- [6] Akbay C, Bilgic A. The Opinions of the Community on the Effects of Thermal Power Plants on the Environment and Human Health in Afsin and Elbistan Districts. *KSU Journal of Agriculture and Nature*. 2020; 23(6):1587-1597.
- [7] Anonymous. Environmental Impacts of Thermal Power Plants and Measures to be Taken; 2020 (15.09.2023). Available from: <https://www.akradyo.net/5790315496,87115,6,Termik-santrallerin-.aspx>.
- [8] Pacyna, J. M. Atmospheric emissions of arsenic, cadmium, lead and mercury from high temperature processes in power generation and industry." *Lead, mercury, cadmium and arsenic in the environment*. 1987;23:69.
- [9] Karaca A, Türkmen C, Arcaç S, Haktanir K, Topcuoglu B, Yıldız H. The Determination of the Effect of Cayirhan Coal-Fired Power Plant Emission on Heavy Metals and Sulphur Contents of Regional Soils. *Ankara University Journal of Environmental Sciences*. 2009;1(1).
- [10] Karaca A. Effects Of Afsin-Elbistan Power Plant Emissions On The Physical, Chemical And Biological Properties Of Nearby Soils. *Pamukkale University Engineering College Journal of Engineering Sciences*. 2001;7(1):95-102.
- [11] Turkmenoglu M, Mert BA, Anil M. Investigation of Fly Ash Originated Heavy Metal Distribution in the Close Surroundings of Afsin Elbistan-A Thermal Power Plant with Gaussian Semivariogram Model. *Bayburt University Journal of Science*. 2022; 5(2):215-222
- [12] Rosenstein JS. Sanitary toxicological assesment of low concentrations of As₂O₃ in the athmosphere. *Gg Sanit*. 1970;35(1):15-20.
- [13] Pandey J, Pandey U. Accumulation of heavy metals in dietary vegetables and cultivated soil horizon in organic farming system in relation to atmospheric deposition in a seasonally dry tropical region of India. *Environmental Monitoring and Assessment*. 2009;148(1-4):61-74.
- [14] Xu Y, Dai S, Meng K, Wang Y, Ren W, Zhao L et al. Occurrence and risk assessment of potentially toxic elements and typical organic pollutants in contaminated rural soils. *Science of the Total Environment*. 2018;630:618-629.
- [15] Kirpik M, Buyuk G, Memet İ, Çelik A. The heavy metal content of some herbal plants on the roadside of Adana-Gaziantep highway. *Journal of Agricultural Faculty of Gaziosmanpasa University (JAFAG)*. 2017;34(1):129-136.
- [16] Anonymous.<https://www.cinergroup.com.tr/enerji-madenci-lik/silopi-elektrik-uretim;2023a>. Accessed On: 20.09.2023.
- [17] Demirci S, Sivrikaya O, Vapur H. Asphaltite as Energy Source; Formation, Content, Turkey Reserves, Cleaning. *Omer Halisdemir University Journal of Engineering Sciences*. 2019; 8(1), 312-325.
- [18] Lebkuchner RF, Orhun F, Wolf M. Asphaltic substances in southeastern Turkey. *AAPG Bulletin*, 1972; 56(10): 1939-1964.
- [19] Saltoglu T, Akyuz T, Alparslan E. Quantitative determination of molybdenum, nickel, vanadium and titanium in the asphaltites and asphaltite ashes by XRF-spectroscopy. *Bulletin of the Mineral Research and Exploration Institute of Turkey*. 1978; 91: 89-93.
- [20] Kosen İ. Functional Characteristics of Silopi City (MSc). Karabuk University, Department of Geography, Karabuk, Turkey; 2019.
- [21] Anonymous.https://www.meteoblue.com/en/weather/historyclimate/climatemodelled/silopi_turkey_300797;2023b. Accessed On: 21.09.2023.
- [22] TKKY. T.C. Official Gazette, Turkish Soil Pollution Control Regulation (TKKY), July 3, No: 5403, Prime Ministry Press Office, Ankara; 2005.
- [23] Lindsay WL, Norvell WA. Development of A DTPA Soil Test for Zinc, Iron, Manganese and Copper. *Soil Science Society of American Proceeding*. 1978;42:421-428. <https://doi.org/10.2136/sssaj1978.03615995004200030009x>
- [24] Hossner LR. Dissolution for Total Elemental Analysis. 3rd Edition. *Methods of Soil Analysis. Part 3, Chemical Methods*, D.L. Sparks, 46-64. Madison, WI: Soil Science Society of America and American Society of Agronomy; 1996.
- [25] SASS. Sas user's guide: Statistic. statistical anal. systems institute inc.;1999.
- [26] Mehra A, Farago ME, Banerjee DK. Impact of fly ash from coal-fired power stations in Delhi, with particular reference to metal contamination. *Environmental Monitoring and Assessment*. 1998;50:15-35.
- [27] Polat M, Guler E, Akar G, Mordogan H, Ipekoglu Ü, Cohen HJ. Neutralization of acid mine drainage by Turkish lignitic fly ashes: role of organic additives in the fixation of toxic elements, *J. Chem. Technol. Biotechnol*. 2002;(77):372–376.
- [28] Koseoglu K, Polat M, Polat H. Encapsulating fly ash and acidic process waste water in brick

- structure. *Journal of hazardous materials*. 2010;176(1-3):957-964.
- [29] Simsek T, Kalkanci N, Büyük G. Determination of heavy metal pollution levels in agricultural soils: the case of Osmaniye. *Mustafa Kemal University Journal of Agricultural Sciences*. 2021; 26 (1):106-116.
- [30] Haktanir K, Ok SS, Karaca A, Arcak S, Cimen F, Topcuoglu B. et al. Generating Pollution Database of the Agricultural and Forest Soils Affected by Mugla-Yatagan Coal-Fired Power Plant Emissions and Investigating Vegetation Effects. *Ankara University Journal of Environmental Sciences*. 2010;2(1):13-30.
- [31] Akbay C, Dikici H, Ari H, Bilgic A. 2011. Economic analysis of environmental pollution caused by Afsin-Elbistan thermal power plant. TUBİTAK TAGOV, 109R027.
- [32] Kabata-Pendias A, Pendias H. *Biochemistry of Trace Elements*, Warszawa, PWN; 1993.
- [33] Khan MR, Khan MM. Effect of varying concentration of nickel and cobalt on the plant growth and yield of chickpea. *Australian Journal of Basic and Applied Sciences*. 2010; 4(6):1036-1046.
- [34] Dartan G, Toroz İ. Investigation of Heavy Metal Pollution on Agricultural Lands in the South of Marmara Region. *Marmara University Journal of Science*. 2013; 25(1):24-40.
- [35] Kubier, A., Wilkin, R. T., & Pichler, T. Cadmium in soils and groundwater: a review. *Applied Geochemistry*. 2019; 108, 104388.
- [36] Mejstřík, V., & Švácha, J. Concentrations of Co, Cd, Cr, Ni and Zn in crop plants cultivated in the vicinity of coal-fired power plants. *Science of the total environment*. 1988; 72, 57-67.
- [37] Çancı, B. Geochemical assessment of environmental effects of fly ash from Seyitömer (Kütahya) thermal power plant (Master's thesis) Middle East Technical University; 1998.
- [38] Sushil S, Batra VS. Analysis of fly ash heavy metal content and disposal in three thermal power plants in India. *Fuel*. 2006; 85(17-18):2676-2679.
- [39] Seven T, Busra C, Darende BN, Sevda O. Heavy Metals Pollution in Air and Soil. *National Research Journal of Environmental Sciences*. 2018; 1(2): 91-103.
- [40] Turer D, Maynard JB, Sansalone JJ. Heavy metal contamination in soils of urban highways comparison between runoff and soil concentrations at Cincinnati, Ohio. *Water, Air, and Soil Pollution*. 2001; 132: 293-314.

Forage Yield and Quality Characteristics of Winter Legume / Grass Mixtures Harvested at Different Phenological Stages

Emre KARA^{1*} , Mustafa SÜRME¹ 

¹ Aydın Adnan Menderes University, Faculty of Agriculture, Department of Field Crops, Aydın, Türkiye
Emre KARA ORCID No: 0000-0002-5535-8398
Mustafa SÜRME ORCID No: 0000-0001-9748-618X

*Corresponding author: emre.kara@adu.edu.tr

(Received: 25.09.2023, Accepted: 12.12.2023, Online Publication: 28.12.2023)

Keywords

Winter forage crops, Annual forage mixture, Forage quality, Harvest time

Abstract: Winter forage crop mixtures are important sources of quality forage as well as the benefits they bring to the soil and the main crop. In regions with year-round production, leaving the soil fallow during the winter months and preferring maize-maize or cotton-cotton production model may negatively affect the nutrient balance in the soil. For this purpose, forage yield and quality characteristics of 12 different winter forage crop applications (4 pure and 8 mixtures) were investigated between 2014-2016 in Büyük Menderes basin (Aydın / Türkiye). The experiment was designed according to the split-plot in randomized blocks and harvest were carried out in 2 different phenological periods with 4 replications. Herbage yield (kg da⁻¹), ADF (%), NDF (%), ADL (%), crude protein ratio (%), crude protein yield (kg da⁻¹) and relative feed value averages were measured. According to the results obtained from the experiment, there are differences between crude protein yield and relative feed values. When analyzed in line with the production purpose, 75% forage pea + 25% oat mixtures stand out in terms of crude protein yield, while 55% forage pea + 45% annual ryegrass stands out in terms of relative feed value. Due to the changes in harvest times depending on the characteristics, it is thought that it would be ideal to perform harvest operations between 50%-100% flowering.

Farklı Fenolojik Dönemlerde Biçilen Kışlık Baklagil / Buğdaygil Karışımlarının Yem Verim ve Kalite Özellikleri

Anahtar Kelimeler

Kışlık ara ürün yem bitkileri, Tek yıllık yem bitkileri karışımları, Yem kalitesi, biçim zamanı

Öz: Kışlık yem bitkileri karışımları kaliteli kaba yem kaynağı olmaları yanı sıra toprağa ve ana ürüne kazandırdıkları ile önemli kaynaklardır. Yıl boyu üretim yapılan bölgelerde kış aylarında toprağın nadasa bırakılıp mısır-mısır ya da pamuk-pamuk üretim modelinin tercih edilmesi toprakta bitki besin elementi dengesini olumsuz yönde etkileyebilmektedir. Bu amaçla Büyük Menderes havzasında (Aydın / Türkiye) 2014-2016 yılları arasında 4 saf ve 8 karışım olmak üzere 12 farklı kışlık ara ürün yem bitkileri uygulamasının yem verim ve kalite özellikleri incelenmiştir. Deneme tesadüf bloklarında bölünmüş parsellere göre 4 tekerrürlü olarak tasarlanmış ve 2 farklı fenolojik dönemde biçim işlemleri gerçekleştirilmiştir. Denemede kuru ot verimi (kg da⁻¹), ADF(%), NDF(%), ADL(%), ham protein oranı (%) değerleri ölçülürken ham protein verimi (kg da⁻¹) ve nispi yem değeri ortalamaları hesaplanmıştır. Denemeden elde edilen neticelere göre ham protein verimi ve nispi yem değerleri arasında farklılıklar söz konusudur. Üretim amacı doğrultusunda incelendiğinde ham protein verimi açısından %75 yem bezelyesi + %25 yulaf karışımları öne çıkarken nispi yem değeri açısından %55 yem bezelyesi + %45 tek yıllık çim öne çıkmaktadır. Biçim zamanlarında özelliklere bağlı olarak yaşanan değişimlerden dolayı %50-%100 çiçeklenme arasında biçim işlemlerinin gerçekleştirilmesinin ideal olacağı düşünülmektedir.

1. INTRODUCTION

Food products derived from livestock have become very important in meeting the increasing demand for food worldwide. With the increasing population in developing countries, meat demand has increased by 5-6% and dairy demand by 3.4-3.8% compared to the end of the 20th century [1]. As a result of these data, it is clear that feeding livestock will be one of the main issues of our future with the increasing human population. One of the main objectives of livestock feeding management is to provide the forage of sufficient quality, high efficiency and at the same time cheap. While species selection is a factor that directly affects feed quality, the effect of area selection on feed quality by itself is low [2]. In addition to being included in the cropping pattern, forage crops, which contain the nutrients necessary for the gastric microflora of livestock in a sufficient and balanced ratio, contain the nutrients necessary for microorganisms that help the digestive systems of livestock to function more regularly [3]. In addition to being a source of quality roughage, legume forage crops make elemental nitrogen useful to the plant thanks to *Rhizobium* bacteria [4].

In Türkiye, forage production is quite inadequate according to the livestock population [5] and our dry forage production, which can be qualified as high quality, is around 4 million tons. Field cultivation of forage crops share was 1.6% in the early 2000s, to 8.2% in 2010 with the impact of subsidies and in 2019, it increased to 13%. Although the Ministry of Agriculture and Forestry of the Republic of Türkiye provides subsidies for forage crops today, production has not reached the desired point. It is clear that the subsidies have increased the cultivation areas of forage crops [6]. Although there are approximately 17.220.903 livestock in Türkiye in 2018, we are in a very insufficient situation in terms of animal product production. In today's conditions, it is not possible to close the forage deficit by growing traditional forage crops as the main crop and utilizing rangeland-pasture areas.

In Aegean region, wheat and cotton are the traditional main crops in the field. In the form of cotton-cotton cultivation, the field can remain empty for 5-6 months in winter and in wheat-wheat cultivation, the field can remain empty for 4-5 months in summer [7]. Also, in terms of land use efficiency, especially in countries bordering the Mediterranean Sea, mixed cultivation of annual legume and cereal forage crops has been adopted more than growing them separately today [8]. In this cropping pattern, cropping areas are better utilized, and the legumes in the mixture play a role in increasing soil fertility in a way to meets the needs of the cereals with the nitrogen they release into the soil. Due to this effect of legumes, the use of pesticides and chemical fertilizers is reduced and the damage caused by agriculture to the environment is minimized. In addition to reducing diseases and pests, intercropping increases forage quality and yield as it increases crude protein yield [3,9,10].

One of the most important legumes that can be used as a winter forage crop in mixtures is common vetch (*Vicia sativa* L.), which we are at the forefront of the world in

terms of production and is an important forage crop in Türkiye. Another one is forage pea (*Pisum sativum* ssp. *arvense* (L.) Asch.), whose production and importance are increasing today. The species that can be used in mixtures are oat (*Avena sativa* L.), which can provide good yield and is easy to produce, and annual ryegrass (*Lolium multiflorum* Lam.), which is known to protect the soil with its dense root structure as well as its ability to dry quickly due to its thin stems. These crops can be planted in mixtures and have high yield potential [35].

This study was conducted to determine the most suitable forage crop mixtures for winter cover crop in Aydın province and similar ecologies. It is thought that the findings obtained from the study can be an example for agricultural enterprises in this region and agricultural organizations and researchers working on the subject can benefit from these results.

2. MATERIAL AND METHOD

2.1. Material

Forage pea (*Pisum sativum* ssp. *arvense* (L.) Asch. cv. Ürünlü), common vetch (*Vicia sativa* L. cv. Alper), oat (*Avena sativa* L. cv. Sari) and annual ryegrass (*Lolium multiflorum* Lam. cv. Caramba) were used as mixture materials.

2.2. Method

The research was conducted in the experimental fields of Aydın Adnan Menderes University, Faculty of Agriculture (37° 45' 51" N, 27° 45' 32" E, 27 m altitude) during the 2014-2016 winter production seasons. Soil analysis of the experimental field was carried out in the laboratories of the Department of Soil Science and Plant Nutrition, Faculty of Agriculture, Aydın Adnan Menderes University. Soil texture was determined by Bouyoucos hydrometer method [11]. Soil pH was measured by pH meter according to Richards [12]. Phosphorus content was calculated calorimetrically. Potassium content was measured by flame photometer method as described by Richards [12]. Organic matter content was determined by wet burning and organic carbon value was multiplied by Van Benmelen factor [13].

According to the results of the soil sample analysis, the soil with high sand content had a loamy texture and showed an alkaline characteristic with a pH of 8.10. Phosphorus, which is a macronutrient element, was high in the soils, which were also observed to be low in terms of organic matter. When analyzed in terms of micronutrients, it is seen that K, Na, Fe, are high, Mg is very high, but Ca mineral are sufficient (Table 1.).

Table 1 Analysis results of the experimental area soil (0-30 cm)

P	K	Ca	Mg	Na	Fe	pH	Total Salt	Organic Matter
ppm	ppm	ppm	ppm	ppm	ppm		(%)	(%)
19	903	274	116	46	8.32	8.1	0.009	1.20
		0	4			6	3	

According to the averages of climate data of the experiment area during the production period and long-term climate data, the first-year temperature values are similar to the long-term data except December. However, in the second year temperatures were fluctuating and higher than the first year (Figure 1). According to the precipitation data, the higher and irregular precipitation of the first year compared to the long-term data caused negative effects on the plants during the development

period. In the second year, there was no precipitation data collected in December, but the precipitation during the vegetation period did not cause any obvious negative effects on development. The fact that differences were observed in both years compared to the long-term data was seen as a sign of how the mixtures may react under extreme conditions.

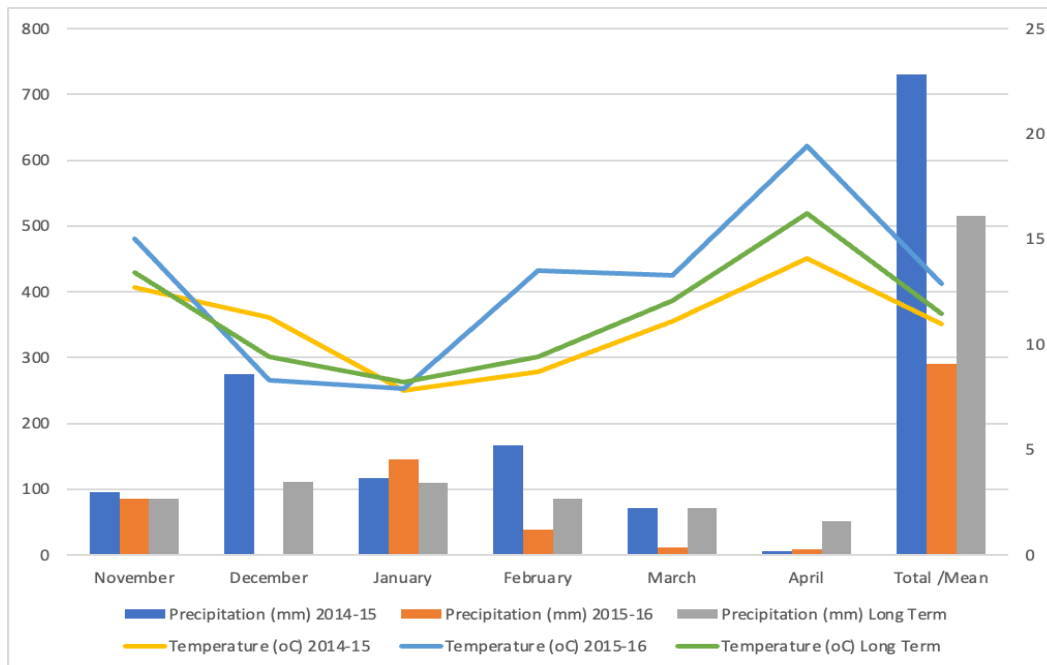


Figure 1. Climatic data during the experiment and according to long-term averages

Sowing was done manually with lines in November in both years. In the experiment, a plot of $2\text{m} \times 5\text{m} = 10\text{m}^2$ was planted in 10 rows with 4 replications. In order to control weeds, a gap of 2 meters was left between blocks and 50 cm between plots. There were 12 treatments as 4 pure (100% forage pea, 100% common vetch, 100% oat, 100% annual ryegrass) and 8 legume:grass mixtures (75:25, 55:45). The research was designed according to the randomized block design with split plots. In pure plots, 12 kg da^{-1} forage pea, 12 kg da^{-1} common vetch, 18 kg da^{-1} oat, and 2 kg da^{-1} annual ryegrass were used [14,15]. Before sowing, legumes were inoculated with *Rhizobium* bacteria in the evening hours in an environment without high light, and according to the results of soil analysis, 3 kg da^{-1} pure nitrogen and 7 kg da^{-1} pure phosphorus were applied as base fertilizer. Forage pea, common vetch and their mixtures were harvested at 50% and 100% flowering time of legumes. During this period, oats were in Zadoks 73 (milking season) and annual ryegrass was in full flowering. Herbage yield was measured after both harvest times.

Herbage yield (kg da^{-1}) was measured by fan drying oven (Mikrotest, MST, Ankara, Türkiye) at 70°C until the weight was fixed [16]. The dried samples were ground in a mill passed through a 1 mm screen. The crude protein ratio (%) of the samples taken from the experiment was measured with Kjeldahl method according to AOAC

[17]; NDF, ADF and ADL contents (%) were measured (ANKOM A200, Macedon, NY, USA) according to Van Soest et al. [18]. The crude protein yield (kg da^{-1}) and relative feed value were calculated by the obtained data by following the procedures of Horrocks and Vallentine [4].

To compare values, the analysis of variance was performed with the LSD multiple comparison method using the 'agricolae' package [19] in R Studio (V4.1.2). Correlogram was created in R Studio using the 'metan' package [20]. Heat map was made in R Studio using the heatmap.2 command within the 'gplots' package [21].

3. RESULTS AND DISCUSSION

According to the data obtained from the experiment, statistically significant treatments and interactions are presented in Table 2. According to these data, while the mixture treatments have statistically significant differences in terms of all the examined traits, the same is also seen in the interaction with harvest time.

Table 2. Sources of variation in the experiment and statistical significance levels of interactions between each other

	HY	ADF	NDF	ADL	CPR	CPY	RFV
Year (Y)	**	**	**	ns	ns	**	**
Mixtures (Mx)	**	**	**	**	**	**	**
Harvest (Har)	**	ns	**	ns	ns	**	**
Y x Mx	**	**	*	**	ns	**	**
Y x Har	**	ns	**	ns	**	**	**
Mx x Har	**	**	**	**	**	**	**
Y x Mx x Har	**	*	**	**	**	**	**

*: P≤0.05 **: P≤0.01 ns: non-significant

HY: Herbage yield; CPR: Crude Protein Ratio; CPY: Crude Protein Yield; RFV: Relative Feed Value;

While there was a difference between the two years in terms of herbage yield values, the average of the values obtained in the second year was higher with 469.64 kg da⁻¹. In terms of harvesting time, it was observed that the harvest at 100% flowering period was in the lead with 437.71 kg da⁻¹. Among the treatments, the application with the highest herbage yield was found in pure oat application with 578.89 kg da⁻¹, while 75% common vetch + 25% annual ryegrass had the highest value among the mixtures (Appendix A,B). Kocer and Albayrak [22] reported that in a mixture trial with forage pea, oat and barley, oat had the highest yield in terms of herbage yield and in mixtures, forage pea - oat mixtures had high values. In some studies, it was stated that pure sowing had higher values than mixtures [23,24], while in some others mixtures had higher values [25,26]. In addition, Aşçı et. al. [27] stated that harvesting in phenologically later periods according to the harvest time will provide yield increase. The reason for the change between the years and

the increase in yield in the second year is thought to be the ponding of water in the area where cultivation was carried out in the first year due to irregular precipitation during the vegetation period. Especially in legumes, waterlogging can reduce photosynthesis, plant growth, grain yield, the formation, function and survival of nodules, biological nitrogen fixation, and cause plant death during or some weeks after the end of waterlogging [28].

When ADF averages were analyzed, statistically significant differences were found between years. In the first year of the experiment, higher ADF value was obtained with 36.49%. There was no difference between harvest times. Among the treatments, the highest values were observed in %55CV %45AR, %55CV %45O, %75FP %25AR, and pure common vetch treatments, while the lowest value was obtained from pure annual ryegrass (Table 3).

Table 3. Mean values of Herbage yield and ADF parameters for year, time of harvest and mixture values

	Herbage yield (kg da⁻¹)			ADF (%)		
	1st Harvest	2nd Harvest	Mean	1st Harvest	2nd Harvest	Mean
Years						
2015	346.22 B			36.49 A		
2016	469.64 A			34.87 B		
Mixtures						
%100 FP	362.70	320.49	341.60 F	34.87	35.84	35.36 CF
%100 CV	345.25	382.26	363.76 EF	37.58	36.30	36.94 AC
%100 Oat	598.16	559.61	578.89 A	33.54	35.99	34.76 EF
%100 AR	389.68	507.69	448.69 C	32.53	33.11	32.82 G
%75FP %25O	534.22	533.68	533.95 B	34.10	36.06	35.08 DF
%55FP %45O	226.95	336.53	281.74 G	32.27	35.42	33.85 FG
%75FP %25AR	279.20	365.45	322.33 FG	36.60	36.74	36.67 AC
%55FP %45AR	315.40	391.13	353.27 EF	33.68	34.50	34.09 FG
%75CV %25O	371.23	461.84	416.54 CD	34.09	38.68	36.38 BD
%55CV %45O	360.15	422.70	391.43 DE	37.06	38.43	37.74 AB
%75CV %25AR	437.50	459.23	448.37 C	37.02	35.50	36.26 BE
%55CV %45AR	317.47	511.86	414.67 CD	41.91	34.42	38.16 A
Mean	378.16 B	437.71 A		35.44	35.92	

Table 4. shows that there were significant differences between harvest time and mixture treatments according to NDF averages. 46.89% value was lower in the first harvest time with 50% flowering than in the second harvest time. There was also a change in NDF values between years. Among all forage crops and mixtures, the highest NDF was found in pure oat with 53.95%. The lowest values were in %100 FP, %55FP, %45AR, %75CV, %25AR treatments. While it was concluded that the time of harvest and years did not cause significant differences in terms of ADL, the lowest value among the treatments was observed in pure oat treatment. Alatrürk et.

al. [29] stated that legumes were lower in terms of ADF, NDF and ADL. It was stated that legumes should be lower because they contain less fiber than grass. Although these were the expected results, in terms of ADF and ADL contents, legume and grass values were similar to each other. In terms of NDF, legumes were lower. This situation was thought to be due to competition between plant species. Sohail et. al. [30] similarly obtained lower values for legumes and their mixtures.

Table 4. Mean values of NDF and ADL parameters for year, time of harvest and mixture

	NDF (%)			ADL (%)		
	1st Harvest	2nd Harvest	Mean	1st Harvest	2nd Harvest	Mean
Years						
2015	49.84 A			7.63		
2016	45.61 B			7.86		
Mixtures						
%100 FP	44.85	43.45	44.15 F	9.76	8.81	9.28 A
%100 CV	39.72	41.07	40.39 G	7.44	9.26	8.35 BC
%100 Oat	52.67	55.22	53.95 A	5.79	5.69	5.74 F
%100 AR	49.50	46.85	48.18 CE	4.73	4.44	4.59 G
%75FP %25O	48.15	52.24	50.20 C	10.51	7.82	9.17 A
%55FP %45O	48.05	52.44	50.25 BC	6.75	6.49	6.62 E
%75FP %25AR	47.43	47.45	47.44 DE	8.95	8.28	8.62 AB
%55FP %45AR	42.60	47.81	45.20 F	8.49	8.08	8.28 BC
%75CV %25O	49.96	49.26	49.61 CD	6.62	7.69	7.15 DE
%55CV %45O	49.31	55.56	52.43 AB	6.44	8.91	7.67 CD
%75CV %25AR	41.23	48.24	44.73 F	8.44	9.22	8.83 AB
%55CV %45AR	49.17	43.22	46.19 EF	8.74	8.55	8.64 AB
Mean	46.89 B	48.57 A		7.72	7.77	

The mean values of crude protein ratio and crude protein yield, which are important quality criteria in forage crops, are given in Table 5. It is seen that harvest time and years did not cause significant differences among forage crops mixtures in crude protein ratio averages. The highest values among the treatments were found in the mixtures including common vetch and common vetch. In terms of crude protein yield, it was observed that there were statistically significant differences between the years and

the time of harvest depending on the herbage yield, while an increase in crude protein ratio could be detected as the phenological period progressed. The highest value among the mixture treatments was obtained from 75% common vetch + 25% oat with 103.74 kg da⁻¹. In terms of protein values, legumes have higher values than grasses. This has also been reported in some studies [31,32].

Table 5. Mean values of crude protein ratio and crude protein yield parameters for year, harvest time and mixture

	Crude Protein Ratio (%)			Crude Protein Yield (kg da ⁻¹)		
	1st Harvest	2nd Harvest	Mean	1st Harvest	2nd Harvest	Mean
Years						
2015	18.35			60.42 B		
2016	18.32			85.68 A		
Mixtures						
%100 FP	19.83	18.53	19.18 C	71.91	57.57	64.74 CD
%100 CV	24.16	24.51	24.34 A	78.44	96.84	87.64 B
%100 Oat	11.84	12.09	11.96 F	68.43	68.60	68.52 CD
%100 AR	14.96	12.46	13.71 E	57.60	66.19	61.89 D
%75FP %25O	18.83	20.03	19.4 C	105.79	101.70	103.74 A
%55FP %45O	16.09	16.51	16.30 D	38.13	52.23	45.18 E
%75FP %25AR	19.64	20.44	20.04 BC	50.76	79.31	65.04 CD
%55FP %45AR	18.85	21.61	20.23 BC	63.66	79.42	71.54 C
%75CV %25O	17.16	16.60	16.88 D	69.04	68.37	68.70 CD
%55CV %45O	16.70	16.45	16.57 D	65.70	62.34	64.02 D
%75CV %25AR	21.35	19.23	20.29 BC	87.66	88.56	88.11 B
%55CV %45AR	20.78	21.40	21.09 B	63.08	111.91	87.49 B
Mean	18.42	18.25		68.35 B	77.75 A	

When the relative feed value averages were examined, significant differences were found in terms of harvest time, and it was observed that the first harvest time had a higher relative feed value. Among the treatments, pure

common vetch stood out, while the mixtures with the highest values were %55FP-%45AR and %75CV-%25AR.

Table 6. Averages of years, harvest time and mixture values of relative feed value

	Relative Feed Value		
	1st Harvest	2nd Harvest	Mean
Years			
2015	114.41 B		
2016	127.90 A		
Mixtures			
%100 FP	129.57	130.60	130.08 B
%100 CV	147.31	137.53	142.42 A
%100 Oat	111.22	102.85	107.03 F
%100 AR	119.70	125.73	122.72 CD
%75FP %25O	121.61	108.73	115.17 E

%55FP %45O	124.34	109.28	116.81 DE
%75FP %25AR	118.90	118.66	118.78 DE
%55FP %45AR	139.36	120.82	130.09 B
%75CV %25O	118.07	111.48	114.77 E
%55CV %45O	113.95	98.93	106.44 F
%75CV %25AR	139.77	119.07	129.42 BC
%55CV %45AR	106.59	133.66	120.12 DE
Mean	124.20 A	118.11 B	

According to Pearson's correlation in Figure 2., the highest positive significance was found in Herbage yield and crude protein yield, while the most significant negative correlation was found between relative feed value and %NDF. Rizvi et. al [33] and Zaeem et. al. [34] obtained similar results, while Rizvi et. al [33] stated that ADF and NDF had a negative correlation with RFV. Zaeem et. al. [34] stated that NDF has a negative correlation with total digestible nutrient affecting RFV.

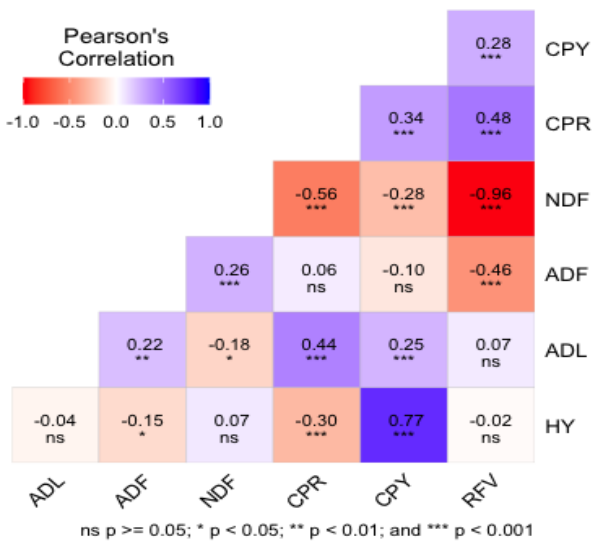


Figure 2. Pearson's correlation between features

4. CONCLUSION

In order to ensure sustainability in agricultural production, crop rotation practices are inevitable in year-round production. Mixtures including legumes can both protect the soil and enrich the soil in terms of nitrogen. At the same time, these mixtures are very important in terms of being a source of quality roughage. The results revealed that legumes and the mixtures in which they were included had higher values in terms of quality, while there were fluctuations in some traits between the harvests, but in general, it was concluded that harvesting between at 50%- 100% flowering periods could be preferred. The mixture of 75% forage pea + 25% oat produced better crude protein yield, and the mixtures of 55% forage pea + 45% annual ryegrass and 75% common vetch + 25% annual ryegrass had higher relative feed values.

Acknowledgement

The first year of this study was presented as MSc thesis.

REFERENCES

- [1] Bruinsma J. Livestock commodities. World agriculture: Towards 2015-2030 an FAO perspective. Earthscan Pub., 85-86, London, UK. 2003.
- [2] Barnes RF, Miller DA, Nelson CJ. Forages Volume 1: An introduction to grassland agriculture fifth edition, Iowa State University Press, 9-369, Iowa, USA. 1995.
- [3] Altın M, Orak A, Tuna C. Yembitkilerinin sürdürülebilir tarım açısından önemi. Yembitkileri (Avcioglu, R., Hatipoğlu, R., Karadağ, Y.), Yembitkileri, T.C. Tarım ve Köyişleri Bakanlığı Tarımsal Üretim ve Geliştirme Genel Müdürlüğü, Cilt 1: 11-24, İzmir. 2009. (In Turkish)
- [4] Horrocks RD, Vallentine JF. Harvested Forages, Academic Press, 3-87, San Diego, California, USA. 1999.
- [5] Yolcu H, Tan M. Ülkemiz yem bitkileri tarımına genel bir bakış. Tar. Bil.Der. 2008;14(3): 303-312. (In Turkish)
- [6] Yavuz T, Kır H, Gül V. Türkiye'de Kaba Yem Üretim Potansiyelinin Değerlendirilmesi: Kırşehir İli Örneği. Türkiye Tarımsal Araştırmalar Dergisi. 2020; 7(3): 345-352. (In Turkish)
- [7] Demiroğlu Topçu G, Kır B, Çelen A, Kavut YT. Değişik Fiğ + Tahıl Karışımları İçin En Uygun Karışım Oranı ve Biçim Zamanının Belirlenmesi. ISPEC Journal of Agricultural Sciences. 2020 Jun 1;4(2):146-56. (In Turkish)
- [8] Papastilianou I. Effect of rotation system and N fertilizer on barley and vetch grown in various crop combinations and cycle lengths. J. of Agric. Sci. 2008;142(1): 41-48.
- [9] Budaklı Carpıcı E, Celik N. Forage yield and quality of common vetch mixtures with triticale and annual ryegrass. Turk. J. of Field Crops 2014;19(1): 66-69.
- [10] Lithourgidis AS, Dordas CA, Damalas CA, Vlachostergios DN. Annual intercrops: An alternative pathway for sustainable agriculture. Australian J. of Crop Sci. 2011;5(4): 396-410.
- [11] Bouyoucos GJ. Hydrometer method improved for making particle size analysis of soil. Agron. J. 1962;54(5).
- [12] Richards LA. Diagnosis and improvement of saline and alkaline soils, USDA, Salinity Laboratory Agricultural Handbook, 110-118, Riverside, USA. 1954.
- [13] Black CA. Methods of soil analysis. Part 1,2, American Soc. of Agr., Madison, USA
- [14] Açıkgöz E, 2021. Yem Bitkileri (Vol 1). Tarım ve Orman Bakanlığı, Bitkisel Üretim Genel Müdürlüğü, Ankara, Türkiye (In Turkish)
- [15] Tuna C, Orak A. The role of intercropping on yield potential of common vetch (*Vicia sativa* L.) / oat

- (*Avena sativa* L.) cultivated in pure stand and mixtures. J. of Agric. and Biol. Sci. 2007;2(2): 14-19.
- [16] Cook CW, Stubbendieck J. Range research: basic problems and techniques. Society for Range Management. Colorado. 1986;317.
- [17] AOAC. Official methods of analysis of AOAC International. 17th Ed. 2nd Rev. Gaithersburg, MD, USA. Association of Analytical Communities. 2003
- [18] Van-Soest PJ, Robertson JB, Lewis BA Method for dietary fiber, neutral detergent fiber, and starch polysaccharides in relation to animal nutrition. Journal of dairy science 1991;74: 3583-3597.
- [19] De Mendiburu F, de Mendiburu MF. Package 'agricolae'. 2019. R Package, Version, 1.3. [cited: 13.10.2023] Available from: <https://cran.rproject.org/web/packages/agricolae/agricolae.pdf>
- [20] Olivoto T, Lúcio AD. "metan: An R package for multi-environment trial analysis." Methods in Ecology and Evolution 2020;11(6): 783-789.
- [21] Warnes GR, Bolker B, Bonebakker L, Gentleman R, Huber W, Liaw A, Lumley T, Maechler M, Magnusson A, Moeller S, Schwartz M, Venables B, Galili T. Package 'gplots'. Various R Programming Tools for Plotting data. R Package, Version, 3.1.3. 2022.
- [22] Kocer A, Albayrak S. Determination of forage yield and quality of pea (*Pisum sativum* L.) mixtures with oat and barley. Turkish Journal of Field Crops 2012;17(1): 96-99.
- [23] Giacomini SJ, Ventruseolo ERO, Cubilla M, Nicoloso RS, Fries MR. Dry matter, C/N ratio and nitrogen, phosphorus and potassium accumulation in mixed soil cover crops in Southern Brazil. Rev. Bras. Ciencia Solo 2003;27: 325-334.
- [24] Aasen A, Baron VS, Clayton GW, Dick AC, McCartney DHSwath grazing potential of spring cereals, field pea and mixtures with other species. Canadian Journal of Plant Science. 2004;84(4): 1051-1058.
- [25] Caballero AR, Goicoechea-Oicoechea EL, Hernaiz Ernaiz PJ. Forage yields and quality of common vetch and oat sown at varying seeding ratios and seeding rates of vetch. Field Crops Research. 1995;41: 135-140
- [26] Carr PM, Horsley RD, Poland WW. Barley, oat, and cereal-pea mixtures as dryland forages in the Northern Great Plains. Agronomy Journal. 2004;96: 677-684.
- [27] Aşçı ÖÖ, Zeki A, Arıcı, YK. Herbage yield, quality traits and interspecies competition of forage pea-triticale mixtures harvested at different stages. Turkish Journal of Field Crops. 2015;20(2): 166-173.
- [28] Pampana S, Masoni A, Arduini I. Response of cool-season grain legumes to waterlogging at flowering. Canadian Journal of Plant Science. 2016;96(4): 597-603.
- [29] Alatürk F, Gökkuş A, Ali B. Effects of Annual Grass with the Mixtures of Legume on Agronomic Growth of Plants. Acta Nat. Sci 2021;2(2): 166-176.
- [30] Sohail S, Ansar M, Skalicky M, Wasaya A, Soufan W, Ahmad Yasir T, et al. Influence of tillage systems and cereals-legume mixture on fodder yield, quality and net returns under Rainfed conditions. Sustainability 2021;13(4): 2172.
- [31] Yavuz T, Karadağ Y. Bazı buğdaygil ve baklagil yem bitkileri ile bunların karışımlarının kıraç mera koşullarındaki performansları. Journal of Agricultural Faculty of Gaziosmanpaşa University (JAFAG) 2016;33(2): 63-71. (In Turkish)
- [32] Albayrak S, Türk M. Changes in the forage yield and quality of legume-grass mixtures throughout a vegetation period. Turkish Journal of Agriculture and Forestry 2013;37(2):139-147.
- [33] Zaeem M, Nadeem M, Pham TH, Ashiq W, Ali W, Gillani SSM, et. al. Corn-soybean intercropping improved the nutritional quality of forage cultivated on Podzols in boreal climate. Plants, 2021;10(5): 1015.
- [34] Rizvi SA, Gondal MR, Naseem W, Umair A, Basit A, Muhammad G, et. al. Evaluating environmental adaptive variability of various Alfalfa (*Medicago sativa* L.) fodder cultivars. International Journal of Agricultural Technology. 2022;18(4):1767-1782.
- [35] Yazgi A, Aykas E, Dumanoglu Z, Demiroğlu Topcu G. Seed Mixture Flowing Characteristics of a Seed Drill for Mixed Seeding. Applied Engineering in Agriculture. 2017 Jan 30;33(1):63-71.

Appendices

372.85	9.95	39.28	46.76	19.74	72.97	117.98	214.8	8.94	38.2	42.82	19.92	42.97	131.92	1
320.99	9.23	38.21	47.88	20.25	84.15	117.2	214.89	9.37	36.44	41.6	48.08	60.42	136.44	2
988.09	4.84	33.21	54.26	11.13	73.57	108.62	484.2	6.36	37.53	57.36	12.56	60.49	96.44	3
465.44	4.59	31.27	49.82	17.03	79.25	121.01	451.92	4.71	32.18	49.27	12.89	56.16	120.96	4
466.22	9.92	35.68	51.17	18.55	86.85	112.18	401.22	7.47	38.57	53.82	19.12	79.95	102.18	5
210.01	5.78	31.74	49.13	15.57	32.84	123.18	302.71	6.5	36.74	54.79	16.61	47.92	102.83	6
231.91	7.64	37.02	49.79	19.02	43.33	112.54	278.36	7.95	36.72	48.96	20.26	56.35	115.34	7
277.42	7.1	34.84	47.09	19.12	51.17	123.51	296.69	6.01	35.94	48.41	18.59	54.65	117.26	8
355.26	6.33	36.37	54.32	18.31	63.29	105.43	438.99	7.54	38.84	60.02	16.02	68.67	110.05	9
262.55	6.53	37.52	52.03	18	47.13	107	315.73	6.96	39.38	57.14	15.41	47.92	94.98	10
411.51	9.11	37.33	47.96	19.38	78.78	116.97	280.95	9.02	37.02	49.14	23.33	64.63	114.42	11
319.48	11.66	41.77	49.57	19.13	59.93	106.13	207.36	9.26	35.44	43.12	22.43	59.98	152.26	12
HY	ADL	ADF	NDF	CPR	CPY	RFV	HYtwo	ADLtwo	ADFtwo	NDFtwo	CPRtwo	CPYtwo	RFVtwo	

Appendix A. Heatmap values of the traits examined at two harvest times with mixture treatments in 2014-2015

352.56	9.68	30.47	42.94	20.12	70.86	141.16	426.38	8.69	35.5	44	16.94	72.18	129.69	1
369.52	5.66	36.96	31.56	24.77	91.74	117.42	549.63	9.16	36.16	40.55	24.26	133.26	139.04	2
528.24	6.75	33.87	51.1	12.08	63.3	113.82	635.01	5.03	34.45	53.09	12.11	76.73	108.77	3
313.93	4.89	33.79	49.19	11.45	35.96	118.4	563.47	4.19	34.05	44.45	13.49	76.22	130.52	4
902.23	11.12	32.51	45.13	21.11	125.73	131.06	666.14	8.18	33.57	50.67	18.96	126.45	115.29	5
243.99	7.73	32.81	46.98	17.75	43.62	125.5	370.36	6.49	34.11	50.1	15.27	56.55	115.74	6
326.51	10.27	36.19	45.08	18.24	58.2	125.26	452.55	8.62	36.77	45.95	22.66	102.28	121.99	7
353.39	9.89	32.52	38.12	21.79	76.15	155.21	485.58	10.15	33.06	47.22	21.44	104.19	124.38	8
387.2	6.92	31.82	45.71	19.12	74.78	130.71	484.69	7.85	38.42	48.51	14.08	68.08	112.93	9
457.76	6.36	36.59	46.6	18.45	84.27	120.91	529.68	10.86	37.51	53.98	14.45	76.76	102.88	10
463.5	7.79	36.71	34.5	20.86	96.65	162.96	637.53	8.94	33.49	47.34	17.62	112.49	123.72	11
315.47	5.8	41.04	48.78	21.23	66.24	107.05	756.37	7.86	33.42	43.32	21.56	104.84	135.06	12
HY	ADL	ADF	NDF	CPR	CPY	RFV	HYtwo	ADLtwo	ADFtwo	NDFtwo	CPRtwo	CPYtwo	RFVtwo	

Appendix B. Heatmap values of the traits examined at two harvest times with mixture treatments in 2015-2016

(1: % 100 Forage Pea; 2: % 100 Common vetch; 3: % 100 Oat; 5: % 75FP %25O; 6: % 55FP %45O; 7: % 75FP %25AR; 8: % 55FP %45AR; 9: % 75CV %25O; 10: % 55CV %45O; 11: % 75CV %25AR; 12: % 55CV %45AR – HY: Herbage yield; CPR: Crude Protein Ratio; CPY: Crude Protein Yield; RFV: Relative Feed Value; HYtwo: Herbage yield-Second Harvest)

Genetic Diversity of *Pelophylax cerigensis*-like Population on the Anatolian Mainland in Türkiye (Amphibia: Anura: Ranidae)

Çiğdem AKIN PEKŞEN^{1,2*} , Emel ÇAKMAK³ 

¹ Başkent University, Faculty of Science and Letters, Department of Molecular Biology and Genetics, Ankara, Türkiye

² Başkent University, Institute of Transplantation and Gene Sciences, Ankara, Türkiye

³ Aksaray University, Faculty of Science and Letters, Department of Molecular Biology and Genetics, Aksaray, Türkiye

Çiğdem AKIN PEKŞEN ORCID No: 0000-0001-5736-3062

Emel ÇAKMAK ORCID No: 0000-0002-6231-1950

*Corresponding author: cerigensis@gmail.com

(Received: 09.11.2023, Accepted: 12.12.2023, Online Publication: 28.12.2023)

Keywords

Genetic diversity,
Water frog,
Pelophylax cerigensis,
Anatolia,
Türkiye

Abstract: Genetic diversity is increasingly used as a vital component in planning appropriate conservation strategies. Water frogs in the eastern Mediterranean consist of several endemic species. The Critically Endangered Karpathos water frog (*Pelophylax cerigensis*) is one such species, restricted to Karpathos Island, but recently *P. cerigensis* specific haplotypes were also found in Rhodes and southwestern Türkiye. Since, geologically Karpathos and Rhodes have been separated from the Anatolian mainland million years ago, the genetic diversity of *P. cerigensis*-like populations on the Anatolian mainland are not known. Here, we aim to evaluate the genetic diversity of this mainland population (N=52) in southwestern Anatolia by using five polymorphic microsatellite loci. According to results, a total of 38 alleles which five loci exhibited a moderate level of genetic diversity (observed heterozygosity, $H_o=0.423$). The population has not gone through a bottleneck anytime soon; however, signs of inbreeding were determined ($F_{is}=0.401$). Due to restricted occurrence from Antalya to Aydın provinces in southwestern Türkiye and a moderate level of genetic diversity, they should be considered a third Management Unit (MU) of *P. cerigensis* populations in addition to previous Karpathos and Rhodes MUs. This approach is very crucial to formulate suitable management strategies for conservation of these threatened populations.

Türkiye’de Anadolu Anakarasında *Pelophylax cerigensis* benzeri (Amphibia: Anura: Ranidae) Popülasyonun Genetik Çeşitliliği

Anahtar Kelimeler

Genetik çeşitlilik,
Su kurbağası
Pelophylax cerigensis,
Anadolu,
Türkiye

Öz: Genetik çeşitlilik, uygun koruma stratejilerinin planlanmasında giderek daha hayati bir bileşen olarak kullanılmaktadır. Doğu Akdeniz’deki su kurbağaları çok sayıda endemik türden oluşmaktadır. Kritik Tehlike Altındaki Karpathos su kurbağası (*Pelophylax cerigensis*) bu türlerden biridir ve Karpathos Adası ile sınırlıdır, ancak yakın zamanda Rodos ve güneybatı Türkiye’de de *P. cerigensis*’e özgü haplotipler bulunmuştur. Jeolojik olarak Karpathos ve Rodos milyonlarca yıl önce Anadolu anakarasından ayrıldığından, Anadolu anakarasındaki *P. cerigensis* benzeri popülasyonların genetik çeşitliliği bilinmemektedir. Burada, beş polimorfik mikrosatellit lokusu kullanarak Güneybatı Anadolu’daki bu anakara popülasyonlarının (N=52) genetik çeşitliliğini değerlendirmesi amaçlanmıştır. Sonuçlara göre, beş lokusta bulunan toplam 38 alel orta düzeyde genetik çeşitlilik sergilemiştir (gözlenen heterozigotluk, $H_o=0.423$). Popülasyon yakın zamanda bir darboğaza girmemiştir; ancak yakın bireyler arasında üreme belirtileri tespit edilmiştir ($F_{is}=0.401$). Türkiye’nin güneybatısında Antalya’dan Aydın’a kadar olan bölgede kısıtlı olarak görülmesi ve orta düzeyde genetik çeşitliliğe sahip olması nedeniyle, daha önceki Karpathos ve Rodos MU’larına ek olarak *P. cerigensis* popülasyonları üçüncü bir Yönetim Birimi (MU) olarak düşünülmelidir. Bu yaklaşım, tehdit altındaki bu popülasyonların korunması için uygun yönetim stratejilerinin formüle edilmesi açısından çok önemlidir.

1. INTRODUCTION

Genetic diversity is an indispensable component of populations to adapt to changing environmental conditions and to compensate them against unpredictable sudden events such as climate changes or outbreak of diseases [1]. Thus, genetic diversity is increasingly used as crucial component in the planning of suitable conservation and management strategies for many threatened populations, aiming to keep as much genetic diversity as possible [2, 3]. Anatolia, the Asian part of Türkiye, is one of the richest biodiversity areas since the Caucasus, Irano-Anatolian and Mediterranean Basin biodiversity hotspots all converge on the region. Besides its high biodiversity with many plant and animal species, it is also the one of the most threatened terrestrial regions of the world [4, 5].

Eastern Mediterranean water frogs (genus *Pelophylax*) are a genetically and phylogenetically diverse group which consist of both older and recently diverged lineages which are widely distributed or restricted to specific regions such as in southwestern Anatolia [6, 7]. The genus also comprises several cryptic lineages and endemic species such as *Pelophylax cretensis* on the island Crete, *P. cerigensis* on Karpathos [8], and *P. cypriensis* in Cyprus [9].

Because of its limited distribution and ongoing population decline, *P. cerigensis* is categorized as Critically Endangered (CR) according to the IUCN Red List of Threatened Species [10, 11]. It is recognized that anthropogenic factors, in particular the drying of wetlands for agriculture and tourism, most strongly affect the survival of the species, and are considered in management actions related to the restoration of their habitats [12].

The island of Karpathos is situated about 47 kilometres southwest of Rhodes. It is the second largest island of the Dodecanese archipelago on the South Aegean Sea. According to fossil data and research on tectonic movements in the Aegean, Rhodes and the Anatolian mainland cluster were isolated from Karpathos about 3 million years ago during Pliocene, while Rhodes was separated from the Anatolian mainland in early Pleistocene about 1.8 million years ago [13, 8].

Several studies were carried to understand phylogenetic relationships of *P. cerigensis* with other eastern Mediterranean water frog lineages, their population genetic structure and genetic diversity based on distinct marker systems. *P. cerigensis* was described as a new species characterized by a unique multi-locus combination of electrophoretic alleles, which also segregated within the Rhodes Island populations [8]. In previous phylogenetic studies, water frogs from Rhodes and Karpathos were grouped with *Pelophylax* cf. *bedriagae* from East Aegean and Türkiye, not with *P. bedriagae* from Cyprus and Syria [8, 14]. Various past studies [6, 7, 15, 16] indicated that both populations from Karpathos and Rhodes islands shared *P. cerigensis*-specific haplotypes. *Pelophylax cerigensis*-specific haplotypes were not only found on Karpathos and Rhodes, but also in the coastal parts of southwestern Anatolia [6, 7]. In southwestern Anatolia

four distinct type of *P. cerigensis*-specific haplotypes were found on Avlan Lake (CER3), Dalaman (CER3), Fethiye (CER2, CER3, CER5), Kaş (CER1, CER3), Girdev Plateau (CER3), Köyceğiz (CER1) where they were found to be coexist with *P. cf. bedriagae*-specific haplotypes or *P. cf. caralititanus*-specific haplotypes or both in some localities. CER3 were the most frequent *P. cerigensis*-specific haplotype [17]. Rhodes and Karpathos had one type of haplotype (CER4) and (CER1) respectively and CER1 was only identically shared haplotype with Anatolian populations and thus, the populations from Karpathos, Rhodes and southwestern Anatolia formed a single monophyletic group [6, 7, 17]. Akın Pekşen [17] found that serum albumin intron 1 (SAI1) of frogs from Karpathos and Rhodes was similar but not identical to populations from southwestern Anatolia which exhibited *cerigensis*-specific mtDNA. This indicates that the mainland populations can be differentiated from island populations based on nuclear genes, but not on mitochondrial haplotypes. The combination of low mitochondrial DNA diversity and different nuclear diversity can be explained by male-mediated gene flow [18]. Female natal philopatry and male-biased dispersal could be seen in species [19, 20]. Additionally, different regions of mitochondrial DNA show different polymorphisms, which may reflect different levels of mtDNA genetic diversity for populations of species.

The study on the population genetic structure of *P. cerigensis* populations on Karpathos Island using AFLP markers revealed similar levels of genetic diversity and also a low but statistically significant genetic divergence between two breeding populations on Karpathos which indicates the importance of a conservation plan to maintain genetic diversity [15]. According to our mtDNA data, the *cerigensis*-lineage has a rather small distribution area on the Anatolian mainland [7, 17]. There is almost no information on the diversity of the nuclear genome of these mitochondrial lineages. Only we know from Beerli et al. [8] that Karpathos and Rhodes populations shared alleles at 30 of 31 loci, but the Rhodes population segregated for alternative alleles at 5 loci which were also seen in *P. cf. bedriagae* on the adjacent Anatolian mainland. They suggested that ancestral alleles could probably become extinct on the Anatolian mainland. Thus, we aim here to evaluate genetic structure and genetic diversity of this mainland population using five polymorphic microsatellite loci.

2. MATERIAL AND METHOD

2.1. Material and Laboratory Procedures

A total of 52 tissue samples were collected at 15 distinct localities in southwestern Anatolia, ranging from Antalya to Aydın provinces. The sample design was based build on the previous *P. cerigensis* specific haplotype records [17] (Table 1, Figure 1). Total genomic DNA was extracted as described by Akın et al. [7].

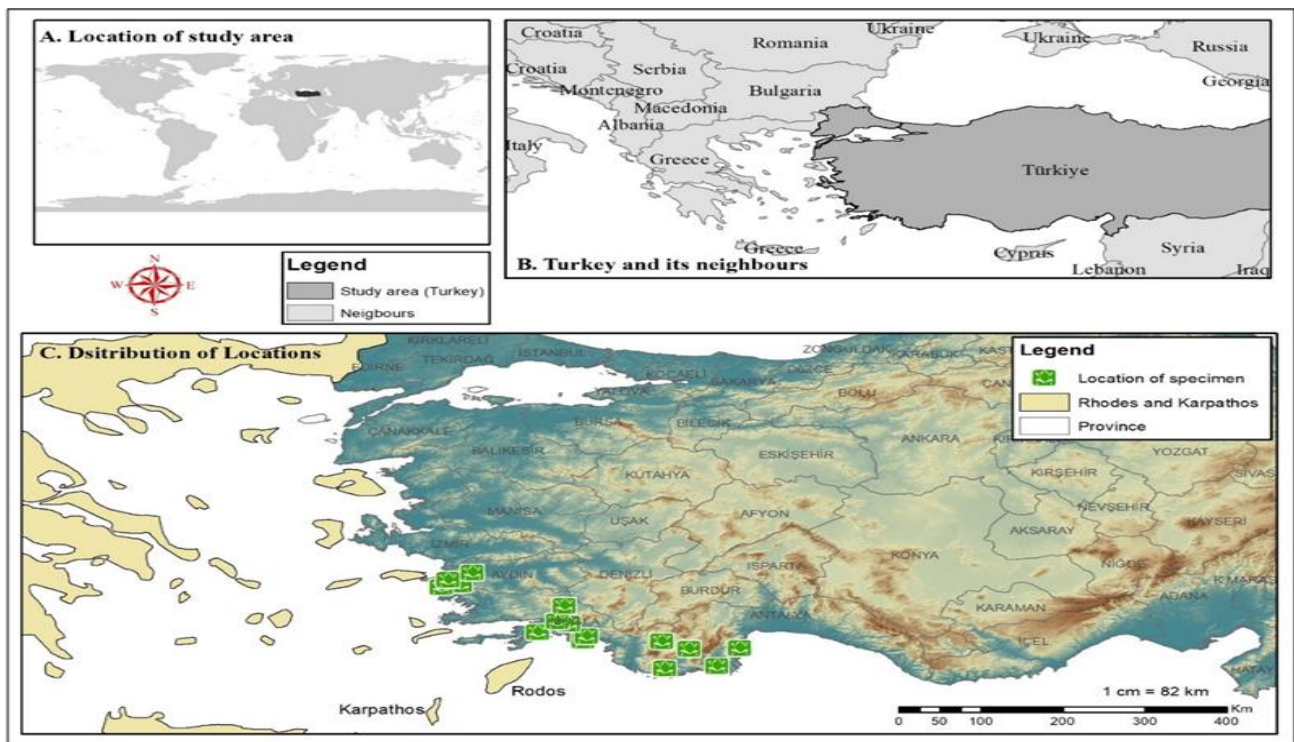


Figure 1. Distribution of the sampling sites.

Five nuclear polymorphic microsatellite loci were used to assess genetic diversity: Res5, Res16 [21], RICA1b5, RICA1b20 and RICA5 [22]. Locus-specific fluorescently labelled (HEX or FAM) forward primers were used at the 5'-end in a multiplex reaction (Table 2). Because RICA5 exhibited inconclusive results, it was excluded from multiplex PCR and amplified separately.

All PCR were carried out in a final volume of 25 μ l containing 5x HOT FIREPol Blend Master Mix RTL (HOT FIREPol DNA polymerase, 5x blend master mix, 12.5 mM MgCl₂, 1 mM dNTP, BSA, blue and yellow dyes) (Solis BioDyne), 0.3 μ M of each primer pair, and 1 μ l of genomic DNA. Using the touchdown method, PCR was performed under the following conditions: 15 min of 95 °C heat activation followed by 34 cycles of 20 s at 95 °C, 1 min at 57 °C, 1 min at 72 °C, and a final extension step of 10 min at 72 °C. PCR products were checked on 2% agarose gels. PCR products were analysed on an ABI-PRISM 3100 sequencer (Applied Biosystems).

Allele sizes obtained from raw data were evaluated with PEAK SCANNER 2.0 (Applied Biosystems) by means of the GS400HD size standard. In the case of low peak signal, genotyping was repeated three times per sample.

2.2. Data Analyses of Microsatellites

Frequencies of null alleles were calculated with FREENA [23] with 10 000 replicates. Using MICROCHECKER 2.2.3 [24], genotyping errors, scoring of stutter peaks, and allelic dropout were evaluated statistically.

Genotypic linkage disequilibrium between each pair of microsatellite loci and basic statistics, e.g., number of alleles and allelic richness, were calculated using FSTAT

2.9.3 [25]. Deviations from Hardy-Weinberg equilibrium (HWE) was tested with CERVUS 3.0.7 [26, 27] and GenAlEx 6.5 [28]. Inbreeding coefficients [FIS] for each locus and population were predicted with GENEPOP 3.4 [29]. In addition, polymorphic information content (PIC), indicating the possible utility of markers in identifying individuals, was estimated with CERVUS 3.0.7 [26, 27]; where $PIC > 0.5$ is highly informative, $0.5 > PIC > 0.25$ is highly informative, and $PIC < 0.25$ is somewhat informative [30].

To reveal any recent bottlenecks, the software BOTTLENECK 1.2.02 [31, 32] was used. Under the two-phase mutation model (TPM), the statistical significance of heterozygosity excess was measured by means of Wilcoxon's sign rank test; the mode-shift graphical method was applied to estimate allele frequency shift after a bottleneck event [33]. It is expected that allele carrying intermediate frequencies (about 0.1–0.2) is more widespread than alleles carrying low frequencies (< 0.1) [34].

Table 1. Locality information, samples IDs and sex of the investigated individuals (F: female; M: male)

SAMPLE ID	Sex	Locality	Latitude	Longitude
HS07165	unknown	Antalya Avlan Lake	36.5825	29.9482
CA07218	unknown	Antalya Kaş	36.2769	29.6839
CA07219	unknown			
CA1865	M	Antalya Kemer	36.5954	30.5045
CA1866	F			
CA1868	unknown	Antalya Kumluca	36.3168	30.2512
CA1801	unknown	Aydın Azap Lake	37.5844	27.447
CA1802	unknown			
CA1803	unknown			
CA1785	F	Aydın Bıyıklı pond	37.7716	27.5741
CA1787	F			
CA1788	F			
CA1789	F			
CA1796	M	Aydın Menderes River	37.5476	27.2371
CA1798	M	Aydın Söke water channel	37.6607	27.3087
CA1790	unknown			
CA1792	F			
ISCA307	unknown	Muğla Dalaman	36.7138	28.7856
ISCA308	unknown			
ISCA309	unknown			
ISCA310	unknown			
ISCA311	unknown			
ISCA312	unknown			
CA1845	F	Muğla Dalaman Tersakan	36.7794	28.8252
CA1846	M			
CA1847	M			
CA1848	M			
CA1849	M			
CA1850	unknown			
CA1851	F	Muğla Girdev Plateau	36.7007	29.6509
CA1853	F			
CA1854	F			
CA1855	F			
CA1856	unknown			
CA1857	unknown			
CA1858	unknown			
CA1859	unknown			
CA1860	unknown			
CA1861	unknown			
CA1840	F	Muğla Köyceğiz Zaferler Village	36.9718	28.6299
CA1841	F			
CA1842	F			
CA1843	F			
CA1844	F			
AKCA48212	unknown	Muğla Marmaris	36.8467	28.2879
CA1837	unknown	Muğla Ula Nannan River	37.0129	28.5105
CA1839	unknown			
CA1830	F	Muğla Yemişendere	37.2516	28.5810
CA1832	unknown			
CA1833	M			
CA1834	M			
CA1835	unknown			

Table 2. Locus name and characterization of five polymorphic microsatellite primers used to analyse *P. cerignensis* population.

Locus	Primer Sequence (5' – 3')	Repeat motif	Tag	TA (0C)	Expected allele size	Observed Allele size
RES16	F:GATCCTGATTTCTGCT R:GTTTATTTACTCTGTCTCTT	(CA) ₁₀	HEX	57	102-114	114-126
RES5	F:ATACTGCCAATAAGCTGGCAATGTTTAGC R:GGCCGACTTCAAAGGGGTGCTC	(GT) ₁₅	FAM	57	129-151	141-157
RICA1b5	F:CCCAGTGACAGTGAGTACCG R:CCCACTGGAGGACCAAAAG	(CA) ₁₇	HEX	57	145	122-140
RICA5	F:CTTCCACTTTGCCCATCAAG R:ATGTGTCGGCAGCTATGTTC	(CA) ₁₇	FAM	57	250	238-264
RICA1b20	F:GGGCAGGTATTGTAATCAATATCAC R:CAACACAAGGACTCCACTGC	(CA) ₈ (C) ₁₃	FAM	57	87	78-86

3. RESULTS

3.1. Reliability of Data

DNA isolation from tissue samples of 52 individuals was successfully performed (Supplementary Table S1). All microsatellite loci were amplified successfully in all individuals (Table S1). All loci proved to be polymorphic in the *P. cerigensis* population studied. No loci were detected to contain null alleles ($r \leq 0.2$) when tested with FREENA.

Looking at possible comparisons between pairs of loci in the population, no significant linkage disequilibrium was detected after Bonferroni correction ($p=0.005$ for 5% nominal level), and each locus was evaluated independently.

Analyses using FREE showed no evidence for the presence of null alleles among the five loci in the population, but MICROCHECKER detected null alleles which may be present due to the general excess of homozygotes for most allele size classes in loci RICA1b5 and RICA1b20. However, because this finding was not consistent with other software, we kept the locus for further analysis. There was also no evidence of genotyping errors due to stuttering or large allele dropout at any of the five loci in the study population based on MICROCHECKER.

3.2. The Genetic Diversity, Inbreeding and Bottleneck

Five nuclear loci were successfully genotyped for all samples ($n=52$). A total of 35 alleles were detected in all loci throughout the population. These five loci exhibited moderate genetic diversity based on number of alleles (N_a), observed heterozygosity (HO) and gene diversity (Table 3). The number of alleles was the highest in loci RICA1b5 and RICA5 (Table 3). The five loci used were found to be highly informative loci ($PIC > 0.5$) in the *P. cerigensis* population (Table 3). The loci RICA1b5 and RICA1b20 were not in HWE. No private population-specific allele was also detected in any of the population. All the estimates of inbreeding coefficient (FIS) differed from zero, so the high signs of inbreeding were determined which means non-random mating (Table 3).

According to the Wilcoxon test, the observed proportion of heterozygotes showed no deviation from expectation under mutation-drift equilibrium using a TPM (one-tailed for H excess: $P = 0.5$) in the pooled sample. This indicates that the mainland *P. cerigensis* population was not going through a bottleneck. The proportion of alleles in different allele frequency classes (0-0.1 low; 0.9-1 high allele frequency class) showed the normal L-shaped distribution rather than the mode-shifting distribution that would be expected for bottleneck populations (Figure 2). This also supports the idea that the population is in mutation-drift equilibrium and is not going through a bottleneck anytime soon.

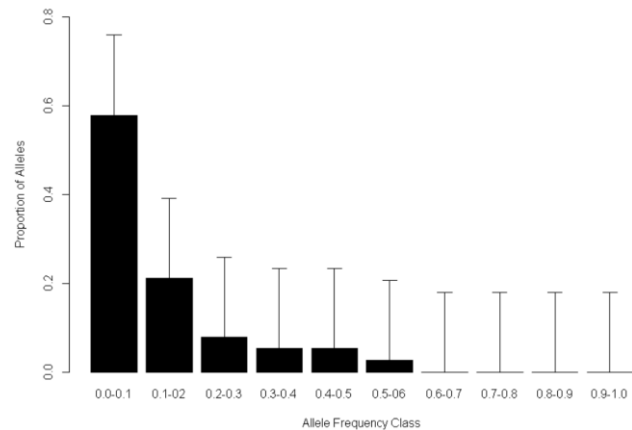


Figure 2. Mode shift of the allele frequencies indicating the occurrence of a recent genetic bottleneck.

4. DISCUSSION AND CONCLUSION

The level of heterozygosity observed was consistent with estimates from other water frog populations [35, 36]. In the study of Leuenberger et al. [36] 16 individuals yielded no amplicons for the marker RICA5, but all water frog samples in our study were amplified in all loci. In the analysis of the *Pelophylax esculentus* complex (*Pelophylax lessonae*, *Pelophylax esculentus*, and *Pelophylax ridibundus*) and Anatolian *Pelophylax* cf. *bedriagae* revealed that four loci (RICA1b5, Res16, RICA1b20, and RICA5) from eight microsatellites are the most discriminative loci between species [35] which were all used in this study. As found in *P. lessonae* and *P. ridibundus* populations in Belgium, genetic diversity results indicated that observed heterozygosity values (H_o) for all loci (RES 16, RES 5, RICA1b5, RICA5, RICA1b20) in mainland *P. cerigensis* populations are less than expected heterozygosity values like our results. Although the limited number of individuals (about 52 individuals) were analysed in the *P. cerigensis* population in comparison with *P. lessonae* and *P. ridibundus* (both 150 individuals each), the observed heterozygosity value (0.423) is moderate and higher than those found in *P. lessonae* and *P. ridibundus* (0.319 and 0.389 respectively) [35]. Additionally, a total of 35 alleles was found in the Anatolian population. The average number of alleles per locus ranges from 5 to 13. Although Holsbeek et al., [35] studied the same five loci, they found only 21 alleles in *P. lessonae* populations and 32 alleles in *P. ridibundus* populations. Regarding the genetic diversity of *P. cerigensis* populations on Karpathos Island, there is only one study based on AFLP markers, where samples collected from two known breeding sites also revealed moderate levels of genetic diversity and differentiation [15].

The inbreeding coefficient (FIS) varied between 0.257 to 0.562, while the Hardy-Weinberg ratios were not met in the two loci which showed an excess of homozygotes for most allele size classes. This may be due to the fact that small number of individuals involved in reproduction or in the last few decades mating has been occurred among closely related animals. The heterozygote deficiency could also be explained as a Wahlund effect if population subdivision is

Table 3. Genetic diversity at five loci studied. Mean allele number (Na), observed heterozygosity (HO), expected heterozygosity (HE), polymorphic information content (PIC), Hardy-Weinberg Equilibrium (HWE) and inbreeding coefficient (F_{is}) values.

	Locus	N	Na	Ho	H _E	Gene diversity	PIC	HWE	F _{is}
<i>cerigensis</i>	RES16	52	6	0.442	0.588	0.595	0.533	NS	0.257
	RES5	52	6	0.404	0.647	0.656	0.578	NS	0.384
	RICA1b5	52	8	0.462	0.723	0.733	0.678	***	0.370
	RICA5	52	13	0.519	0.876	0.888	0.863	NS	0.415
	RICA1b20	52	5	0.288	0.649	0.659	0.592	***	0.562
Mean		52	7.6	0.423	0.697	0.706	0.648		0.401

NS: non-significant; ***: significant (with Bonferroni correction, P value<0.001)

occurring, linkage with loci under selection (genetic hitchhiking), population heterogeneity, null alleles (non-amplifying alleles) or inbreeding. Positive FIS value suggested inbreeding to be one of the main causes for shortage of heterozygotes in this population [37]. Therefore, a significant inbreeding event (F_{is}>0.25) can be true for *P. cerigensis* population since they were found range within the restricted geographic region from Antalya province to Aydın province (i.e. only the southwestern Anatolia), a fact that was previously derived from mitochondrial ND2 and ND3 and nuclear SAI-1+*Rana*CR1 data [17], but also now supported by specific allele sizes of RES16 and RICA1b5 microsatellite loci. In the study of Coltman and Slate [38], to detect inbreeding depression on a life history trait using microsatellites have recruited more than 600 individuals to detect an average effect size ($r = 0.10$) with reasonable statistical power (0.80) shows that sampling is required. However, as known, very few published studies have used sample sizes approaching this value. On the other hand, Hale et al. [39] showed that there appears to be little benefit in sampling more than 25 to 30 individuals per population for population genetic studies based on microsatellite allele frequencies. The mainland *P. cerigensis* population is bounded in the north, west and east by two other Anatolian water frog lineages *Pelophylax* cf. *caralitanus* and *P. cf. bedriagae*. Therefore *P. cerigensis* population was unable to expand further and got entrapped within this region (possibly also due to mountain barriers). This would lead to increased inbreeding and excess homozygosity, and hence, moderate levels of heterozygosity within populations. However, a full understanding of the consequences of inbreeding in wild populations would require not only detection of inbreeding but also long-term measurements of reproductive success and survival [40, 41].

We detected no signs of a genetic bottleneck. This finding is not surprising since southwestern Anatolia, where *P. cerigensis* population is located, is considered an important refuge for many animal and plant species during the Quaternary ice ages. Populations that could sustain themselves during glacial periods often spread throughout Europe and the Caucasus during the following interglacial intervals [42]. Due to the mountainous topography up to 3000 m, densely forested areas could have acted as a biodiversity center for certain Anatolian water frogs (*Pelophylax*) lineages. Several other reptile and amphibian species, for example *Lyciasalamandra flavimembris* [43], *Lyciasalamandra fazilae* [44], *Ophiomorus kardesi* [45], and *Anatololacerta pelasgiana* (Mertens, 1959) are known to be largely restricted in the same geographic area [46].

Phylogenetic studies based on one or two mitochondrial genes [6, 7, 15, 17] and complete mitogenomes [16] revealed that *P. cerigensis* occurs on Karpathos Island but is also present in Rhodes Island. Interestingly, Akın et al. [7] and Akın Pekşen [17] indicated that all *P. cerigensis* specific haplotypes from Karpathos, Rhodes and southwestern Anatolia formed a single monophyletic group. However, analyses of nuclear SAI-1+*Rana*CR1 gene Akın Pekşen [17] revealed that southwestern Anatolian population (*P. cerigensis*) on the other hand, and Karpathos and Rhodes Island populations on the others have distinct albumin alleles, and they formed two distinct but closely related clades.

Geological studies indicate that Karpathos separated from Rhodes and Asia Minor during the Pliocene [47, 8], and it is believed that Rhodes served as a springboard for the colonisation and spread of species from Asia Minor (mainland Anatolia) [48]. However, the results show that the mainland and island populations could be differentiated in terms of nuclear markers, but still have the shared mitochondrial haplotypes from most probably human mediated dispersal like that seen in Cyprus water frog populations [49]. These results clearly show the need for a taxonomic reassessment of *P. cerigensis* using more samples from island populations of Karpathos and Rhodes by applying and nuclear markers as a very limited sample were originated from those islands.

In conclusion, both mtDNA and nuclear marker [17] showed that Karpathos and Rhodes Islands and mainland populations of *P. cerigensis* are closely related. Because of their restricted range and moderate genetic diversity of *P. cerigensis* population in southwestern Anatolia, they should be a considered as a third Management Unit (MUs) in addition to those as previously suggested for Karpathos and Rhodes populations [16]. It is crucial to develop and implement appropriate conservation strategies to assure future survival and conservation of these threatened *P. cerigensis* populations.

Acknowledgement

We are grateful to Dr. Jörg Plötner and Prof. Dr. C. Can Bilgin their valuable comments on the manuscript. We also thank to Dr. Banu Kaya Özdemirel for preparation of the locality map.

REFERENCES

- [1] Lacy RC. Loss of genetic diversity from managed populations: interacting effects of drift, mutation, immigration, selection, and population subdivision. *Conservation Biology*. 1987;1:143-158.
- [2] Amos W, Balmford A. When does conservation genetics matter? *Heredity*. 2001;8:7:257.
- [3] Hoban S, Bruford MW, Chris Funk W, Galbusera P, Patrick Griffith M, Grueber CE, et al. Global commitments to conserving and monitoring genetic diversity are now necessary and feasible. *BioScience*. 2021;71(9):964–976.
- [4] Conservation International. Biodiversity Hotspots. 2021. Biodiversity Hotspots. viewed 31 August 2021, from <https://www.conservation.org/priorities/biodiversity-hotspots>.
- [5] Gür H. The future impact of climate and land-use changes on Anatolian ground squirrels under different scenarios. *Ecological Informatic*. 2022;70:1-12.
- [6] Plötner J, Uzzell T, Beerli P, Akin Ç, Bilgin C, Haefeli C, et al. Genetic divergence and evolution of reproductive isolation in eastern Mediterranean water frogs. In: Glaubrecht M (ed.). *Evolution in Action*. Berlin, Heidelberg: Springer. 2010; p. 373–403.
- [7] Akin Ç, Can Bilgin C, Beerli P, Westaway R, Ohst T, Litvinchuk SN, et al. Phylogeographic patterns of genetic diversity in eastern Mediterranean water frogs were determined by geological processes and climate change in the late Cenozoic. *J. Biogeogr*. 2010;37:2111-2124.
- [8] Beerli P, Hotz H, Tunner HG, Heppich S, Uzzell T. Two new water frog species from the Aegean islands Crete and Karpathos (Amphibia, Salientia, Ranidae). *Not. Nat*. 1994;470:1-9.
- [9] Plötner J, Baier F, Akin C, Mazepa G, Schreiber R, Beerli P, et al. Genetic data reveal that water frogs of Cyprus (genus *Pelophylax*) are an endemic species of Messinian origin. *Zoosyst. Evol*. 2012;88:261-283.
- [10] Beerli P, Uzzell T, Lymberakis P. *Pelophylax cerigensis*. The IUCN Red List of Threatened Species, 2009: e. T58567A11787309. <https://amphibiaweb.org/species/5000>.
- [11] IUCN, SSC Amphibian Specialist Group. *Pelophylax cerigensis* (errata version published in 2022). The IUCN Red List of Threatened Species 2022: e.T58567A89696593. [cited 2023 Decem 1] Available from: <https://dx.doi.org/10.2305/IUCN.UK.2020-3.RLTS.T58567A89696593.en>.
- [12] Pafilis P, Deimezis-Tsikoutas A, Kapsalas G, Maragou P. Action Plan for *Pelophylax cerigensis*. LIFEIP 4 NATURA project: integrated actions for the conservation and management of Natura 2000 sites, species, habitats and ecosystems in Greece (LIFE16 IPE/GR/000002). Deliverable Action A.1. Ministry of Environment and Energy, Athens. 2020;43 pages-Annexes, 40 pp.
- [13] Meulenkamp JE. Aspects of the late Cenozoic evolution of the Aegean region. In: Stanley, D. J. and F. C. Wezel (Eds.): *Geological evolution of the Mediterranean basin*. Springer, New York. 1985;307-321.
- [14] Lymberakis P, Poulakakis N, Manthou G, Tsigenopoulos C, Magoulas A, Mylonas M. Mitochondrial phylogeography of *Rana* (*Pelophylax*) populations in the eastern Mediterranean region. *Mol. Phylogen. Evol*. 2007;44:115-125.
- [15] Toli E, Siarabi S, Bounas A, Pafilis P, Lymberakis P, Sotiropoulos K. New insights on the phylogenetic position and population genetic structure of the critically endangered Karpathos marsh frog *Pelophylax cerigensis* (Amphibia: Anura: Ranidae). *Acta Herpetol*. 2018;13:117-123.
- [16] Toli EA, Bounas A, Christopoulos A, Pafilis P, Lymberakis P, Sotiropoulos K. Phylogenetic analysis of the critically endangered Karpathos water frog (Anura, Amphibia): conservation insights from complete mitochondrial genome sequencing. *Amphibia-Reptilia*. 2023;44(3):277-287.
- [17] Akin Pekşen Ç. Molecular evolution and phylogeography of the eastern Mediterranean water frog (*Pelophylax*) complex. Ph.D dissertation. Middle East Technical University. 2015;342 pp.
- [18] Martínez-Cruz B, Godoy JA. Genetic evidence for a recent divergence and subsequent gene flow between Spanish and Eastern imperial eagles. *BMC Evolutionary Biology*. 2007;7:1-8.
- [19] Lopes F, Hoffman JI, Valiati VH, Bonatto SL, Wolf JBW, Trillmich F. et al. Fine-scale matrilineal population structure in the Galapagos fur seal and its implications for conservation management. *Conserv. Genet*. 2015;16:1099–1113.
- [20] Doyle JM, Katzner TE, Bloom PH, Roemer GW, Cain JW, Millsap B, et al. Genetic structure and viability selection in the Golden Eagle (*Aquila chrysaetos*), a vagile raptor with a Holarctic distribution. *Conserv. Genet*. 2016;17:1–16.
- [21] Zeisset I, Rowe G, Beebee TJC. Polymerase chain reaction primers for microsatellite loci in the north European water frogs *Rana ridibunda* and *R. lessonae*. *Molecular Ecology*. 2000;9:1173–1174.
- [22] Garner TWJ, Gautschi B, Rothlisberger S, Reyer HU. A set of CA repeat microsatellite markers derived from the pool frog, *Rana lessonae*. *Molecular Ecology*, 2000;9,2173–2175.
- [23] Chapuis MP, Estoup A. Microsatellite null alleles and estimation of population differentiation. *Mol. Biol. Evol*. 2006;24:621–631.
- [24] Van Oosterhout C, Hutchinson WF, Wills DP, Shipley P. MICRO-CHECKER: software for identifying and correcting genotyping errors in microsatellite data. *Mol. Ecol. Resour*, 2004; 4:535–538.
- [25] Goudet J. FSTAT; a program to estimate and test gene diversities and fixation indices version. 2001;2.9. 3. Available at: <https://www2.unil.ch/popgen/softwares/fstat.htm> (accessed 23 Sep 2023).
- [26] Marshall T, Slate J, Kruuk L, Pemberton J. Statistical confidence for likelihood-based paternity inference in natural populations. *Molecular Ecology*. 1998;7:639–655.
- [27] Kalinowski ST, Taper ML, Marshall TC. Revising how the computer program CERVUS accommodates genotyping error increases success in paternity

- assignment. *Molecular Ecology*. 2007;16:1099–1106.
- [28] Peakall R, Smouse P. GenAlEx 6.5: genetic analysis in Excel. Population genetic software for teaching and research – an update. *Bioinformatics*. 2012;28:2537–2539.
- [29] Raymond M, Rousset F. GENEPOP (Version 1.2): population genetics software for exact tests and ecumenicalism. *Journal of Heredity*. 1995;86: 248–249.
- [30] Botstein D, White RL, Skolnick M, Davis RW. Construction of a genetic linkage map in man using restriction fragment length polymorphisms. *American Journal of Human Genetics*. 1980;32:314.
- [31] Cornuet JM, Luikart G. Description and power analysis of two tests for detecting recent population bottlenecks from allele frequency data. *Genetics*. 1996;144:2001–2014.
- [32] Piry S, Luikart G, Cornuet JM. Computer note. BOTTLENECK: a computer program for detecting recent reductions in the effective size using allele frequency data. *Journal of Heredity*. 1999;90:502–503.
- [33] Luikart G, Allendorf F, Cornuet, J, Sherwin W. Distortion of allele frequency distributions provides a test for recent population bottlenecks. *Journal of Heredity*. 1998;89:238–247.
- [34] Ganapathi P, Rajendran R, Kathiravan P. Detection of occurrence of a recent genetic bottleneck event in Indian hill cattle breed Bargur using microsatellite markers. *Trop. Anim. Health Prod.* 2012;44:2007–2013.
- [35] Holsbeek G, Maes GE, De Meester L, Volckaert FAM. Conservation of the introgressed European water frog complex using molecular tools. *Molecular Ecology*. 2009;18:1071–1087.
- [36] Leuenberger J, Gander A, Schmidt BR, Perrin N. Are invasive marsh frogs (*Pelophylax ridibundus*) replacing the native *P. lessonae*/*P. esculentus* hybridogenetic complex in Western Europe? Genetic evidence from a field study. *Conservation Genetics*. 2014;15:869–878.
- [37] De Meeüs T, Chan CT, Ludwig JM, Tsao JI, Patel J, Bhagatwala J, et al. Deceptive combined effects of short allele dominance and stuttering: An example with *Ixodes scapularis*, the main vector of Lyme disease in the USA. *Peer Community Journal*. 2021;1.
- [38] Coltman DW, Slate J. Microsatellite measures of inbreeding: A Meta-Analysis. *Evolution*. 2003;57(5):971–983.
- [39] Hale ML, Burg TM, Steeves TE. Sampling for microsatellite based population genetic studies: 25 to 30 individuals per population is enough to accurately estimate allele frequencies. *PLoS ONE*. 2012;7: e45170.
- [40] Pemberton J. Measuring inbreeding depression in the wild: the old ways are the best. *Trends Ecol Evol*. 2004;19(12):613-5.
- [41] Brzeski KE, Rabon DRJr, Chamberlain MJ, Waits LP, Taylor SS. Inbreeding and inbreeding depression in endangered red wolves (*Canis rufus*). *Molecular Ecology*. 2014;23(17):4241-55.
- [42] Hewitt GM. Speciation, hybrid zones and phylogeography – or seeing genes in space and time. *Mol.Ecol.* 2001;10:537-549.
- [43] Mutz T, Steinfartz S. *Mertensiella luschani flavimembris* ssp. n., Eine Neue Unterart des Lykischen Salamanders aus der Türkei (Caudata: Salamandridae). *Salamandra*. 1995;31:137-148.
- [44] Baçoğlu M, Atatür MK. The subspecific division of the Lycian salamander, *Mertensiella luschani* (Steindachner) in Southwestern Anatolia. *İstanbul Üniversitesi Fen Fakültesi Mecmuası Seri B*. 1974;39(3-4):147-155.
- [45] Kornilios P, Kumlutaş Y, Lymberakis P, Ilgaz Ç. Cryptic diversity and molecular systematics of the Aegean *Ophiomorus* skinks (Reptilia: Squamata), with the description of a new species. *Journal of Zoological Systematics and Evolutionary Research*. 2018;56(3):364-381.
- [46] Baran İ, Avcı A, Kumlutaş Y, Olgun K, Ilgaz Ç. *Türkiye Amfibi ve Sürüngenleri*. Palme Press, Ankara. 2021;236 pp.
- [47] Boger H, Dermitzakis MD. Neogene paleogeography in the Central Aegean region. In: VIIIth International Neogene Congress, Budapest. 1985; vol.70.
- [48] Lymberakis P, Poulakakis N. Three continents claiming an archipelago: the evolution of Aegean's herpetofaunal diversity. *Diversity*. 2010;2:233-255.
- [49] Plötner, J, Akın Pekşen Ç, Baier F, Uzzell T, Bilgin CC. Genetic evidence for human-mediated introduction of Anatolian water frogs (*Pelophylax* cf. *bedriagae*) to Cyprus (Amphibia: Ranidae). *Zoology in the Middle East*, 2015;61:125–132.

Appendices

Appendix A. Table S1

Table S1. Sample ID and microsatellite profiles for 52 individuals.

ID	RES 16		RES 5		RICA1b5		RICA5		RICA1b20	
1842	118	118	143	143	124	124	242	254	82	82
1843	114	118	143	143	122	122	254	254	80	80
1847	114	118	141	145	122	130	240	262	82	82
1848	114	118	141	145	122	122	240	240	82	82
1854	118	118	141	141	124	130	242	258	84	84
1855	114	118	141	143	122	130	258	258	82	82
1856	118	118	143	143	124	130	250	264	82	82
1865	118	118	143	153	126	128	250	254	80	80
1868	118	118	153	157	124	128	242	252	82	82
1840	118	118	143	143	122	122	254	254	80	84
1841	118	118	141	143	122	122	240	254	80	80
1845	118	118	143	143	122	122	262	262	80	86
1846	114	118	143	143	122	132	262	262	82	82
1851	118	122	141	143	128	128	250	250	82	84
1853	114	124	143	143	128	128	248	250	86	86
309	116	118	143	143	122	122	240	254	80	86
310	118	118	141	143	122	122	242	254	82	82
311	118	118	143	143	124	124	238	244	80	84
312	114	118	141	143	122	122	238	242	82	82
218	114	118	141	143	122	130	240	240	80	84
219	114	118	141	143	130	130	240	240	82	82
212	118	118	141	143	130	130	242	242	82	82
165	118	118	141	141	128	140	250	262	80	86
308	114	118	143	143	122	122	254	254	82	86
307	114	118	143	143	122	122	254	254	82	86
1830	114	118	141	141	130	130	240	240	80	80
1832	118	118	141	145	130	132	242	250	82	82
1833	118	118	141	145	130	130	242	242	82	86
1834	118	118	141	145	130	130	242	254	82	82
1835	118	118	141	141	130	130	248	248	80	80
1837	118	118	145	145	122	122	250	250	82	86
1839	114	118	143	143	122	130	260	260	82	86
1844	116	118	143	143	122	122	240	240	82	82
1849	118	118	143	145	122	122	240	242	82	82
1850	114	118	145	145	122	122	240	242	82	82
1857	114	118	141	143	122	130	250	250	80	86
1858	114	116	141	143	128	130	244	250	86	86
1859	118	118	141	141	124	130	242	258	82	82
1860	118	118	143	143	124	124	240	248	82	82
1861	118	124	143	143	128	130	250	250	82	82
1866	118	126	151	153	128	132	254	264	80	80
1796	116	116	141	141	122	130	240	240	80	80
1798	114	116	141	141	122	130	240	244	80	80
1801	116	116	141	141	124	124	246	264	82	82
1802	114	114	141	141	124	130	246	246	82	82
1803	114	114	141	141	124	130	242	248	82	82
1785	116	116	145	145	122	122	244	250	80	80
1787	114	114	141	141	130	130	242	248	80	80
1788	116	116	141	141	124	130	242	242	80	86
1789	116	116	141	145	124	134	244	248	80	82
1790	114	114	141	145	122	130	248	248	80	80
1792	116	118	141	141	122	130	244	244	78	78

An effective DNN-based Approach for Detecting Energy Theft in Smart Grids through User Consumption Patterns

Muhammed Zekeriya GÜNDÜZ^{1*} , Resul DAŞ² 

¹ Bingöl University, Vocational School of Technical Sciences, Department of Computer Science and Technology, Bingöl, Türkiye

² Fırat University, Technology Faculty, Department of Software Engineering, Elazığ, Türkiye
Muhammed Zekeriya GÜNDÜZ ORCID No: 0000-0003-4278-7123
Resul DAŞ ORCID No: 0000-0002-6113-4649

*Corresponding author: mzgunduz@bingol.edu.tr

(Received: 30.10.2023, Accepted: 15.12.2023, Online Publication: 28.12.2023)

Keywords

AMI,
DNN,
Cyber security,
Energy theft,
Smart grid
security

Abstract: The advancement of the Internet has been progressively easing human life. The development of mobile communication technologies has led to the widespread adoption of Internet of Things (IoT) applications. Thus, most systems and devices have connected to the Internet more efficiently. The integration of communication systems into critical infrastructures, such as electricity grids, has given rise to the concept of IoT-based smart grids. In smart grid systems, data communication is facilitated through the Advanced Metering Infrastructure (AMI). Due to the inherent characteristics of communication systems, AMI may be vulnerable to cyber-attacks. Some vulnerabilities have resulted in the emergence of cyber-attack vectors against energy consumption data obtained from smart meters. In this study, an effective energy theft intrusion detection system (IDS) based on users' consumption patterns is proposed. A Deep Neural Network (DNN) based classification model was employed to assess the predictability of both honest and malicious consumption patterns. The proposed model exhibits high and adjustable performance. Extensive experiments have been carried out on a real consumption dataset of approximately 2000 customers. Manipulated data from real readings with two different attack vectors were injected into the dataset. K-fold cross-validation technique was used. The proposed model performed a high performance reaching up to 97.4% accuracy.

Kullanıcı Tüketim Kalıpları Aracılığıyla Akıllı Şebekelerdeki Enerji Hırsızlığını Tespit Etmek İçin Etkili Bir DNN Tabanlı Yaklaşım

Anahtar Kelimeler

AMI,
DNN,
Siber güvenlik,
Enerji
hırsızlığı,
Akıllı şebeke
güvenliği

Öz: İnternetin ilerlemesi insan hayatını giderek kolaylaştırmaktadır. Mobil iletişim teknolojilerinin gelişmesi, Nesnelerin İnterneti (Internet of Things-IoT) uygulamalarının yaygın olarak benimsenmesine yol açmıştır. Böylece, çoğu sistem ve cihaz internete daha verimli bir şekilde bağlanmıştır. İletişim sistemlerinin elektrik şebekeleri gibi kritik altyapılara entegre edilmesi, IoT tabanlı akıllı şebekeler kavramını ortaya çıkarmıştır. Akıllı şebeke sistemlerinde veri iletişimi, Gelişmiş Ölçüm Altyapısı (Advanced Metering Infrastructure - AMI) aracılığıyla sağlanmaktadır. İletişim sistemlerinin doğal özellikleri nedeniyle, AMI siber saldırılara karşı savunmasız olabilir. Bazı güvenlik açıkları, akıllı sayaçlardan elde edilen enerji tüketim verilerine karşı siber saldırı vektörlerinin ortaya çıkmasına neden olmuştur. Bu çalışmada, kullanıcıların tüketim modellerine dayalı etkili bir enerji hırsızlığı saldırı tespit sistemi önerilmektedir. Hem dürüst hem de kötü niyetli tüketim kalıplarının tahmin edilebilirliğini değerlendirmek için Derin Sinir Ağı (Deep Neural Network - DNN) tabanlı bir sınıflandırma modeli kullanılmıştır. Önerilen model yüksek ve ayarlanabilir performans sergilemektedir. Yaklaşık 2000 müşteriden oluşan gerçek bir tüketim veri kümesi üzerinde kapsamlı deneyler gerçekleştirilmiştir. Veri kümesine iki farklı saldırı vektörü ile gerçek okumalardan elde edilen manipüle edilmiş veriler enjekte edilmiştir. K-katlı çapraz-doğrulama tekniği kullanılmıştır. Önerilen model %97,4 doğruluğa ulaşarak yüksek bir performans göstermiştir.

1. INTRODUCTION

IoT is a revolutionary technology that connects daily objects and devices to the Internet [1]. Thanks to the IoT, daily devices and systems can communicate with each other, share information, and make autonomous decisions more efficiently. It leads to development of new applications that can facilitate processes and improve quality of life [2]. Smart grids, which are critical infrastructures, have increased their usability with the development of IoT technologies. An IoT-based smart grid application uses IoT technologies to optimize energy generation, transmission, distribution, and consumption processes. AMI and smart meter are main elements of a smart grid system [3]. A smart meter is an electronic device designed to continuously monitor and log electricity consumption at regular time intervals [4]. Smart meters facilitate real-time monitoring of electricity consumption and offer valuable analytics for consumers and utilities [5]. By enabling bidirectional communication between service providers and consumers, smart meters improve the accuracy of billing, promote demand response, and empower customers to make conscious decisions regarding their energy consumption [6]. Cyber security issues are critical for the development of smart grid applications [7]. AMI causes many different cyber-attacks that occur in the smart grid applications due to its nature [7, 8]. Most of the attacks exploit security vulnerabilities in smart meters. While consumption data in a smart meter, which is an important component of AMI, passes through different stages, it can be sensitive against local and remote data tampering [9]. Storing and transmitting the data are the stages. Illegal manipulation of users' energy consumption data represents an important and major cyber security problem for smart grid systems [10]. Therefore, it is important to develop an effective IDS that can detect data manipulation attacks such as False Data Injection (FDI) in AMI with high accuracy [11].

Non-technical losses (NTLs) resulting from FDI attacks present a significant global concern [12]. While complete elimination of fraud may be unattainable for smart grid suppliers but implementing measures to detect, prevent, and reduce fraud is a viable approach [13]. Classification-based methods utilize detailed electricity consumption data obtained from smart meters. Customer consumption follows a specific statistical pattern in normal conditions [14]. Usage pattern irregularities may indicate malicious activities [15]. Deep learning (DL) models can be used to train a classifier based on real samples and synthetically generated samples. In our work honest samples are obtained from the real dataset. Malicious samples are obtained synthetically. We present a consumption pattern-based energy theft detector that utilize DNN.

DL approaches have gained popularity due to their superior performance compared to traditional machine learning (ML) methods in recent times [16]. The DNN-based IDS was trained using historical data of the honest consumers and synthetic attack data. The attack datasets

were generated from honest samples. The classifier was then used to determine whether a new sample is honest or malicious. We have presented a novel IDS for detecting energy theft in AMI. It detects anomalies in the consumption pattern of customers, offering a cost-efficient and high-performing solution for identifying energy theft and detecting data manipulation. In place of current classification-based techniques, the introduced IDS is resilient to attacks and benign alterations in consumption patterns. It achieves higher accuracy, sensitivity, and lower FPR. We obtained promising results with the model that we proposed. The proposed model was trained separately on balanced and imbalanced datasets using cross-validation technique. As a result of the training and testing, confusion matrices were created to measure the performance of the model. Performance metrics were obtained from these matrices. We tested the performance of the IDS with real data from nearly 2000 customers. The dataset serves as a valuable reference point for assessing and comparing various energy theft detection methods. The outcomes affirm the efficiency of our method.

FDI cyber-attacks, which can result in NTL, involve transmitting consumption data to the center with a value that is less than the actual one [17]. Many academic studies have been conducted to detect and prevent these cyber-attacks. Viegas et al. [14] used statistical and ML methods in the study focusing on electricity demand profile and achieved a forecast success of up to 76%. Jokar et al. [18] proposed an IDS using statistical methods based on consumption pattern in AMI and achieved accuracy in the range of 83.25% and 98.75%. Nagi et al. [12] proposed an approach with the SVM method based on load profile for NTL detection and achieved 60% accuracy. Otuoze et al. [19] proposed a framework for energy theft detection insight of smart city planning, but did not mention the performance rate of the proposed framework. Baskaran et al. [8] proposed a framework for detecting FDI data falsification attacks that may occur in AMI, but did not mention the performance rate of the proposed framework. Na et al. [10] created an FDI detector model using CNN and weighted random forest together and achieved an accuracy of up to 95.7% from the model. Kocaman and Tümen [17] created a LSTM-based model achieved an accuracy of up to 93.60%. DNN-based IDS system that we recommended has achieved 97.46% accuracy.

The rest of the paper is organized as follows: materials and methods are presented in section 2, and the experimental results are presented in section 3. Consequently, the conclusion remarks and future work are given in section 4.

2. MATERIAL AND METHOD

Real smart meter consumption data has recently been made available to researchers for academic and commercial studies. The Irish Social Science Data Archive (ISSDA) shares smart meter data that is difficult for individuals to obtain through real-life applications [20]. However, it is almost impossible to obtain data that

has been subjected to real cyber-attacks [21]. Therefore, hacked synthetic datasets are widely used in cyber security works. This, facilitates the development of artificial intelligence applications. Current DL models generally provide better performance than ML methods [22, 23]. Therefore, an up-to-date and high-performance DNN model was presented in this study.

2.1. Dataset and Attack Vectors

The ISSDA made available a dataset in January 2012, obtained through a collaboration with the Irish Commission for Energy Regulation (CER) [20]. This dataset comprises half-hourly electricity usage data for over 5,000 Irish households and businesses over a 536-day period in 2009 and 2010. The participants had smart meters and willingly took part in the project. All the data came from honest users. The size of dataset, diversity of participants, extended data collection period, and public accessibility make it a valuable resource for research in the analysis of smart meter data. In our tests, consumption data of 1948 customers for ten weekdays are used in half-hour periods by creating a 1948 rows and 480 columns dataset. Honest samples are labeled as 1, malicious samples are labeled as 0.

The hacked consumption data was obtained synthetically. Two different attack vectors were used in the study to create synthetic attack data. The attacks are named f_1 and f_2 . While the f_1 attack aims the multiplication of the real data by a random number between 0.1 – 0.8, the f_2 attack aims the reduction of the values at a specific time of the day to zero. The equations of attack vectors f_1 and f_2 are as in (1) and (2).

$$f_1 = \text{random}(0.1-0.8) * \text{all honest data} \quad (1)$$

$$f_2 = 0 * \text{honest data (specific time range, } t=37-41) \quad (2)$$

There are 48 consumption data per day for a customer. While the first reading is done at 00.30, the last reading is done at 00.00. In this context, the 37th, 38th, 39th, 40th, 41th readings between 18.30 and 20.30, where the consumption is high, were selected for the f_2 attack vector. It is important to visualize how an FDI attack vector that aims to reduce energy consumption data changes the actual data. In this context, the honest consumer pattern of a customer and the f_1 , f_2 attack forms are shown in figure 1.

2.2. Deep Neural Network

A DNN model employs techniques to automatically adjust its weights during training on large datasets, allowing it to capture intricate patterns [16]. A DNN model comprises various layers, such as input, dense (fully connected), convolutional, recurrent, activation, and output layers, depending on the architecture. Each of these output neurons serves as input for subsequent layers. Dense layers, prevalent in DNNs, are often combined with other layers to construct models capable of extracting hierarchical features and representations from the input data.

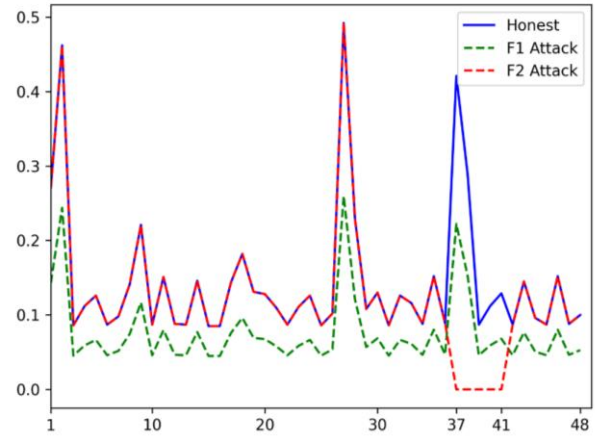


Figure 1. Honest consumer pattern of a customer with f_1, f_2 attacks

The arrangement and quantity of dense layers in a neural network structure are determined by the specific problem at hand and the desired level of model complexity [23]. DNN encompasses diverse areas such as computer vision, natural language processing, and pattern recognition. The training process involves fine-tuning the weights through backpropagation, enabling the DNN to learn and generalize from the provided datasets. DNNs have played a crucial role in advancing the capability of deep learning across a wide range of applications, showcasing their adaptability and effectiveness in capturing complex patterns within data.

2.3. Proposed Approach

Users with no missing data were selected as samples. Hence 10-days consumption data of approximately 2000 customers was designed in 30-minutes periods. The dataset was converted into 1×480 input data for each customer. Synthetic attack datasets were obtained by applying f_1 and f_2 attacks on all honest-data (h). These datasets were normalized by combining them as $h + f_1, h + f_2, h + f_1 + f_2$. Honest data labeled as 1 and malicious ones as 0. While $h + f_1$ and $h + f_2$ are balance datasets, $h + f_1 + f_2$ is an imbalance dataset. In the training phase, confusion matrices are obtained for each fold using the k-fold cross validation technique. The value of k is five. Model performance results were got from the performance metrics that are obtained from these confusion matrices.

The dataset obtained from ISSDA is consumption data belongs completely honest customers. This honest dataset was exposed to $f_1, f_2, f_1 \& f_2$ attacks. Thus, different datasets that were exposed to three different cyber-attacks were obtained. f_1 attack dataset, f_2 attack dataset, and $f_1 \& f_2$ attack dataset were generated separately. The dataset created with $f_1 \& f_2$ is imbalanced while the others are balanced. After these datasets were normalized, they were given to the DNN algorithm as input for the training and validation processes. Our model consists of seven layers, including the input layer, five fully connected layers and the output layer. The architecture of the energy theft detector is shown in figure 2.

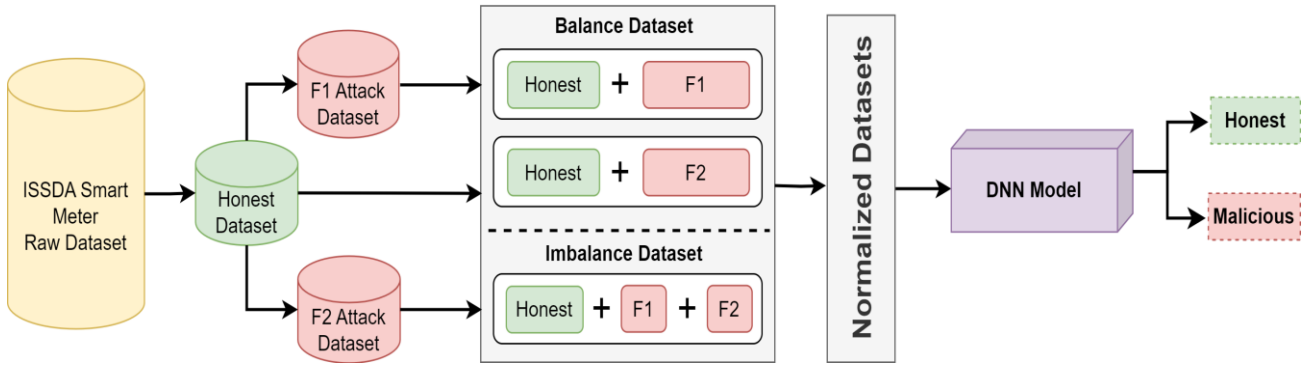


Figure 2. The architecture of the DNN-based energy theft detector

The model accepts 1-by-480 consumption pattern into the input layer. Glorot uniform initializer, ReLU activation function, dropout, early stopping and L2 regularization were preferred to prevent over-fitting with batch normalization in every fully connected layer.

The model flow is as follows:

The input data is represented as a vector. Mathematical output of fully connected (dense) layers is stated as

$$Z^{[i]} = \sum_{i=1}^5 W^{[i]} A^{[i-1]} + b^{[i]}$$

$$A^{[i]} = \text{Re } LU(Z^{[i]})$$

Where:

$A^{[0]}$ represents the input data vector.

$W^{[i]}$ is the weight matrix layer i .

$b^{[i]}$ is the bias vector for layer i .

$Z^{[i]}$ is the linear operation result at layer i .

$A^{[i]}$ is the activation at layer i , computed using the *ReLU* activation function. Output layer is stated as

$$Z^{[6]} = W^{[6]} A^{[5]} + b^{[6]}$$

$$\hat{Y} = \text{Sigmoid}(Z^{[6]})$$

Where:

\hat{Y} is the output prediction, typically using sigmoid activation function for binary classification.

2.4. Evaluation of the Proposed Model

The confusion matrix, also called as the error matrix, is a common method for evaluating a model's effectiveness. It is generated when the model compares its predicted outcomes with the actual samples, resulting in four key indicators. True Positives (TP - correctly predicted positives), True Negatives (TN - correctly predicted negatives), False Positives (FP - incorrectly predicted positives), False Negatives (FN - incorrectly predicted negatives) [16]. The number of TP and TN represent the number of correctly recognized malicious and honest samples respectively. The number of FP and FN represent the number of misclassified malicious and

honest samples respectively. The structure of the confusion matrix used in the study is shown in figure 3.

		Actual Values	
		Malicious (0) Energy Theft	Honest (1) No Theft
Predicted Values	Malicious (0) Energy Theft	TP	FP
	Honest (1) No Theft	FN	TN

Figure 3. Confusion matrix for 2-classes

Evaluation metrics derived from a confusion matrix include several key indicators used to assess the performance of classification models. These metrics are calculated based on the values present in the confusion matrix. Table 1 shows prominent performance metrics such as sensitivity, specificity, precision, F1-score, accuracy, and False Positive Rate (FPR) obtained from the confusion matrix. Meanwhile recall, True Positive Rate (TPR), hit rate, Detection Rate (DR) and sensitivity represent the same metric. These metrics help in assessing different aspects of a classification model's performance, considering both the correct and incorrect classifications made by the model in comparison to the actual values.

In our experiments, we employed k-fold cross-validation technique to ensure reliable and generalized outcomes. This approach involves partitioning the dataset into training and validation sets to evaluate and compare model performance. During the k-fold cross-validation process, every data point is utilized for both training and validation across each fold of the dataset. K-fold cross-validation serves two fundamental objectives in model assessment. Firstly, it rigorously evaluates a model's performance using the provided dataset, developing its ability to yield accurate predictions or classifications on entirely novel, unseen data. This process ensures a comprehensive understanding of the model's generalization capabilities beyond the training set.

Table 1. Performance metrics obtained from the confusion matrix

Metrics	Equation	Short Description
Sensitivity	$\frac{TP}{TP + FN}$	The performance of the model in detecting malicious samples.
Specificity	$\frac{TN}{TN + FP}$	The performance of the model in detecting honest samples.
Precision	$\frac{TP}{TP + FP}$	The ratio of malicious samples predicted as malicious to all malicious samples.
F1-score	$\frac{2TP}{2TP + FP + FN}$	It is expressed as the harmonic mean between precision and sensitivity.
Accuracy	$\frac{TP + TN}{TP + FP + FN + TN}$	Measures the overall correctness of predictions by the model.
FPR	$\left(\frac{FP}{FP + TN}\right)$	Measures the proportion of actual honest that were incorrectly classified as malicious samples.

Secondly, by systematically partitioning the data into subsets for training and validation, k-fold cross-validation facilitates a comparative analysis of the model performances. This methodological approach aids in determining the optimal model among various algorithms based on their performance metrics within the dataset. As a result, it empowers the informed selection of the algorithm that exhibits superior predictive ability and robustness, crucial considerations for addressing specific problem domains effectively.

3. EXPERIMENTAL RESULTS

We used *Python 3.10* and *Google Colab Pro* (A100 GPU and V100 GPU) platforms for all processes. The honest and malicious datasets were trained and tested using the five-fold cross-validation method. Hyper parameters are given in table 2.

Table 2. Hyper parameters used in the DNN-based model

Hyper parameters	Values
Epoch	100
Batch Size	64
Optimizer	SGD
Learning Rate	0.01
L2 Regularization	0.0001
Kernel Initializer	Glorot_uniform
Seed	12

Balance datasets and imbalance dataset were trained with the model using the stratified five-fold cross-validation technique. Confusion matrices were obtained for each fold of each dataset. The confusion matrices obtained for each fold of each dataset is given in table 3.

The performances of the models were measured with the accuracy, precision, specificity, sensitivity, F1-score, and FPR performance metrics. The standard deviations were also calculated. Performance metrics were obtained with the related confusion matrices presented in table 3. The results of these metrics are given in table 4. According to the results, 84.68% accuracy was obtained with the

Honest + f₁ attack dataset, while 97.46% accuracy was obtained with the *Honest+f₂* attack dataset. These results were obtained from balanced datasets. An accuracy of 85.28% was achieved with the *Honest+ f₁ + f₂* attack dataset, which is the imbalance dataset. According to these results, the best performance result was obtained with *Honest + f₂* attack dataset, which includes *f₂* attack vector. Accuracy, specificity, sensitivity, and FPR performance metrics were used sequentially. Therefore, 84.68%, 89.16%, 81.32%, 10.84% were achieved in the *Honest+ f₁* attack respectively. 97.46%, 99.90%, 95.38%, 0.10% were achieved in the *Honest+f₂* attack respectively. 85.28%, 81.08%, 87.30%, 18.92% were achieved in the *Honest+f₁+f₂* attack respectively.

Figure 4 shows the ROC curves of the models trained with different balanced datasets. The AUC values of the model trained with *Honest + f₁* attack data at each fold are 89.97%, 90.60%, 90.67%, 90.89%, and 90.59%, respectively. The AUC values of the model trained with *Honest + f₂* attack data at each fold are 99.94%, 99.16%, 99.84%, 99.42%, and 99.71%, respectively. As can be seen from the curves and AUC values in figure 4, the *Honest + f₂* attack dataset showed a higher accuracy rate than other datasets.

The ROC curve demonstrates the model's capacity to reasonably differentiate malicious samples, even within the context of the dataset's inherent imbalance. ROC analysis serves as a critical indicator of the stability of the trained deep learning model, particularly in challenging scenarios involving imbalanced dataset, where achieving high accuracy presents difficulties.

Figure 5 exhibits ROC curves of the folds corresponding model trained with imbalanced (*Honest + f₁ + f₂*) dataset. The AUC values of the model trained with *Honest + f₁ + f₂* attack data on each fold were calculated as 92.50%, 91.90%, 91.02%, 90.59%, and 92.61%, respectively. Additionally, figure 5 shows loss-accuracy graphs of the folds corresponding to the imbalanced dataset. When examining the epochs, it becomes apparent that the accuracy generally increases while the loss curve decreases at a certain rate, ultimately reaching a reasonable level. Hence, the model has undergone the learning process in a determined manner, effectively avoiding overfitting.

The information regarding the balancing or imbalancing of datasets in articles is often unclear, which adds complexity to examining the distribution nature of the datasets utilized in various studies. Table 5 shows the comparison of our study with some existing studies. All studies work on the same dataset with different sample rates. In [14], statistical and ML methodologies were explored to forecast consumer demand profiles. Among these models, the support vector machine (SVM) algorithm achieved an accuracy rate as high as 75.8% for this particular application.

Table 3. Confusion matrices for each fold of the proposed model

Dataset	Fold 1		Fold 2		Fold 3		Fold 4		Fold 5	
<i>Honest + f₁ Attack</i>	362 ^a	28 ^b	355 ^a	34 ^b	354 ^a	35 ^b	339 ^a	51 ^b	349 ^a	41 ^b
	97 ^c	293 ^d	104 ^c	286 ^d	80 ^c	310 ^d	61 ^c	328 ^d	66 ^c	323 ^d
<i>Honest + f₂ Attack</i>	390 ^a	0 ^b	389 ^a	0 ^b	388 ^a	1 ^b	390 ^a	0 ^b	389 ^a	1 ^b
	9 ^c	381 ^d	20 ^c	370 ^d	12 ^c	378 ^d	49 ^c	340 ^d	7 ^c	382 ^d
<i>Honest + f₁&f₂ Attack</i>	695 ^a	84 ^b	720 ^a	59 ^b	686 ^a	93 ^b	717 ^a	63 ^b	738 ^a	41 ^b
	79 ^c	311 ^d	116 ^c	274 ^d	92 ^c	298 ^d	113 ^c	276 ^d	120 ^c	269 ^d

TP (^a), FP (^b), FN (^c), TN (^d)

Table 4. Performance results and standard deviation of the proposed model according to balance and imbalance datasets

	Accuracy (%)	Precision (%)	Specificity (%)	Sensitivity (%)	F1-score (%)	FPR (%)
<i>Honest + f₁ Attack</i>	84.68±1.41	90.30±1.99	89.16±1.55	81.32±2.88	85.51±1.0	10.84±1.55
<i>Honest + f₂ Attack</i>	97.46±1.95	99.90±0.13	99.90±0.13	95.38±3.44	97.56±1.81	0.10±0.13
<i>Honest + f₁&f₂ Attack</i>	85.28±0.76	91.27±2.38	81.08±3.55	87.30±1.47	89.20±0.67	18.92±3.55

Mean ± standard deviation

Table 5. A comparison of exist studies on the same dataset

Reference	Year	Simulation Platform	Proposed Model	Dataset Resource	Accuracy(%)
[14]	2015	N/A	SVM	ISSDA	75.8
[24]	2017	N/A	Density-based clustering	ISSDA	93.2
[25]	2016	N/A	SVM-based	ISSDA	94.0
[26]	2020	N/A	MP-ANN	ISSDA	93.4
[13]	2018	Python 3.x	DNN-based	ISSDA	93.0
Our study	2023	Python 3.10	DNN-based	ISSDA	97.4

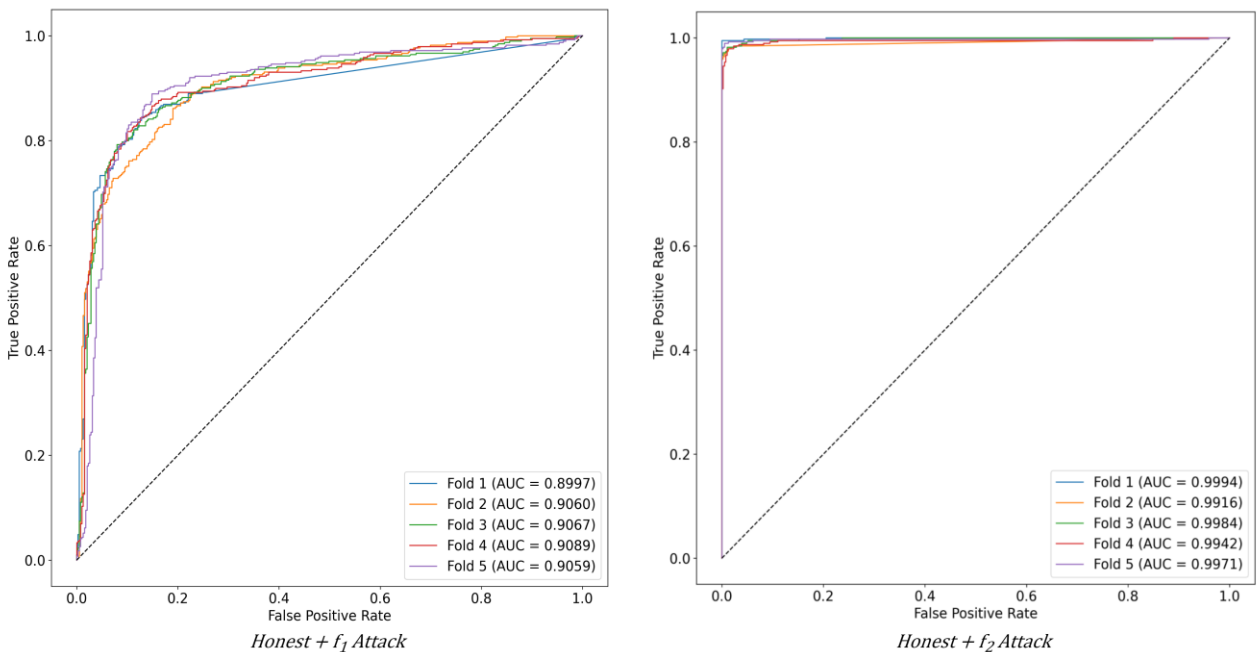


Figure 4. The ROC curves of the DNN models for balanced datasets

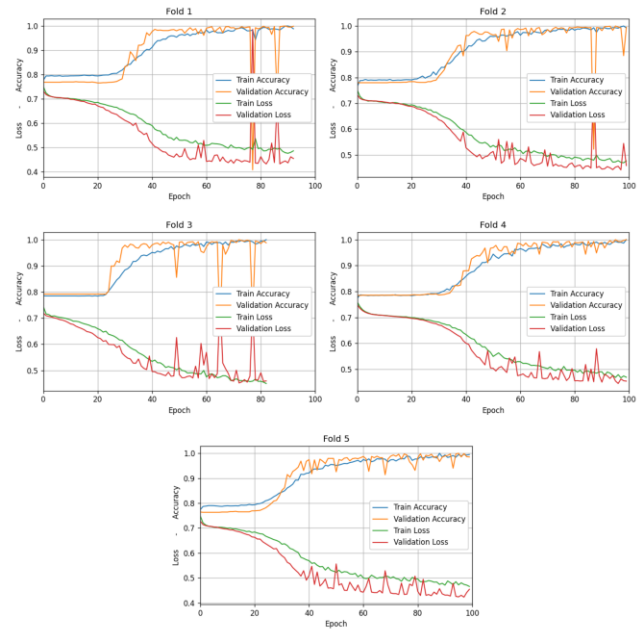
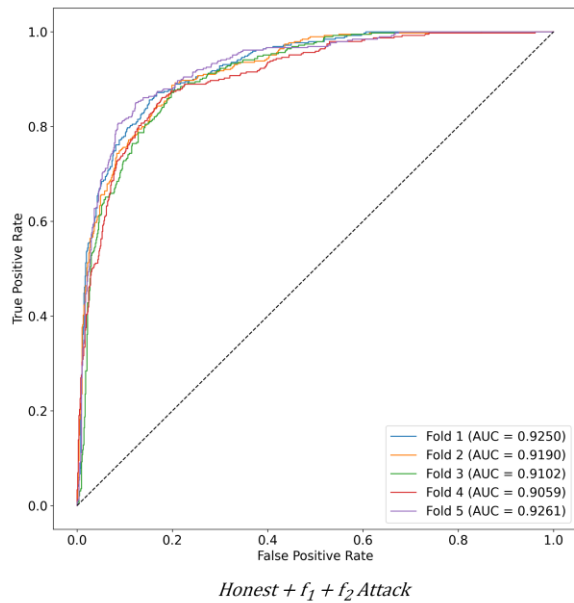


Figure 5. The ROC curve and loss-accuracy graphs along with epochs for imbalanced dataset

In [24], the method using smart meter data effectively detects energy theft by focusing on abnormal load profiles, outperforming traditional unsupervised techniques like k-means clustering, GMM clustering, and DBSCAN. It has high accuracy. The technique is helpless for attackers that do not generate load profiles with an abnormal shape. Moreover, the proposed SVM-driven detector in [25] exhibits notable efficacy, demonstrating an average detection rate of 94% alongside a false alarm rate of 11%. In [26], a multilayer perceptron was developed the detection of energy theft in distribution systems using the Multilayer Perceptron Artificial Neural Network (MP-ANN) algorithm. They obtained 93.4% accuracy. In [13], a DNN based system was designed for identifying energy theft on a per-customer basis. This specialized DNN-based detector attains a detection rate reaching 93%. Simulation outcomes underscore a considerable advancement in performance when compared with state-of-the-art shallow detection methodologies. In some studies, it has not been clearly stated the real data exposed to which attack vectors and whether the data is imbalanced or balanced. In our proposed model, real data were exposed to f_1 and f_2 attacks separately and together, as explained before. Our energy theft detector provides up to 97.4% accuracy.

4. CONCLUSION

In this study, the detection of energy theft in smart grids was investigated on synthetic data obtained from a real dataset with a DNN-based approach. The method relies on consumption data patterns. The manipulated values were injected into the dataset with two different attack vectors. Both balanced and imbalanced datasets were investigated with the same DNN network. Stratified five-fold cross-validation technique was used to obtain more generalizable results during the training phase. The results were compared. Widely accepted performance metrics such as accuracy, precision, specificity,

sensitivity, FPR, and AUC-ROC were used to evaluate the performance of the model. We observed that the classification done with the *Honest+ f_2* balanced dataset performed better results than the imbalanced dataset. The model achieved 97.46% accuracy, 99.9% precision, 99.9% specificity, 95.38% sensitivity, 97.56% F1-score, 0.1% FPR, and up to 99% AUC-ROC when it was tested on *Honest+ f_2* balanced dataset. Compared to other data-driven methods evaluated on the same dataset, we achieved the best accuracy of 97.46% among existing studies. By proactively identifying irregularities in consumption patterns, the DNN-based approach offers a robust IDS, enhancing the reliability and resilience of energy distribution systems. In future work, a study will be done with more cyber-attack vectors and a CNN-based hybrid model will be developed on a larger balanced dataset.

Declaration of Competing Interest

The authors declare no conflicts of interest.

Acknowledgment

The authors would like to thank ISSDA and CER for providing the real smart meter consumption data.

This manuscript was produced from Muhammed Zekeriya Gündüz's Ph.D. thesis ("Development of New Approaches for the Detection and Solution of Security Vulnerabilities in the Internet of Things Based Smart Grids").

REFERENCES

- [1] Gunduz MZ and Das R. Internet of things (IoT): Evolution, components and applications fields. *Pamukkale University Journal of Engineering Sciences*. 2018; 24(2). doi: 10.5505/pajes.2017.89106.
- [2] Gunduz MZ and Das R. Analysis of cyber-attacks on smart grid applications. *International*

- Conference on Artificial Intelligence and Data Processing (IDAP)*. 2018; doi: 10.1109/IDAP.2018.8620728.
- [3] Gündüz MZ and Daş R. Akıllı Şebekelerde İletişim Altyapısı ve Siber Güvenlik. *İğdır Üniv. Fen Bil. Enst. Der.* 2020;10(2). doi: 10.21597/jist.655990.
- [4] Sahoo S, Nikovski D, Muso T, and Tsuru K. Electricity theft detection using smart meter data. *IEEE Power & Energy Society Innovative Smart Grid Technologies Conference (ISGT)*. 2015; doi: 10.1109/ISGT.2015.7131776.
- [5] Emmanuel M and Rayudu R. Communication technologies for smart grid applications: A survey. *Journal of Network and Computer Applications*. 2016;74 doi: 10.1016/j.jnca.2016.08.012.
- [6] Otuoze AO *et al.* Electricity theft detection framework based on universal prediction algorithm. *Indonesian Journal of Electrical Engineering and Computer Science*. 2019;15(2) doi: 10.11591/ijeecs.v15.i2.pp758-768.
- [7] Gunduz MZ and Das R. Cyber-security on smart grid: Threats and potential solutions. *Computer Networks*. 2020;169. doi: 10.1016/j.comnet.2019.107094.
- [8] Baskaran H., Al-Ghaili AM, Ibrahim ZA, Rahim FA, Muthaiyah S and Kasim H. Data falsification attacks in advanced metering infrastructure. *Bulletin of Electrical Engineering and Informatics*. 2021;10(1). doi: 10.11591/eei.v10i1.2024.
- [9] Das R and Gunduz MZ. Analysis of cyber-attacks in IoT-based critical infrastructures. *International Journal of Information Security Science*. 2019;8(4).
- [10] Na L, Xiaohui X, Xiaoqin M, Xiangfu M, and Peisen Y. Fake Data Injection Attack Detection in AMI System Using a Hybrid Method. *IEEE Sustainable Power and Energy Conference (iSPEC)*. 2021. doi: 10.1109/iSPEC53008.2021.9735875.
- [11] Bhattacharjee S and Das SK. Detection and Forensics against Stealthy Data Falsification in Smart Metering Infrastructure. *IEEE Transactions on Dependable and Secure Computing*. 2021;18(1) doi:10.1109/TDSC.2018.2889729.
- [12] Nagi J, Yap KS, Tiong SK, Ahmed SK, and Mohamad M. Nontechnical Loss Detection for Metered Customers in Power Utility Using Support Vector Machines. *IEEE Transactions on Power Delivery*. 2010;25(2). doi: 10.1109/TPWRD.2009.2030890.
- [13] Ismail M, Shahin M, Shaaban MF, Serpedin E and Qaraqe K. Efficient detection of electricity theft cyber attacks in AMI networks. *IEEE Wireless Communications and Networking Conference (WCNC)*. 2018. doi: 10.1109/WCNC.2018.8377010.
- [14] Viegas JL, Vieira SM, Sousa JMC, Melício R, and Mendes VMF. Electricity demand profile prediction based on household characteristics. *12th International Conference on the European Energy Market (EEM)*. 2015. doi: 10.1109/EEM.2015.7216746.
- [15] Viegas JL, Esteves PR, Melício R, Mendes VMF, Vieira SM. Solutions for detection of non-technical losses in the electricity grid: A review. *Renewable and Sustainable Energy Reviews*. 2017;80. doi: 10.1016/j.rser.2017.05.193.
- [16] Ayaz I, Kutlu F, Cömert Z, DeepMaizeNet: A novel hybrid approach based on CBAM for implementing the doubled haploid technique. *Agronomy Journal*. doi: 10.1002/agj2.21396.
- [17] Kocaman B and Tümen V. Detection of electricity theft using data processing and LSTM method in distribution systems. *Sādhanā*. 2020; 45(1) doi: 10.1007/s12046-020-01512-0.
- [18] Jokar P, Arianpoo N, Leung VCM. Intrusion detection in advanced metering infrastructure based on consumption pattern. *IEEE International Conference on Communications (ICC)*. 2013. doi: 10.1109/ICC.2013.6655271.
- [19] Otuoze AO, Mustafa MW, Mohammed OO, Saeed MS, Surajudeen-Bakinde NT, Salisu S. Electricity theft detection by sources of threats for smart city planning. *IET Smart Cities*. 2019; 1(2) doi: 10.1049/iet-smc.2019.0045.
- [20] ISSDA, Irish Social Science Data Archive. <https://www.ucd.ie/issda/data/commissionforenergyregulationcer/>
- [21] Şahin K, Hizal S, Zengin A. Design and Implementation of ADevs-Based Cyber-Attack Simulator for Cyber Security. *IJSIMM*. 2022; 21(1). doi: <https://doi.org/10.2507/IJSIMM21-1-587>.
- [22] Dinçer Y, İnik Ö. Çevresel Seslerin Evrişimsel Sınır Ağları ile Sınıflandırılması. *KONJES*. 2023;11(2). doi: 10.36306/konjes.1201558.
- [23] Haq EU, Pei C, Zhang R, Jianjun H, Ahmad F. Electricity-theft detection for smart grid security using smart meter data: A deep-CNN based approach. *Energy Reports*. 2023;9 doi: 10.1016/j.egyr.2022.11.072.
- [24] Zheng K, Wang Y, Chen Q, Li Y, Electricity theft detecting based on density-clustering method. *IEEE Innovative Smart Grid Technologies (ISGT-Asia)*. 2017. doi: 10.1109/ISGT-Asia.2017.8378347.
- [25] Jokar P, Arianpoo N, Leung VCM. Electricity Theft Detection in AMI Using Customers' Consumption Patterns. *IEEE Transactions on Smart Grid*. 2016;7(1) doi: 10.1109/TSG.2015.2425222.
- [26] Souza MA, Pereira JLR, Alves GO, Oliveira BC, Melo ID, Garcia PAN. Detection and identification of energy theft in advanced metering infrastructures. *Electric Power Systems Research*. 2020; 182. doi: 10.1016/j.epsr.2020.106258.

Erratum: Determination of Ground-Based Structural Problems in the Historical Four-Legged Minaret with Ground Penetration Radar

Süleyman İPEK^{1*}, Nursen IŞIK², Fatma Meral HALİFEOĞLU³

¹ Bingöl University, Engineering and Architecture Faculty, Architecture Department, Bingöl, Türkiye

² Dicle University, Architecture Faculty, Architecture Department, Diyarbakır, Türkiye

³ Dicle University, Architecture Faculty, Architecture Department, Diyarbakır, Türkiye

Süleyman İPEK ORCID No: 0000-0001-8891-949X

Nursen IŞIK ORCID No: 0000-0002-6125-1896

Fatma Meral HALİFEOĞLU ORCID No: 0000-0003-2032-3774

*Corresponding author: sipek@bingol.edu.tr

(Received: 25.12.2022, Accepted: 22.06.2023, Erratum Online Publication: 28.12.2023)

Keywords

Historical structure, Ground-penetrating radar, Masonry structure, Minaret, Nondestructive testing method

Abstract: The Four-Legged Minaret, which has an important place thanks to its building period and unique architecture, is located in the southeastern part of the historical Suriçi region of Diyarbakır. This structure located outside the courtyard of Sheikh Mutahhar Mosque and inside the Dört Ayaklı Minare Street was built on a monolithic stone column from basalt stone in a tetragon plan and is carried by four columns that are in cylindrical form. After 2015, partial damages occurred to the minaret. During the restoration works carried out between 2016-2019, these partial damages were tried to be repaired. But the condition of the ground was not instrumentally detected and investigated in these restoration works. In the present study, observational geological and instrumental geophysical studies were carried out on the Four-Legged Minaret and its surrounding area. The ground condition of the Four-Legged Minaret and the situation of its construction materials were determined by scannings achieved from the ground penetration radar and whether the damages in the structure were related to the ground condition was analyzed. As a consequence of the study, fractures and cracks were detected in the wall, and fractures, cracks, and water leakage-dependent collapses were detected on the floor. Besides, finally, repair recommendations for these damages are also presented in this study.

Düzeltilmiş: Tarihi Dört Ayaklı Minare'de Zemine Dayalı Strüktürel Sorunların Yer Radarı ile Belirlenmesi

Anahtar

Kelimeler

Tarihi yapı, Yer radarı, Yığma yapı, Minare, Tahribatsız deney yöntemi

Öz: Hem inşa edildiği dönem hem de sahip olduğu eşsiz mimariyle önemli bir yere sahip olan Dört Ayaklı Minare, Diyarbakır'ın tarihi Suriçi Bölgesinin güneydoğu diliminde yer almaktadır. Şeyh Mutahhar Cami avlusu dışında ve Dört Ayaklı Minare Sokak içinde bulunan bu yapı, yekpare taş sütun üzerinde bazalt malzemeden dört köşeli olarak inşa edilmiş olup, dört adet silindirik formlu sütunla taşınmaktadır. 2015 yılından sonra minarede kısmi hasarlar meydana gelmiştir. 2016-2019 yılları arasında yapılan restorasyon çalışmalarında bu kısmi hasarlar giderilmeye çalışılmıştır. Ancak yapılan bu restorasyon çalışmalarında zemine yönelik herhangi bir aletsel tespit ve inceleme yapılmamıştır. Bu çalışmada, Dört Ayaklı Minare ve çevresinde gözlemsel olarak jeolojik ve aletsel olarak jeofizik etütler yapılmıştır. Dört Ayaklı Minare'nin zemin durumu ve yapı malzemelerinin durumu, yer radarından yapılan taramalarla tespit edilmiş ve yapıda meydana gelen hasarların zemin durumu ile ilgili olup olmadığı analiz edilmiştir. Yapılan çalışma neticesinde, duvarda kırık ve çatlaklar, zeminde kırık, çatlak ve su sızıntılarına bağlı çökmeler olduğu tespit edilmiştir. Son olarak, bu hasarlara yönelik onarım önerileri de bu çalışmada sunulmuştur.

1. INTRODUCTION

The United Nations Educational, Scientific and Cultural Organization (UNESCO) describes the term 'cultural heritage' as the legacy, inherited from past generations, reaching today, and endowing for the benefit of future generations, that is associated with intangible attributes and physical science artifacts of a society or group [1,2]. But this term has been applied to tangible cultural heritages such as monuments, historical places, buildings, works of art, artifacts, and books, as well as intangible cultural heritages such as beliefs, traditions, language, folklore, knowledge, and customs, and natural heritages such as culturally significant marine ecosystems, landscapes, and biodiversity [1]. However, not all legacies passed down through the centuries qualify as legacy; rather, the item is designated as heritage by society [3]. In this manner, the preservation of historical buildings in all their physical forms makes this an important issue as it is a special component of the collective identity [4]. Human involvement and natural disasters like earthquakes, landslides, floods, etc. are typical causes of the deterioration of such buildings as time passes. Therefore, finding a route that combines and safeguards such historical structures should be created and followed to boost the efficiency of the fortification, conservation, and restoration method [4,5].

In this context, historical mosques, which are centers of worship and belief that have an important place in the social and cultural life of cities from past to present, can be regarded as tangible cultural heritage, implicitly also intangible cultural heritage. After the acceptance and spread of Islam, mosques were built in different forms and plans, reflecting the characteristics of the period in which they were built and used as places of worship. In many periods from the past to the present, minarets have been built in mosques for the purpose of reciting the azan and making reciting the azan heard. In this context, the first minaret example in the mosque was built in the Mosque of 'Amr ibn al-'As in Egypt in 673 AD, and it was built with a balcony to announce the azan [6].

Minarets, which were built from stones, bricks, and wood, did not have a certain shape in the beginning and there are two styles of minarets that might be described in general: the first style is inspired by ancient lighthouses and/or bell towers having a square/rectangular cross-section in-plane and the second style that originated in Asia constructed in a cylindrical slender body [7]. Minarets can be considered one of the distinctive and essential structural components of the Islamic cityscape [8]. Throughout history, countless majestic minarets have been built in various parts of the world adapting structural approaches and utilizing various materials [6]. Similar to many other ancient structures, the historical minarets are made of brick/stone and mortar and they are regarded as tower-like structures [9].

Diyarbakır which has hosted many civilizations and still has born traces of these civilizations is located in southeast Turkey. In the course of these periods, the social, cultural, religious, and interaction of communities

from different cultures and traditions with the local resident increased over time. With the spread of Islam, the majority of the city community perpetuated living according to Islamic traditions and rules. In this manner, mosques have become the buildings where the people of the city performed their religious worship and have been actively used in many parts of the city [10].

In the yearbooks of Diyarbakır, it is stated that there were 24 mosques and 21 masjids in the city center in the 1900s. In the Suriçi region, a limited number of the mosques that were constructed during the early Islamic period have survived to the present day, and a majority of the structures have been destroyed. Besides, there are no mosques or masjids that have survived to the present day from the Umayyad period, while information about the mosques belonging to the Abbasid period is learned from the inscriptions and reliefs on the city walls. The oldest mosque in the city is the Diyarbakır Ulu Mosque, which was built in the 7th century with the characteristics of Arabic architecture. Many of the other mosques were built during and after the Akkoyunlu period.

Khoja Ahmet (Ayn Minaret) Mosque (in 1489) was built in the southwest of the Suriçi region, Sheikh Mutahhar and the Four-Legged Minaret (in 1500) and Lala Kasım Bey Mosque in the southeast of the Suriçi region, Nebi Mosque (in 1503) and some masjids (such as İbrahim Bey, Hacı Büzruk, Tacettin masjids) were built in the northwest of the Suriçi region. Fatih Pasha (Kurşunlu) Mosque (in 1516-1520) and Nasuh Pasha Mosque (in 1601) in the northeast of the Suriçi region, Hüsrev Pasha Mosque and its madrasa (in 1521-1528) in the southeast of the Suriçi region, Ali Pasha Mosque (in 1534-1537) and Defterdar Mosque (in 1594) in the south of the Suriçi region, İskender Pasha Mosque (in 1551) and Melik Ahmet Pasha Mosque (in 1587-1591) in the northwest of the Suriçi region, Behram Pasha Mosque (in 1564-1567) in the southwest of the Suriçi region are among the Ottoman period mosques [11]. In Diyarbakır mosques, the minarets are built in either square (or nearly square) form or cylindrical form, while the minaret of the Khoja Ahmet (Ayn Minaret) Mosque has an octagonal form. The minarets of the Ulu Mosque, Nebi Mosque, Hz. Süleyman Mosque, Hüsrev Pasha Mosque, and Sheikh Mutahhar Mosque are in a square plan order. However, there are cylindrical annexes in most of these minarets. Figures 1a-n exhibit the mosques and their minarets in the Suriçi region in Diyarbakır.

Among the aforementioned minarets, the Four-Legged Minaret has an important status from the point of cultural heritage, due to its building period and peerless architecture, and the historical events it has witnessed. During the repair and restoration works carried out on the minaret, drilling works and compression tests were carried out in 2011 by the Regional Directorate of Foundations to determine the soil condition of this area. However, after this date, there is no convenient and useful examination of the soil condition of this building and its surrounding area. For this reason, the present study has importance since it is aimed to examine the

structural status of the building in regard to its soil condition. Because of that, the investigation of cracks, fractures, and partial axis slippage problems in the minaret depending on the soil structure was carried out with a non-destructive measurement method called ground-penetrating radar, and thereby, the structure was evaluated in this context. Here, it can be stated that nondestructive testing (NDT) is the examination of a system and its components and materials, in terms of situations and features using a number of analytical procedures [12]. Though fast progress in NDT technology has been witnessed due to increasing performance expectations from current buildings and engineering materials, the process of adapting NDT technologies to historical buildings is still in its infancy [5]. However, Moropoulou et al. [13] have recently defined NDT methods as essential instruments for cultural heritage buildings. The capacity to use NDT methods in situ and the elimination of the necessity for disruptive sample taking are the two most important benefits of using them on ancient buildings. They can be used not only to determine material situations and

characteristics like density, moisture content, strength, dimension, stiffness, etc., but also to detect discontinuities, anomalies, internal cracks, and voids in structure and/or its components. Additionally, they can be employed in displaying the architectural detailing and layouts, evaluating frame and structural performances of the building, and monitoring anomalies underground. Examining the qualities of historical materials, studying the origins of these materials, analyzing the environmental consequences, considering prior interferences, and, most importantly, searching the historical records may all be done as part of extensive studies on historical structures [4,13,14]. NDT methods which can be grouped into four major groups: electromagnetic, penetrating radiation, sound, and optical, can be particularly considered a valuable diagnostic tool for determining material qualities, environmental influences, and prior interferences [5]. In this way, using NDT methods on historical buildings prior to attempting any conservation or restoration may reveal specific scientific knowledge of the structure.



Figure 1. The photographic view of mosques and their minarets in the Suriçi region in Diyarbakır (taken in 2021): (a) Ulu Mosque, (b) Hz. Süleyman Mosque, (c) Safa (Parlı) Mosque, (d) Khoja Ahmet Mosque, (e) Sheikh Mutahhar Mosque (Four-Legged Minaret), (f) Nebi Mosque, (g) Fatih Pasha Mosque, (h) Hüsrev Pasha Mosque, (i) Ali Pasha Mosque, (j) İskender Pasha Mosque, (k) Behram Pasha Mosque, (l) Lala Kasım Bey Mosque, (m) Melik Ahmet Mosque, and (n) Nasuh Pasha Mosque

The GPR technique, which is one of the significant NDT methods, has been used frequently in the literature to assess and monitor the condition of historic buildings. By incorporating another nondestructive testing method, Alani et al. [15], for example, employed GPR to monitor the state of the stone arch bridges. Imposa [16], on the other hand, used the GPR technique to examine the inside walls of the “Sala delle Nicchie” of Florence’s Pitti Palace. Similar to this, before the Collemaggio Basilica, a medieval church in L’Aquila (central Italy), was restored, Ranalli et al. [17] assessed the Collemaggio Basilica’s façade’s condition of conservation and determined the thickness of its walls using the GPR approach. In order to create a structural model based on finite elements, Lubowiecka et al. [18] also used the GPR technique to determine the homogeneity or heterogeneity of the interior construction of an old bridge. Masini et al. [19] also provided three instances of GPR prospecting to see historical monuments. Three distinct constructional components, including a wall, a masonry pillar, and a marble column, were chosen for this study to describe the masonry, detect and locate fractures, and document the metallic reinforcing bars. In another investigation, Pieraccini et al. [20] used the GPR method to find cracks in the stone walls of the famous “Salone dei 500” chamber in the Palazzo Vecchio (Firenze, Italy). In addition to the investigations stated above, Yağciner et al. [21] employed the GPR technique to find a new temple at the Nysa archaeological site in western Turkey.

In this context, the target of the study is to investigate the subject of geological formations, the sequence changes, geometric behavior patterns, underground cavity structures and dimensions of ground/sub-structure fractures. For that purpose, a GPR device having 100-MHz and 1.8-GHz antennas were used for measurements. The working area was separated into distinct places, and GPR sections in the shape of lines/profiles were obtained at each of these places. Penetration depths differ in regard to the measurement location: for example, 2.00 m was designated for the scanning of the load-bearing elements whereas 10 m as the shallowest and 20 m as the deepest were chosen for the ground scanning.

2. ARCHITECTURAL PROPERTIES AND LOCATION OF THE FOUR-LEGGED MINARET

Diyarbakır which is also included in the UNESCO Cultural Heritage List owing to its historical city walls [22] is located in the southeast of Turkey, as shown in Figure 2. Sheikh Mutahhar Mosque and Four-Legged Minaret, located in the southeast part of the Suriçi region that is surrounded by city walls and 82 towers as shown in Figure 2, were constructed in 1500 during the Akkoyunlu’s period [23]. The Suriçi region is largely populated with historical buildings [24].

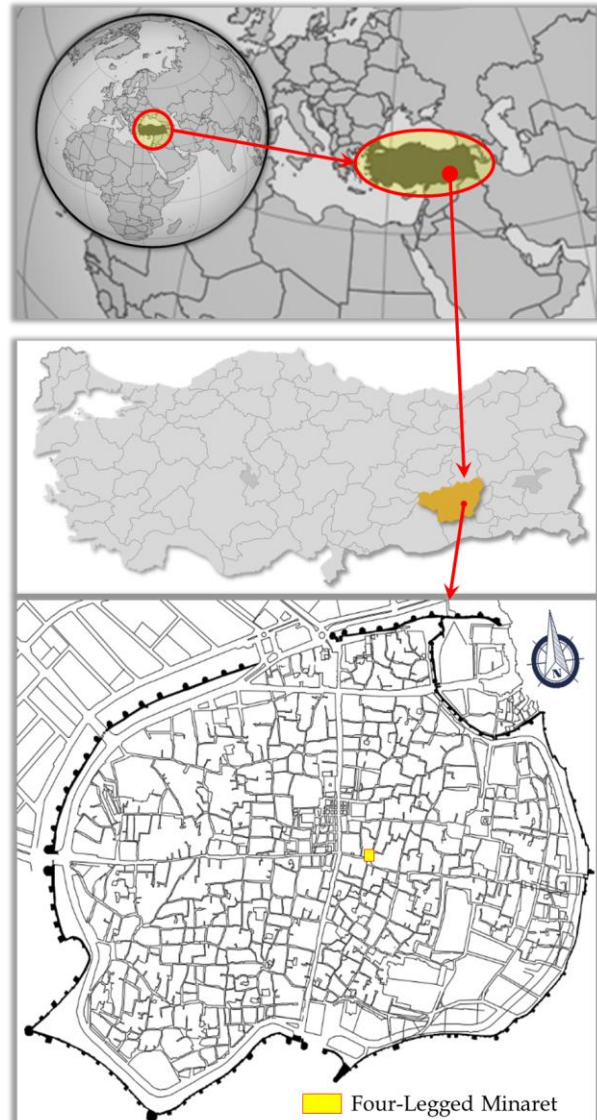


Figure 2. The location of Diyarbakır province on the map [25,26] and the Four-Legged Minaret in the Suriçi region

The Four-Legged Minaret is one of these historical buildings and it is located to the northeast of the Sheikh Mutahhar Mosque. The minaret has been repaired and restored many times from the time it was built to the present day in order to eliminate the existing problems in the minaret. However, nowadays, the minaret remained outside the borders of the mosque due to the widening of the street and the introduction of a wall boundary for the mosque, and hence, the minaret remained as an independent minaret in Yenikapı Street (known also as Four-Legged Minaret Street). The square-formed minaret is carried by four cylindrical columns as can be seen in Figure 3a. The minaret, which was built with the masonry technique, has a height of 18.54 m up to the spire and 22.44 m up to the top including the finial as marked in Figure 3b. The main building material used in the minaret is basalt; however, at certain intervals, brick was also used as a girder as indicated in Figure 3b. Besides, there are four wooden girders above the cylindrical columns and under the square minaret base as shown in Figure 3c.

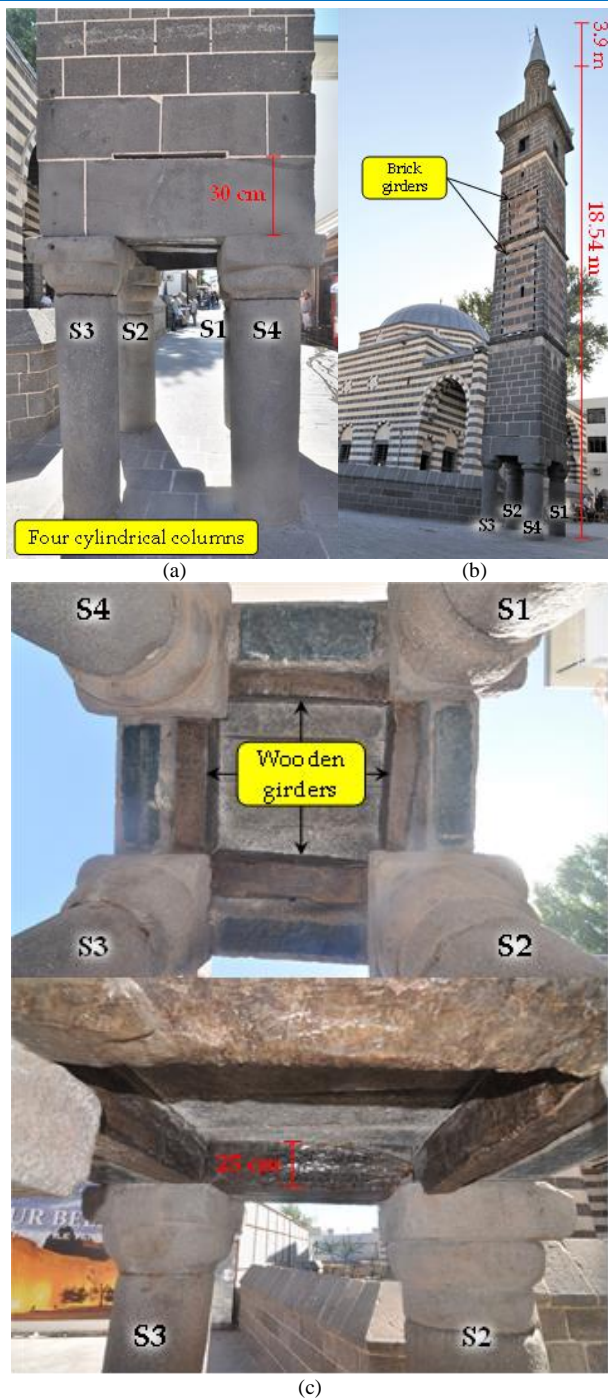
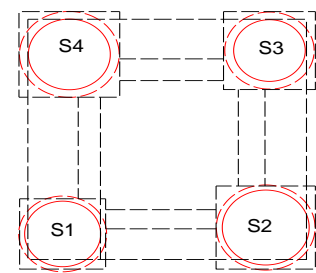


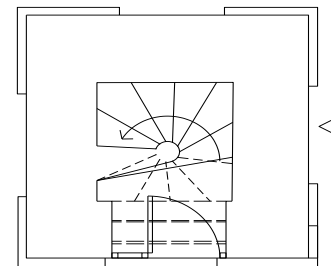
Figure 3. Photographic view of: (a) four cylindrical columns (west view), (b) brick girders (west and north views), and (c) wooden girders (bottom view)

The diameter of each load-bearing column in the Four-Legged Minaret is different from the other: the diameters of the S1 (in the northwest direction) and S4 (in the northeast direction) labeled columns are about 51 and 55 cm, respectively, whereas that of the S2 (in the southwest direction) and S3 (in the southeast direction) named columns are 59 and 49 cm, respectively. For the array and labeling of the columns, see Figure 4a. There are wooden beams having a 25-cm height on these columns as shown in Figure 3c and a basalt lintel with a height of approximately 30 cm above these beams as can be seen in Figure 3a. A spiral staircase that can also be seen in Figure 4b starts after the level of +1.00 m in the minaret.



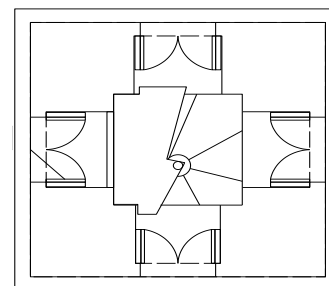
+1.00 level

(a)



+4.00 level

(b)



+14.00 level

(c)

Figure 4. Plans of Four-Legged Minaret at: (a) +1.00, (b) +4.00, and (c) +14 levels

There are basalt cornices as three horizontal bands on the body. Between these cornices on the surfaces of the body, there is brickwork as partial stripes. The upper body section of the square planned minaret is located after a height of 15.37 m. This body in the basalt cylindrical form was completed with a lead spire as shown in Figure 3b. Besides, in the last section of the body, there is a window on each surface of the minaret, as can be seen in Figure 3b and shown in the plan view presented in Figure 4c.

During the restoration work of the Four-Legged Minaret carried out between 2011-2012, the cracks in the north and east directions were reinforced by injection. In addition, steel clamps were added to the lintels as part of this restoration as shown in Figure 5a. However, in 2015, the clamp added around the minaret was removed. Besides, the lintels on the columns of the minaret were strengthened using carbon fiber strips as can be seen in Figure 5b.

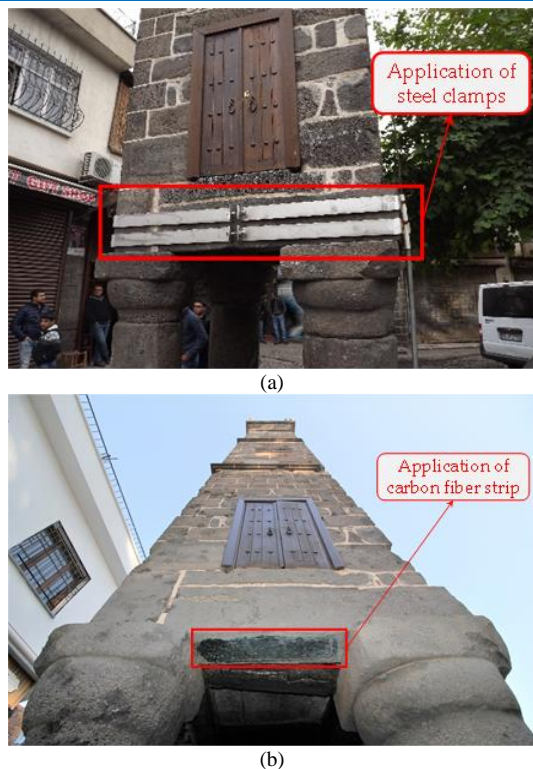


Figure 5. Photographic view of strengthening work on the Four-Legged Minaret: (a) application of steel clamps (taken in 2015) and (b) application of carbon fiber strip (taken in 2021)

3. MEASUREMENT METHOD

The GPR measuring technique consists of a simple system involving a recording device (computer) and two antennas named receiving and transmitting, as schematically exhibited in Figure 6.

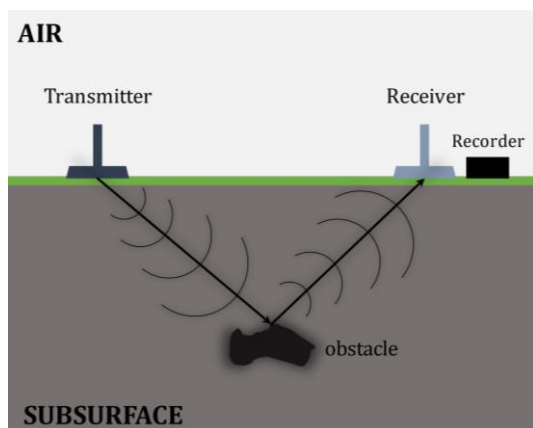


Figure 6. Schematic demonstration of the working principle of a typical GPR system

The transmitting antenna generates multi-nanosecond electromagnetic waves in the horizontal direction, parallel to the electric field vector. During the measurement progress, any anomaly, obstacle, disturbances, and/or negativity leads to the reflection and scattering of the waves under the ground and on the surface. In such conditions, waves are reflected and start to move through the upstream direction, and thereby, they are captured by the receiving antenna, and then the receiving antenna transfers these waves to the computer. In broad, this method is based on the difference between

electromagnetic signals produced by the transmitting antenna and captured by the receiving antenna, during its underground travel [27]. The most important components of these signals are the electrical and magnetic constants of the energy transfer process. The resulting data and fluctuations are therefore called “radar traces”. These nanosecond measurements and radar traces are concatenated into a time unit, and the resulting portions are called “radargrams” [28].

GPR signals arrive at the objective by determining their speed according to the physical and chemical characteristics of the environment it is traveling to, thus collecting information about the target during this travel. In situations where the travel time is known and the speed of the medium is also known, the target depth can be determined with precision. Herein, the most important factors are the signal distribution and the environments in which the travel of electromagnetic signals can be affected. As previously stated, the receiving (R_x) and transmitting (T_x) antennas constitute the GPR system where the short high-frequency radio signals are emitted by transmitting antennas and the signals are picked up by the receiving antennas while being reflected by the obstacle or target, or by layers with different dielectric constant. Unlike seismic reflections, GPR produces reflections from both strata and buried objects. Objects with different electromagnetic properties such as water tables, sediment layers, foundation structures, buried tanks, and archaeological remains lead to reflections in the GPR. In other words, GPR reflections generally occur because objects have different dielectric constants. The dielectric constant reveals how much charge an object can store when an electromagnetic charge is applied to it. In this context, Conyers [27] graphically demonstrated an inverse relationship between radar travel speed and partial dielectric constant, as shown in Figure 7.

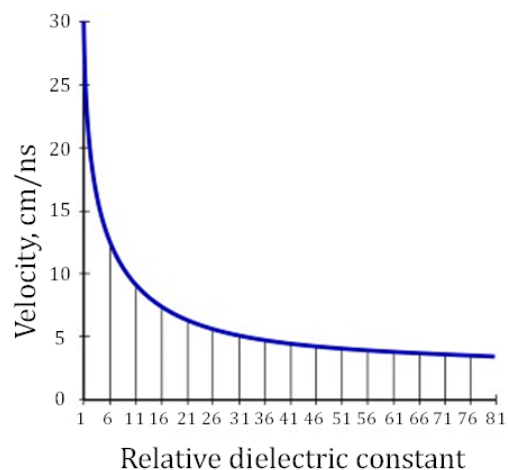


Figure 7. The inverse relationship between radar travel speed and partial dielectric constant [27]

There are just a few studies in the literature that look at the dielectric constants of various materials [29-31]. In radar frequencies, the dielectric constant of dry rocks usually ranges from 3 to 5, while water has dielectric values of 80-81. In general, dielectric constants of rocks,

which contain water, vary between 6 and 30, depending on the amount of water they retain. In the present study, a device setup having a constant width between the transmitting and receiving antennas was used to examine the ground and structure-dependent damages of the Four-Legged Minaret. Sheltered antennas were used in the measurements and both the transmitting and receiving antennas were placed into a box then, it was moved on the ground, and thereby traces under the ground were collected in the course of this movement process. Subsequently, thousands of traces were collected, which form the profile when they are put together. After some measurements, anomaly situations on the surface were clarified with the help of three-dimensional images. In order to carry out the GPR scanning on both Four-Legged Minaret and its surrounding area, a Python-3 named GPR device having frequency values of 250/100/50/38/25 MHz and the antenna length changing between 1 to 4 m depending on the frequency value was employed [32] and besides, Prism 2 named software was used to manage the data processing steps in the GPR measurement works. The internal Wi-Fi system in the device provided the data transmission to the computer. The device may be used with both default and custom digital filters, and it can display 16-bit digital data. The device also features a user-selectable time range of 1 to 2500 ns with a 1 ns step, as well as a 28 and 1024x16-bit scan rate and samples per scan, respectively. 100 MHz and 1.6 GHz antennas were used for measurements in this study.

The subject of geological formations, the sequence changes, geometric behavior patterns, underground cavity structures, and dimensions of ground/sub-structure fractures are included in this study. Besides, the conditions and changes of the formations and the classifications according to the characteristics of the host rocks and their electromagnetic permeability were also taken into consideration. In this case, the working area was separated into distinct places, and GPR sections in the shape of lines/profiles were obtained at each of these places. The exact depth capability of the GPR is highly dependent on the antenna frequency, the soil conditions and material properties, the quality and capability of the equipment, and the size of the target. The depth of radar penetration and the ability to identify the target object at any depth depends on the soil properties in that area. If the soil is highly conductive, the GPR method may be ineffective. In this regard, the maximum penetration depth of the GPR into the ground can be determined by the total propagation loss, which is determined by the electrical properties of the materials. Different penetration depths have been determined depending on the GPR equipment and antenna used in this study, the soil characteristics of the area being surveyed, and the size of the target. For example, 4.00 m was designated for scanning the structural elements, while 10 m was chosen as the shallowest and 20 m as the deepest for scanning the ground. Figure 8 shows some representative photographs taken during the GPR measurements.



Figure 8. A typical application of the GPR on: (a) the ground of the surrounding area of the minaret, (b) the basalt lintel of the minaret, and (c) the column of the minaret

For good data to be generated, it is necessary to perform proper filtering after careful measuring, which is suitable for interpreting [21]. Converting the obtained numerical data into understandable images is the basis of data processing in GPR measurements. The following filtering processes which are explained in detail by Işık et al. [14] are applied to obtain understandable images once the pure data is obtained from the site [33]:

- i. First-time filter
- ii. Current correction (Dewow)
- iii. Energy delay
- iv. Average value cleaning:
- v. Velocity analysis

4. RESULTS AND DISCUSSION

As previously noted, the research location, which has a 5-degree slope and a 660 elevation, is located in Diyarbakır province's Sur district (called Suriçi region). The lithological sequence from the earth's surface to the subterranean in this study region, its near surrounds, and certain section cuts are detected as vegetable soil unit, clayey sandy unit, and clayey silty sand unit in accordance with the prior geological and geotechnical research. Despite these sequence alterations revealing local variances in areas, they generally follow the same pattern as the one described above.

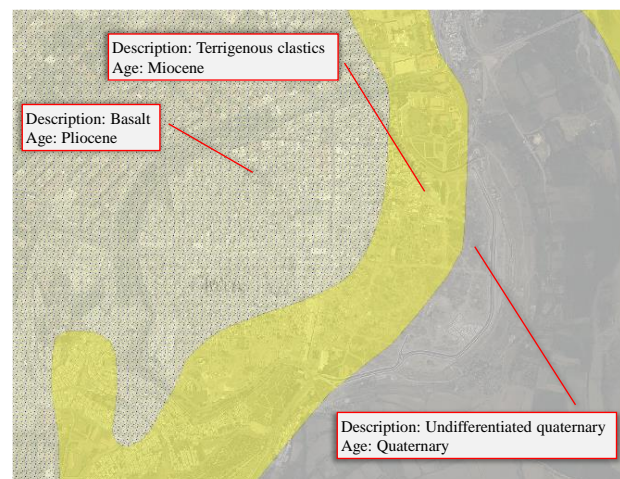


Figure 9. Possible geology map related to the immediate environment of the study area [34]

In regard to the General Directorate of Mineral Research and Exploration, as shown in Figure 9, the geology of the research region and its close surrounds comprises basalt, terrigenous clastics, and undifferentiated quaternary belonging to the Pliocene epoch, Miocene epoch, and quaternary period, respectively. Terrigenous clastics from the Miocene epoch, on the other hand, are widespread in this research region and its close surroundings.

4.1. Observationally Detected Structural Problems in the Four-Legged Minaret

Due to the fact that the minaret was outside the courtyard of the mosque due to its location, partial material losses occurred due to vehicle hits. In addition, in 2015, damage such as fragmentation and abrasion due to firearms occurred on columns S1 and S2 in the northwest direction of the minaret, and bullet holes occurred in some places (see Figure 10).



Figure 10. Photographic views of damages caused by firearms on: (a) the body and (b) columns of the Four-Legged Minaret (taken in 2021)

During the restoration work carried out between 2016-2017, no comprehensive repairs were made to the minaret, except for cleaning and removing mortar losses. Especially, there has not been any attempt to complete the material losses in the minaret during the period of vehicle traffic. The existing crack in the lintel of the minaret in the northwest direction was filled with injection during the repair works. In addition, macro-sized (visible) cracks were detected on the lintels on the

columns in the northeast and southeast directions (see Figure 11).

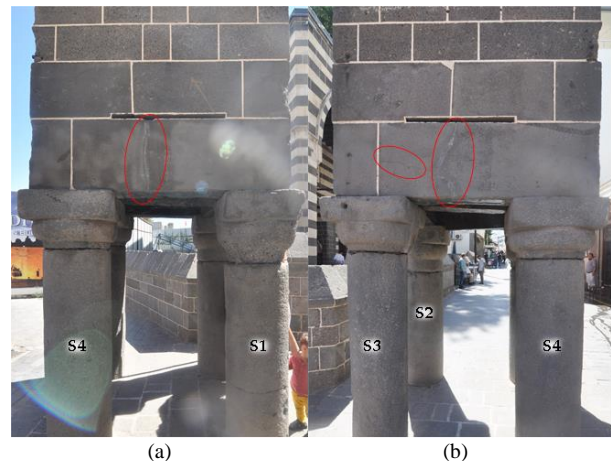
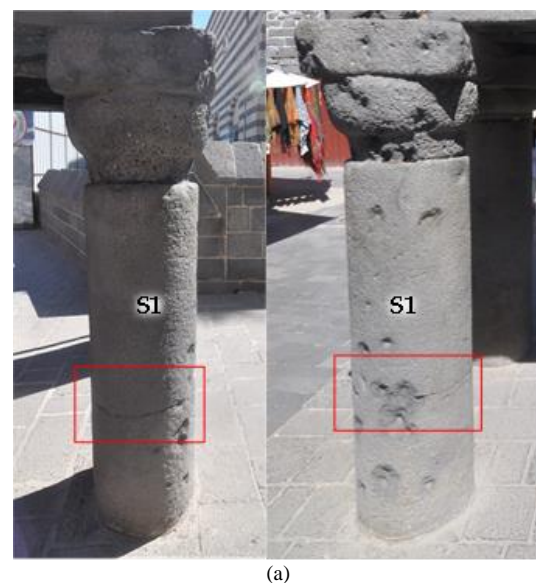


Figure 11. Photographic view of crack damage on lintels on: (a) S1-S4 columns in the northeast direction and (b) S3-S4 columns in the southeast direction (taken in 2021)

There are level irregularities on the street floor where the minaret is located. Although the street floor where the minaret is located was renewed with cut stone during the repair works, no detailed examination was done on the cause and correction of the level irregularities on the street floor. Besides, partial axis slippage due to vehicle hit, vibration, and level irregularity on the street floor has been observationally detected at the column heads. However, these irregularities and damages were not eliminated during the repairs. In addition, there is a horizontal crack in the middle part of the S1 column due to the loss of material because of the hit of a large number of bullets in that area and the impact of these bullets (see Figure 12). The wooden girders on the minaret columns are original but partially damaged. During the repair work, they were maintained by applying impregnation and protective paint for wood protection, and thereby, the current condition of the wooden girders was preserved.



(a)

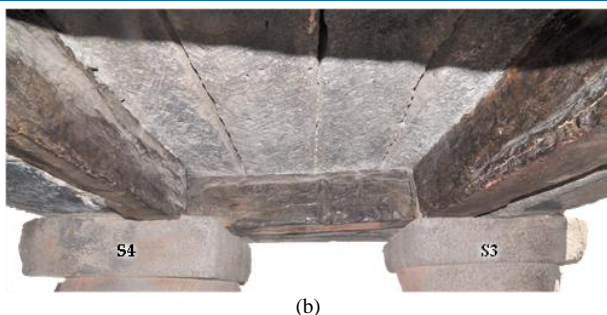


Figure 12. Photographic view of: (a) the horizontal crack on column S1 and its location and (b) the current condition of wooden girders

4.2. GPR Measurements and Evaluations on the Four-Legged Minaret

4.2.1. Ground scanning

GPR scanings on the ground of the Four-Legged Minaret were carried out by dividing the area into zones. Figure 13 indicates the location and border of each zone in which the GPR scanings were carried out. The GPR Z1 labeled zone had a profile length of 80.0 m while the GPR Z2 and GPR Z3 labeled zones had profile lengths of 50.0 m and 74.0 m, respectively. In all zones, the penetration depth was designated as 20.0 m.

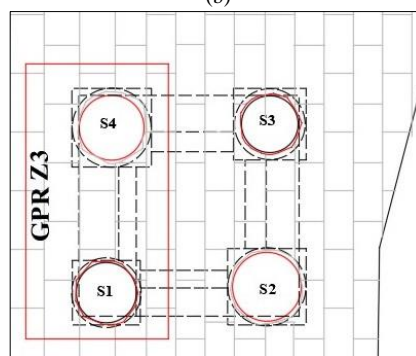
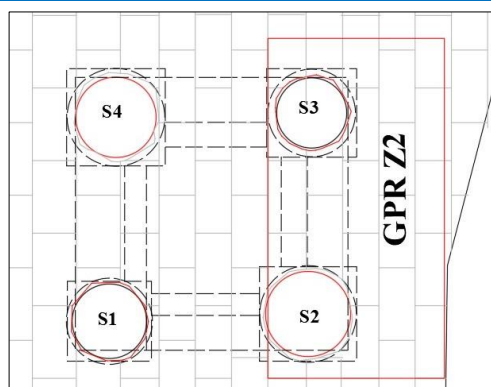
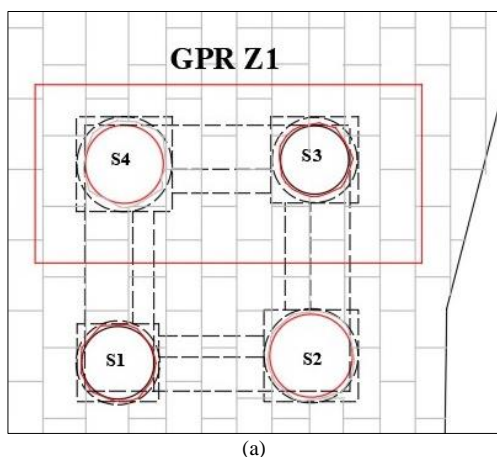
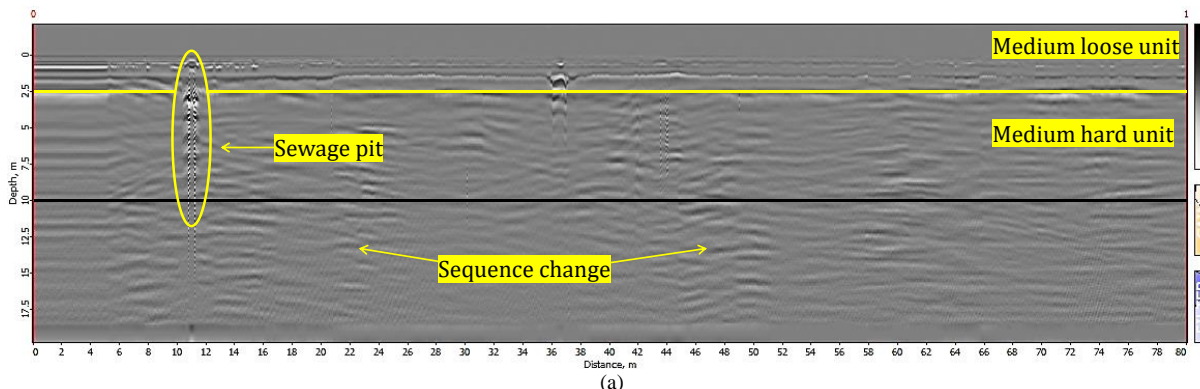


Figure 13. The locations and borders of the GPR scanning zones on the ground (each zone is shown by the box in red color)

Figures 14a-c demonstrate the 2-dimensional GPR sections taken at zones 1, 2, and 3, respectively. As marked in these figures, 2 different levels were observed from the radargram section of each zone. It is considered to be a medium loose unit of about 2.50 m in the upper part, and a medium hard unit between 2.50 and 10.00 m. As indicated in Figure 14a, there is a sewer pit starting at a depth of 2.50 m and lasting about 10.00-12.00 m throughout the profiling of zone 1. Additionally, in this zone, there is no anomaly formation on the ground, except for the sequence changes. On the other hand, subsidence anomaly formations were identified in the profiling of zone 2. As can be seen in Figure 14b, the regions starting at a depth of 7.50 m lasting through 10.00 and 26.00 m took in water, thus collapsed. In the profiling of zone 3, only subsidence deformations caused by taking in water were detected, as pointed out in Figure 14c. These anomalies are starting at the depth of 5.00 m and lasting through the 50.00 and 52.00 m.



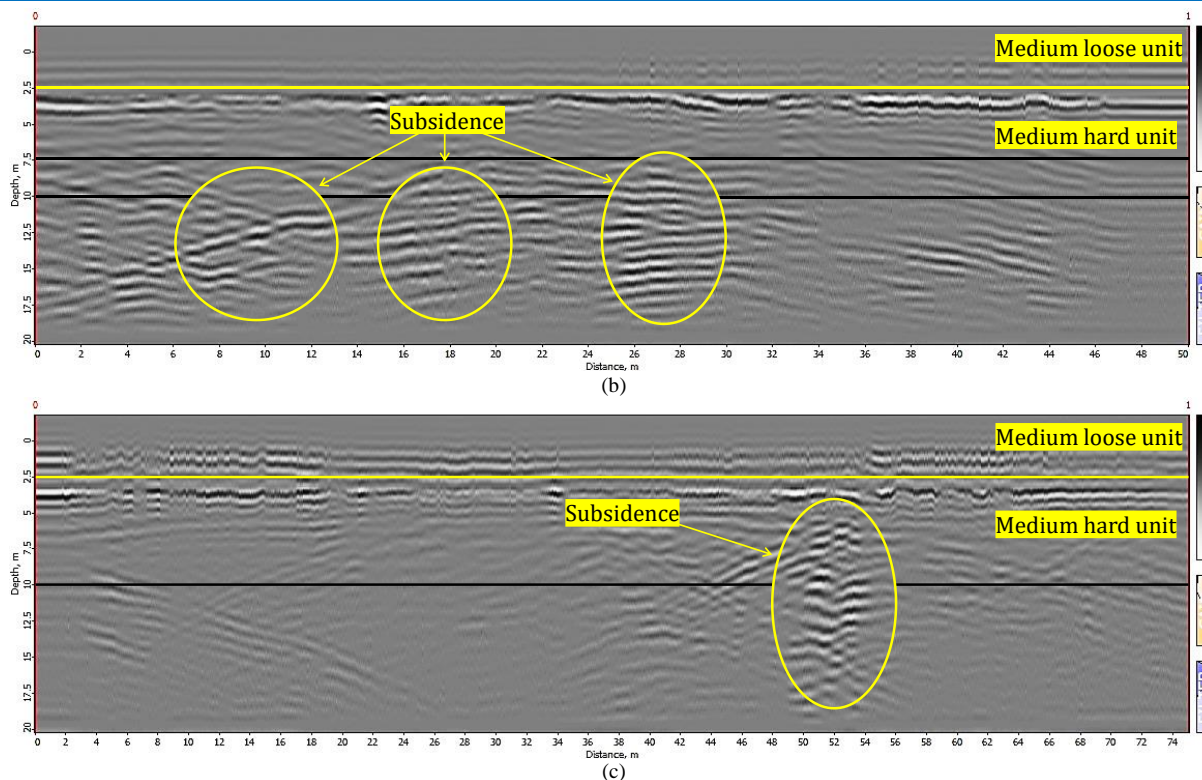


Figure 14. GPR sections: (a) taken at zone 1, (b) taken at zone 2, and (c) taken at zone 3

4.2.2. Lintel scanning

In addition to the GRP scanings on the ground, the lintels on the columns of the Four-Legged Minaret were also scanned by dividing the area into two regions named GPR 1 and GPR 2. Figure 15 indicates the border of each region in which the GPR scanings of lintels were carried out. In the scanning of the region named GPR 1, the profile length was designed as 10.0 m while in the GPR 2 labeled region, it was chosen as 15.0 m. In both regions, the 4.00-m penetration depth was designated. Region 1 involves the lintels on the S2-S3 columns and S3-S4 columns while region 2 includes the lintels on the S1-S2 columns and S1-S4 columns.

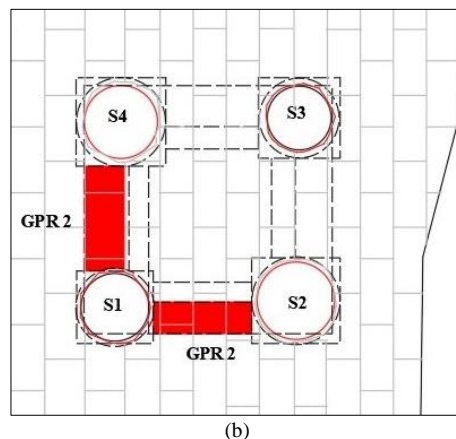
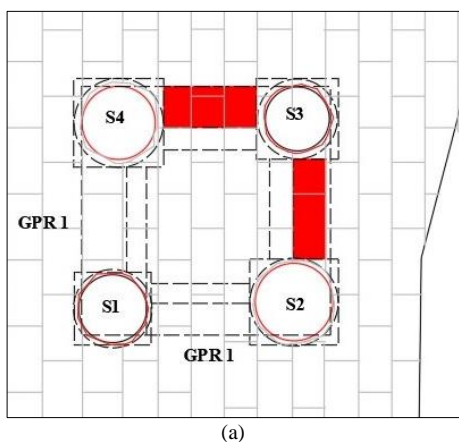


Figure 15. The indication of the GPR scanning regions on the lintels (each region is shown by the red color)



In regard to the radargram section obtained from region 1 (see Figure 16a), it can be stated that it has been observed that the cracks and fractures in the lintels are at a level that will affect the load-bearing system of the minarets. It is considered that cracks and fractures, the smallest 12.00 cm and the largest 20.00 cm, have been detected on the lintels in this area. On the other hand, broken V-type crack systems are at the maximum level in the lintels of region 2, as pointed out in Figure 16b. It is thought that the detected damages on the lintels may adversely influence the load-bearing system of the minaret.

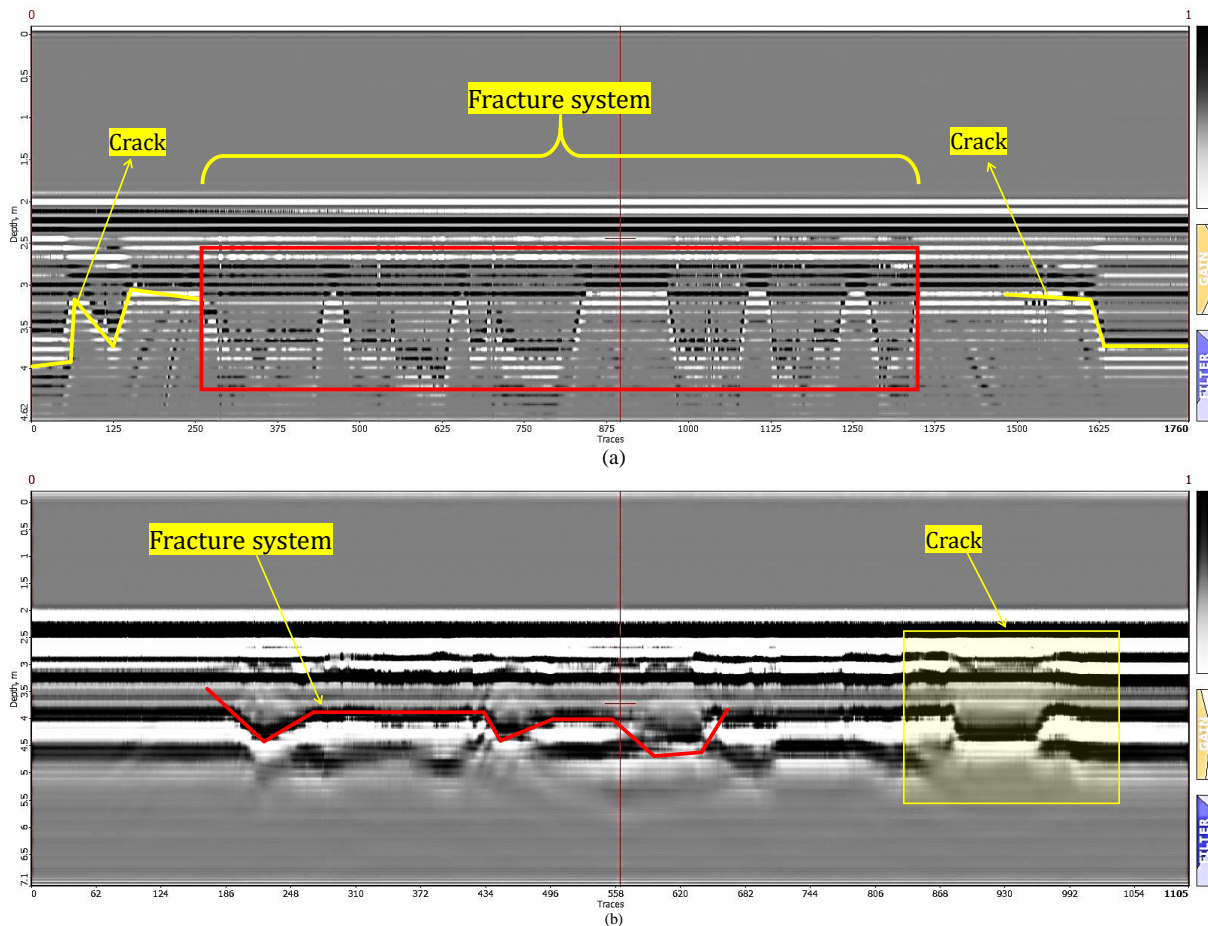


Figure 16. GPR sections: (a) taken at Region 1 and (b) taken at Region 2

5. CONCLUSIONS AND RECOMMENDATIONS

Based on the findings presented above, the following conclusions and recommendations can be drawn:

GPR scans and studies were carried out for the existing damages under the ground and on the load-bearing members of the Four-Legged Minaret in the Suriçi region of Diyarbakır province. In the studies carried out, the current condition of the ground and possible damages and deformations in the load-bearing members were determined and revealed by the radargram sections obtained from the GPR scanings. In the scanings carried out on the Four-Legged Minaret, the conditions of the deformations, their variations, the properties of the surrounding rocks, and their classification according to their electromagnetic permeability were taken into account. As a result of the ground scanning, it was observed that the sequence changes were differentiated at 2 different levels. A medium loose unit was detected from the ground to a depth of 2.50 m, and a medium-hard unit formation was detected between 2.50-10.00 m. It was detected that there was a sewage pit in the scanning zone named GPR Z1 to the east of the minaret. On the south of the minaret, in the scanning zone named GPR Z2, deformations caused by water leakage and related collapse were detected after the levels of 7.50-10.00 m. In the ground scans of the zone called GPR Z3 to the north of the minaret, voids due to collapse were detected in the soil. Some cracks and fractures can be visually seen on lintels in the north and east directions of

the Four-Legged Minaret. During the restoration works carried out in 2012 and 2017, the existing cracks were filled with injections. However, in the GPR scans, it was detected that the existing cracks and fractures continued into the inside of the lintels. On the other hand, fragment losses caused by vehicle hits during the periods when the street was open to vehicle traffic were detected on the columns by observational investigation. In addition, by the time, axis slippages have occurred due to the absence of any tension ring or any protective application between the top caps of the columns and the column bodies. The column diameters of the minaret are close to each other. There are fragmentations and abrasions caused by firearms in 2015 in the columns (S1 and S2) in the northwest and southwest directions of the minaret.

To repair the existing damages on the Four-Legged Minaret, comprehensive survey and restoration projects should be prepared under the leadership of the relevant experts, and reinforcement applications should be carried out immediately. In addition to the determination of the damages on the minaret with non-destructive methods, observation pits should be opened in the regions determined by the experts and the physical condition of the ground should be determined. Soil improvements should be carried out around the building, and also columns and walls having axis slippages should be suspended, and reinforcement work should be conducted. In the past years, GPR scanning was not carried out during the restoration works carried out on the ground and load-bearing members of the Four-

Legged Minaret. For this reason, it is very important because it is the first study to determine the problems in this cultural heritage using the GPR technique. In recent years, damage assessment studies using non-destructive methods employed for historical buildings continue increasingly. The GPR technique is an important non-destructive geophysical method used for historical buildings. For this reason, it is thought that this method, which will be used for historical buildings, will be an up-to-date guide for all historical buildings, specific to the Four-Legged Minaret.

REFERENCES

- [1] Sullivan AM. Cultural Heritage & New Media: A Future for the Past. *John Marshall Rev Intel Prop Law*. 2016;15(3):604-46.
- [2] UNESCO [Internet]. Cultural Heritage; 2022 [cited 2022 November 19]. Available from: https://en.unesco.org/creativity/sites/creativity/files/cdis/heritage_dimension.pdf
- [3] Logan WS. Closing Pandora's Box: Human rights conundrums in cultural heritage protection. In: Silverman H, Ruggless DF, editors. *Cultural Heritage and Human Rights*. Springer, New York-ABD, 2007; p. 33-52.
- [4] Ortega-Ramirez J, Bano M, Cordero-Arce MT, Villa-Alvarado LA, Frafa CC. Application of Non-invasive Geophysical Methods (GPR and ERT) to Locate the Ancient Foundations of the First Cathedral of Puebla, Mexico: A case study. *J Appl Geophy*. 2020;174:103958.
- [5] Işık N, Halifeoğlu FM, İpek S. Nondestructive testing techniques to evaluate the structural damage of historical city walls. *Constr Build Mater*. 2020;253:119228.
- [6] Bağbancı, MB, Bağbancı, ÖK. Structural health monitoring through vibration-based approaches. *Shock Vibr*. 2018;2018:9853896.
- [7] Usta, P. Assessment of seismic behavior of historic masonry minarets in Antalya, Turkey. *Case Stud Constr Mater*. 2021;15:e00665.
- [8] Günaydın, M, Tonyalı, Z. Dynamic response of a reinforced concrete minaret. *J Struct Eng App Mech*. 2018;1(2):62-72.
- [9] Ercan, E, Arısoy, B, Hökelekli, E, Nuhoglu, A. Estimation of seismic damage propagation in a historical masonry minaret. *Sigma J Eng Nat Sci*. 2017;5(4):647-666.
- [10] Beysanoğlu Ş. Anıtları ve Kitabeleri ile Diyarbakır Tarihi 2, İrmak Matbaası, Ankara-Turkey; 1998.
- [11] Han Z. Diyarbakır kültür envanteri, Cilt 1, T.C. Diyarbakır Valiliği İl Kültür ve Turizm Müdürlüğü, Müze Müdürlüğü, Diyarbakır-Turkey; 2015.
- [12] Umar, MU, Hanafi, MH, Latip, NA. Analysis of non-destructive testing of historic building structures. *Australian J Basic App Sci*. 2015;9(7):326-330.
- [13] Moropoulou, A, Labropoulos KC, Delegou, ET, Karoglou, M, Bakolas, A. Non-destructive techniques as a tool for the protection of built cultural heritage. *Constr Build Mater*. 2013;48,1222-1239.
- [14] Işık N, Halifeoğlu FM, İpek S. Detecting the ground-dependent structural damages in a historic mosque by employing GPR. *J App Geophy*. 2022;199:104606.
- [15] Alani AM, Tosti F, Ciampoli LB, Gagliardi V, Benedetto A. An integrated investigative approach in health monitoring of masonry arch bridges using GPR and InSAR technologies. *NDT&E Inter*. 2020;115:102288.
- [16] Imposa S. Infrared Thermography and Georadar Techniques Applied to the "Sala delle Nicchie" (Niches Hall) of Palazzo Pitti, Florence (Italy). *J Cult Herit*. 2010;11:259-264.
- [17] Ranalli D, Scozzafava M, Tallini M. Ground penetrating radar investigations for the restoration of historic buildings: the case study of the Collemaggio Basilica (L'Aquila, Italy). *J Cult Herit*. 2004;5(1):91-99.
- [18] Lubowiecka I, Armesto J, Arias P, Lorenzo H. Historic bridge modelling using laser scanning, ground penetrating radar and finite element methods in the context of structural dynamics. *Eng Struct*. 2009;31(11):2667-2676.
- [19] Masini N, Persico R, Rizzo E. Some examples of GPR prospecting for monitoring of the monumental heritage. *J Geophy Eng*. 2010;7(2):190-199.
- [20] Pieraccini M, Noferini L, Mecatti D, Luzi G, Atzeni C, Persico R, Soldovieri R. Advanced processing techniques for step-frequency continuous-wave penetrating radar: The case study of "Palazzo Vecchio" Walls (Firenze, Italy). *Res Nondestruct Eva*. 2006;17(2):71-83.
- [21] Yalçiner CÇ, Bano M, Kadioglu M, Karabacak V, Meghraoui M, Altunel E. New temple discovery at the Archaeological Site of Nysa (Western Turkey) using GPR method. *J Archaeol Sci*. 2009;36:1680-1689.
- [22] UNESCO [Internet]. United Nations Educational, Scientific and Cultural Organization – World Heritage in Turkey; 2016 [cited 2022 November 19]. Available from: http://www.unesco.org.tr/Content_Files/Content/Yayinlar/wht_2016.pdf
- [23] Atılğan A [Internet]. Diyarbakır'da Dört Ayaklı Minare; 2015 [cited 2022 December 04]. Available from: <http://mimdap.org/2015/12/diyarbakyrda-dort-ayakly-minare-arif-atylgan>
- [24] Işık N, Halifeoğlu FM, İpek S. A Proposal for the Conservation and Integration of Historic Diyarbakır City Walls: the Urfa Gate. *Towers and City Walls, Turkish J Nat Sci*. 2020;9(2):146-156.
- [25] Wikipedia [Internet]. Turkey; 2022 [cited 2022 November 20]. Available from: <https://commons.wikimedia.org/w/index.php?curid=7818230>
- [26] Wikipedia [Internet]. Diyarbakır; 2022 [cited 2022 November 20]. Available from: <https://commons.wikimedia.org/w/index.php?curid=7123114>
- [27] Conyers LB. *Ground-Penetrating Radar for Archaeology (Geophysical Methods for Archaeology)*, 3th Edition, Lanham, AltaMira Press, Rowman & Littlefield Publishers; 2013.

- [28] Kadiođlu S, Uluggerli EU. Determination of cavities using ground penetrating radar in Dalaman-Akköprü Dam construction area. The 16th International Geophysical Congress and Exhibition of Turkey, 7-10 December, Ankara; 2004.
- [29] Davis JL, Annan, AP. Ground-penetrating radar for high-resolution mapping of soil and rock stratigraphy. *Geophysical Prospecting*, 1989;37:531-551.
- [30] Reynolds JM. *An Introduction to Applied and Environmental Geophysics*, John Wiley & Sons, New York-USA; 1997.
- [31] Daniels DJ. *Ground Penetrating Radar (Radar, Sonar and Navigation)*, 2nd Edition, The Institution of Electrical Engineers, London-England; 2004.
- [32] Phthon-3 GPR [Internet]. Radar Systems Inc. Products; 2022 [cited 2022 November 23]. Available from: <http://www.radsys.lv/en/products-soft/products/prod/6>
- [33] Leucci G, Negri S. Use of ground penetrating radar to map subsurface archaeological features in an urban area. *J Archaeol Sci*. 2006;33:502-512.
- [34] MTA [Internet]. Geoscience Mapviewer and Drawing Editor, General Directorate of Mineral Research and Exploration; 2022 [cited 2022 November 26]. Available from: <http://yerbilimleri.mta.gov.tr/anasayfa.aspx>

Erratum: Evaluation of benzaldehyde derivatives as being bovine kidney aldose reductase inhibitors

Bülent ŞENGÜL^{1*} 

¹ Department of Health Care Services, Vocational School of Health Services, Bayburt University, Bayburt, Turkey
Bülent ŞENGÜL ORCID No: 0000-0002-9998-6564

*Corresponding author: bulentsengul@bayburt.edu.tr

(Received: 14.11.2022, Accepted: 22.06.2023, Erratum Online Publication: 28.12.2023)

Keywords

Inhibition,
molecular
docking,
polyol
pathway,
benzaldehydes

Abstract: Aldose reductase (AR) catalyzes the production of sorbitol from glucose in the polyol pathway, and it is a critical enzyme that causes an aberrant aggregation of sorbitol in insulin-independent tissues, create some problems including retinopathy, neuropathy, and nephropathy. AR inhibition has been shown to be a viable approach for reducing these side effects. The current study aimed to introduce new AR inhibitors to the literature. For this purpose, benzaldehydes were examined as being AR inhibitors. Firstly, the homogenate was prepared from the bovine kidney, then inhibition studies were carried out. It was found that all derivatives inhibited AR. The inhibitory potency of 4- Phenyl benzaldehyde (3) and 2- Bromobenzaldehyde (6), having IC₅₀ values as 0.23 and 1.37 µM, respectively, was determined higher than standard inhibitor sorbinil. After *in vitro* inhibition studies, estimated binding energies and binding modes of derivatives with enzyme were predicted by molecular docking. Compound 3 exhibited a maximum docking score of -8,61 kcal/mol. In conclusion, these compounds especially compound 3 may be guiding agents that can be used to synthesise new drug candidate molecules to treat or prevent diabetic complications.

184

Düzeltilmiş: Benzaldehit türevlerinin sığır böbrek aldoz redüktaz inhibitörleri olarak değerlendirilmesi

Anahtar

Kelimeler
İnhibisyon,
moleküler
doking,
poliol yolu,
benzaldehit

Öz: Aldoaz redüktaz (AR), poliol yolunda glikozdan sorbitol üretimini katalize eder ve insülin bağımsız dokularda anormal sorbitol agregasyonuna neden olan, retinopati, nöropati ve nefropati gibi bazı problemler yaratan kritik bir enzimdir. AR inhibisyonunun bu yan etkileri azaltmak için uygun bir yaklaşım olduğu gösterilmiştir. Mevcut çalışma, literatüre yeni AR inhibitörlerini tanıtmayı amaçlamıştır. Bu amaçla AR inhibitörleri olarak benzaldehitler incelenmiştir. İlk olarak sığır böbreğinden homojenat hazırlanmış, ardından inhibisyon çalışmaları yapılmıştır. Çalışılan bütün benzaldehit türevlerinin AR'yi inhibe ettiği bulundu. 0,23 ve 1,37 µM IC₅₀ değerlerine sahip olan 4- Phenyl benzaldehide (3) ve 2- Bromobenzaldehide (6)'in inhibitör aktivitesi, standart inhibitör sorbinilden daha yüksek olduğu tespit edildi. *In vitro* inhibisyon çalışmalarından sonra, tahmini bağlanma enerjileri ve türevlerin enzime bağlanma modları moleküler docking ile tahmin edildi. Bileşik 3, -8,61 kcal/mol'lük bir maksimum yerleştirme puanı sergiledi. Sonuç olarak, bu bileşikler, özellikle bileşik 3, diyabetik komplikasyonların tedavisinde veya önlenmesinde yeni ilaç aday moleküllerinin sentezi için yol gösterici moleküller olabilir.

1. INTRODUCTION

Diabetes is a chronic metabolic disease marked by high blood sugar levels that cause long-term damage to blood vessels, nerves, kidneys, heart, and eyes [1, 2] Type 2 diabetes, the most prevalent type, develops in adults when the body becomes insulin resistant or produces

insufficient insulin [3]. According to the 2019 data of the International Diabetes Federation (IDF), the incidence of diabetes in adults between the ages of 20-79 was 9.33%. The number of people with diabetes was reported as 463 million in 2019 and the IDF predicts that this number may increase to approximately 580 million in 2030 and 700 million in 2045 [4]. In Turkey, its prevalence increased to

21% in 2015 [5]. In the 2020 data on diabetes prevalence it has been reported that nearly 15% of the total adult population in Turkey has diabetes [6].

Many pathways are regulated during the development and evolution of diabetes to deal with excess glucose in the body. One of these mechanisms is the polyol pathway (PP) [5,6]. Aldose reductase (AR, EC 1.1.1.21) is the first enzyme of PP and reduces glucose to sorbitol in the presence of cofactor NADPH [8]. And then, in the presence of NAD^+ , sorbitol dehydrogenase (SOD, EC 1.1.1.14) transforms sorbitol to fructose [9].

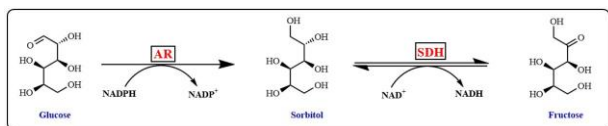


Figure 1. Polyol pathway

In a healthy body, only a small amount of glucose is converted to sorbitol so, blood glucose levels are within normal ranges [10,11]. Sorbitol is not able to penetrate through cell membranes and accumulate in the cell and produced an osmotic effect, causing tissue hydration [12]. Diabetic patients will have difficulties as a result of the problems that have occurred for their health quality. As sorbitol builds up in tissues, it sets in motion a cascade of events that leads to long-term diabetes consequences such as kidney damage, retinal disease, and cardiovascular disease [9-11]. Inhibition of AR activity of the AR for preventing glucose conversion to sorbitol could help avoid cell-level complications [16]. AR converts aldehydes derived from reactive oxygen species (ROS) into inert alcohols in the presence of the NADPH cofactor, in addition to converting glucose to sorbitol [17], [18]. The loss of NADPH induces an increase in GSH levels in cells with high AR activity, resulting in an increase in oxidative stress [15, 19, 20].

The function of aldose reductase in diabetes has been completely elucidated using AR inhibitors and knockout animals, and its inhibitors have been demonstrated to be able to ameliorate diabetes [21]. AR deletion or knockout investigations in mice have showed that AR deletion prevents the development of diabetes-induced retinal capillary degeneration, which is mediated by the creation of superoxide. AR knockout mice have also been shown to develop resistance to diabetic nephropathy [14,15]. Based on the above-mentioned explanations, the goal of this research was to study the *in vitro* inhibition effects of benzaldehyde derivatives (Figure 2) on AR to guide the synthesis of drugs that can be used in the treatment of diabetes. Besides, inhibitor-enzyme interactions were predicted by molecular docking study.

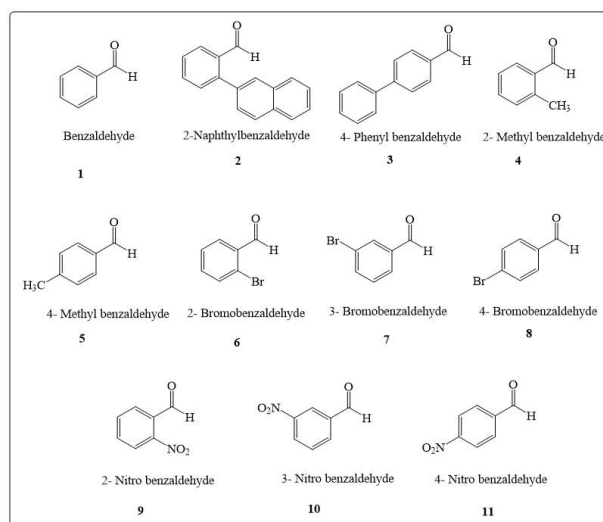


Figure 2. Benzaldehyde derivatives with investigated inhibition profile

2. MATERIAL AND METHOD

2.1. Materials

All chemicals that are used in activity determination and as inhibitors were procured from Sigma-Aldrich Co. and Merck (Darmstadt, Germany). The bovine kidney was obtained from a local butcher in Erzurum, Turkey.

2.2. Preparation of Kidney Homogenate

Kidney samples were washed with isotonic NaCl (0.9%) solution three times. About 10 g of the kidney tissue was chopped into small pieces, and then the cell membranes were ruptured by treatment with liquid nitrogen. The prepared sample was homogenized in 30 mL of 0.01 M phosphate buffer (pH 7.4) and was centrifuged at 13.500xg, at +4° for an hour by using refrigerated centrifuge. Then, the precipitated cell wastes were removed [24].

2.3. AR Activity Assay

The enzyme activity was measured using a modified method put by Cerelli et al.[25]. The depleted amount of NADPH at 340 nm was monitored spectrophotometrically for 3 minutes at 25°C. About 1mL total volume of the enzymatic reaction mix contained 0.8 M Naphosphate buffer (pH=5.5), 4.7 mM DL-glyceraldehyde, 0.11mM NADPH and enzyme solution.

2.4. Determination *In vitro* Inhibition Effects

For the determination of compounds' *in vitro* effects, the enzyme activities were assayed in the presence of at least five various compound concentrations. The control measurement having no compound was assumed as 100% and measurements in the presence of compounds were calculated as % activity [26]. Data were drawn as Activity%-[compound] graphs, and IC₅₀ values were calculated from the equations of these graphs [27].

2.5. Molecular Docking Studies

The three-dimensional (3D) structure of the aldose reductase (PDB ID: 2FZD, 1.08 Å) [28] was received from the PDB (Protein Data Bank). The structure of the receptor was arranged, minimized and optimized with the assistance of the Protein Preparation Wizard [29] module using the OPLS3e force field in the Maestro interface [30]. The LigPrep module was used to create two-dimensional drawings and three-dimensional conversions of the benzaldehyde derivative ligands. The OPLS3e force field was utilized to prepare and minimize protonation shows at pH 7.0 ± 2.0 and tautomers. The docking grid was created using the Receptor Grid Generation instrument and was placed on the center of the co-crystallized ligand, Tolrestat. The Glide extra precision (XP) method was used to molecularly attach all of the benzaldehyde derivatives to the target receptor AR [31]. In addition, Tolrestat was isolated from the crystal structure of the enzyme (AR) and docked again in order to validate the docking procedure. The best ligand pose was superpositioned with the co-crystallized ligand subsequent the re-docking method, and the RMSD (Root Mean Square Deviation) value was computed. Following the re-docking method, the top ligand posture was superpositioned with the co-crystal ligand, and the Root Mean Square Deviation (RMSD) value was calculated. The docking protocol's validation is shown by an RMSD value of less than 2 Å [32].

3. RESULTS

To examine the *in vitro* inhibition effects of benzaldehydes, bovine kidney homogenate was used as the source of AR enzyme. It was found that all benzaldehydes inhibited enzyme and 4- phenyl benzaldehyde (3) was the most effective inhibitor with IC₅₀ value of 0.23 μM which was lower than the IC₅₀ value of standard inhibitor determined by Rakowitz et al. [33] as 3.420 μM (Table 1).

Table 1. IC₅₀ values of benzaldehyde derivatives on bovine kidney AR

Compound No	Compound Name	IC ₅₀ (μM)
1	Benzaldehyde	6300
2	2-Naphthylbenzaldehyde	34.65
3	4- Phenyl benzaldehyde	0.23
4	2- Methyl benzaldehyde	2650
5	4- Methyl benzaldehyde	2400
6	2- Bromobenzaldehyde	1.37
7	3- Bromobenzaldehyde	23.1
8	4- Bromobenzaldehyde	57.75
9	2- Nitro benzaldehyde	19.25
10	3- Nitro benzaldehyde	10.5
11	4- Nitro benzaldehyde	18.2
SOR (Rakowitz et al. 2006)	Sorbinyll	3.420

For the prediction of binding affinities and best poses, molecular docking studies were performed with AR receptor. Firstly, docking validation was performed with the co-crystallized ligand. The current study's docking results revealed that compound 3 had the highest effect, with a docking score of -8.31 kcal/mol, as shown in Table 2.

Table 2. XP docking scores and binding energies of benzaldehyde derivatives with AR receptor. Predicted docking scores and binding energy values were calculated as kcal/mol.

Compound Number	Docking Score	XP GScore	Glide emodel
1	-6,33	-6,33	-30,54
2	-8,01	-8,01	-39,57
3	-8,61	-8,61	-41,74
4	-6,84	-6,84	-30,15
5	-6,74	-6,74	-30,53
6	-6,57	-6,57	-27,34
7	-6,91	-6,91	-30,75
8	-6,81	-6,81	-31,7
9	-5,14	-5,14	-29,75
10	-6,05	-6,05	-34,18
11	-6,03	-6,03	-34,39
Sorbinyll*	-8,3	-8,35	-44,78

* Sorbinyll was used as standard inhibitor for AR.

4. DISCUSSION AND CONCLUSION

Diabetes Mellitus (DM), a common disease, can cause health issues including blindness, neuron diseases, heart, and kidney failure [34]. In diabetic management, the level of PP becomes the most strategic aims to achieve [33, 34]. AR is the first enzyme of the PP. Various AR inhibitors have been studied extensively, with encouraging results in terms of preventing and reducing diabetes progression [37], [38]. In this paper, some benzaldehyde derivatives were examined being bovine kidney AR. Besides, molecular interactions of compounds and enzyme were estimated by the molecular docking method. As a result of *in vitro* inhibition studies, all derivatives were found to inhibit the enzyme and activity%-[derivative] graphs were drawn. The graphs of the two best inhibitors are given in Figure 3. Compound concentrations that halved the activity were calculated from the equations of these graphs (Table 1). The two most effective inhibitors were found as derivatives 3, 4-phenylbenzaldehyde and 6, 2-Bromobenzaldehyde, with IC₅₀ values of 0.23 and 1.37 μM correspondingly. These results determined that 3 and 6 are more effective than standard inhibitor, sorbinyll of which IC₅₀ value was found as 3.420 μM by Rakowitz et al. [33]. It was seen from Table 1 that benzaldehyde had 6300 μM IC₅₀ value and methyl derivatives of benzaldehyde had less inhibitory potency than other derivatives.

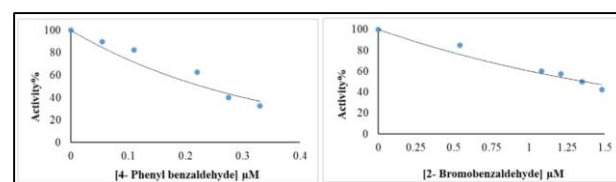


Figure 3. Activity%-[derivative] graphs of the two best inhibitors

The earlier study also found that a large number of synthesized derivatives such as thiazole-based compounds, 4H-1,2,4-triazole derivatives, N-benzyl(oxotriazinoindole), 2,4-thiazolidinediones, benzothiazolone-based carboxylic acid inhibited AR [25,26]. The study finds the inhibition potencies of 3 and 6 were higher than thiazole-based compounds, 4H-1,2,4-triazole derivatives and coumarin-thiosemicarbazone

hybrids [11,37,39]. The effectiveness of inhibitory effects of benzaldehyde derivatives was determined less than N-benzyl(oxotriazinoindole) and benzothiazolone-based carboxylic acid [35, 38, 40, 41, 42].

Molecular docking studies were also completed to theoretically support the experimental inhibition effects of benzaldehyde derivatives on the AR enzyme. Benzaldehyde derivatives and the positive control compound sorbinyl were docked to the ligand-binding site identified for the target protein using the extra precision (XP) docking methodology. The docking scores and estimated binding energies of benzaldehyde derivatives for the AR target enzyme are summarized in Table 2.

The re-docking approach was employed to verify the docking methodology in this research. Tolrestat was isolated from the crystal structure of the enzyme (AR) and docked again in order to validate the docking procedure. The best ligand pose was superpositioned with the co-crystallized ligand following on re-docking procedure, and the RMSD (Root Mean Square Deviation) value was computed. For the tolrestat ligand, the RMSD value was discovered to be 0,103 Å (Figure 4).

The earlier study also found that a large number of synthesized derivatives such as thiazole-based compounds, 4H-1,2,4-triazole derivatives, N-benzyl(oxotriazinoindole), 2,4-thiazolidinediones, benzothiazolone-based carboxylic acid inhibited AR [25,26]. The study finds the inhibition potencies of 3 and 6 were higher than thiazole-based compounds, 4H-1,2,4-triazole derivatives and coumarin-thiosemicarbazone hybrids [11,37,39]. The effectiveness of inhibitory effects of benzaldehyde derivatives was determined less than N-benzyl(oxotriazinoindole) and benzothiazolone-based carboxylic acid [35, 38, 40, 41, 42].

Molecular docking studies were also completed to theoretically support the experimental inhibition effects of benzaldehyde derivatives on the AR enzyme. Benzaldehyde derivatives and the positive control compound sorbinyl were docked to the ligand-binding site identified for the target protein using the extra precision (XP) docking methodology. The docking scores and estimated binding energies of benzaldehyde derivatives for the AR target enzyme are summarized in Table 2. The re-docking approach was employed to verify the docking methodology in this research. Tolrestat was isolated from the crystal structure of the enzyme (AR) and docked again in order to validate the docking procedure. The best ligand pose was superpositioned with the co-crystallized ligand following on re-docking procedure, and the RMSD (Root Mean Square Deviation) value was computed. For the tolrestat ligand, the RMSD value was discovered to be 0,103 Å (Figure 4).

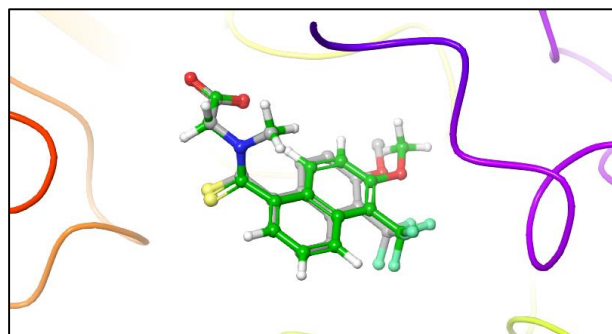


Figure 4. Docking validation of tolrestat adduct AR enzyme. AR receptor is depicted in the ribbon model. The co-crystallized ligand is represented in gray ball and stick modeling, while the re-docked ligand is shown in green ball and stick modeling.

As seen from Table 2, only the docking score of derivative 3 (-8,61 kcal/mol) was found to be higher than the standard inhibitor, sorbinyl, which had a docking score of -8,3 kcal/mol. Trp79, Trp20, Trp219, Trp111, Leu300, and Phe122 are among the residues in the highly hydrophobic active site pocket of AR [30,31]. When we examine the forms of interactions, we can see that; sorbinyl had an H bond with HIS110 residue and also showed pi-pi stacking interaction upon benzene moiety with indole moieties of Trp79 and Trp111 amino acids. And it displayed so many hydrophobic interactions with the active side pocket (Figure 5). Derivative 3, which is the most effective inhibitor based on the results of *in vitro* inhibition experiments and molecular docking estimations, affected AR in a similar manner with standard inhibitor. As seen from Figure 6, compound 3, had two hydrogen bonds with TYR48 and HIS110 residues. Benzene moiety of 3 also exhibited a pi-pi stacking interaction with the indole group of TRP111. Derivative 3 had so many polar and hydrophobic interactions through the same residues as sorbinyl. These interactions are consistent with a previous study, which was conducted by Salem et al. [47]. They reported in their study on the inhibition effects of novel meglitinides on AR that 15C and 12B had interaction with residues similar to those of our study.

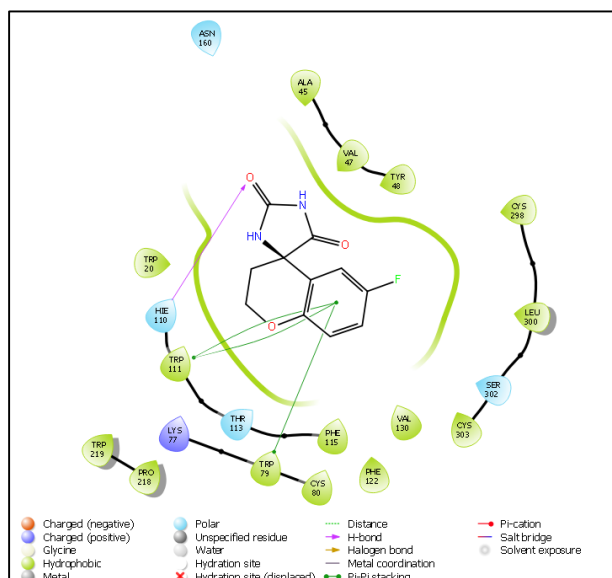


Figure 5. 2D ligand-receptor interaction diagram of standard AR inhibitor sorbinil

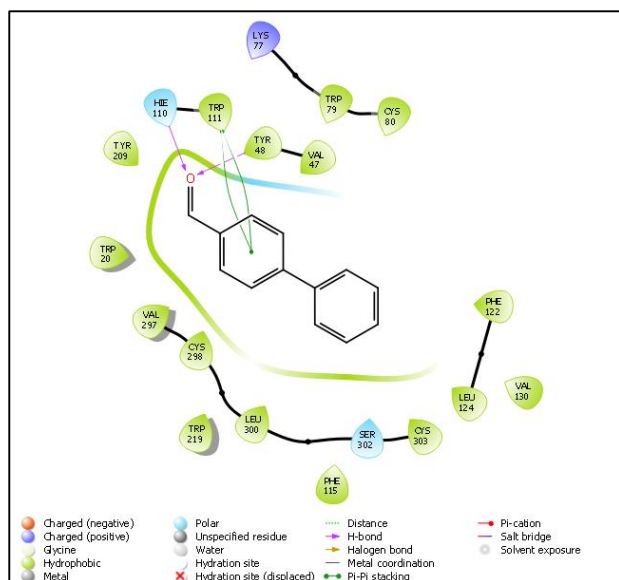


Figure 6. 2D ligand-receptor interaction diagram of best-scored compound derivative 3.

In conclusion, the PP is activated when blood glucose levels are high and it is critical for preventing diabetes and diabetes-related complications. As a result, the AR inhibition strategy holds promise for the treatment of diabetes and related illnesses. In conclusion, all benzaldehyde derivatives inhibited AR in the micromolar range and compounds 3 and 6 had higher inhibitory potency than standard inhibitor with IC_{50} values of 0.23 and 1.37 μ M respectively. The docking score of 3 was also found to be higher than the standard inhibitor with the value of -8.61 kcal/mol. The results of the current study are hoped to be able to guide for further research on new drug candidates in the treatment of diabetes.

Conflict of Interest

The author declares that there is no potential conflict of interest.

Acknowledgments

Since enzyme inhibition studies were performed in the Biochemistry Research Laboratory of Atatürk University, Faculty of Science, Department of Chemistry, the author is thankful to Atatürk University, Faculty of Science, Department of Chemistry.

CRedit authorship contribution statement

Bülent Şengül: Conceptualization, Methodology, Data curation, Visualization, Investigation, Writing - review & editing.

Data Availability Statement

The data that support the findings of this study are available from the corresponding author upon reasonable request.

REFERENCES

- [1] Y. Demir, H. E. Duran, L. Durmaz, P. Taslimi, Ş. Beydemir, and İ. Gulçin, "The Influence of Some Nonsteroidal Anti-inflammatory Drugs on Metabolic Enzymes of Aldose Reductase, Sorbitol Dehydrogenase, and α -Glycosidase: a Perspective for Metabolic Disorders," *Appl. Biochem. Biotechnol.*, vol. 190, no. 2, pp. 437–447, Feb. 2020, doi: 10.1007/s12010-019-03099-7.
- [2] F. Erdemir *et al.*, "Novel 2-aminopyridine liganded Pd(II) N-heterocyclic carbene complexes: Synthesis, characterization, crystal structure and bioactivity properties," *Bioorg. Chem.*, vol. 91, p. 103134, Oct. 2019, doi: 10.1016/j.bioorg.2019.103134.
- [3] L. Gilbert *et al.*, "A pilot study of pi-class glutathione S-transferase expression in breast cancer: correlation with estrogen receptor expression and prognosis in node-negative breast cancer.," *J. Clin. Oncol.*, vol. 11, no. 1, pp. 49–58, Jan. 1993, doi: 10.1200/JCO.1993.11.1.49.
- [4] IDF diabetes atlas, "No Title," in *IDF diabetes atlas.* International Diabetes Federation (9th editio). Retrieved from <http://www.idf.org/about-diabetes/facts-figures>, 2019.
- [5] A. Oğuz, "The Prospective Urban Rural Epidemiology (PURE) study: PURE TURKEY," *Turk Kardiyol. Dern. Arsivi-Archives Turkish Soc. Cardiol.*, 2018, doi: 10.5543/tkda.2018.32967.
- [6] Anonim, "No Title," *Dünya Diyabet Günü*, 2020. <https://sggm.saglik.gov.tr/TR-76887/dunya-diyabet-gunu-2020.html>
- [7] W. H. Tang, S. Wu, T. M. Wong, S. K. Chung, and S. S. M. Chung, "Polyol pathway mediates iron-induced oxidative injury in ischemic-reperfused rat heart," *Free Radic. Biol. Med.*, vol. 45, no. 5, pp. 602–610, Sep. 2008, doi: 10.1016/j.freeradbiomed.2008.05.003.
- [8] S. S. M. Chung, E. C. M. Ho, K. S. L. Lam, and S. K. Chung, "Contribution of Polyol Pathway to Diabetes-Induced Oxidative Stress," *J. Am. Soc. Nephrol.*, vol. 14, no. suppl 3, pp. S233–S236, Aug. 2003, doi: 10.1097/01.ASN.0000077408.15865.06.
- [9] R. I. Lindstad, K. Teigen, and L. Skjeldal, "Inhibition of sorbitol dehydrogenase by nucleosides and nucleotides," *Biochem. Biophys. Res. Commun.*, vol. 435, no. 2, pp. 202–208, May 2013, doi: 10.1016/j.bbrc.2013.04.081.
- [10] Y. Demir, M. S. Özasan, H. E. Duran, Ö. İ. Küfrevioğlu, and Ş. Beydemir, "Inhibition effects of quinones on aldose reductase: Antidiabetic properties," *Environ. Toxicol. Pharmacol.*, vol. 70, p. 103195, Aug. 2019, doi: 10.1016/j.etap.2019.103195.
- [11] B. Sever, M. D. Altıntop, Y. Demir, G. Akalın Çiftçi, Ş. Beydemir, and A. Özdemir, "Design, synthesis, in vitro and in silico investigation of aldose reductase inhibitory effects of new thiazole-based compounds," *Bioorg. Chem.*, vol. 102, p. 104110, Sep. 2020, doi: 10.1016/j.bioorg.2020.104110.
- [12] T.-S. Kim *et al.*, "Overcoming NADPH product inhibition improves D-sorbitol conversion to L-

- sorbose,” *Sci. Rep.*, vol. 9, no. 1, p. 815, Dec. 2019, doi: 10.1038/s41598-018-37401-0.
- [13] T. Petrova *et al.*, “Factorizing selectivity determinants of inhibitor binding toward aldose and aldehyde reductases: structural and thermodynamic properties of the aldose reductase mutant Leu300Pro-fidarestat complex,” *J. Med. Chem.*, vol. 48, no. 18, pp. 5659–65, Sep. 2005, doi: 10.1021/jm050424+.
- [14] C. Yabe-Nishimura, “Aldose reductase in glucose toxicity: a potential target for the prevention of diabetic complications,” *Pharmacol. Rev.*, vol. 50, no. 1, pp. 21–33, Mar. 1998, [Online]. Available: <http://www.ncbi.nlm.nih.gov/pubmed/9549756>
- [15] M. Brownlee, “Biochemistry and molecular cell biology of diabetic complications,” *Nature*, vol. 414, no. 6865, pp. 813–820, Dec. 2001, doi: 10.1038/414813a.
- [16] Q. Huang, Q. Liu, and D. Ouyang, “Sorbinil, an Aldose Reductase Inhibitor, in Fighting Against Diabetic Complications,” *Med. Chem. (Los Angeles)*, vol. 15, no. 1, pp. 3–7, Jan. 2019, doi: 10.2174/1573406414666180524082445.
- [17] M. S. Özasan, R. Sağlamtaş, Y. Demir, Y. Genç, İ. Saraçoğlu, and İ. Gülçin, “Isolation of Some Phenolic Compounds from *Plantago subulata* L. and Determination of Their Antidiabetic, Anticholinesterase, Antiepileptic and Antioxidant Activity,” *Chem. Biodivers.*, vol. 19, no. 8, Aug. 2022, doi: 10.1002/cbdv.202200280.
- [18] C. Türkes, Y. Demir, and Ş. Beydemir, “Anti-diabetic Properties of Calcium Channel Blockers: Inhibition Effects on Aldose Reductase Enzyme Activity,” *Appl. Biochem. Biotechnol.*, vol. 189, no. 1, pp. 318–329, Sep. 2019, doi: 10.1007/s12010-019-03009-x.
- [19] Y. Demir, M. Işık, İ. Gülçin, and Ş. Beydemir, “Phenolic compounds inhibit the aldose reductase enzyme from the sheep kidney,” *J. Biochem. Mol. Toxicol.*, vol. 31, no. 9, p. e21936, Sep. 2017, doi: 10.1002/jbt.21935.
- [20] F. S. Tokalı *et al.*, “Synthesis, biological evaluation, and in silico study of novel library sulfonates containing quinazolin-4($<sc>3 H</sc>$)-one derivatives as potential aldose reductase inhibitors,” *Drug Dev. Res.*, Sep. 2021, doi: 10.1002/ddr.21887.
- [21] N. Trueblood and R. Ramasamy, “Aldose reductase inhibition improves altered glucose metabolism of isolated diabetic rat hearts,” *Am. J. Physiol. Circ. Physiol.*, vol. 275, no. 1, pp. H75–H83, Jul. 1998, doi: 10.1152/ajpheart.1998.275.1.H75.
- [22] H. Liu *et al.*, “Genetic deficiency of aldose reductase counteracts the development of diabetic nephropathy in C57BL/6 mice,” *Diabetologia*, vol. 54, no. 5, pp. 1242–1251, May 2011, doi: 10.1007/s00125-011-2045-4.
- [23] J. Tang, Y. Du, J. M. Petrush, N. Sheibani, and T. S. Kern, “Deletion of Aldose Reductase from Mice Inhibits Diabetes-Induced Retinal Capillary Degeneration and Superoxide Generation,” *PLoS One*, vol. 8, no. 4, p. e62081, Apr. 2013, doi: 10.1371/journal.pone.0062081.
- [24] B. Şengül and Ş. Beydemir, “The interactions of cephalosporins on polyol pathway enzymes from sheep kidney,” *Arch. Physiol. Biochem.*, vol. 124, no. 1, pp. 35–44, Jan. 2018, doi: 10.1080/13813455.2017.1358749.
- [25] M. J. Cerelli, D. L. Curtis, J. P. Dunn, P. H. Nelson, T. M. Peak, and L. D. Waterbury, “Antiinflammatory and aldose reductase inhibitory activity of some tricyclic arylacetic acids,” *J. Med. Chem.*, vol. 29, no. 11, pp. 2347–2351, Nov. 1986, doi: 10.1021/jm00161a033.
- [26] I. N. Korkmaz, “2-Amino thiazole derivatives as inhibitors of some metabolic enzymes: An in vitro and in silico study,” *Biotechnol. Appl. Biochem.*, Jul. 2022, doi: 10.1002/bab.2388.
- [27] I. N. KORKMAZ, “In Vitro Inhibition Effects of 2-Amino Thiazole Derivatives on Lactoperoxidase Enzyme Activity,” *Cumhur. Sci. J.*, vol. 43, no. 1, pp. 33–37, Mar. 2022, doi: 10.17776/csj.1017247.
- [28] H. Steuber, M. Zentgraf, C. Gerlach, C. A. Sottriffer, A. Heine, and G. Klebe, “Expect the Unexpected or Caveat for Drug Designers: Multiple Structure Determinations Using Aldose Reductase Crystals Treated under Varying Soaking and Co-crystallisation Conditions,” *J. Mol. Biol.*, vol. 363, no. 1, pp. 174–187, Oct. 2006, doi: 10.1016/j.jmb.2006.08.011.
- [29] G. Madhavi Sastry, M. Adzhigirey, T. Day, R. Annabhimoju, and W. Sherman, “Protein and ligand preparation: parameters, protocols, and influence on virtual screening enrichments,” *J. Comput. Aided. Mol. Des.*, vol. 27, no. 3, pp. 221–234, Mar. 2013, doi: 10.1007/s10822-013-9644-8.
- [30] Schrödinger, “No Title,” vol. 3, 2020.
- [31] R. A. Friesner *et al.*, “Glide: A New Approach for Rapid, Accurate Docking and Scoring. 1. Method and Assessment of Docking Accuracy,” *J. Med. Chem.*, vol. 47, no. 7, pp. 1739–1749, Mar. 2004, doi: 10.1021/jm0306430.
- [32] E. Yuriev, M. Agostino, and P. A. Ramsland, “Challenges and advances in computational docking: 2009 in review,” *J. Mol. Recognit.*, vol. 24, no. 2, pp. 149–164, Mar. 2011, doi: 10.1002/jmr.1077.
- [33] D. Rakowitz, R. Maccari, R. Ottanà, and M. G. Vigorita, “In vitro aldose reductase inhibitory activity of 5-benzyl-2,4-thiazolidinediones,” *Bioorg. Med. Chem.*, vol. 14, no. 2, pp. 567–574, Jan. 2006, doi: 10.1016/j.bmc.2005.08.056.
- [34] B. F. Schrijvers, A. S. De Vriese, and A. Flyvbjerg, “From Hyperglycemia to Diabetic Kidney Disease: The Role of Metabolic, Hemodynamic, Intracellular Factors and Growth Factors/Cytokines,” *Endocr. Rev.*, vol. 25, no. 6, pp. 971–1010, Dec. 2004, doi: 10.1210/er.2003-0018.
- [35] C. Türkes, M. Arslan, Y. Demir, L. Çoçaj, A. R. Nixha, and Ş. Beydemir, “ $<sc>N</sc>$ -substituted $<sc>N</sc>$ -phthalazine sulfonamide derivatives as non-classical aldose reductase inhibitors,” *J. Mol. Recognit.*, vol. 35, no. 12, Dec. 2022, doi: 10.1002/jmr.2991.
- [36] M. Akdağ, A. B. Özçelik, Y. Demir, and Ş. Beydemir, “Design, synthesis, and aldose reductase

- inhibitory effect of some novel carboxylic acid derivatives bearing 2-substituted-6-aryloxy-pyridazinone moiety,” *J. Mol. Struct.*, vol. 1258, p. 132675, Jun. 2022, doi: 10.1016/j.molstruc.2022.132675.
- [37] Y. Demir *et al.*, “Determination of the inhibition profiles of pyrazolyl–thiazole derivatives against aldose reductase and α -glycosidase and molecular docking studies,” *Arch. Pharm. (Weinheim)*, vol. 353, no. 12, p. 2000118, Dec. 2020, doi: 10.1002/ardp.202000118.
- [38] Y. Demir and Z. Köksal, “Some sulfonamides as aldose reductase inhibitors: therapeutic approach in diabetes,” *Arch. Physiol. Biochem.*, vol. 128, no. 4, pp. 979–984, Jul. 2022, doi: 10.1080/13813455.2020.1742166.
- [39] B. Sever *et al.*, “A new series of 2,4-thiazolidinediones endowed with potent aldose reductase inhibitory activity,” *Open Chem.*, vol. 19, no. 1, pp. 347–357, Mar. 2021, doi: 10.1515/chem-2021-0032.
- [40] Y. Lei *et al.*, “Design of Benzothiazolone-Based Carboxylic Acid Aldose Reductase Inhibitors,” *ChemistrySelect*, vol. 6, no. 20, pp. 4874–4880, May 2021, doi: 10.1002/slct.202101443.
- [41] A. Imran *et al.*, “Development of coumarin-thiosemicarbazone hybrids as aldose reductase inhibitors: Biological assays, molecular docking, simulation studies and ADME evaluation,” *Bioorg. Chem.*, vol. 115, p. 105164, Oct. 2021, doi: 10.1016/j.bioorg.2021.105164.
- [42] M. Hlaváč *et al.*, “Novel substituted N-benzyl(oxotriazinoindole) inhibitors of aldose reductase exploiting ALR2 unoccupied interactive pocket,” *Bioorg. Med. Chem.*, vol. 29, p. 115885, Jan. 2021, doi: 10.1016/j.bmc.2020.115885.
- [43] M. Ceylan *et al.*, “Synthesis, carbonic anhydrase I and II isoenzymes inhibition properties, and antibacterial activities of novel tetralone-based 1,4-benzothiazepine derivatives,” *J. Biochem. Mol. Toxicol.*, vol. 31, no. 4, p. e21872, Apr. 2017, doi: 10.1002/jbt.21872.
- [44] Y. Temel and S. BAYINDIR, “The Synthesis of Thiosemicarbazone-Based Aza-Ylides as Inhibitors of Rat Erythrocyte Glucose 6-Phosphate Dehydrogenase Enzyme,” *J. Inst. Sci. Technol.*, pp. 1503–1512, Sep. 2019, doi: 10.21597/jist.518012.
- [45] P. Alexiou, K. Pegklidou, M. Chatzopoulou, I. Nicolaou, and V. Demopoulos, “Aldose Reductase Enzyme and its Implication to Major Health Problems of the 21st Century,” *Curr. Med. Chem.*, vol. 16, no. 6, pp. 734–752, Feb. 2009, doi: 10.2174/092986709787458362.
- [46] J. Sangshetti, R. Chouthe, N. Sakle, I. Gonjari, and D. Shinde, “Aldose Reductase: A Multi-disease Target,” *Curr. Enzym. Inhib.*, vol. 10, no. 1, pp. 2–12, Oct. 2013, doi: 10.2174/15734080113096660007.
- [47] M. G. Salem, Y. M. Abdel Aziz, M. Elewa, M. S. Nafie, H. A. Elshihawy, and M. M. Said, “Synthesis, molecular modeling, selective aldose reductase inhibition and hypoglycemic activity of novel meglitinides,” *Bioorg. Chem.*, vol. 111, p. 104909, Jun. 2021, doi: 10.1016/j.bioorg.2021.104909.